

The Haemodynamics of Aneurysms:

A Spectral Element Analysis of the Effects of
Wall Stiffness

by

Nicholas Boustead

A thesis submitted to Monash University
for the degree of
Doctor of Philosophy

November 2012

Department of Mechanical and Aerospace Engineering
Monash University

Copyright notices

Under the Copyright Act 1968, this thesis must be used only under the normal conditions of scholarly fair dealing. In particular no results or conclusions should be extracted from it, nor should it be copied or closely paraphrased in whole or in part without the written consent of the author. Proper written acknowledgement should be made for any assistance obtained from this thesis.

I certify that I have made all reasonable efforts to secure copyright permissions for third-party content included in this thesis and have not knowingly added copyright content to my work without the owner's permission.

For Mum and Dad

Statement of Originality

This thesis contains no material that has been accepted for the award of a degree or diploma in this or any other university. To the best of the candidate's knowledge and belief, this thesis contains no material previously published or written by another person except where due reference is made in the text of this thesis.

Nicholas Boustead

<30/11/2012>

Abstract

The prevalence of abdominal aortic aneurysms is increasing with an ageing population. Aneurysms present a major health risk; in the event of aneurysm rupture, patients exhibit a mortality rate of 70-95% (Lindholt *et al.* 2005). Treatment of aneurysms involves invasive surgery, which carries an inherent risk, therefore it is preferable to intervene only when the aneurysm is close to rupture. Currently, the aneurysm initiation, growth and rupture mechanisms are not fully understood and accurate predictions of aneurysm growth-rate and rupture time cannot be made.

Research in this field has identified haemodynamic stimuli as the principal factor in aneurysm growth. As such, in-depth fluid-dynamic investigations can contribute greatly to developing appropriate models for patient prognosis and treatment. Previous investigations into aneurysm haemodynamics have largely been focused on blood flows with rigid-wall dynamics. To realistically model the flow, a moving boundary condition must be applied to account for the elasticity of the aneurysm wall.

A fluid-structure interaction was studied in the context of abdominal aortic aneurysms. The effects of an elastic wall were modelled using a numerical technique. To this end, a new coupling scheme is proposed based around an Arbitrary Lagrangian–Eulerian (ALE) algorithm. The monolithic ALE solver uses a modified iterative over unequal time step coupling routine. The use of an ALE algorithm for modelling aneurysm flows maximises the accuracy of flow field data in the near-wall region where the haemodynamic environment is most pertinent.

The biological material that comprises the artery wall is highly complex in nature. To accurately model the wall response, the wall is modelled as a multi-layered, hyper-elastic and heterogeneous material. A novel time stepping algorithm was developed and tested to model the wall response in the aneurysm. Spectral elements were used for the spatial discretisation while a backward differencing time stepping scheme was proposed for the temporal evolution. A two-step operator splitting scheme was proposed in order to implicitly solve for the displacement at the next time step. This algorithm is capable of modelling both the inertial and non-linear response of the wall, which is important in the context of biological applications.

Once formulated, two fluid-structure interaction studies were conducted. The first investigated the effects of heterogeneous wall properties, such as those formed around

lesions and calcification, on the haemodynamics in arteries. It was found that previous models based on a rigid-wall assumption misrepresent the flow conditions in aneurysms.

Furthermore, it was shown that local variations in wall elasticity can affect the wall shear stress environment both locally and downstream of the lesion or calcification. Weakening of the aneurysm wall was shown to increase the wall shear stress downstream. This occurred as the greater wall motion led to higher variations in flow rate.

In terms of the local effects, local variations in wall stiffness led to additional variations in aneurysm geometry and wall velocity. These changes led to a local change in boundary layer thickness which in turn affected the local wall shear stress distribution. In cases when the wall was weakened the wall shear stress decreased locally. Conversely the stiffer wall case corresponded to an increase in local wall shear stress.

Finally an investigation into the effect of wall stiffness on established aneurysm geometries was conducted. Using an elastic-wall model, the wall motion was shown to cause significant flow reversal in the boundary layer. As a result, in addition to the vortex ring shed from the proximal neck, a distal vortex ring formed. The proximity of these vortices to the aneurysm wall affects the shear layer at the wall and consequently the wall shear stresses.

In cases where there was large motion, the shear layer is drawn into a secondary distal vortex ring. At intermediate levels of wall motion, the formation of this secondary distal vortex ring is suppressed. The presence of the primary distal vortex ring protects the wall from the impact of the strong proximal vortex ring.

Local variations in wall stiffness were investigated at three locations in the aneurysm bulge. All weakened wall cases exhibited similar changes in wall dynamics compared to the uniformly stiff case. However, it has been shown that a weakened region upstream of the distal neck provided the greatest change in wall shear stress distribution. The case of a weakened central region represents the least favourable haemodynamic conditions for healthy endothelial wall function. In terms of the stiffened cases, the least protective distribution was the stiffening at the distal neck. These results indicate that aneurysms that feature a weakened wall region upstream of the distal neck present the greatest risk of rupture.

Acknowledgements

For their unrelenting guidance and support throughout my candidature, I would like to thank my supervisors Dr Kris Ryan and Dr Gregory J Sheard. On countless occasions when I found myself in the depths of despair, I could always count on one of you sitting next to me guiding me back to the path.

I am grateful to the Department of Mechanical and Aerospace Engineering, Monash University, for providing the work environment and resources necessary for the completion of this study. Furthermore, I wish to acknowledge the Monash e-Research Centre (MeRC), for granting access to their high performance computing facility. I also wish to express my gratitude for the financial backing provided through an Australian Post-graduate Award (APA) scholarship, and briefly, a Monash e-Research Centre early adopters scholarship.

To Chris, Sarah, Tim and the rest of my fellow postgraduate students: Thank you for the intimidating research discussions which always drove me to try harder, for the good company at lunch times that provided some relief, and for the sympathetic ears when things weren't what I wanted them to be. I wish you all the very best in your future endeavours.

I would also like to thank my family, Mum, Dad, Matthew and Helen. Regardless of the choices I make they offer nothing but love, guidance and support. I always have someone to look up to, someone to feel comfortable with and someone to show me how to have fun.

Finally, I must acknowledge those many friends who have stuck with me throughout my studies. Joel, Marty, Lachlan, Michael, David, Paul and Tom have provided countless hours of fun and relaxation; Eloise and Hannah who plied me with chocolate and lunch time retreats; James for his unwavering interest in my other pursuits; and of course Karryn whose levels of understanding extend beyond reasonable.

Nomenclature

A list of nomenclature used throughout the thesis is included here. Mathematical symbols are presented, followed by Greek alphabet nomenclature and English alphabet nomenclature.

Symbol	Description
\S	Thesis section
\int	Integration
∇	Vector gradient operator (grad)
∇^2	Del squared (or div-grad) operator, also known as the Laplacian
$(\cdot)^T$	The transpose of a matrix
(\cdot)	Matrix inner product
$(\cdot)^{-1}$	The inverse of a matrix
$tr(\cdot)$	The trace of a tensor
\circ	The tensor composition operator
\mathbf{I}	The identity matrix
$\frac{D}{Dt}$	The total time derivative (material derivative)
i	The imaginary number
τ	Shear stress
μ	Classical fluid viscosity
ν	Kinematic fluid viscosity
χ	Position vector in ALE referential coordinates
γ_T	The shear rate tensor for a fluid
γ_s	The shear rate scalar for a fluid
ν	The kinematic viscosity
ρ	Density
ω	Angular frequency

Continued on the next page.

Continued from previous page.

Symbol	Description
α	The Womersley number
Ω	A generic domain of interest (not necessarily an entire body)
$\partial\Omega$	Boundary of the domain Ω
Ω^e	Elemental sub-domain of the domain Ω
Ω^{st}	Standard element Ω
ϕ	The deformation mapping from material to spatial coordinates
Φ	The mapping from referential to spatial coordinates
Ψ	The mapping from spatial to referential coordinates
ε	The true strain also known as the infinitesimal strain in small strain approximation
ε_G	The Green strain
γ_{ij}	The shear strain in the i - j plane
ε_{log}	The logarithmic strain tensor
λ	The stretch ratio
ε	The infinitesimal strain tensor
σ	Stress
λ_L	A Lamé coefficient
μ_L	A Lamé coefficient
ν	Poisson's ratio
Υ	Is a generic extensive quantity of the Schottky system
\prod^Υ	Schottky system source term
\sum^Υ	Schottky system supply term
\mathbf{J}^Υ	Schottky system flux term
Γ	Path along which work is done
α_i	Finite differencing coefficient for $n - i$ time step
κ	Finite differencing coefficient for $n + 1$ time step
β_i	Polynomial extrapolation coefficient for $n - i$ time step
ω	The vorticity vector
κ_s	Solid solver finite differencing coefficient for $n + 1$ time step
α_i^s	Solid solver finite differencing coefficient for $n - i$ time step

Continued on the next page.

Continued from previous page.

Symbol	Description
Φ_i	Set of trial functions in Rayleigh Ritz problem
ϕ_i	Set of local element trial functions
χ	Map from standard element coordinates to elemental coordinates
ξ	Standard element coordinate
Λ	The diagonal matrix
$\dot{\epsilon}$	The strain rate
ς	Courant condition
δ	Boundary layer thickness
h	Characteristic length of elements in h -type finite element solvers
p	Polynomial order of spectral solver
R_X	Lagrangian coordinate system
R_x	Eulerian coordinate system
R_χ	ALE referential coordinate system
\mathbf{x}	Position vector in spatial coordinates
\mathbf{X}	Position vector in material coordinates
\mathbf{u}	Displacement vector in spatial coordinates
\mathbf{U}	Displacement vector in material coordinates
\mathbf{v}	The velocity vector in spatial coordinates
\mathbf{V}	The velocity vector in material coordinates
\mathbf{a}	The acceleration vector in spatial coordinates
\mathbf{A}	The acceleration vector in material coordinates
x_i	The i^{th} component of position \mathbf{x} in spatial coordinates
X_i	The i^{th} component of position \mathbf{X} in material coordinates
u_i	The i^{th} component of displacement \mathbf{u} in spatial coordinates
U_i	The i^{th} component of displacement \mathbf{U} in material coordinates
v_i	The i^{th} component of velocity \mathbf{v} in spatial coordinates
V_i	The i^{th} component of velocity \mathbf{V} in material coordinates
a_i	The i^{th} component of acceleration \mathbf{a} in spatial coordinates

Continued on the next page.

Continued from previous page.

Symbol	Description
A_i	The i^{th} component of acceleration \mathbf{A} in material coordinates
\mathcal{V}	Volume
$d\mathcal{V}$	Infinitesimal volume
Re	The Reynolds number
V_m	The mean velocity of a fluid
D	Characteristic length scale, Maximum diameter of aneurysm bulge
Q	The volumetric efflux rate of distilled water from a tube
ΔP	Pressure differential
L	Length
d	Pipe diameter
K'	Poiseuille's constant
R	The maximum radius of a pipe Residual of finite approximation
r	Radial position
A	Amplitude Area
f	Frequency
\mathbf{J}_0	A Bessel function
t	Time
P	Pressure, A generic material particle
WSS_{mean}	Mean wall shear stress
$WSSG$	Wall shear stress gradient
OSI	Oscillating shear index
\mathcal{B}	An arbitrary continuous body
\mathcal{S}	The surface of the body \mathcal{B}
\mathbb{R}	The set of Real numbers
\mathbf{F}	The deformation gradient
J	The Jacobian

Continued on the next page.

Continued from previous page.

Symbol	Description
$\bar{\epsilon}$	The engineering strain
ℓ	The new length of the fibre
\mathbf{C}	The right Cauchy-Green strain tensor
\mathbf{b}	The left Cauchy-Green strain tensor
\mathbf{E}	The Green-Lagrange strain tensor
\mathbf{H}	Hencky strain tensor
$\bar{\mathbf{F}}$	Total force
\bar{F}_n	The normal component of force
\bar{F}_t	The tangential component of force
$\bar{\mathbf{B}}$	The body forces in a material reference frame
$\bar{\mathbf{b}}$	The body forces in a spatial reference frame
$\boldsymbol{\sigma}$	The Cauchy stress tensor
\mathbf{P}	The First Piola-Kirchhoff stress tensor
\mathbf{S}	The Second Piola-Kirchhoff stress tensor
\bar{E}	The total energy
E	The Youngs modulus
E_m	The Youngs modulus of the medial layer
E_i	The Youngs modulus of the intimal layer
E_a	The Youngs modulus of the adventitia layer
E_{mean}	The average Youngs modulus of the arterial wall
t_{total}	The total wall thickness
t_m	The thickness of the medial layer
t_i	The thickness of the intimal layer
t_a	The thickness of the adventitia layer
G	Shear modulus
m	Mass
$\bar{\mathbf{p}}$	The linear momentum
W	Strain energy density
I^C	An invariant of the tensor C

Continued on the next page.

Continued from previous page.

Symbol	Description
$\hat{\mathbf{v}}$	Mesh velocity
$\hat{\mathbf{L}}$	A Linear operator
\mathbf{w}	Particle velocity in the referential domain
\mathbf{c}	Convective velocity
$\hat{\mathbf{L}}$	A linear operator
\hat{L}_m	The m^{th} linear component of a Linear operator
$(\cdot)^n$	Time step identifier
J_e	The order of integration (explicit)
J_i	The order of integration (implicit)
J_p	The order of integration (pressure boundary condition)
J_s	The order of integration (solid solver)
$\hat{\mathbf{N}}$	A nonlinear advection operator
$\hat{\mathbf{v}}$	An intermediate velocity field
$\hat{\mathbf{U}}$	An intermediate displacement field
$\hat{\hat{\mathbf{v}}}$	An intermediate velocity field
$\hat{\hat{\mathbf{U}}}$	An intermediate displacement field
\mathbf{n}	The unit normal vector
\mathbf{t}	The unit tangent vector
\mathcal{F}	Quadratic functional
\hat{u}_i	Set of trial functions coefficients in Rayleigh Ritz problem
w	The test (or weight) function
N_{dof}	The degrees of freedom in system
N^{el}	Number of elements in solution domain Ω
u^δ	The approximate solution
g_D	Constants for Dirichlet boundary conditions
g_N	Constants for Neumann boundary conditions
$u^{\mathcal{H}}$	The homogeneous boundary contributions
$u^{\mathcal{D}}$	The Dirichlet boundary contributions
\mathcal{A}	Local to global assembly matrix

Continued on the next page.

Continued from previous page.

Symbol	Description
h_p	Lagrange polynomial
\mathbf{M}	The mass matrix
\mathcal{J}	Interpolant of an integration
L_P	Is the Legendre polynomials or order P
L'_P	Derivative of the Legendre polynomials of order P
\hat{P}	The Jacobi polynomials
Q	The number of quadrature points
\mathbf{W}	The weight matrix
\mathbf{D}	The differentiation matrix
L_2	The L_2 norm of a vector field
\mathbb{R}	The set of real numbers

Contents

Introduction	1
Arbitrary Lagrangian–Eulerian (ALE) modeling	2
Spectral- <i>hp</i> element methods	4
Thesis structure	6
1 A review of the literature	7
1.1 Vascular structure of healthy aorta	7
1.2 Haemodynamics of blood flow	9
1.3 Aneurysm sites	12
1.4 Aneurysm evolution	13
1.4.1 Initiation	13
1.4.2 Aneurysm growth	15
1.5 Methods of investigation	17
1.5.1 Experimental	17
1.5.2 Computational	18
1.5.3 Compliant models	19
1.5.4 Fluid-Solid-Growth (FSG)	21
1.6 Arterial flow investigations	22
1.6.1 Flow in a straight pipe	22
1.6.2 Flow in flexible vessels	26
1.6.3 Haemodynamics of aneurysm geometries	28
1.6.3.1 Rigid-wall models	28
1.6.3.2 Compliant-wall models	33
1.6.3.3 Effect of wall mechanics on FSI	36
1.6.3.4 Further medical complications: Calcification and thrombus	39
1.7 Restrictions of previous work	40
1.8 Research aims	43
1.8.1 Developing a new method for investigating FSI in aneurysm	44
1.8.2 Investigation: Heterogeneous wall stiffness effects on established aneurysms	44

1.8.3	Investigation: The effect of heterogeneous wall stiffness on aneurysm initiation	46
1.9	Closure	46
2	A review of continuum mechanics	49
2.1	Introduction to continuum mechanics	49
2.2	Kinematics of deformation	50
2.2.1	Kinematics of local deformations	54
2.3	Strain measures	58
2.3.1	Tensor representations of strain measures	60
2.4	Stress measures	62
2.5	Balance laws	64
2.5.1	Conservation of mass	65
2.5.2	Conservation of momentum	66
2.5.3	General balance equations	67
2.6	Constitutive Equations	70
2.6.1	Strain energy density, W	71
2.6.2	Hookean materials	71
2.6.3	Neo-Hookean materials	74
2.6.4	Fluids	75
2.7	Closure	77
3	The arbitrary Lagrangian–Eulerian method	79
3.1	Introduction	79
3.2	Lagrangian and Eulerian viewpoints	82
3.2.1	Lagrangian	82
3.2.2	Eulerian	84
3.3	ALE referential frame	84
3.4	Fundamental ALE equations	86
3.4.1	Time derivatives	87
3.4.2	Conservation equations in the ALE formulation	89
3.5	ALE algorithms for FSI	90
3.5.1	ALE time marching algorithm	95
3.5.1.1	Coupling: The information flow	95
3.5.1.2	Mesh movement scheme	99
3.6	Closure	101
4	Numerical methods for fluids and solids	103
4.1	Introduction	103
4.2	Time stepping algorithm	105
4.2.1	Operator splitting schemes	105

4.2.2	Time evolution of the Navier–Stokes equations	106
4.2.3	Time evolution of the solid mechanics equations	109
4.2.3.1	Time evolution of a Hookean solid	109
4.2.3.2	Time evolution of a neo-Hookean solid	110
4.3	Fundamental concepts in one-dimension	112
4.3.1	The method of weighted residuals	113
4.3.2	The Galerkin method	114
4.4	Spatial discretisation scheme	116
4.4.1	Forming the discrete system h -type decomposition	117
4.4.2	Interpolating within an element: The p -type decomposition . . .	121
4.4.2.1	Gauss–Legendre–Lobatto quadrature	122
4.4.3	Numerical integration	124
4.4.4	Differentiation	126
4.5	Forming global operators	127
4.5.1	The Jacobian	127
4.5.2	Mass matrix, \mathbf{W}	128
4.5.3	Differentiation matrix, \mathbf{D}	129
4.5.4	Forming higher-order operators	130
4.5.5	The surface integral	130
4.6	Static condensation	133
4.6.1	The Schur complement, \mathbf{M}_{sc}	134
4.7	Closure	136
5	The neo-Hookean solver	139
5.1	Introduction	139
5.2	Splitting the governing equations	140
5.3	Sub-step 1	141
5.4	Sub-step 2	144
5.5	Closure	146
6	Validation	149
6.1	Introduction	149
6.2	Hookean solver	150
6.3	Neo-Hookean solver	152
6.4	Arbitrary Lagrangian–Eulerian algorithm	155
6.4.1	Oscillating cylinder	155
6.4.2	Pressure driven bulging membrane	158
6.4.3	Flow in a lid driven cavity with a membrane	162
6.5	Closure	167

7	Parameter space	169
7.1	Introduction	169
7.2	Geometry	169
7.2.1	Healthy aorta	170
7.2.2	Aneurysm	171
7.3	Fluid parameters	174
7.3.1	Fluid properties	174
7.3.2	Boundary conditions	174
7.3.2.1	FSI interface boundary conditions	178
7.3.3	Flow properties	178
7.4	Solid parameters	178
7.4.1	Wall thickness	180
7.4.2	Wall stiffness	182
7.4.2.1	Layer stiffness	183
7.4.3	Wall assumptions	185
7.4.4	Solid boundary conditions	186
7.5	Summary	187
8	Investigation 1: Aneurysm initiation	189
8.1	Introduction	189
8.2	Geometry	191
8.2.1	Fluid properties and boundary conditions	192
8.2.2	Solid properties and boundary conditions	195
8.3	Solution validation	196
8.3.1	Mesh optimisation	196
8.3.2	Domain size	203
8.3.2.1	Upstream	203
8.3.2.2	Downstream	205
8.3.3	h_2 -type refinement	206
8.3.4	Solid domain p -type refinement	207
8.3.5	Fluid-solid coupling p -type refinement	210
8.4	Temporal resolution	211
8.4.1	Time step	212
8.4.2	Time period	213
8.5	Results	216
8.5.1	Flow in a rigid pipe	216
8.5.1.1	Analytical solution	217
8.5.2	Flow in a healthy artery	220
8.5.3	Flow dynamics with localised stiffness variations	224
8.5.4	Wall shear stress in a perfectly rigid aorta	233

8.5.5	Wall shear stress in an elastic aorta	235
8.5.5.1	Analytical approach	235
8.5.5.2	Simulated wall shear stresses	243
8.5.6	Effects of stiffened band thickness	252
8.5.7	Flow in an expanded pipe with a rigid-wall	257
8.6	Closure	260
9	Investigation 2: Haemodynamics and wall shear stress in an established aneurysm	265
9.1	Introduction	265
9.2	Geometry	266
9.2.1	Fluid and solid properties and boundary conditions	267
9.3	Solution validation	269
9.3.1	Mesh optimisation and p -type refinement	270
9.3.2	Domain size	277
9.3.2.1	Upstream	278
9.3.2.2	Downstream	279
9.3.3	h_z -type refinement	281
9.3.4	Solid domain p -type refinement	282
9.3.5	Fluid-solid coupling p -type refinement	284
9.4	Temporal resolution	285
9.4.1	Time step	286
9.4.2	Time period	287
9.5	Results	290
9.5.1	Flow in a rigid-walled aneurysm	290
9.5.2	Flow conditions with a healthy arterial wall stiffness	294
9.5.3	The effect of wall elasticity on wall shear stress in an aneurysm .	301
9.5.4	The effect of heterogeneous wall properties	309
9.5.4.1	Proximal region	310
9.5.4.2	Central region	318
9.5.4.3	Distal region	325
9.5.5	Comparison of heterogeneous wall stiffness scenarios	332
9.5.6	Effects of the perianeurysmal environment	335
9.6	Closure	340
10	Conclusions	345
10.1	FSI algorithm	346
10.2	Aneurysm initiation	347
10.3	Haemodynamics in established aneurysms	349
10.4	Directions for future work	351

Appendices	373
A Wall shear stress	375

Introduction

In the context of an ageing population the incidence of aneurysm has risen greatly, with the prevalence of Abdominal Aortic Aneurysms (AAAs) alone reaching 8.8% in people above 65 (Newman *et al.* 2001). In 44% of cases, the rupture of a cerebral aneurysm will cause death within 30 days, with many more leading to permanent injury (Olafsson *et al.* 1997). Due to the risks associated with invasive surgery, it is important to target treatment by identifying aneurysms that are most likely to rupture. However, this is made difficult by an inability to predict the growth rate and rupture time of an aneurysm.

Aneurysms may be categorised as one of two types, dependent on their geometry and location. Aneurysms may be fusiform or saccular, as depicted in figure I. Fusiform aneurysms are characterised by a uniform dilation of the vessel wall along a longitudinal section. Saccular aneurysms are spherical in shape and involve the localised ballooning of just a small section of the artery wall. The fusiform type is predominantly found in the abdominal aorta just above the iliac junction, but is also often located in the knee joint and with a lower prevalence, in the circle of Willis (Lasheras 2007; Sforza *et al.* 2009). Saccular aneurysms are principally found in the circle of Willis, such aneurysms are often termed cerebral aneurysms owing to their location.

The development of arterial aneurysms results from a variety of factors: haemodynamics¹, wall biomechanics, mechanobiology², and the perianeurysmal environment³ (Sforza *et al.* 2009). Once formed, an aneurysm will undergo gradual expansion under the influence of repetitive pressure and shear stresses: these are exerted by the blood on the weakened arterial wall. Wall geometry, composition and strength continue to change throughout the expansion process, culminating in rupture when the wall is no

¹The study of the fluid motion of blood.

²The interaction between physical forces and changes in cell or tissue mechanics throughout the development of physiology, and disease.

³The surrounding tissue and supportive structures which support the exterior vessel wall of an aneurysm.

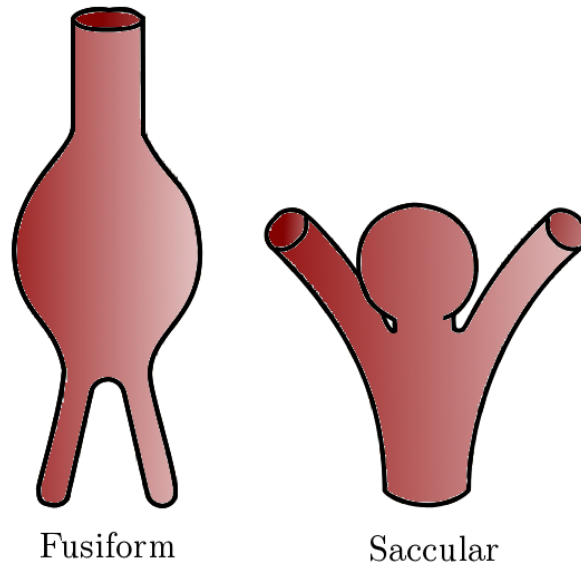


FIGURE I: Aneurysm classification based on geometry.

longer able to support the haemodynamic stresses exerted by the blood (Sforza *et al.* 2009).

Complete computer modelling of wall dynamics may increase our ability to predict this end-point. However, previous research in the area has not been able to show a sufficient peak pressure to cause rupture on a mechanical basis (Sforza *et al.* 2009). As such many researchers draw a comparison to the structural engineering problem of flow in a bulging pipe, where fatigue may be a factor (Lasheras 2007). Haemodynamic studies to date have focused on *in vitro* idealised models, and some Computational Fluid Dynamics modelling (CFD) of both idealised cases and patient-specific models. Due to the complexity of the artery-flow interaction and a lack of specific knowledge about changing wall properties, the majority of models employ a rigid boundary condition, Sforza *et al.* (2009) highlight this lack of knowledge about wall behaviour as a major restriction in this field of research.

Arbitrary Lagrangian–Eulerian (ALE) modeling

The numerical simulation of multi-dimensional problems in fluid and solid mechanics often results in large distortions of the continuum under consideration. Large or rapid distortions may introduce numerical errors into the computed solution.

In solid mechanics, Lagrangian algorithms are typically employed. Lagrangian al-

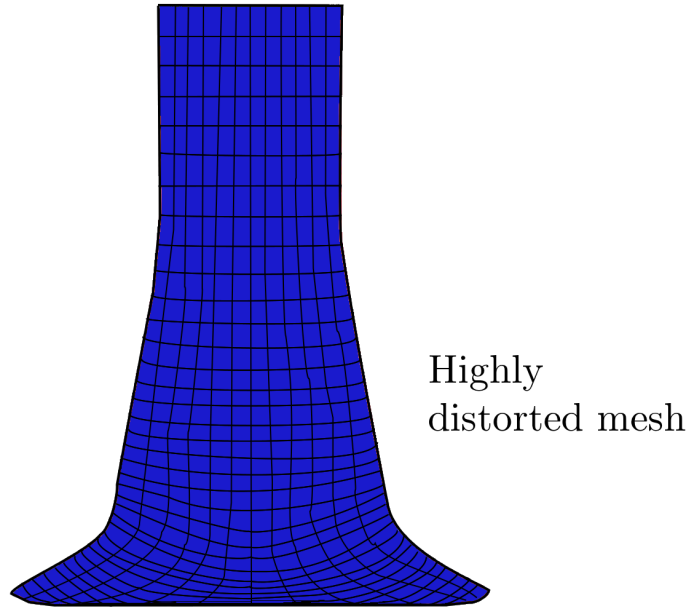


FIGURE II: A hyperelastic material impacting on a rigid wall (bottom of the mesh) with deformed Lagrangian mesh shown.

gorithms associate each individual computational mesh node with a single material particle throughout the motion. The Lagrangian description allows interfaces, such as the the artery wall-blood interface, to be easily and accurately tracked. However, its weakness lies in its inability to follow large distortions. See for example figure II in which a hyperelastic material impacts on a wall at high speed. The Lagrangian approach begins to break down along the impact surface between the material and the rigid-wall. The mesh in this region becomes highly distorted and will not yield accurate results.

In fluid mechanics, Eulerian algorithms are typically employed. Here the computational mesh is fixed in space and the continuum moves with respect to the grid. In the Eulerian description large deformations of the continuum can be handled with relative ease. This advantage is derived at the expense of accurate knowledge of the continuum interface locations. For example, if an artery wall moves to decrease the aneurysm volume, information about the location of the wall is compromised. Figure III demonstrates how such a movement introduces an uncertainty.

To overcome the shortcomings of the purely Lagrangian or Eulerian approaches a technique has been developed to combine the best features of both the Lagrangian

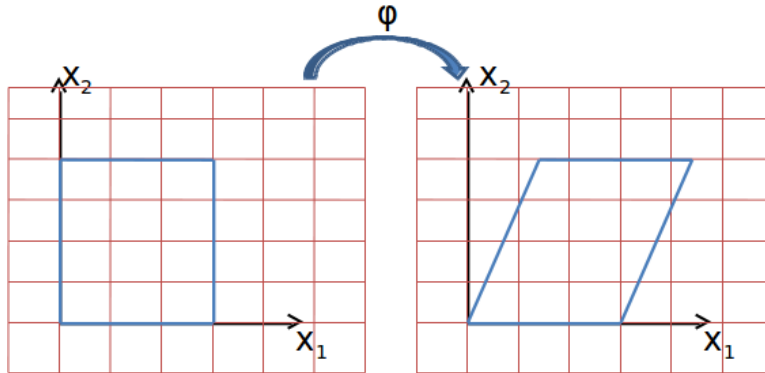


FIGURE III: An Eulerian mesh in undeformed state with interface defined by nodal positions and deformed state in which interface lies between nodal locations.

and Eulerian methods. This technique is known as the Arbitrary Lagrangian–Eulerian (ALE) description. In this formulation the nodes of the mesh may move with the continuum in a Lagrangian fashion or be held fixed in an Eulerian manner, or, they may behave in an arbitrary intermediate way to give a continuous rezoning capability. The advantages of this become clearer when considering the aforementioned block-impact example. Figure IV shows the result produced using an ALE mesh, the result is a much more regular element shape than was achieved with the Lagrangian description in figure II. Moving the interface or boundary nodes in a purely Lagrangian fashion allows the extents of the domain to be well defined. Meanwhile, the continuous rezoning capability of the ALE formulation maintains a regular grid for accurate computation. Further details of this can be found in chapter 3.

Spectral- hp element methods

The ALE method was initially developed by Noh (1963), Franck & Lazarus (1964), Trulio (1966), and Hirt *et al.* (1974) for finite element algorithms. Since then, a class of solvers known as spectral- hp element methods have been developed and successfully applied to fluid dynamic problems. First developed by Gottlieb & Orszag (1981) and Patera (1984), spectral- hp solvers combine the high geometric flexibility of finite element solvers with the high numerical efficiency and exponential spatial convergence characteristics of spectral solvers. Finite element solvers, of which spectral element solvers are a subset, may be categorized by their expansion bases as either h -type or p -type.

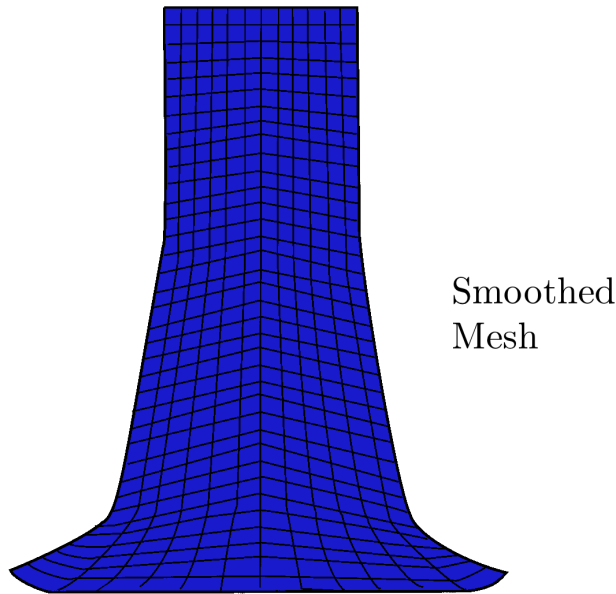


FIGURE IV: A hyperelastic material impacting on a rigid wall with deformed ALE mesh shown.

h -type solvers split the domain into a set of subdomains known as elements. The sum of the set of elements forms the entire solution domain. h -type finite element solvers use a fixed order polynomial in every element with convergence to the exact solution attained by reducing the element size. This type of extension allows high geometric flexibility.

p -type solvers use a fixed mesh which encompasses the entire solution domain. A polynomial of variable order, p , is used to approximate the solution across the entire domain, fitting through fixed mesh points. Convergence to the exact solution is achieved by increasing the polynomial order used to interpolate across the domain. This type of expansion allows rapid convergence for smooth problems, but is complicated in geometrically difficult domains. For the special case where the entire solution domain is modelled with only one element, then this kind of solver is a spectral method.

The spectral- hp element method, of which the algorithm developed in this thesis is a type, combines attributes of both extensions. While widely used in fluid dynamics, spectral- hp element methods have found limited use in solid mechanics problems. Furthermore, spectral- hp methods are rarely combined with ALE in order to solve fluid-structure interactions.

Thesis structure

While a statement of the hypotheses tested in this thesis and the justification for them is given in the literature review of chapter 1, an outline of the structure of this document is given here. First, the aforementioned literature review is presented. This review attempts to present the state of knowledge in the field of fluid-structure interactions in aneurysms, and to identify some of the key areas where knowledge is lacking. From these areas, hypotheses have been formed to guide the present study.

Chapter 2 outlines the physics behind continuum mechanics and derives the system of equations required to solve the fluid-structure interactions in aneurysms.

Having established the equations, chapter 3 goes on to describe the ALE method, how it is implemented in this body of work, and what information is communicated between each of the solver segments.

Building on the description of the respective continuum equations and the ALE algorithm, chapter 4 and 5, describe in detail the temporal discretisation scheme for the solid and fluid dynamics solvers and the spatial discretisation scheme associated with the spectral element method. This forms a numerical framework for the fluid-structure interaction algorithm.

Having described the new spectral element arbitrary Lagrangian–Eulerian algorithm in detail, chapter 6 presents a validation of each aspect of the solver, testing the consistency of each component of the solver as well as the sum of its parts.

Chapter 7 departs from the discussion of the numerical method developed in this thesis. It describes in detail the justification of the parameter space to be studied in the aneurysm investigations presented in chapters 8 and 9.

Chapter 8 presents the investigation into the effect of changing wall stiffness in a straight pipe. The motivation for this investigation is to determine if changes in wall stiffness may indicate the initiation of aneurysms.

In chapter 9 the fluid dynamics of established aneurysms is studied. The effects of heterogeneous wall stiffness is discussed in a fluid-structure interaction context. These results show the impact of the stiffened regions on aneurysm growth-rate.

Finally, the overall conclusions of the thesis are presented in chapter 10. These focus on the most important findings, and how the results obtained relate to the hypotheses posed in chapter 1.

Chapter 1

A review of the literature

The study of fluid-structure interactions in engineering systems is complicated, in and of itself, by the interaction of two continua each with their own distinct fundamental dynamics. The study of fluid-structure interactions in a biological system, such as an aneurysm, adds another level of complexity to the model. Throughout the sections to follow, the relevant biological and anatomical intricacies will be addressed and previous studies of flow through aneurysms with fixed walls and compliant walls will be reviewed in turn. Despite the limitations of the scope of the present study to idealistic fusiform geometries; a more complete overview of the haemodynamics for all geometries is considered.

1.1 Vascular structure of healthy aorta

Blood is periodically pumped by the heart into a complex network of elastic arteries that carry the oxygen and nutrient rich blood around the body to capillaries which irrigate muscle tissue. A complex arrangement of veins then return the blood to the heart. During each cardiac cycle the heart ejects 70 ml of blood at a pressure of 120 mmHg into the aorta where the mean pressure is 80 mmHg (in a resting patient) (Nichols & O'Rourke 1990).

The walls of the large arteries are comprised of three layers, the tunica intima, tunica media and tunica adventitia (see figure 1.1). The thickness and composition of each layer depends on multiple factors, including distance from the heart, geometry, age, and function of the particular artery. The intima layer is made up of a single layer of vascular endothelial cells¹ (VECs) that adhere to a basal laminar which covers

¹Vascular endothelial cells line the entire circulatory system. These cells have very distinct and unique functions that are paramount to vascular biology. These functions include fluid filtration, blood vessel tone, haemostasis (blood cell coagulation), nutrient recruitment, and hormone trafficking.

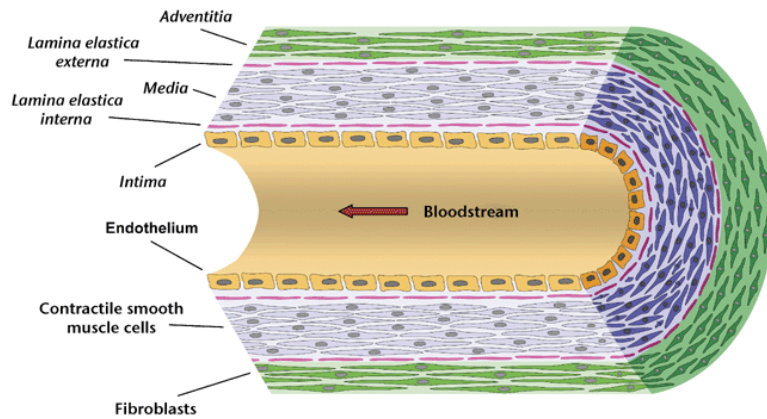


FIGURE 1.1: Structure of a medium sized muscular artery. Reproduced with the permission of Wiley and sons from Lorkowski & Cullen (2001).

a sub-endothelial layer composed of connective tissue, elastic fibrils, and collagenous bundles².

The median layer accounts for most of the mechanical properties of the wall and consists primarily of layers of smooth muscle cells³ (SMCs), a number of elastic sheets, a complex network of elastic fibrils, and bundles of collagenous fibres embedded in an extracellular matrix (ECM) (Lasheras 2007). The smooth muscle cells produces enzymes and proteins that control cellular migration and cell death in the arterial wall, which in turn control the walls elasticity (Lasheras 2007).

The tunica adventitia contributes little to the mechanical properties of the arterial wall. It is composed of collagen and its function is to anchor the blood vessel to nearby organs, lending stability.

Elastin fibres have a modulus of elasticity of 0.6 MPa (6×10^6 dynes/cm²) and can stretch in excess of 250% of their original length. Collagen fibres are much stiffer with a modulus of elasticity of 500 MPa (5×10^9 dynes/cm²), almost 1000 times larger than elastin (Dorbin 1978).

Vascular endothelial cells of the tunica media as well as blood cells (platelets and erythrocytes) are shear-sensitive (Lasheras 2007) . In particular, fluid shear forces from blood flows regulate many VEC activities through “mechanotransduction”⁴ (Davies *et al.* 1984; Traub & Berk 1998; Blackman *et al.* 2002). Flow shear effects endothelial

²Bundles of protein which make up part of the inter-cellular connective tissue.

³Smooth muscle is an involuntary non-striated muscle.

⁴Mechanotransduction refers to the mechanisms by which cells convert mechanical stimulus into chemical activity.

secretion of prostacyclin and nitric oxide, these act to inhibit platelet and leukocyte adhesion and aggregation and change the contractile tone (and hence elasticity) of SMCs (Ben Driss *et al.* 1997; Chiu *et al.* 2003, 2004). As such, the elasticity of the wall constantly changes through a remodelling process. It is believed biological factors coupled with a change in haemodynamic stimuli may destabilize the remodelling process (Lasheras 2007). Unfortunately, due to the short time scales over which the wall may adapt its material properties in response to haemodynamic stimuli (such as those found when exercising) a comprehensive model for the wall has not yet been developed. The longer-term remodelling that leads to the development of an aneurysm is also not fully understood. This forms a key stumbling block precluding the prediction of both expansion rate and risk of rupture of aneurysms (Lasheras 2007).

1.2 Haemodynamics of blood flow

It is clear that the haemodynamic conditions in the aorta are integral to healthy arterial function. Lasheras (2007) describes how the haemodynamic conditions can destabilize the wall remodelling process. This process, which ensures the health of the artery wall, involves an interaction between the biological particles that make up blood and the endothelial cells of the artery wall. Blood has a complex composition, it is comprised of large cells suspended in plasma rather than the small molecules that other fluids such as air or water consist of. This gives it some unique properties that are worth detailing here.

Blood is composed of approximately 55% plasma and 45% blood cells. Plasma consists of 90% water, 8% proteins, 1.1% organic substances and 0.9% inorganic salts. Immersed in the plasma are the blood cells; red blood cells (Erythrocytes) make up 93.4% of the blood cells, platelets (Thrombocytes) make up 6.2%, with the remaining 0.4% consisting of a variety of white blood cells (Leukocytes). Red blood cells deliver oxygen to the body while the white blood cells and platelets fight disease and deliver vital nutrients to the cells to ensure arterial health.

The composition of blood affects its fluid properties. In a Newtonian fluid, the local strain rate is proportional to the applied viscous stresses, the constant of proportionality is the dynamic viscosity of the fluid, μ . Physically this describes the resistance of the fluid to flow. An example of a fluid with a high viscosity is honey, which reacts quite slowly to pouring when compared to fluids with a low viscosity such as alcohol or

water. As the blood cells exist within the plasma, the viscosity of blood depends on the viscosity of the plasma. While plasma may be considered a Newtonian fluid, i.e. a fluid with a linear stress-strain relationship, blood in general cannot be due to the cellular interactions of the large scale blood cells. A Newtonian fluid is described by the stress strain relationship,

$$\tau = -\mu \frac{dv_i}{dx_i}, \quad (1.1)$$

where τ is the shear stress, μ is the viscosity and $\frac{dv_i}{dx_i}$ is the velocity gradient perpendicular to the direction of shear. A non-Newtonian fluid does not have a constant viscosity and so a viscosity for blood cannot be specified. Rodkiewicz *et al.* (1990) showed that if blood reaches a shear rate of approximately 100 s^{-1} the shear rate reaches a linear or Newtonian limit and a viscosity can be specified. At shear rates greater than 100 s^{-1} the viscosity of blood is approximately 5 times that of water at $(3 - 4) \times 10^{-3} \text{ Pa} \cdot \text{s}$. In the context of the present study Wootton & Ku (1999) found blood to behave largely as a Newtonian fluid in larger vessels. Furthermore, in Rodkiewicz *et al.* (1990) the non-Newtonian properties of arterial blood flow were considered, with variation from Newtonian flow being isolated to the centreline of arteries, away from the walls where the shear rate is high. The near-wall region where blood can be considered a Newtonian fluid is of principal interest to the present study.

The density of blood is 1060 kg/m^3 which is very close to that of water at 1000 kg/m^3 the extra density coming from the small amounts of protein and inorganic salts in the plasma and blood cells.

Subsequent sections (§ 1.6.3) discuss the importance of the Wall Shear Stress (WSS) parameter in maintaining healthy arterial wall function. Wall shear stress is commonly referred to as the shear stress normal to the artery wall. Shear stress is mathematically described in equation 1.1. Physically, at a boundary the no-slip condition requires that the fluid have zero velocity relative to the boundary. The fluid near the boundary can have a non-zero velocity, creating a velocity gradient at the wall. The shear stress is imparted onto the boundary as a result of the velocity gradient.

Given the difficulty in determining a fluid viscosity for blood due to its non-Newtonian nature, some studies (Tolouei *et al.* 2011; Butler *et al.* 2012) use shear rate rather than shear stress to measure the effect of shearing forces. These studies have typically focused on thrombotic geometries. The shear rate tensor is

$$\gamma_T = \nabla \mathbf{v} + (\nabla \mathbf{v})^T, \quad (1.2)$$

where the shear rate tensor describes the shear rate in each plane, \mathbf{v} is the velocity vector and ∇ is the gradient operator. The gradient field ($\nabla\mathbf{v}$) describes the rate at which the velocity changes at each point in any plane.

Most previous investigations using the shear rate have considered Poiseuille flow in which the maximum shear rate occurs at the wall. However, Nesbitt *et al.* (2009) and Tolouei *et al.* (2011) revealed flaws in this methodology; identifying that local variations in shear are significant within realistic geometries. Their studies indicate that in realistic flows, components of the velocity gradient in directions non-normal to the boundary may be of sufficient size as to have a significant effect. As such a better measure would be the shear rate scalar which accounts for the shear rate contributions in all planes at each position. In this way it acts as a measure of the total rather than maximum shear rate at a point. The shear rate scalar may be described by

$$\gamma_s = \sqrt{0.5 \times \gamma_T : \gamma_T} \quad (1.3)$$

where γ_T is the shear rate defined as a tensor and the $(:)$ operator denotes a matrix inner product.

Despite the advantages of shear rate and shear rate scalar in describing the shear at the wall, most studies use wall shear stress alone to describe the shear environment felt by the endothelial cells. In order to facilitate comparison of results with those published in previous investigations, wall shear stress will be used in this thesis. For simple flows such as those in a rigid walled pipe, equation 1.1 is sufficient to describe the shear stress at the wall. However, with a non-zero wall-normal velocity this is no longer the case. Instead a generalisation of the wall shear stress is required in order to fully describe the shear stress exerted at the wall. With a non-zero wall velocity the wall shear stress can be described by

$$\tau_{WSS} = 2\mu \begin{bmatrix} (\tau_{11} - \tau_{22})\underline{n}_{122} + (\tau_{11} - \tau_{33})\underline{n}_{133} + \\ \tau_{12}(\underline{n}_2 - 2\underline{n}_{211}) + \tau_{13}(\underline{n}_3 - 2\underline{n}_{311}) - 2\tau_{23}\underline{n}_{123} \\ (\tau_{22} - \tau_{11})\underline{n}_{211} + (\tau_{22} - \tau_{33})\underline{n}_{233} + \\ \tau_{12}(\underline{n}_1 - 2\underline{n}_{122}) + \tau_{23}(\underline{n}_3 - 2\underline{n}_{322}) - 2\tau_{13}\underline{n}_{123} \\ (\tau_{33} - \tau_{11})\underline{n}_{311} + (\tau_{33} - \tau_{22})\underline{n}_{322} + \\ \tau_{13}(\underline{n}_1 - 2\underline{n}_{133}) + \tau_{23}(\underline{n}_2 - 2\underline{n}_{233}) - 2\tau_{12}\underline{n}_{123} \end{bmatrix}, \quad (1.4)$$

where

$$\underline{n}_{ijk} = \underline{n}_i \underline{n}_j \underline{n}_k. \quad (1.5)$$

and τ_{ij} are the i^{th} and j^{th} component of the strain rate tensor.

Investigations that do not include these extra terms when calculating the wall shear stress may well underestimate the wall shear stress in the wall plane. Many investigations into elastic-walled aneurysms have reported a reduction in the peak wall shear stress achieved (Perktold & Rappitsch 1995; Dempere-Marco *et al.* 2006; Oubel *et al.* 2007). None of these papers indicate how they define the wall shear stress; failure to use the full three-dimensional form of the wall shear stress may partially explain the reduced wall shear stress observed in their investigations.

Equation 1.4 describes the wall shear stress in the plane normal to the wall. However, just as with shear rate and shear rate scalar this may not be the maximum shear stress at the wall. The tensor nature of shear stress implies there may exist a different plane in which the maximum wall shear stress could occur. This is certainly the case when a non-zero wall velocity exists. To calculate the maximum wall shear stress in any plane an eigenvalue problem can be solved. For a detailed discussion and derivation of the eigenvalue approach and the generalised wall shear stress equations the reader is referred to appendix A.

It is not clear from the literature whether it is the maximum shear stress (regardless of the shearing direction) that is physiologically relevant or whether it is simply the wall shear stress in the wall normal plane. Physiological studies of endothelial cell response do not indicate which definition of shear stress is critical. As such, the physiological merit of each shear stress definition cannot be determined. In order to facilitate an accurate comparison of the current work with previous investigations the generalised definition of wall shear stress (equation 1.4) is used herein.

1.3 Aneurysm sites

As discussed earlier aneurysms are primarily found in the abdominal aorta as fusiform AAAs or in the circle of Willis as saccular cerebral aneurysms. Anatomically these locations are quite distinct, though they do present some similarities in terms of localised flow conditions that may cause aneurysm formation. A non-uniform distribution of WSS at bifurcations and sharp curves corresponds to regions where aneurysms normally form (Sheard *et al.* 2007; Sforza *et al.* 2009). Fusiform aneurysms are mostly

found just upstream of bifurcations, most common in AAAs. Saccular aneurysms form at the apex of the bifurcation where there is a thin or absent elastic lamina and the median layer is absent leaving the wall weakened (figure I). Saccular aneurysms may also occur on side walls at large curvatures (Foutrakis *et al.* 1999). At these locations deviation from normal anatomy results in a redistribution of wall pressure and wall shear stress at branch points (Sforza *et al.* 2009).

A further confounding factor may be the pressure pulse which travels with the blood flow through the arterial wall. The pressure pulse is reflected at each branching point which then constructively interferes with the incoming pressure waves (Lasheras 2007).

1.4 Aneurysm evolution

1.4.1 Initiation

The precise initiation process of aneurysms is currently unknown. However, many physiological studies have identified a series of factors which contribute to aneurysm formation as well as a set of risk factors that enhance the risk of aneurysm formation. Risk factors include smoking, sex, alcohol, hypertension, atherosclerosis, disease or infection (e.g. syphilis) (Lasheras 2007; Sforza *et al.* 2009).

Atherosclerosis is no longer considered as important as sites of concentrated plaque rarely correlate with aneurysms location (Lasheras 2007). However, age is considered to be the greatest risk factor, with aneurysms being most prevalent in the elderly. Age makes arteries thicker and stiffer. The median layer thins and loses its orderly arrangement of elastin changing to a disordered “patchwork” of elastin grain. The elastin to collagen ratio becomes more collagenous which leads to a stiffening of the arterial wall (Lasheras 2007). A stiffer wall means an increase in speed of the pulse wave from 6.5 m/s in young patients to 11 m/s in patients over 66 yrs (Nichols & O’Rourke 1990). This may be connected to the location of aneurysms and their progression.

Histological studies have shown that in the early stages of aneurysm formation there is a degeneration of endothelial cells and internal elastic lamina. A thinning of the medial layer through apoptosis (programmed cell death) of smooth muscle cells is also evident (Stehbens 1963, 1989). Furthermore, disruptions in the remodelling process have been identified with increased levels of elastase (Chaytte & Lewis 1997) and matrix metalloproteinase (Bruno *et al.* 1998). This could lead to a weakening of the wall.

Nichols & O'Rourke (1990) suggest that fatigue through cyclic stresses causes the fracture of the load-bearing elastic sheets. Under the pulsatile haemodynamic forces, the polymerised structure of elastin sheets and fibres reorganises, causing them to fail at lower tensional stresses. The tearing of these sheets is associated with a loss in elastic recoil which may cause a permanent dilation of the vessel. The permanent stretching of the smooth muscle tissue is accompanied by a permanent remodelling process whereby collagen content in the muscular layer increases. The end result of this irreversible process is the creation of an aneurysm.

A genetic predisposition to endothelial degradation may also be a contributing factor in the onset of aneurysm formation. A Japanese study by Onda *et al.* (2001) found a genetic locus for cerebral aneurysms localised within or close to the elastin gene locus on chromosome 7. Furthermore, endothelial gene expression is related to wall shear stress. Therefore triggering of any genetic traits may be attributed to haemodynamic conditions.

Haemodynamic factors play a key role due to the capacity of endothelial cells to sense and react to wall shear stresses. Studies have shown that low wall shear stress and high oscillatory patterns of wall shear stress correlate with intimal wall thickening (Friedman *et al.* 1981; Ku *et al.* 1985; Dardik *et al.* 2005). A uniform shear stress field tends to stretch and align endothelial cells. Furthermore, studies on animals show an increase in WSS can fragment the internal elastic lamina or damage the endothelium (Sforza *et al.* 2009).

The current medical standard for predicting risk of aneurysm rupture is based on aneurysm diameter alone. A patient-specific study has previously demonstrated that maximum wall stress was 12% more specific and 13% more sensitive in predicting AAA rupture than maximum diameter (Fillinger *et al.* 2003). Sonesson *et al.* (1999) conducted an epidemiological study assessing the efficacy of using wall stiffness as a predictor of aneurysm rupture. Their study involved following 285 patients. They used an echo tracking instrument interfaced with a real-time ultrasound scanner to measure the peak systolic and diastolic deflections of the aneurysm wall. The deflections, combined with blood pressure measurements were used to give an indicator of wall stiffness. Sonesson *et al.* (1999) found that there was no statistically significant correlation between wall stiffness and incidence of rupture, nor could they find any statistically significant correlation with aneurysm diameter and incidence of rupture. These results

call into question the current practice for assessing aneurysm risk of rupture. While the results of Sonesson *et al.* (1999) do not indicate wall stiffness should provide a better risk indicator, they did not measure wall stiffness accurately and they did not correlate the effects of wall stiffness in a heterogeneous manner, such effects may alter the haemodynamics of the blood flow and affect the aneurysm growth-rate.

In summary, the primary cause is a coupling between changes in vessel structure and the induced change in haemodynamics (Lasheras 2007).

1.4.2 Aneurysm growth

After the formation of an aneurysm the haemodynamics within the bulbous structure are significantly different from that of a healthy artery. The new complex haemodynamic environment drives the continued growth of the aneurysm. Haemodynamic studies have not been able to show a sufficient peak pressure to cause rupture on a mechanical basis (Steiger *et al.* 1988). The yield stress of aneurysms is found to be slightly higher than the systolic peak stress. Aneurysm growth could be understood by a passive fatigue based yielding to blood pressure and reactive healing and thickening of the wall (Sforza *et al.* 2009).

Animal models suggest that increased wall shear stress can degenerate the vascular endothelium and smooth muscle cells (Kondo *et al.* 1997). Low wall stress and high oscillatory patterns of WSS cause intimal wall thickening in a disorganised way. If WSS is increased locally then it may cause local enlargement and consequently damage to the arterial wall (Sforza *et al.* 2009).

Sforza *et al.* (2009) summarise two theories on the continued growth of aneurysms based on an interaction between haemodynamics and wall mechanotransduction. In high flow theory, WSS elevation causes endothelial injury (Sheard *et al.* 2007), which initiates wall remodelling and possible degradation. A high WSS can cause over production of nitric oxide (NO) upon which the endothelium is dependent. This leads to a lower non-physiological arterial tone, which disturbs the equilibrium between blood pressure forces and internal wall forces and subsequently dilates the wall. The distension of the artery stretches collagen and elastin leading to a stiffening of the wall (Sforza *et al.* 2009). In low flow theory, localised blood flow stagnation causes a dysfunction of flow induced nitric oxide. This leads to a build up of red blood cells and an accumulation of leukocytes and platelets. The build up may cause intimal damage

which lets white blood cells and fibrin into the arterial wall and locally degrades the wall. A lower pressure threshold is then present, increasing the susceptibility to rupture of the aneurysm (Sforza *et al.* 2009).

For the case of fusiform aneurysms, regions of stagnant flow form. Stagnation of blood flow leads to the aggregation of red blood cells and the adhesion of platelets and leukocytes. The process is exacerbated by evolving endothelial injury which attracts these substances. This can lead to thromboses (Salsac 2005; Sheard *et al.* 2007; Lasheras 2007). Thrombus formation causes the destruction of the endothelial layer by hypoxia. After thrombus formation the blood is no longer in contact with the vessel wall (see figure 1.2), instead it is flowing through an internal lumen (Salsac 2005). This renders the shear-VEC layer interaction redundant in the growth of the aneurysm. Thus permanent remodelling may play a role, as the arterial wall distends and stiffens. The permanently stretched SMCs are progressively deprived of the cyclic stimulation required for synthesis of connective tissue and healthy proliferation (Lasheras 2007). Alternately inside the thrombus chemical and enzyme interactions may further damage the wall (Lasheras 2007). Di Martino *et al.* (1998) suggest that the presence of a thrombus may act as a cushioning or protective layer against extreme haemodynamic forces as wall thickness is uniform. In saccular cases the flow enters and forms one or two 3D vortices and this flow pattern persists into the diastolic phase. There is a constant flushing of blood and therefore no thrombus forms (Lasheras 2007).

Fluid dynamics may contribute to this field of study through a complete understanding of the haemodynamic stimuli. The capacity of endothelial cells to regulate wall activity based on wall shear stress makes it the most important haemodynamic parameter. WSS affects:

- Base set point of many genes via transcription regulation (Chien *et al.* 1998).
- Endothelial secretion of prostacyclin (a vasodilator which inhibits platelet adhesion), and Nitric Oxide which reduces leukocyte adhesion (Qiu & Tarbell 2000a).
- Endothelial cell permeability; high WSS damages endothelial cells (Fry 1968).
- Endothelial cell shape. In the presence of low WSS or oscillating WSS stimuli, endothelial cells become more round (Ku *et al.* 1985).
- Cell division rate. High Wall Shear Stress Gradient (WSSG) induces an increased

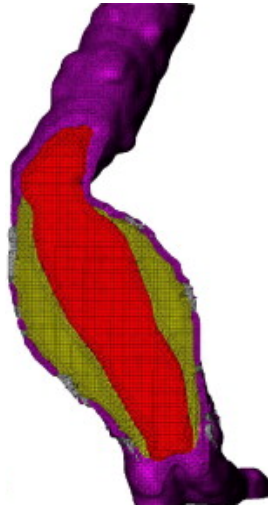


FIGURE 1.2: Fusiform aneurysm with intraluminal thrombus. The thrombus sits between the arterial wall and the blood preventing delivery of nutrients to endothelial cells. The purple region represents the arterial wall, the olive green section represents the thrombus, and the red region represents the blood flowing through the artery. Reproduced with the permission of Elsevier from Li *et al.* (2008).

net cell division rate (Davies *et al.* 1995; Nagel *et al.* 1999) and leads to a migration of cells away from these areas.

Other factors that may contribute to aneurysm growth include non-uniform haemodynamics and the perianeurysmal environment. Non-uniform haemodynamics trigger an increase in local wall permeability allowing cross wall mass transfer of low density lipoproteins (Buchanan *et al.* 1998), such proteins may be detrimental to the wall mechanics. The perianeurysmal environment is the structure surrounding the aneurysm. The perianeurysmal environment supports sections of the aneurysm. However, this is seldom uniform and therefore may lead to more complicated flow (Sforza *et al.* 2009). Such effects are seen in studies of asymmetric and patient specific models of aneurysms such as Shojima *et al.* (2004), Scotti *et al.* (2005), and Finol *et al.* (2003b).

1.5 Methods of investigation

1.5.1 Experimental

A variety of approaches have been employed to investigate haemodynamics in aneurysms. Experimental techniques may be categorised as either *in vitro* or in surgically created aneurysms (Sforza *et al.* 2009). These techniques take measurements using Doppler

Ultrasound or tagged image velocimetry and DPIV (Sheard *et al.* 2007).

Research using these techniques can be limited in their ability to resolve fluid forces such as shear near the walls. *In vitro* modelling is also restricted in that it enforces a rigid boundary condition on the aneurysm wall which is non-physical.

1.5.2 Computational

Computational modelling has also been performed (Di Martino *et al.* 2001; Shojima *et al.* 2004; Sforza *et al.* 2009; Sheard 2009). Computational fluid dynamic techniques have provided better resolution of wall shear stresses as well as better temporal resolution. Finite element methods have proven more popular (Di Martino *et al.* 2001; Shojima *et al.* 2004; Sforza *et al.* 2009) with spectral element codes (Sheard *et al.* 2007) and finite volume codes (Buchanan *et al.* 1998) yielding equivalent results.

CFD models may be categorized as either idealised or patient specific. Idealised models simplify the aneurysm geometry in order to systematically evaluate the effects of different parameters on the flow. Patient specific models (Di Martino *et al.* 2001; Shojima *et al.* 2004; Dempere-Marco *et al.* 2006; Sforza *et al.* 2009) are preferred by clinicians who may use the flows to make a judgement on the risk to patients.

Patient specific models use angiogram or CT scanned (Shojima *et al.* 2004) two-dimensional medical imagery and construct a three-dimensional model of the aneurysm. Dempere-Marco *et al.* (2006) describes a typical method used to extract the data to form a three-dimensional model that they used to measure the temporal distortion to the vessel wall. Image registration is employed across the 2D slices which establish correspondences between points in two different images. A 2D version of the non-rigid registration algorithm, based on free form deformations proposed by Rueckert *et al.* (1999) was applied by Dempere-Marco *et al.* (2006). By moving a set of control points originally distributed into a regular lattice, a smooth and continuous transformation is obtained that is subsequently used for deforming one image into the other. The control points are moved in order to maximize the similarity between the two images. For each series of sequential X-ray projection images, a set of landmarks can be manually delineated in the first frame, and subsequently propagated by using the transformations derived from the image registration procedure. The complete series was registered to the initial reference frame. A combination of blurring and sharpening operations, followed by a region growing segmentation and iso-surface extraction is finally used to create

the 3D model. Such methods for extracting wall motions and geometry are limited by the resolution of the medical imagery; experts must be employed to determine the landmarks in each 2D slice. Furthermore often wall heterogeneity cannot be accurately determined due to the presence of a thrombus (Di Martino *et al.* 2001)

1.5.3 Compliant models

A seemingly large downfall in the majority of CFD work is the assumption of rigid-walls. This assumption is made due to a lack of information on mechanical properties of the arterial layers (Dempere-Marco *et al.* 2006; Sforza *et al.* 2009). Furthermore the complex wall remodelling processes in response to haemodynamic stimuli form a non-isotropic material which is difficult to model. Lasheras (2007) and Sforza *et al.* (2009) highlight a lack of knowledge of the wall mechanical properties and changing environment as the limiting factor in forming a wall-fluid model.

The early works of Witzing (1914) and Womersley (1957a) pioneered research into fluid-structure interactions in pipes. Witzing (1914) solved the equations of motion for an inviscid fluid-filled elastic thin walled tube. Womersley (1957a), in solving the linearised Navier–Stokes equations for a thin walled isotropic elastic cylinder containing a Newtonian fluid, derived the analytic solution for the coupling of a viscous fluid and wall motion in a deformable vessel.

Cox (1969) extended the work of Womersley to include the study of thick walled tubes which included models for viscoelastic and anisotropic material behaviour despite using a model which included only linear-wall motion. His study also incorporated the non-linear terms in the Navier–Stokes equations.

Much of the work of Witzing (1914); Womersley (1957a) and Cox (1969) was subsequently supported by experimental studies of flow in flexible vessels (see § 1.6.2). In terms of computationally investigating these flows, development of methods for handling moving boundaries was the first step. Reuderink (1991) and Pietrabissa & Inzoli (1994) present the simplest examples of boundary motion handling in an aneurysmal environment. Their studies used a method which decoupled the fluid and solid solutions. For a given flow, the pressure wave was computed using a linear wave propagation theory. Then the predicted time evolution of the pressure field was applied independently as a boundary condition of the solid domain and used to solve the solid equilibrium equations. The mesh for the fluid domain was then deformed accordingly. Reuderink

(1991) deformed the outermost elements only of their 3D carotid artery mesh, whereas in their later publication on a 2D tube model, all elements were deformed (Reuderink *et al.* 1993). The works of Reuderink *et al.* (1993) and Pietrabissa & Inzoli (1994) neglect the velocity of interior nodal points relative to the stationary frame as a result of the mesh boundary movement. Their work also neglected the effects that the instantaneous feedback of a changed geometry, velocity and pressure field will have on the flow and the parameters being passed between the two solvers. In this way their algorithm is described as very weakly coupled.

Perhaps the biggest obstacle impeding Reuderink *et al.* (1993) and Pietrabissa & Inzoli (1994) was the lack of a suitable wave propagation model due to the complex nature of the material and geometry. Hilbert (1986); Steinman & Ethier (1994) and Perktold & Rappitsch (1995) partially negated the issue by solving the equations of motion with a weakly coupled method. In each case the flow was prescribed at the inlet; the experimentally tabulated pressures from Perktold & Rappitsch (1995) were used as the outlet boundary condition while Hilbert (1986); Steinman & Ethier (1994) solved for the outlet pressure dynamically using linear wave theory and a penalty method for the fluid solver.

Qiu & Tarbell (2000b) used the free surface function of FIDAP[R]7.62 to simulate the moving walls of coronary artery based on experimental measurements in dogs. Lee & Xu (2002) coupled ABAQUS and CFX4.2 to simulate blood flow in elastic arteries. De Hart *et al.* (2003a) used a fictitious domain technique and loose coupling method to simulate 2D aortic valve motion in systolic phase, however their model neglected the elasticity of the vessel wall and used a quasi-static model for the heart valve. They also used implicit coupling methods to simulate 3D aortic valve motion to increase accuracy and stability of the algorithm (De Hart *et al.* 2003b).

Rather than using the loose coupling method of De Hart *et al.* (2003a), Figueroa *et al.* (2006) developed a strongly coupled method for simulating three-dimensional blood flow in arteries. The method is proposed as a simpler solution to using arbitrary Lagrangian–Eulerian methods for coupling the fluid and solid solution. The method couples the equations for the deformation of the vessel wall at the variational level as a boundary condition for the fluid domain. This is contrary to ALE methods which solve the wall deformation equations separately and pass the results to the fluid domain as a boundary condition. A linear membrane model is used for the vessel wall. While a

robust and efficient scheme is presented using this momentum coupling method, it does not account for the full effect that thick walls will have on the mechanics. As such, schemes such as the ALE may be more accurate.

Many investigations into aneurysms have favoured the ALE technique for coupling the fluid and solid solutions (Bazilevs *et al.* 2006). Applications of ALE to haemodynamics are discussed in Di Martino *et al.* (2001); Formaggia *et al.* (2001) and Gerbeau *et al.* (2005). This technique is widely used in haemodynamic simulations due to the high degree of accuracy afforded by the technique, especially in regards to the level of coupling and the position of fluid-structure interfaces. For further discussions of the ALE technique the reader is referred to chapter 3.

1.5.4 Fluid-Solid-Growth (FSG)

In their review, Humphrey & Taylor (2008) highlight the need for a new class of models that can describe the evolving geometry, non-linear-wall properties, and haemodynamics, which in turn dictate the evolving cell mechanobiology that is responsible for matrix turnover and the possible rupture of aneurysms. They believe it is important to go beyond the coupling of fluid and structural mechanics in FSI models to incorporate long-term growth and remodelling models of the evolving arterial wall. This class of coupled computational tools is referred to as Fluid-Solid-Growth (FSG) models.

Figueroa *et al.* (2009) present a computational framework for fluid-solid-growth modelling in cardiovascular simulations. The framework is built primarily on four separate advances in: Biomechanics of growth and remodelling (Baek *et al.* 2006), momentum methods for fluid-solid interactions during a cardiac cycle (Figueroa *et al.* 2006), a theory for coupling biosolid and biofluid mechanical models (Baek *et al.* 2007), and improved approaches for modeling fluid boundary conditions in complex vascular systems (Vignon-Clementel *et al.* 2006). Figueroa *et al.* (2009) were able to show that the inclusion of a growth and remodelling model allowed them to accurately model the arterial remodelling and mechanical response to a lesion in an artery wall. Humphrey & Taylor (2008) along with Figueroa *et al.* (2009) cite a need for more complicated models of the remodelling process, more efficient and accurate FSI coupling methods as well as improved computing facilities in order to advance studies in this field. **The work presented in this thesis seeks to advance the FSI coupling methods and provide information about wall stiffening in aneurysm which may be**

useful in developing models of growth and remodelling.

1.6 Arterial flow investigations

Investigations into haemodynamic stimuli in aneurysmal environments have been conducted using many different methods. Physiological studies have included imaging of aneurysm geometries (e.g. Wilman *et al.* 1998; Potkin *et al.* 1990), biopsies of burst arteries (e.g. Raghavan & Vorp 2000; Carmo *et al.* 2002), induced aneurysms in rabbit and canine aorta (e.g. Jiang *et al.* 2009; Reinald *et al.* 2010; Mardal *et al.* 2010) and epidemiological studies (Sonesson *et al.* 1999; Wanhainen 2008). Engineering investigations have focused more closely on the underlying physics of the flow moving through an aneurysm, for reviews on this topic the reader is directed to Lasheras (2007), Humphrey & Taylor (2008) and Sforza *et al.* (2009). The fluid flow studies may be categorised by the choice of geometry, i.e. idealised or patient specific, the investigative technique, i.e. CFD or experimental, the boundary and initial conditions applied, i.e. physiological, idealised, steady state or oscillatory, and finally using either a rigid-wall assumption or a compliant-wall.

Using a rigid-wall assumption simplifies the arterial model to that of a straight pipe: as such, investigations into flows through straight pipes with steady and oscillatory flows marks the starting point of fundamental study in this field.

1.6.1 Flow in a straight pipe

The earliest experiments investigating flow in a straight pipe were conducted by Reynolds (1883). Reynolds (1883) described the motion of water through a section of straight pipe as he changed three key parameters, namely the input velocity, the fluid viscosity and the pipe diameter. He observed that “the general character of the motion of fluids in contact with solid surfaces depends on the relation (1) between the dimensions of the space occupied by the fluid and a linear physical constant of the fluid; (2) between the velocity and a physical constant of the fluid”, namely its viscosity. Sommerfeld (1908) coined the term Reynolds number to describe the relationship that Reynolds had discovered,

$$Re = \frac{V_m \times D}{\nu}, \quad (1.6)$$

where Re is the Reynolds number, ν is the kinematic viscosity, V_m is the mean velocity and D is the diameter of the pipe. While demonstrating the relationship Reynolds

found two critical values of the ratio. The critical ratios found by Reynolds correspond to a lower critical Re of 2260 and an upper critical Re of 12000. Below 2260 the flow was steady and laminar, above 2260 the flow was susceptible to different levels of perturbation leading to a transition to turbulent flow, finally above 12000 the flow was fully turbulent regardless of the level of perturbation. This series of experiments have raised the maximum upper critical Re observed to a value in excess of 10^5 (Pfenninger 1961). However, the minimum lower critical value for transition to occur has remained close to the value obtained by Reynolds. Studies by Binnie & Fowler (1947); Lindgren (1958); Leite (1959) and Wygnanski *et al.* (1975) have placed it in the range $1800 < Re < 2300$.

Also of early significance is the work of Poiseuille. Poiseuille (1847) set out to find a functional relationship among four variables: the volumetric efflux rate of distilled water from a tube Q , the driving pressure differential ΔP , the tube length L , and the tube diameter d . His investigation was extended to study the relationship of these parameters to changes in temperature and fluid. The result of this work was Poiseuille's equation for pipe flow, first written as

$$Q = K' \frac{\Delta P d^4}{L}, \quad (1.7)$$

where Q is the volumetric efflux rate, K' is a function of the fluid and temperature, P is the pressure drop, d is the pipe diameter, and L is the pipe length. Later Hagenbach (1860) derived Poiseuille's equation from the Navier–Stokes equation recognising the relationship between viscosity and Poiseuille's constant K' , and rewriting the relation to the common form,

$$Q = \frac{\pi}{128\mu} \frac{\Delta P d^4}{L}, \quad (1.8)$$

where μ is the viscosity of the fluid. The Hagen–Poiseuille law gives the pressure drop in a fluid flowing through a long cylindrical pipe, assuming the flow is laminar, viscous and incompressible. In 1960, Hagenbach (1860) and (although not published at the time) Stokes (1967) derived the the Poiseuille equation from the Navier–Stokes equations. One corollary of this derivation was the velocity profile for a circular pipe is parabolic with the form,

$$v_z = -\frac{1}{4\mu} \frac{\partial P}{\partial z} (R^2 - r^2), \quad (1.9)$$

where v_z is the velocity in the axial direction, μ is the viscosity, $\frac{\partial P}{\partial z}$ is the pressure gradient along the pipe, R is the maximum radius of the pipe and r is the radial

position.

While the works of Hagan, Poiseuille and others provides a comprehensive knowledge of steady laminar flow along a straight pipe, the underlying physics is irrevocably changed when the motion is oscillatory. Such knowledge is essential if correct hydrodynamic principals are to be applied to the circulatory system as blood flow in arteries and the large veins is pulsatile in nature (Helps & McDonald 1954; Womersley 1955). Womersley and collaborators were instrumental in developing an understanding of oscillatory flows in straight pipes.

In a landmark paper, Womersley (1955) derived an exact solution of the equations of viscous flow in a circular tube under a pressure gradient that is a periodic function of time. This work is analogous to the work completed by Poiseuille (1847) on steady flows. Womersley showed the velocity profile for flow in a straight pipe is given by

$$v_z = Re \left\{ \frac{A}{\rho} \frac{1}{i\omega} \left[1 - \frac{J_0 \left(\alpha y i^{\frac{3}{2}} \right)}{J_0 \left(\alpha i^{\frac{3}{2}} \right)} \right] e^{i\omega t} \right\}, \quad (1.10)$$

where A is an amplitude, ρ is the fluid density, $i = \sqrt{-1}$ is an imaginary number, ω is the angular frequency of the pressure wave form, J_0 is a Bessel function of the first kind and order 0, y is a measure of the radial distance defined by $y = \frac{r}{R}$, t is the time, and α is the Womersley number. The Womersley number characterises the pulsatile frequency, and is written as

$$\alpha = R \sqrt{\frac{2\pi f}{\nu}}, \quad (1.11)$$

where R is the radius of the pipe, f is the frequency of pressure oscillation, and ν is the kinematic viscosity.

Having derived the equations of motion for a time dependent pressure gradient, Womersley (1955) showed that for the limit of the frequency approaches zero (i.e. when the pressure gradient is constant), that the parabolic Hagen–Poiseuille profile is achieved. He also showed that there is a phase-lag between the fluid motion and the pressure gradient which causes it.

The Womersley number of the flow dictates the phase lag between the flow field and pressure gradient. It is a dimensionless expression of the pulsatile flow frequency in relation to viscous effects (i.e. the ratio of the transient or oscillatory inertia force to the shear force). When α is small (1 or less), the frequency of pulsations is sufficiently low that the Hagen–Poiseuille parabolic velocity profile has time to develop during

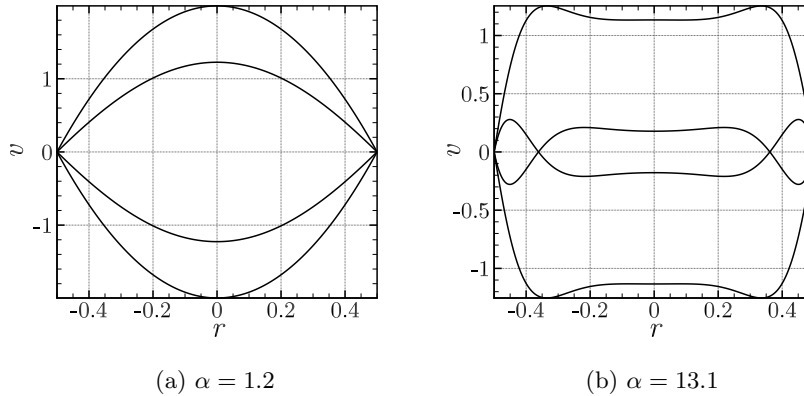


FIGURE 1.3: The velocity profiles of the flow resulting from a sinusoidal pressure gradient in a pipe ($\cos \omega t$) at 90° intervals of the oscillating pressure gradient. Sub-plot (a) depicts the nearly classic Hagen–Poiseuille velocity profile achieved at a low Womersley number of $\alpha = 1.2$. Sub-plot (b) shows the Womersley profile which forms at high Womersley numbers $\alpha = 13.1$.

each cycle. The flow will be very nearly in phase with the pressure gradient. When α is large (10 or more), the frequency of pulsations is sufficiently large that the rapid acceleration-deceleration states of the pressure gradient causes flow reversal near to the walls, and the velocity profile in the interior of the pipe is relatively flat or plug-like, the mean flow may lag the pressure gradient by up to 90 degrees. Hale *et al.* (1955) showed the effect that increasing Womersley number has on velocity profile. Figure 1.3 depicts the departure from the classic Hagen–Poiseuille parabolic profile at large Womersley numbers. The large Womersley number flattens the profile making it plug like. As the pressure gradient reverses direction, the reversal of flow starts in the laminae near the wall. The effects of the larger Womersley number is seen in figure 1.3(b), there is a distinct flattening of the profile of the central region, a reduction of amplitude of the flow and the rate of reversal of flow increases close to the wall. The greater the Womersley number the further accentuated these effects are. For very high Womersley numbers (figure 1.3(b)), the rapidly varying part of the flow lies between $r = 0.35$ and $r = 0.5$, the central mass of the fluid reciprocates almost like a solid core.

1.6.2 Flow in flexible vessels

Blood flow through arteries is more complicated than simple flow through straight pipes. The elastic nature of the walls plays an important role defining the haemodynamics. When a flow is driven through a deformable tube, interactions between the fluid and elastic forces lead to a variety of biologically significant phenomena. These include wave propagation through both the fluid and walls, non-linear pressure-drop/flow rate relations, and the generation of extra instability modes (Grotberg & Jensen 2004). In understanding the complex flow through aneurysms it is important to know the physical origins and nature of these phenomena.

The earliest works on flow in distensible tubes was completed by Euler in 1775 (Euler 1844). In this paper Euler set out the one-dimensional equations for the conservation of mass and momentum in a distensible tube. In his notation these respective conservation equations are written as

$$\left(\frac{ds}{dt}\right) + \left(\frac{d \cdot V_m s}{dx}\right) = 0, \quad (1.12)$$

and

$$2\rho \left(\frac{dP}{dz}\right) + V_m \left(\frac{d \cdot V_m}{dz}\right) + \left(\frac{dV_m}{dt}\right) = 0, \quad (1.13)$$

where s is the cross-sectional area, V_m is the average velocity, P is the pressure, ρ is the density, t is time and z is the axial distance. Since Euler, many theoretical works have been devoted to this subject.

Luchini *et al.* (1991) identifies the most prominent feature of flow in distensible, as opposed to rigid, tubes is the propagation of pressure waves with finite velocity. Young (1808) provided the first estimate of the velocity of the pressure wave using a one-dimensional model of an inviscid fluid. He used an effective compressibility of the fluid in place of an elastic-wall. Later, Lamb (1898), improved on Young's model introducing the differential equations of motion of the tube walls replacing the effective compressibility model. Witzing (1914) built on the work of his predecessors and expressed the complex wave velocity as a function of frequency for periodic solutions. This solution was generalised by Womersley (1957b) to include viscous effects for the fluid and viscoelastic properties for the wall. Womersley pointed out that both velocity and the damping coefficient of the wave are increased by viscous effects in the wall. All of these papers only deal with the one-dimensional evolution of the cross-section-averaged fluid pressure. The problem of the complete theoretical determination of the

fluid flow field in a distensible tube remains.

Atabek (1968) redefined the equations including the effect of pre-stressing the tube with a hydrostatic load and considered the presence of external loading of *in vivo* arteries through its contact with the surrounding tissue. Others have since modified these results to include non-linear elastic models for the tube to more closely match biological data, this has the result of making the wave disturbance dependent on the state of pre-stressing in the wall. Anliker *et al.* (1968, 1969) observed this effect on anaesthetized dogs. They found for a given transmural pressure, the phase velocity increases with distance from the heart. They conclude the pressure pulse will exhibit a steepening of its wave front as it propagates.

Krindel & Silberberg (1979) studied the flow of a Newtonian fluid in a gel-walled tube, and observed that the transition Reynolds number and the drag law are very different from those of rigid tubes. Kumaran (1995b) argued the flow near a flexible surface is very different to flow near a rigid surface due to the non zero normal velocity, this results in a breaking of Rayleigh theorem and leads to non-trivial solutions for the temporal stability problem. The Reynolds number analysis of Kumaran (1995b,a) revealed the possibility of unstable fluctuations when the fluid velocity is increased beyond a critical value. Kumaran (1995a) performed an energy balance and showed the transfer of energy from the mean flow to the fluctuations due to the Reynolds stress in the wall layer is exactly cancelled by an opposite transfer of equal magnitude due to deformation work done at the interface and that there is no net transfer from the mean flow to the fluctuations.

Pertinent to the healthy function of the artery is the wall shear stress. The one-dimensional models based on continuity of mass and momentum and tube laws for the wall require a flow-dependent WSS expression to solve the set of equations (Zagzoule *et al.* 1991). Often it is the case (Rockwell 1969; Stettler *et al.* 1981) that the local velocity profile is assumed to be parabolic, allowing the WSS to be deduced from Poiseuille's law. As shown by Womersley (1955) for unsteady pulsatile flows a parabolic velocity profile does not develop, the WSS always has a phase lead on the mean and centre line velocities. The use of the Poiseuille approximation ignores this feature of the flow and as a consequence the WSS is underestimated from these one-dimensional models (Zagzoule *et al.* 1991). Several attempts have been made to improve the WSS model in one-dimensional equations. Streeter *et al.* (1964) used a turbulent type friction

expression and showed that the Poiseuille approximation underestimates the WSS in laminar and turbulent régimes. Olsen & Shapiro (1967) used the first harmonic in a Womersley velocity profile in a rigid pipe to deduce the WSS in an elastic tube. This approximation yielded good results in high or low Womersley number ranges but provided inaccurate information at biologically realistic régimes. While this was a good advancement they neglected the phase lag of the pressure and velocity solutions and the variations in cross sectional area.

The one-dimensional models for fluid flow in an elastic tube over-simplifies the system. Attempts to combine components of two-dimensional models and one-dimensional models (Atabek 1980) have yielded inefficient techniques with marginal gains in accuracy. Accuracy in modelling these flows requires a full direct numerical simulation with appropriate boundary conditions.

1.6.3 Haemodynamics of aneurysm geometries

Many different approaches have been taken to investigate aneurysmal flow conditions. *In vitro* experiments have been used in conjunction with PIV techniques to visualise flow through aneurysms. Computational Fluid Dynamics (CFD) models have proven more useful in determining shear stresses near the wall. Another advantage of CFD models is the ability to look at both idealised and patient specific models. Needless to say, the complex nature of the fluid-structure interaction has made complete modelling of the system difficult. Much of the research conducted has used a rigid-wall assumption to simplify their models, let this form a starting point for our discussion of haemodynamics in aneurysms.

1.6.3.1 Rigid-wall models

Salsac *et al.* (2006) completed a parametric study in symmetric glass models. The models were characterised by their aspect ratio $\frac{L}{d}$ and dilation ratio $\frac{D}{d}$ as depicted in figure 1.4. The maximum aneurysm diameter D was restricted to be less than 4.5 cm as larger aneurysms may form thromboses. Water was used as the fluid in the investigation and assumptions were made that blood is a Newtonian fluid which is reasonable in large vessels (Attinger 1964; El-Khatib & Damiano 2003).

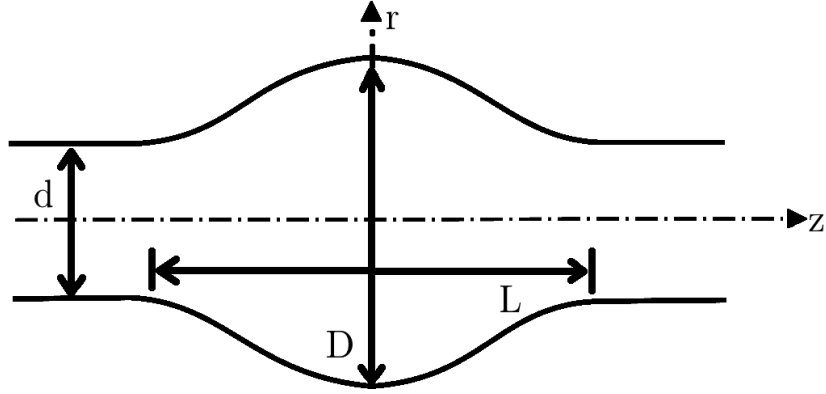


FIGURE 1.4: Fusiform symmetric glass models used by Salsac *et al.* (2006) and defining parameters. Reproduced with the permission of Cambridge University Press from Salsac *et al.* (2006).

Salsac *et al.* (2006) found that in the healthy aorta during systole⁵ a top hat flow profile is formed with boundary layer increasing with Womersley number.

During diastole⁶ the bulk flow of the fluid motion is forward with backward movement beginning at the boundaries. It is important to note that flow remains laminar throughout the entire cycle. For a healthy aorta it was found that the $WSS_{mean} = 0.27$, $WSS_{mag} = 1.5$ and the oscillating shear index, $OSI = 0.4$. The mean wall shear stress is given by

$$WSS_{mean} = \frac{1}{T} \int_0^T WSS dt, \quad (1.14)$$

where T is the time period, the wall shear stress magnitude is given by

$$WSS_{mag} = \frac{1}{T} \int_0^T |WSS| dt, \quad (1.15)$$

and the oscillating shear index is given by

$$OSI = \frac{1}{2} \left(1 - \frac{WSS_{mean}}{WSS_{mag}} \right). \quad (1.16)$$

Both Finol *et al.* (2003b) and Salsac *et al.* (2006) describe the flow evolution (see figure 1.5 in detail):

1. Systolic acceleration involves downstream ejection of the residual vortices left from the previous cycle, yielding an attached laminar flow pattern thanks to the

⁵Systole refers to the gathering and contraction of the heart, this is linked to the expulsion of blood from the heart and is represented by a positive volumetric flow rate.

⁶Diastole is the period of time in which the heart refills with blood after systole, it is represented by a negative or minimum in the volumetric flow rate.

positive pressure gradient of systole. The temporal acceleration of the flow is at this point larger than the convective deceleration resulting from the upstream (proximal) diverging walls of the artery.

2. Systolic deceleration is characterized by flow separation at the proximal neck, toroid-shaped single-vortex growth and its translation downstream, followed by a free shear layer in which secondary vortices form due to the Kelvin–Helmholtz instability. The vortex ring will eventually impact on the distal neck, causing a region of higher shear stress.
3. Early diastole is characterized by partial shedding of the vortex left from systole towards the main stream. Flow recirculation is reduced in size, as the centreline velocity increases in accord with the pressure gradient imposed by the inlet flow condition.
4. Late diastole is the phase where the most significant flow disturbance takes place. It is largely influenced by the effect of secondary disorganized recirculation regions that depart from the symmetric toroidal shape. These are present downstream of the aneurysm midsection until the onset of systolic acceleration in the next cardiac cycle.

In terms of the wall shear stresses, the presence of the primary vortex ring so close to the distal wall at impact induces the boundary layer to roll up into a counter-rotating vortex of smaller size. A strong $WSSG$ is observed in the proximal and distal necks where flow detaches from the wall and when the changes in WSS are maximum. The formation of the vortex ring also creates regions of high $WSSG$ up and downstream of it. Regions of low WSS_{mean} correspond to Oscillating Shear Index (OSI) of 0.5 (oscillatory), most of the wall experiences OSI greater than 0.5 indicating a flow reversal. While the work of Salsac *et al.* (2006) comprehensively describes the flow evolution in a fusiform aneurysm, they fail to capture the complete physics of flow through an aneurysm. The rigid wall is not physiologically realistic and its exclusion could lead to a change in flow dynamics as suggested by other studies such as Finol *et al.* (2003b).

Geometry has a large impact on the distribution of wall stresses and flow evolution (Buchanan *et al.* 1998; Finol *et al.* 2003b; Salsac *et al.* 2006; Sheard *et al.* 2007; Sforza *et al.* 2009). A change in aspect ratio L/d , changes the distance along the axis that

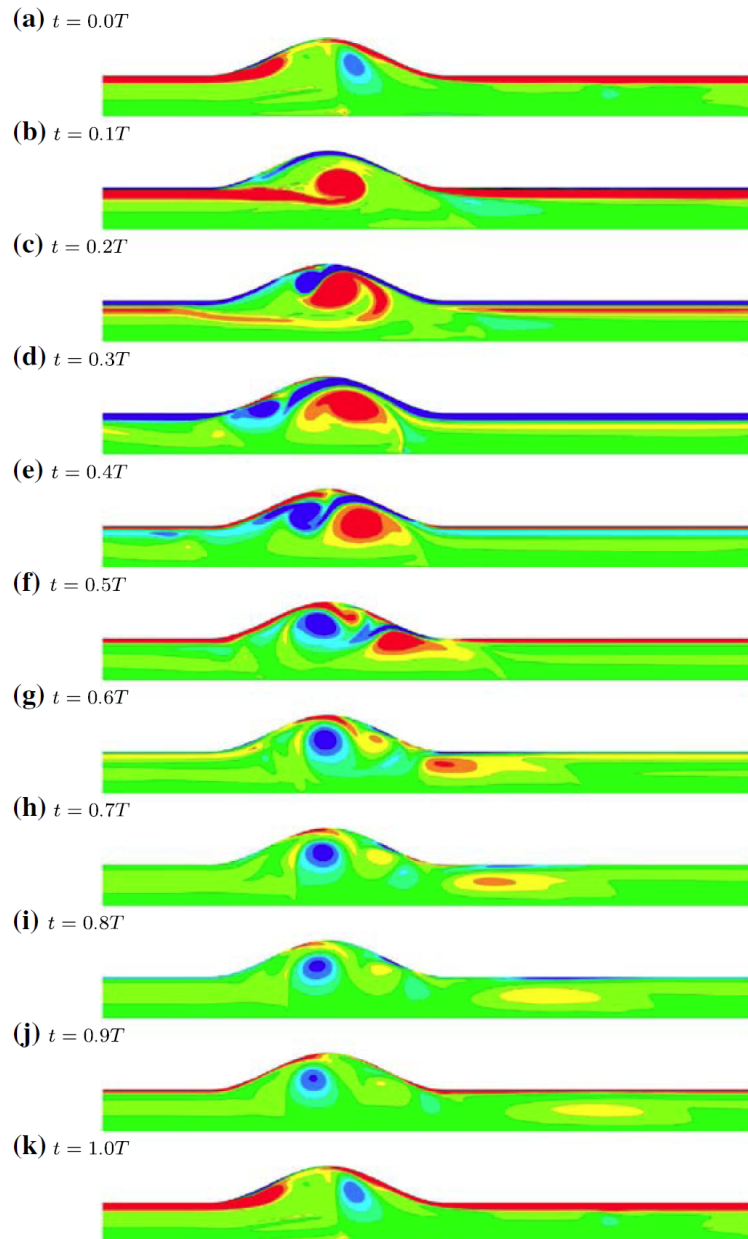


FIGURE 1.5: Flow in a fusiform aneurysm. Flow is left to right and the Meridional half plane is plotted. Contours are of-out-of plane vorticity, with red positive and blue negative. Note the large red primary vortex ring in the systolic acceleration phase and the blue secondary vortices in the diastolic phase. Reproduced with the permission of Sheard from (Sheard 2009).

the vortex ring must travel. Aspect ratio may limit the evolution of the vortex ring as the length scale is less than that defined by the Strouhal number. Higher aspect ratios lead to a later separation and hence a weaker vortex (Salsac *et al.* 2006). A change in aspect ratio alone has little effect on wall shear stress, in fact it typically acts to reduce the intensity of WSS patterns, this is due to weaker vortex formation for larger aspect ratios (Salsac *et al.* 2006). However, dilation factor D/d enhances WSS patterns. As D/d increases the point of flow separation moves closer to the proximal neck, the mean WSS increases, and recirculation regions increase in size. The time at which flow separation occurs is not dependent on dilation factor (Salsac *et al.* 2006).

Sheard *et al.* (2007) investigated the effects of changing the radius of curvature of the proximal and distal necks. A spectral element CFD technique was employed and results were compared to a healthy aorta and Poiseuille's laws for straight pipes. They found that the rate at which fluid is flushed from the bulge is dependent on pulse frequency and not geometry. The heart rate frequency, f , is defined by the non-dimensionalised Womersley number. Optimal fluid removal was found at $\alpha = 20$ (Sheard *et al.* 2007). However, wall shear stress and pressure drop were dependent on geometry, with an increased radius of curvature corresponding to lower WSS .

It is unlikely that an aneurysm of medium or large size ($D > 4.5$ mm) be of fusiform or axisymmetric shape (Finol *et al.* 2003b). Di Martino *et al.* (2001); Finol *et al.* (2003b) and Scotti *et al.* (2005) all analysed the effects of asymmetry using finite element CFD techniques. Finol *et al.* (2003b) explains the effects of asymmetry on the flow through a rigid-walled fusiform aneurysm. They explain that during systolic deceleration the effect of asymmetry is to reduce the intensity of the vortex along the posterior wall, creating an asymmetric annular structure. During early diastole aneurysm asymmetry yields stronger velocity gradients along the anterior wall at the distal end. Finally, during late diastole the geometric asymmetry creates secondary vortex structures which cause disorganized recirculation regions that depart from the symmetric toroidal shape. In terms of WSS as the asymmetry increases so too does the peak WSS in a non-linear manner.

Like both Finol *et al.* (2003b) and Scotti *et al.* (2005), Vorp *et al.* (1998) investigated the effect of geometric asymmetry on the wall shear stress experienced in a fusiform aneurysm. Using a finite element technique and rigid-walls they found the magnitude of the peak wall shear stress increased non-linearly with increasing maximum diameter

(for constant asymmetry) and increasing the level of asymmetry (for constant maximum diameter). In terms of the shear stress distribution, it was found that different levels of asymmetry changed the location of the peak wall shear stress from the midsection to the distal neck. Their findings were later corroborated by the works of Di Martino *et al.* (2001); Finol *et al.* (2003b); Scotti *et al.* (2005).

The ultimate application of this research sees an integration of CFD software with medical imagery in order to realistically measure the flow through patient specific aneurysms. Shojima *et al.* (2004), investigated 20 such models, they concluded that the average WSS in the vessel was significantly higher than in the aneurysm (Shojima *et al.* 2004). Geometry had a profound effect on their results; small aneurysm with low aspect ratio $L/d = 0.56$ had no decrease in intra-aneurysmal flow. But larger with high aspect ratio of $L/d = 1.58$ saw the formation of a recirculation region leading to a decrease in intra-aneurysmal flow and consequently a low average shear stress (Shojima *et al.* 2004). These studies suggested that a $WSS = 2 \text{ N/m}^2$ will maintain endothelial cells while a WSS of 1.5 N/m^2 begins to degrade them. This is contrary to the results presented by Salsac *et al.* (2006) who suggested healthy WSS be 1.5 N/m^2 .

Other authors suggest other factors that could be important in terms of patient specific haemodynamics. Egelhoff *et al.* (1999) indicate under medium exercise inflow conditions a transitional stage exists that may see the vortex ring bursting into turbulence at late diastole. However, Finol *et al.* (2003b) and Finol & Amon (2002) did not capture any numerical instabilities or singularities for time dependent flow conditions that would lead to turbulence. Buchanan *et al.* (1998), while working on rabbit aorto-celiac junctions, indicated the significance of secondary spiral or helical flows. Sforza *et al.* (2009) through work on cerebral aneurysms also stated that helical or swirling secondary flows induced by the curving geometry of cerebral arteries are fundamentally important as they govern the areas of local flow.

1.6.3.2 Compliant-wall models

The enlargement of aneurysms has been linked to a disruption in the mechanotransduction process which keeps arterial walls healthy. This disruption is closely associated with both the haemodynamic shear stresses exerted on the wall as well as the mechanical characteristics of the vessel wall. The arterial endothelial lining is exposed to both wall shear stress caused by pulsatile blood flow and circumferential stress caused

by pulsating arterial pressure. The interaction of these two stresses, and not the sole contribution of each, plays an important role in determining a healthy mechanotransduction process (Qiu & Tarbell 2000b). Given the importance of the stress interaction it seems prudent to perform investigations which include a compliant wall model (Lasheras 2007). Lasheras (2007) and Sforza *et al.* (2009) highlight a lack of knowledge of the wall mechanical properties and changing environment as the limiting factor in forming a wall-fluid model. Simple models have however been tested to see the effects that a fluid-structure interaction has on the fluid flows.

The nature of the interaction is complex. Arteries deform under pressure fluctuation generated by the heart. The blood transmits the pressure wave as a result of energy exchange between the artery wall and the blood itself; this makes modelling of the arterial haemodynamics a fluid-solid interaction problem. Lasheras (2007) highlighted the lack of knowledge of the arterial wall properties as one obstacle hindering research in this area, as few such investigations had been attempted.

It is anticipated that a compliant wall model will have an effect on the haemodynamic metrics we use to assess aneurysms. The reported findings seem inconsistent with some studies (e.g. Scotti *et al.* 2005) reporting that compliant walls increase peak wall shear stress, while others Perktold & Rappitsch (1995); Dempere-Marco *et al.* (2006); Oubel *et al.* (2007) reported contradictory findings.

Dempere-Marco *et al.* (2006) and Oubel *et al.* (2007) applied the pulsation of the artery wall to patient specific cases. To do this they measured the wall motion of different regions in the aneurysm using medical imaging. They then made a first-order approximation of the wave, including only the fundamental frequency of the wave form, and scaled the amplitude of the oscillation with the observed wall movement. They used this wave form as a velocity boundary condition on a fixed-wall patient specific fluid model. Both Dempere-Marco *et al.* (2006) and Oubel *et al.* (2007) found that a purely rigid model with no-slip boundary condition, over-estimates the peak wall shear stress, while compliant models yielded slightly larger areas of elevated WSS . While they did account for the velocity of the fluid introduced as a result of the wall motion, they did not account for the change in shape that the wall motion creates. The change in shape is an important factor in resolving the temporal evolution of aneurysm haemodynamics, particularly in the boundary layer.

Di Martino *et al.* (2001) and Scotti *et al.* (2005) modelled a full fluid-structure in-

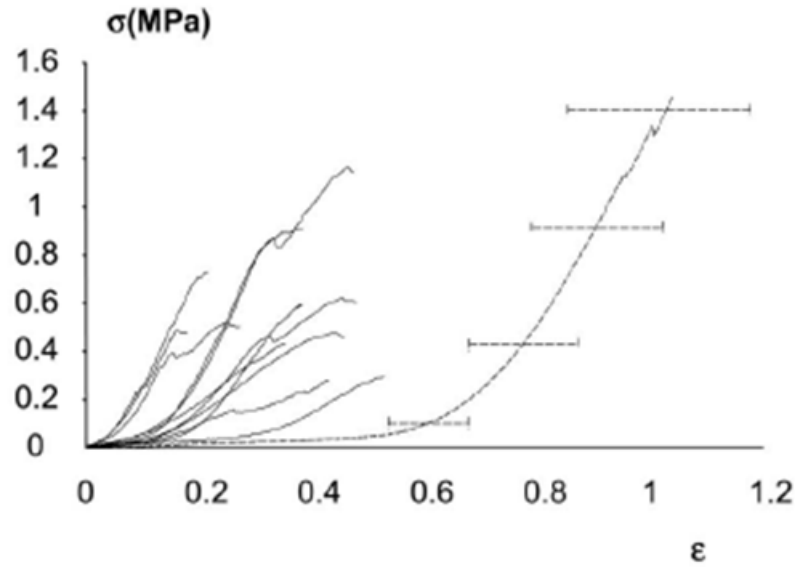


FIGURE 1.6: Stress-deformation curves from aneurysm specimens tested using a uni-axial tensile test. The dashed line represents the stress-deformation curve of a healthy artery. Reproduced with the permission of Elsevier from Di Martino *et al.* (2001).

teraction within AAAs. Contrary to the findings of both Dempere-Marco *et al.* (2006) and Oubel *et al.* (2007), Scotti *et al.* (2005) found that non-compliant models drastically underestimated stresses in the wall. Perktold & Rappitsch (1995) reported a 25% decrease in wall shear stress in an elastic model compared to a solid model. Both studies used a finite element solver in conjunction with an arbitrary Lagrangian–Eulerian algorithm to solve the system. The ALE algorithm seeks at each time step the convergence of three blocks of equations, fluid flow (Navier–Stokes), solid (CSD) and mesh movements (CMD) which must then converge together before a new step is initiated. The mechanical properties of the wall were measured using cadaver specimens. Their stress-strain relationships are reproduced in figure 1.6. The code was limited to a linear elastic homogeneous approximation of the non-linear behaviour shown in figure 1.6. A linear elastic approximation is insufficient to describe this behaviour. At high stresses the strain predicted by a linear model will be markedly different to the actual strain shown from these uni-axial stress tests. Recently, Raghavan & Vorp (2000) showed that the wall behaviour may be described successfully by means of a non-linear isotropic, hyper-elastic material model defined through uni-axial tests.

Cebral *et al.* (2002) used magnetic resonance images to construct a model of an

artery wall. They concluded that in rigid models, the regions with low shear stress ($< 10 \text{ dyn/cm}^2$) were smaller compared to those in elastic models.

Scotti *et al.* (2005) found that the wall was displaced by an amplitude of 5 mm. This is contradictory to the measurements from medical images which indicated a wall movement only 2.5 mm (Dempere-Marco *et al.* 2006). With the fluid-structure interaction, Scotti *et al.* (2005), showed at or just after peak systolic pressure there are no vortices customary of systolic acceleration. This is contrary to results from rigid models as energy stored by the expanding compliant vessel ejects the vortex downstream shortly after peak flow. A phase delay is detected between the velocity inlet and pressure outlet waveforms (Scotti *et al.* 2005). The same vortex dynamics are produced regardless of asymmetry, but they remain in the midsection of the distal end in the symmetric case and in the asymmetric case it moves toward the proximal end (Scotti *et al.* 2005).

The effects of a diameter dependent wall thickness are much greater than asymmetry for aneurysm models including a fluid-structure interaction. Scotti *et al.* (2005) showed a uniform thickness in a symmetric fusiform aneurysm will yield smooth laminar flow; however, heterogeneous wall causes vortex formation near the distal neck. Flow reversal occurs twice as often in the variable wall thickness model. Assumptions of uniform wall thickness gives an underestimation of stresses by 77% compared to a variable thickness model (Scotti *et al.* 2005). The work of Scotti *et al.* (2005) provides a good description of the effects of simple changes in wall thickness have on flow dynamics. However, Lasheras (2007), among others, describes the stiffening or weakening of the arterial wall that coincides with changes in wall thickness. The work of Scotti *et al.* does not account for the changed stiffness conditions in the aneurysm wall that would correspond to the imposed change in thickness. Furthermore, calcification, cell death and intraluminal thrombus can all cause a very complex and heterogeneous wall thickness distribution. Modelling the wall with more localised variations in wall thickness may exacerbate the effect of a variable wall thickness.

1.6.3.3 Effect of wall mechanics on FSI

It has been widely accepted that arterial tissue has a non-linear elastic response. Many constitutive material models have been developed to mimic the stress strain material behaviour of the arterial wall (e.g. Lally *et al.* 2004; Fung *et al.* 1979). Largely, these

models simplify the complex structures of the arterial wall using a single homogeneous material. In reality the different material structures and properties of the media, intima and adventitia contribute to the material response. Elastin in the media bears most of the pressure load at low strains. The collagen fibre network limits the radial deformability at higher blood pressure, and causes the steep rise in wall stiffness at higher blood pressures, resulting in a material with non-linear elasticity (Oscui *et al.* 2007). An alternative approach to modelling the wall as a homogenous material with complex material model is to consider the wall as a multi-layered structure with differing material parameters for each layer of the wall reflecting the properties of the biological structures that comprise each layer.

Schulze-Bauer *et al.* (2003) observed an average wall layer thickness ratio of intima/media/adventitia of 13/56/31 for arteries. Driessen *et al.* (2004) used a thickness ratio of 2/1 for media/adventitia. Gao *et al.* (2006) use a ratio of 1/6/3. The ratios used in both Gao *et al.* (2006) and Driessen *et al.* (2004) are an approximation of that measured in Schulze-Bauer *et al.* (2003).

In terms of wall stiffness, Mosora *et al.* (1993) used a Young's modulus range of 2 MPa to 6.5 Mpa. In their bending experiments, Xie *et al.* (1995) showed the Young's modulus of the inner layer (intima and media) was three to four times larger than that of the outer layer (adventitia), and it can be deduced from the experimental data in Cabrera-Fischer *et al.* (2002) that the Young's modulus of the intima is smaller than that of the media. Gao *et al.* (2006) uses a Young's modulus of the media three times that of the adventitia and intima. Since the mean Young's modulus of the vessel wall across the whole wall volume is invariable, the Young's modulus of each layer is in inverse proportion to the area of the layer in the cross section (Gao *et al.* 2006).

Gao *et al.* (2006) presented the effects of fluid-structure interaction on the aortic arch using a multi-layered wall model. They showed that variations of circumferential stress are very similar to variations of pressure. The composite stress in the aortic wall plane was shown to be much higher in the media than in the intima and adventitia across the wall thickness. These results indicate that a single layered homogeneous material model may underestimate wall stresses in the aneurysm.

Leung *et al.* (2006) directly compared using a rigid-wall model and a fluid-structure interaction model for three patient specific aneurysms. The aneurysm was given a uniform thickness (1.5 mm) and stiffness (2.7 MPa) for the aneurysm wall. The aneurysm

wall was modelled using a hyperelastic material defined by Raghavan & Vorp (2000). The arbitrary Lagrangian–Eulerian formulation was used to couple the fluid and solid solution. They demonstrated that including fluid flow can change the wall stress distribution slightly. However, as far as the peak wall stress is concerned, this effect is negligible as the difference between rigid-wall and FSI models is less than 1%. While presenting plots of peak wall shear stress in the aneurysm for the FSI simulations, they do not comment on how this distribution is affected by an FSI model compared to a rigid-wall model, nor do they comment on the effect these parameters may have to the future health of the aneurysm.

Oscuii *et al.* (2007) investigated the effects of varying wall stiffness on the flow in a fusiform brachial aneurysm. They used the arbitrary Lagrangian–Eulerian formulation to loosely couple the incompressible Navier–Stokes equations for the fluid region with an incompressible elastic material undergoing large deformations. Pressure and velocity waveforms were applied specifically to the brachial artery. Resultant flow, wall displacement, wall shear stress, wall circumferential strain waves and their phase differences were determined. Oscuii *et al.* (2007) showed a significant decrease in flow rate and axial velocity profile for stiffer walled models. A ten-fold increase in wall stiffness caused maximum wall shear stress values to decrease 51%, leading to negative minimum shear that lasted almost one quarter of the pressure pulse duration. An analysis also showed the stress phase angle was altered by stiffening of the arterial wall. It was concluded that for elastic moduli corresponding to wall displacements less than 1%, the blood flow and wall shear stress were not sensitive to wall stiffness.

Torii *et al.* (2008) compared the effect of using a linear elastic small strain model, a neo-Hookean model and a hyperelastic Fung-type model for the material wall. A patient specific cerebral aneurysm geometry previously shown to have flow patterns that developed in compliant wall simulations but not in rigid-wall simulations was used to demonstrate the effect of each wall model. They found that the neo-Hookean material had the largest displacement at 0.346 mm compared to 0.333 mm for the Hookean and 0.222 mm for the Fung material. The larger displacement in the neo-Hookean material compared to the Hookean material was expected due to the change in thickness of the artery wall throughout the large displacements. The neo-Hookean model takes this change in volume into account while the Hookean material does not. Regardless of material model the flow patterns observed in the aneurysm lumen were consistent,

characterised by large wall shear stress areas compared to solid state models and the shedding of a secondary vortex. Torii *et al.* (2008) conclude that both linearly elastic and hyper-elastic models can be useful to investigate aneurysm FSI. The displacements of the aneurysm walls described in Torii *et al.* (2008) are small compared with the 1.2 – 2.5 mm wall dilation measured in abdominal aortic aneurysm (Stefanadis *et al.* 1995). Possible reasons for the underestimation of wall motion could be the choice of material properties in each material model, the difference in the mechanical properties in cerebral aneurysms compared to aortic aneurysms or a failure to model the effect of a perianeurysmal environment.

1.6.3.4 Further medical complications: Calcification and thrombus

Commonly associated with AAAs is calcification and Intraluminal Thrombus (ILT). These are generally associated with a dimmer cardiovascular prognosis. The effect of calcification on biomechanical wall shear stress in AAAs has not been fully studied (Detrano *et al.* 1999; Schmermund *et al.* 1999). ILT has been heavily investigated in an aortic aneurysm context; however, a conclusive finding on their effects has not been determined. Some believe ILT increases the risk of rupture (Satta *et al.* 1996; Vorp *et al.* 2001), others believe ILT may significantly reduce wall stress and therefore protect from rupture (Inzoli *et al.* 1993; Mower *et al.* 1997), still others suggest ILT has no effect on rupture risk (Dobrin 1989). Li *et al.* (2008) studied the effect of both ILT and calcification on AAAs. Their study conducted a finite element analysis on some patient specific aneurysm geometries with varying degrees of thrombus formation and calcification. For the artery wall and ILT they used the hyperelastic model, which was described in Raghavan & Vorp (2000). They used a Mooney–Rivlin type material for the calcification deposits. A finite element structural analysis with large deformations was conducted independent of blood flow information. Their findings indicated no correlation between the peak values of wall stress in each case and the median values. They found that the peak wall stress was not correlated with the percentage of calcification in the AAA, and was negatively correlated with the percentage of ILT. Results showed calcification led to a median 14% increase in maximum stress and that ILT led to a 24% increase in median peak wall stress. The effect of ILT and calcification is clearly significant to AAA wall mechanics. In order to remove the effect of thrombus from this investigation the geometry is limited to aneurysms with Diameter $D < 4.5$ cm which

have been clinically shown to be typically devoid of an endoluminal thrombus (Harter *et al.* 1982).

1.7 Restrictions of previous work

Due to the large parameter space involved in modelling aneurysms, many assumptions and simplifications have been made in previous investigations. Experimental methods for measuring haemodynamic forces are restricted in their resolution of wall shear stresses. Theoretical models of flexible vessels use assumptions that underestimate the wall shear stresses. Conversely, while *in vivo* studies are possible, current methods for measuring flow conditions are primitive compared to the accuracy achieved outside of the body. This is also true of methods for assessing wall stresses and wall stiffnesses of the aneurysm *in situ*. This leads to a basic lack of data in this field.

Of the computational studies conducted to date, many consider vessel compliance to be only of secondary importance and neglect it (Sforza *et al.* 2009). As such, most CFD modelling is conducted with a rigid-wall condition. As highlighted in this literature review this can lead to an underestimation of the mechanical wall stresses and a variation in the wall shear stress distribution in the fluid. Furthermore, non-Newtonian behaviour is ignored and the blood is assumed incompressible. What little work that has been done with fluid-structure interactions has been fraught with simplified models that lead to contradictory results. Largely, these simplifications have been driven by either inefficient numerical methods which have made accurate modelling of the system too expensive a task, or a lack of basic information about the aneurysmal environment. In aneurysm investigations the most advanced simulations use a fluid-solid-growth model FSG, these are largely limited by the lack of knowledge about the wall remodelling processes (Sforza *et al.* 2009).

In order for FSG models to be viable it is vital that the fundamental aspects of the flow through aneurysms is mastered. As such, a comprehensive understanding of the underlying physics of the flow is necessary and therefore accurate modelling techniques for modelling fluid-structure interactions are essential. Current fluid-structure models are limited by one or several of the following points.

- *They do not fully couple the fluid and solid solutions.* The momentum method of Figueroa *et al.* (2006) only loosely couples the fluid and solid solutions. Some works have used the varying pressure gradient in the aneurysm as a pressure

boundary condition on the solid and solved for its motion separately. This is then applied this as a wall velocity to the fluid (Di Martino *et al.* 1998). Others have used medical imaging of the aneurysm to determine the wall motion of the solid and imposed this as a velocity boundary condition on the fluid (Oubel *et al.* 2007). Each of these methods fails to account for local variations in the pressure as a result of fluid-structures such as vortices that change the local pressure on the wall. Currently the ALE method is the best method for coupling the two solutions.

- *They do not account for large deformations in the solid domain.* Linear elastic models of the arterial wall assume that the strain is small and as such the difference in undeformed and deformed coordinate systems is small. In aneurysm simulations this is simply not the case with wall motion being as large as 15% of the wall thickness. Some non-linear models are also constructed using a small strain approximation.
- *They do not accurately maintain information of the location of the fluid-solid interface.* Methods that do not use an ALE method, or those that employ an Eulerian reference frame only, cannot accurately define the position of the artery wall. This occurs in the Eulerian formulation when the wall passes through an element as opposed to being mapped out by its edge.
- *They do not include inertial terms in the solid structural mechanics.* The majority of studies (Di Martino *et al.* 1998; Scotti *et al.* 2005; Finol *et al.* 2003b) use a quasi-static approximation for the boundary. This means the boundary conditions are time dependent but the structural response is instantaneous. Such simplifications means pressure waves which travel in the solid are not resolved (Lasheras 2007). Some investigations (Li & Kleinstreuer 2005) have solved the wave equation in conjunction with thin membrane models to partially overcome this problem.
- *They do not account for forces being spread from inner wall to medial and outer walls (Scotti et al. 2005).* Most investigations have modelled the wall using either a thick or thin membrane theory or as a single layered homogeneous material. Gao *et al.* (2006) showed that single layered models underestimate wall stresses. While non-linear material models do come close to approximating the overall mechanical response of the wall it is a simplification of the multi-layered aneurysm

environment. Elastin in the media bears most of the pressure load at low strains. The collagen fibre network limits the radial deformability at higher blood pressure, and causes the steep rise in wall stiffness at higher blood pressures. This results in a material with non-linear elasticity (Oscuii *et al.* 2007).

- *They do not account for highly heterogeneous wall thicknesses and stiffnesses.* While some investigations (Di Martino *et al.* 2001; Scotti *et al.* 2005) have investigated the effect of changing wall thickness in an aneurysm they have done so in a very uniform fashion, i.e. a function of wall diameter. In reality the wall thickness and stiffness will change as a result of haemodynamic stimuli and as aneurysm imaging has shown the wall thickness is highly heterogeneous.
- *They do not account for non-linear elastic material properties of the wall (Scotti et al. 2005).* While many investigations of aneurysm walls themselves have been modelled using highly complex anisotropic, hyperelastic material models (Holzapfel & Weizsäcker 1998), investigations that include fluid-structure interactions rarely use complex material models for the wall in order to conserve computational efficiency. Furthermore if a non-linear elastic material is solved a single layer model is invariably used.
- *They do not account for the effects of a thrombus (Scotti et al. 2005).* In large aneurysms, formation of thrombus drastically changes the lumen shape. large sections become occluded due to the build up of platelets in low WSS areas.
- *They do not account for the forces from the perianeurysmal environment (Sforza et al. 2009).* The boundary conditions applied to the solid region are of the utmost importance. Having the outer edge of the arterial wall free to move with no force upon it or fixed in place is unrealistic. Humphrey & Taylor (2008) highlight the importance of using a force feedback model on the outer surface of the arterial wall to model the effect of the aneurysm pushing against the perianeurysmal environment. The treatment of the perianeurysmal environment in this research is discussed in § 7.4.4.
- *They do not account for the effects of bifurcations and inlet flow conditions.* Humphrey & Taylor (2008) highlight the importance of using appropriate boundary conditions in modelling the flow through an aneurysm. Currently many stud-

ies use simplified models for the inflow and outflow conditions, not allowing physiologically accurate flows to evolve. Impedance models based on the downstream pressure in the venous branches are recommended, as is modelling outflow through the renal branches upstream and the femoral artery bifurcation downstream.

Research that seeks to contribute to this field must strive to rectify these shortcomings. The work of this thesis looks to improve on the current numerical simulation methods as well as performing investigations on aneurysms with physiologically appropriate boundary conditions.

1.8 Research aims

Lasheras (2007) and Sforza *et al.* (2009) both emphasized a lack of knowledge regarding aneurysm wall properties and models. They also indicated the importance of such models in forming a predictive model for aneurysm growth and rupture. Scotti *et al.* (2005) showed that modelling of a fluid-structure interaction alters the evolution of flow in the aneurysm compared to rigid-wall models. Following this, the present research aims to:

1. Create a spectral element CFD algorithm facilitating the accurate modeling of the fluid-structure interaction in an aneurysm. The FSI model should incorporate:
 - (a) A wall constructed of multiple layers each with different material properties,
 - (b) The heterogeneous nature of the wall, and,
 - (c) Non-linear elastic material properties of the wall.
2. Implement this fluid-structure modelling tool to assess the flow through a fusiform abdominal aortic aneurysm and assess the effects of:
 - (a) Wall mechanical properties. Previous models have not accounted for the different mechanical properties associated with the different layers of the wall,
 - (b) Heterogeneous wall stiffness. Scotti *et al.* (2005) investigated the effect of diameter-dependent wall thickness on an aneurysm. They showed a uniform thickness underestimates wall stresses by up to 77%; as such a heterogeneous wall will have significant effects on the fluid forces. The thickness of the wall

is also linked to its deformation and stiffness; heterogeneous stiffness should drastically change the onset of vortex shedding as well as altering the wave speed of the pressure pulse travelling along the walls.

(c) Heterogeneous wall stiffness in the context of aneurysm initiation.

1.8.1 Developing a new method for investigating FSI in aneurysm

This phase of the project proposes to address research aims 1a-1c. In this stage a non-linear solid solver is developed and integrated into an existing fluid solver. The arbitrary Lagrangian–Eulerian method will be used to couple the fluid and solid solvers. This method permits accurate determination of the boundary interface while providing a strong coupling of the fluid and solid dynamics equations, therefore improving on current computational practices.

Humphrey & Taylor (2008) cite the work of Wolters *et al.* (2005) as being the most advanced FSI solver currently being used in aneurysm research. Wolters *et al.* (2005) uses a neo-Hookean model for the artery wall material with large strain capabilities, an incompressible Newtonian fluid solver and physiologically accurate boundary conditions. The methodology implemented in this thesis intends to make a similar implementation but using the highly efficient spectral element method for both the fluid and the solid discretisations, as well as including the inertial term in the solid mechanics thus improving on the current investigative tools. Spectral elements have rarely been used in solid mechanics and are less common in non-linear solid mechanics. A 2-step operator splitting method with penalty function for enforcing incompressibility is proposed for solving the constitutive equations for a neo-Hookean solid. Throughout the development phase a series of validation tests will be performed to ensure the algorithms performance.

1.8.2 Investigation: Heterogeneous wall stiffness effects on established aneurysms

This investigation proposes to address the research aim 2a and 2b by answering the following questions:

How will the perianeurysmal environment affect the flow through the aneurysm?

Hypothesis: An increase in the force feedback from the perianeurysmal environment will have the same affect as a global decrease in wall stiffness. It will reduce the

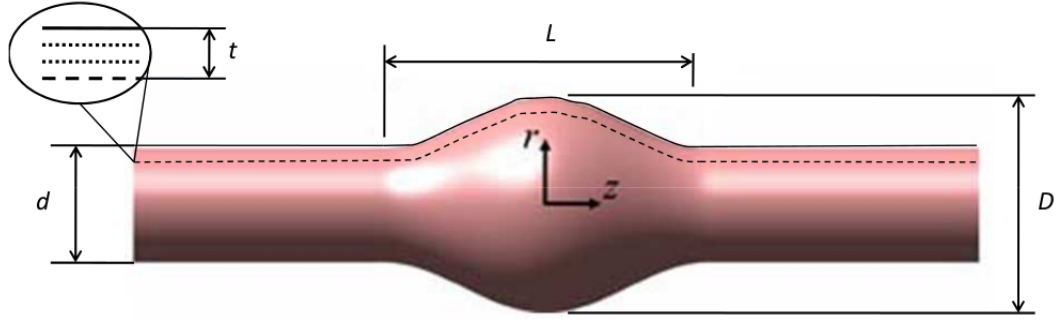


FIGURE 1.7: Aneurysm geometry for investigation. $D = 2$ cm, $d = 1$ cm and $L = 3$ cm, t may change as required.

size of areas with positive normalised wall shear stress. A stronger perianeurysmal response will mean less elastic-wall motion. Therefore the effects of the elastic-wall on the flow dynamics should be decreased. The less wall motion, the closer to the rigid-wall approximation which has been shown to underestimate wall stresses.

How will local wall stiffness affect the flow through the aneurysm?

Hypothesis: A local increase in wall stiffness will introduce secondary regions of flow separations and potentially the development of a secondary vortex ring system. A local difference in wall stiffness could lead to a localised differential in displacements causing a less smooth geometry which could act like a “backward facing step” leading to flow separation.

Is a Hookean material model for the aneurysm wall sufficient to model the wall response in Aneurysms?

Hypothesis: A hyper-elastic material law will cause the model to exhibit higher wall stress at points of greatest deformation. Conversely, subject to a given pressure, a hyper-elastic material model will predict a smaller strain or wall motion than a linear-Hookean elastic material model. This hypothesis will be addressed in chapter 6 when comparing the relative strain in a Hookean and neo-Hookean material.

For the established aneurysm investigations, the geometry modelled is a fusiform aneurysm with dimensions shown in figure 1.7.

The wall mechanical properties are chosen as per Fung (1993) to describe the mean mechanical properties of each layer in the artery wall (for detailed discussion of the choice of parameter space see chapter 7). To assess the effect of changed material

properties, the material properties of each layer are altered locally in locations at the proximal neck, distal neck and extrema of the arterial bulge.

1.8.3 Investigation: The effect of heterogeneous wall stiffness on aneurysm initiation

This investigation proposes to address the research aim 2c by answering the following questions:

How will a stiffer (or less stiff) band of arterial wall affect the flow through a straight pipe?

Hypothesis: A local stiffening of the artery wall will reduce the wall motion in that local region creating a geometry similar to a stenosis. This will cause flow recirculation and a change in the WSS patterns that could initiate aneurysm growth. A local stiffening of the material wall should physiologically mimic three scenarios:

- the effect of cell death in the arterial wall,
- the formation of plaque build up, or,
- the tethering of artery by upstream branches such as the femoral and renal artery bifurcations

Hypothesis: A local reduction in wall stiffness will lead to extra ballooning of the arterial wall. This extra bulge will change the flow dynamics and WSS distributions which could create a cascade affect.

Hypothesis: Wider stiffened regions will lead to less adverse flow conditions as the gradient of the nozzle effect or ballooning effect will be reduced.

1.9 Closure

Previous research into haemodynamics in aneurysms has largely been focused on rigid-wall dynamics. To realistically model the flow, a moving boundary condition must be applied to account for the elasticity of the aneurysm wall. A fluid-structure interaction problem will be studied in the context of an abdominal aortic aneurysm, with the effects of an elastic-wall modelled using a numerical analysis. An ALE algorithm will be employed to solve fluid-mechanics, solid-mechanics, and mesh-mechanics equations, thus allowing both fluid flows and mechanical structures to be modelled concurrently. Once formulated, the fluid-structure model will be employed to measure the haemodynamics

of flow through an aortic aneurysm with variable wall stiffness. An investigation will also be undertaken to assess the effect wall stiffness may play on aneurysm initiation.

Chapter 2

A review of continuum mechanics

In modelling the mechanical response of the arterial wall and the dynamics of blood flow a comprehensive understanding of continuum mechanics is essential. This chapter briefly summarizes the fundamental relations of the kinematics of large deformations, it outlines the balance laws that govern both fluid, and solid mechanics and alludes to the subtle differences which differentiate the Hookean, neo-Hookean and fluid dynamics constitutive models. The similarity of the governing equations presented herein provides the background that motivates the development of the time stepping algorithm for a neo-Hookean solid. This class of algorithms has previously been applied to fluid dynamics simulations. The material revised in this chapter closely follows Müller & Ferber (2008) and Bower (2009).

2.1 Introduction to continuum mechanics

All matter is inherently discontinuous. Regardless of its classification it may be decomposed and shown to comprise of distinct building blocks. Biological materials can be broken down into cells, the cells into molecules and so on. Similarly, metals and composites too can be deconstructed into a finite number of atoms, which in turn consist of finite numbers of nucleons and electrons.

Many important physical phenomena involve matter on large length and time scales. This is the case when considering fluid flows in the human body or the response of the artery wall to pressure. In these cases matter is being considered at a length scale much larger than the characteristic length of atomic spacings ($1 - 5 \text{ \AA}$) and similarly at time scales significantly larger than phonons ($1 - 10 \text{ fs}$). If the physical problem of interest occurs at length and time scales of several orders of magnitude higher than these limiting scales, it is possible to ignore these small-scale heterogeneities and to consider

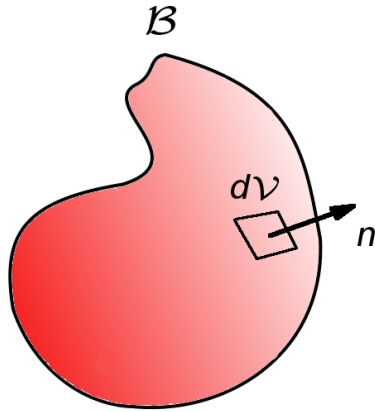


FIGURE 2.1: Arbitrary solid body \mathcal{B} .

matter as a continuous medium. A continuous medium may be conceptually defined as a finite amount of matter whose physical properties are independent of its actual size or the time over which they are measured. In terms of computational simulations of a continuous medium, the assumption of a continuum holds until the resolution of the mesh reaches length scales on the order of the atomic spacing and the solver reaches temporal resolution equivalent to phonon sizes. If one were able to resolve past this point a sudden change in the physical properties would be observed.

Mathematical theories developed for continuous media, such as the Navier–Stokes equations for fluids and the Hookean relations for solids, are phenomenological in the sense that they capture the observed physics response without directly accounting for the discrete structure of matter. The subsequent sections look at developing a mathematical equation set for which modelling both solid and fluid continua is based.

2.2 Kinematics of deformation

Let us consider a continuous body (e.g. figure 2.1), whether it be a fluid or solid, whose particles at a particular point in time occupy the region $\mathcal{B} \subset \mathbb{R}^3$. This body at this time, t_0 , may be considered to be in a certain reference placement. Each of the material particles, $P \in \mathcal{B}$ are defined by their position vectors $\mathbf{X}(P)$, which may be described without loss of generality by their components $\{X_1, X_2, X_3\}_P$ relative to an orthonormal-based $(\mathbf{E}_1, \mathbf{E}_2, \mathbf{E}_3)$ coordinate system centred at some convenient origin

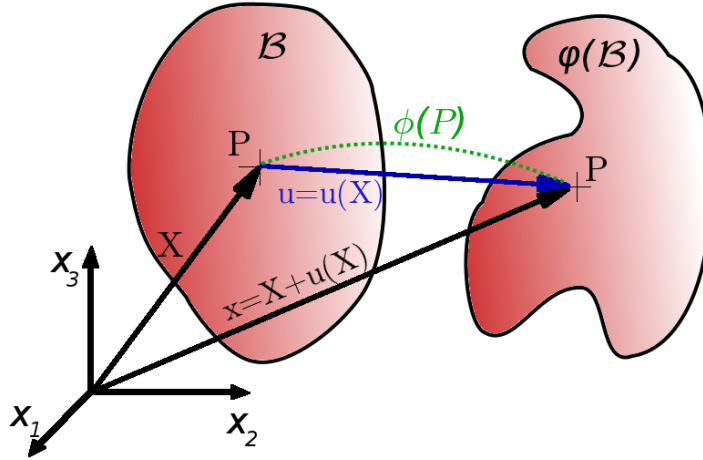


FIGURE 2.2: A representation of a deformation in the Lagrangian point of view. The deformation occurs from original coordinates X to deformed coordinates x through the mapping $\mathbf{x} = \phi(\mathbf{X})$.

O , so that in this reference configuration

$$\mathbf{X} = X_i \mathbf{E}_i.$$

This reference system will herein be referred to as the material reference frame. The reference placement of the body is arbitrarily represented in figure 2.2.

Subject to an external load, the body \mathcal{B} subsequently deforms over a period of time δt . A deformation of the body \mathcal{B} is a mapping $\phi : \mathcal{B} \rightarrow \mathbb{R}^3$ that preserves the distinctness of all points in the body; that is to say it is injective and one-to-one.

After an external force has caused a deformation to the material over time δt , the body sits in the current or deformed position described mathematically by $\phi(\mathcal{B})$ and shown in figure 2.3. Each material particle $P \in \phi(\mathcal{B})$ is now defined by its new position vector $\mathbf{x}(P)$. The components $\{x_1, x_2, x_3\}_P$ are relative to an orthonormal coordinate system $(\mathbf{e}_1, \mathbf{e}_2, \mathbf{e}_3)$ centred at o (in the deformed coordinates), in which,

$$\mathbf{x} = x_i \mathbf{e}_i.$$

This position is referred to as the spatial reference frame.

For an arbitrary point P the deformation mapping is defined as

$$x_i = \phi_i(\mathbf{X}). \tag{2.1}$$

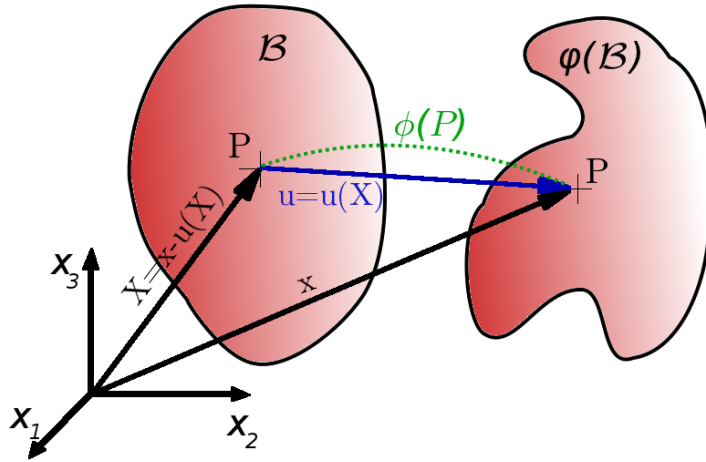


FIGURE 2.3: A representation of a deformation in the Eulerian reference frame. In this case the reference frame is in the original position x and the descriptions of the deformations must be mapped back onto it using: $\mathbf{X} = \phi^{-1}(x)$.

This deformation mapping describes for each component how the position vector changes from material to spatial coordinates through this particular deformation over this given time. Since by definition the mapping ϕ is one-to-one, the inverse of the deformation map is well defined:

$$X_i = \phi_i^{-1}(x). \quad (2.2)$$

As indicated earlier the motion of the body \mathcal{B} during a time interval $[t_1, t_2]$ may be described by the deformation mapping $\phi(x, t)$. In other words a motion is defined as a single set of parametric mappings indexed by time, describing a path or trajectory for all particles in a body,

$$\mathbf{x} = \phi_t(\mathbf{X}).$$

In describing the motion of a particle the initial and final positions of the particle may be used. Given the definitions of position described in equations 2.1 and 2.2 the spatial (or direct) motion and material (or inverse) motion of a particle must be distinguished in order to describe its displacement.

A Lagrangian reference frame is used in the case of direct motion. The position of material particles are followed from the fixed material position \mathbf{X} along the path of motion to their spatial or deformed position. If the coordinate system follows the particle, this point of view is known as the Lagrangian reference frame. In contrast to

this, the Eulerian reference frame is used if the inverse motion description is adopted. The motion of physical particles are followed through the ambient material at fixed spatial positions \mathbf{x} . In this case the coordinate system is fixed in space and the material particles are defined by their relative motion to this fixed point.

The displacement field, \mathbf{U} , for a particle relates its current (deformed) position at time, t , to its original (reference) position at time, t_0 . Using a Lagrangian reference frame the displacement field may be written

$$\mathbf{U}(\mathbf{X}, t) = \mathbf{x}(\mathbf{X}, t) - \mathbf{X}, \quad (2.3)$$

where $\mathbf{x}(\mathbf{X}, t)$ denotes the final deformed position of the particle (in material coordinates) and \mathbf{X} denotes its original position (in material coordinates). The Eulerian form of the displacement field is given by,

$$\mathbf{u}(\mathbf{x}, t) = \mathbf{x} - \mathbf{X}(\mathbf{x}, t), \quad (2.4)$$

where \mathbf{x} denotes the final deformed position of the particle (in spatial coordinates) and $\mathbf{X}(\mathbf{x}, t)$ denotes its original position (in spatial coordinates). The two definitions in equations 2.3 and 2.4 are equally valid in their respective reference frames and are shown to be related through the inverse deformation mapping,

$$\mathbf{U}(\mathbf{X}, t) = \mathbf{U}(\phi^{-1}(\mathbf{x}, t)) = \mathbf{u}(\mathbf{x}, t). \quad (2.5)$$

In formulating a mathematical model for continuum mechanics, definitions may also be required for the velocity and acceleration of the body \mathcal{B} . The instantaneous velocity of a material point in the material (Lagrangian) reference frame is

$$\mathbf{V}(\mathbf{X}, t) = \frac{\partial \phi_i}{\partial t}(\mathbf{X}, t). \quad (2.6)$$

The analogous velocity field in the Eulerian reference frame may be written

$$\mathbf{v}(\mathbf{x}, t) = \mathbf{V}(\phi(\mathbf{X}, t), t) = \frac{\partial \phi}{\partial t}(\phi^{-1}(\mathbf{x}, t), t) = (\mathbf{V} \circ \phi^{-1})(\mathbf{x}, t), \quad (2.7)$$

where $(\cdot) \circ (\cdot)$ denotes the tensor composition.

Listing the instantaneous acceleration, \mathbf{A} , of a material point at position \mathbf{X} at time t in Lagrangian coordinates,

$$\mathbf{A}(\mathbf{X}, t) = \frac{\partial \mathbf{V}_i}{\partial t}(\mathbf{X}, t), \quad (2.8)$$

and in the Eulerian reference frame, the acceleration, \mathbf{a} , of the material occupying the spatial location \mathbf{x} at time t is,

$$\mathbf{a}(\mathbf{x}, t) = \mathbf{A}(\phi(\mathbf{X}, t), t) = \frac{\partial \mathbf{V}}{\partial t}(\phi^{-1}(\mathbf{x}, t), t) = (\mathbf{A} \circ \phi^{-1})(\mathbf{x}, t). \quad (2.9)$$

Given a smooth spatial velocity field $\mathbf{v}(\mathbf{x}, t)$, the material time derivative of equation 2.9 simplifies to

$$\mathbf{a}(\mathbf{x}, t) = \frac{\partial \mathbf{v}}{\partial t}(\mathbf{x}, t) + \mathbf{v}(\mathbf{x}, t) \cdot \nabla \mathbf{v}(\mathbf{x}, t). \quad (2.10)$$

The first term of equation 2.10 describes the local acceleration of the material incident at point \mathbf{x} , the second term describes a convective acceleration field. This form of the acceleration term is particularly useful in fluid mechanics as the spatial acceleration can be determined without knowing the motion of the particles explicitly, i.e. the position vector is never determined.

The Eulerian descriptions will be used in solving the fluid mechanics equations due to the advantages described earlier. In keeping with convention the model for solid continua will be formulated using a Lagrangian reference frame.

Finally, a note on sequential deformations or transient deformations: If one chose to consider a small strain approximation then the total deformation of a body subject to subsequent deformations or analogously deformations over a series of time steps, δt , is simply the sum of the deformation maps, or alternatively a superposition of the displacement vector fields u ,

$$\phi(\mathbf{X}, t) = \phi_2(\mathbf{X}, t) + \phi_1(\mathbf{X}, t) \equiv (\phi_1 + \phi_2)(\mathbf{X}, t). \quad (2.11)$$

This is only possible because under a small strain assumption the difference between the spatial and material coordinate systems is negligible. When considering successive large deformations, e.g. figure 2.4, the total or combined deformation of the body is

$$\phi(\mathbf{X}, t) = \phi_2(\phi_1(\mathbf{X}, t), t) \equiv \phi_2 \circ \phi_1(\mathbf{X}, t). \quad (2.12)$$

The composition of deformation mappings has a multiplicative group structure in contrast with the additive structure in the superposition of small strain assumptions.

2.2.1 Kinematics of local deformations

Having defined the Lagrangian and Eulerian reference frames and their respective displacements, velocities and accelerations; attention is now paid to more fully defining the

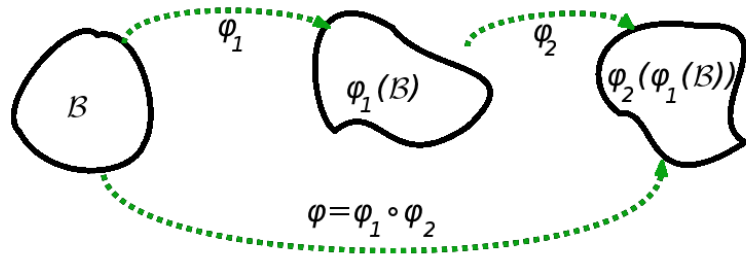


FIGURE 2.4: Composition of deformations.

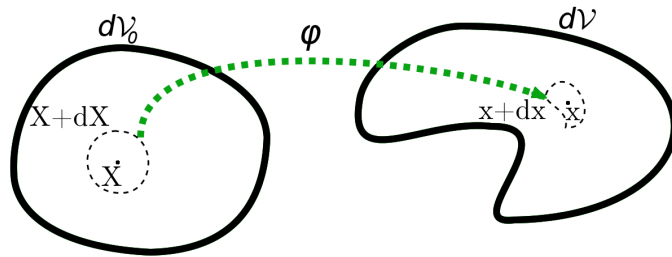


FIGURE 2.5: Local deformation of an infinitesimal material Volume dV_0 .

basis for each of these vector fields, i.e. the deformation map ϕ . In measuring the local deformation for a particular point, ϕ_i , the principle of local action is presumed valid. This principle states that the local energy density of a material point, \mathbf{X} , depends only on the state of the infinitely small volume within which the point exists.

Let $dV_0 \subset \mathcal{B}$ define the infinitely small volume containing the point \mathbf{X} in the Lagrangian material reference frame and dV be the corresponding deformed volume in the spatial coordinate. A neighbouring point must also be considered located at $\mathbf{X} + d\mathbf{X}$ but still located within the volume dV_0 . The location in the deformed spatial volume of point \mathbf{X} can be defined as \mathbf{x} similarly, a point located an infinitesimally small distance from the original point, $\mathbf{X} + d\mathbf{X}$, is located at $\mathbf{x} + d\mathbf{x}$ in the spatial coordinates (see figure 2.5). These two states may be linked with the definition of a deformation described in equation 2.1. This permits the components of $\mathbf{x} + d\mathbf{x}$ to be defined as,

$$x_i + dx_i = \phi_i(\mathbf{X} + d\mathbf{X}, t). \quad (2.13)$$

While equation 2.13 fully describes the components of the deformation for the point $\mathbf{x} + d\mathbf{x}$, it does not give any further insight into the form the deformation ϕ . In fact

the deformation may be non-linear and highly complex. In an effort to simplify the description and determine a more tangible form of the deformation, a Taylor series expansion of 2.13 at the position \mathbf{X} is used:

$$x_i + dx_i = \phi_i(\mathbf{X} + d\mathbf{X}, t) = \phi_i(\mathbf{X}, t) + \frac{\partial \phi_i}{\partial X_j}(\mathbf{X}, t) dX_j + O(d\mathbf{X}). \quad (2.14)$$

Here, X_j is the j^{th} component of the position vector \mathbf{X} in material coordinates, dX_j is similarly the change in the j^{th} component of \mathbf{X} , and $O(d\mathbf{X})$ denotes the higher order terms in the expansion. It is important to recognise that with sufficient spatial resolution, i.e. if the volume dV_0 is sufficiently small as to make $d\mathbf{X}$ small, these higher order terms will approach zero faster than $d\mathbf{X}$ and therefore these higher order terms become negligible. By neglecting these terms equation 2.14 forms a linearised differential relation which will have a unique solution,

$$x_i + dx_i \simeq x_i + \frac{\partial \phi_i}{\partial X_j}(\mathbf{X}, t) dX_j \Rightarrow dx_i = \frac{\partial \phi_i}{\partial X_j}(\mathbf{X}, t) dX_j. \quad (2.15)$$

The deformation gradient, \mathbf{F} , is now defined as

$$F_{ij}(\mathbf{X}, t) = \frac{\partial \phi_i}{\partial X_j}(\mathbf{X}, t) \Rightarrow dx_i = F_{ij}(\mathbf{X}, t) dX_j, \quad (2.16)$$

which may be written as

$$F_{ij}(\mathbf{X}, t) = \frac{dx_i}{dX_j}. \quad (2.17)$$

The deformation gradient is fundamental to non-linear continuum mechanics as it fully describes the deformation mapping at time t on an infinitesimal material region $d\mathbf{X}$ of \mathbf{x} . The final form of the deformation gradient, equation 2.17, is a two-point tensor which describes the change in the coordinate direction dx_i relative to the original coordinate system dX_j . In this way it fully describes the deformation mapping. If the original position in three-dimensional space (X_1, X_2, X_3) is considered, and the deformed position at (x_1, x_2, x_3) the expanded form of 2.17 is

$$F_{ij}(\mathbf{X}, t) = \begin{bmatrix} \frac{dx_1}{dX_1} & \frac{dx_1}{dX_2} & \frac{dx_1}{dX_3} \\ \frac{dx_2}{dX_1} & \frac{dx_2}{dX_2} & \frac{dx_2}{dX_3} \\ \frac{dx_3}{dX_1} & \frac{dx_3}{dX_2} & \frac{dx_3}{dX_3} \end{bmatrix}. \quad (2.18)$$

The kinematics described in § 2.2 suggests that in terms of making use of this deformation gradient map between initial and deformed coordinate space it may be more prudent to describe the deformation gradient in terms of displacements u_i over the time

interval rather than original positions X_i and final positions x_i . To make this change, equation 2.4 is substituted into the deformation gradient giving

$$F_{ij}(\mathbf{X}, t) = \begin{bmatrix} \frac{du_1}{dX_1} + \frac{dX_1}{dX_1} & \frac{du_1}{dX_2} + \frac{dX_1}{dX_2} & \frac{du_1}{dX_3} + \frac{dX_1}{dX_3} \\ \frac{du_2}{dX_1} + \frac{dX_2}{dX_1} & \frac{du_2}{dX_2} + \frac{dX_2}{dX_2} & \frac{du_2}{dX_3} + \frac{dX_2}{dX_3} \\ \frac{du_3}{dX_1} + \frac{dX_3}{dX_1} & \frac{du_3}{dX_2} + \frac{dX_3}{dX_2} & \frac{du_3}{dX_3} + \frac{dX_3}{dX_3} \end{bmatrix}.$$

Given $\mathbf{X} = X_i \cdot E_i$, where E_i is an orthonormal base, the terms

$$\frac{dX_i}{dX_j} = \delta_{ij},$$

where δ_{ij} is the Kronecker delta function. Thus $F_{ij}(\mathbf{X}, t)$ may be simplified to

$$F_{ij}(\mathbf{X}, t) = \begin{bmatrix} 1 + \frac{du_1}{dX_1} & \frac{du_1}{dX_2} & \frac{du_1}{dX_3} \\ \frac{du_2}{dX_1} & 1 + \frac{du_2}{dX_2} & \frac{du_2}{dX_3} \\ \frac{du_3}{dX_1} & \frac{du_3}{dX_2} & 1 + \frac{du_3}{dX_3} \end{bmatrix}. \quad (2.19)$$

Finally, before using the deformation gradient to define strain, some properties of the deformation gradient are considered. Firstly an infinitesimal material volume dV_0 of finite extent $\mathbf{X} + d\mathbf{X}$ is considered. This volume is given by the parallelepipedic product

$$dV_0 = \left(d\mathbf{X}^{(1)} \times d\mathbf{X}^{(2)} \right) \cdot d\mathbf{X}^{(3)}$$

where $\mathbf{X}^{(i)}$ are position vectors defining the extents of the volume. Similarly the corresponding volume may be defined in the deformed coordinate by,

$$\begin{aligned} dV &= \left(d\mathbf{x}^{(1)} \times d\mathbf{x}^{(2)} \right) \cdot d\mathbf{x}^{(3)} \\ &= \left(F_{1i} dX_i^{(1)} \times F_{2i} dX_i^{(2)} \right) \cdot F_{3i} dX_i^{(3)} \\ &= \det(\mathbf{F}) \left(d\mathbf{X}^{(1)} \times d\mathbf{X}^{(2)} \right) \cdot d\mathbf{X}^{(3)} \\ &= \det(\mathbf{F}) dV_0. \end{aligned} \quad (2.20)$$

Consequently the following relation holds

$$\frac{dV}{dV_0} = J(\mathbf{X}, t), \quad (2.21)$$

where

$$J(\mathbf{X}, t) = \det(\mathbf{F}(\mathbf{X}, t)) \quad (2.22)$$

is the Jacobian of the deformation. Equation 2.21 states that the ratio of the volume in the final and initial states is equal to the Jacobian and in turn the determinant of the deformation gradient. This is an important property for continuum mechanics as the enforcement of incompressibility requires the Jacobian $J = 1$. Because the deformation mappings are one-to-one and injective, it follows that the Jacobian $J(\mathbf{X}, t) \geq 1$.

2.3 Strain measures

Strain is a normalised measure of deformation, which represents the displacement of particles in the deformed configuration relative to some reference length (this is normally a length in the undeformed configuration). Different measures of strain are used throughout the literature depending on the amount of strain, the local deformation and whether large (general) strain theory or small strain theory is being applied. The engineering strain is defined as

$$\bar{\epsilon} = \frac{\ell - L}{L}, \quad (2.23)$$

where ℓ is the new length of a fibre and L is the original length. This is the most common definition for materials subject to very small deformations. It represents the total deformation of the body to which forces are being applied. Materials that are subject to large deformations such as rubbers, elastomers, and biological materials do not exhibit a simple linear relationship between stress and strain; rather the strain may vary locally through a material. This renders the engineering strain inapplicable. More complex definitions of strain such as stretch, logarithmic strain, or the Green strain are required.

The stretch ratio is a measure of normal strain of a differential line element. The fact that it is a differential line element rather than the entire length of the body implies that this is a localised strain measure. The stretch ratio may be defined in either the deformed or undeformed configuration by

$$\lambda = \frac{\ell}{L}. \quad (2.24)$$

For the special case when strains are not localised the stretch ratio may be related to the engineering strain by

$$\bar{\epsilon} = \frac{\ell - L}{L} = \lambda - 1. \quad (2.25)$$

This implies that the normal strain is zero so there is no deformation when the stretch ratio is equal to unity.

Other commonly used strain measures include the true strain, also known as logarithmic strain, Hencky strain or incremental strain. The true strain proves to be the correct measure of strain when the deformation takes place in a series of increments.

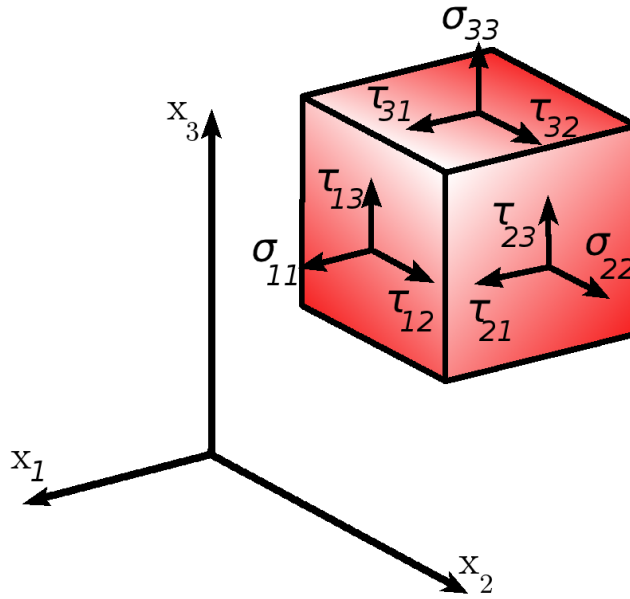


FIGURE 2.6: Differential cube of material with normal stresses σ_{ii} and shear stresses τ_{ii} shown.

The true strain is defined as

$$\begin{aligned}
 \varepsilon &= \ln\left(\frac{\ell}{L}\right) = \ln(\lambda) \\
 &= \ln(1 + \bar{e}) \\
 &= \bar{e} - \bar{e}^2/2 + \bar{e}^3/3 - \dots
 \end{aligned}
 \tag{2.26}$$

Important to the analysis of rubber-like materials such as those found in the arterial wall is the capacity to describe large deformations of the material. The correct strain measure to use to describe the total strain over a body (not localised like the stretch ratio) for a material undergoing large deformations is the Green strain. The Green strain is defined as

$$\varepsilon_G = \frac{1}{2} \left(\frac{\ell^2 - L^2}{L^2} \right) = \frac{1}{2}(\lambda^2 - 1).
 \tag{2.27}$$

Finally, the difference between normal strains and shear strains is defined. Consider a three-dimensional differential material element that undergoes an arbitrary deformation as shown in figure 2.6. Normal strains are those which act perpendicular to an element face. In a linearly elastic material they are the result of normal stresses and result in dilations. Shear strains act in the plane along a face of the differential element. While normal strains are measured by a dilation or change in length, shear strain may

be conceptualised as the change in angle between two line elements (e.g. the edge of the plane in the differential element) as a result of a given deformation. So referring to figure 2.7, for a normal strain (an engineering strain acting in the same direction of the applied force),

$$\varepsilon_x = \frac{\text{extension}}{\text{original length}} = \frac{\text{length}(ab) - \text{length}(AB)}{\text{length}(AB)} = \frac{\partial u_x}{\partial x}, \quad (2.28)$$

where u_x is the displacement in the x -direction. Defining a shear strain (γ_{xy}) is considerably more complex. Consider a single plane of the differential element shown in figure 2.6, which is redrawn in figure 2.7. The shear strain is defined as the change in angle between the lines \overrightarrow{AC} and \overrightarrow{AB} , i.e.

$$\gamma_{xy} = \alpha + \beta$$

where α is the resulting angle between the initial and deformed configurations of the line segment \overrightarrow{AB} and β is the resulting angle between the initial and deformed configurations of the line segment \overrightarrow{AC} . This is shown in figure 2.7; using a small angle approximation it can be shown that the shear stress becomes

$$\gamma_{xy} = \alpha + \beta = \frac{\partial u_y}{\partial x} + \frac{\partial u_x}{\partial y}, \quad (2.29)$$

where the subscripts u_x and u_y represent the component of the displacement vector \mathbf{u} in the x and y directions, respectively.

2.3.1 Tensor representations of strain measures

For a multidimensional strain, the strain measures outlined in § 2.3, which describe the strain in one dimension only cannot be relied upon. A two-point tensor is required to fully describe the strain in an infinitesimal body. It is critical that all tensor strain measures represent strain but vanish for rigid body rotations. This requirement imposes a symmetry on the strain tensor. With this in mind the tensor representations of the aforementioned strain measures are outlined. These include the right Cauchy–Green tensor,

$$\mathbf{C} = \mathbf{F}^T \mathbf{F} = \mathbf{U}^T \mathbf{U} = \mathbf{U}^2, \quad (2.30)$$

the left Cauchy–Green strain tensor

$$\mathbf{b} = \mathbf{F} \mathbf{F}^T, \quad (2.31)$$

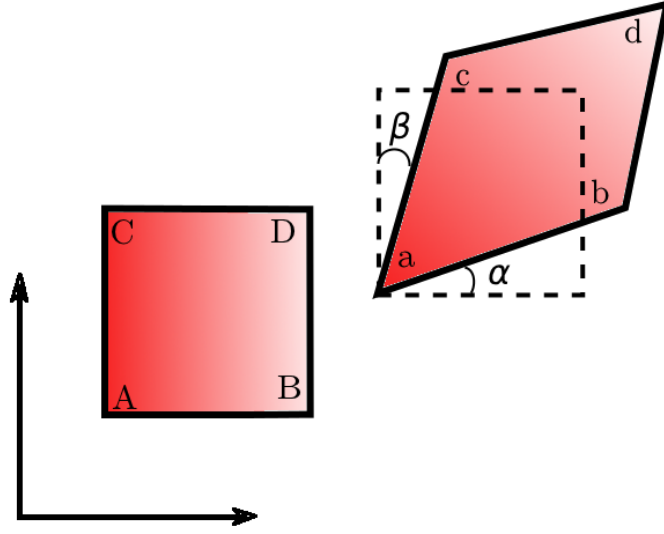


FIGURE 2.7: A shear deformation of a plane of the differential element.

and the Green–Lagrange strain tensor

$$\mathbf{E} = \frac{1}{2} (\mathbf{F}^T \mathbf{F} - \mathbf{I}), \quad (2.32)$$

where \mathbf{I} is the identity matrix. The Green–Lagrange strain tensor has the additional property of being zero for the case of zero deformation. Each of these strain tensors are equally valid for large deformations and local strains: the choice of strain tensor generally depends on the convention used in a particular branch of mechanics. The logarithmic strain for incremental applications of strain is

$$\boldsymbol{\varepsilon}_{log} = \frac{1}{2} \ln(\mathbf{C}). \quad (2.33)$$

As an example the right Cauchy–Green strain tensor is expanded using the definition of \mathbf{F} in equation 2.19

$$\mathbf{C} = \begin{bmatrix} 1 + \frac{du_1}{dX_1} & \frac{du_2}{dX_1} & \frac{du_3}{dX_1} \\ \frac{du_1}{dX_2} & 1 + \frac{du_2}{dX_2} & \frac{du_3}{dX_2} \\ \frac{du_1}{dX_3} & \frac{du_2}{dX_3} & 1 + \frac{du_3}{dX_3} \end{bmatrix} \cdot \begin{bmatrix} 1 + \frac{du_1}{dX_1} & \frac{du_1}{dX_2} & \frac{du_1}{dX_3} \\ \frac{du_2}{dX_1} & 1 + \frac{du_2}{dX_2} & \frac{du_2}{dX_3} \\ \frac{du_3}{dX_1} & \frac{du_3}{dX_2} & 1 + \frac{du_3}{dX_3} \end{bmatrix} \quad (2.34)$$

which after some expansion leaves a highly non-linear description of strain. To complete this section note that under the assumption of small strains the non-linear terms in equation 2.34 approach zero, leaving the infinitesimal strain tensor

$$\boldsymbol{\varepsilon} = \frac{1}{2} (\nabla \mathbf{u} + \nabla \mathbf{u}^T), \quad (2.35)$$

where \mathbf{u} is the displacement vector. In matrix form this strain tensor is,

$$\boldsymbol{\varepsilon} = \begin{bmatrix} \varepsilon_{xx} & \varepsilon_{xy} & \varepsilon_{xz} \\ \varepsilon_{yx} & \varepsilon_{yy} & \varepsilon_{yz} \\ \varepsilon_{zx} & \varepsilon_{zy} & \varepsilon_{zz} \end{bmatrix} = \begin{bmatrix} \varepsilon_{xx} & \frac{1}{2}\gamma_{xy} & \frac{1}{2}\gamma_{xz} \\ \frac{1}{2}\gamma_{yx} & \varepsilon_{yy} & \frac{1}{2}\gamma_{yz} \\ \frac{1}{2}\gamma_{zx} & \frac{1}{2}\gamma_{zy} & \varepsilon_{zz} \end{bmatrix}. \quad (2.36)$$

This shows the components of the strain tensor. ε_{ii} represents the normal strains described in § 2.3 and γ_{ij} the shear strains.

2.4 Stress measures

Stress is defined as a measure of the internal forces acting within a deformable body, \mathcal{B} , in response to some external loading. The external loading may be body forces such as gravity or electric fields which act at a distance and affect the entire material body, or, tractions which act as a result of contact with the body. Quantitatively the stress is the average force acting per unit area of a surface within the body on which internal forces act. The internal forces are distributed continuously throughout the body as a result of the material deformation. If the surface is coincident with an external interface upon which an external force is acting, this external force is equal to the “internal force” at this surface. The stress in a solid body is critical to failure in aneurysms. As with any solid the artery wall has a material strength represented by a yield stress. If the applied loads lead to a deformation which causes an internal stress exceeding this yield stress, permanent deformation of the material or even material rupture will occur.

By definition, the stress in deformable continua is a function of the strain. As such there are multiple definitions of the stress tensor. Broadly there are two main categories of stress, normal stresses and shear stresses. Normal forces are analogous to normal strains, (see figure 2.6), a normal stress relates the force normal to the strain plane which causes a deformation or displacement in the normal plane direction. Similarly, shear stresses are related to shear strains. A shear stress is the component of the force acting at a tangent to a strain plane which causes a shear strain. For a simple linearly elastic material for which small strains are assumed, the normal stress is simply,

$$\sigma_{avg} = \frac{\bar{F}_n}{A}, \quad (2.37)$$

where σ_{avg} is the average normal stress across the surface, \bar{F}_n is the normal force at the surface and A is the area of the surface element. Similarly, for a simple linearly elastic

material under small deformations the shear stress may be defined as

$$\tau_{avg} = \frac{\bar{F}_t}{A}, \quad (2.38)$$

where τ_{avg} is the average shear stress acting across the surface and \bar{F}_t is the component of the force acting on the surface element which is acting at a tangent to the surface. These two definitions of stress (equations 2.37 and 2.38) give the average or total stress in a body, \mathcal{B} . Generally, the composition and geometry of the material body causes a non-uniform stress distribution. Consequently the stress at a given point differs for each infinitesimal volume within the material. Cauchy developed a stress tensor, that relates the internal force felt after the deformation at a material point to the area in the deformed configuration. Under the small strain approximation this is easy as the difference between the deformed and undeformed configurations is negligible. Cauchy's theory states that the stress at any point of a body may be described by nine stress components, three orthogonal normal stresses and 6 orthogonal shear stresses: these form the Cauchy stress tensor

$$\boldsymbol{\sigma} = \begin{bmatrix} \sigma_{11} & \sigma_{12} & \sigma_{13} \\ \sigma_{21} & \sigma_{22} & \sigma_{23} \\ \sigma_{31} & \sigma_{32} & \sigma_{33} \end{bmatrix} \equiv \begin{bmatrix} \sigma_{xx} & \sigma_{xy} & \sigma_{xz} \\ \sigma_{yx} & \sigma_{yy} & \sigma_{yz} \\ \sigma_{zx} & \sigma_{zy} & \sigma_{zz} \end{bmatrix} \equiv \begin{bmatrix} \sigma_x & \tau_{xy} & \tau_{xz} \\ \tau_{yx} & \sigma_y & \tau_{yz} \\ \tau_{zx} & \tau_{zy} & \sigma_z \end{bmatrix}. \quad (2.39)$$

The similarities between equation 2.39 and equation 2.36 are evident. In each tensor, the normal stresses and strains and the shear stresses and strains are coincident. Certain invariants are associated with the stress tensor whose values do not depend upon the coordinate system chosen or the area element upon which the stress tensor operates. These are the three eigenvalues of the stress tensor, which are known as the principal stresses.

While the Cauchy stress tensor is valid for small strains, when the initial and deformed configurations are essentially the same, it does not hold when deformations are large. When a small strain approximation is not assumed, other measures of stress are required that take into account the change in configuration, in this case the First and Second Piola–Kirchhoff stress tensors must be used. The Piola–Kirchhoff tensors account for the difference in configuration by expressing the stress relative to the undeformed or initial configuration rather than the deformed configuration like the Cauchy stress. To preserve generality the Piola–Kirchhoff tensors are identical to the Cauchy stress tensor for vanishingly small deformations.

Whereas the Cauchy stress tensor, $\boldsymbol{\sigma}$, relates stresses in the deformed configuration, the deformation gradient and strain tensors are described by relating the motion to the undeformed configuration; thus not all tensors describing the state of the material are in either the undeformed or deformed configuration. The First Piola-Kirchhoff stress tensor, \mathbf{P} , relates forces in the deformed configuration with areas in the undeformed (“material”) configuration.

$$\mathbf{P} = J \boldsymbol{\sigma} \cdot \mathbf{F}^{-T} \quad (2.40)$$

where \mathbf{F} is the deformation gradient and $J = \det(\mathbf{F})$ is the Jacobian of the deformation gradient. The Second Piola-Kirchhoff stress tensor, \mathbf{S} , relates forces in the undeformed configuration to areas in the undeformed configuration. The force in the undeformed configuration is obtained via the deformation gradient mapping that preserves the relationship between the force direction and the area normal in the deformed configuration.

$$\mathbf{S} = J \mathbf{F}^{-1} \cdot \boldsymbol{\sigma} \cdot \mathbf{F}^{-T}. \quad (2.41)$$

The advantage the Second Piola-Kirchhoff has over the First is it remains constant irrespective of material orientation, this allows it to deal with rigid body rotations. One may easily transform from one stress tensor to the other using the deformation gradient. The following relationships hold:

$$\boldsymbol{\sigma} = J^{-1} \mathbf{F} \mathbf{S} \mathbf{F}^T,$$

and

$$\mathbf{P} = \mathbf{F} \mathbf{S}.$$

2.5 Balance laws

The set of balance laws for mass, linear and angular momentum, energy and entropy, form the fundamental laws of continuum mechanics. These laws form the state equations of matter, and in conjunction with a constitutive model for the stress, fully describe the continuous system. The conservation of these three primary physical quantities results in a set of equations that must be obeyed for all continua. The balance laws are generally cast in integral form derived from the consideration of the conservation of each property. The integral acts to assess that quantity over the entire body \mathcal{B} . By obeying these laws the physical quantity contained in the system may not be created or destroyed. However, it may be transferred from one part of the system to another,

or in the case of energy, from one form to another. Once formed, the global balance equations may be used to develop a specific set of field equations that are valid for the particular reference frame being used and the type of continua whether it be fluid or solid. These field equations will prove valid at all points within the body and on its boundary.

In the following sections the conservation laws for mass and momentum are outlined. The system is assumed to be at constant temperature and as such is not subject to thermodynamic effects. This allows the omission from this discussion of the conservation of entropy. Furthermore the discussion is limited to incompressible continua. With this assumption conservation of energy may be ignored as energy can only be stored in the system as kinetic energy (not potential energy). This means the energy is fully described by

$$\bar{E}(t) = \frac{1}{2} \int |\mathbf{v}|^2 d\mathbf{x},$$

where $\bar{E}(t)$ is the total energy in the system at time t , and \mathbf{v} is the velocity field. Given linear momentum is loosely described as

$$\bar{\mathbf{p}} = m \cdot \mathbf{v}, \tag{2.42}$$

where $\bar{\mathbf{p}}$ is the linear momentum, m is the mass and \mathbf{v} is the velocity field, the conservation of mass in conjunction with the conservation of momentum implies the conservation of energy (Cheskidov *et al.* 2008).

2.5.1 Conservation of mass

In the undeformed configuration the mass density per unit undeformed volume is represented by $\rho_0(\mathbf{X}, t)$. In the deformed configuration the corresponding mass density per unit deformed volume is $\rho(\mathbf{x}, t)$. Consider an infinitesimal volume $d\mathcal{V}_0$ containing the point \mathbf{X} at time t_0 which is subject to a deformation to form the new volume $d\mathcal{V}$ at time t . Given both volumes completely correspond due to the injective nature of the deformation mapping, the total mass contained in each volume $d\mathcal{V}_0$ and $d\mathcal{V}$ must be the same, i.e.

$$dm = \rho_0(\mathbf{X}, t) d\mathcal{V}_0 = \rho(\mathbf{x}, t) d\mathcal{V}. \tag{2.43}$$

Combining this relation with equation 2.21 gives the Lagrangian form of the mass balance

$$\rho_0 = J\rho. \tag{2.44}$$

The Eulerian form of the mass balance is given by

$$\frac{d\rho_0}{dt} = \rho \frac{dv_i}{dx_i}. \quad (2.45)$$

where v_i are the velocity field components and x_i is the position of the deformed configuration.

When considering an incompressible continuum the density of the continuum remains constant at all times. This means that the conservation of mass is equivalent to a conservation of volume. Under these conditions the conservation of mass, sometimes referred to as the incompressibility condition, is mathematically described by the divergence of the vector field.

$$\nabla \cdot \mathbf{v} = 0. \quad (2.46)$$

Note: This holds true for both the divergence of the displacement field and the velocity field as it is independent of time.

2.5.2 Conservation of momentum

The total linear momentum, $\bar{\mathbf{p}}$, of a body in the deformed configuration is

$$\bar{\mathbf{p}} = \int_{\mathcal{B}} \rho_0 \mathbf{V} d\mathcal{V}, \quad (2.47)$$

where \mathbf{V} denotes the material velocity, \mathcal{V} denotes the material volume and ρ_0 the initial material density.

In an isolated system (one in which external forces are absent) the total momentum will be constant; this is implied by Newton's first law of motion. Newton's third law of motion is the law of reciprocal actions, which dictates that the forces acting between systems are equal in magnitude, but opposite in sign. This law is a product of the conservation of momentum. The applied forces, $\bar{\mathbf{F}}$, may be broken down into body forces $\bar{\mathbf{B}}$ and tractions on the surface so that

$$\bar{\mathbf{F}} = \int_{\mathcal{B}} \rho_0 \bar{\mathbf{B}} d\mathcal{V} + \int_{\mathcal{S}} \rho_0 \mathbf{P} \cdot \underline{\mathbf{n}} d\mathcal{S}, \quad (2.48)$$

where \mathcal{S} is the surface of the body \mathcal{B} , \mathbf{P} is the First Piola–Kirchhoff stress tensor and $\underline{\mathbf{n}}$ is the surface outward unit normal. By applying Newton's second law of motion

$$\frac{d\bar{\mathbf{p}}}{dt} = \bar{\mathbf{F}},$$

and using equation 2.42, the force balance equations are

$$\int_{\mathcal{B}} \rho_0 \mathbf{A} d\mathcal{V} = \int_{\mathcal{B}} \rho_0 \bar{\mathbf{B}} d\mathcal{V} + \int_{\mathcal{S}} \rho_0 \mathbf{P} \cdot \underline{\mathbf{n}} d\mathcal{S}, \quad (2.49)$$

where \mathbf{A} is the material acceleration defined in equation 2.8. As in the conservation of mass discussion, the assumption of an incompressible continuum is enforced. Gauss' divergence theorem is then used to express 2.49 as

$$\int_{\mathcal{B}} (\rho_0 (\mathbf{A} - \bar{\mathbf{B}}) - \nabla \cdot \mathbf{P}) \, d\mathcal{V} = 0. \quad (2.50)$$

This balance equation applies for all subsets of the body \mathcal{B} . Thus the integrand must also equal zero, and therefore the Lagrangian form of the linear momentum balance is

$$\rho_0 \mathbf{A} = \rho_0 \bar{\mathbf{B}} + \nabla \cdot \mathbf{P}. \quad (2.51)$$

In the Eulerian reference frame

$$\rho \mathbf{a} = \rho \bar{\mathbf{b}} + \nabla \cdot \boldsymbol{\sigma}, \quad (2.52)$$

where \mathbf{a} is the Eulerian acceleration defined in equation 2.9, $\bar{\mathbf{b}}$ are the body forces in the Eulerian frame of reference and $\boldsymbol{\sigma}$ is the Cauchy stress tensor.

2.5.3 General balance equations

In this section a Schottky system is considered. A Schottky system such as the one depicted in figure 2.8 is a generic material domain $\Omega(t)$ which exchanges heat, power and material with its surrounding environment. The Schottky system can be considered an extension of the previously defined body, \mathcal{B} , of constant mass. By considering the generic Schottky system a set of general balance equations may be derived. These balance equations may be applied to any continua regardless of the principal quantity (displacement for solids and velocity for fluids) that is specific to each continuum category.

Let $\Upsilon(\mathbf{x}, t)$ be the generic extensive quantity of the Schottky system. Again, it must be reiterated that this may be a displacement, velocity or some other scalar quantity which forms the basis for describing the deformation of that system. A change in Υ may occur in three ways. Υ may change due to addition from a source within the volume, which will be denoted as \prod^Υ . It may change through a supply \sum^Υ from outside the system, or via an outward flux, \mathbf{J}^Υ , over the boundaries of the volume Ω . These are used to construct the generic form of a global balance equations

$$\begin{aligned} \frac{d\Upsilon}{dt} &= \frac{d}{dt} \int_{\Omega(t)} \rho \Upsilon(\mathbf{x}, t) \, d\mathcal{V} \\ &= - \int_{d\Omega(t)} \mathbf{J}^\Upsilon(\mathbf{x}, t) \cdot \underline{\mathbf{n}} \, d\mathbf{S} + \int_{\Omega(t)} \left(\prod^\Upsilon(\mathbf{x}, t) + \sum^\Upsilon(\mathbf{x}, t) \right) \, d\mathcal{V}, \end{aligned} \quad (2.53)$$

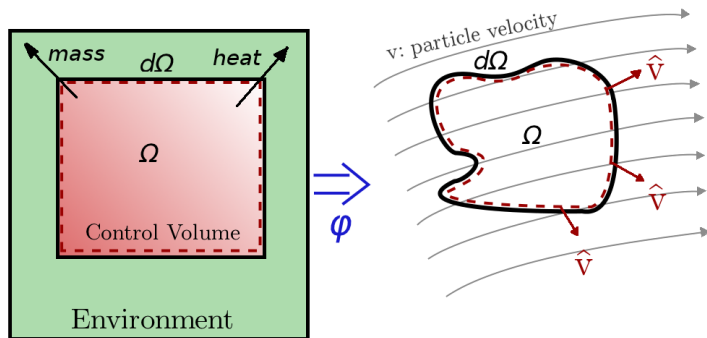


FIGURE 2.8: Generic Schottky system Ω with boundary $\partial\Omega$, velocity $\hat{\mathbf{v}}$ and particle velocity \mathbf{v} .

where \mathbf{n} is the unit vector normal to the boundary $\partial\Omega$, $\mathbf{S} \equiv \partial\Omega$ and $\rho\Upsilon$ are the quantity $\Upsilon(\mathbf{x}, t)$ per unit volume.

If the entire body, \mathcal{B} , is chosen as the system, Ω , so no particle transfer occurs over the boundary, $\partial\Omega$, then the mass in the system is conserved and the general balance equation 2.53 becomes

$$\frac{d}{dt} \int_{\Omega(t)} \rho(\mathbf{x}, t) d\mathcal{V} = 0. \quad (2.54)$$

This special case of the general balance equation is found by modelling the Schottky system as closed and setting $\Upsilon \equiv 1$, $\mathbf{J}^\Upsilon = \mathbf{\Pi}^\Upsilon = \mathbf{\Sigma}^\Upsilon \equiv 0$. If alternately the system is considered to be open and a constant volume which is moving through space (e.g. figure 2.8) with velocity $\hat{\mathbf{v}}$ and material particles move through the control volume with speed v then

$$\frac{d}{dt} \int_{\Omega(t)} \rho\Upsilon(\mathbf{x}, t) d\mathcal{V} = - \int_{\partial\Omega(t)} \mathbf{J}^\Upsilon(\mathbf{x}, t) d\mathbf{S},$$

where the flux of the quantity Υ is given by the relative velocity for the particles to the system

$$\mathbf{J}^\Upsilon = \rho(\mathbf{v} - \hat{\mathbf{v}}).$$

Note that if the domain Ω and the body \mathcal{B} are fully coincident then $\mathbf{v} = \hat{\mathbf{v}}$. The consideration of such a system becomes important later in this thesis for consideration of an arbitrary Lagrangian–Eulerian reference frame.

Using the Reynolds transport theorem and Gauss' divergence theorem the generic local form of the balance equations is obtained (i.e. true at any material point not just

over the entire domain),

$$\frac{\partial \rho \Upsilon}{\partial t} + \nabla \cdot (\hat{\mathbf{v}} \rho \Upsilon + \mathbf{J}^\Upsilon) = \prod^\Upsilon + \sum^\Upsilon. \quad (2.55)$$

To close this discussion the values of Υ , \mathbf{J}^Υ , \prod^Υ and \sum^Υ are outlined that give the mass and momentum balance equations.

For the conservation of mass, the principal quantity is $\Upsilon \equiv 0$, $\mathbf{J}^1 \equiv (\mathbf{v} - \hat{\mathbf{v}})$, $\prod^1 \equiv 0$ and $\sum^1 \equiv 0$, resulting in equation 2.54.

For the conservation of momentum, the principal quantity is

$$\Upsilon \equiv \mathbf{v},$$

where \mathbf{v} is the particle velocity,

$$\mathbf{J}^v \equiv (\mathbf{v} - \hat{\mathbf{v}}) \mathbf{v} - \boldsymbol{\sigma}^T,$$

where $\boldsymbol{\sigma}$ is the stress tensor in the relevant coordinate system,

$$\prod^v \equiv 0$$

and

$$\sum^v \equiv \rho \bar{\mathbf{b}},$$

where $\bar{\mathbf{b}}$ is any body forces being applied to the system in an Eulerian reference frame.

Substitution of these quantities into equation 2.55 yields

$$\rho \frac{\partial \mathbf{v}}{\partial t} + \nabla \cdot (\mathbf{v}^2) = \nabla \cdot \boldsymbol{\sigma}^T + \rho \bar{\mathbf{b}}. \quad (2.56)$$

Expanding the $\nabla \cdot \mathbf{v}^2$ term gives

$$\rho \frac{\partial \mathbf{v}}{\partial t} + \mathbf{v}^T (\nabla \cdot \mathbf{v}) + (\mathbf{v} \cdot \nabla) \mathbf{v}^T = \nabla \cdot \boldsymbol{\sigma}^T + \rho \bar{\mathbf{b}}.$$

If an incompressible material is considered the incompressibility condition can be enforced by substituting equation 2.46 into the second term, giving

$$\rho \frac{\partial \mathbf{v}}{\partial t} + (\mathbf{v} \cdot \nabla) \mathbf{v}^T = \nabla \cdot \boldsymbol{\sigma}^T + \rho \bar{\mathbf{b}} \quad (2.57)$$

The left hand side of equation 2.57 is easily recognisable as the acceleration in the Eulerian reference frame from equation 2.9. Equations 2.57 and 2.46 are the general governing equations for an incompressible continuum in an Eulerian reference frame.

Eulerian reference frames are typically used in fluid mechanics; conversely, solid mechanics typically use a Lagrangian reference frame. Rewriting equations 2.57 and 2.46 in a Lagrangian reference frame is as simple as changing the Eulerian description of the acceleration to the Lagrangian and replacing body forces in the Eulerian frame with those in the Lagrangian. In this case the governing equations for an incompressible material in the Lagrangian reference frame are

$$\begin{aligned}\rho \frac{\partial \mathbf{V}}{\partial t} &= \nabla \cdot \boldsymbol{\sigma}^T + \rho \bar{\mathbf{B}}, \\ \nabla \cdot \mathbf{V} &= 0.\end{aligned}\tag{2.58}$$

The set of equations 2.46, 2.57 and 2.58 form the equations of state for a continuous system. These relations must be obeyed both globally and locally within a continuous body \mathcal{B} . To form the set of governing equations for a particular type of continuum (e.g. a fluid, elastic solid or hyperelastic solid), one needs only to determine which frame of reference, Lagrangian or Eulerian, to solve the system in and to define the stress tensor $\boldsymbol{\sigma}$. The definition of the stress tensor for a particular continuum is determined by its constitutive equations: this is the subject of the next section.

2.6 Constitutive Equations

Section 2.2 developed the kinematic equations necessary to describe the motion and deformation of a body. Section 2.5 used these relations to build the differential equations of state that determine the time evolution of the primary vector fields. Combined these mathematical constructs do not form a closed system of equations because they fail to distinguish one material from another. This section outlines the constitutive laws required to specify the material behaviour by forming a definition of the stress, $\boldsymbol{\sigma}$, in terms of a strain measure in the material.

A constitutive model is a relation between two physical quantities that is specific to a material or substance and approximates the response of that material to external forces. Some constitutive models are derived from first principles but largely they are phenomenological, being based on observations and generalizations. Given the material dependence of the constitutive relations and the plethora of material categories that exist this discussion is limited to an incompressible fluid, an elastic Hookean solid and a hyperelastic neo-Hookean solid. At the conclusion of this section a relationship for the stress, $\boldsymbol{\sigma}$, for each material type will be formed to complete the set of governing equations.

2.6.1 Strain energy density, W

The strain energy density function $W(\mathbf{F})$ is a function that relates the energy formed by a strain on the material, i.e. the result of a deformation, to the deformation gradient. It is analogous to the work done on the material to cause the deformation. The work done by a particular deformation described by the deformation gradient \mathbf{F} along a certain path Γ is

$$Work = \int_{t_1}^{t_2} \mathbf{P}(t) \cdot \mathbf{F}(t) dt \quad (2.59)$$

where \mathbf{P} is the First Piola–Kirchhoff stress. A material is said to be elastic if the work done to cause the deformation is path independent. All materials considered herein will be considered elastic, isotropic and isothermal. The definition of elasticity implies for any deformation path the strain energy density W is of the form

$$W(\mathbf{F}) = \int_{\Gamma} \mathbf{P} d\mathbf{F}. \quad (2.60)$$

This definition clearly states the strain energy density is a function of the deformation only. Equation 2.60 may be rearranged to give an expression for the First Piola–Kirchhoff stress tensor,

$$P_{ij}(\mathbf{F}) = \frac{\partial W}{\partial F_{ij}}(\mathbf{F}). \quad (2.61)$$

To complete this section definitions of the Cauchy stress tensor and Second Piola–Kirchhoff stress tensors are provided in terms of the strain energy function, as well as some alternate identities based on the use of a strain measure rather than the deformation gradient. Note, that these are completely analogous with equation 2.61. The Cauchy stress tensor, $\boldsymbol{\sigma}$, is

$$\boldsymbol{\sigma} = \frac{1}{J} \mathbf{F}^T \frac{\partial W}{\partial \mathbf{F}^T}, \quad (2.62)$$

where J is the Jacobian of the deformation gradient. The Second Piola–Kirchhoff stress tensor, \mathbf{S} , is

$$\mathbf{S} = \frac{\partial W}{\partial \mathbf{F}^T} = \frac{\partial W}{\partial \mathbf{E}} = 2 \frac{\partial W}{\partial \mathbf{C}}, \quad (2.63)$$

where \mathbf{E} is the Green–Lagrange strain tensor and \mathbf{C} is the right Cauchy–Green tensor.

2.6.2 Hookean materials

A Hookean material is a special case of elastic isotropic materials which has a simple linear relationship between stress and strain. If a uni-axial tensile test is conducted on almost any material, and the stress levels are kept sufficiently low, the following behaviour will be observed (Bower 2009):

- The specimen deforms reversibly: If you remove the loads, the solid returns to its original shape.
- The strain in the specimen depends only on the stress applied to it. It does not depend on the rate of loading, or the history of loading.
- For most materials, the stress is a linear function of strain. Because the strains are small, this is true whatever stress measure is adopted (Cauchy stress or nominal stress), and is true whatever strain measure is adopted (Lagrange strain or infinitesimal strain).
- For most, but not all, materials, the material has no characteristic orientation. Thus, if you cut a tensile specimen out of a block of material, the stress-strain curve will be independent of the orientation of the specimen relative to the block of material. *Such materials are said to be isotropic.*
- If you heat a specimen of the material, increasing its temperature uniformly, it will generally change its shape slightly. If the material is isotropic (no preferred material orientation) and homogeneous, then the specimen will simply increase in size, without shape change.

Such a material is referred to as a Hookean material, it obeys Hooke's law,

$$\boldsymbol{\sigma} = \langle 4 \rangle \mathbb{C} \boldsymbol{\varepsilon}, \quad (2.64)$$

where $\boldsymbol{\varepsilon}$ is the infinitesimal strain measure, $\boldsymbol{\sigma}$ is the Cauchy stress and $\langle 4 \rangle \mathbb{C}$ is a linear four-point tensor relating the two. One of the major assumptions in Hooke's law is that the deformation is small, which is why the infinitesimal strain tensor and the Cauchy stress are used. The deformed configuration is assumed to be the same (within error) as the initial configuration. The strain energy density for the Hookean material is

$$W(\boldsymbol{\varepsilon}) = \frac{\lambda_L}{2} [\text{tr}(\boldsymbol{\varepsilon})]^2 + \mu_L \text{tr}(\boldsymbol{\varepsilon}^2), \quad (2.65)$$

where $\text{tr}(\cdot)$ denotes the trace of a tensor, μ_L and λ_L are Lamé coefficients defined by

$$\lambda_L = \frac{Ev}{(1+\nu)(1-2\nu)}, \quad \mu_L = \frac{E}{2(1+\nu)} \quad (2.66)$$

and E is a measure of the material stiffness, the Young's modulus, and

$$\nu = \frac{\epsilon_t}{\epsilon_L} \quad (2.67)$$

is the Poisson ratio in which ϵ_t is the transverse component of strain and ϵ_L is the longitudinal component of strain.

By applying the differential in equation 2.62 the Cauchy stress can be determined. The derivative of a function with respect to a tensor is conducted relative to the principal invariants of the tensor, for a detailed description of this the reader is directed to Synge *et al.* (1978). The Cauchy stress for a Hookean solid becomes,

$$\boldsymbol{\sigma} = \lambda_L \text{tr}(\boldsymbol{\varepsilon}) \mathbf{I} + 2\mu_L \boldsymbol{\varepsilon}, \quad (2.68)$$

where \mathbf{I} is the identity matrix. Using the definition of the infinitesimal strain tensor $\boldsymbol{\varepsilon}$ given in equation 2.35, the Cauchy stress tensor in extended form is,

$$\boldsymbol{\sigma} = \begin{bmatrix} \sigma_{11} & \sigma_{12} & \sigma_{13} \\ \sigma_{21} & \sigma_{22} & \sigma_{23} \\ \sigma_{31} & \sigma_{32} & \sigma_{33} \end{bmatrix}, \quad (2.69)$$

where

$$\begin{aligned} \sigma_{11} &= \lambda_L \left(\frac{du_1}{dx_1} + \frac{du_2}{dx_2} + \frac{du_3}{dx_3} \right) + 2\mu_L \frac{du_1}{dx_1} \\ \sigma_{22} &= \lambda_L \left(\frac{du_1}{dx_1} + \frac{du_2}{dx_2} + \frac{du_3}{dx_3} \right) + 2\mu_L \frac{du_2}{dx_2} \\ \sigma_{33} &= \lambda_L \left(\frac{du_1}{dx_1} + \frac{du_2}{dx_2} + \frac{du_3}{dx_3} \right) + 2\mu_L \frac{du_3}{dx_3} \\ \sigma_{12} &= \sigma_{21} = \mu_L \left(\frac{du_1}{dx_2} + \frac{du_2}{dx_1} \right) \\ \sigma_{13} &= \sigma_{31} = \mu_L \left(\frac{du_1}{dx_3} + \frac{du_3}{dx_1} \right) \\ \sigma_{23} &= \sigma_{32} = \mu_L \left(\frac{du_2}{dx_3} + \frac{du_3}{dx_2} \right). \end{aligned} \quad (2.70)$$

With an expression for the Cauchy stress in terms of the primary variables, and the displacement \mathbf{u} , equation 2.69 can be substituted into equation 2.58 to form the final form of the governing equations for a Hookean material. The Lagrangian reference frame is used widely in solid mechanics, and in keeping with convention it is chosen here. Note that the time derivative on the left hand side of 2.58 becomes a second derivative because the primary variable is a displacement, not a velocity. The governing equation for a Hookean material is

$$\begin{aligned} \rho \frac{\partial^2 \mathbf{u}}{\partial t^2} &= \nabla \cdot (\lambda_L \text{tr}(\boldsymbol{\varepsilon}) \mathbf{I} + 2\mu_L \boldsymbol{\varepsilon}^T) + \rho \bar{\mathbf{B}} \\ &= \hat{\mathbf{L}}(\mathbf{u}) + \rho \bar{\mathbf{B}}, \end{aligned} \quad (2.71)$$

where $\hat{\mathbf{L}}(\mathbf{u})$ is a linear derivative operator, which contains a combination of derivatives. Equation 2.71 fully describes the state of any point within a Hookean material subject to an external load. A Hookean material does not require a conservation of mass equation as this is inherent in the Hookean constitutive model through the Poisson ratio. A Poisson ratio of $\nu = 0.5$ gives a completely incompressible material.

2.6.3 Neo-Hookean materials

Organic materials and rubber-like materials require a more sophisticated constitutive model than the Hookean model. Features of the behaviour of a solid rubber or biological material include (Bower 2009):

- The material is close to ideally elastic. i.e. (i) when deformed at constant temperature or adiabatically, stress is a function only of current strain and independent of history or rate of loading, (ii) the behaviour is reversible: no net work is done on the solid when subjected to a closed cycle of strain under adiabatic or isothermal conditions.
- The material strongly resists volume changes. The bulk modulus (the ratio of volume change to hydrostatic component of stress) is comparable to that of metals or covalently bonded solids;
- The material is very compliant in shear. Shear modulus is in the order of 10^{-5} times that of most metals;
- The material is isotropic, its stress-strain response is independent of material orientation.
- The shear modulus is temperature dependent. The material becomes stiffer as it is heated, in sharp contrast to metals.

The structure of these materials allows very large strains, up to 400% in some materials. Experimental stress testing has shown that they exhibit a non-linear stress-strain relationship (Di Martino *et al.* 2001). Examples of this can be seen in figure 1.6. The non-linearity of the material is due to both the complex structure of the material absorbing stresses at different strain levels and the large deformations which it is undertaking. The neo-Hookean material model captures the non-linearity which results

from the large deformations experienced by the material. To assure incompressibility the strain energy function takes the form,

$$W^{incompressible} = W(\mathbf{C}) + P(\det(\mathbf{F}) - 1), \quad (2.72)$$

where \mathbf{C} is the right Cauchy–Green strain tensor and P is a Lagrange multiplier introduced to enforce the incompressibility condition,

$$\det(\mathbf{F}) = 1.$$

The physical interpretation of this pressure is a hydrostatic pressure in the solid. The strain energy density for a neo-Hookean material is given by

$$W^{incompressible}(\mathbf{C}) = \frac{G}{2}(I_1^C - 3) + p(\det(\mathbf{F}) - 1), \quad (2.73)$$

where G is the shear modulus of the material and I_1^C is the first invariant of the right Cauchy–Green strain tensor. As a neo-Hookean material takes into account the finite strains, the First Piola–Kirchhoff stress tensor is required to describe the relations. By substituting equation 2.73 into equation 2.61 and again utilising tensor calculus, the stress term for a neo-Hookean material is

$$\mathbf{P} = \mathbf{F}^{-T} p \mathbf{I} + G \nabla^2 \mathbf{u}, \quad (2.74)$$

Again, this relation is substituted into equation 2.58 to form the governing equations for an incompressible neo-Hookean material in the Lagrangian reference frame,

$$\begin{aligned} \rho \frac{\partial^2 \mathbf{u}}{\partial t^2} &= G \nabla^2 \mathbf{u} + \mathbf{F}^{-T} p \mathbf{I} + \rho \bar{\mathbf{B}}, \\ \nabla \cdot \mathbf{u} &= 0. \end{aligned} \quad (2.75)$$

Equation 2.75 holds many similarities to the Hookean governing equation 2.71. Both are cast in the Lagrangian reference frame, both have displacement, \mathbf{u} , as their primary variable and as such a second-order temporal term for the right hand side acceleration and both have a linear operator acting on \mathbf{u} on the left hand side. For the neo-Hookean material, $\hat{\mathbf{L}}(\cdot) \equiv \nabla^2$. The incompressible neo-Hookean also requires the hydrostatic pressure term and the mass conservation term to enforce incompressibility and to complete the set of equations.

2.6.4 Fluids

A fluid is a continuum that continually deforms under an applied shear stress. Fluids are a subset of matter that include liquids, gases, plasmas and, to some extent, plastic

solids. In this thesis, an incompressible Newtonian fluid is modelled. A Newtonian fluid implies a linear relationship between shear stress and strain rate. The shear stress is given by

$$\boldsymbol{\tau} = \mu (\nabla \mathbf{v} + \nabla \mathbf{v}^T), \quad (2.76)$$

where $\boldsymbol{\tau}$ is the shear stress, \mathbf{v} is the velocity field, and μ is the fluid viscosity. This is analogous to the time derivative of the infinitesimal strain tensor. The total stress tensor for a fluid includes a pressure term to enforce incompressibility and is given by,

$$\boldsymbol{\sigma} = -P\mathbf{I} + \mu (\nabla \mathbf{v} + \nabla \mathbf{v}^T) \quad (2.77)$$

where P is the pressure.

Due to the large deformations common in fluid mechanics, an Eulerian reference frame is used. By substituting the stress (equation 2.77) into the Eulerian form of the generalised balance equation 2.57, the Navier–Stokes equations are recovered. These govern time-dependent fluid flows,

$$\begin{aligned} \frac{\partial \mathbf{v}}{\partial t} + (\mathbf{v} \cdot \nabla) \mathbf{v} &= -\nabla P + \nu \nabla^2 \mathbf{v} + \rho \bar{\mathbf{B}}, \\ \nabla \cdot \mathbf{v} &= 0 \end{aligned} \quad (2.78)$$

where ν is the kinematic viscosity, P is the total kinematic pressure and \mathbf{v} is the velocity. The $\frac{\partial \mathbf{v}}{\partial t}$ term is known as the inertial term and represents the local temporal acceleration of the material.

The $(\mathbf{v} \cdot \nabla) \mathbf{v}$ term is known as the advection term and describes a convective acceleration field. Convective acceleration is the effect of time-independent acceleration of a fluid with respect to space. The convective acceleration of the flow field is a spatial effect, one example is a fluid speeding up in a contracting nozzle.

The $-\nabla P$ term is known as the pressure term and accounts for the isotropic components of stress arising from normal stresses. When modelled with the conservation of mass equation 2.46, the pressure term enforces the incompressibility of the system.

The $\nu \nabla^2 \mathbf{v}$ term is known as the diffusion term. This term arises from the anisotropic terms in the stress tensor. Diffusion describes the spread of particles through random motion from regions of higher velocity to regions of lower velocity.

Finally, the $\rho \bar{\mathbf{B}}$ term accounts for any body forces experienced by the material. Such forces may include gravity or the action of magnetic fields in charged fluids.

To close this section the similarity between the Navier–Stokes equations 2.78 and the incompressible neo-Hookean governing equation 2.75 is considered. In each equation

there is a pressure gradient term, a Laplacian diffusion term, a body forces term and an inertial term. The only difference between these sets of equation is the convective acceleration term which arises from the use of an Eulerian reference frame rather than a Lagrangian reference frame. The similarity is hardly surprising given both materials are continua. The similarity stimulates the notion of using a similar computational method to solve for the mechanics of each kind of material. Such a method will be outlined in chapter 4.

2.7 Closure

In this chapter, a review is presented describing how the governing equations for continuum mechanics are derived from first principles. For any continuum the change in a body is fully described by a deformation mapping. This deformation mapping can be used in either the Lagrangian or the Eulerian reference frame to describe displacements, velocities, accelerations and measures of strain such as the Green–Lagrange strain tensor. These form the fundamental basis through which a change in a system can be described.

Considering a continuous body as part of a system that interacts with its surrounding environment the conservation of mass and conservation of momentum equations in general form were derived. These equations form the equations of state for a continuous system and describe how the system changes in time.

Finally a description of the constitutive models for various materials were formed and substituted into the state equations to fully describe different continuous systems such as the Hookean and neo-Hookean solids and the incompressible Navier–Stokes equations for fluids.

Moving forward, the significance of the similarity in the Navier–Stokes and neo-Hookean equations is recognised. Many of the terms are identical, which should permit a similar numerical algorithm to be used to solve both the fluid and solid equations. Perhaps the reason for the similarity comes down to the initial premise of this chapter, i.e. both fluids and solids are examples of continua, for which the equations of state are identical. Different constitutive models (and in turn a different primary variable, displacement rather than velocity), is all that separates the two systems.

Chapter 3

The arbitrary Lagrangian–Eulerian method

This chapter serves to introduce the background mathematics of an Arbitrary Lagrangian–Eulerian (ALE) method (§ 3.1-3.4), describe the different types of ALE implementations that have previously been used (§ 3.5) and present the new implementation that has been developed in this thesis (§ 3.5.1). The mathematical framework reviewed in this chapter closely follows the works of both Hirt *et al.* (1974) and Donea *et al.* (2004).

3.1 Introduction

Large deformations of continua pose a significant problem for numerical simulations. Lagrangian descriptions subject to large deformations suffer from element skew which can reduce the accuracy of a solver. Eulerian reference frames are bound by tight time step restrictions when modeling large deformations. Accurate numerical investigations of fluid-structure interactions and non-linear solid mechanics often requires coping with strong distortions of the continua while maintaining precise information of the free surface or the fluid-structure interface.

In chapter 2 the two classical descriptions of motion, the Lagrangian and Eulerian, were described. Algorithms of continuum mechanics usually make use of one of these descriptions by solving the governing equations for the continuum with respect to a reference frame or mesh which is either Lagrangian or Eulerian (see, for instance Malvern 1969). The ALE description was developed in order to combine the advantages of each classical frame of reference while minimizing their weaknesses.

Original developers included Noh (1963), Franck & Lazarus (1964), and Trulio (1966), but perhaps the greatest contribution came from Hirt *et al.* (1974); this last

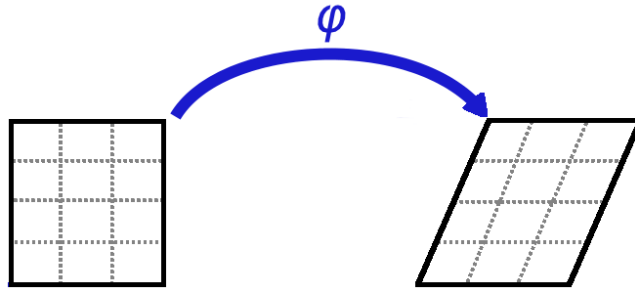


FIGURE 3.1: Lagrangian description of motion. The Lagrangian reference frame (depicted by the dashed mesh) is fixed to the deforming material and deforms with it.

contribution was reprinted in 1997. Subsequent to the development of the ALE method was its implementation. It was adopted in finite element codes in work by Donea *et al.* (1977), Belytschko & Kennedy (1978), Belytschko *et al.* (1980), and Hughes *et al.* (1981). Since then it has been widely used in many applications, including free surface flows, fluid-structure interactions, and non-linear solid mechanics.

In solid mechanics, the Lagrangian reference frame is most commonly used. Lagrangian algorithms force each individual node of the computational mesh to follow the material particle it is associated with during the deformation (see Figure 3.1). The benefits of using a Lagrangian description is it allows convenient tracking of the free surface; or in structural interactions, the interface between fluids and structures. While accurate boundary tracking is critical to the accuracy of fluid-structure interactions in aneurysms, the Lagrangian reference frame is not without its limitations. It is unable to follow large distortions of the material as this results in high levels of skew in the computational mesh. Numerically, skew introduces large errors into the solution. This occurs because the accuracy of the mapping from a regular shaped standard domain to the realistic element shape is compromised. The accuracy of the quadrature used to solve the equations over the elemental domain rely on accurately placed quadrature nodes. Skew reduces the accuracy of the solver and eventually leads to divergence because of invalidated elements (singularities in the mapping functions) or extreme Courant–Friedrichs–Lewy conditions.

In fluid dynamics, the Eulerian reference frame is almost exclusively used. Eulerian algorithms separate the computational mesh from the continuum; the mesh is fixed in

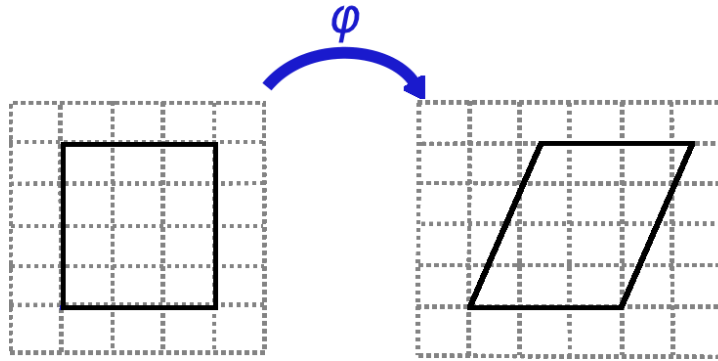


FIGURE 3.2: Eulerian description of motion. The Eulerian reference frame (depicted by the dashed mesh) is fixed in space and the material deforms independently of the mesh.

space and the continuum is free to move with respect to the grid (see Figure 3.2).

The advantages of an Eulerian description is it can handle large deformations of the continuum with ease, simply restricting the time step allows arbitrary deformations to be computed. However, the Eulerian reference frame has its drawbacks: figure 3.3 shows the interface between two continuous media on a finite element mesh. When mesh nodes are coincident with the interface the position of the interface is accurately determined. However, when the interface lies within an element, the exact location of the interface is not known, it is located with some uncertainty between grid points.

The ALE technique was developed as a compromise whereby the best features of the Lagrangian and Eulerian descriptions are combined so that an algorithm can handle large deformations while still maintaining accurate information about the location of boundaries and interfaces. In the ALE description, the nodes of the computational mesh are permitted to move with the continuum in the normal Lagrangian fashion (allowing accurate interface information), or be held fixed in an Eulerian manner (to handle large deformations). Later implementations allowed the mesh to be moved in an arbitrary fashion which gives a continuous rezoning capability.

The freedom to move the computational mesh allows greater distortions of the continuum to be modelled while accurately resolving free surfaces or material interfaces. To demonstrate the advantages of an ALE formulation, Donea *et al.* (2004) offer the example of using a coarse finite element mesh to model the detonation of an explosive charge in an extremely strong cylindrical vessel partially filled with water. A comparison is made between the mesh configuration after $t = 1.0$ ms using an ALE description,

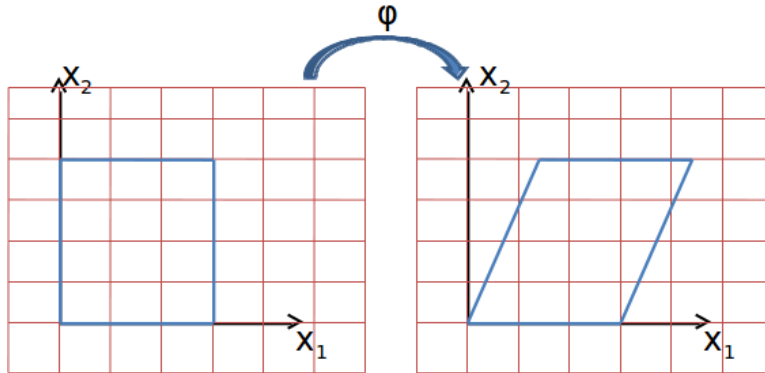


FIGURE 3.3: The interface of a two continua solved on an Eulerian mesh. The location of the interface cannot be accurately determined as it lies within an element.

and a purely Lagrangian description. Figure 3.4 demonstrates that a Lagrangian mesh becomes highly degraded with skewed and inverted elements. The ALE mesh in contrast preserves a regular mesh configuration of the charge-water interface.

In this chapter, a referential domain upon which the ALE technique is based is introduced and the relevant changes to the governing equations are derived based on the new frame of reference. A description of the ALE time stepping algorithm for fluid-structure interactions is outlined in § 3.5, which will include a discussion of relevant details for implementation.

3.2 Lagrangian and Eulerian viewpoints

The Lagrangian and Eulerian reference frames have been extensively covered in chapter 2. Here a summary of the salient points is presented before moving on to a description of the kinematics of the ALE-referential coordinate system. The review presented herein follows closely the work of Donea *et al.* (2004).

3.2.1 Lagrangian

A Lagrangian reference system denoted by R_X is fixed to the material as it deforms (figure 3.2). The material points in the Lagrangian reference frame are denoted by \mathbf{X} while the spatial coordinates are denoted by \mathbf{x} . The map ϕ denotes the injective deformation mapping from the material coordinates \mathbf{X} to the spatial coordinates \mathbf{x} , i.e.,

$$x_i = \phi_i(\mathbf{X}).$$

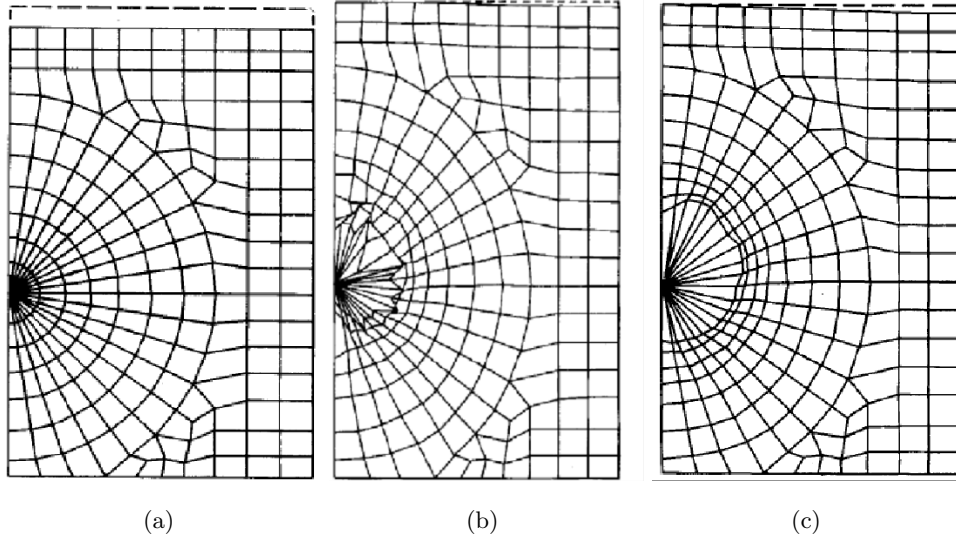


FIGURE 3.4: An illustration of a detonation of an explosive charge in an extremely strong cylindrical vessel partially filled with water. Lagrangian versus ALE descriptions are shown. (a) shows the initial FE mesh; (b) shows the Lagrangian mesh at $t = 1$ ms; and (c) shows ALE mesh at $t = 1$ ms. The ability of the ALE description to accommodate significant distortions of the computational mesh is shown. The Lagrangian approach suffers from a severe degradation of the computational mesh, exhibiting highly skewed and inverted elements, in contrast the ALE approach is able to maintain a quite regular mesh configuration of the charge-water interface. Reproduce with the permission of Wiley and sons from Donea *et al.* (2004).

The mapping ϕ is time dependent and describes the motion over an interval δt . As such a velocity and acceleration may also be described. Let the material velocity be defined as

$$\mathbf{v}(\mathbf{X}, t) = \left. \frac{\partial \mathbf{x}}{\partial t} \right|_x, \quad (3.1)$$

where $|_x$ signifies that the derivative is relative to a fixed material coordinate \mathbf{X} .

Since the material points coincide with the same grid points during the whole motion, there are no convective effects in Lagrangian calculations and the total material derivative reduces to a simple time derivative. The fact that each element of a Lagrangian mesh always contains the same material particles represents a significant advantage from the computational viewpoint, especially in cases such as modeling an arterial wall where different layers have different mechanical properties.

When large material deformations do occur, Lagrangian algorithms undergo a loss in accuracy due to excessive distortions of the computational mesh linked to the material.

3.2.2 Eulerian

An Eulerian reference system denoted by R_x is fixed in the spatial coordinates \mathbf{x} and the continuum moves with respect to the mesh. The conservation equations are formulated in terms of the spatial coordinates \mathbf{x} and time t . The deformation ϕ in this case can be interpreted as the inverse of the Lagrangian description,

$$X_i = \phi_i(\mathbf{x}).$$

The Eulerian description of motion only involves variables which have instantaneous significance in a fixed region of space. The material velocity \mathbf{v} at a given mesh node corresponds to the velocity of the material at the node at the given time, t . The velocity, \mathbf{v} , is consequently expressed with respect to the fixed spatial mesh and requires no reference to an initial configuration of the material coordinates \mathbf{X} , i.e. $\mathbf{v} = \mathbf{v}(\mathbf{x}, t)$.

As the material points convect past the Eulerian reference frame, convective effects are required to describe the time derivative of the material vector field. Convective effects appear because of the relative motion between the deforming material and the computational grid. That is, both a spatial and temporal term appear in the time derivative of the vector field.

3.3 ALE referential frame

Having reviewed the classical Lagrangian and Eulerian descriptions of motion, a clear understanding of the advantages and disadvantages of each reference frame is understood. Furthermore, the potential benefits of combining aspects of the classical descriptions of motion are clear. In order to implement the ALE description of motion we recognise that neither the material (Lagrangian) configuration (R_X) or the spatial configuration (R_x) provide a sufficiently general reference frame such that an application is not shielded from their disadvantages. As such, Donea *et al.* (2004) describe a third reference frame which is needed: the referential configuration R_χ , where χ are the reference coordinates which are introduced to identify the grid points. Figure 3.5 shows these configurations and the injective transformations relating each of the domains. Let the mappings Φ and Ψ describe the maps from the referential coordinate system to the material and spatial configurations respectively. The particle motion ϕ described at length in § 2.2 may be expressed through the alternate path,

$$\phi = \Psi^{-1} \circ \Phi. \tag{3.2}$$

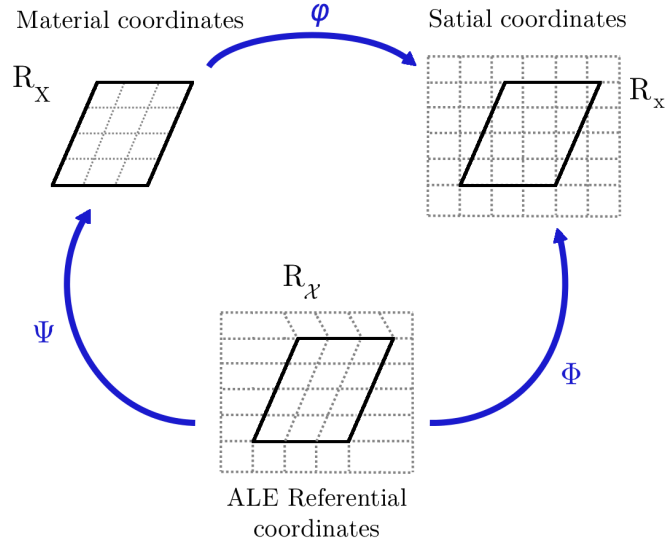


FIGURE 3.5: The motion of the ALE computational mesh is independent of the motion of the material. The maps ϕ represents the mapping from material to spatial coordinates, i.e. a Lagrangian map whose inverse mapping is an Eulerian map, Ψ is a map from the referential reference frame to the material configuration, and Φ is a map from the referential reference frame to the spatial coordinates.

Each of the mappings may be interpreted physically. As discussed, the map ϕ describes the motion of the particles with respect to the spatial coordinates. The map Φ from the referential domain to the spatial domain can be understood as the motion of the grid points in the spatial domain. The map Ψ^{-1} from the material configuration to the referential domain can be interpreted as the particle movement relative to the referential domain.

Just as in the Eulerian and the Lagrangian reference frames where the time derivative of the deformation ϕ gave rise to a velocity and acceleration, the time derivative of the maps Φ and Ψ also yield a velocity. From the time derivative of the map Φ we derive the velocity of the referential mesh in the spatial domain as the mesh velocity,

$$\hat{\mathbf{v}} = \left. \frac{\partial \mathbf{x}}{\partial t} \right|_{\mathbf{x}}. \quad (3.3)$$

Similarly, from the temporal derivative of the map Ψ^{-1} , we derive the particle velocity in the referential domain,

$$\mathbf{w} = \left. \frac{\partial \boldsymbol{\chi}}{\partial t} \right|_{\mathbf{X}}. \quad (3.4)$$

In equation 3.2 an alternate description of the deformation ϕ was described using the referential coordinate system. That relation demonstrates the link between the

coordinate systems which allows us to define a relationship between each of the velocities described previously, i.e. \mathbf{v} , $\hat{\mathbf{v}}$, and \mathbf{w} . This relationship is

$$\mathbf{v} = \hat{\mathbf{v}} + \frac{\partial \mathbf{x}}{\partial \boldsymbol{\chi}} \cdot \mathbf{w}, \quad (3.5)$$

where $\frac{\partial \mathbf{x}}{\partial \boldsymbol{\chi}}$ relates the spatial and referential coordinate system and is analogous to the convective velocity terms in the governing equations in § 2.5. Note this arises from the arbitrary motion of the referential coordinate system, its motion is not inextricably linked to the motion of the material, nor is it fixed in space. This equation may be rewritten as

$$\mathbf{c} := \mathbf{v} - \hat{\mathbf{v}} = \frac{\partial \mathbf{x}}{\partial \boldsymbol{\chi}} \cdot \mathbf{w}, \quad (3.6)$$

thus defining the convective velocity \mathbf{c} (that is, the relative velocity between the material and the mesh). To clarify precisely, \mathbf{w} is the particle velocity as seen from the referential domain $R_{\boldsymbol{\chi}}$, whereas \mathbf{c} is the particle velocity relative to the mesh as observed from the spatial domain R_x .

To emphasize the fact that the referential description of the ALE is a generalisation of both the Lagrangian and Eulerian reference frames, it can be demonstrated that both the Lagrangian and Eulerian descriptions of motion can be obtained from equation 3.2. With the choice that $\boldsymbol{\Psi} = \mathbf{I}$ (the identity matrix), the referential system is the material coordinate system, i.e. $\mathbf{X} \equiv \boldsymbol{\chi}$, which results in a Lagrangian description of motion. In this instance the material and mesh velocities, (equations 3.1 and 3.3) coincide, and the convective velocity \mathbf{c} vanishes, i.e. there are no convective terms in the conservation laws (see § 2.5). Conversely, with the choice that $\boldsymbol{\Phi} = \mathbf{I}$, the referential system is the spatial coordinate system, i.e. $\mathbf{x} \equiv \boldsymbol{\chi}$, thus implying an Eulerian description. In this case the mesh velocity $\hat{\mathbf{v}} = 0$ and the convective velocity \mathbf{c} is simply the material velocity \mathbf{v} .

3.4 Fundamental ALE equations

Fundamental to the balance equations developed in § 2.5 is an expression for the total time derivative $\frac{D}{Dt}$. It was shown that in an Eulerian reference frame

$$\frac{D}{Dt} \equiv \frac{\partial}{\partial t} + (\mathbf{v} \cdot \nabla) \mathbf{v}, \quad (3.7)$$

which includes both a temporal derivative and a spatial convective derivative term. In the Lagrangian reference frame the total derivative consists of only a time derivative,

$$\frac{D}{Dt} \equiv \frac{\partial}{\partial t}. \quad (3.8)$$

To express the governing equations in an ALE framework an expression for the total derivative is required.

3.4.1 Time derivatives

Before deriving the total derivative for the ALE framework (following the work in Donea *et al.* (2004)), an expression for the total derivative expressed in equations 3.7 and 3.8 is required. Let us consider a physical scalar quantity $f(\mathbf{x}, t)$ in the spatial domain, $f^*(\boldsymbol{\chi}, t)$ in the referential domain, and $f^{**}(\mathbf{X}, t)$ in the material domain. The star superscripts emphasize that the functional form of the scalar field is different in each of the domains.

Figure 3.5 shows that the deformation can be described by the mapping ϕ and so the spatial description $f(\mathbf{x}, t)$ of the scalar quantity and the material description, $f^{**}(\mathbf{X}, t)$, may be related as

$$f^{**} = f \circ \phi, \quad (3.9)$$

with gradients expressed by

$$\frac{\partial f^{**}}{\partial(\mathbf{X}, t)}(\mathbf{X}, t) = \frac{\partial f}{\partial(\mathbf{x}, t)}(\mathbf{x}, t) \frac{\partial \phi}{\partial(\mathbf{X}, t)}(\mathbf{X}, t). \quad (3.10)$$

The $(\cdot) \circ (\cdot)$ operation implies a multiplicative structure of the relationship, as such a matrix form of the relation in equation 3.10 can be written

$$\begin{bmatrix} \frac{\partial f^{**}}{\partial \mathbf{X}} & \frac{\partial f^{**}}{\partial t} \end{bmatrix} = \begin{bmatrix} \frac{\partial f}{\partial \mathbf{x}} & \frac{\partial f}{\partial t} \end{bmatrix} \begin{bmatrix} \frac{\partial \mathbf{x}}{\partial \mathbf{X}} & \mathbf{v} \\ \mathbf{0}^T & 1 \end{bmatrix}, \quad (3.11)$$

which after block manipulation yields

$$\begin{aligned} \left(\frac{\partial f^{**}}{\partial \mathbf{X}} \right) &= \left(\frac{\partial f}{\partial \mathbf{x}} \right) \left(\frac{\partial \mathbf{x}}{\partial \mathbf{X}} \right), \\ \left(\frac{\partial f^{**}}{\partial t} \right) &= \left(\frac{\partial f}{\partial t} \right) + \left(\frac{\partial f}{\partial \mathbf{x}} \right) \cdot \mathbf{v}. \end{aligned} \quad (3.12)$$

The second term in this expression is the well-known total derivative for an Eulerian reference frame, in 3-space this equation is recast as

$$\frac{Df}{Dt} = \frac{\partial f}{\partial t} + \mathbf{v} \cdot \nabla f, \quad (3.13)$$

which is the generic expression for any field f of the total derivative in equation 3.7. This may be interpreted in the usual way as the variation of a physical quantity for a given particle at position \mathbf{X} . This variation consists of the local variation in time plus a convective term taking into account the relative motion between the material and spatial reference frame. Of course, if a Lagrangian algorithm is employed the relative velocity between the material and spatial domains is zero (i.e. $\mathbf{v} = 0$), thus recovering the Lagrangian expression for the total derivative (equation 3.8).

Having derived the total derivative for an Eulerian and Lagrangian reference frame, the discussion is extended to include the ALE-referential configuration R_χ . As such the mapping Ψ^{-1} is used to transform the referential description of the physical quantity $f^*(\chi, t)$ to the material description $f^{**}(\mathbf{X}, t)$ through

$$f^{**} = f^* \circ \Psi^{-1}. \quad (3.14)$$

Just as before, through describing the gradient of this field in matrix form and applying some block manipulation, the expressions

$$\begin{aligned} \left(\frac{\partial f^{**}}{\partial \mathbf{X}} \right) &= \left(\frac{\partial f^*}{\partial \chi} \right) \left(\frac{\partial \chi}{\partial \mathbf{X}} \right), \\ \left(\frac{\partial f^{**}}{\partial t} \right) &= \left(\frac{\partial f^*}{\partial t} \right) + \left(\frac{\partial f^*}{\partial \chi} \right) \cdot \mathbf{w}, \end{aligned} \quad (3.15)$$

are obtained. The second of these two equations relates the material and referential time derivatives. Again a convective term $\left(\frac{\partial f^*}{\partial \chi} \right) \cdot \mathbf{w}$ appears, with the velocity \mathbf{w} being the relative velocity between the material and the referential domain. Unfortunately equation 3.15 requires the evaluation of the considered quantity in the referential domain. While possible, in implementation it is easier to work in either the material or spatial domains. To facilitate this the expression for \mathbf{w} developed in equation 3.4 is used to remove any spatial derivatives in the referential domain in the total derivative. The fundamental ALE relationship is finally cast as

$$\left. \frac{\partial f^{**}}{\partial t} \right|_{\mathbf{X}} = \left. \frac{\partial f^*}{\partial t} \right|_{\chi} + \mathbf{c} \cdot \nabla f. \quad (3.16)$$

This shows that the time derivative for a physical quantity f at a given position \mathbf{X} is its local derivative plus a convective term taking into account the relative velocity, \mathbf{c} , between the material and reference system. Note that this is equivalent to equation 3.13, but instead of the spatial frame being the laboratory frame, the referential frame is the laboratory, which may move independently of the deformation.

The total derivative defined in this section for the ALE referential domain may now be used to augment the governing equations for fluid and solid mechanics, thus allowing an ALE implementation to be solved.

3.4.2 Conservation equations in the ALE formulation

The ALE differential form of the conservation equations for mass and momentum are readily obtained from the corresponding Eulerian descriptions outlined in equations 2.57 and 2.46. These are rewritten here in their general form:

$$\text{Mass: } \frac{D\rho}{Dt} = -\rho\nabla \cdot \mathbf{v}, \quad (3.17a)$$

$$\text{Momentum: } \rho \frac{D\mathbf{v}}{Dt} = \nabla \cdot \boldsymbol{\sigma} + \rho\mathbf{b}, \quad (3.17b)$$

where \mathbf{b} is the net body force, ρ is the material density, $\boldsymbol{\sigma}$ is the stress tensor, and \mathbf{v} is the Eulerian velocity in the spatial domain. Equations 3.17a and 3.17b differ from equations 2.57 and 2.46 only in that the general form of the total derivative is used on the left hand side of the equation. This is done for generality purposes as the desired form of the total derivative, Lagrangian (3.8), Eulerian (3.7) or ALE (3.16) may be substituted as desired.

Substituting the ALE description of the total derivative given in equation 3.16 gives the ALE form of the governing equations,

$$\text{Mass: } \left. \frac{\partial \rho}{\partial t} \right|_{\mathbf{x}} + \mathbf{c} \cdot \nabla \rho = -\rho\nabla \cdot \mathbf{v}, \quad (3.18a)$$

$$\text{Momentum: } \rho \left(\left. \frac{\partial \mathbf{v}}{\partial t} \right|_{\mathbf{x}} + (\mathbf{c} \cdot \nabla) \mathbf{v} \right) = \nabla \cdot \boldsymbol{\sigma} + \rho\mathbf{b}. \quad (3.18b)$$

When comparing equation 3.18 to the Eulerian balance equation we note that the only difference is that instead of the convective term on the LHS including the relative velocity between the material and spatial reference frames \mathbf{v} , it now uses the convective velocity $\mathbf{c} = \mathbf{v} - \hat{\mathbf{v}}$ which is the relative velocity between the material and the mesh. Of course in the Eulerian reference frame the velocity of the mesh $\hat{\mathbf{v}}$ is zero so this relative velocity is the velocity between the material and the spatial (fixed) configuration. This shows that they are completely analogous.

It is also important to note that the right hand side of equation 3.18 is written in classical Eulerian form. This reflects that these terms vary only spatially and so are consistent regardless of the reference frame chosen.

3.5 ALE algorithms for FSI

A combination of convention, numerical accuracy, efficiency and application, has led to a raft of different fluid-structure interaction solvers. In most applications the fluid and solid solver components are modelled using different techniques with different levels of complexity. As an example, some solvers employ a full three-dimensional fluid dynamics solver which is highly accurate, yet they may use a one-dimensional thin shell model for wall dynamics (Formaggia *et al.* 2001). In addition to the choice of accuracy in each component of the solver, solvers may also differ in the way they transfer information across the physical interface. For the case of information transfer, the choices are somewhat more limited as they must be transferred at the interface and at the beginning or end of each time step (or sub-step). A summary of these coupling techniques may be found in Giannopapa (2006), which is reproduced herein figure 3.6. Giannopapa (2006) identified five methods of data transfer: non iterative over all time, iterative over all time, non-iterative over time step, iterative over time step and the single solution method. Figure 3.6 shows the information flow for each of these methods. Solid lines represent solution solves in the fluid (F) or solid (S) solvers while dashed lines represent an information transfer between the solvers. The core elements of each of these methods are as follows:

- **Method 1** is the most basic approach: non iterative over all time, the system is completely uncoupled. Each equation of state (for fluid and solid) is solved separately for the entire simulation time. Typically the fluid is solved first to gather the time history of pressure along the boundary and this is specified as a time varying boundary condition on the solid. There is no feedback in this method at all.
- **Method 2** is iterative over all time. This method is similar to the non-iterative over all time approach in that information is not passed at each time step, it is instead passed at the end of the solution. In the iterative over all time method, the fluid solver is typically solved first and the pressure history that is determined is then passed as a boundary condition to the solid. The motion of the solid in response to the pressure boundary condition is then passed back to the fluid solver as a time varying velocity boundary condition and the fluid is recomputed. In this way, feedback between the solvers is achieved. This process is repeated until

the solution reaches a predetermined convergence limit.

- **Method 3** is non-iterative over each time step. The boundary conditions are passed between fluid and solid at the end of each individual time step. This has advantages over Method 1 as it provides some feedback from the solid to the fluid at regular intervals.

Method 3a non-iterative over each time step with equal time steps. This means that at every time step the fluid and solid solvers pass boundary information to each other.

Method 3b is identical to Method 3a except that it relaxes the requirement that both the fluid and solid algorithms have the same time step. It is known as the non-iterative over unequal time steps method. This variant is useful in physical problems in which temporal changes occur much faster in one continuum. A small downside in this case is the exchange of boundary data cannot occur after every time step, it only occurs at the beginning and end of the largest time step.

- **Method 4** is iterative over each time step. This method is similar to Method 2 in that the fluid equations are solved in a continuous feedback loop with the solid solver. However, instead of being iterated over the total time domain, the iterations occur over each sub-step. Typically, the fluid solver is solved for a single time step and the pressure solution becomes the boundary condition for the solid equations. The solid equations are then solved for the same time step and the solution is returned to the fluid as a velocity boundary condition. This process is repeated until convergence is achieved at each time step. This is the most highly coupled solution approach and as a result gives the most accurate answers. However, it has an associated computational cost as the number of iterations within each time step is high. Despite this, it may reach equivalent convergence levels faster than Method 2 due to the smaller time scale over which change may occur in each iteration.
- **Method 5** is a special kind of fluid-structure solver referred to as a single solution solver. In this, the governing equations for fluids and solids are constructed to be based on the same primary variables, which are solved simultaneously in the one matrix solve. The two domains may be separated by a coefficient only. This is highly efficient, though the method does have its drawbacks. These include the

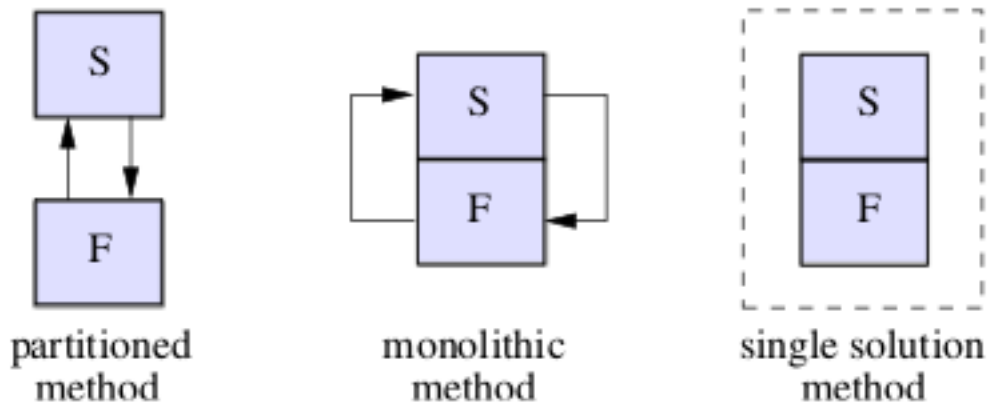


FIGURE 3.7: Fluid-structure interactions conventional terminology. Reproduced with the permission of Giannopapa from Giannopapa (2006).

complexity of the fluid and solid mechanic models being used, the order of the boundary conditions being shared, and depending on the time-stepping scheme the stability of the solver.

For Methods 1, 3a and 3b, information is only passed one way from the fluid to the solid solver. Physically, this does not make sense as the response of each component will have an effect on the other. When a fluid-structure interaction is being solved, a fully coupled algorithm (Method 2 or Method 4) should be used, in which a two-way transfer of information occurs. Furthermore, data exchange should occur at small intervals to get the most realistic simulation (Giannopapa 2006).

Fluid-structure interaction solvers can be categorised more broadly by their treatment of time discretisation. According to the conventional terminology in the literature, current numerical methods can be categorised as either partitioned, monolithic or single solution (figure 3.7).

Partitioned methods are based on the separation of the fluid and the solid solution. Each equation set is solved alternately and the interface conditions are exchanged asynchronously. Typically this kind of algorithm involves two separate methods for solving the fluid and solid components, while merging the different software packages is possible it is a complex task and the computational overhead of running such a code is restrictive (Belytschko *et al.* 1986). The data transfer between the solvers usually

requires a third programme, this also has its drawbacks in file-input/file-output bottlenecks. Finally, partitioning can lead inherently to degradation of the conservation of properties of the continua (fluid and structure).

Alternately coupled methods can be used, coupled methods offer advantageous in terms of accuracy by ensuring both the fluid and solid are satisfied in a two-way fashion at each time step. Despite the accuracy considerations, partitioned methods offer computational efficiency benefits that may make them attractive in some applications.

Monolithic approaches use separate sets of equations (fluid and solid) and couple the fluid and solid dynamics implicitly. They solve the dynamics of the interface through an iterative procedure as suggested in Method 4 at each time step: examples of this include Blom (1998) and Le Tallec & Mouro (2001). Van Brummelen *et al.* (2003) showed that if an Osher scheme (an algorithm capable of capturing shocks in fluid dynamics) is used for the fluid elements these methods are unconditionally stable. Despite the obvious advantages over partitioned methods, the sub-step iterations can make them quite computationally expensive.

Single solution methods have been proposed by Giannopapa (2006). The single solution method treats both the fluid and solid as a single continuum, thus the whole computational domain, both fluid and solid, is a single entity in a single grid. The behaviour of this continuum is described by a single set of equations rather than a pair of equations. There is no explicit exchange of information between the fluid and solid interface as it is inherently implicit. As such the computational expense of the sub-iterations can be avoided.

So far, fluid-structure interaction algorithms have been categorised based on the level of coupling in the time stepping scheme. Along with this point of difference there is also an enormous range of solvers that use different algorithms to solve either the fluid or solid mechanic equations. Furthermore, in the context of aneurysm simulations many investigations differ further on the types of boundary conditions applied to the computational domain. For a full discussion of different methods in an aneurysm context the reader is directed to chapter 1 and the reviews of Humphrey & Taylor (2008) and Lasheras (2007).

The following sections in this chapter detail the newly developed coupling algorithm used herein. This method is an implicit fully coupled iterative scheme with unequal time steps: in essence it is a combination of Method 3b and Method 4 outlined in

figure 3.6. To the authors knowledge, such a time stepping scheme for a fluid-structure interaction has not been previously developed. The iterative nature of Method 4 over each time step ensures convergence to the correct solution over each increment in time. Iterating at each time step is more computationally efficient and accurate than doing so over an entire time period as small changes in the solution are immediately accounted for. The unequal time steps for the fluid and solid (Method 3b) are used to improve the stability characteristics of the solver. The time marching scheme developed in this thesis improves on the combination of these two methods by interpolating the boundary condition values for each fluid sub-step in order to continuously pass information between the two solvers and to remove step changes in the solution which may introduce numerical errors.

3.5.1 ALE time marching algorithm

The arbitrary Lagrangian–Eulerian time stepping scheme developed in this thesis is a new formulation. The time marching scheme uses a monolithic approach. An existing in-house fluid dynamics package, *Viper*, which solves the time dependent incompressible Navier–Stokes equations is used as a basis for the new solver. A spectral-element solid mechanics solver for neo-Hookean materials was developed and fully integrated into the existing *Viper* code. Details of the spectral discretisation schemes and the time stepping algorithm for each of these individual solvers can be found in chapter 4. This section focuses on the implementation of the arbitrary Lagrangian–Eulerian algorithm, in particular the coupling of the two components and the impact it has on the governing equations.

3.5.1.1 Coupling: The information flow

Broadly, the algorithm is inspired by the method used by Bodard & Deville (2006). It is an *iterative over each time step* method, described schematically in figure 3.8. In their algorithm, the following steps are completed:

Step 1: Initialise the fluid and solid solvers. Based on the initial positions of the solvers, the matrices for each solver are created. At this stage the referential domain is the initial configuration so the mesh has no velocity ($\hat{\mathbf{v}} = 0$) associated with it. As such, the fluid solver is simply a classical Eulerian solver, and the solid a Lagrangian solver.

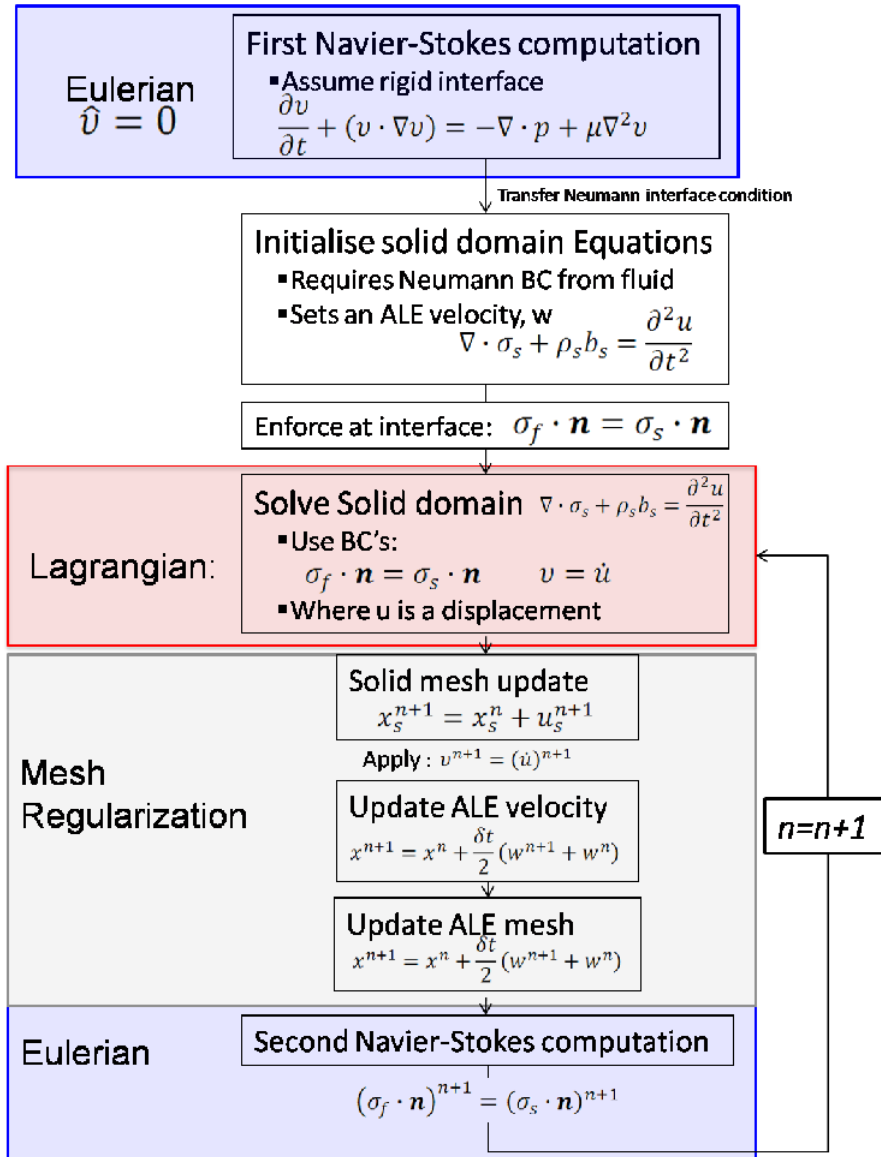


FIGURE 3.8: The ALE algorithm inspired by Bodard & Deville (2006). This time stepping algorithm is used for simulations where the motion of the solid body is well defined such as the forced oscillation of a cylinder.

Step 2: Calculate the first fluid time step. This is done based on the fluid dynamics boundary conditions only. The walls of the domain are assumed to be rigid with a no-slip wall boundary condition. This is a purely Eulerian solve. It is also implicit so the resulting fields at the completion of this step are the field values corresponding to the next time step.

Step 3: Complete a solid mechanics solve using as boundary conditions the pressure determined in the previous pressure solve. As the solid solver is also implicit the

pressure that is passed by the fluid solver is the pressure at the end of the solid time step.

Step 4: Having solved the solid mechanics equation the position of the fluid and solid meshes must be updated. This is known as the mesh regularisation phase: the strategy for this is discussed in § 3.5.1.2. Vectors holding the mesh position are updated. The movement of the mesh also has associated with it a mesh velocity \hat{v} : this velocity is calculated and made available to the fluid solver.

Step 5: At this stage, because the mesh has moved, the Jacobians and matrix operators must be reinitialised based on the new mesh position.

Step 6: Finally, the fluid is re-updated using the new mesh position and mesh velocity, i.e. the fluid is solved for using an ALE referential domain. The velocity of the wall determined in Step 4 is used as a velocity boundary condition in the fluid step.

Step 7: Update the time step. If the new pressure, velocity and mesh position are within a predetermined convergence criterion update the time to the next time step. If not, iterate by repeating Steps 3 to 6.

In this thesis a variation on this algorithm is proposed. Figure 3.9 shows schematically the new algorithm, it follows a similar stepping and iterative procedure as just described except a different-sized time step is used for the fluid and solid in order to improve stability. It was found for fluid-structure interactions where there was direct feedback between fluid and solid, there was some stability concerns when using the fluid and solid time stepping algorithms outlined in chapter 4. It was found for some problems that a larger time step for the solid domain delivered a more stable algorithm. Information exchange still occurs at each time step and each sub-step in at least one direction. To illustrate how this solver works, consider a solid time step that is five times bigger than the fluid time step, $\Delta t_s = 5 \times \Delta t_f$. Let it also be assumed that the fluid time step $\Delta t_f = 1$. The following time step headings describe what steps are being completed when the fluid solver is at t_f and the solid solver is at t_s . The solution starts at $t_f = t_s = 0$ and one complete step is completed at $t_f = t_s = 5$.

$t_f = 0$ $t_s = 0$ The first time through, the algorithm outlined in Bodard & Deville (2006) (figure 3.8) is used until convergence is reached. Pressures are passed to

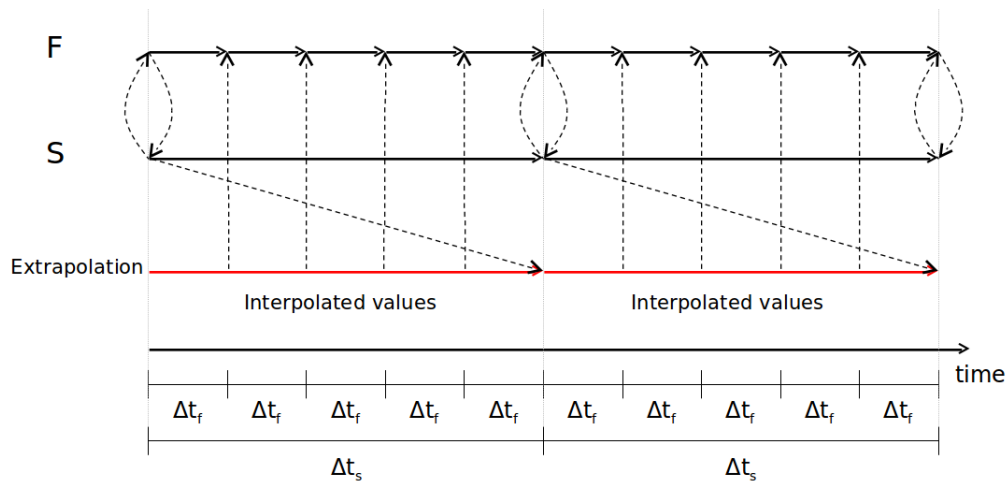


FIGURE 3.9: Schematic representation of information flow in the fluid-structure interaction solver developed in this thesis. It consists of different fluid and solid time step to allow better stability of the algorithm. At each solid step the solid and mesh positions are extrapolated to the next time step. Intermediate values are interpolated and passed to the fluid at each fluid time step. When fluid and solid time steps occur together a correction is made to the extrapolated value.

the solid; position and velocities are passed back to the fluid, and the referential mesh positions (and velocities) are updated within each iteration. To complete an iterative solve of the fluid dynamic equations given in chapter 4, the updated mesh velocity at the boundary and fluid velocity in the domain is used as the new guess of the velocity field in the first sub-step. The previous time history remains the same.

$t_f = 1 - 4 t_s = 0$ At this point the previous history of solid movement is used to extrapolate forward in time to the end of the next solid time step; this gives a prediction of the solid displacement at the end of the time next solid time step. This is done using a third order accurate polynomial extrapolation. Once the prediction has been made, a third order accurate Aitken's interpolation scheme is used to determine what the solid position and velocity will be at the next fluid time step (which is between the current time step and the next solid step). These predicted velocities and positions are used to reposition the mesh and define the mesh velocity, \hat{v} , for the next fluid time step. This extrapolation/interpolation routine replaces the solid stepping algorithm for these intermediate fluid time steps. Note: mesh regularization and reforming the Jacobians must still occur

based on the interpolated values.

The fluid solver is then computed for the next fluid time step using the extrapolated/interpolated values for the mesh velocity in the ALE equations and as the appropriate boundary conditions.

Next the time is progressed by one fluid time step and the interpolation is completed once more to determine the mesh velocity, position, and boundary conditions for the fluid region at the end of the next time step. The fluid is again updated as per the previous step. This is continued a total of five times until the point when the fluid and the solid solvers are next evaluating for the same time. Note: For these intermediate fluid time steps the pressure is not passed back to the solid solver.

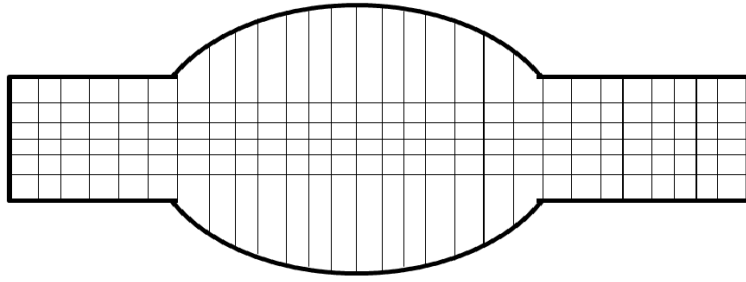
$t_f = 5 t_s = 5$ When $t_s = t_f$ once more, the time step is updated in the same manner as the algorithm of figure 3.8 using an iterative procedure. This corrects any discrepancy between the extrapolated value and the real value.

For cases where the deformation of the solid body is known, e.g. a forced oscillation of a cylinder, the different time stepping is not required and the algorithm shown in figure 3.8 is used. This is simply achieved in the algorithm by setting the different time steps to the same size. Despite not passing the pressure back to the solid for reconsideration at every time step (this is only done when $t_f = t_s$) the use of a consistent third-order accurate polynomial extrapolation is sufficient to accurately predict the updated positions with a high degree of accuracy. The results presented in chapter 6 will demonstrate that the scale of the error introduced by this technique is small.

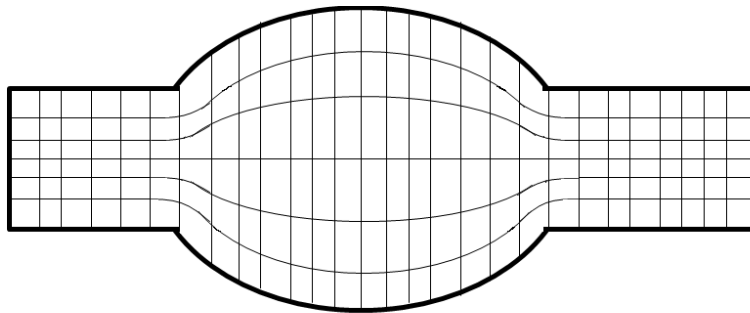
3.5.1.2 Mesh movement scheme

The advantage of using an arbitrary Lagrangian–Eulerian technique is the ability to have a moving reference frame. The movement of this referential frame is arbitrary. The type of problem being looked at has some impact on how the mesh will be moved, the desire to conserve the accuracy of a mesh is another consideration.

In the context of a fluid–structure interaction, the location of the interface is paramount to the accuracy of the simulation. As such, the mesh is chosen to move with the solid phase in a Lagrangian manner in order to accurately map out the location of the interface. This will in turn change the position of the fluid mesh. In this way, the problem being investigated has driven the way in which the mesh will move: it must follow the



(a)



(b)

FIGURE 3.10: Flow through a flexible pipe undergoing a large localised dilation. Sub-plot (a) shows the case when only the boundary nodes are moved; this leads to large distortion of elements along the wall and under resolution. Sub-plot (b) shows the case of using the Hookean solid model for the mesh regularisation scheme, which leads to conservation of the mesh quality.

interface. However, this only defines the movement of the boundary of the fluid region, not the interior mesh nodes.

For accuracy purposes it is advantageous to maintain equal, non-deformed mesh elements. If for example, flow through a distensible pipe was being simulated and the pipe underwent a large dilation, simply moving the mesh nodes on the boundary interface would cause large stretching of the elements nearest the wall (see figure 3.10(a)) resulting in undesirable aspect ratios and reduced resolution in this area. If instead a technique to cause all of the nodes in the mesh to move is used, such that they each absorb some of the dilation, the accuracy of the elements can be conserved. An example of this type of mesh regularization can be seen in figure 3.10(b).

In this implementation the mesh regularisation scheme used considers the fluid mesh

region as a solid body. Similar strategies have been used in Winslow (1963); Benson (1989) and Le Tallec & Martin (1996), this strategy is a natural choice in fluid-structure interactions in which a solid mechanics code already exists and is readily adaptable to the mesh regularization. The displacement of the interface is applied as the boundary conditions. All other boundaries are taken to be fixed. The mesh region is modelled as a steady-state Hookean solid. This requires the solution of the elliptic problem

$$\nabla \boldsymbol{\sigma} = 0, \tag{3.19}$$

where $\boldsymbol{\sigma}$ is the Cauchy stress. Details of how the solver handles Hookean materials can be found in chapter 4. By using a high material stiffness in the Cauchy stress tensor (in equation 3.19), an even distribution of the dilation throughout the mesh region is ensured, which allows the relative spacing of mesh nodes to be conserved.

3.6 Closure

The kinematic relations for the arbitrary Lagrangian–Eulerian formulation are not too dissimilar from those of an Eulerian formulation. In fact the Arbitrary Lagrangian–Eulerian formulation represents a generalisation of both the classical domains. The referential domain introduced for the Arbitrary Lagrangian–Eulerian formulation allows continuous rezoning capability as the laboratory frame moves independently of the material. Careful choice of the mesh regularisation scheme, which may be interpreted as the motion of the laboratory frame, allows for accurate knowledge of the interface while allowing large deformations of the fluid region and a changing geometry of the fluid domain. Such capability is not possible with either classical reference frame.

The governing equations for the ALE formulation are only changed in the total derivative term. The convective velocity is used in the convective acceleration term in place of the velocity in the spatial coordinates. The right hand side of the governing equation 3.18 is written in classical Eulerian form. This is because these terms vary only spatially and so are consistent regardless of the reference frame chosen.

A monolithic solver is used with a modified iterative over unequal time step coupling routine. The unequal time stepping algorithm ensures information is updated in the fluid solver at each fluid time step using an extrapolation/interpolation method on intermediate time steps and a full iterative feedback method during time steps when both the fluid and the solid are being updated. To preserve the relative spacing of mesh

nodes in the fluid region as the domain size changes, a Hookean solid model is used to regulate the mesh movement.

The arbitrary Lagrangian–Eulerian time stepping scheme developed in this thesis allows the coupling of the fluid and solid mechanics solvers. This enables the solver to handle the complex fluid-structure interactions found in arterial flows. This work is integral to aim 1 defined in chapter 1. While the mathematical background of the ALE technique is well defined, this algorithm represents a novel contribution to the field with its new information transfer scheme. Having defined the full set of governing equations for solids and fluids and outlining the time stepping algorithm for the ALE method the following chapter clarifies the details of the temporal and spatial discretisation of each of the individual solver components.

Chapter 4

Numerical methods for fluids and solids

Presented in this chapter are the numerical methods used to solve the governing fluid and solid dynamics equations. The mathematical framework relating to the spectral element method described herein follows closely the work of Karniadakis & Sherwin (1999). While the temporal discretisation of the Navier–Stokes equations in § 4.2.2 is based on Karniadakis *et al.* (1991), here a new method is developed for the temporal discretisation of the neo-Hookean and Hookean governing equations.

4.1 Introduction

A variety of techniques are available to discretise a set of governing mathematical equations both in space and time. Within the class of mesh-based methods, where the domain is discretised into a grid of elements, three discretisation paradigms are popular: the Finite Element Method, Finite Difference Method, and Finite Volume Method. The Finite Element Method was developed primarily to solve problems in the area of structural mechanics. The Finite Volume Method, which was developed from the Finite Difference Method, has been applied with great success in fluid mechanics and heat transfer applications. The Spectral Element Method (SEM) is a highly efficient subset of the Finite Element Method, that has recently been applied largely to Computational Fluid Dynamics (CFD) problems with limited use in structural mechanics. Spectral element methods use adaptive high-order basis functions to discretise the spatial domain which provides them with exponential convergence properties compared with the linear or low order polynomial basis functions used in traditional finite element methods.

In chapter 3 the governing equations for fluid flows (the Navier–Stokes equations)

and those of a neo-Hookean hyperelastic solid were shown to contain very similar terms. The similarity of the two equation sets suggests a similar discretisation scheme could reasonably be adapted for both the solid and fluid domains. Such an approach would have some obvious efficiency benefits when it comes to coupling a fluid-solid solver. The emerging need to simulate multi-physics processes such as Fluid Structure Interactions (FSI) that are governed by a number of interactive physical phenomena, drives the construction of integrated solvers that improve efficiency by reducing input and output (Giannopapa 2006). This chapter provides both the time stepping algorithm and outlines the existing mathematical framework that underpins the algorithm used to solve the fluid and solid domains described in chapter 3.

This chapter will present the algorithm for the solution of fluid and solid mechanic problems. For fluid mechanics the time dependent incompressible Navier–Stokes equations are solved for Newtonian fluids, comprising the momentum equation

$$\frac{\partial \mathbf{v}}{\partial t} + (\mathbf{v} \cdot \nabla) \mathbf{v} = -\nabla P + \nu \nabla^2 \mathbf{v}, \quad (4.1)$$

where \mathbf{v} is the velocity vector $\mathbf{v} = (v_1, v_2, v_3) = \left(\frac{du_1}{dt}, \frac{du_2}{dt}, \frac{du_3}{dt} \right)$ where u_i are components of the displacement vector, P is the kinematic pressure, ν is the kinematic viscosity and t is time. The incompressibility condition requires

$$\nabla \cdot \mathbf{v} = 0. \quad (4.2)$$

For solid mechanics problems a similar momentum equation is solved,

$$\rho \frac{\partial^2 \mathbf{u}}{\partial t^2} = \rho \bar{\mathbf{b}} + \nabla \cdot \boldsymbol{\sigma}, \quad (4.3)$$

where $\mathbf{u} = (u_1, u_2, u_3)$ is the displacement vector, ρ is the solid material density, $\boldsymbol{\sigma}$ is a stress tensor, and $\bar{\mathbf{b}}$ are the body forces. The stress tensor $\boldsymbol{\sigma}$ will take a different form depending on the constitutive model being used, for further discussion on this refer to chapter 3.

Equations 4.1 and 4.3 must be discretised in both space and time. Section 4.2 describes the numerical algorithm used to evolve the solution in time. Sections 4.3 to 4.5 will then outline the mathematical framework used by the numerical algorithm to spatially discretise the governing partial differential equations and recast them into a set of ordinary differential equations and subsequently algebraic expressions that may be efficiently solved numerically.

4.2 Time stepping algorithm

In continuum mechanics (fluid or solid) the governing equations are formed under the basis of a series of conservation laws. These are commonly referred to as the conservation of mass, momentum and energy. Their conservative nature implies a time dependent aspect such that as time progresses, changes in the quantity in question can only occur in balance with fluxes in and out of the domain and subject to any sources or sinks inside the domain (see chapter 3).

Given the time dependent nature of the continuum mechanics governing equations the presence of the time derivative is recognised in both the fluid and solid governing equations (4.1 and 4.3) respectively. This implies a dynamic system in which boundary conditions may be transient and an environment in which the conserved quantities may propagate through the domain. This captures important physics; indeed neglecting this term implies that mass, momentum and energy transfer throughout the domain instantaneously, which in many systems is physically inaccurate. This is particularly important in fluid dynamics in which convective transfer is the principal mechanism of energy and mass transfer.

Unlike many fluid-structure interaction solvers, the algorithm developed in this project includes a time stepping scheme for both the fluid and the solid, thus accounting for the inertial term. The following section details the time stepping scheme employed for each continuum.

Many different formulations have been developed to handle the temporal discretisation of conservative equations. For a detailed description of fluid dynamic formulations see Quartapelle (1993), Gunzburger *et al.* (1993), and Karniadakis & Sherwin (1999); and in solid mechanics Glowinski & Tallec (1989), and Glowinski (2008). The time stepping algorithm described herein applies an operator-splitting approach described by Karniadakis *et al.* (1991) for incompressible fluid flows. This scheme is then adapted for the temporal discretisation of the solid domain equations.

4.2.1 Operator splitting schemes

To evolve the Navier–Stokes equations forward in time, Karniadakis *et al.* (1991) propose a stiffly-stable operator-splitting scheme for high-order accurate Navier–Stokes solvers. This high-order stiffly-stable splitting algorithm builds directly on Adams type operator-splitting schemes for fluid dynamics also described in Karniadakis *et al.* (1991).

These stiffly-stable schemes have since been recognised as a class of backwards-multistep schemes by Blackburn & Sherwin (2004). The stiffly-stable algorithm was chosen for its improved stability characteristics at high-orders of accuracy.

Operator splitting schemes (Yanenko 1971) were first applied to Navier–Stokes problems by Issa (1986). The basis of generic splitting schemes may be explained by considering a general equation of the form

$$\frac{\partial \mathbf{u}}{\partial t} = \hat{\mathbf{L}}(\mathbf{u}) \quad (4.4)$$

where $\hat{\mathbf{L}}$ is a linear operator that advances the vector \mathbf{u} in time (Press 2007). Assuming the operator can be written as a linear sum of m pieces,

$$\mathbf{L}\mathbf{u} = \hat{\mathbf{L}}_1\mathbf{u} + \hat{\mathbf{L}}_2\mathbf{u} + \dots + \hat{\mathbf{L}}_m\mathbf{u}, \quad (4.5)$$

the solution that eventually updates the variable \mathbf{u} to the next time step ($n + 1$) can be derived simply by summing the contribution of each $\hat{\mathbf{L}}_m$ operating on \mathbf{u} separately (Press 2007).

4.2.2 Time evolution of the Navier–Stokes equations

In applying the operator-splitting scheme to the Navier–Stokes equations (4.1) the type of differencing scheme is first chosen for the temporal derivative term. Blackburn & Sherwin (2004) identified the stiffly-stable scheme of Karniadakis *et al.* (1991) as a class of backward multi-step methods which employ backward differencing to evolve the solution in time.

Backward differencing evaluates the time derivative at the next time step ($n + 1$) using a weighted sum of values at previous time steps, the number of previous time steps required and the value of the weights are determined by the level of accuracy required of the approximation. Weights (and hence the combination of previous time steps) are determined through combining Taylor series expansions at antecedent time steps in order to have the leading error term of the Taylor series at the desired accuracy level for the solution (Ames 1965). It is noted that increasing the order of the solver does affect its stability.

For the incompressible Navier–Stokes equations, Karniadakis *et al.* (1991) propose an implicit three-step ($m = 3$) time splitting scheme

$$\frac{\partial \mathbf{v}}{\partial t} = -(\mathbf{v} \cdot \nabla) \mathbf{v} - \nabla P + \nu \nabla^2 \mathbf{v}, \quad (4.6)$$

becomes

$$\frac{\hat{\mathbf{v}} - \sum_{q=0}^{J_i-1} \alpha_q \mathbf{v}^{n-q}}{\Delta t} = \sum_{q=0}^{J_e-1} \beta_q \hat{\mathbf{N}}(\mathbf{v}^{n-q}), \quad (4.7)$$

$$\frac{\hat{\hat{\mathbf{v}}} - \hat{\mathbf{v}}}{\Delta t} = -\nabla P^{n+1}, \quad (4.8)$$

$$\frac{\kappa \mathbf{v}^{n+1} - \hat{\hat{\mathbf{v}}}}{\Delta t} = \nu \nabla^2 \mathbf{v}^{n+1}, \quad (4.9)$$

where $\hat{\mathbf{v}}$ and $\hat{\hat{\mathbf{v}}}$ are intermediate velocity fields, $\hat{\mathbf{N}} = \sum_{q=0}^{J_e-1} \beta_q [(\mathbf{v} \cdot \nabla) \mathbf{v}]^{n-q}$ is the non-linear advection operator and J_e and J_i represents the order of integration: for third-order accuracy in time $J_e = J_i = 3$. We note here that this is analogous to the operator-splitting form of equation 4.5, i.e.

$$(\mathbf{v} \cdot \nabla) \mathbf{v} = \hat{\mathbf{L}}_1 = \sum_{q=0}^{J_e-1} \beta_q \hat{\mathbf{N}}(\mathbf{v}^{n-q}), \quad (4.10)$$

$$\nabla P = \hat{\mathbf{L}}_2 = -\nabla P^{n+1}, \quad (4.11)$$

$$\nu \nabla^2 \mathbf{v} = \hat{\mathbf{L}}_3 = \nu \nabla^2 \mathbf{v}^{n+1}, \quad (4.12)$$

by back substitution of each sub-step the Navier–Stokes equations (equation 4.6) are recovered with a backwards differencing approximation to the inertial term and a stiffly-stable polynomial approximation of the advection term.

The first sub-step, equation 4.7, involves an explicit solve for the advection term. The contribution of the non-linear advection term at the $(n+1)^{\text{st}}$ time step is approximated using an appropriate-order polynomial extrapolation. In this implementation, third-order accuracy is achieved using $J_e = 3$ and the coefficients $\beta_0 = 3, \beta_1 = -3$ and $\beta_2 = 1$, where β_q applies to the $(n-q)^{\text{th}}$ time-step. To maintain third-order temporal accuracy the coefficients for the inertial terms are $\kappa = 11/6, \alpha_0 = 3, \alpha_1 = -3/2$ and $\alpha_2 = 1/3$, where again α_q applies to the $(n-q)^{\text{th}}$ time-step (Karniadakis & Sherwin 1999).

In the second sub-step, equation 4.8, the intermediate velocity field $\hat{\mathbf{v}}$ is corrected to account for the contribution of the pressure term; finding the second intermediate velocity field $\hat{\hat{\mathbf{v}}}$. This first requires evaluation of the kinematic pressure, P . In this sub-step the incompressibility condition, $\nabla \cdot \mathbf{v} = 0$, is also enforced. The first step is to take the divergence of both sides of equation 4.8,

$$\nabla \cdot \left(\frac{\hat{\hat{\mathbf{v}}} - \hat{\mathbf{v}}}{\Delta t} \right) = \nabla \cdot (-\nabla P^{n+1}), \quad (4.13)$$

which becomes

$$\frac{\nabla \cdot \hat{\mathbf{v}} - \nabla \cdot \hat{\mathbf{v}}}{\Delta t} = -\nabla^2 P^{n+1} \quad (4.14)$$

and by enforcing the incompressibility constraint on the second intermediate velocity field $\hat{\mathbf{v}}$, this becomes a Poisson problem

$$\nabla^2 P^{n+1} = \frac{\nabla \cdot \hat{\mathbf{v}}}{\Delta t}. \quad (4.15)$$

The intermediate velocity field $\hat{\mathbf{v}}$ is calculated during the first sub-step, so the right-hand side of equation 4.15 is known and this equation can be solved as a Poisson equation for the kinematic pressure P at time t^{n+1} . Once found, the kinematic pressure P can be substituted back into equation 4.8 to find the second intermediate velocity field, $\hat{\mathbf{v}}$. The Galerkin formulation (described in detail in § 4.3.2) provides a course for implementing the appropriate high-order Neumann pressure boundary conditions imposed on homogenous boundaries. The pressure boundary condition imposed at the $(n+1)^{\text{st}}$ time step written in rotational form is

$$\frac{\partial P^{n+1}}{\partial \mathbf{n}} = - \left[\frac{\partial \mathbf{v}^{n+1}}{\partial t} + \nu \sum_{q=0}^{J_p-1} \beta_q (\nabla \times \boldsymbol{\omega})^{n-q} + \sum_{q=0}^{J_e-1} \beta_q \hat{\mathbf{N}}(\mathbf{v}^{n-q}) \right] \cdot \mathbf{n}, \quad (4.16)$$

where \mathbf{n} is the unit normal vector, and $\boldsymbol{\omega}$ is the vorticity. This is simply the Navier–Stokes equations rearranged in terms of P in the direction of the unit normal vector on homogenous boundaries. To ensure it provides the boundary conditions at the next time step $(n+1)$ the non-linear advection term is again determined using a polynomial extrapolation method based on past velocity fields \mathbf{v}^{n-q} , a third-order accurate approximation of this term, $J_e = 3$ is maintained. However, for the pressure term a second-order integration $J_p = 2$ is used. Karniadakis *et al.* (1991) show that using a rotational formulation with a second-order extrapolation $J_p = 2$, maintains third-order accuracy and improves stability conditions. The β_i coefficients for $J_p = 2$ are $\beta_0 = 2$ and $\beta_1 = -1$ (Karniadakis *et al.* 1991).

The pressure boundary condition is written in rotational form to reinforce the incompressibility condition on the boundaries. This allows the time step to directly control the divergence at the boundary (Petersson 2001, see) and to preserve the ellipticity of the Laplacian diffusion term. Leriche & Labrosse (2001) demonstrate this characteristic and the importance of maintaining ellipticity in preserving the stability of the algorithm.

The third sub-step, equation 4.9, involves solving a Helmholtz equation for the final velocity field \boldsymbol{v}^{n+1} . The intermediate velocity field, $\hat{\boldsymbol{v}}$, is known and provides contributions from the pressure and advection terms as well as the enforced incompressibility condition. Velocity boundary conditions are prescribed during this sub-step. Dirichlet boundary conditions are strongly enforced in the familiar fashion, while again the Galerkin formulation allows Neumann velocity boundary conditions to be imposed on the velocity field with ease.

4.2.3 Time evolution of the solid mechanics equations

The underlying physics that governs both fluid and solid mechanics is summarised by the conservation of mass and momentum. These are the basis for the Navier–Stokes equations (4.1) and also the solid mechanics equations (4.3). Given this common basis many analogous terms can be found in each set of equations. For instance, both equations have an inertial term of the same form. For the Hookean solid governing equations the Cauchy stress term (at least in terms of a computational implementation) can be seen to be analogous to the diffusion term in the Navier–Stokes equations. For a neo-Hookean solid the Cauchy stress term has components analogous to the diffusion term and a penalty pressure term is introduced to maintain incompressibility just as in the Navier–Stokes equations. Given the similarity in the equations a very similar time-stepping algorithm is presented to evolve the solution in time. The time stepping scheme outlined in the forthcoming sections is novel in solid mechanics and, along with the new implementation of the ALE in § 3.5.1 represent the contribution of a new methodology for solving fluid-structure interactions in aneurysms.

4.2.3.1 Time evolution of a Hookean solid

Given the relatively simple linear structure of the Cauchy stress tensor in the Hookean solid, a splitting scheme is not required. The algorithm uses a second-order accurate implicit scheme to solve for the updated displacement field, \boldsymbol{U}^{n+1} . A second-order accurate backwards difference approximation is used for the second-order derivative in the inertial term, and a high-order linear operator is formed from the Cauchy stress term which is analogous to the diffusion term in the Navier–Stokes equations. Because a Lagrangian reference system is used for the solid mechanics the displacement in the material frame \boldsymbol{U} is used rather than the displacement in the spatial (Eulerian) reference

frame, \mathbf{u} . Rewriting 4.3 with the approximations gives

$$\rho \frac{\kappa^s \mathbf{U}^{n+1} + \sum_{q=0}^{J_s} \alpha_q^s \mathbf{U}^{n-q}}{(\Delta t)^2} = \hat{\mathbf{L}} \cdot \mathbf{U}^{n+1}, \quad (4.17)$$

where for second-order accuracy $J_s = 2$, $\kappa^s = -2$, $\alpha_0^s = 5$, $\alpha_1^s = -4$ and $\alpha_2^s = 1$. To form the Helmholtz equation 4.17 is recast as

$$\left[\rho \frac{\kappa^s}{(\Delta t)^2} - \hat{\mathbf{L}} \right] \cdot \mathbf{U}^{n+1} = -\rho \frac{\sum_{q=0}^{J_s} \alpha_q^s \mathbf{U}^{n-q}}{(\Delta t)^2}. \quad (4.18)$$

The forces applied to a solid cause the deformations that are described by this equation. These forces are described in terms of a pressure on a boundary and appear in the stress tensor for the boundary nodal positions. The Galerkin formulation described in § 4.3.2 again allows explicit prescription of the boundary conditions as they appear in a separate surface integral term in which the boundary forces may be inserted. Dirichlet displacement boundary conditions are handled in the standard manner using the static condensation technique described in § 4.6.

4.2.3.2 Time evolution of a neo-Hookean solid

The neo-Hookean solid has a more complex structure for the Cauchy stress tensor, i.e.

$$\boldsymbol{\sigma} = P \mathbf{I} + \mathbf{F} \left(\frac{\partial W}{\partial \mathbf{F}} \right)^T, \quad (4.19)$$

where W is the (non-linear) neo-Hookean strain energy function, \mathbf{F} is the deformation gradient (a function of \mathbf{U}), P is the pressure arising to maintain incompressibility, and \mathbf{I} is the identity matrix. When substituted into equation 4.3 this yields

$$\rho \frac{\partial^2 \mathbf{U}}{\partial t^2} = \rho \bar{\mathbf{b}} + \nabla \cdot P_s \mathbf{I} + \nabla^2 (\mathbf{U}), \quad (4.20)$$

where $\nabla^2(\cdot)$ is the linear component of the divergence of the stress tensor term, the Laplacian. The similarity of this equation and the Navier–Stokes momentum equation is remarkable. Both contain an inertial term (one is Lagrangian, the other Eulerian which contains a non-linear convective term). They both have a $\nabla \cdot P$ term, and a high-order linear operator ($\hat{\mathbf{L}}$ in the Navier–Stokes equations and the Laplacian in the neo-Hookean equation). These similarities inspire the use of an operator-splitting scheme similar to that of the Navier–Stokes solver to evolve the solid domain. A two-step splitting scheme is proposed that is implicit, second-order accurate, and utilises backwards differencing for the temporal discretisation as described in § 4.2.3.1,

$$\rho \frac{\hat{\mathbf{U}} - \sum_{q=0}^{J_i} \alpha_q^s \mathbf{U}^{n-q}}{(\Delta t)^2} = -\nabla P_s^{n+1}, \quad (4.21)$$

$$\frac{\kappa^s \mathbf{U}^{n+1} - \hat{\mathbf{U}}}{\Delta t} = \hat{\mathbf{L}} \mathbf{U}^{n+1}. \quad (4.22)$$

In the first sub-step, equation 4.21, the contributions of the previous displacement field $\sum_{q=0}^{J_i} \alpha_q^s \mathbf{U}^{n-q}$ are used to account for the contribution of the pressure term finding the intermediate displacement field $\hat{\mathbf{U}}$. This first requires evaluation of the kinematic pressure, P . Taking the divergence of both sides of 4.21,

$$\nabla \cdot \left(\frac{\hat{\mathbf{U}} - \sum_{q=0}^{J_i} \alpha_q^s \mathbf{U}^{n-q}}{(\Delta t)^2} \right) = \nabla \cdot (-\nabla P^{n+1}), \quad (4.23)$$

and rearranging gives

$$\frac{\nabla \cdot \hat{\mathbf{U}} - \sum_{q=0}^{J_i} \alpha_q^s \nabla \cdot \mathbf{U}^{n-q}}{(\Delta t)^2} = -\nabla^2 P^{n+1}. \quad (4.24)$$

The pressure P introduced in the neo-Hookean Cauchy stress is introduced as a penalty function to enforce incompressibility. As such it is recognised that the vector field should satisfy an incompressibility constraint. In fluid mechanics this constraint is described by

$$\nabla \cdot \mathbf{v} = 0 \quad (4.25)$$

where \mathbf{v} is a velocity vector. In the solid equations the principal variable is displacement. Because velocity is simply the time derivative of displacement we see that if equation 4.25 holds then so to must

$$\nabla \cdot \mathbf{U} = 0. \quad (4.26)$$

Therefore the incompressibility constraint is enforced on the intermediate displacement field $\hat{\mathbf{U}}$, leaving

$$\frac{-\nabla \cdot \sum_{q=0}^{J_i} \alpha_q^s \mathbf{U}^{n-q}}{(\Delta t)^2} = \nabla \cdot (-\nabla P^{n+1}). \quad (4.27)$$

The inertial contribution to the displacement field $\sum_{q=0}^{J_i} \alpha_q^s \mathbf{U}^{n-q}$ is calculated explicitly, so this equation can be solved as a Poisson equation for the kinematic pressure P . Once found, the kinematic pressure, P , is substituted back into equation 4.21 to find the intermediate displacement field $\hat{\mathbf{U}}$. The Galerkin formulation detailed in § 4.3.2 provides a method for implementing the appropriate high-order Neumann pressure boundary conditions imposed on homogenous boundaries. The pressure boundary condition imposed at the $(n+1)^{\text{st}}$ time step is

$$\frac{\partial P^{n+1}}{\partial \mathbf{n}} = - \left[\frac{\partial^2 \mathbf{U}^{n+1}}{\partial t^2} + \rho \sum_{q=0}^{J_p-1} \beta_q^s \nabla^2 (\mathbf{U})^{n-q} \right] \cdot \mathbf{n}, \quad (4.28)$$

where \underline{n} is the unit normal vector. Just as with the Navier–Stokes pressure boundary condition, this is simply the governing equations rearranged in terms of P and dotted with the unit normal vector on homogenous boundaries. To ensure it provides the boundary conditions at the next time step ($n + 1$) the non-linear stress term is determined using a polynomial extrapolation method based on past displacement fields \mathbf{U}^{n-q} , where second-order accuracy ($J_e = 2$) is maintained for this term. The coefficients for the polynomial extrapolation in the boundary condition of the pressure step ($J_p = 2$) are $\beta_0 = 2$ and $\beta_1 = -1$ (Karniadakis & Sherwin 1999).

The second sub-step, equation 4.22, involves solving a Helmholtz equation for the final displacement field \mathbf{U}^{n+1} . The intermediate displacement field, $\hat{\mathbf{U}}$, is known and provides contributions from the pressure and inertial terms as well as the enforced incompressibility condition. Displacement boundary conditions can be prescribed at this point. Dirichlet boundary conditions may be prescribed in the familiar fashion while the Galerkin formulation allows high-order displacement boundary conditions to be imposed with ease.

4.3 Fundamental concepts in one-dimension

Having described the numerical algorithm used for temporal discretisation of equations 4.1 for fluid dynamics and 4.3 for solid mechanics the mathematical framework of the spatial discretisation used to construct the matrix operators used in the governing equations is presented. The spectral element spatial discretisation presented herein is well documented in texts such as Karniadakis & Sherwin (1999) and is presented only to demonstrate understanding of the computational methods employed in developing the FSI solver.

Modelling of continuum mechanics has primarily been driven by finite element modelling of solid structures. The finite element model can be shown to be a case of the Rayleigh–Ritz problem (Courant & Hilbert 1989). In these modelling techniques a variational form of the problem is considered, which can be shown to approximate the original differential equation.

For example, following Karniadakis & Sherwin (1999), the quadratic functional

$$\mathcal{F}(u) = \int_0^1 \left[p(x) (u'(x))^2 + q(x) (u(x))^2 - 2f(x) u(x) \right] dx \quad (4.29)$$

has a minimum with respect to a variation in $u(x)$ given by the Euler equation

$$-\frac{d}{dx} \left(p(x) \frac{du(x)}{dx} \right) + q(x) u(x) = f(x). \quad (4.30)$$

So rather than solving the partial differential equation 4.30 to determine $u(x)$, an alternate and, importantly, equivalent solution is to find the value $u(x)$ which minimises equation 4.29.

Using the Rayleigh–Ritz approach, the solution $u(x)$ is approximated by a finite number of functions Φ_i ,

$$u(x) = \sum_i^N q_i \Phi_i, \quad (4.31)$$

and the weights q_i are determined in order to minimise the functional-variational form of equation 4.29.

The finite element method is analogous to the Rayleigh–Ritz problem (Courant & Hilbert 1989). In the finite element method the solution domain is typically broken into smaller local segments over which the solution approximation is enforced. In addition to the global-local difference, the finite element method would use the differential equation 4.30 recast in the integral-Galerkin form as the mathematical basis for the discretisation scheme. The Galerkin form of the differential equation is mathematically equivalent to the variational functional form of 4.29, which provides the connection between the Rayleigh–Ritz problem and the finite element technique. Once in this form the method aims to reduce the system to a series of algebraic expressions which can be solved numerically.

It has since been shown that a functional form is not required to reach the Galerkin form of the problem. A more general formulation is possible using the method of weighted residuals which leads to the standard Galerkin formulation.

4.3.1 The method of weighted residuals

In describing the method of weighted residuals consider first a linear differential equation arbitrarily denoted by equation 4.32 which is subject to appropriate initial boundary conditions,

$$\hat{\mathbf{L}}(u) = 0. \quad (4.32)$$

The solution, $u(\mathbf{x}, t)$, is assumed to be accurately represented by an infinite expansion, which is approximated with the finite sum

$$u^\delta(\mathbf{x}, t) = u_0(\mathbf{x}, t) + \sum_{i=1}^{N_{dof}} \hat{u}_i(t) \Phi_i(\mathbf{x}) \quad (4.33)$$

where $\Phi_i(\mathbf{x})$ are known as trial functions, \hat{u}_i are the unknown trial function coefficients and u_0 satisfies the initial and boundary conditions. By definition $\Phi_i(\mathbf{x})$ satisfies homogeneous boundary conditions allowing u_0 to account for all Dirichlet values on the boundary. Given this is only a finite approximation of an infinite solution when substituting equation 4.33 into 4.32 a residual $R(u^\delta)$ remains. In order to solve for the exact solution a restriction is placed on the residual, which has the added advantage of reducing the system of equations to a linear first-order system.

Defining the restriction enforced on the residual first requires definition of the Legendre inner product

$$(f, g) = \int_{\Omega} f(x) g(x) dx, \quad (4.34)$$

where f and g are arbitrary functions.

The desired restriction of the residual is that the inner product (equation 4.34) with respect to a weight function (sometimes referred to as a test function) is equal to zero, that is

$$(w_j(\mathbf{x}), R) = 0, \quad j = 1, \dots, N_{dof}, \quad (4.35)$$

where w_j is the weight function: the weighted residual is then said to be zero.

As the number of degrees of freedom, N_{dof} , approaches infinity, the residual tends to zero and the approximation u^δ approaches the exact solution u . The type of computational method is determined by the choice of the trial and test functions. To obtain the standard Galerkin formulation the same analytical function is used for both the test and trial function (Finlayson 1972).

4.3.2 The Galerkin method

The Rayleigh–Ritz problem and equivalently the method of weighted residuals forms a mathematical basis for finite element and spectral-*hp* element solvers. In this section, the Galerkin formulation is introduced and used to manipulate a series of Partial Differential Equations (PDEs) into a set of Ordinary Differential Equations (ODEs) which may be solved using numerical techniques.

Consider for example the one-dimensional Poisson equation

$$\hat{\mathbf{L}}(u) \equiv \frac{\partial^2 u}{\partial x^2} + f = 0, \quad (4.36)$$

with domain

$$\Omega = \{x \mid 0 \leq x \leq 1\}$$

and boundary conditions

$$u(0) = g_D, \quad \frac{\partial u}{\partial x}(1) = g_N,$$

where g_D and g_N are given constants for the Dirichlet and Neumann boundary conditions, respectively. In a variational formulation, Dirichlet type boundary conditions can be expressed explicitly using equation 4.33. However, Neumann boundary conditions prove difficult to enforce. Inherent in the Galerkin formulation is a method in which Neumann boundary conditions are explicitly expressed. However, the method for handling Dirichlet conditions is dependent on the choice of trial and test functions. To complete the Galerkin formulation and manage the Neumann boundary conditions the equations must be recast in “weak form”.

Finding the weak form is analogous to taking the Legendre inner product of the ODE with a weight or test function¹, $w(x)$. It is important for the implementation of the Dirichlet boundary conditions that the test function by definition is zero on all boundaries. The inner product of equation 4.36 is

$$(w, \mathbb{L}(u)) = \int_0^1 w \left(\frac{\partial^2 u}{\partial x^2} \right) + wf \, dx = 0. \quad (4.37)$$

Remember that equation 4.37 is equivalent to setting the weighted residual to zero and as such the approximation, u^δ , will approximate u as N_{dof} tends to infinity.

In forming the Galerkin formulation, the next step is to apply Gauss’ Divergence theorem to obtain

$$\int_0^1 \frac{\partial w}{\partial x} \frac{\partial u}{\partial x} \, dx = \int_0^1 wf \, dx + \left[\frac{\partial u}{\partial x} \right]_0^1. \quad (4.38)$$

Using the fact that the test function is zero on the boundaries allows the enforcement of the Neumann boundary condition $\frac{\partial u}{\partial x} = g_N$ via a direct substitution into the final term (see equation 4.39). The ease with which the Neumann boundary conditions are implemented is a direct result of the integral in the weak formulation. This operation

¹A test function, is a functional space against which the subject is checked. It attributes different weight (or importance) to the value of the subject across its domain and is used to check it meets the prescribed criteria (Karniadakis & Sherwin 1999)

implements Neumann boundary conditions, reduces the maximum order of derivatives in the discrete problem, and makes the resulting matrix equation symmetric, giving

$$\int_0^1 \frac{\partial w}{\partial x} \frac{\partial u}{\partial x} dx = \int_0^1 v f dx + w(1) g_{\mathcal{N}}. \quad (4.39)$$

In order to solve equation 4.39 the Galerkin approximation must be completed by substituting the exact solution $u(x)$ with a finite expansion u^δ and the continuous test function $w(x)$ with a finite test function w^δ such as

$$\int_0^1 \frac{\partial w^\delta}{\partial x} \frac{\partial u^\delta}{\partial x} dx = \int_0^1 w^\delta f dx + w^\delta(1) g_{\mathcal{N}}. \quad (4.40)$$

By casting the equations in their weak form, the Neumann boundary conditions are intrinsically handled. Dirichlet boundary conditions require further treatment through a process known as “lifting the solution”. To lift a boundary condition the approximate solution u^δ is split into a known lifted-Dirichlet function $u^{\mathcal{D}}$ which satisfies the Dirichlet boundary conditions and an unknown homogenous function $u^{\mathcal{H}}$ which has a zero value on the boundaries, i.e.,

$$u^\delta = u^{\mathcal{H}} + u^{\mathcal{D}} \quad (4.41)$$

By substituting 4.41 into 4.40,

$$\int_0^1 \frac{\partial w^\delta}{\partial x} \frac{\partial u^{\mathcal{H}}}{\partial x} dx = \int_0^1 w^\delta f dx + w^\delta(1) g_{\mathcal{N}} - \int_0^1 \frac{\partial w^\delta}{\partial x} \frac{\partial u^{\mathcal{D}}}{\partial x} dx. \quad (4.42)$$

Since $u^{\mathcal{D}}$ is a known function satisfying the boundary condition, the right hand side of equation 4.42 contains only known quantities. Note: the gradient of the Dirichlet boundary condition is known because $u^{\mathcal{D}}$ is approximated by the weighted sum of a set of trial functions (see equation 4.50) which has a generic shape which is scaled using $u^{\mathcal{D}}$ and the shape of the element, both of which are known. The left hand side contains only $u^{\mathcal{H}}$ and w^δ which are a finite number of functions. Essentially, the Galerkin formulation has taken a continuous partial differential equation and converted it to a matrix problem which can be solved computationally.

4.4 Spatial discretisation scheme

Due to the historical use of Taylor expansions to form approximate solutions to complex functions, polynomials are by far the most dominant form of expansion bases for finite element solvers (Karniadakis & Sherwin 1999). Finite element solvers, of which spectral

element solvers are a subset, may be categorized by their expansion bases as either h -type or p -type.

h -type solvers split the domain, Ω , into a set of N^{el} elements, Ω^e . The sum of the set of elements forms the entire solution domain. h -type solvers use a fixed-order polynomial in every element with convergence to the exact solution attained by reducing the size of elements; this is true of classical finite element solvers (Karniadakis & Sherwin 1999). The h represents the characteristic size of an element. This type of extension allows high geometric flexibility (Karniadakis & Sherwin 1999).

p -type solvers use a fixed mesh that encompasses the entire solution domain. A polynomial of order p is used as the test function across the entire domain fitting through a set of fixed mesh points. Convergence to the exact solution is achieved by increasing the polynomial order used to interpolate across the domain. Here, p represents the order of the polynomial function used to interpolate across the solution domain. This type of expansion allows rapid convergence in smooth problems, but is complicated in geometrically difficult domains. For the case where the whole solution domain is modelled with only one element then this kind of solver is a spectral method (Karniadakis & Sherwin 1999).

The spectral- hp element method, of which the algorithm developed in this thesis is a type, combines attributes of both extensions.

The following sections discuss the required components to form numerical operators that are capable of performing integration and differentiation. In the context of spectral- hp elements, the contribution of the h -type and p -type refinement in forming a global solution is recognised. This type of refinement dictates the procedure in which integration and differentiation operators are formed. An integral or differential operator may be formed over a standard element using a p -type discretisation, this can then be mapped to any local element coordinates before the h -type refinement maps this onto the global solution domain.

4.4.1 Forming the discrete system h -type decomposition

h -type methods subdivide the solution domain into non-overlapping sub-domains termed elements, within which the polynomial expansion basis is expressed.

Consider the domain Ω , which is partitioned into the arbitrarily sized N^{el} elements, each of spatial extent Ω^e , such that the domain is fully expressed by the union of the

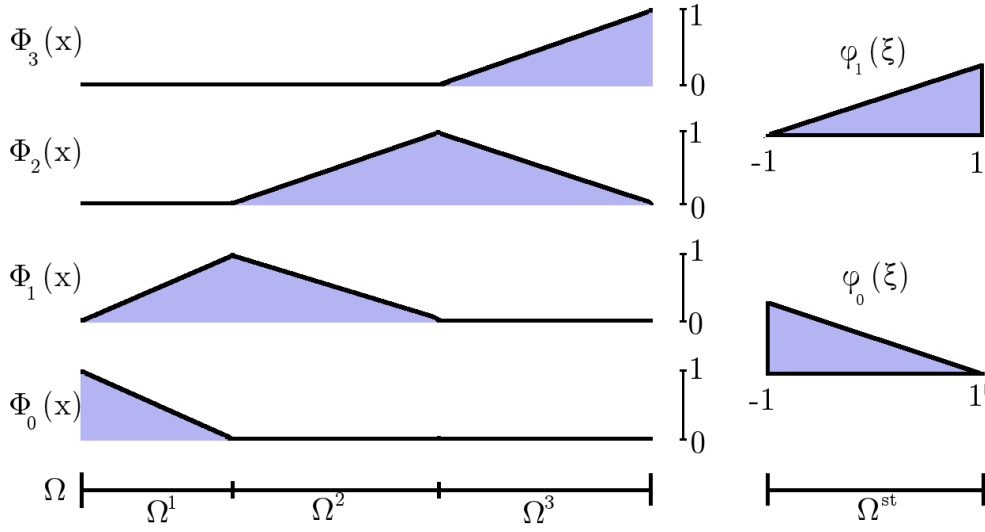


FIGURE 4.1: Elemental decomposition of the solution domain Ω into three elements Ω^1 , Ω^2 and Ω^3 . Above the domain the global expansion modes $\Phi_0(x)$, $\Phi_1(x)$, $\Phi_2(x)$ and $\Phi_3(x)$ are shown for a linear finite element expansion over the domain Ω . On the right are local expansion bases $\phi_0(\xi)$ and $\phi_1(\xi)$ defined in the standard region Ω^{st} which can be used to define the global expansion modes. Reproduced with the permission of Karniadakis & Sherwin and oxford university press from Karniadakis & Sherwin (1999).

individual elements. As an example consider the domain shown in figure 4.1 describing the 1-Dimensional domain $\Omega = \{x \mid 0 \leq x \leq 1\}$.

Figure 4.1 depicts the global expansion modes for a linear finite element expansion. Each mode has a value of one at the end of one of the elemental domains with a linear decay to zero at the other. Figure 4.1 also shows the four global degrees of freedom in this expansion $\Phi_0(x)$, $\Phi_1(x)$, $\Phi_2(x)$ and $\Phi_3(x)$. The global modes are non-zero in no more than two neighbouring elements.

On an elemental level each global mode consists of two linearly varying functions. If a one-dimensional standard element, $\Omega^{st} = \{\xi \mid -1 \leq \xi \leq 1\}$, is considered then an equivalent linear function can be defined over the standard element described by:

$$\phi_0(\xi) = \begin{cases} \frac{1-\xi}{2}, & \xi \in \Omega_{st}, \\ 0, & \xi \notin \Omega_{st}, \end{cases} \quad \phi_1(\xi) = \begin{cases} \frac{1+\xi}{2}, & \xi \in \Omega_{st}, \\ 0, & \xi \notin \Omega_{st}. \end{cases} \quad (4.43)$$

This is the standard form of a linear expansion basis for a one-dimensional element. To move from the standard element to any local elemental domain the mapping function $\chi^e(\xi)$ is used where

$$x = \chi^e(\xi) = \frac{1-\xi}{2}x_{e-1} + \frac{1+\xi}{2}x_e, \quad \xi \in \Omega_{st}. \quad (4.44)$$

and for mathematical completeness the inverse mapping is

$$\xi = (\chi^e)^{-1}(x) = 2 \frac{x - x_{e-1}}{x_e - x_{e-1}} - 1, \quad \xi \in \Omega^e. \quad (4.45)$$

This mapping function can be used to express the global modes Φ_i (h -type discretisation) in terms of the local elemental expansions ϕ_p (p -type discretisation).

The final step is to move from the elemental sub-space to the global domain through a process called the direct stiffness summation, or global assembly. In terms of global modes the finite element expansion u^δ is

$$u^\delta(x) = \sum_{i=0}^{N_{dof}-1} \hat{u}_i \Phi_i(\mathbf{x}). \quad (4.46)$$

This is expressed in terms of local-elemental modes as

$$u^\delta(x) = \sum_{i=0}^{N_{dof}-1} \hat{u}_i \Phi_i(\mathbf{x}) = \sum_{e=1}^{N_{el}} \sum_{p=0}^p \hat{u}_p^e \phi_p^e(\xi), \quad (4.47)$$

where p is the polynomial order of the expansion (spectral methods are not restricted to the linear expansion mode of equation 4.43), $\Phi_i(x)$ is the global expansion modes, and ϕ_p the local expansion modes. Note that $\phi_p^e(\xi) = \phi_p([\chi^e]^{-1}(x))$, where the superscript, e , denotes the element in which the function is non-zero.

As a result of the division of the domain into sub-domain regions there exists a necessary bordering of elements in order to account for the entire solution region. As such, in this discretisation there exists more local expansion coefficients \hat{u}_p^e than global expansion coefficients \hat{u}_i . As such, further conditions are required to relate the local and global definitions of the solution. Therefore, a constraint is enforced at element boundary edges in which u^δ must have the same value in each element expansion. In the example of Figure 4.2, the constraint may be expressed by

$$\begin{aligned} \hat{u}_1^1 &= \hat{u}_0^2, \\ \hat{u}_1^2 &= \hat{u}_0^3. \end{aligned} \quad (4.48)$$

In this way C^0 -continuity is enforced across the domain.

To facilitate the implementation of the local to global mapping the global boundary mapping matrix also known as the assembly matrix, \mathcal{A} , is introduced.

$$\hat{u}_l = \mathcal{A} \hat{u}_g, \quad (4.49)$$

where \hat{u}_g denotes the vector of all global coefficients and \hat{u}_l denotes the vector of all local coefficients within an element. \mathcal{A} is simply a mapping between global and local coordinates.

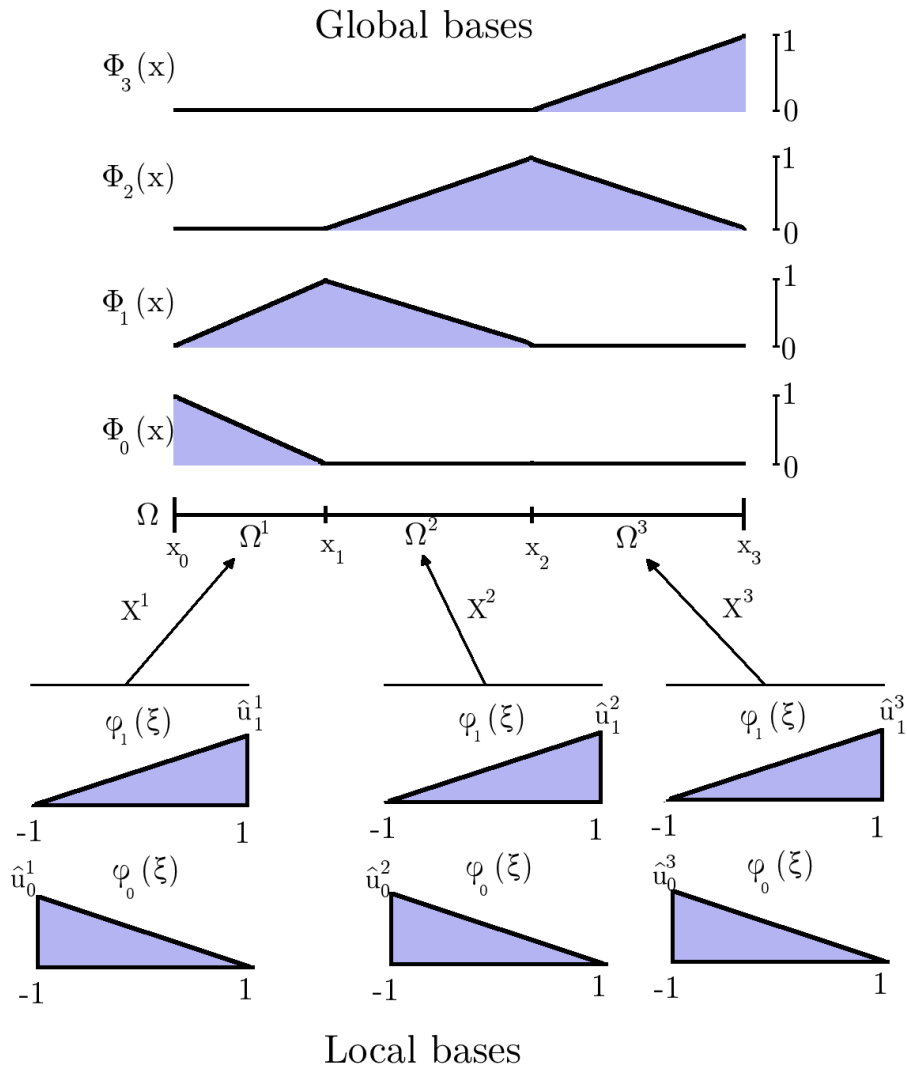


FIGURE 4.2: Global and local expansion coefficients and bases in a three-element decomposition of the domain Ω . Reproduced with the permission of Karniadakis & Sherwin and Oxford University Press from Karniadakis & Sherwin (1999).

In the Galerkin formulation it is advantageous to consider the inverse of the mapping, which can be mathematically shown to be the transpose of the assembly matrix (\mathcal{A}^T). The integral structure of the Galerkin formulation implies the summation of the elemental contributions of each test function in order to find the global solution. As such, operations may be performed on a local level before assembly into the global solution. This can be quite advantageous in terms of computational efficiency as matrix inverse problems are very expensive in large degree-of-freedom systems. Furthermore,

the mapping from standard element to local element coordinate $\chi^e(\xi)$, can also be exploited to perform all integrals on a standard elemental level, thus minimising the number of degrees of freedom in each matrix system solve.

In closing this discussion on the h -type expansion, it is recognised that in practice the global assembly matrix \mathcal{A} is never explicitly formed. The matrix is extremely sparse and so for implementation it is easier to represent the matrix as a mapping array.

4.4.2 Interpolating within an element: The p -type decomposition

While complex geometries, different scaling and localised structures necessitate h -type decomposition of a solution domain, it can be very numerically efficient and accurate at lower levels of h -type refinement to then use p -type extensions within elements to approximate the solution. In all that follows the p -type extension is interpreted as increasing the polynomial order of the polynomial expansion within the elemental region.

There are many types of polynomial expansions acceptable to spectral- hp element implementations, these can be classified in two groups as either modal or nodal expansions. The fluid and solid continuum algorithms used in this investigation are of nodal type; as such, modal expansion bases will not be discussed here. For further information on modal type expansion bases see Karniadakis & Sherwin (1999). Nodal expansion sets are based on a set of predetermined nodal points x_q . As an example consider a Lagrange polynomial

$$h_p(x) = \frac{\prod_{q=0, q \neq p}^P (x - x_q)}{\prod_{q=0, q \neq p}^P (x_p - x_q)}, \quad p = 0, \dots, P. \quad (4.50)$$

The Lagrange polynomial has the property that at the nodal points, $x = x_q$, the Lagrange polynomial represents a Kronecker-delta function. This property implies that

$$u^\delta(x_q) = \sum_{p=0}^P \hat{u}_p h_p(x_q) = \sum_{p=0}^P \hat{u}_p \delta_{pq} = \hat{u}_q, \quad (4.51)$$

where the expansion coefficient \hat{u}_p can be defined in terms of the approximate solution at the nodal points x_q . Therefore the coefficients, \hat{u}_p , physically represent the approximate solution at the nodal points. Linear finite elements use nodal expansions with the nodal points located at either end of the solution domain; for the Gauss–Legendre–Lobatto quadrature used in this solver, nodal points are chosen to be internal and include all extremes of the solution domain.

The choice of nodal expansion basis is influenced by numerical efficiency and approximation properties. Consider for example, the Galerkin approximation of a smooth function, $f(x)$,

$$(w^\delta, u^\delta) = (w^\delta, f). \quad (4.52)$$

Using a Galerkin formulation the test and trial functions have the same form, $u^\delta(x) = w^\delta(x) = \sum_{p=0}^p \hat{u}_p \Phi_p(x)$. As such, equation 4.52 can be transformed to a matrix problem of the form,

$$w^T [\mathbf{M} \hat{u} = f] \Rightarrow \mathbf{M} \hat{u} = f_p, \quad (4.53)$$

where,

$$\mathbf{M}_{pq} = (\Phi_p, \Phi_q), \quad \hat{u} = [\hat{u}_0, \dots, \hat{u}_p]^T, \quad \mathbf{f}_p = (\Phi_p, f). \quad (4.54)$$

The matrix \mathbf{M} is known as the mass matrix and contains the global expansion base coefficients, \hat{u} is the solution vector at the p nodal points, and f_p is the elemental nodal values of the forcing term in the ODE. The matrix \mathbf{M} may be inverted to find the solution to the algebraic equation 4.53. The numerical efficiency associated with the choice of expansion base stems from the cost of constructing and inverting the matrix. As such, to promote numerical efficiency the expansion base used is chosen on the basis of generating a matrix with a predetermined structure that is conducive to construction and inversion.

From this perspective, the Lagrange polynomial is particularly useful as it produces a purely diagonal mass matrix, on an elemental level, by virtue of the Kronecker-delta function. The diagonal structure is very inexpensive to construct and invert. Lagrange–Legendre polynomials have the added advantage of being orthogonal, leading to excellent matrix conditioning which is important to numerical accuracy in terms of the numerical matrix inversion process.

4.4.2.1 Gauss–Legendre–Lobatto quadrature

As described earlier, nodal expansions are based on the value of a function at a set of nodal points, i.e. they are based on the Lagrange polynomial. In the algorithm employed herein, the nodal points may be spaced in any way throughout the solution domain with the only restriction being they include nodal points at the extremes of the domain (this is in order to enforce C^0 -continuity between elements). The location of nodes does impact on the stability of the numerical method. Using nodal points at the zeros of Gauss–Legendre–Lobatto integration rules creates a particularly efficient,

stable and accurate expansion. Unlike the pure Gaussian quadrature, Gauss–Legendre–Lobatto quadrature includes nodal points at the edges of the domain, for a small cost in accuracy.

Lagrange polynomials, h_p , are unique polynomials that have the value of unity at the node x_p and zero at all other nodes x_q ,

$$h_p(x_q) = \delta_{pq}. \quad (4.55)$$

Note the Lagrange polynomial, as defined by equation 4.50, can be expressed at the nodal locations using the property 4.55. The test function interpolation approximation requires the interpolant \mathcal{J} which is a function of u ,

$$\mathcal{J}u(x_q) = u(x_q),$$

and therefore the interpolant can be written as

$$\mathcal{J}u(x) = \sum_{p=0}^P \hat{u}_p h_p(x). \quad (4.56)$$

If $u(x)$ is a polynomial of order p the relationship is exact. For the particularly accurate case of Gauss–Legendre–Lobatto quadrature, the p -type expansion in the standard element is

$$\phi_p(\xi) \mapsto h_p(\xi) = \begin{cases} 1, & \xi = \xi_p, \\ \frac{(\xi - 1)(\xi + 1)L'_P(\xi)}{p(p+1)L_P(\xi_p)(\xi_p - \xi)}, & \text{otherwise,} \end{cases} \quad (4.57)$$

where L_P is the Legendre polynomial, L'_P is its derivative and p is the polynomial order of the expansion. The shapes of these modes for a polynomial order $p = 3$ are shown in figure 4.3

Owing to its nodal construction, all modes are polynomials of order p . The boundary modes ϕ_0 and ϕ_3 are the only modes to exhibit a value other than zero on the boundaries; this allows the h -type decomposition of the solution domain to enforce C^0 -continuity.

As the Galerkin formulation with Gauss–Legendre–Lobatto quadrature uses the same nodal points on which the expansion was defined for the test function; the property in equation 4.51 implies that the mass matrix is diagonal rather than full.

$$\mathbf{M}^e[p][q] = (h_p, h_q) \simeq \sum_{i=0}^p w_i h_p(\xi_i) h_q(\xi_i) = \sum_{i=0}^p w_i \delta_{pi} \delta_{pq} = w_p \delta_{pq}, \quad (4.58)$$

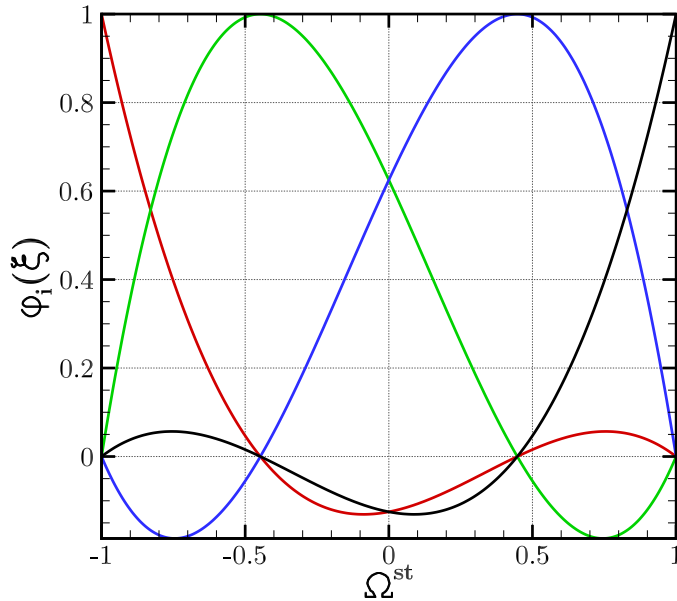


FIGURE 4.3: Nodal expansion modes for a polynomial order of $p = 3$ in the standard element. The red, green, blue and black lines represent the ϕ_0 , ϕ_1 , ϕ_2 , and ϕ_3 modes respectively.

where w_i are the weights for Gauss–Legendre–Lobatto quadrature using $p + 1$ points. Using the same nodal points for both the quadrature rule and Lagrange polynomial ensures discrete orthogonality, which ensures an exact solution for polynomials of order $2p - 1$ (Karniadakis & Sherwin 1999).

4.4.3 Numerical integration

Having developed a numerical basis for decomposing the global expansion basis into elemental sub-domains and mapping them onto a standard region over which a polynomial expansion base is expressed, the Gauss–Legendre–Lobatto quadrature can now be used to integrate and differentiate within the standard region.

Given the Galerkin formulation is cast in weak form which is based on the sum of elemental integrals, a technique is required to evaluate the integral of each function across the standard domain. Once established in the standard domain this may then be mapped to local-elemental co-ordinates. The integral over a standard domain is

$$\int_{-1}^1 u(\xi) \, d\xi, \quad (4.59)$$

where $u(\xi)$ may be made up of products of the polynomial basis functions (e.g. equation 4.57).

Given the form of $u(\xi)$ is application-specific a generic evaluation technique must be employed. This provides the motivation to use numerical quadrature techniques such as Gaussian quadrature.

Gaussian quadrature represents the integrand as a Lagrange polynomial using the Q points ξ_i in

$$u(\xi) = \sum_{i=0}^{Q-1} u(\xi_i) h_i(\xi) + \varepsilon(u), \quad (4.60)$$

where $\varepsilon(u)$ is the approximation error. Combining this with the integration equation 4.59 gives,

$$\int_{-1}^1 u(\xi) d\xi = \sum_{i=0}^{Q-1} w_i u(\xi_i) + R(u), \quad (4.61)$$

where,

$$w_i = \int_{-1}^1 h_i(\xi) d\xi, \quad (4.62)$$

and

$$R(u) = \int_{-1}^1 \varepsilon(u) d\xi. \quad (4.63)$$

Equation 4.62 describes the integration weights in terms of integrals of the Lagrange polynomial. All that is required then to perform the integration is the nodal locations, namely the zeros ξ_i (also known as abscissae). If the nodal positions are equispaced, an exact solution for $u(\xi)$ which is represented by a polynomial of order $Q - 1$; could only be achieved with a polynomial of $Q - 1$ (Karniadakis & Sherwin 1999). In Gaussian quadrature non-equispaced zeros are chosen. To facilitate easy implementation of global boundary decomposition a sub-class of the more accurate Gaussian quadrature, Gauss–Legendre–Lobatto quadrature is employed. This form of Gaussian quadrature has zeros at either end of the standard region. i.e.

$$\begin{aligned} \xi_i &= \begin{cases} -1, & i = 0, \\ \xi_{i-1, Q-2}^{1,1}, & i = 1, \dots, Q-2, \\ 1, & i = Q-1, \end{cases} \\ w_i^{0,0} &= \frac{2}{Q(Q-1)[L_{Q-1}(\xi_i)]^2}, & i = 0, \dots, Q-1 \\ R(u) &= 0 & \text{if } u(\xi) \in \hat{P}_{2Q-3}([-1, 1]). \end{aligned} \quad (4.64)$$

where $L_Q(\xi)$ is the Legendre polynomial ($L_Q(\xi) = \hat{P}_Q^{0,0}(\xi)$). The zeros of the Jacobi polynomial \hat{P} are $\xi_{i,m}^{\alpha,\beta}$ for which there is no analytical solution. Karniadakis & Sherwin (1999) describes a recursive strategy for determining the Jacobi zeros.

4.4.4 Differentiation

Using the polynomial approximation,

$$u^\delta(x) = \sum_{p=0}^p \hat{u}_p \phi_p(\chi^{-1}) = \sum_{p=0}^p \hat{u}_p \phi_p(\xi), \quad (4.65)$$

where $\chi(\xi)$ is the standard-to-elemental domain mapping, differentiating using the chain rule to obtain,

$$\frac{du^\delta(x)}{dx} = \frac{du^\delta(\xi)}{d\xi} \frac{d\xi}{dx} = \sum_{p=0}^p \hat{u}_p \frac{d\phi_p(\xi)}{d\xi} \frac{d\xi}{dx}. \quad (4.66)$$

Thus in approximating the differential of the unknown u a method for evaluating $\frac{d\phi_p(\xi)}{d\xi}$ and $\frac{d\xi}{dx}$ is required. Given a polynomial expansion using Lagrange polynomials (see equation 4.50) and utilizing Gauss–Legendre–Lobatto quadrature the derivative of u in the standard domain (i.e. in ξ - space) is

$$\frac{du(\xi)}{d\xi} = \sum_{i=0}^{Q-1} u(\xi_i) \frac{d}{d\xi} h_i(\xi), \quad (4.67)$$

Typically, we only require the derivative at the nodal points ξ_i which is given by

$$\left. \frac{du(\xi)}{d\xi} \right|_{\xi=\xi_i} = \sum_{j=0}^{Q-1} d_{ij} u(\xi_j), \quad (4.68)$$

where

$$d_{ij} = \left. \frac{dh_j(\xi)}{d\xi} \right|_{\xi=\xi_i}. \quad (4.69)$$

For the specific case of Gauss–Legendre–Lobatto quadrature the standard element differentiation matrices may be described by

$$\xi_i = \begin{cases} -1, & i = 0, \\ \xi_{i=1, Q-2}^{1,1}, & i = 1, \dots, Q-2, \\ 1, & i = Q-1, \end{cases} \quad (4.70)$$

$$d_{ij} = \begin{cases} \frac{-Q(Q-1)}{4}, & i = j = 0, \\ \frac{L_{Q-1}(\xi_i)}{L_{Q-1}(\xi_j)} \frac{1}{\xi_i \xi_j}, & i \neq j, 0 \leq i, j \leq Q-1, \\ 0, & 1 \leq i = j \leq Q-2, \\ \frac{Q(Q-1)}{4}, & i = j = Q-1. \end{cases}$$

Note: Just as with the quadrature formulae the construction of the differentiation matrices requires the numerically determined quadrature zeros which are found using a recursive formula given in Appendix A of Karniadakis & Sherwin (1999).

4.5 Forming global operators

In the discussion thus far the merits of the Galerkin approximation and the choice of a nodal-based Gauss–Legendre–Lobatto quadrature scheme to discretise a set of partial differential equations has been outlined. It has been shown how this mathematical framework may be used to perform integration and differentiation over a standard domain. It has also been demonstrated how the Galerkin formulation allows easy enforcement of boundary conditions. The following sections illustrate how this mathematical basis is used to solve complex systems by mapping the solution from a standard region to a local elemental space and finally how this is connected to form the global solution. Algebraic matrix operators are formed from the mathematical framework and special operators for higher-order operations and enforcing boundary conditions are expressed.

4.5.1 The Jacobian

As discussed earlier when performing elemental operations, integrals and differentials are efficiently computed by performing them over a standard region and then mapping them onto the elemental domain. It has been shown how such a mapping may be formed in one dimension. In two and three dimensions the concept of Jacobian mapping is introduced. Just as in one dimension the integral becomes

$$\int_{\Omega^e} u(x_1, x_2) dx_1 dx_2 = \int_{\Omega_{st}} u(\xi_1, \xi_2) |J_{2D}| d\xi_1 d\xi_2. \quad (4.71)$$

Here J_{2D} is defined as

$$J_{2D} = \begin{vmatrix} \frac{\partial x_1}{\partial \xi_1} & \frac{\partial x_1}{\partial \xi_2} \\ \frac{\partial x_2}{\partial \xi_1} & \frac{\partial x_2}{\partial \xi_2} \end{vmatrix}, \quad (4.72)$$

and for completeness J_{3D} is defined as

$$J_{3D} = \begin{vmatrix} \frac{\partial x_1}{\partial \xi_1} & \frac{\partial x_1}{\partial \xi_2} & \frac{\partial x_1}{\partial \xi_3} \\ \frac{\partial x_2}{\partial \xi_1} & \frac{\partial x_2}{\partial \xi_2} & \frac{\partial x_2}{\partial \xi_3} \\ \frac{\partial x_3}{\partial \xi_1} & \frac{\partial x_3}{\partial \xi_2} & \frac{\partial x_3}{\partial \xi_3} \end{vmatrix}, \quad (4.73)$$

where $|\dots|$ represents the determinant of the matrix.

Given the form of the mapping $x_i = \chi(\xi_1, \xi_2)$, all partial derivatives required for the Jacobian can be calculated. For a straight-sided quadrilateral element with corner nodes at $\{(x_1^A, x_2^A), (x_1^B, x_2^B), (x_1^C, x_2^C), (x_1^D, x_2^D)\}$ the mapping is described by

$$x_i = \chi(\xi_1, \xi_2) = x_i^A \frac{1 - \xi_1}{2} \frac{1 - \xi_2}{2} + x_i^B \frac{1 + \xi_1}{2} \frac{1 - \xi_2}{2} + x_i^C \frac{1 + \xi_1}{2} \frac{1 + \xi_2}{2} + x_i^D \frac{1 - \xi_1}{2} \frac{1 + \xi_2}{2}. \quad (4.74)$$

The simple form of these mappings ensures that the partial derivatives and Jacobians are constant for all quadrilateral regions of this shape. For deformed elements the Jacobian may be evaluated and stored at the quadrature points, thus storing the standard-to-elemental mapping at each of the nodal points.

An analogous application of the Jacobian mapping may be applied to differential operations. A chain rule expansion shows that the differential operator may be given by

$$\nabla = \begin{bmatrix} \frac{\partial}{\partial x_1} \\ \frac{\partial}{\partial x_2} \end{bmatrix} = \begin{bmatrix} \frac{\partial \xi_1}{\partial x_1} \frac{\partial}{\partial \xi_1} + \frac{\partial \xi_2}{\partial x_1} \frac{\partial}{\partial \xi_2} \\ \frac{\partial \xi_1}{\partial x_2} \frac{\partial}{\partial \xi_1} + \frac{\partial \xi_2}{\partial x_2} \frac{\partial}{\partial \xi_2} \end{bmatrix}. \quad (4.75)$$

Through a process of manipulating the coordinate mapping (in 2D)

$$\frac{\partial \xi_1}{\partial x_1} = \frac{1}{J} \frac{\partial x_2}{\partial \xi_2}, \quad \frac{\partial \xi_1}{\partial x_2} = -\frac{1}{J} \frac{\partial x_1}{\partial \xi_2}, \quad \frac{\partial \xi_2}{\partial x_1} = -\frac{1}{J} \frac{\partial x_2}{\partial \xi_1}, \quad \frac{\partial \xi_2}{\partial x_2} = \frac{1}{J} \frac{\partial x_1}{\partial \xi_1}. \quad (4.76)$$

At this point computation of the two-dimensional gradient operator equation 4.75 is possible using the relationships in equation 4.76, as all partial derivatives can be expressed in terms of the standard elemental co-ordinates (ξ_1, ξ_2) . This allows us to pre-compute and store the differential operators using the Jacobian mapping, just as with the integral formulae.

4.5.2 Mass matrix, \mathbf{W}

As a consequence of the Galerkin formulation a method of numerically performing an integral is required. The following discusses the development of the \mathbf{W} matrix (Karniadakis & Sherwin 1999, following), a matrix operator which performs integrals in the numerical algorithm.

As solutions are computed across a standard region and then mapped to elemental space, let the vector \mathbf{u} denote the evaluation of $\mathbf{u}(\xi)$ at the standard elemental points.

The weight matrix, \mathbf{W} , is a diagonal matrix which contains the Gaussian quadrature weights, augmented by the elemental Jacobian at each quadrature point. It is designed to be consistent with \mathbf{u} evaluated at each of the quadrature points. This forms the matrix implementation of the numerical integration formulae discussed in § 4.4.3 in one dimension.

$$\mathbf{W} [m(ijk)] [n(rst)] = J_{ijk} w_i w_j w_k \delta_{mn}, \quad (4.77)$$

where δ_{mn} is the Kronecker-delta function, and $m(ijk)$ and $n(rst)$ are integer values which run consecutively from 0 to the number of quadrature points N_Q thus relating

all nodes in the domain. The use of the Jacobian in forming the matrix \mathbf{W} allows it to perform integration in the local-elemental coordinate system. In global co-ordinates the assembly matrix, \mathcal{A} , is used to combine the degrees of freedom.

4.5.3 Differentiation matrix, \mathbf{D}

The final matrix required to complete the set of discrete operators is the differentiation matrix (analogous to the one-Dimensional operation in equation 4.67), extended to global co-ordinates. The partial derivative of local-elemental co-ordinates with respect to standard co-ordinates is defined by

$$\frac{\partial u}{\partial \xi_1}(\xi_{1i}, \xi_{2j}, \xi_{3k}) = \sum_{r=0}^{Q_1} \sum_{s=0}^{Q_2} \sum_{t=0}^{Q_3} \frac{dh_r(\xi_1)}{d\xi_1} \Big|_{\xi_{1,i}} h_s(\xi_{2j}) h_t(\xi_{3k}) u_{rst}, \quad (4.78)$$

where $h_r(\xi)$ is the one-dimensional Lagrange polynomials through the Q Gauss–Legendre–Lobatto quadrature points. A differentiation matrix may be formed,

$$\mathbf{D}_{\xi_i} = \frac{dh_r(\xi_1)}{d\xi_1} \Big|_{\xi_{1,i}} h_s(\xi_{2j}) h_t(\xi_{3k}), \quad (4.79)$$

which acts on the global vector \mathbf{u} evaluated at the quadrature points to form the derivative at the quadrature points in each of the ξ_i directions. To finalize this discussion it is recognized that the derivative with respect to the local coordinates may be obtained from the chain rule (i.e. equation 4.75). Given this definition, the differential operator must be pre-multiplied by a diagonal matrix containing the factors $\frac{d\xi}{dx}$ evaluated at each of the quadrature points. This may be represented by the diagonal component notation $\mathbf{\Lambda}(f(\xi_1, \xi_2, \xi_3)) = f(\xi_{1i}, \xi_{2j}, \xi_{3k}) \delta_{mn}$. Finally the differentiation matrix in global coordinates takes the form,

$$\frac{\partial \mathbf{u}}{\partial x_1} = \left[\mathbf{\Lambda} \frac{\partial \xi_1}{\partial x_1} \mathbf{D}_{\xi_1} + \mathbf{\Lambda} \frac{\partial \xi_2}{\partial x_1} \mathbf{D}_{\xi_2} + \mathbf{\Lambda} \frac{\partial \xi_3}{\partial x_1} \mathbf{D}_{\xi_3} \right] \mathbf{u}. \quad (4.80)$$

In this discussion it has been shown that by casting the equations in the weak Galerkin form enables the reconstruction of the partial differential equations in a form that may be approximated using polynomial functions. Using Gauss-type quadrature rules it is evident that the equations may be cast into simple algebraic matrix equations. Equipped with the quadrature rules and the standard-local Jacobian mappings enables construction of the matrices \mathbf{W} and \mathbf{D} . Finally, the assembly matrix \mathcal{A} can be used to combine local degrees of freedom to form a global system. A numerical toolbox has been described which may be used to solve complicated PDEs with integral and differential operators.

4.5.4 Forming higher-order operators

While it has been shown that integrals and differentials can be easily performed, a non-trivial extension that is required is the formation of high-order operators such as the Laplacian, ∇^2 . These higher-order operators are required in this implementation for the viscous term in the Navier–Stokes equations (4.1) and the stress gradient term in the solid mechanics equations (4.3). To illustrate this consider the example used in Karniadakis & Sherwin (1999) of the Galerkin approximation of a Poisson equation

$$\nabla^2 u(x) = f(x). \quad (4.81)$$

Taking the Legendre inner product and applying Gauss’ Divergence theorem (as per Galerkin approximation) obtains

$$(\nabla v, \nabla u) = \int_{\partial\Omega} v \nabla u \cdot \mathbf{n} \, dS - (v, f), \quad (4.82)$$

where $\partial\Omega$ is the boundary of the problem domain and \mathbf{n} is the unit normal vector to the boundary. The weak Laplacian is $(\nabla v, \nabla u)$, and in two dimensions may be written as

$$(\nabla v, \nabla u) = \left(\frac{\partial v}{\partial x_1}, \frac{\partial u}{\partial x_1} \right) + \left(\frac{\partial v}{\partial x_2}, \frac{\partial u}{\partial x_2} \right). \quad (4.83)$$

Given that the Galerkin approximation uses the same test and trial functions, the matrix form of the weak Laplacian, becomes

$$\begin{aligned} L^e &= \left[\mathbf{\Lambda} \left(\frac{\partial \xi_1}{\partial x_1} \right) D_{\xi_1} + \mathbf{\Lambda} \left(\frac{\partial \xi_2}{\partial x_1} \right) D_{\xi_2} \right]^T W \left[\mathbf{\Lambda} \left(\frac{\partial \xi_1}{\partial x_1} \right) D_{\xi_1} + \mathbf{\Lambda} \left(\frac{\partial \xi_2}{\partial x_1} \right) D_{\xi_2} \right] \\ &+ \left[\mathbf{\Lambda} \left(\frac{\partial \xi_1}{\partial x_2} \right) D_{\xi_1} + \mathbf{\Lambda} \left(\frac{\partial \xi_2}{\partial x_2} \right) D_{\xi_2} \right]^T W \left[\mathbf{\Lambda} \left(\frac{\partial \xi_1}{\partial x_2} \right) D_{\xi_1} + \mathbf{\Lambda} \left(\frac{\partial \xi_2}{\partial x_2} \right) D_{\xi_2} \right]. \end{aligned}$$

Note the transpose in the pre-multiplied differentiation matrix is simply a result of the matrix algebra required to recover the form of the Laplacian (see equation 4.83).

4.5.5 The surface integral

As a direct consequence of the Galerkin formulation and specifically the step involving Gauss’ Divergence theorem, a surface integral (in 3D) or a line integral (in 2D) must be performed. See for example the Galerkin form of the Helmholtz equation. Physically

this line or surface integral may be interpreted as representing the enforcement of boundary conditions on the reformulated equations

$$(\nabla v, \nabla u)_\Omega + \lambda(v, u)_\Omega = \langle v, \nabla u \cdot \mathbf{n} \rangle - (v, f)_\Omega. \quad (4.84)$$

It is noted that the surface integral which results from the Galerkin approximation allows explicit enforcement of the Neumann boundary conditions. To solve the PDE an operator which evaluates the surface integral is required,

$$\langle v, \nabla u \cdot \mathbf{n} \rangle = \langle v, g_{\mathcal{N}} \rangle = \int_{\partial\Omega_{\mathcal{N}}} v g_{\mathcal{N}} \, dS = \sum_{e=1}^{N_{el}} \int_{\partial\Omega_{\mathcal{N}} \cap \partial\Omega^e} v^e g_{\mathcal{N}} \, dS^e. \quad (4.85)$$

As with regular integrals the strategy is to perform the integration using efficient Gaussian quadrature across a standard element and subsequently map these to each individual element in order to find their elemental contribution. In following this approach the surface Jacobian is introduced, which is analogous to the Jacobian for full integrals. Let us first consider the two-dimensional case, which is simply a line integral of the form

$$\int_a^b f(x_1, x_2) \, ds, \quad (4.86)$$

where $ds = \sqrt{(dx_1)^2 + (dx_2)^2}$ is the differential length along the path of integration. The differential length, ds , may be expressed in terms of the local co-ordinates, ξ , through knowledge of the mapping χ , i.e.

$$x_1 = \chi_1(\xi_1, \xi_2), x_2 = \chi_2(\xi_1, \xi_2), \quad (4.87)$$

allowing dx_1 and dx_2 to be expressed as

$$dx_1 = \frac{\partial x_1}{\partial \xi_1} d\xi_1 + \frac{\partial x_1}{\partial \xi_2} d\xi_2, \quad dx_2 = \frac{\partial x_2}{\partial \xi_1} d\xi_1 + \frac{\partial x_2}{\partial \xi_2} d\xi_2. \quad (4.88)$$

A method for solving the partial derivatives (equation 4.68) has already been developed. Along a boundary the element edge is completely parametrised by only one of the standard co-ordinates. That is to say, one of the standard coordinates ξ_1 or ξ_2 will be constant on the edge. Thus evaluation of ds can be made in terms of the differential change in the other dimension, equation 4.89 is for the case where ξ_2 is held constant

$$ds = \sqrt{(dx_1)^2 + (dx_2)^2} = \sqrt{\left(\frac{\partial x_1}{\partial \xi_1} \Big|_{\xi_2=-1} \right)^2 (d\xi_1)^2 + \left(\frac{\partial x_2}{\partial \xi_1} \Big|_{\xi_2=-1} \right)^2 (d\xi_1)^2}. \quad (4.89)$$

Thus the contribution to the e^{th} element in the integral equation may be found using

$$\int_{\partial\Omega^e \cap s} f(x_1, x_2) ds = \int_{-1}^1 f(\xi_1, \xi_2) \sqrt{\left(\frac{\partial x_1}{\partial \xi_1}\right)^2 + \left(\frac{\partial x_2}{\partial \xi_1}\right)^2} d\xi_1, \quad (4.90)$$

which may be simply evaluated using the Gaussian quadrature rules.

The extension to three dimensions is slightly more complex because on any surface only one of the standard co-ordinates is constant while the other two vary, for example for a surface for which ξ_3 is fixed

$$x_1 = \chi_1(\xi_1, \xi_2, -1), \quad x_2 = \chi_2(\xi_1, \xi_2, -1), \quad x_3 = \chi_3(\xi_1, \xi_2, -1). \quad (4.91)$$

To relate the differential change in surface area dS in terms of parametric coordinates it is recognised that a change in position dx , will be the vector $[dx_1, dx_2, dx_3]^T$ and in parametric co-ordinates,

$$dx = \frac{\partial \mathbf{x}}{\partial \xi_1} d\xi_1 + \frac{\partial \mathbf{x}}{\partial \xi_2} d\xi_2, \quad (4.92)$$

where \mathbf{x} is the position vector and $\frac{\partial \mathbf{x}}{\partial \xi_i}$ are surface tangent vectors along lines of constant ξ_1 and ξ_2 (in the case that ξ_3 is constant). Given this interpretation, along lines of constant ξ_2 the change in differential length $d\mathbf{l}_{\xi_2}$ is

$$d\mathbf{l}_{\xi_2} = \left. \frac{\partial \mathbf{x}}{\partial \xi_1} \right|_{\xi_2} d\xi_1 = \begin{bmatrix} \frac{\partial x_1}{\partial \xi_1} \\ \frac{\partial x_2}{\partial \xi_1} \\ \frac{\partial x_3}{\partial \xi_1} \end{bmatrix} d\xi_1. \quad (4.93)$$

Finally, these differential tangent vectors may be used to determine the change in area on the surface using a cross product rule

$$dS = |d\mathbf{l}_{\xi_2}| |d\mathbf{l}_{\xi_1}| \sin \theta, \quad (4.94)$$

where θ is the angle between the two vectors $d\mathbf{l}_{\xi_1}$ and $d\mathbf{l}_{\xi_2}$ which expressed explicitly as a cross product becomes

$$dS = |d\mathbf{l}_{\xi_2} \times d\mathbf{l}_{\xi_1}| = \left| \frac{\partial \mathbf{x}}{\partial \xi_1} \times \frac{\partial \mathbf{x}}{\partial \xi_2} \right| d\xi_1 d\xi_2 \quad (4.95)$$

It may be easier to interpret this as finding the component of the vector normal to the surface. Finally the surface integral may be evaluated as

$$\int_{\partial\Omega^e \cap s} f(x_1, x_2, x_3) dS = \int_{-1}^1 \int_{-1}^1 f(\xi_1, \xi_2, -1) \left| \frac{\partial \mathbf{x}}{\partial \xi_1} \times \frac{\partial \mathbf{x}}{\partial \xi_2} \right| d\xi_1 d\xi_2 \quad (4.96)$$

This completes the numerical toolbox needed to construct algebraic approximations of the partial differential equations to be solved in this thesis.

4.6 Static condensation

Having described the mathematical framework described in Karniadakis & Sherwin (1999), which transforms a partial differential equation into a set of algebraic matrix equations, an efficient technique is now described for solving the system, known as static condensation. For details on the derivation of the static condensation technique, the reader is directed to the discussion in Karniadakis & Sherwin (1999). It is assumed the matrix system to be solved is of the form

$$\mathbf{M}\mathbf{x} = \mathcal{A}^T \underline{\mathbf{M}}^e \mathcal{A}\mathbf{x} = \mathbf{f}, \quad (4.97)$$

where \mathbf{x} is a vector of global unknowns \mathbf{M} is a block diagonal matrix formed from the Laplacian, local mass matrices, or both. In the static condensation technique use is made of the global elemental decomposition to perform the matrix inversion over an elemental matrix domain, which is far more efficient due to the smaller matrix sizes. Each of the elemental matrices $\underline{\mathbf{M}}^e$ can be broken down into components containing boundary and interior contributions (as a result of the numbering scheme employed), that is,

$$\underline{\mathbf{M}}^e = \begin{bmatrix} \mathbf{M}_b^e & \mathbf{M}_c^e \\ (\mathbf{M}_c^e)^T & \mathbf{M}_i^e \end{bmatrix}, \quad (4.98)$$

Where \mathbf{M}_b^e is the boundary-boundary mode interactions, \mathbf{M}_c^e is the components resulting from a coupling between boundary and interior nodes and \mathbf{M}_i^e is from interior-interior mode interactions. Just as with the matrix $\underline{\mathbf{M}}^e$ the vectors \mathbf{x} and \mathbf{f} may be broken into the boundary and interior components \mathbf{x}_b , \mathbf{x}_i and \mathbf{f}_b , \mathbf{f}_i respectively, that is,

$$\mathbf{x} = \begin{bmatrix} \mathbf{x}_b \\ \mathbf{x}_i \end{bmatrix}, \quad \mathbf{f} = \begin{bmatrix} \mathbf{f}_b \\ \mathbf{f}_i \end{bmatrix}, \quad (4.99)$$

then equation 4.97 can be written as

$$\begin{bmatrix} \mathbf{M}_b^e & \mathbf{M}_c^e \\ (\mathbf{M}_c^e)^T & \mathbf{M}_i^e \end{bmatrix} \begin{bmatrix} \mathbf{x}_b \\ \mathbf{x}_i \end{bmatrix} = \begin{bmatrix} \mathbf{f}_b \\ \mathbf{f}_i \end{bmatrix}. \quad (4.100)$$

To solve this system a standard block elimination can be performed (Karniadakis & Sherwin 1999). After block elimination, equation 4.100 becomes

$$\begin{bmatrix} \mathbf{M}_b^e - \mathbf{M}_c^e (\mathbf{M}_i^e)^{-1} (\mathbf{M}_c^e)^T & 0 \\ (\mathbf{M}_c^e)^T & \mathbf{M}_i^e \end{bmatrix} \begin{bmatrix} \mathbf{x}_b \\ \mathbf{x}_i \end{bmatrix} = \begin{bmatrix} \mathbf{f}_b - \mathbf{M}_c^e (\mathbf{M}_i^e)^{-1} \mathbf{f}_i \\ \mathbf{f}_i \end{bmatrix}. \quad (4.101)$$

The equation for the boundary unknowns is therefore

$$\left(\mathbf{M}_b^e - \mathbf{M}_c^e (\mathbf{M}_i^e)^{-1} (\mathbf{M}_c^e)^T\right) \mathbf{x}_b = \mathbf{f}_b - \mathbf{M}_c^e (\mathbf{M}_i^e)^{-1} \mathbf{f}_i. \quad (4.102)$$

Once the boundary unknowns \mathbf{x}_b are determined the internal degrees of freedom \mathbf{x}_i can be determined from the second row of equation 4.101 since

$$\mathbf{x}_i = (\mathbf{M}_i^e)^{-1} \mathbf{f}_i - (\mathbf{M}_i^e)^{-1} (\mathbf{M}_c^e)^T \mathbf{x}_b. \quad (4.103)$$

To solve the matrix system (equation 4.97) no longer requires finding the inverse of \mathbf{M} . Instead evaluation of \mathbf{M}_i alone is required. Since \mathbf{M}_i is a block diagonal matrix (due to the choice of Legendre polynomials for the basis function) the local matrices \mathbf{M}_i^e and its inverse $(\mathbf{M}_i^e)^{-1}$ are also diagonal. This can be inverted locally within each element which is much less computationally expensive than a global inversion of the \mathbf{M}_i matrix. Once this inverse is found, simple matrix multiplication can be used to form $\mathbf{M}_c^e (\mathbf{M}_i^e)^{-1} = \left[(\mathbf{M}_i^e)^{-1} (\mathbf{M}_c^e)^T \right]^T$.

The final component is to form and invert the *Schur complement*, $\mathbf{M}_{sc} = \mathbf{M}_b^e - \mathbf{M}_c^e (\mathbf{M}_i^e)^{-1} (\mathbf{M}_c^e)^T$. Once these three components have been formed equations 4.102 and 4.103 can be easily solved for \mathbf{x}_b and \mathbf{x}_i . Most of the memory is used in storing this large matrix. Although it may be formed on an elemental level it cannot be inverted on an elemental level as it is not in a block diagonal form. By using the static condensation technique the size of the global inversion matrix has been drastically reduced. Section 4.6.1 goes on to discuss how the Schur complement matrix (which has all of the boundary-boundary and boundary-interior node information) can be solved more efficiently while enforcing both the homogenous and Dirichlet boundary conditions.

4.6.1 The Schur complement, \mathbf{M}_{sc}

The Schur complement matrix has all of the boundary-boundary and boundary-interior node information. As such it is where the boundary conditions must be enforced (recall § 4.3.2 in which the lifting of boundary conditions was discussed). The Galerkin formulation allows a direct implementation of Neumann boundary conditions. Other boundary nodes may be considered to be either homogenous or Dirichlet. As before, the homogenous unknown solution of \mathbf{x}_b is denoted by $\mathbf{x}_b^{\mathcal{H}}$ and the Dirichlet component by $\mathbf{x}_b^{\mathcal{D}}$ so the total boundary vector \mathbf{x}_b may be written

$$\mathbf{x}_b = \mathbf{x}_b^{\mathcal{H}} + \mathbf{x}_b^{\mathcal{D}}. \quad (4.104)$$

For the efficient manipulation of the Schur complement matrix and to easily handle the different homogeneous and Dirichlet boundary conditions, a numbering system is adopted whereby the Dirichlet degrees of freedom are listed after the homogenous degrees of freedom. In this way the boundary degree-of-freedom vector may be written

$$\mathbf{x}_b = \begin{bmatrix} \mathbf{x}_b^{\mathcal{H}} \\ \mathbf{x}_b^{\mathcal{D}} \end{bmatrix}. \quad (4.105)$$

Similarly, the Schur complement matrix is reordered into

$$\mathbf{M}_{sc} = \begin{bmatrix} \mathbf{M}_{sc}^{\mathcal{H}\mathcal{H}} & \mathbf{M}_{sc}^{\mathcal{H}\mathcal{D}} \\ \mathbf{M}_{sc}^{\mathcal{D}\mathcal{H}} & \mathbf{M}_{sc}^{\mathcal{D}\mathcal{D}} \end{bmatrix}, \quad (4.106)$$

where the sub-matrices $\mathbf{M}_{sc}^{\mathcal{H}\mathcal{H}}$, $\mathbf{M}_{sc}^{\mathcal{H}\mathcal{D}}$, $\mathbf{M}_{sc}^{\mathcal{D}\mathcal{H}}$ and $\mathbf{M}_{sc}^{\mathcal{D}\mathcal{D}}$ correspond to the homogenous and Dirichlet solutions $x_b^{\mathcal{H}}$ and $x_b^{\mathcal{D}}$, respectively. This matrix may be used to solve the problem

$$\begin{bmatrix} \mathbf{M}_{sc}^{\mathcal{H}\mathcal{H}} & \mathbf{M}_{sc}^{\mathcal{H}\mathcal{D}} \\ \mathbf{M}_{sc}^{\mathcal{D}\mathcal{H}} & \mathbf{M}_{sc}^{\mathcal{D}\mathcal{D}} \end{bmatrix} \begin{bmatrix} \mathbf{x}_b^{\mathcal{H}} \\ \mathbf{x}_b^{\mathcal{D}} \end{bmatrix} = \begin{bmatrix} \hat{\mathbf{f}}_b^{\mathcal{H}} \\ \hat{\mathbf{f}}_b^{\mathcal{D}} \end{bmatrix}, \quad (4.107)$$

where $\hat{\mathbf{f}}^{\mathcal{H}}$ and $\hat{\mathbf{f}}^{\mathcal{D}}$ are the homogenous and Dirichlet components of the vector $\hat{\mathbf{f}}$ respectively. $\hat{\mathbf{f}}$ is the right hand side of the boundary equation 4.102, i.e.

$$\hat{\mathbf{f}} = \mathbf{f}_b - \mathbf{M}_c^e (\mathbf{M}_i^e)^{-1} \mathbf{f}_i.$$

Having already constructed the vector $\hat{\mathbf{f}}$, equation 4.107 may be solved with enforcement of the Dirichlet boundary conditions. The sub-matrices $\mathbf{M}_{sc}^{\mathcal{D}\mathcal{H}}$ and $\mathbf{M}_{sc}^{\mathcal{D}\mathcal{D}}$ are not part of the Galerkin problem as they contain weight functions that are not zero at Dirichlet boundary conditions. To enforce the Dirichlet boundary conditions the system is manipulated to

$$\mathbf{M}_{sc}^{\mathcal{H}\mathcal{H}} \mathbf{x}_b^{\mathcal{H}} = \hat{\mathbf{f}}_b^{\mathcal{H}} - \mathbf{M}_{sc}^{\mathcal{H}\mathcal{D}} \mathbf{x}_b^{\mathcal{D}}, \quad (4.108)$$

where the known Dirichlet boundary conditions have been moved to the right hand side. The symmetry of the system $\mathbf{M}_{sc}^{\mathcal{H}\mathcal{H}}$ has been maintained, essentially lifting the known solution from the problem. Now all that remains is the inversion of the $\mathbf{M}_{sc}^{\mathcal{H}\mathcal{H}}$ matrix in order to solve the system of equations 4.97. Despite containing the majority of the connectivity data, $\mathbf{M}_{sc}^{\mathcal{H}\mathcal{H}}$ remains a sparse matrix. It is of much smaller size than the original matrix \mathbf{M} of equation 4.97, which makes it much more efficient to solve. This static condensation technique also shows how the Dirichlet boundary conditions may be accounted for.

Numerically, the matrix manipulation is handled by two separate packages. The LAPACK package is used for linear algebra operations including the inversion and multiplication of matrices on an elemental level where the matrices are dense. The sparse matrix solver PARDISO (Schenk & Gärtner 2004) is used for all higher level matrix manipulation due to its excellent efficiency properties when handling sparse matrices.

4.7 Closure

In solving continuum mechanics, fluid or solid, the conservation laws of mass and momentum are modelled. This common underlying physics precipitates mathematically into quite similar mathematical expressions for the evolution of each primary variable through time. This similarity was exploited to develop very similar and highly accurate time stepping schemes for both the fluid and solid mechanics equations based on operator-splitting and backwards differencing approaches. In both cases polynomial extrapolation was used to determine the contribution of non-linear terms at the updated time-step as the algorithm uses an implicit matrix solve.

The Galerkin formulation allows each step in the three-step splitting schemes to be recast in integral form and allows a simple way to enforce higher-order Neumann boundary conditions such as those required for the pressure sub-step in the Navier–Stokes problem and for the forces applied at the boundaries to solid domains. A spectral- hp element spatial discretisation was chosen for both solvers to take advantage of the highly efficient refinement of p -type discretisations. Gauss–Legendre–Lobatto quadrature was chosen as the basis for the nodal expansion for its efficiency, accuracy and the ease it offers for enforcing C^0 continuity between elements.

Using this discretisation scheme a series of matrix-based numerical operators can be formed for conducting integration differentiation and higher-order operations, these were constructed for the numerical implementation of this model.

A mathematical toolbox for spatial discretisation and a framework for the temporal discretisation has been outlined. This framework can be similarly applied to fluid dynamics and both linear and non-linear solid mechanics. This work leads to the completion of aim 1c of this thesis, construction of a fluid-structure interaction solver capable of modelling the non-linear elastic material properties of the wall.

The validity of this algorithm will be proven in chapter 6. While the algorithm

is well documented for fluid mechanics problems, it has not explicitly been used in solid mechanics and fluid-structure interactions. With the successful validation of the algorithm, the similarity of the fluid and solid algorithms prove advantageous in FSI problems with the efficient and accurate passing of boundary information.

Chapter 5

The neo-Hookean solver

5.1 Introduction

Chapter 4 detailed the mathematical framework used for the temporal and spatial discretisation of the Navier–Stokes and neo-Hookean governing equations. Typically investigations into aneurysm haemodynamics that involve an elastic wall do not include the inertial term in the neo-Hookean governing equations. Instead, previous solvers solve a quasi-static system in which a time varying boundary condition is employed in conjunction with a steady state solver. The temporal discretisation described briefly in § 4.2.3.2 includes the inertial term. A combination of a finite differencing approach and an operator splitting method is used to solve the set of equations.

A spectral element discretisation is used for the spatial terms. In solid mechanics, finite element schemes are by far the most popular methods used. Spectral element methods have been shown to exhibit exponential convergence properties in their applications to fluid mechanics. In the context of solid mechanics, the spectral element discretisation in addition to the inclusion of the inertial term and using an operator splitting method for the temporal discretisation represents a new algorithm. Such an algorithm has not previously been developed to solve the neo-Hookean governing equations.

In the following description the neo-Hookean algorithm will be presented in more detail. Also developed in this thesis is a new coupling method for fluid-structure interactions. For details on this the reader is directed to § 3.5.1.

5.2 Splitting the governing equations

For solid mechanics problems the governing equations are

$$\rho \frac{\partial^2 \mathbf{U}}{\partial t^2} = \rho \bar{\mathbf{b}} + \nabla \cdot \boldsymbol{\sigma}, \quad (5.1)$$

where $\mathbf{U} = (U_1, U_2, U_3)$ is the displacement vector, ρ is the solid density, $\boldsymbol{\sigma}$ is the stress tensor, $\bar{\mathbf{b}}$ are the body forces and t is time. The stress tensor $\boldsymbol{\sigma}$ will take a different form depending on the constitutive model being used; for further discussion on this refer to chapter 2.

As described in chapter 2, the neo-Hookean solid has a complex structure for the Cauchy stress tensor, i.e.

$$\boldsymbol{\sigma} = P \mathbf{I} + \mathbf{F} \left(\frac{\partial W}{\partial \mathbf{F}} \right)^T, \quad (5.2)$$

where W is the neo-Hookean strain-energy-density function, which is non-linear in nature, \mathbf{F} is the deformation gradient (a function of \mathbf{U}), P is the pressure arising to maintain incompressibility, and \mathbf{I} is the identity matrix. Substitution into equation 5.1 obtains

$$\rho \frac{\partial^2 \mathbf{U}}{\partial t^2} = G \nabla^2 \mathbf{U} + \mathbf{F}^{-T} p \mathbf{I} + \rho \bar{\mathbf{b}}, \quad (5.3)$$

$$\nabla \cdot \mathbf{U} = 0,$$

where G is the shear modulus, \mathbf{F}^{-T} is the inverse transpose of the deformation gradient \mathbf{F} which describes the map from deformed to original coordinates. The physical ramifications of this term will be treated in § 5.3

As discussed in § 4.2.1, operator splitting schemes assume an operator can be written as a linear sum of m components

$$\mathbf{L} \mathbf{u} = \hat{\mathbf{L}}_1 \mathbf{u} + \hat{\mathbf{L}}_2 \mathbf{u} + \dots + \hat{\mathbf{L}}_m \mathbf{u}, \quad (5.4)$$

the solution that eventually updates the variable \mathbf{u} to the next time step $n + 1$ can be derived simply by summing the contribution of each $\hat{\mathbf{L}}_m$ operating on \mathbf{u} separately (Press 2007).

Using a second-order accurate backwards differencing approach for the inertial term, the present work proposes a two-step splitting scheme (§ 4.2.3.2). This scheme is implicit, second-order accurate and utilises backwards differencing for the temporal discretisation as described in § 4.2.3.2,

$$\rho \frac{\hat{\mathbf{U}} - \sum_{q=0}^{J_i} \alpha_q^s \mathbf{U}^{n-q}}{(\Delta t)^2} = -\nabla \cdot (\mathbf{F}^{-T} P^{n+1}), \quad (5.5)$$

$$\frac{\kappa^s \mathbf{U}^{n+1} - \hat{\mathbf{U}}}{\Delta t} = \nabla^2 \mathbf{U}^{n+1}. \quad (5.6)$$

Details of the finite differencing coefficients κ and α can be found in §4.2.3.2. The following sections describe in detail the matrix operators used and the solution method to solve each of the sub-steps defined in equations 5.5 and 5.6.

5.3 Sub-step 1

In the first sub-step, equation 5.5, the contribution of the previous displacement field, $\sum_{q=0}^{J_i} \alpha_q^s \mathbf{U}^{n-q}$ is used to account for the contribution of the pressure term and to determine the intermediate displacement field $\hat{\mathbf{U}}$. This first requires evaluation of the kinematic pressure, P . Toward this goal, one must take the divergence of both sides of equation 5.5,

$$\nabla \cdot \left(\frac{\hat{\mathbf{U}} - \sum_{q=0}^{J_i} \alpha_q^s \mathbf{U}^{n-q}}{(\Delta t)^2} \right) = \nabla \cdot (-\nabla \mathbf{F}^{-T} P^{n+1}), \quad (5.7)$$

which becomes

$$\frac{\nabla \cdot \hat{\mathbf{U}} - \sum_{q=0}^{J_i} \alpha_q^s \nabla \cdot \mathbf{U}^{n-q}}{(\Delta t)^2} = -\nabla^2 (\mathbf{F}^{-T} P^{n+1}). \quad (5.8)$$

The pressure P introduced in the neo-Hookean Cauchy stress is introduced as a penalty function to enforce the incompressibility. As such the vector field should satisfy an incompressibility constraint (Bower 2009),

$$\nabla \cdot \mathbf{U} = 0. \quad (5.9)$$

To enforce the incompressibility constraint on the intermediate displacement field, $\hat{\mathbf{U}}$, $\nabla \cdot \hat{\mathbf{U}} = 0$ is substituted leaving

$$\frac{-\nabla \cdot \sum_{q=0}^{J_i} \alpha_q^s \mathbf{U}^{n-q}}{(\Delta t)^2} = -\nabla^2 (\mathbf{F}^{-T} P^{n+1}). \quad (5.10)$$

Equation 5.10 is the final form of equation 5.5 that must be solved. The inertial contribution to the displacement field $\sum_{q=0}^{J_i} \alpha_q^s \mathbf{U}^{n-q}$ is calculated explicitly from knowledge of the displacement field history. As such, it is a known quantity and forms the right hand side of a Poisson matrix equation, which shall be called f . Equation 5.5 must then be solved for the kinematic pressure, P . To do this the framework in chapter 4 is followed; recasting the equation

$$-\nabla^2 (\mathbf{F}^{-T} P^{n+1}) = f, \quad (5.11)$$

in its weak form by taking the Legendre inner product with respect to a test function $w(x)$,

$$-(w, \nabla^2 (\mathbf{F}^{-T} P^{n+1})) = (w, f). \quad (5.12)$$

Since $\nabla^2 P = \nabla \cdot \nabla P$, Gauss' divergence theorem can be applied to obtain

$$(\nabla w, \nabla (\mathbf{F}^{-T} P^{n+1})) + \langle w, \nabla P \cdot \underline{\mathbf{n}} \rangle = (w, f) \quad (5.13)$$

where

$$\langle w, \nabla P \cdot \underline{\mathbf{n}} \rangle = \int_{\partial\Omega} w \nabla P \cdot \underline{\mathbf{n}} \, d\mathbf{x} \quad (5.14)$$

and $\underline{\mathbf{n}}$ is the outward normal to the boundary $\partial\Omega$.

The flux contribution in equation 5.13, and explicitly defined in 5.14, only makes a contribution on the Neumann boundary since, by definition, $w(\partial\Omega_D)$ is zero on all Dirichlet boundaries. Equation 5.14 therefore allows us to weakly enforce the Neumann boundary conditions

$$\nabla P \cdot \underline{\mathbf{n}} = g_{\mathcal{N}}, \quad (5.15)$$

where $g_{\mathcal{N}}$ are the Neumann boundary conditions. These boundary conditions can simply be enforced by substituting the value $g_{\mathcal{N}}$ into the integral 5.14. As the contribution of $g_{\mathcal{N}}$ is zero on all Dirichlet boundaries and known for all Neumann type boundaries it may be moved to the right hand side of the equation and enveloped into the forcing function f^* ,

$$\begin{aligned} (\nabla w, \nabla (\mathbf{F}^{-T} P^{n+1})) &= (w, f) - \langle w, \nabla P \cdot \underline{\mathbf{n}} \rangle \\ &= f^*, \end{aligned} \quad (5.16)$$

where $f^* = (w, f) - \langle w, \nabla P \cdot \underline{\mathbf{n}} \rangle$. Handling of Dirichlet boundary conditions is performed through lifting the solution as discussed in the static condensation technique description in § 4.6.

Having manipulated the equations into their weak form, a method for solving equation 5.16 is considered. The mathematical framework of chapter 4 provides a method for developing the appropriate differential, integral and higher-order operators necessary to solve the equation. Initially a single element will be considered, and later the global system will be constructed. Within each element a discrete approximation is made of the solution using a polynomial expansion

$$P^e = \mathbf{M}^e \hat{P}^e, \quad (5.17)$$

where P^e is the elemental pressure, \mathbf{M}^e is the elemental mass matrix (comprising the test function weights), and \hat{P}^e are the discrete trial functions in the elemental domain. Similarly, the forcing function (or right hand side) of equation 5.16, f^* , is denoted by f^e at the quadrature points. Using Gauss–Legendre–Lobatto quadrature and Legendre polynomial basis functions the elemental contribution of equation 5.16 can be written as

$$\mathbf{L}^e \mathbf{F}^{-T} \hat{P}^e = \mathbf{W}^e f^e - \mathbf{S}^e \left(g_{\mathcal{N}} + \nabla P^{\mathcal{H}} \right) \quad (5.18)$$

where it is recalled from chapter 4 that,

$$\mathbf{W} [m (ijk)] [n (rst)] = J_{ijk} w_i w_j w_k \delta_{mn}, \quad (5.19)$$

$$\begin{aligned} \mathbf{L}^e = & \left[\mathbf{\Lambda} \left(\frac{\partial \xi_1}{\partial x_1} \right) D_{\xi_1} + \mathbf{\Lambda} \left(\frac{\partial \xi_2}{\partial x_1} \right) D_{\xi_2} \right]^T W \left[\mathbf{\Lambda} \left(\frac{\partial \xi_1}{\partial x_1} \right) D_{\xi_1} + \mathbf{\Lambda} \left(\frac{\partial \xi_2}{\partial x_1} \right) D_{\xi_2} \right] \\ & + \left[\mathbf{\Lambda} \left(\frac{\partial \xi_1}{\partial x_2} \right) D_{\xi_1} + \mathbf{\Lambda} \left(\frac{\partial \xi_2}{\partial x_2} \right) D_{\xi_2} \right]^T W \left[\mathbf{\Lambda} \left(\frac{\partial \xi_1}{\partial x_2} \right) D_{\xi_1} + \mathbf{\Lambda} \left(\frac{\partial \xi_2}{\partial x_2} \right) D_{\xi_2} \right], \end{aligned} \quad (5.20)$$

and \mathbf{S}^e is the surface integral from § 4.5.5. $P^{\mathcal{H}}$ represents the homogeneous pressure boundary contributions.

At this point the definition of \mathbf{F} is considered. This describes the map between the original and deformed coordinates. The inverse transpose, \mathbf{F}^{-T} , describes the map from deformed to original coordinates. Physically, the effect that this has is to link each state of matter. If the derivative matrices are formed with respect to the deformed coordinates this term can be omitted from the matrix equation 5.18. To form the matrices at this deformed configuration the third-order accurate polynomial extrapolation, i.e.

$$\mathbf{x}^{n+1} = 3\mathbf{x}^n - 3\mathbf{x}^{n-1} + \mathbf{x}^{n-2}, \quad (5.21)$$

is used to predict the position of the solid at the next time step. Then this geometry is used to form the matrix operators \mathbf{L}^e . This simplifies the equations to

$$\mathbf{L}^e \hat{P}^e = \mathbf{W}^e f^e - \mathbf{S}^e \left(g_{\mathcal{N}} + \nabla P^{\mathcal{H}} \right). \quad (5.22)$$

The next step is to form the global matrix solution. To form the global matrix system, the assembly matrix \mathcal{A} is used. The assembly matrix is described in § 4.4.1 as

$$\hat{P}_l = \mathcal{A} \hat{P}_g, \quad (5.23)$$

where \hat{P}_l is the discrete local coordinates and \hat{P}_g are the discrete global coordinates. \mathcal{A} can be stored as a vector, as it links global and local coordinate systems. As such, to

go from local to global coordinates simply substitute equation 5.23 and pre-multiply equation 5.22 by \mathcal{A}^T to obtain

$$\mathcal{A}^T \mathbf{L}^e \mathcal{A} \hat{P}_g = \mathcal{A}^T \mathbf{W}^e f^e - \mathcal{A}^T \mathbf{\Gamma}, \quad (5.24)$$

where

$$\mathbf{\Gamma} = \mathbf{S}^e \left(g_{\mathcal{N}} + \nabla P^{\mathcal{H}} \right), \quad (5.25)$$

is the non zero surface integral terms from equation 5.22.

Before solving for P using the static condensation method outlined in § 4.6, which allows the strong enforcement of the Dirichlet pressure boundary conditions, the homogeneous pressure boundary contributions $\nabla P^{\mathcal{H}}$ are described. The pressure boundary condition imposed at the $(n + 1)^{\text{st}}$ time step is

$$P^{\mathcal{H}} \cdot \underline{\mathbf{n}} = \frac{\partial P^{n+1}}{\partial \underline{\mathbf{n}}} = - \left[\frac{\partial^2 \mathbf{U}^{n+1}}{\partial t^2} + \rho \sum_{q=0}^{J_p-1} \beta_q^s \nabla^2 (\mathbf{U})^{n-q} \right] \cdot \underline{\mathbf{n}}. \quad (5.26)$$

This homogenous boundary condition is derived by rearranging the governing equations in terms of P and taking the component which is normal to the homogenous boundaries. To ensure it provides the boundary conditions at the next time step $(n + 1)$ the non-linear stress term is determined using a polynomial extrapolation method (see equation 5.21) based on past displacement fields \mathbf{U}^{n-q} . The pressure boundary condition can be explicitly determined based on the previous displacement fields. Once found, $P^{\mathcal{H}}$ can easily be substituted directly into equation 5.25 and in turn equation 5.24 to form the known right hand side of the matrix equation.

Finally, to solve the matrix equation the static condensation technique (§ 4.6) is applied. The kinematic pressure P that is determined is then substituted back into equation 5.5 to find the intermediate displacement field $\hat{\mathbf{U}}$.

5.4 Sub-step 2

The second sub-step, solving equation 5.6, involves solving a Helmholtz equation for the final displacement field \mathbf{U}^{n+1} . The intermediate displacement field, $\hat{\mathbf{U}}$, is known from the solution to equation 5.5, and provides contributions from the pressure and inertial terms as well as the enforced incompressibility condition. To construct the matrix operator system for sub-step 2, the same steps are followed as were outlined in § 5.3. The subsequent matrix operator system may be solved using the static condensation technique described in § 4.6.

Firstly, equation 5.6 is rewritten with all of the known quantities on the right hand side

$$\frac{\kappa^s \mathbf{U}^{n+1}}{\Delta t} + \nabla^2 \mathbf{U}^{n+1} = \frac{\hat{\mathbf{U}}}{\Delta t}. \quad (5.27)$$

Next equation 5.27 is recast in weak form by taking the Legendre inner product with respect to the test function $w(x)$

$$(w, \nabla^2 \mathbf{U}^{n+1}) + \frac{\kappa^s}{\Delta t} (w, \mathbf{U}^{n+1}) = \left(w, \frac{\hat{\mathbf{U}}}{\Delta t} \right). \quad (5.28)$$

Since $\nabla^2 \mathbf{U} = \nabla \cdot \nabla \mathbf{U}$, Gauss' divergence theorem can be applied to obtain

$$\langle w, \nabla \mathbf{U} \cdot \underline{\mathbf{n}} \rangle - (\nabla w, \nabla \mathbf{U}^{n+1}) + \frac{\kappa^s}{\Delta t} (w, \mathbf{U}^{n+1}) = \left(w, \frac{\hat{\mathbf{U}}}{\Delta t} \right), \quad (5.29)$$

where

$$\langle w, \nabla \mathbf{U}^{n+1} \cdot \underline{\mathbf{n}} \rangle = \int_{\partial\Omega} w \nabla \mathbf{U}^{n+1} \cdot \underline{\mathbf{n}} \, d\mathbf{x}. \quad (5.30)$$

Following § 5.3 the flux contribution defined in equation 5.30 allows weak enforcement of the Neumann boundary conditions,

$$\nabla \mathbf{U}^{n+1} \cdot \underline{\mathbf{n}} = g_{\mathcal{N}}, \quad (5.31)$$

where $g_{\mathcal{N}}$ are the Neumann boundary conditions. As the contribution of this is zero on all Dirichlet boundaries and known for all Neumann type boundaries it may be moved to the right hand side of the equation

$$(\nabla w, \nabla \mathbf{U}^{n+1}) - \frac{\kappa^s}{\Delta t} (w, \mathbf{U}^{n+1}) = \langle w, g_{\mathcal{N}} \rangle - \left(w, \frac{\hat{\mathbf{U}}}{\Delta t} \right). \quad (5.32)$$

Again the Dirichlet boundary conditions are handled through lifting the solution as discussed in the static condensation technique in § 4.6.

In following the method of § 5.3, the differential, integral, and higher-order operators developed in chapter 4 are now substituted into equation 5.32. A single element is initially considered and the global system constructed later. Within each element a discrete approximation is made of the solution using a polynomial expansion

$$\mathbf{U}^e = \mathbf{M}^e \hat{\mathbf{U}}^e, \quad (5.33)$$

where \mathbf{U}^e is the elemental displacement vector, \mathbf{M}^e is the elemental mass matrix (made of the test function weights) and $\hat{\mathbf{U}}^e$ are the discrete trial functions in the in the elemental domain. Using Gauss–Legendre–Lobatto quadrature and Legendre polynomial basis functions the elemental contribution of equation 5.32 can be written as

$$\mathbf{L}^e \mathbf{U}^{e,n+1} - \frac{\kappa^s}{\Delta t} \mathbf{W}^e \mathbf{U}^{e,n+1} = \mathbf{S}^e g_{\mathcal{N}} - \mathbf{W}^e \frac{\hat{\mathbf{U}}}{\Delta t} \quad (5.34)$$

where \mathbf{W}^e , \mathbf{L}^e and \mathbf{S}^e are defined in both § 5.3 and chapter 4.

Unlike sub-step 1 (equation 5.5) there is no \mathbf{F}^{-T} term. This means that the matrix operators may be formed using the current geometry.

The next step is to form the global matrix solution. To form the global matrix system assembly matrix \mathcal{A} is used. Just as in § 5.3, to go from local to global coordinates equation 4.49 is substituted into equation 5.34 and pre-multiplied by \mathcal{A}^T to obtain

$$\mathcal{A}^T \left[\mathbf{L}^e - \frac{\kappa^s}{\Delta t} \mathbf{W}^e \right] \mathcal{A} \mathbf{U}^{e,n+1} = \mathcal{A}^T \mathbf{\Gamma}, \quad (5.35)$$

where

$$\mathbf{\Gamma} = \mathbf{S}^e g_{\mathcal{N}} - \mathbf{W}^e \frac{\hat{\mathbf{U}}}{\Delta t}, \quad (5.36)$$

is the non zero surface integral terms from equation 5.22.

By setting $\mathbf{H} = \left[\mathbf{L} - \frac{\kappa^s}{\Delta t} \mathbf{W} \right]$ as the global Helmholtz operator equation 5.35 may finally be rewritten as

$$\mathbf{H} \mathbf{U}^{n+1} = \mathbf{\Gamma}. \quad (5.37)$$

All of the components of $\mathbf{\Gamma}$ on the right hand side are known having been explicitly calculated in sub-step 1. As such the matrix equation for the displacement field at the next time step \mathbf{U}^{n+1} is finally able to be solved using the static condensation technique (§ 4.6). Displacement boundary conditions are prescribed through the static condensation process.

5.5 Closure

The governing equations for an incompressible neo-Hookean material are solved using a backward differencing temporal discretisation and a spectral element spatial discretisation. A two-step operator splitting scheme is proposed in order to implicitly solve for the displacement at the next time step. The Galerkin approximation of the equations allows weak enforcement of the Neumann boundary conditions. Once the matrix system is formed the static condensation method described in § 4.6 is used to simultaneously enforce the Dirichlet boundary conditions and solve for the system of equations.

The combination of a two-step operator splitting scheme, the inclusion of the inertial term and the use of a spectral element spatial discretisation makes this a new technique for solving the governing equations for an incompressible neo-Hookean solid. When simulating the response of the arterial wall in an aneurysms, a hyperelastic material

model such as the neo-Hookean is essential. This algorithm in conjunction with the new fluid-structure interaction coupling scheme described in § 3.5.1 represents a new and highly accurate tool for investigating FSI in aneurysms. Validation of this technique can be found in chapter 6, while preliminary results on aneurysm haemodynamics are presented in chapters 8 and 9.

Chapter 6

Validation

The purpose of this chapter is to present a series of validation cases which were used to confirm the accuracy of the numerical techniques developed in chapters 3 to 5. The fluid-structure interaction solver consists of both solid-structural and fluid dynamics components. The fluids component of the algorithm has been rigorously validated and used in many published papers, for examples of its validation the reader is directed to Sheard & Ryan (2007). The validation presented in this chapter focuses on the accuracy of the Hookean and neo-Hookean solid solvers and the Arbitrary Lagrangian–Eulerian (ALE) algorithm for coupling the solvers.

6.1 Introduction

The validation of a numerical algorithm is a process whereby the accuracy of the algorithm is assessed. This is performed using a test case for which the results are well defined. The capacity of the algorithm to model the desired physics is determined by how closely it reproduces the known solution.

The numerical algorithms developed in this thesis were constructed in a sufficiently broad manner so as to allow their application to a wide range of engineering problems. A series of validation cases were constructed to determine the accuracy of each component of the algorithm and the sum of their parts. The variability in the function of each model means that the same testing procedure cannot be applied to each problem. As such, the series of validation cases presented in the following sections focus on very different problems. The generality with which the algorithm was developed allows testing to be conducted on simple known solutions rather than complicated application-specific examples for which data may not be readily available.

To this end, the accuracy of the Hookean solver is tested using a simple three-

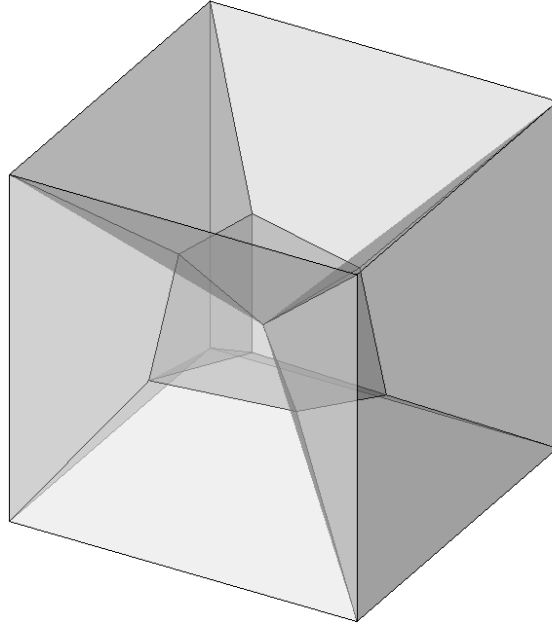


FIGURE 6.1: The seven-element patch test mesh used for Hookean model verification.

dimensional patch test, the neo-Hookean solver is compared to an existing algorithm and some experimental data for a rubbery material; and the ALE solver is tested using three different test cases.

6.2 Hookean solver

Testing of the Hookean solver is conducted using a simple uni-axial stress test. The test uses the patch test mesh which is widely used in the testing of linear finite element solid mechanics codes (see for example Pierson *et al.* 2004; Koterias *et al.* 2006; Scherzinger & Hammerand 2007). The mesh, shown in figure 6.1, is a cube consisting of seven elements. The elements in this mesh are not parallelepipeds, which makes the mesh useful in assessing the linear consistency of the hexahedral elements used in the spatial discretisation of the domain. The patch-test mesh has eight exterior nodes that are used to define boundary conditions. The boundary conditions can be either prescribed displacements or tractions.

A simple uni-axial stress test is used to validate the Hookean model solver. A uni-axial stress is prescribed using displacement control in the x -direction and traction-free boundary conditions are applied in all other directions. One face of the cube which

Displacement	Predicted			% error		
	u_x	ε	σ	u_y	ε	σ
0.005	0.995	1.05×10^7	-1.2461×10^{-3}	0.0	0.12	0.1
-0.005	-0.005	9.95×10^6	1.2539×10^{-3}	0.0	0.13	0.15

TABLE 6.1: Comparison of the predicted lateral displacements and stresses to simulated values. Simulations were conducted using a polynomial order of $n = 8$.

is oriented normal to the x -direction is fixed in space while the corresponding face on the opposite side of the cube has displacements of 0.005 m and -0.005 m prescribed as boundary conditions for two tests. All other surfaces are free to move. A polynomial order of $n = 8$ was used in both test cases, at this resolution the solution has reached a mesh independent result which exhibits very little numerical error.

The material constants for the Hookean model used in this problem are: Young's modulus, $E = 10 \times 10^6$ Pa, and Poisson ratio, $\nu = 0.25$.

Given a uni-axial strain problem on a unit cube with zero lateral tractions, the stress calculated using a Hookean elastic model is

$$\boldsymbol{\sigma} = E\boldsymbol{\varepsilon}, \quad (6.1)$$

where E is the Young's modulus and $\boldsymbol{\varepsilon}$ is the true strain. Given the axial displacements prescribed on the unit cube, the true strain and axial stress may be calculated as known values, these are shown in table 6.1. Since the lateral surfaces are traction free they are free to contract. The displacement of the lateral surfaces is

$$u_y = u_z = \frac{1}{(1 + u_x)^\nu} - 1. \quad (6.2)$$

Using the prescribed displacements, the minimum and maximum lateral displacements are tabulated in table 6.1

Figure 6.2 shows the patch test cube after it has undergone the deformation. When an axial displacement elongated the domain (figure 6.2(a)) the lateral surfaces contracted, forming an hourglass shape. When the axial displacement compressed the domain (figure 6.2(b)) the lateral surfaces bulged outward. The lateral displacements and stresses determined from the simulation show excellent correspondence with the predetermined solution. Table 6.1 shows that when using a polynomial order of $n = 8$ the maximum error was less than 0.2%.

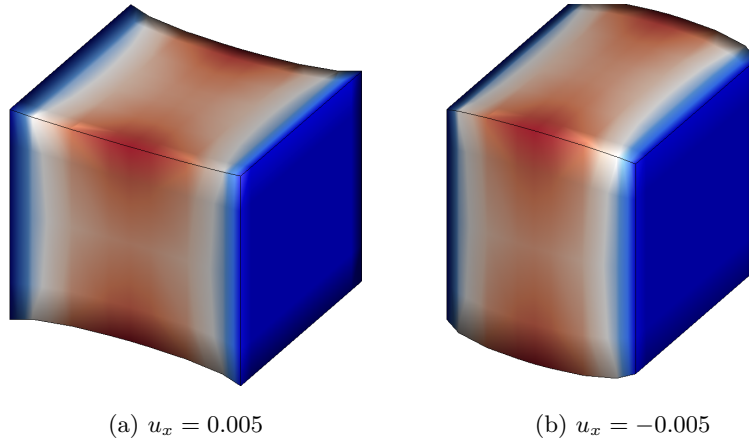


FIGURE 6.2: Elongated and compressed unit cube in Hookean model patch test. Sub-plot (a) shows the case with a displacement of 0.005 enforced on the right hand face and sub-plot (b) shows the case with a displacement of -0.005 enforced on the right hand face. Contours are of lateral displacement magnitude.

6.3 Neo-Hookean solver

Testing of the neo-Hookean solver was conducted using a simple compression test. The results of the neo-Hookean simulation were validated against the experimental and numerical results presented in Mesa Múnica (2011). Mesa Múnica (2011) measured the deformation of an 80 mm diameter by 70 mm height cylinder fabricated from silicone rubber Ecoflex 00-10. They then developed a neo-Hookean model and determined the elasticity of the material which best matched the deformation characteristics of the silicone specimen. They found that the elastic modulus of the silicone was $E = 8769$ MPa.

The current validation simulation aims to replicate the conditions of the experimental and numerical work conducted in Mesa Múnica (2011). To this end, figure 6.3(a) shows the mesh created to test the compression of the silicone block (a polynomial order of $n = 6$ is used within the macro elements). The dimensions are 80 mm in diameter and a height of 70 mm. A uniform pressure force was applied to the top and bottom surfaces of the cylinder causing a compression of the material. Figure 6.3(b) shows the deformed configuration of the material. As expected, the material has compressed in the axial direction and expanded laterally. The side walls do not exhibit the bulging shape seen in the Hookean displacement test results (figure 6.2(b)), because in this test

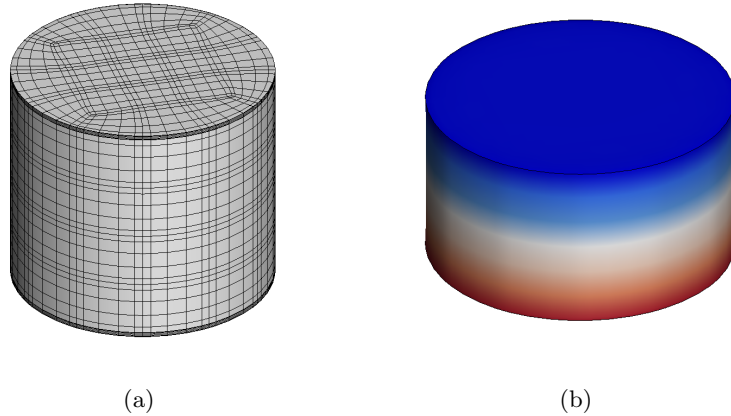


FIGURE 6.3: Compression test of a rubbery cylindrical block. Sub-plot (a) shows the initial mesh of the cylindrical block, while sub-plot (b) shows the case after deformation using a neo-Hookean material model. The simulation was conducted with a polynomial order $n = 6$. The contours are of axial displacement.

the boundary conditions do not limit the diameter of the top and bottom surfaces where the pressure is applied. This matches the results published in Mesa Múnica (2011) in which they indicate the surfaces of the silicone block were lubricated in order to allow free movement of the upper and lower surfaces in the compression rig.

Figure 6.4 compares the stress-strain curve produced from the neo-Hookean solver developed in this thesis to the published data in Mesa Múnica (2011). The results show an excellent agreement between the neo-Hookean models used in the literature and the one developed in this thesis. Using a polynomial order of $n = 6$ (shown in figure 6.4), the maximum error between the neo-Hookean solvers is 0.52%. Table 6.2 shows the performance of the neo-Hookean solver as the resolution is increased which shows good convergence towards the published data in Mesa Múnica (2011). This verifies the neo-Hookean algorithm developed in this thesis as accurate in describing neo-Hookean constitutive models.

One of the aims in this thesis is to determine the efficacy of using a linear elastic-wall model for modelling the fluid-structure interaction in aneurysms. The results presented in figure 6.4 show that at large stresses, such as those found in the natural function of the arterial wall, the linear elastic assumption of the material properties grossly overestimates the wall motion. At an intermediate stress of 1000 Pa the linear elastic model predicted a strain 20.5% greater than the neo-Hookean model. These results

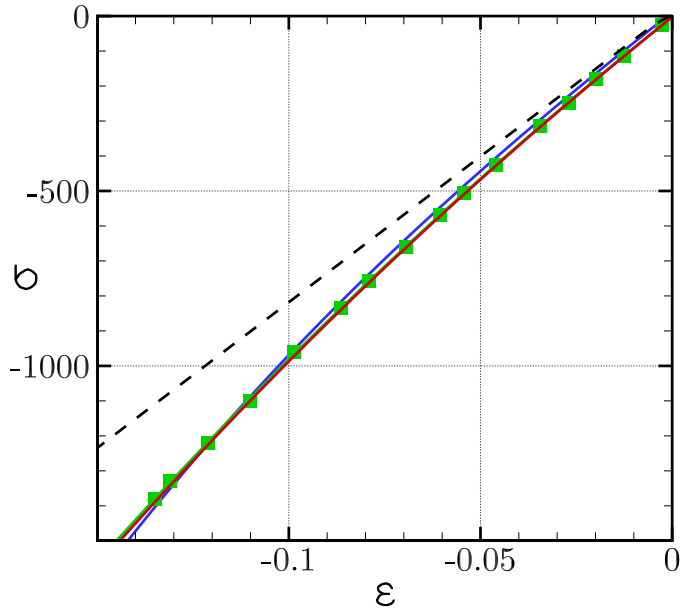


FIGURE 6.4: Comparison of neo-Hookean solver results to the results presented in Mesa Múnera (2011). The blue line represents the experimental data from Mesa Múnera (2011), green squares ■ represent the neo-Hookean simulations conducted by Mesa Múnera (2011) and the red line represents the neo-Hookean model developed in this thesis. The dashed black line shows the Hookean response for the same test case.

p	ϵ	%-error
2	7.786×10^{-2}	1.44
3	7.776×10^{-2}	1.58
4	7.819×10^{-2}	1.02
5	7.847×10^{-2}	0.67
6	7.859×10^{-2}	0.52
7	7.860×10^{-2}	0.51

TABLE 6.2: Results of a grid resolution study for the neo-Hookean solver. Strains were measured at $\sigma = 750$ and compared to the neo-Hookean solver used in Mesa Múnera (2011)

indicate that use of a linear elastic model would overestimate the wall displacement in an aneurysm. As such, a linear elastic model is not sufficient for modelling the fluid-structure interaction in an aneurysm. The results presented in chapter 9 will show the impact that wall motion has on the haemodynamic environment.

6.4 Arbitrary Lagrangian–Eulerian algorithm

The previous sections have verified the accuracy of the Hookean and neo-Hookean algorithms. These algorithms were coupled with an existing in-house fluid solver (Sheard & Ryan 2007) to form a solver capable of studying fluid-structure interactions. As the accuracy of each of the fluid and solid components has been confirmed, the remaining validation concentrates on the accuracy of the arbitrary Lagrangian–Eulerian coupling scheme.

To this end three benchmark tests were conducted. The first was a case of forced solid body motion in which the motion of the solid body was predetermined and prescribed as a boundary condition on the fluid domain. Next, the conservation of mass was confirmed using the case of a pressure driven flow against a membrane separating two chambers. The final test case simulated a strongly coupled system in which two-way coupling is dominant in the system. A velocity driven flow in a lid driven cavity was used for this test case. These test cases were designed to verify all aspects of the coupling between the two solvers. The first case (§ 6.4.1; oscillating cylinder) describes the case of a one-way information flow. The second case (§ 6.4.2; bulging membrane) verifies the code in terms of conservation of mass and in the framework of a pressure driven flow. Finally, the third case validates the capacity of the ALE algorithm in a fully coupled two-way information flow in which the results are driven via a mixed pressure-velocity boundary response (§ 6.4.3; lid driven cavity).

6.4.1 Oscillating cylinder

The first test of the ALE solver investigated the performance when the motion of the solid was prescribed as a boundary condition on the fluid. To this end, the forced transverse oscillation of a cylinder in a cross flow was considered. Under various flow conditions, notably the Reynolds number, the frequency of oscillation and amplitude of oscillation, the wake shed behind the oscillating cylinder will form different flow patterns. Leontini *et al.* (2006) presented a study which mapped the energy transitions and

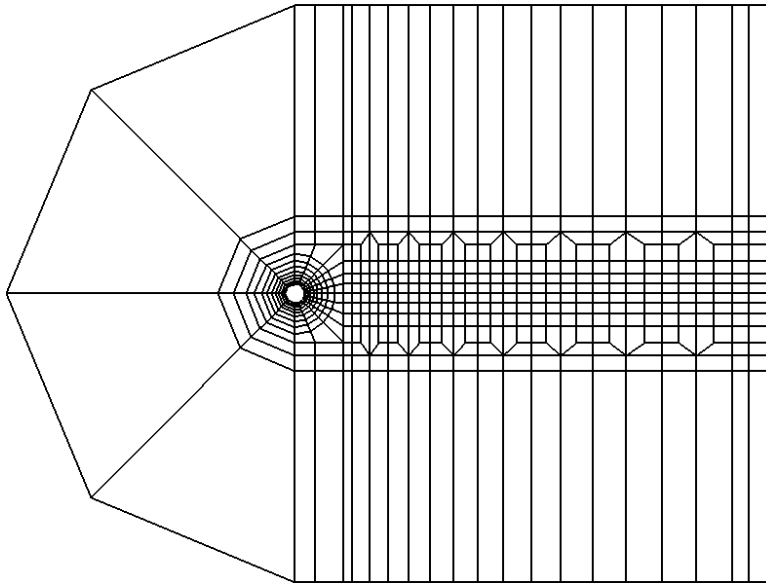


FIGURE 6.5: Macro-element mesh used in the forced oscillation validation case of an oscillating cylinder.

wake states formed across a large combination of Reynolds numbers, frequencies and amplitudes of oscillation. Their study was conducted using a moving reference frame algorithm and solved the incompressible Navier–Stokes equations. This validation case endeavours to repeat the simulations conducted in Leontini *et al.* (2006) and identify identical wake states under the different flow regimes.

The mesh used in this analysis is identical to that used in Leontini *et al.* (2006). The spatial domain is discretised into 508 elements, with the majority concentrated in the wake and boundary-layer regions. This macro-element mesh is shown in figure 6.5. Leontini *et al.* (2006) chose this mesh after an extensive mesh and domain optimization study. Similarly, a polynomial order of $n = 8$ was used for verification purposes, matching that used in the spectral element discretisation in Leontini *et al.* (2006).

The cross flow is applied on the left hand boundary and the top and bottom walls with a non-dimensionalised velocity $v^* = 1$. A prescribed reference value is imposed on pressure at the right-hand side of the domain where the fluid exits, along with a zero normal gradient condition on the velocity field. At the cylinder wall a no-slip condition

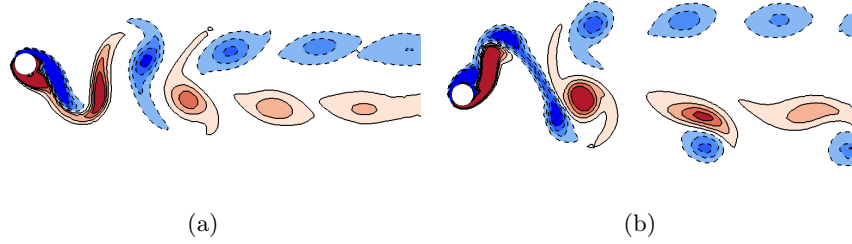


FIGURE 6.6: Flow in the near wake region behind an oscillating cylinder in a cross flow. Sub-plot (a) shows the wake when the amplitude of oscillation is $A^* = 0.7D$ and (b) shows the wake when the amplitude of oscillation is $A^* = 1.1D$. The simulation was conducted at a Reynolds number of 100 and an oscillating frequency $f = f_{st}$. Red and blue contours show positive and negative vorticity, respectively which range from -2 to 2.

is imposed. The motion of the cylinder is prescribed by the function,

$$u_y = \frac{A^*}{D} \sin(2\pi ft), \quad (6.3)$$

where A^* is the amplitude of oscillation, D is the diameter of the cylinder, and f is the frequency of oscillation of the cylinder (The Strouhal frequency was determined to be $f_{st} = 0.189$). The Reynolds number of the simulation is controlled via the kinematic viscosity. For this validation case a Reynolds number of 100 was used. The amplitude of oscillation was set at $0.7D$ and $1.1D$ and the frequency of oscillation was selected such that $\frac{f}{f_{st}} = 1$.

Figure 6.6 shows the wake formed behind the oscillating cylinder at the two amplitudes of oscillation $0.7D$ and $1.1D$. In the region directly behind the cylinder, two different wake modes were observed. At the lower value of $A^* = 0.7D$, a synchronized 2 S shedding mode is observed, with two single vortices shed per oscillation cycle. This is depicted in figure 6.6(a). At the higher value of $A^* = 1.1D$, a synchronized P + S shedding mode occurs, with one single and one pair of vortices of opposite sign shed per shedding cycle (see figure 6.6(b)). This reflects the findings of Leontini *et al.* (2006) which are reproduced in figure 6.7.

A quantitative comparison of the results presented in Leontini *et al.* (2006) was also conducted. Figure 6.8 shows the coefficient of lift on the cylinder for the case of $A^* = 0.7D$ and $Re = 200$. These results demonstrate an excellent correlation with those presented in Leontini *et al.* (2006), the maximum error was found to be 1.9% at the time of peak coefficient of lift.

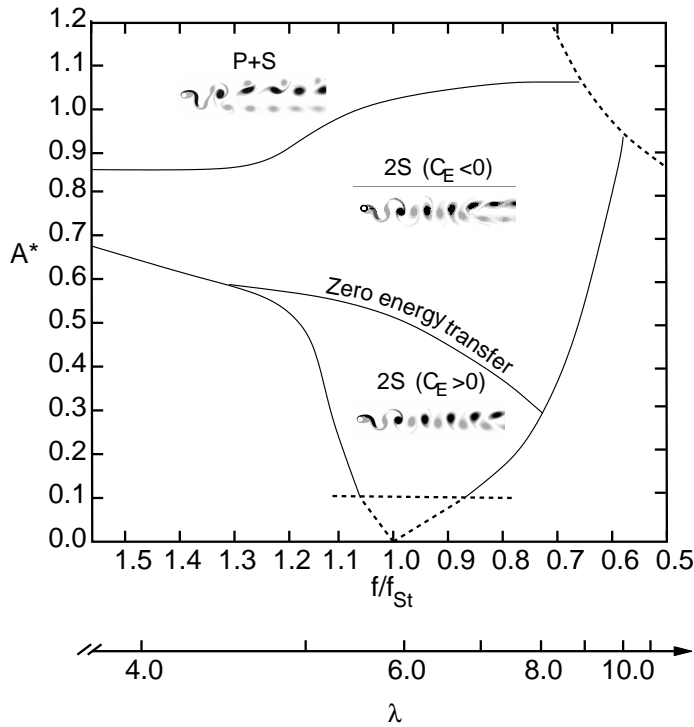


FIGURE 6.7: Flow regimes for a $Re = 100$ in the primary synchronization region. It is clear that at various values of cylinder oscillation amplitude and oscillation different flow regimes are achieved. Reproduced with the permission of Leontini, Stewart, Thompson & Hourigan from Leontini *et al.* (2006)

These results show that the ALE formulation is capable of achieving results in the fluid domain when the motion of a solid boundary is prescribed as a boundary condition. These results extend to the validation of three-dimensional examples. While the 3D cases are not explicitly shown here, the extra degree of freedom serves only to increase the dimensions of the matrix and not the fundamentals of the algorithm. As such validation of the 2D or 3D case provides sufficient validation of the solver.

6.4.2 Pressure driven bulging membrane

The case of a bulging membrane in a fluid is used to verify that mass is conserved throughout the fluid and solid domains. This is important as both the fluid and solid constitutive relationships are incompressible. To this end, an adaptation of the bulging membrane problem suggested in Van Loon *et al.* (2007) is presented. Different boundary conditions are imposed compared to Van Loon *et al.* (2007) which mimic the type of

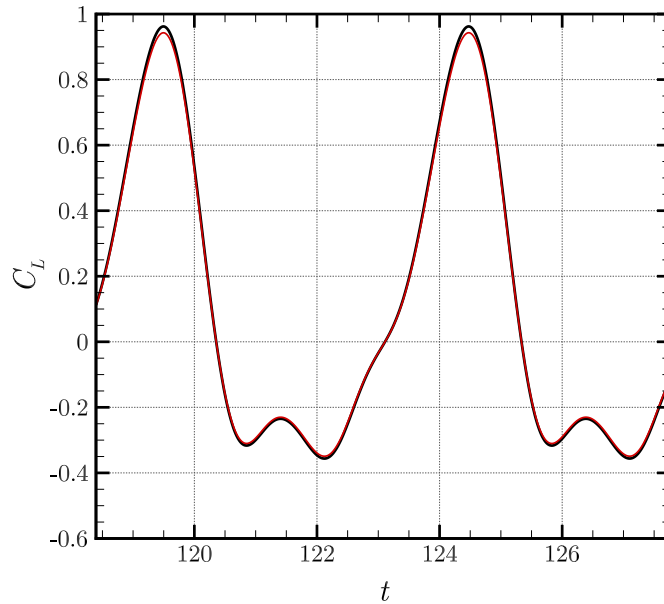


FIGURE 6.8: The change in coefficient of lift as a function of time as the vortices are shed downstream for the case of $A^* = 0.7D$, $Re = 200$ and $\frac{f}{f_{st}} = 1.01$. The black line shows the reported data from Leontini *et al.* (2006) found using the moving reference frame technique, the red line shows the lift calculated using the ALE formulation developed in this thesis.

boundary conditions used in the aneurysm studies presented in chapter 8. As such, the aim of this validation case is not to compare studies, rather it is purely to verify the mass conservation properties of the algorithm. Measurements of flow rate through the domain inlet and outlet and the rate of volumetric displacement of the membrane are monitored to determine any error associated with mass conservation. Similar studies have been used to assess the accuracy of FSI algorithms, see for example the bulging pipe case in Bathe & Ledezma (2007).

In this test case a slender solid membrane is considered that separates the fluid domain in two parts as shown in figure 6.9. The boundary conditions applied to the fluid domain are a linearly increasing pressure boundary condition on the lower inlet Γ_1 ,

$$P = h(t) = 25000t, \quad (6.4)$$

where $h(t)$ is a linear function of time. A zero pressure boundary condition is applied at the outlets of the second chamber Γ_2 . A no-slip boundary condition is applied at all surfaces including the surface of the membrane

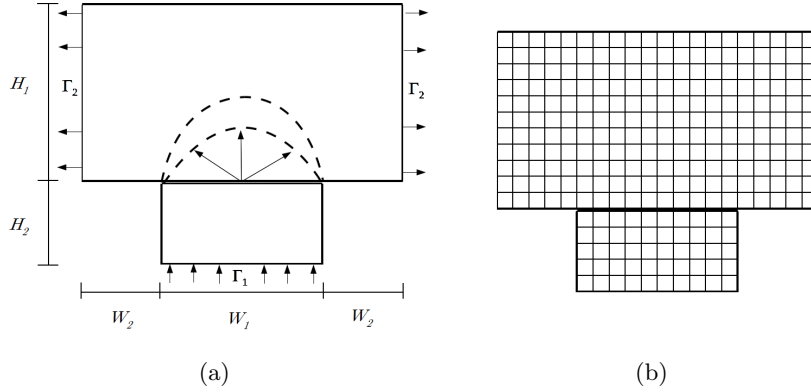


FIGURE 6.9: Details of the fluid domain used in the pressure driven bulging membrane test. Sub-plot (a) shows the detail of the domain including dimensions, inlet and outlets; while (b) shows the undeformed macro-element mesh used in the simulation.

Dimension	Fluid parameters	Solid parameters
W_1	ν 0.004	E 2×10^6
W_2	ρ_f 1000	ρ_s 1000
H_1	1	
H_2	0.5	
t_{mem}	0.016	

TABLE 6.3: Dimensions of the bulging membrane problem and relevant physical parameters.

Since no flow is allowed through the membrane, an influx through Γ_1 will cause the pressure to rise in the bottom part of the fluid chamber and induce deformation of the membrane. Due to the incompressibility of the fluid, the amount of fluid that enters the domain will equal the amount leaving the domain through Γ_2 . The increase in pressure leads to a deformation in the membrane and increase in the volume of the lower chamber. This in turn leads to a flow rate through Γ_1 . Due to the incompressibility conditions, this flow rate is also equal to the fluid volume displaced by the membrane, i.e.

$$\int_t \int_{A_{in}} Q_{in} dA_{in} dt \Big|_{\Gamma_1} = \int_t \int_{A_{mem}} Q_{mem} dA_{mem} dt = \int_t \int_{A_{out}} Q_{out} dA_{out} dt \Big|_{\Gamma_2}, \quad (6.5)$$

where Q represents the flow rate through a surface of area A . This observation can be used to monitor the flow conservation at various stages of the coupling.

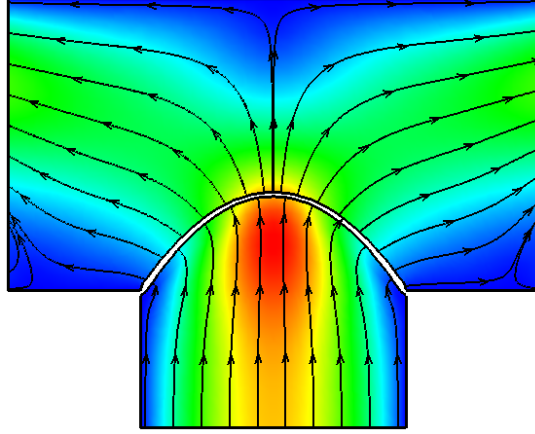


FIGURE 6.10: Visualisation of the flow in the bulging membrane domain. Flooded contours are of velocity magnitude (varying from 0 to 0.07) with streamlines overlaid.

The macro-element mesh used for the computations is shown in Figure 6.9(b), and a polynomial order of $n = 7$ is used as the basis function within each element. Dimensions of the domain and the relevant physical parameters are detailed in table 6.3. The solid membrane was modelled using ten quadrilateral macro-elements, and the same polynomial order was used for the solid domain to allow efficient transfer of data from one domain to the next. As a final note, the membrane is fixed in all degrees of freedom where it connects to the channel walls at the edges of the fluid domain.

Figure 6.10 shows the flow field in the two cavities at an advanced stage of the simulation. The solid membrane has bulged outwards into the upper chamber decreasing its volume and increasing the volume of the lower chamber. Fluid is seen to be drawn in from the bottom boundary, Γ_1 , and as a result of conservation of mass, the fluid is forced out of outlets of the upper chamber. Figure 6.11 shows the flow rate results of the simulation. It is evident that the algorithm conserves mass with excellent precision. The flow rate at the inlet and outlet are within 0.012% of each other with the membrane flow rate remaining at an equivalent value. Figure 6.11(b) shows the error in the flow rate as a function of time. As the membrane is increasingly stretched,

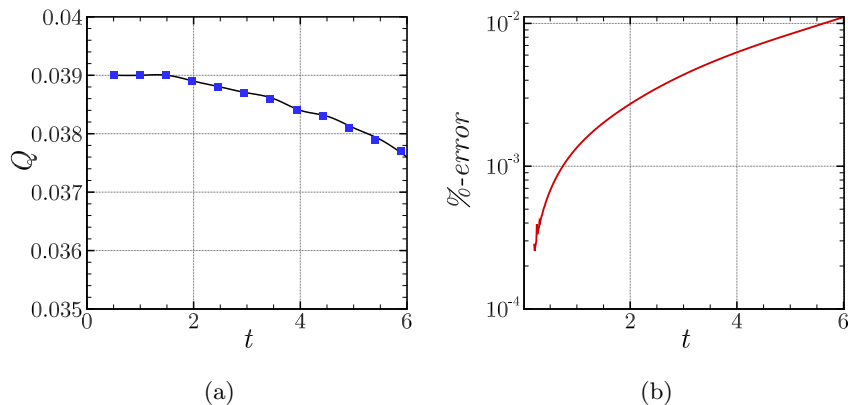


FIGURE 6.11: Flow rate results for the bulging membrane study. Sub-plot (a) shows the flow rate through the inlet ■ in the lower cavity and out the outlets in the top cavity ■. Sub-plot (b) shows the error between the inlet and outlet flow rates.

the quality of the mesh begins to degrade and as a result, the accuracy of the mass conservation is reduced. This highlights a shortfall in the current implementation of the ALE solver. When modelling multiple fluid-solid interfaces, as the deformation between interfaces gets large mesh elements may become skewed. This limitation is a result of the Lagrangian fashion with which the solid is modelled. This interface tracking strategy ensures high accuracy at the interface boundary but may lead to poorly structured meshes at very large deformations. For the aneurysm investigations studied in this thesis the deformations are small enough that this is not of concern.

These results demonstrate that this implementation of the ALE algorithm is very capable of modelling a pressure driven flow in which the fluid pressure causes a deformation of the solid which in turn affects the velocity of the fluid. These results show that mass is well conserved throughout both the fluid and solid domains.

6.4.3 Flow in a lid driven cavity with a membrane

The final validation case for the fluid-structure interaction solver is the strongly coupled case of a lid driven cavity with an elastic membrane at the bottom surface. This example was first introduced in Wall (1999) and has since been reproduced in many validation studies (Mok & Wall 2001; Förster *et al.* 2007; Küttler & Wall 2008; Bathe & Zhang 2009; Jog & Pal 2011). It is a variant of the classical lid-driven cavity problem in fluid mechanics, where the bottom is a flexible membrane of non-dimensional thickness

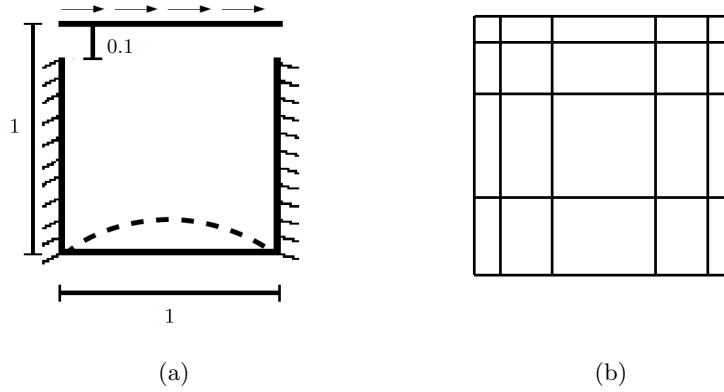


FIGURE 6.12: Details of the fluid domain used in the lid driven cavity study. Sub-plot (a) shows the details of the domain including dimensions, inlet and outlets; while (b) shows the undeformed macro-element mesh used in the simulation.

$0.002L$, and there are apertures near the top through which fluid can flow in or out as shown in figure 6.12. In this example, the high elasticity (low elastic moduli) of the membrane causes it to distort rapidly as the velocity field in the near field region changes.

No-slip boundary conditions are applied on all walls and the surface of the membrane. A gap in the wall is made either side of the lid in order to allow flow to enter and exit the domain to conserve mass as the motion of the membrane changes the volume in the cavity. A traction-free, zero normal pressure gradient boundary condition is applied at these openings. The lid of the cavity is driven by an oscillating velocity acting at a tangent to the lid (in the x -direction). The lid velocity boundary condition is prescribed by

$$v_x = 1 - \cos\left(\frac{2\pi t}{5}\right), \quad (6.6)$$

which has a maximum non-dimensionalised amplitude of 1 m/s and a period of oscillation of 5 time units. The solid membrane is fixed at each edge in both the x and y -directions. A zero reference pressure boundary condition is applied to the outer surface while the inner surface is subject to the pressure conditions in the fluid domain.

The properties of the fluid are the same as used in the work of Bathe & Zhang (2009) and Jog & Pal (2011). For the fluid domain these are: fluid density $\rho_f = 1 \text{ kg/m}^3$, dynamic viscosity $\mu_f = 0.01 \text{ Pa} \cdot \text{s}$ which gives a Reynolds number of $Re = 100$. The flexible membrane of thickness 0.002 mm , has a stiffness of $E = 250 \text{ Pa}$. The mesh used

to discretise the fluid domain consists of 20 macro-elements with a polynomial order of $n = 7$ used as the basis function for interpolation (see figure 6.12(b)). The solid domain consists of a strip extending across the bottom boundary, 5 macro-elements long and 1 element thick, with an identical polynomial order to allow efficient and accurate transfer of data between the solid and fluid domains.

Figure 6.13 shows the computed flow field and membrane displacement at three snapshots in time. The motion of the membrane can clearly be seen to be oscillating in response to the changing velocity boundary condition at the lid. The motion of the wall is dominated by the presence of the recirculation region which forms in the main chamber. At the times shown in figure 6.13(c) the response of the membrane to the presence of the recirculation region is most obvious as the asymmetric shape of the deformation is reflected in the offset of the recirculation region. Such deformations of the membrane and flow fields mimic (qualitatively) the results presented in Kassiotis *et al.* (2011). This indicates the high level of coupling between the membrane deformation and the local flow dynamics.

Figure 6.14 shows the vertical displacement of the midpoint of the membrane as a function of time. There is reasonable qualitative agreement with the corresponding solution presented in Jog & Pal (2011) and Bathe & Zhang (2009). The membrane moves in the mean upwards direction, the oscillations of the membrane reach a steady state and oscillate at a steady amplitude (after the initial transients have died out) reflecting the findings presented in the literature. The time period of the oscillation is almost exactly 5 time units as is expected from the velocity boundary condition and was reported by Jog & Pal (2011).

Despite the good qualitative agreement with the corresponding solutions presented in the literature, some discrepancies and limitations must be discussed. Firstly, Jog & Pal (2011) highlight that the solution to the problem is extremely sensitive to the boundary conditions imposed on the gaps left in the wall near the lid of the domain. In this case a zero normal pressure gradient boundary condition has been applied. Other studies impose a zero y -velocity component (Jog & Pal 2011), while some use a zero velocity gradient at the boundary (Bathe & Zhang 2009). The sensitivity of the solution to the boundary conditions is also stated by Bathe & Zhang (2009), who note that in their solution the bottom membrane moves in the mean downwards direction, whereas in the solution of Küttler & Wall (2008) (who do not indicate what type of boundary

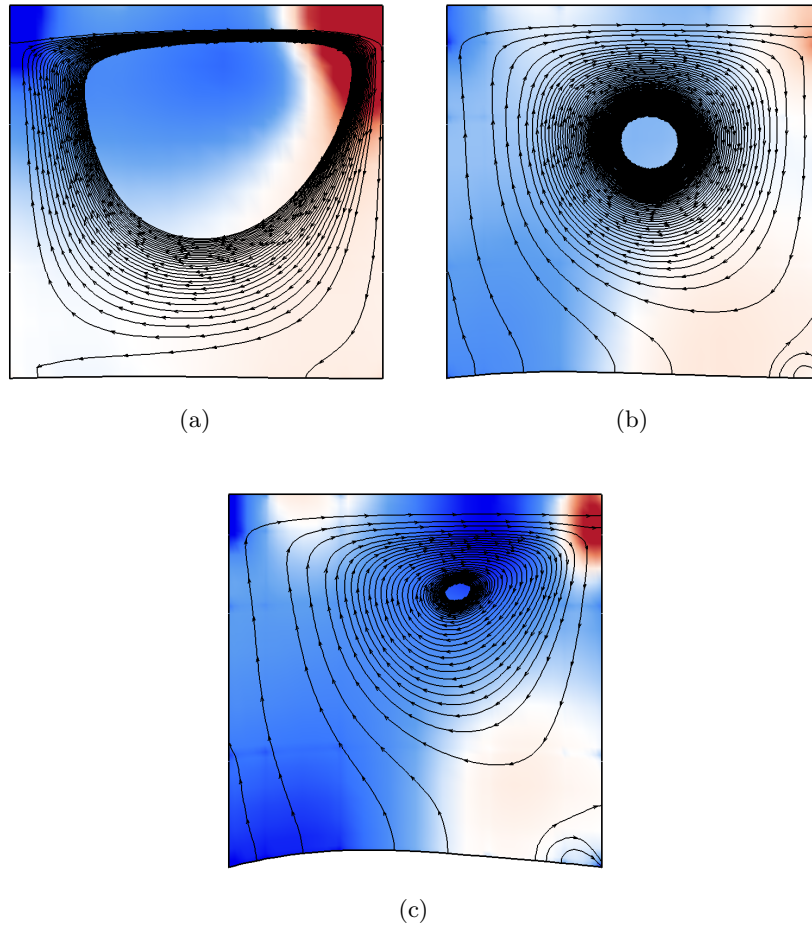


FIGURE 6.13: Visualisation of the flow in the lid driven cavity. Colour flood is of pressure with red indicating positive pressure (maximum +0.1) and blue indicating negative pressure (maximum -0.1). Streamlines of velocity are also shown.

condition they impose) it moves upwards.

Finally, in terms of the limitations, the membrane displacements reported herein are smaller than those reported in Bathe & Zhang (2009) and Jog & Pal (2011). This is a result of the difference in membrane stiffness employed in this study compared to their works. In this study the membrane was stiffened to reduce its motion. In the event that the membrane motion became too large, the solution became unstable and diverged. This emphasizes an important aspect of the coupling between the fluid and solid solvers. Owing to their construction, the stability characteristics of each algorithm (fluid and solid) are quite similar. However, the appearance of a first-order time derivative in the fluid and a second-order time derivative in the solid, leads to a difference in the Courant

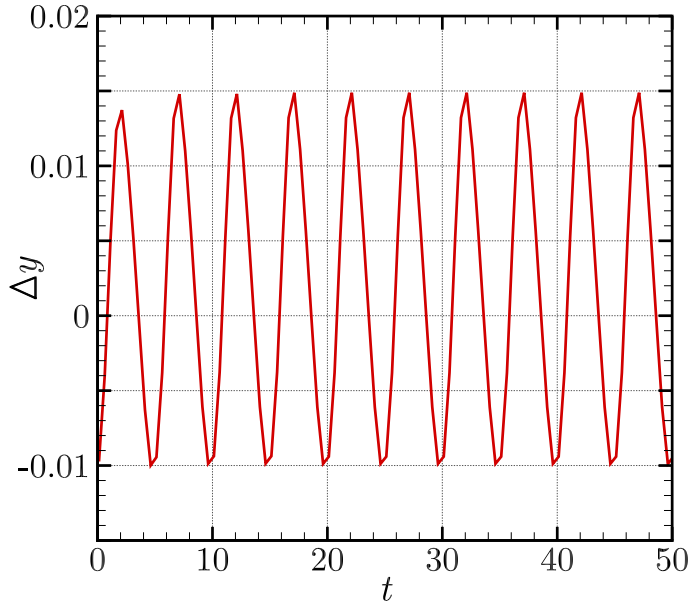


FIGURE 6.14: Displacement of the central point of the membrane $(0.5, 0)$ as a function of time.

condition, which scales as

$$\varsigma_f = \frac{1}{Re} \frac{\Delta x}{\Delta t},$$

for the fluid and

$$\varsigma_s = E \frac{\Delta x}{\Delta t^2},$$

for the solid. This presents a challenge when coupling the solvers. The fluid algorithm is most stable using smaller time steps and lower Reynolds numbers, while the solid solver is more stable at larger stiffnesses and smaller time steps. Furthermore, issues arise when the time step is lowered to satisfy the stability of the fluid solver, the Δt^2 term in the stability condition of the solid solver can cause extrema (either very large or very small numbers). Extreme values can induce significant round-off errors. Furthermore, matrices formed with extrema may be poorly conditioned; not satisfying diagonal dominance which is a problem for some linear solvers. Finally, the difference in the scale of the Reynolds number and wall stiffness typically modelled presents a problem, this leads to a larger time step being preferential to solve the solid domain and a lower time step for the fluid.

In order to circumvent some of the stability concerns a different time step can be

applied to each of the solution domains. This helps some cases to run more smoothly, though if the required difference in time step is too large it can produce step changes in the solution (as the extrapolation used to supply information at intermediate steps misrepresents the change in the solution over that time) which can lead to solution divergence. This proved to be the case in the lid driven cavity problem presented here. Despite these limitations, these results demonstrate that the algorithm is capable of solving a strongly coupled problem in which changes in the velocity field effect the local wall deformation. These results also show that for the stability of the solution, the solver is best suited to solving problems in which the pressure and stiffness of the wall is high (as is the case in the bulging membrane test case and the arterial flows investigated in chapters 8 and 9).

6.5 Closure

In this chapter, the numerical algorithms developed in chapters 3, 4 and 5 were tested against a series of benchmark studies. Each component of the solver was tested independently to verify its accurate performance before ensuring the coupling algorithm was capable of combining the solutions and resolving complex fluid-structure interactions. Previously validation has been conducted on the fluid dynamics solver. This validation showed excellent accuracy and solution convergence properties (Sheard & Ryan 2007).

The Hookean solver was tested using a simple uni-axial patch test. The results of the simulation were compared with known analytical solutions for both the displacement and stress in the material. In all cases the Hookean algorithm performed excellently producing results within 0.2% of the analytical solution. The patch test also involved using non-orthogonal mesh elements which tested the linear consistency of the spatial discretisation.

The neo-Hookean solver was validated against experimental and numerical data from Mesa Múnica (2011). In this, the strain response in a rubber specimen was assessed in a uni-axial compression test. Like the Hookean solver, the neo-Hookean solver proved highly accurate with the maximum error reported as 0.52%. In conducting this compression test, a Hookean model was also used, These results showed that even at intermediate levels of stress, the Hookean material drastically overestimated the strain in the material. This result implies that using a Hookean material model to model the wall dynamics in an aneurysm would lead to an over-estimate of the wall

motion. Consequently it would be inappropriate to use a Hookean elastic model in the context of aneurysm FSI. Such sentiment is widely supported in the literature (see for e.g. Humphrey & Taylor 2008).

Having determined the accuracy of each of the solver components, a series of benchmark studies were conducted to assess the performance of the ALE coupling algorithm. It was determined that the ALE algorithm was capable of simulating a variety of fluid structure problems with varying degrees of coupling between the fluid and solid. The solver performed exceptionally well in unidirectional coupling problems and strongly for cases which were pressure driven. While proving capable of simulating strongly coupled systems such as the lid driven cavity problem in § 6.4.3, stability of the solution did become an issue in large deformation cases. To resolve these issues the algorithm has been constructed such that the time step of the fluid and solid can be varied independently of each other allowing the user extra capabilities to tune the algorithm to the problem at hand. In any case, the solver performs well under conditions where wall stiffnesses are high and the pressure is driven from the boundary conditions. This suits the problems considered in subsequent chapters well.

The first phase of this thesis aimed to develop a numerical method for analysing fluid structure interactions in aneurysms. The numerical method needed to be sufficiently complex so as to consider the non-linear constitutive models of the wall, which included non uniform wall properties. The validation cases presented in this chapter, combined with the numerical algorithm outlined in chapters 3, 4 and 5 achieve this outcome. Furthermore, the unique combination of spectral elements, a new time stepping algorithm for neo-Hookean applications and a modified coupling algorithm for the ALE formulation presents a novel contribution to this field.

Chapter 7

Parameter space

7.1 Introduction

Numerical modelling of fluid-structure interactions necessitates the prior knowledge of a set of parameters pertaining to the geometry, the fluid and solid continuum models, as well as the appropriate physiological boundary conditions for both continuum phases. Humphrey & Taylor (2008) emphasize a major downfall in current fluid-structure interaction models in aneurysms is the use of inappropriate, non physiological, continuum properties and boundary conditions.

Modelling biological material and flows is always fraught with generalisations and simplifications. Firstly, because humans are unique, different genetic predispositions and different environmental stimuli leads to each individual having a particular resting heart rate, artery wall stiffness and aneurysm size. Secondly, because measurement is difficult, biological materials are difficult to work with, and can easily be damaged during measurement. Furthermore, access to the material to accurately test their properties is impossible without causing harm to the patient.

This chapter aims to canvas the literature in order to define a reasonable value for the fluid and solid properties which can be utilised in the subsequent aneurysm investigations. It will also provide justification of the wall stiffness parameter space to be investigated. Finally it will present an explanation of the geometries chosen for the ensuing fluid-structure interaction research.

7.2 Geometry

Aneurysms are prevalent in the large blood vessels throughout the human body. Most commonly they are located in the abdominal aorta just above the iliac junction, but

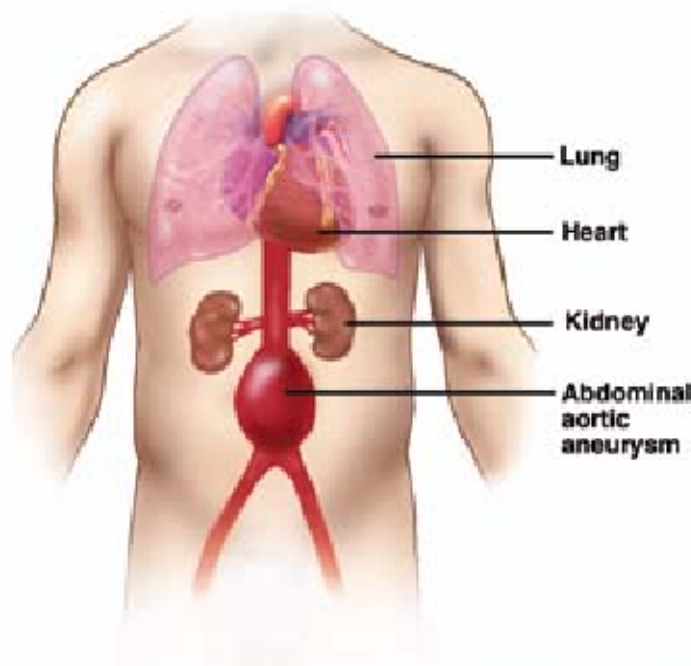


FIGURE 7.1: The location of an abdominal aortic aneurysm with renal arteries above and the iliac junction below. Reproduced with the permission of Annual reviews from Lasheras (2007).

are often also located in the knee joint, and with a lower prevalence, in the circle of Willis (Lasheras 2007; Sforza *et al.* 2009). With the mortality rate of abdominal aortic aneurysms at 70-90% (Lindholt *et al.* 2005) investigation into these aneurysms is crucial. Abdominal aortic aneurysms form in the aorta between the renal artery junction and the iliac junction which sends blood down each of the lower limbs, this location is depicted in figure 7.1.

7.2.1 Healthy aorta

Figure 7.2 shows the computational domain for the aneurysm initiation investigation. It simulates blood flow through a healthy aortic section in which abdominal aortic aneurysms commonly form.

An aortic diameter of 20 mm is used, which is a value commonly used throughout the literature (Di Martino *et al.* 1998; Finol *et al.* 2003a,b; Salsac *et al.* 2006). In their investigation, Stefanadis *et al.* (1995) measured the dilation of the aorta throughout the pressure pulse from the heart. They found the aortic diameter varied from 20.5 mm



FIGURE 7.2: The geometry used in the straight pipe aneurysm initiation investigation. The darker raised region is the aneurysm wall (thickness, $t_{total} = 1.5$ mm), with the brighter red region representing the fluid flowing into the moving wall section (diameter $d = 20$ mm).

at peak diastole to 22.5 mm at peak systole. This is in good agreement with the 20 mm diameter wall used for rigid-wall simulations in the aforementioned studies.

7.2.2 Aneurysm

Aneurysm shapes may be saccular (balloon-like expansions of only a portion of the wall), fusiform (gradual dilation of the complete circumference of the artery), or cylindrical. The different shapes have not been related to any specific cardiovascular disease or clinical manifestation (Morrison 1999). While in the early stages of development abdominal aortic aneurysms are often approximated by a fusiform shape, it is unlikely that well developed aneurysms of medium or large size (diameter > 45 mm) would be fusiform or axisymmetric. In fact, advanced AAAs form truly asymmetric shapes due to the presence of the tissue in the perianeurysmal environment and the vertebral column located posterior to this artery segment. This makes a large AAA less fusiform and asymmetric, accounting for a major anterior dilation and a flattened posterior surface (Finol *et al.* 2003b).

While recognising the departure from the fusiform shape in the late stages of abdominal aortic aneurysm development, the work in this thesis will focus on a fusiform shape only. In their investigation into the effects of asymmetry, Finol *et al.* (2003b) recognise that in early stages of development the aneurysm takes on a nearly fusiform geometry. Furthermore, in order to determine the effect of a heterogeneous wall stiff-

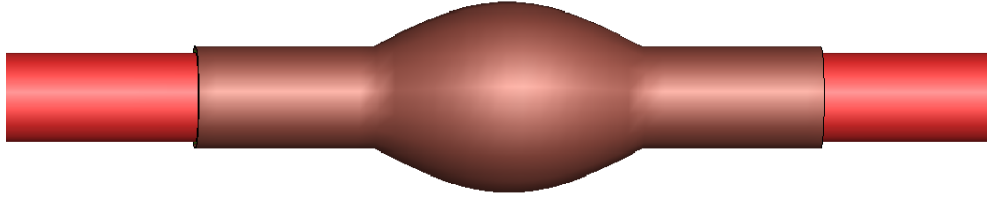


FIGURE 7.3: The geometry used in the established aneurysm investigation. The darker raised region is the aneurysm wall (thickness, $t_{total} = 1.5$ mm), with the brighter red region representing the fluid flowing into the moving wall section (diameter $d = 20$ mm). The bulge may be described by an aspect ratio $\frac{L}{d} = 3$ and dilation ratio $\frac{D}{d} = 2$.

ness on the flow dynamics in an aneurysm all other parameters that have an effect on the haemodynamics are held constant in order to isolate the effect of the variable wall stiffness.

The fusiform bulge created for the aneurysm in this investigation (shown in figure 7.3) is created using the sinusoidal relationship,

$$r(z) = \begin{cases} \frac{d}{2} & \text{if } z < z_0 \text{ or } z > z_0 + L, \\ \frac{d}{2} + \frac{D-d}{2} \left[\sin \left(\frac{\pi(z-z_0)}{L} \right) \right] & \text{if } z_0 < z < z_0 + L, \end{cases} \quad (7.1)$$

where $r(z)$ is the radius of the aneurysm as a function of z -position, z_0 is the starting position of the aneurysm bulge, L is the aneurysm bulge length, D is the maximum diameter of the aneurysm, and d is the diameter of the original artery (Sheard 2009).

Fusiform aneurysms may be characterised by their aspect ratio $\frac{L}{d}$ and dilation ratio $\frac{D}{d}$ as seen in figure 1.4. Previous numerical studies have investigated a range of aspect and dilation ratios (e.g. Salsac *et al.* 2006). Table 7.1 summarises some of the ratios used. In this investigation a dilation ratio $\frac{D}{d} = 2$ and an aspect ratio $\frac{L}{d} = 3$ is chosen. This is within the range of aspect and dilation ratios used in the literature. It also corresponds to a small to medium sized aneurysm, which should not have departed too far from a fusiform shape.

In terms of physical dimensions the maximum diameter of the aneurysm was kept at 40 mm (in accordance with the dilation ratio $\frac{D}{d} = 2$), this was chosen to remove

Bulge shape		
	Aspect ratio $\frac{L}{d}$	Dialation ratio $\frac{D}{d}$
Salsac <i>et al.</i> (2006)	2.9-5.2	1.3-2.4
Sheard (2009)	2.9	1.9
Finol <i>et al.</i> (2003b)	6.0	3.0
Finol <i>et al.</i> (2003a)	9.0	3.0
This study	3.0	2.0

TABLE 7.1: Literature survey of aneurysm aspect and dilation ratios of aneurysms that have been used in numerical simulations.

the likelihood of intraluminal thrombus forming which has been shown to affect flow dynamics (Di Martino *et al.* 1998). Aneurysms with diameter $D < 45$ mm are clinically shown to be typically devoid of an intraluminal thrombus (Harter *et al.* 1982). Again the choice of this parameter is aimed at isolating the effect of wall stiffness on the aneurysm haemodynamics while maintaining a physiologically relevant simulation environment.

The length of the aneurysm will be 60 mm. This parameter is simply chosen based on the aspect ratio which has been commonly used in the literature. It represents an aneurysm of medium size. Large aneurysms can grow up to the full length of the section of the abdominal aorta which lies between the renal arteries and the iliac junction. The average length of this arterial section is 130 mm across both males and females (Hoffmann 2008).

In the following investigations, the length of arterial wall that is allowed to move is 120 mm in both the aneurysm initiation and established aneurysm cases (note: longer inlet and outlet regions are used with solid walls to ensure inlet and outlet conditions do not affect the solution in the region of interest). This closely matches the length of the abdominal aorta described in Hoffmann (2008). The circulatory system is much longer than this section and the vessel wall is compliant throughout, however, junctions such as the renal artery and iliac junctions will form tethering points limiting the local dilation of the artery wall. As such, modelling just the 120 mm section between the renal and iliac junction with the ends tethered closely models the human physiological environment.

7.3 Fluid parameters

In modelling the blood flow in an aneurysm it is important to select a physiologically accurate set of fluid properties and boundary conditions to accurately assess the haemodynamics *in vivo*. The choice of fluid dynamic parameters and boundary conditions used in this study follows closely the works of Finol *et al.* (2003b) and Leung *et al.* (2006).

7.3.1 Fluid properties

The density of blood is widely accepted to be 1060 kg/m^3 (Finol *et al.* 2003b; Leung *et al.* 2006) which is very close to that of water at 1000 kg/m^3 . The extra density is a result of the small amounts of protein and inorganic salts in the plasma and haematocrit.

In § 1.2 the composition of blood is discussed. Due to the level of haematocrit which exists within the plasma, blood is strictly a non-Newtonian fluid (it does not have a linear stress-strain relationship). Regardless, the results presented in this thesis use a Newtonian fluid assumption. The works of Rodkiewicz *et al.* (1990); Perktold & Rappitsch (1995) and (Wootton & Ku 1999) showed that in large vessels such as the abdominal aorta, blood behaves like a Newtonian fluid. In the present study a dynamic viscosity of $\mu = 3.85 \times 10^{-3} \text{ Pa} \cdot \text{s}$ (Finol *et al.* 2003b) is used.

7.3.2 Boundary conditions

The boundary of the fluid domain is divided into the following regions for the assignment of boundary conditions: an inlet, outlet, and the fluid-structure interaction interface. The applied boundary conditions for the fluid inlet and outlet are a time dependent fully developed Poiseuille velocity profile for the inlet, and at the outlet a time dependent pressure boundary condition. The Poiseuille velocity profile is described by

$$v_z = 2 \frac{v_{peak}}{R^2} (R^2 - x^2 - y^2), \quad (7.2)$$

where v_z is the inlet velocity in the z direction, v_{peak} is the time dependent peak inlet velocity (shown in figure 7.4), R is the radius of the artery and x and y are positions in the x - y plane. While the Womersley profile is the naturally forming velocity profile for oscillatory flows in pipes, the Poiseuille flow forced at the inlet will develop into a Womersley profile given enough time before it reaches the proximal neck.

The pressure outlet boundary condition is time dependent due to the pressure pulse

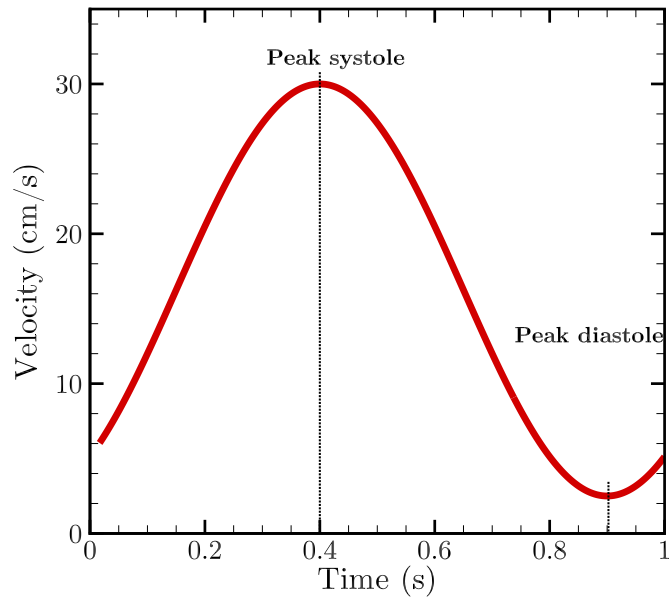


FIGURE 7.4: Time-variation in the peak velocity at the inlet over a single period, used in this thesis.

from the heart driving the flow. The variation in outlet pressure as a function of time is plotted in figure 7.5.

The systolic and diastolic pressures shown in figure 7.5 match those used in Finol *et al.* (2003b) which use the in vivo luminal pressure measured at the iliac junction in Mills *et al.* (1970). Similarly the velocity profile of figure 7.4 matches the peak systolic velocity and velocity range measured in Mills *et al.* (1970) at the renal artery junction. The use of this transient input velocity based on normal arterial conditions (not aneurysm geometries) is justified by the fact that the inlet boundary condition is applied well upstream of the proximal neck of the aneurysm, where the abdominal aorta is undilated. For average resting conditions (heart rate of 60–70 bpm), blood flow in the abdominal aorta is generally laminar (Finol & Amon 2002); flow deceleration achieved after peak systole induces laminar disturbed flow conditions and vortex formation even under simulated exercise conditions (Moore Jr *et al.* 1994). Inlet peak systolic flow occurs at $t = 0.4$ s and outlet peak pressure at $t = 0.5$ s.

Some previous investigations have used Windkessel models to reproduce the physiological influence of the arterial beds distal to the outlets (e.g. Arzani *et al.* 2012). Such

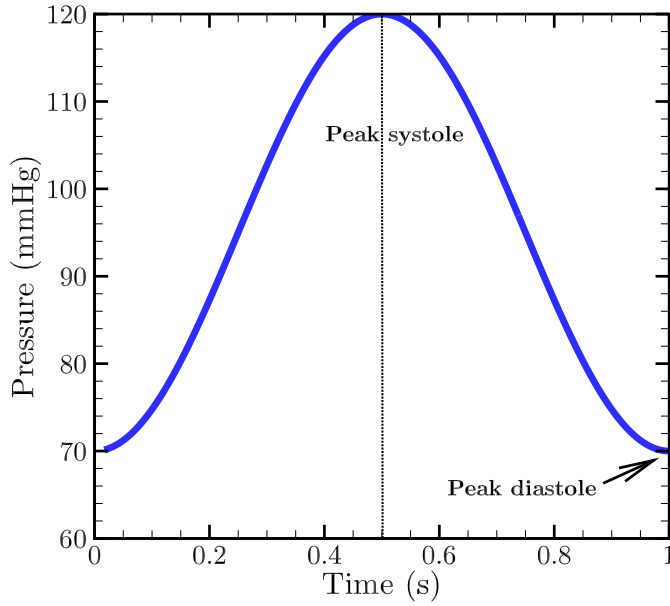


FIGURE 7.5: Pressure outlet boundary condition as a function of time used in this thesis.

models use a three-element Windkessel model coupled to the computational domain using the method described in Vignon-Clementel *et al.* (2006) with outlet volumetric flow rates determined by the Windkessel model. In the Windkessel model of the arterial network, the pressure, flow rate and flow resistance are seen as the voltage, current and resistance in an electric circuit. The pressure is determined by integrating the following equation:

$$Q = C \frac{dP}{dt} + \frac{P}{D} \quad (7.3)$$

where Q is the flow rate in the artery, C is the compliance of the artery, and D is the resistance of the distal arterial network.

In the context of this work, the compliance factor C can be readily calculated, however the resistance D of the distal arterial and vascular network remains unknown. The dependence of the Windkessel model on the pressure drop implies a domain size dependence. If a Windkessel model were adopted, complications could arise with inlet velocity profiles. In order to constrain the number of parameters in this study a Windkessel model is not used.

While the pressure and velocity profiles do not exhibit the same systolic and diastolic acceleration shown in figure 7.6, matching the relevant peak physiological parameters

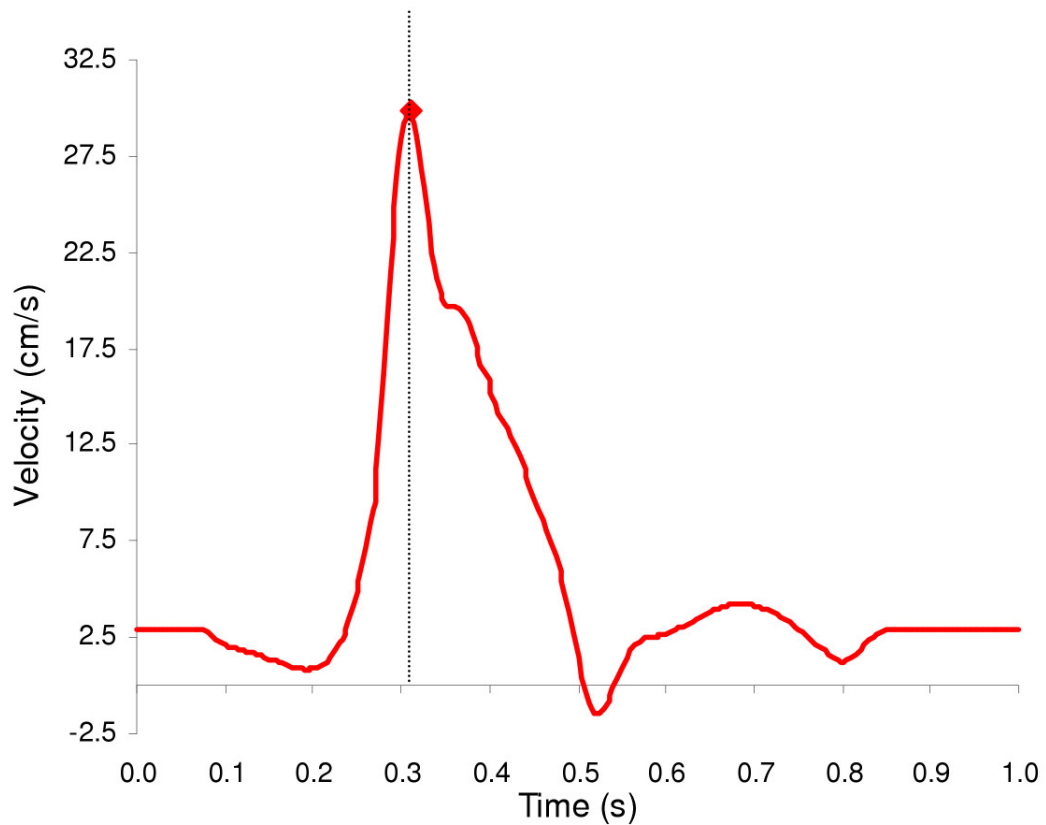


FIGURE 7.6: *In vivo* luminal pulsatile velocity based on the velocity profile in Mills *et al.* (1970). Inlet peak systolic flow occurs at $t = 0.304$ s. Reproduced with the permission of BioMed Central Ltd from Scotti *et al.* (2005).

should give a good approximation of the *in vivo* flow conditions. The peak velocity measured in Mills *et al.* (1970), is reflected in this velocity inlet as it is expected that the peak wall shear stress (in the case of laminar flow) should occur when the velocity is the greatest. The simplification of the time evolution of the velocity and pressure fields does limit how physiologically representative the simulations are. However, an aim of this thesis is to determine the effect of heterogeneous wall stiffness on the haemodynamic stimuli in an aneurysm. By performing simulations that compare changes in stiffness under like boundary conditions; conclusions can be drawn in relation to the variations in wall stiffness. Furthermore, the simplification of the time evolution of the pressure and velocity boundary conditions allows analytical expressions to be developed, providing a platform from which the underlying physics driving the changes in the flow fields may be understood.

7.3.2.1 FSI interface boundary conditions

The boundary conditions applied at the fluid-structure interface are as follows: displacement (u) of the fluid ($\partial\Omega_f$) and solid ($\partial\Omega_s$) domain boundaries must be compatible,

$$u_{\partial\Omega_s} = u_{\partial\Omega_f}, \quad (7.4)$$

the traction (stress, $\boldsymbol{\sigma}$) normal to the wall must equal the pressure (P) applied by the fluid at the wall,

$$\boldsymbol{\sigma} \cdot \underline{\mathbf{n}} = P, \quad (7.5)$$

where $\underline{\mathbf{n}}$ is the unit normal vector to the wall; and the fluid must obey a non-slip boundary condition at the wall, that is,

$$\mathbf{v}_f = \mathbf{v}_s, \quad (7.6)$$

where \mathbf{v}_f is the velocity of the fluid and \mathbf{v}_s is the velocity of the FSI interface.

7.3.3 Flow properties

Finally we define some of the non-dimensionalised parameters that describe the flow. The time-averaged Reynolds number is $Re_{mean} = 410$, which is characteristic of a patient in resting conditions (Milnor 1989). The dynamic range of the Reynolds number is $Re = 61.5 - 758$.

The heart rate of the resting patient for which such a time averaged Reynolds number is appropriate is 60 bpm which implies a period of each heart cycle of $T = 1$ s.

The Womersley number, α , characterizes the flow frequency $\omega = \frac{2\pi}{T}$, the geometry and the fluid viscous properties. For this investigation, which has been based on physiological properties, the Womersley number $\alpha = 9.7$. As the rest of the study is based on the physiologically accurate boundary conditions the Womersley number is also physiologically realistic, $\alpha = 9.7$ is a typical value for the human abdominal aorta under resting conditions (Nichols & O'Rourke 1990; Finol *et al.* 2003b; Scotti *et al.* 2005; Lindholt *et al.* 2005).

7.4 Solid parameters

In their reviews, both Lasheras (2007) and Sforza *et al.* (2009) indicated a major shortcoming in the current modelling of fluid-structure interactions in aneurysms is based

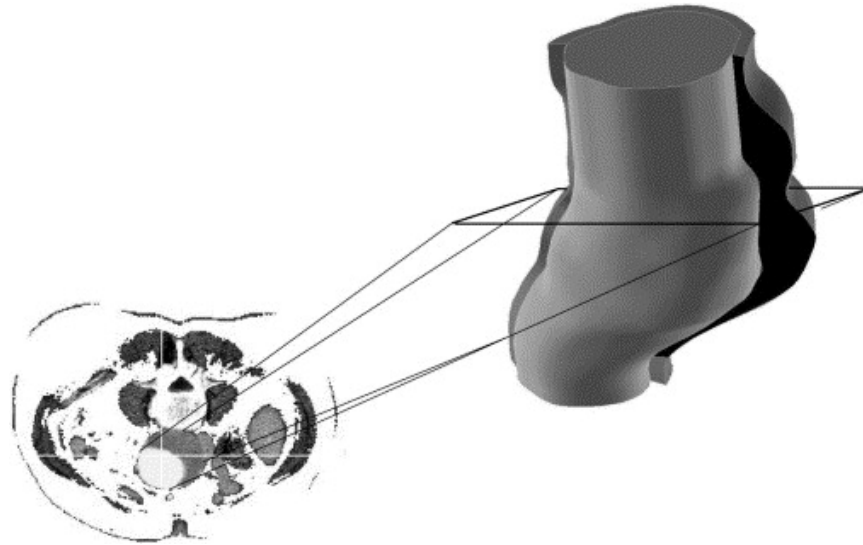


FIGURE 7.7: A computed tomography (CT) scan slice of an abdominal aortic aneurysm. A three dimensional model (also shown) is reconstructed from the series of 2D segments identified in the CT scan. The arterial wall (cross-sectioned) has a highly variable thickness. Reproduced with the permission of Elsevier Ltd from Di Martino *et al.* (2001).

around the lack of information about the mechanical properties of the wall. Furthermore they highlighted the inadequacy of the existing continuum models used for the solid phase. While many models use highly complex constitutive models to describe the wall, incorporating hyperelastic material models (Raghavan & Vorp 2000), linear or non linear viscoelastic models (Pontrelli 2001; Čanić *et al.* 2006) and anisotropic models (Grotberg & Jensen 2004; Rissland *et al.* 2009); very few have accounted for the heterogeneous thickness and stiffness distribution in an aneurysm.

Figure 7.7 shows the reconstruction of an aneurysm from a CT scan. What is readily visible is the high degree of variation in the arterial wall thickness. Furthermore, in figure 7.8, the stress distribution is shown to be highly heterogeneous, with calcification deposits scattered sporadically throughout the aneurysm. The highly heterogeneous wall stiffness environment motivates this study. This examination aims to investigate the effect of localised variations in material stiffness in both a healthy artery and an established aneurysm geometry. The healthy artery investigation focuses on investigating causes of aneurysms while the aneurysm study shows how an uneven stress distribution may cause undesirable haemodynamic properties which could perpetuate the growth of aneurysms.

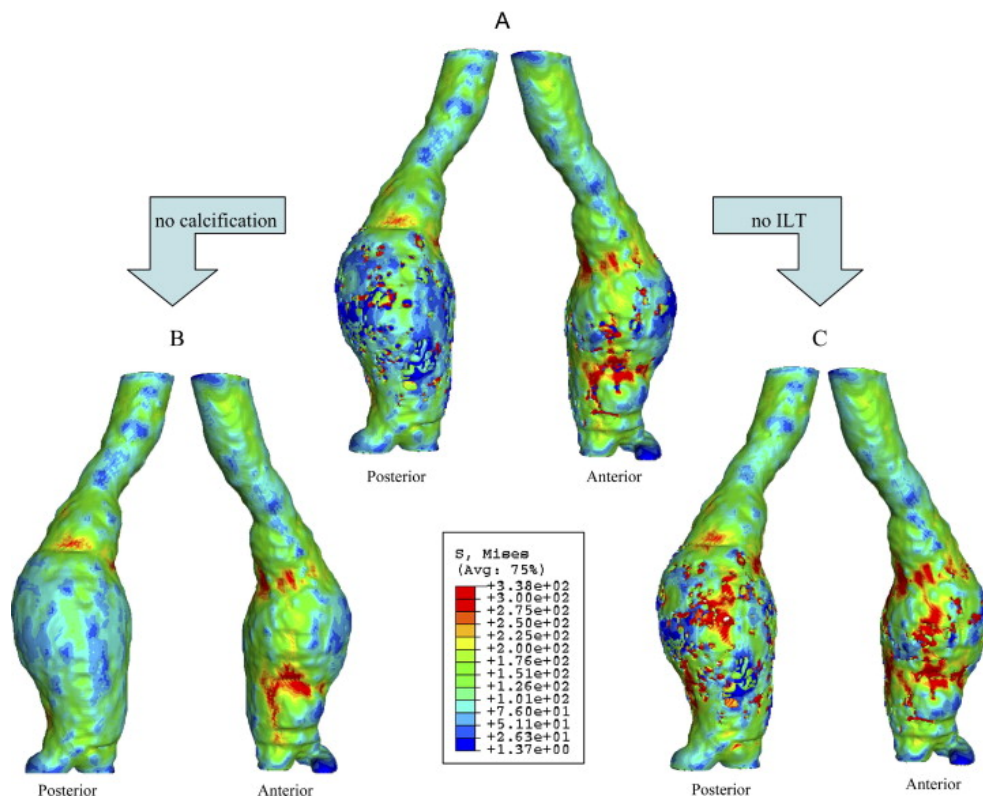


FIGURE 7.8: The computed von-Mises stress distribution in a patient specific aneurysm (A). The stress distribution changes dramatically if calcification regions (B) or Intra-Luminal Thrombus (ILT) (C) are excluded. Reproduced with the permission of Elsevier Ltd from Li *et al.* (2008).

7.4.1 Wall thickness

Previous studies such as Scotti *et al.* (2005), have investigated the effect of a changing wall thickness on the haemodynamics in a fusiform aneurysm. They showed that a variable wall thickness drastically affects the wall stresses. The current study will investigate the effect of varying the other heterogeneous material parameter, the stiffness. The wall response to the haemodynamic forces is not a function of stiffness or thickness alone. If identical forces are applied then a decrease in stiffness or thickness will lead to larger stresses being felt by the wall. In order to isolate the effect of changes in stiffness for the purpose of assessing its feasibility as a risk of rupture indicator, the thickness of the wall will be kept constant and the wall stiffness varied.

The artery wall is made up of three layers, the intima, media and adventitia. Many investigations have either measured the wall and layer thickness of an abdominal aorta or used a derived wall thickness in a simulation. Table 7.2 summarises the range of

Thickness (mm)				
	Intima	Media	Adventitia	Total
Healthy aorta				
Lindsay & Hurst (1979)	0.13	1.00	-	1.63
Restrepo <i>et al.</i> (1979)	0.13	1.00	-	1.63
Åstrand <i>et al.</i> (2005)	-	0.73	-	1.06*
Restrepo <i>et al.</i> (1979)	0.10	-	-	-
Gao <i>et al.</i> (2006)	-	-	-	2.00
Driessen <i>et al.</i> (2004)	-	0.26	0.13	0.41*
Aneurysms				
Raghavan <i>et al.</i> (2006)	-	-	-	1.48
Thubrikar <i>et al.</i> (2001)	-	-	-	1.58-3.19
Scotti <i>et al.</i> (2005)	-	-	-	1.50
Papaharilaou <i>et al.</i> (2007)	-	-	-	2.00
Di Martino <i>et al.</i> (2006)	-	-	-	2.00
This study	0.195*	0.840*	0.465*	1.50

TABLE 7.2: Literature survey of healthy arterial wall and aneurysm wall thicknesses. Both values of wall thickness determined by experiment and implemented in numerical simulations are presented. * represents a value determined using the layer thickness ratio found in Schulze-Bauer *et al.* (2003).

thicknesses quoted in the literature.

From these papers, the mean artery wall thickness is 1.346 mm. For aneurysm measurements and simulations the average thickness is 1.95 mm. Aneurysm formation is usually associated with large variations in wall thickness as cell apoptosis occurs and intraluminal thromboses form. In this study the thickness of the wall was chosen to be a constant across both the aneurysm bulge and the healthy artery sections just as in Scotti *et al.* (2005); Di Martino *et al.* (2006); Gao *et al.* (2006) and Papaharilaou *et al.* (2007). In this study a thickness of $t_{total} = 1.5$ mm is chosen which is close to the average of thicknesses for aneurysms and healthy aorta.

Schulze-Bauer *et al.* (2003) observed a thickness ratio for the artery wall layers of intima/media/adventitia of 13/56/31 for healthy arteries. Driessen *et al.* (2004) used a

ratio of 2/1 for media/adventitia and Gao *et al.* (2006) used a ratio of 1/6/2. The ratios used by both Driessen *et al.* (2004) and Gao *et al.* (2006) are simplifications of the ratio quoted in Schulze-Bauer *et al.* (2003); as such, this ratio is used in determining the layer thicknesses for the model. Given a total thickness $t_{total} = 1.5$ mm, this yields an intima thickness of $t_i = 0.195$ mm, a media thickness of $t_m = 0.84$ mm, and adventitia thickness of $t_a = 0.465$ mm.

7.4.2 Wall stiffness

As with wall thickness, many studies have been completed to assess the stiffness of an artery wall. Determining the stiffness of the wall *in situ* is a complicated prospect. Estimates of the stiffness have been made by observing the dilation or response of the wall to the different pressures of systole and diastole. Other measurements have been performed using ultrasound techniques (Claridge 2010; Couade *et al.* 2010). Some investigations have completed uniaxial and biaxial tensile tests on ruptured aneurysm tissue or animal tissues (Di Martino *et al.* 2006; Lally *et al.* 2004). Table 7.3 compiles the range of stiffnesses determined throughout the literature.

From these papers the median healthy artery stiffness is 0.8 MPa. Some of the papers used in forming this average cite data for artery sections that are not near the abdominal aorta and others use data for elderly subjects with hypertension and other health concerns. Although this does skew the data to a stiffer value of the overall stiffness, the prevalence of aneurysms is greatest in the elderly population. Furthermore, the incidence of aneurysm is often coincident with hypertension, atherosclerosis or other health concerns that adversely affect wall stiffness, making this value of 0.8 MPa plausible. In further support of this argument, figure 7.9 from Claridge (2010) shows the regression of the artery stiffness with age. The stiffness of 0.8 MPa corresponds to a person of approximately 65 years, which is the beginning of the age bracket in which there is a high prevalence of abdominal aortic aneurysms.

The stiffness of aneurysm sections will be varied from 0.2 – 6.0 MPa, this encompasses the full range of stiffnesses quoted in the literature for both healthy and damaged vessels. This range should provide a physiological parameter space sufficient to determine if non-uniform stress distributions affect the flow haemodynamics.

Stiffness		
	Youngs modulus, E (MPa)	Shear modulus, G (MPa)
Healthy aorta		
Di Martino <i>et al.</i> (2006)	0.200	0.066
Laurent <i>et al.</i> (1994)	2.250	0.750
Claridge (2010)	0.250-1.000	0.083-0.333
Couade <i>et al.</i> (2010)	0.300	0.100
Mosora <i>et al.</i> (1993)	0.600-2.000	0.200-0.666
Aneurysms		
Vorp <i>et al.</i> (1996)	3.510-5.690	1.170-1.890
Di Martino <i>et al.</i> (2006)	3.800	1.260
Thubrikar <i>et al.</i> (2001)	1.000-6.000	0.333-2.000
Scotti <i>et al.</i> (2005)	2.700	0.933
Finol <i>et al.</i> (2003a)	5.000	1.666
This study		
Healthy aorta	0.800	0.267
Aneurysm	0.200-6.000	0.066-2.000

TABLE 7.3: Literature survey of the stiffness of both healthy arterial walls and aneurysm walls. Values represented in this table are average wall stiffnesses and not accurate for individual layers of the arterial wall. Both values of wall stiffness determined by experiment and implemented in numerical simulations are presented.

7.4.2.1 Layer stiffness

The measurements of the material stiffness parameters are performed on bisected artery and aneurysm sections (Mosora *et al.* 1993; Claridge 2010; Couade *et al.* 2010). A tensile or compressive test rig is used such as the one shown in Dokos *et al.* (2000). This rig is capable of measuring the stress-strain behaviour of the arterial tissue, and from this, the material parameters of the tissue may be determined. Due to the complex nature of the layers of the artery walls and their thickness it is difficult to accurately dissect the layers in order to measure precisely the material properties of each. As such the stiffness values quoted in table 7.3 are average stiffnesses of the entire arterial cross-section.

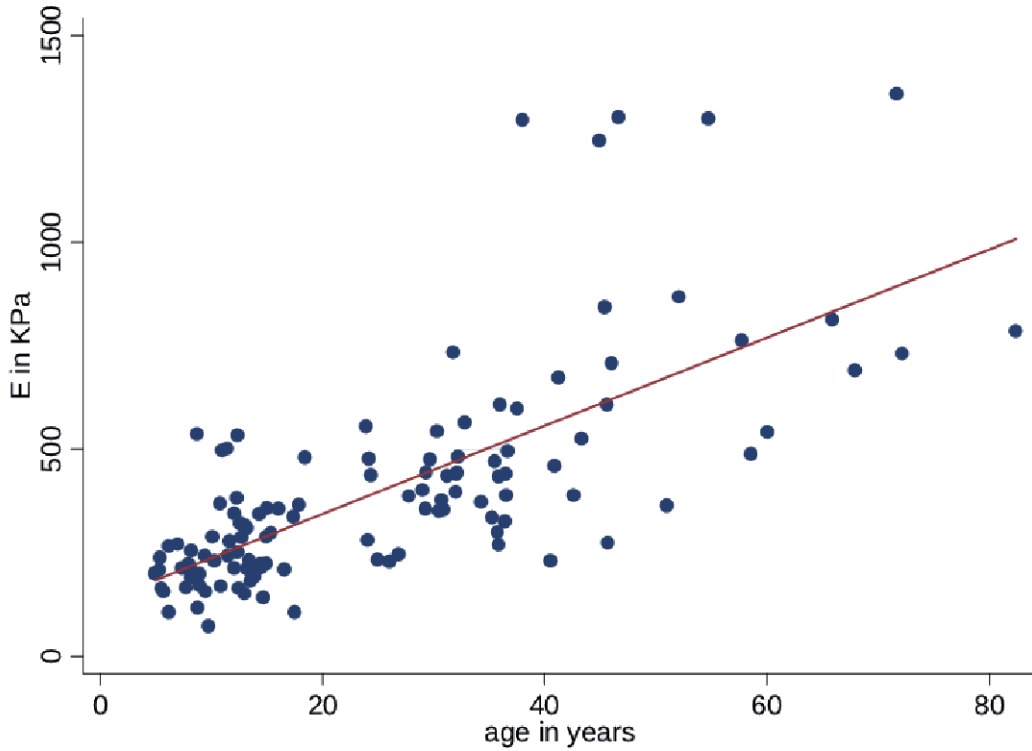


FIGURE 7.9: The regression of the mean Young's modulus (E) in kPa plotted as a function of age. Reproduced with the permission of Claridge from Claridge (2010).

Xie *et al.* (1995) provides a means to determine the stiffness of the individual layers of the artery wall. They found the Young's modulus of the inner layers (intima and media) was three to four times larger than that of the outer layer (adventitia). Cabrera-Fischer *et al.* (2002) presented some experimental data showing that the Young's modulus of the intima is smaller than that of the media. This investigation follows the work of Gao *et al.* (2006). The Young's modulus of the media is set to be three times that of both the adventitia and intima (i.e. 1:3:1). Since the mean Young's modulus of the vessel wall across the entire wall volume is invariable, the Young's modulus of each layer is in inverse proportion to the area of the layer in the cross-section (Gao *et al.* 2006). The stiffness of each layer may be related to the average stiffness of the arterial wall using

$$E_{mean} = \frac{E_i \times t_i + E_m \times t_m + E_a \times t_a}{t_{total}}, \quad (7.7)$$

where E_{mean} is the mean stiffness of the wall, E_i , E_m and E_a are the stiffnesses of the intima, media and adventitia respectively; t_i , t_m and t_a are the thicknesses of the

Layer stiffness, E (MPa)							
Average stiffness, E_{mean}	0.2	0.4	0.6	0.8 (healthy)	2.0	4.0	6.0
Intima stiffness, E_i	0.031	0.063	0.094	0.126	0.314	0.629	0.943
Media stiffness, E_m	0.094	0.189	0.283	0.377	0.943	1.887	2.830
Adventitia stiffness, E_a	0.031	0.063	0.094	0.126	0.314	0.629	0.943

TABLE 7.4: Breakdown of the layer stiffness used at each of the prescribed average stiffnesses used in this investigation.

intima, media and adventitia respectively and t_{total} is the thickness of the wall. Also required is the relation from Xie *et al.* (1995),

$$E_m = 3E_i = 3E_a. \quad (7.8)$$

Using these relations the stiffnesses of each layer is calculated and summarized in table 7.4.

7.4.3 Wall assumptions

At this point some of the assumptions made in choosing these material properties are recognised. Firstly, the wall is modelled as an isotropic incompressible neo-Hookean solid. Biological tissues such as the artery wall have been shown by Raghavan & Vorp (2000) among others to be anisotropic in nature and feature both hyperelastic and viscoelastic properties. This is a result of the highly complex structure of the artery wall. Humphrey & Taylor (2008) indicated that the most advanced FSI solvers currently use a neo-Hookean wall model (Wolters *et al.* 2005). Other investigations such as Torii *et al.* (2008) tested the effect of using more complex material models on the artery wall response. They found that while neo-Hookean material models gave very different results to Hookean material models, more complex models had a negligible impact on the results.

In terms of choosing the wall stiffness and thickness, Lopez-Candales *et al.* (1997) and Thompson *et al.* (1997), identified a thinning of the intima and medial layers during aneurysm formation. In this study the layer thickness is kept constant regardless of whether it is in the aneurysm or healthy aorta region. Lopez-Candales *et al.* (1997) also described the change in the material stiffness that occurs as a result of the wall remodelling process that leads to an aneurysm forming. In this study the overall stiffness

will be changed to simulate the stiffening of different regions. However, individual layer stiffness will remain proportional to the total stiffness of the region. This would be a good subject of further investigation but is beyond the scope of the work completed in this study. Finally, the grain like structure of the stiffness and thickness pattern shown in figure 7.8 is considered. The stiffening that is to be conducted in this investigation is applied across bands of the arterial wall giving a very axisymmetric stiffness profile. This is obviously a simplification of the structure shown in figure 7.8 but is done in order to investigate a pattern or distribution which may be generalized across many aneurysms. While the case of non-symmetric stiffening would be more physiologically accurate and of interest, it is again beyond the scope of this investigation.

7.4.4 Solid boundary conditions

The solid domain boundary consists of the fluid-structure interaction interface, the inlet and outlet cross-sectional ends and the outer surface which interacts with the perianeurysmal environment.

The FSI interface will have the boundary conditions that were described in § 7.3.2.1. The cross-sectional ends at the inlet and outlet of the geometry will be fixed in place, that is,

$$\mathbf{u} = 0, \tag{7.9}$$

where \mathbf{u} is the displacement of the solid material. As discussed in § 7.2.2 the renal and iliac artery junctions provide a stabilising platform which tethers the abdominal aortic section. The length of the simulated section between these two boundary faces is comparable to the abdominal aortic section. Finol *et al.* (2003b) use identical boundary conditions for these surfaces.

The final boundary condition is the outer wall surface. This surface interacts with the perianeurysmal environment. Finol *et al.* (2003b) could find no published data on normal forces exerted by internal organs and tissue on the wall of the abdominal aorta. A further search of the literature yielded no further information about pressures exerted by the perianeurysmal environment. Fixing the outer surface of the artery wall, as is common practice in Finol *et al.* (2003b); Lindholt *et al.* (2005) and Scotti *et al.* (2005), can result in underestimating the movement of the artery wall. Stefanadis *et al.* (1995) measured the dilation of the artery wall in two patients throughout the cardiac cycle. They reported a change in vessel diameter of $\Delta d = 1.2 - 2.5$ mm. A short investigation

found that using an external pressure which matched the diastolic pressure at diastole and varied by 20% of the change in luminal pressure throughout the cycle produces a dilation of 1.54 mm in a healthy artery which falls within the range of values quoted in Stefanadis *et al.* (1995). The external pressure boundary condition that is then applied is,

$$P_{ext} = P_{dia} + 0.2 \frac{P_{peak} - P_{dia}}{2} \left[1 - \cos \left(\frac{2\pi}{T} t \right) \right], \quad (7.10)$$

where P_{ext} is the pressure applied to the external surface of the artery wall, P_{dia} is the diastolic pressure in the lumen, P_{peak} is the peak systolic pressure in the lumen, T is the period of the heart beat and t is time.

7.5 Summary

Through an extensive survey of the literature and careful consideration of the physiological environment; the full parameter space of the subsequent investigations into aneurysm initiation and growth has been justified. Table 7.5 provides a summary of the chosen fluid and solid dynamic parameters used throughout the rest of this thesis.

Summary	
Parameter	value
Geometry	
Length of solid section (aneurysm)	140 mm
Length of solid section (straight pipe)	120 mm
Length aneurysm bulge	60 mm
Aortic diameter d	20 mm
Aspect ratio $\frac{L}{d}$	3
Dilation ratio $\frac{D}{d}$	2
Total wall thickness t_{tot}	1.5 mm
Intima layer thickness t_i	0.195 mm
Media layer thickness t_m	0.84 mm
Adventitia layer thickness t_a	0.465 mm
Fluid	
dynamic viscosity μ	3.85×10^{-3} Pa · s
density ρ	1060 kg/m ³
Inlet velocity mean \mathbf{v}_{mean}	16.25 cm/s
Inlet velocity peak \mathbf{v}_{peak}	30 cm/s
Outlet pressure systolic \mathbf{P}_{sys}	120 mmHg
Outlet pressure diastolic \mathbf{P}_{dia}	70 mmHg
Phase lag (velocity-pressure)	0.1 s
Heart rate (period) T	1 s
Time averaged Reynolds number Re_{mean}	410
Peak Reynolds number Re_{peak}	750
Womersley number α	9.7
Solid	
Stiffness (healthy) E_{mean}	0.800 MPa
Aneurysm stiffness range	0.200-6.000 MPa
density ρ_s	1160 kg/m ³

TABLE 7.5: Summary of the parameter space used in the aneurysm initiation and growth investigations.

Chapter 8

Investigation 1: Aneurysm initiation

8.1 Introduction

The precise initiation process of aneurysms is currently unknown (Lasheras 2007; Sforza *et al.* 2009). Many physiological studies have identified a series of risk factors that increase the risk of aneurysm formation. These include smoking, sex, alcohol, hypertension, atherosclerosis, disease or infection (e.g. syphilis). While these risk factors have been identified, the asymptomatic nature of aneurysms means early detection is unlikely. In fact, generally aneurysms are not identified until they are quite advanced in their evolution. As such, little is known about aneurysm initiation (Lasheras 2007).

Age is considered to be the greatest risk factor, with aneurysms being most prevalent in the elderly. Age makes arteries thicker and stiffer. The median layer thins and loses its orderly arrangement of elastin changing to a disordered “patchwork” of elastin grain. The elastin to collagen ratio becomes more collagenous which leads to a stiffening of the arterial wall (Lasheras 2007). Furthermore, histological studies have shown that in the early stages of aneurysm formation there is a degeneration of endothelial cells and internal elastic lamina (Stehbens 1963, 1989). A thinning of the medial layer through apoptosis (programmed cell death) of smooth muscle cells is also evident (Stehbens 1963, 1989). Disruptions in the remodelling process have been identified with increased levels of elastase (Chaytte & Lewis 1997) and matrix metalloproteinase (Bruno *et al.* 1998). This could lead to a weakening of the wall.

Nichols & O’Rourke (1990) suggest that fatigue through cyclic stresses causes the fracture of the load-bearing elastic sheets. Under the pulsatile haemodynamic forces, the polymerised structure of elastin sheet and fibres reorganises, causing them to fail

at lower tensional stresses. The tearing of these sheets is associated with a loss in elastic re-coil which may cause a permanent dilatation of the vessel. The permanent stretching of the smooth muscle tissue is accompanied by a permanent remodelling process whereby collagen content in the muscular layer increases. The end result of this irreversible process is the creation of an aneurysm.

Haemodynamic factors play a key role due to the capacity of endothelial cells to sense and react to Wall Shear Stresses (WSS). Studies have shown that low wall shear stress and high oscillatory patterns of wall shear stress correlate with intimal wall thickening (Dardik *et al.* 2005; Friedman *et al.* 1981; Ku *et al.* 1985). A uniform shear stress field tends to stretch and align endothelial cells. Furthermore, studies on animals show an increase in WSS can fragment the internal elastic lamina or damage the endothelium (Sforza *et al.* 2009).

Presented in this chapter are the results of an investigation into the initiation of aneurysms. There exists a consensus in the literature (Stehbens 1963, 1989; Nichols & O'Rourke 1990; Bruno *et al.* 1998; Lasheras 2007) that through the ageing process and possible exposure to disease, arterial walls undergo a slow degradation which leads to a localised discontinuity in arterial wall stiffness. Nichols & O'Rourke (1990) suggest the fatigue-like wall degradation triggers an interruption in the mechanotransduction process which leads to the negative progression of arterial wall health and the creation of an aneurysm.

This study aims to address aim 2c from § 1.8, to investigate the effect of a heterogeneous wall stiffness on the haemodynamics in an artery and how this in turn may lead to a haemodynamic environment that could disrupt the mechanotransduction process leading to the initiation of aneurysm growth.

In addressing this aim, blood flow through a straight section of pipe with elastic-walls was simulated. To simulate the localised wall degradation that can occur naturally as part of the ageing process or as a result of disease; sections of the elastic-wall were prescribed a spatially varying stiffness. This investigation shows the effect that lesions, calcification or wall tethering can have on arterial haemodynamics and the eventual initiation of aneurysms.

For the set of hypotheses relating to this investigation the reader is referred to § 1.8.3.

8.2 Geometry

Figure 8.1 shows the computational domain used for this aneurysm initiation investigation. The model simulates blood flow through a healthy aortic section in which abdominal aortic aneurysms commonly form. As discussed in § 7.2.1, an aortic diameter of $d = 20$ mm is used. The length of the elastic-wall region shown in figure 8.1 is 120 mm (or $6d$). Figure 8.1 shows the macro-element mesh used in the meshing of the straight pipe. Gauss–Legendre–Lobatto quadrature points are used to interpolate within each of the macro-elements shown. By using these quadrature points a highly accurate mesh is formed (see § 8.3 for details of the accuracy).

It is clear from figure 8.1(a) that the computational domain extends both upstream and downstream of the elastic region. While physiologically this region does not exist, it must be included to ensure that inlet and outlet boundary conditions do not affect the flow in the region of interest. Further details of the choice of inlet and outlet length can be found in § 8.3.2. The large inlet length allows the Poiseuille velocity profile inlet condition to adopt the stable Womersley profile for oscillating flows by the time it reaches the inlet of the elastic region. The inlet is $9d$ upstream of the entrance to the elastic region and the outlet is $6d$ downstream.

Downstream of the elastic region is a flared section leading to the outlet (figure 8.1(d)). A velocity inlet boundary condition is applied to the side walls of the flared section and a periodic pressure boundary condition is applied at the end of the pipe. Due to the motion of the elastic-wall blood is drawn back into the elastic section periodically throughout the heart-cycle. Figure 7.6 shows the time evolution of velocity in an artery which includes a diastolic phase with reverse flow. In order to simulate this reverse flow through the elastic region in a stable manner, this flared velocity inlet condition was included to ensure positive flow through the pressure outlet at all times while allowing reversed flow in the region close to the elastic-wall. While the boundary condition itself is covered in § 8.2.1 it is noted here that the flared shape was chosen to minimise the energy input into the system thus providing a minimal effect on the elastic region upstream. The flare has a length of $3d$ and expands from the pipe diameter d to $1.5d$ at the downstream boundary.

Hexahedral mesh elements are used to simulate the flow through the three-dimensional domain (see figure 8.1(b)). To maximise accuracy in the elastic region where the moving arterial wall introduces multi-dimensional flow dynamics, the mesh is much denser.

In this region the macro mesh elements are of approximate size $0.2d \times 0.2d \times 0.2d$ (i.e. aspect ratio of unity). A near cube-shaped macro-element should ensure that numerical errors introduced through the matrix inversion process (which is more accurate on diagonally dominant matrices) is minimized.

Outside of the elastic region, the mesh is coarser. The rigid walls and uniform geometry in this region ensures the flow is almost completely unidirectional. As such, less resolution is required to describe the flow in these regions (see § 8.3.3). A coarser mesh was used in these regions to decrease simulation time.

Figure 8.1(c) also shows the solid domain mesh used. This mesh consists of three macro-element layers. Each layer represents a layer in the arterial wall. The wall has a constant initial thickness throughout the geometry and each layer is also initially constant along the length of the artery. The overall thickness is 1.5 mm with the intima thickness, $t_i = 0.195$ mm, the media thickness, $t_m = 0.84$ mm, and the adventitia thickness of $t_a = 0.465$ mm. Justification of these thicknesses can be found in § 7.4.1. Section 8.3.4 demonstrates the accuracy of the mesh.

The investigation into aneurysm initiation involves a local change in wall stiffness. The results presented in § 8.5 include a stiffer band of material that is one element (or $0.2d$) wide, in the centre of the elastic region. All three layers of the wall are stiffened by the same amount. The results presented in § 8.5.6 investigate the effects of expanding this thickened region to two elements (or $0.4d$) wide and three elements (or $0.8d$) wide.

In § 8.5.7 flow through an expanded rigid-walled pipe is simulated, to assess if the geometry alone is responsible for some of the flow structures being observed in the fluid-structure interaction study. For this investigation the geometry from figure 8.1(a) is used. All of the mesh features described for the fluid-structure interaction cases are used with the shape of the bulge determined from the maximum solid response in an FSI simulation.

8.2.1 Fluid properties and boundary conditions

In this investigation blood is modelled as a Newtonian fluid. The viscosity of blood is $\mu = 3.85 \times 10^{-3}$ Pa · s, with a density of $\rho = 1060$ kg/m³. These parameters have been extensively documented in the literature. For justification of the Newtonian model of blood see § 1.2.

The fluid boundary conditions are extensively documented and justified in chapter 7.

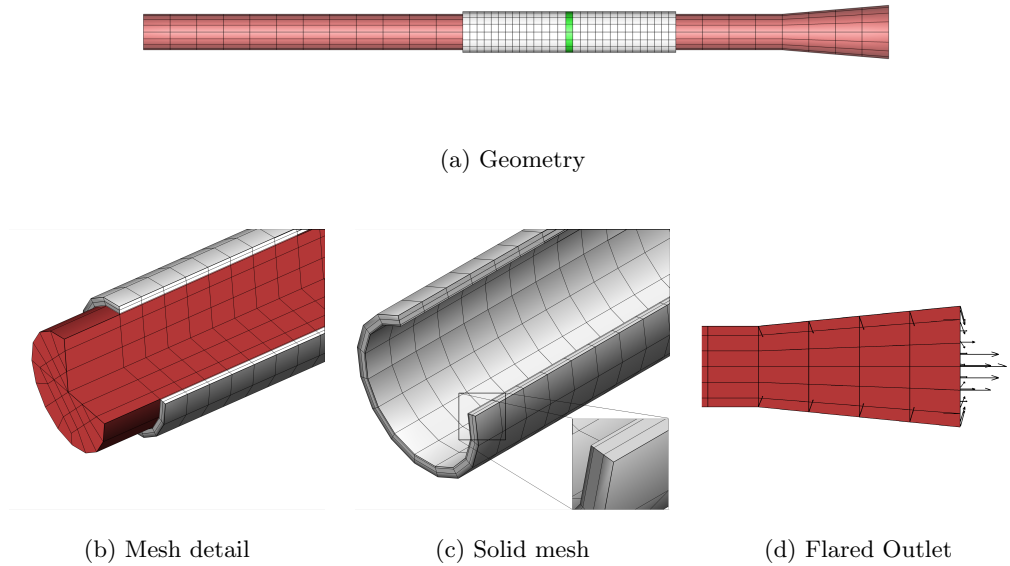


FIGURE 8.1: Mesh detail used in the aneurysm initiation investigation, blood flows from left to right. (a) shows macro-elements in the entire computational domain. Red regions represent blood flow, the green region shows the band of solid material that is to be stiffened. (b) shows a detailed cross-section of the mesh, clearly visible are the cube-shaped elements in the fluid region and the thinner layer of solid elements. (c) shows a detailed cross-section of the solid mesh with its three macro-element layers. (d) shows the outlet flare with vectors representing the inlet boundary conditions and outflow at the pressure outlet.

These consist of a velocity inlet boundary condition with Poiseuille profile. Figure 7.4 showed the temporal flow profile at the velocity inlet, which comprises a sinusoidal profile with a peak inlet velocity of $v_{peak} = 30$ cm/s and a mean velocity of $v_{mean} = 16.25$ cm/s. A time-varying pressure outlet boundary condition is also used. Figure 7.5 shows the time evolution of the pressure boundary condition, which features a sinusoidal profile with a phase lag of 0.1 s behind the inlet velocity profile. The period of both the inlet and outlet boundary conditions is $T = 1$ s. These boundary conditions correspond to a time-averaged Reynolds number of $Re_{mean} = 410$ and a peak Reynolds number of $Re_{peak} = 750$. The Womersley number used in the investigation is $\alpha = 9.7$.

At the vessel wall a no-slip boundary is applied. At the fluid-structure interface in the elastic region, the velocity of the wall is prescribed as the fluid boundary condition. i.e.

$$\mathbf{v}_f = \mathbf{v}_s. \quad (8.1)$$

Finally, the flared inlet boundary condition near the pressure outlet is described. Figure 8.1 shows the velocity vectors on a two-dimensional slice of the flared section. The magnitude of the velocity entering the domain increases linearly from the start of the flared section to the end. This allows the boundary conditions at the end of the straight section (which is a no-slip boundary condition, i.e. $\mathbf{v} = 0$) to match the flared boundary condition at their interface edge. The x , y , and z components of this boundary condition are

$$\begin{aligned}v_x &= -\frac{1}{4} [(z - L_{f_s}) v_f] \cdot \frac{x}{R}, \\v_y &= -\frac{1}{4} [(z - L_{f_s}) v_f] \cdot \frac{y}{R}, \\v_z &= [(z - L_{f_s}) v_f] \cdot \frac{1}{R},\end{aligned}\tag{8.2}$$

where v_x , v_y , v_z are the x , y , and z components of this velocity, L_{f_s} is the length of straight pipe leading to the beginning of the flared section, R is the radius of the pipe, and v_f is

$$v_f = 4 - 2 \cos(2\pi t).\tag{8.3}$$

As discussed in § 8.2 this boundary condition is applied to ensure continuous outflow at the pressure outlet. The time-varying component v_f is used rather than a constant value as throughout the cardiac cycle flow periodically reverses direction. This boundary condition is therefore not required at all times and to minimise the energy it introduces into the system the flow rate through the boundary is reduced (by the sinusoidal time dependence) at times when the velocity through the outlet is naturally outward. The domain size study conducted in § 8.3.2 showed that the addition of this outlet sufficiently far downstream of the elastic region had no measurable impact on the flow through the elastic region of interest.

For the rigid-wall expanded-pipe case the geometry formed at peak systole was captured. Once formed the walls were held fixed in this location while the velocity and pressure boundary conditions at the inlet and outlet respectively were allowed to vary as in the previous investigations. Finally, a no-slip boundary condition is applied to all walls with no fluid-structure interaction occurring.

Justification of each of the parameters and boundary conditions used in this investigation may be found in chapter 7.

8.2.2 Solid properties and boundary conditions

The elastic artery wall represents the second component of the fluid-structure interaction in aneurysms. The wall is modelled as a hyperelastic neo-Hookean material. In chapter 7 a literature survey is used to determine the Young's modulus of the healthy abdominal aorta as $E_{mean} = 0.800$ MPa. Details of the layer stiffness are given in § 7.4.2.1. In conjunction with the Young's modulus, a density of $\rho_s = 1160$ kg/m³ is specified for the healthy arterial wall.

The band of material to be stiffened in the elastic region is shown in figure 8.1(a). This region will have stiffnesses ranging from $E_{mean} = 0.2 - 6.0$ MPa. Specifically, simulations were conducted with a rigid-wall; a uniform healthy stiffness throughout the artery ($E_{mean} = 0.8$ MPa); and adverse conditions ($E_{mean} = 0.2, 0.4, 0.6, 2.0, 4.0$ and 6.0 MPa). This range of stiffnesses were chosen based on the literature survey conducted in chapter 7.

The boundary conditions of the solid domain are described in § 7.4.4. They include a zero displacement boundary condition on the inlet and outlet faces; this mimics the tethering that occurs at the iliac and renal artery junctions at either end of the abdominal aortic section. On the interior surface a pressure boundary condition is applied. The pressure is calculated during the fluid phase and applied as a normal stress to the solid domain, i.e.

$$\boldsymbol{\sigma} \cdot \underline{\mathbf{n}} = P. \quad (8.4)$$

The exterior of the artery wall is in contact with the periarterial environment. To simulate the response of the periarterial environment a pressure boundary condition is applied to the surface,

$$P_{ext} = P_{dia} + 0.2 \frac{P_{peak} - P_{dia}}{2} \left[1 - \cos \left(\frac{2\pi}{T} t \right) \right]. \quad (8.5)$$

The exterior pressure increases as the luminal pressure increases. This simulates the increase in the periarterial response to the dilation caused by the luminal pressure. The period and phase of this pressure boundary condition is the same as the outlet pressure boundary condition for the fluid.

Justification of each of the parameters and boundary conditions used in this investigation may be found in chapter 7.

8.3 Solution validation

Rigorous validation of the numerical techniques, domain size, and mesh independence were conducted as part of this research. The numerical techniques developed in this thesis are validated in chapter 6.

To ensure the mesh used in this investigation provided sufficient spatial and temporal resolution while maintaining a minimal computational cost, a mesh optimisation investigation was conducted (see § 8.3.1). A series of meshing strategies were tested for their accuracy, and based on the time taken to achieve a certain level of accuracy, the mesh shown in figure 8.1 was chosen.

After selecting the optimized mesh, a domain analysis was conducted to guarantee that the inlet and outlet boundary conditions were not affecting the flow through the region of interest. Inlet and outlet lengths extending up to $24D$ upstream and downstream were investigated while monitoring the flow in the elastic region. Section 8.3.2 presents the results of the domain analysis.

Once the most efficient mesh and domain size were established, a grid independence study was performed to determine the spatial accuracy of the simulations. The results of this are detailed in sections 8.3.3 and 8.3.4.

Finally, the accuracy of the temporal discretisation was examined in § 8.4. This study considered the effect of varying the time step of the solver and the number of oscillation cycles were required in order to evolve the flow to its asymptotic fluid-structure interaction state.

In this thesis, an error threshold of $< 1\%$ for global error measures and $< 2\%$ for local error measures was used to direct the choice of spatial and temporal resolution; and domain size.

8.3.1 Mesh optimisation

The spectral- hp element method allows both h -type and p -type refinement of a computational mesh. Spectral methods exhibit exponential convergence properties when the number of degrees of freedom are increased (Karniadakis *et al.* 1991). This means in order to achieve a desired spatial resolution, the spectral element method can use a coarser macro-element mesh with a higher degree polynomial which amounts to fewer degrees of freedom when compared to traditional linear finite element methods. However, the improved spatial convergence properties do not guarantee a reduction in the

computational cost. Simulation time, while strongly linked to the number of degrees of freedom, is also dependent on the density and structure of the matrix system (Karniadakis & Sherwin 1999). The software packages used to perform the matrix solves have different performance results dependent on the structure of the matrix system. To determine the most time-efficient mesh for a prescribed level of accuracy, a mesh optimisation analysis was performed.

Four meshes were created in the mesh optimisation study. Each mesh, shown in figure 8.2, employed a different level of h -type refinement. The meshes were created by linking successive 2D planes of elements. To ensure accuracy at the boundary, element depth (plane spacing) was set to match the width of the element closest to the boundary. This gives an aspect ratio as close to unity as possible for these boundary elements. A near cube-shaped macro-element should ensure that numerical errors introduced through the matrix inversion process (which is more accurate on diagonally dominant matrices) is minimized. Accuracy is especially important at the fluid-structure interface where boundary layers form: in this region vorticity is high and wall shear stresses are to be determined. Mesh 1 in figure 8.2(a) employs very few macro-elements. As such it requires a higher polynomial order, p , to attain spatial convergence. Conversely, Mesh 4 employs a large number of macro-elements, which in turn permits a lower polynomial order to attain spatial convergence. Meshes 2 (figure 8.2(b)) and 3 (figure 8.2(c)) employ intermediate levels of h -type refinement.

To determine the optimal mesh configuration, a p -type grid independence study was conducted for each mesh. As the haemodynamic parameters are of the greatest importance to aneurysm initiation, only the fluid region was simulated with a non-slip rigid-wall boundary condition. The time-dependent inlet velocity and outlet pressure boundary conditions discussed in § 8.2.1 were applied to each mesh, and a number of global and local parameters were recorded in order to assess the accuracy of each mesh. The time taken for the simulation to run was also recorded to give an indication of the computational cost associated with each meshing strategy.

To assess the spatial resolution of the solution produced from each mesh at each level of p -type refinement, a set of global and local flow measurements were taken. The L_2 -norm is used to measure the overall difference between the solutions from different meshes and resolutions. It is a vector norm mathematically described by

$$L_2 = \int_{\Omega} |v|^2 d\Omega, \quad (8.6)$$

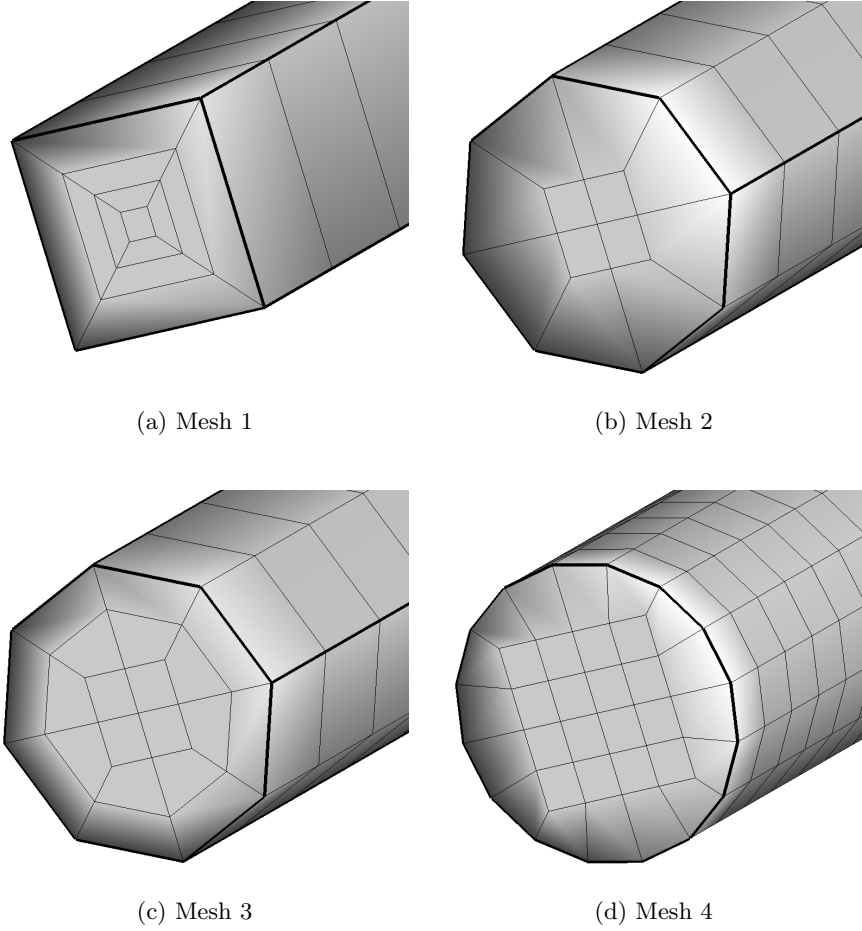


FIGURE 8.2: Macro element meshes used in the mesh optimisation investigation. Meshes 1-4 show an increasing level of h -type refinement. The meshes were created by linking successive 2D planes of elements. To ensure accuracy at the boundary element, depth (plane spacing) was set to match the width of the element closest to the boundary. Note: a curvilinear mapping of the element faces onto the circular pipe is used - the flat faces depicted on the pipe walls here is a product of the plotting package used, which accentuates the poor representation of the geometry at the limit of small p -type resolution.

where Ω represents the computational domain, \mathbf{v} are the velocity vector, and $|\cdot|$ the local magnitude of the vector. The additive nature of the L_2 -norm and the use of a magnitude function make it useful in assessing the global error in a solution as local variations are amalgamated into a single value.

Local variations in the solutions are observed by monitoring v_z , the z -component of velocity, and the strain-rate-magnitude at a point in the global domain. In the results presented in figure 8.3, these parameters are sampled along the centreline at the midpoint of the elastic region $(x, y, z) = (0, 0, 12D)$. The velocity component is a

first-order quantity which should be reasonably smooth due to the use of C^0 -continuous elements. The strain-rate-magnitude defined is by

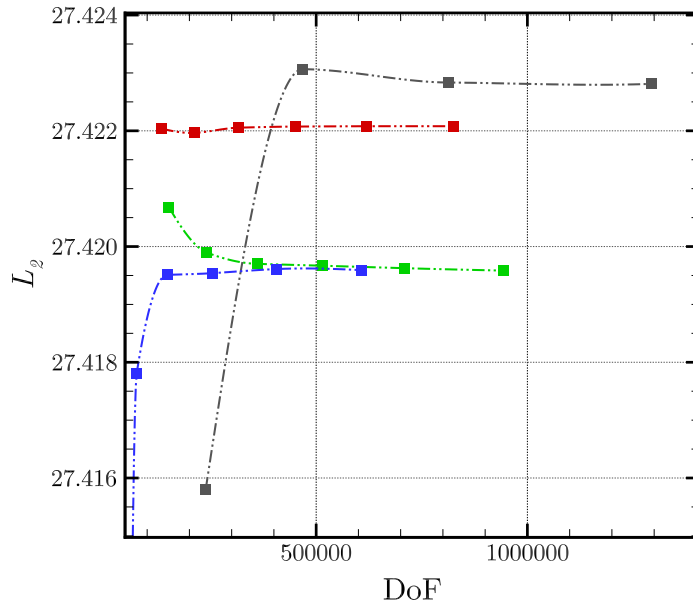
$$|\dot{\epsilon}| = \sqrt{2\dot{\epsilon} : \dot{\epsilon}}, \quad (8.7)$$

where $\dot{\epsilon}$ is the strain rate,

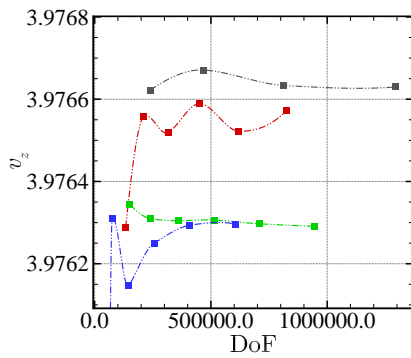
$$\dot{\epsilon}_{ij} = \frac{1}{2} \left(\frac{\partial u_i}{\partial x_j} + \frac{\partial u_j}{\partial x_i} \right), \quad (8.8)$$

is more likely to exhibit resolution-based variation as it is based on spatial derivative quantities $\frac{\partial u_i}{\partial x_j}$. Spatial derivatives reduce by one the order of the polynomial approximation of the field (i.e. $\frac{\partial u_i}{\partial x_j}$ of a fourth-order resolved field becomes a third-order representation of the gradient field). As such, gradient fields require higher resolution (relative to zero-th order fields) to resolve. In this regard, gradient fields are more sensitive to borderline resolution. The numerical “wobble” which presents in some results is a by product of the post-processing of data in which data fields are interpolated across C^0 -continuous element interfaces where the local mismatch has been averaged. As such at large polynomial orders where numerical “wobble” becomes prevalent this property may give the first indications of error in the solution.

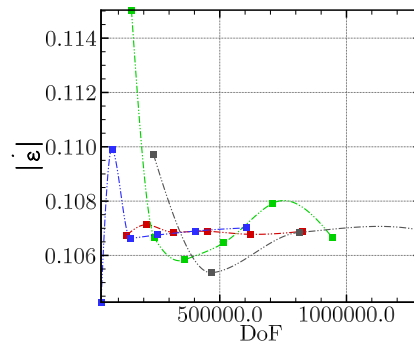
The results presented in figure 8.3 show the p -type grid independence studies conducted for each of the 4 meshes (see figure 8.2). In order to compare the resolution achieved between meshes, the results are plotted against the number of independent degrees of freedom in the solution domain. As expected, as the polynomial order is increased for each mesh the solution converges to a consistent value. The results for the L_2 -norm shows the most consistent convergence behaviour. Mesh 3 produces a slower convergence rate with some fluctuation present in the v_z results. Mesh 2 shows similar wobble characteristics in terms of the strain-rate-magnitude data. The sparse nature of these two meshes meant they were run at higher polynomial orders compared with Mesh 4. Mesh 4 exhibits stable convergence behaviour in both global and local error cases. The higher-degree polynomial basis functions may be responsible for the poor convergence observed for meshes 2 and 3. Mesh 1 is also sparse and simulations were conducted at higher polynomial orders, though similar fluctuations were not observed in this case. This may be due to the larger z -dimension of elements in Mesh 1 as compared to Meshes 2 and 3, which may mean that small-scale flow variations along the longitudinal axis were not resolved and hence did not contribute to the wobble in the solution.



(a)



(b)



(c)

FIGURE 8.3: Results of the p -type grid independence study for each mesh 1-4 shown in figure 8.2. In each sub-plot red, green, blue and grey lines and symbols represent meshes 1, 2, 3 and 4, respectively. For all sub-plots and meshes as the number of degrees of freedom (polynomial order) is increased the mesh solution converges to a stable value. (a) shows the L_2 -norm, a global measure of the energy in the solution. (b) shows the v_z velocity component at a point along the centre line of the pipe and (c) shows the magnitude of strain rate at a point on the pipe centreline. All values were taken at time of peak energy.

% error						
p	Mesh 1			Mesh 2		
	L_2	v_z	$ \dot{\epsilon} $	L_2	v_z	$ \dot{\epsilon} $
7	1.3×10^{-4}	7.1×10^{-3}	0.13	3.9×10^{-3}	1.3×10^{-3}	7.8
8	4.1×10^{-4}	3.4×10^{-4}	0.22	1.1×10^{-3}	4.5×10^{-4}	0.01
9	8.7×10^{-5}	1.3×10^{-3}	0.03	4.2×10^{-4}	3.3×10^{-4}	0.76
10	1.9×10^{-5}	4.3×10^{-4}	2.4×10^{-3}	3.0×10^{-4}	3.7×10^{-4}	0.17
11	3.3×10^{-6}	1.2×10^{-3}	0.10	1.5×10^{-4}	1.5×10^{-4}	1.18
12	0.0	0.0	0.0	0.0	0.0	0.0

p	Mesh 3			Mesh 4		
	L_2	v_z	$ \dot{\epsilon} $	L_2	v_z	$ \dot{\epsilon} $
4	0.157	0.13	2.5	-	-	-
5	6.5×10^{-3}	3.2×10^{-4}	2.70	0.02	1.8×10^{-4}	2.61
6	3.0×10^{-4}	3.7×10^{-3}	0.36	9.2×10^{-4}	1.0×10^{-3}	1.45
7	1.9×10^{-4}	1.1×10^{-3}	0.24	8.0×10^{-5}	9.9×10^{-5}	0.07
8	6.9×10^{-4}	7.5×10^{-5}	0.10	0.0	0.0	0.0
9	0.0	0.0	0.0	-	-	-

TABLE 8.1: Percentage error in each mesh when compared to the most resolved case. Error is shown for global measures (L_2 -norm) and local measures (v_z and $|\dot{\epsilon}|$).

Table 8.1 provides a numerical estimate of the error associated with each mesh at each resolution level. The error was calculated by comparing the flow parameter measured at each resolution level to the most resolved case. Here the assumption is made that each mesh has reached a mesh independent state at the highest resolution case. The data presented in table 8.1 supports the results presented in figure 8.3. As the polynomial order is increased, the error in each case decreases. In all cases the error is small (error < 1%) for the more resolved cases. The smallest error is observed in the global L_2 -norm error estimate, with error converging to less than $10^{-4}\%$ for each mesh. The greatest error was observed in the strain-rate-magnitude with error only converging to ($< 10^{-1}\%$) in most cases. The larger error in the strain-rate-magnitude is to be expected for the reasons outlined previously. Finally, to emphasize the validity of using any of the meshes in solving this system, the maximum difference between any mesh at the most resolved case was 0.011% for L_2 -norm, 0.008% for v_z and 0.25% for

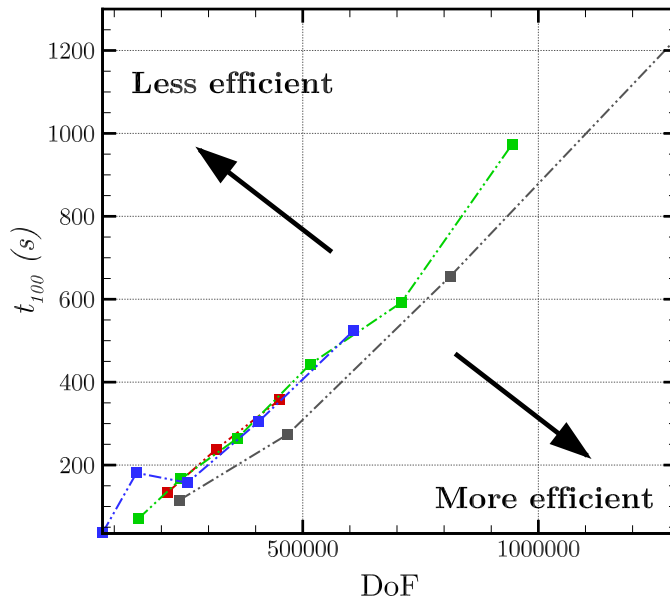


FIGURE 8.4: Simulation time required to complete 100 time steps, t_{100} , is plotted with respect to the number of degrees of freedom for each simulation. As in figure 8.3, red, green, blue and grey lines and symbols represent Meshes 1, 2, 3 and 4, respectively. A more efficient simulation has a shorter run time at higher resolution. Mesh 4 is the most efficient mesh.

strain-rate-magnitude.

The most appropriate mesh for the aneurysm initiation study should provide a grid independent solution at the lowest computational cost. Figure 8.3 and table 8.1 show each meshing strategy is capable of producing a sufficiently accurate mesh. Figure 8.4 shows the physical time taken to complete 100 time steps (t_{100}) in the solver for each mesh at each level of resolution. This clearly shows that Mesh 4 which is based on more macro-elements and a relatively low polynomial order is more efficient than the other meshes. Mesh 4 is capable of running faster at higher levels of resolution than the other meshes.

Figure 8.3 and table 8.1 present a clear case that when using all mesh types a grid independent solution can be achieved. Mesh 4 with the use of relatively low polynomial orders provides the most stable, accurate and efficient solution. This mesh is used throughout the aneurysm initiation study. Finally, a polynomial order of 5 was used as it provided less than 1% error with minimal computational cost. A similar paradigm for balancing h - and p -type refinement can be found in Blackburn *et al.* (2008)

8.3.2 Domain size

The mesh optimisation study conducted in § 8.3.1 simulated flow through a straight rigid section of pipe that represents the abdominal aorta. To ensure that the blood flow through the region of interest is physiologically accurate it is imperative that the proximity of the boundary conditions does not affect the results. The upstream inlet velocity is prescribed with a Poiseuille profile which needs time to adapt to the physiological profile for oscillating flows. Furthermore, the downstream inlet and pressure outlet could introduce back pressure and propagate numerical error. To minimise the effect that each of these have on the region of interest they should ideally be located as far away as possible. A domain size analysis was conducted to determine the minimum upstream and downstream distances required to prevent the boundary conditions affecting the solution.

Five inlet and outlet lengths were simulated in each case, $0d$, $3d$, $6d$, $9d$ and $24d$.

8.3.2.1 Upstream

Simulations were conducted using a constant outlet length and varying the upstream length. The flow was monitored at a series of points throughout the region of interest. Figure 8.5(a) shows the velocity profile at the entrance to the region of interest at $t = 0.4$ s for each of the inlet length cases. For the case of $0d$ upstream the velocity distribution is that of the perfect Poiseuille profile that is described at the outlet. As the inlet length is increased the flow has time to adopt the Womersley profile which is the natural state for oscillating flow. Figure 8.5(b) demonstrates that increasing the inlet length beyond $6d$ yields a negligible change in the velocity profile.

To illustrate precisely the effect of changing the inlet length, figure 8.5(b) plots the error-norm of the axial velocity across the diameter of the pipe at the entrance to the elastic region. As the inlet length is increased, the change in velocity diminishes dramatically. This correlates well with the velocity profile plots of figure 8.5. The percentage change of flow as a result of varying the inlet length is listed in table 8.2. The inlet length has a greater effect on the peak velocity than at the near-wall region. These results show that with an inlet length of $9d$ or greater, the effect of the inlet boundary condition is less than 0.01%. This is sufficiently accurate for this investigation, so an inlet length of $9d$ is used hereafter.

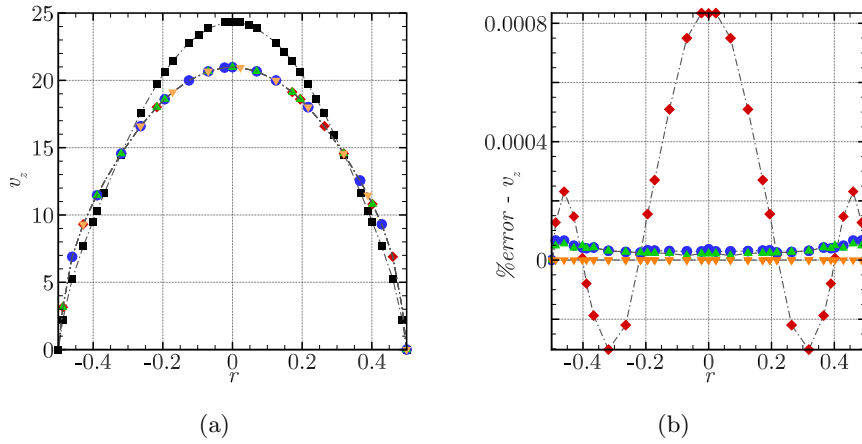


FIGURE 8.5: Velocity profile at the beginning of the elastic zone, velocity is normalised using the period of oscillation and diameter of the vessel. Black squares \blacksquare , red diamonds \blacklozenge , blue circles \bullet , green triangles \blacktriangle , and orange inverted triangles \blacktriangledown represent the profile for an inlet length $0d$, $3d$, $6d$, $9d$ and $24d$ upstream, respectively. (a) shows the velocity profile across the pipe diameter and (b) shows the percentage error of each velocity profile relative to the longest inlet case in (a). As the inlet length is increased, the difference in velocity profiles becomes negligible.

% error		
Inlet length	$r = 0$	$r = 0.3d$
0	13.8	5.7×10^{-1}
3	8.3×10^{-5}	2.7×10^{-4}
6	3.6×10^{-5}	3.0×10^{-5}
9	2.1×10^{-5}	3.0×10^{-5}
24	0.0	0.0

TABLE 8.2: Percentage error of the axial velocity at the centreline and near-wall locations. The error decreases as the inlet length increases.

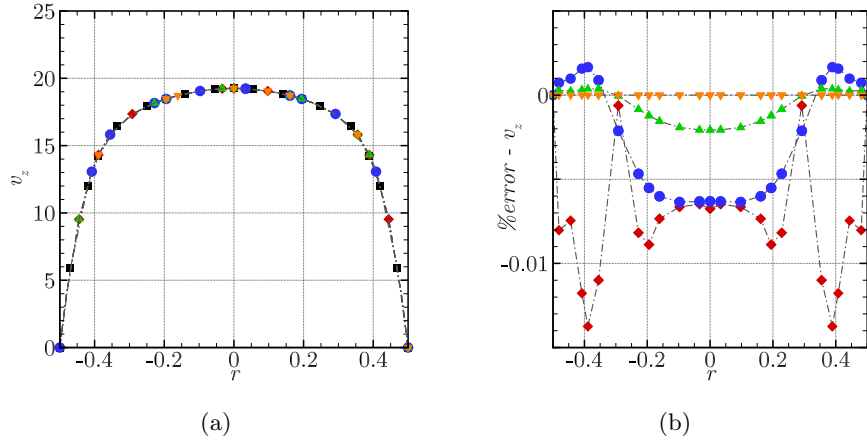


FIGURE 8.6: Velocity profile at the end of the region of interest, velocity is normalised using the period of oscillation and diameter of the vessel. Black squares \blacksquare , red diamonds \blacklozenge , blue circles \bullet , green triangles \blacktriangle , and orange inverted triangles \blacktriangledown represent the profile for an outlet length $0d$, $3d$, $6d$, $9d$ and $24d$ downstream, respectively. (a) shows the velocity profile across the pipe diameter and (b) shows the percentage error of each velocity profile relative to the longest inlet case in (a). As the outlet length is increased, the difference in velocity profiles becomes negligible.

8.3.2.2 Downstream

Having established an inlet length of $9d$, a series of simulations were conducted to determine the appropriate outlet length. The inlet length was fixed at $9d$, while the outlet length (distance from the end of the elastic region to start of the flared region) was varied between $0d$ and $24d$. The flow was monitored at identical locations to the upstream domain study. Figure 8.6(a) shows the velocity profile at the aneurysm bulge outlet (distal neck) at $t = 0.4$ s for each of the outlet length cases. A top-hat profile is clearly visible, as is expected for oscillating flow through a straight pipe. It is clear that for the straight pipe case changing the outlet length has a negligible effect on the flow in the region of interest. Figure 8.6(b) demonstrates that increasing the outlet length beyond $3d$ yields a negligible change in the velocity profile.

To further elucidate the effect of changing the outlet length, figure 8.6(b) shows the error-norm of the axial velocity across the diameter of the pipe at the exit of the elastic region. As the outlet length is increased, the change in velocity diminishes dramatically. Table 8.3 shows the percentage error for each outlet length. The maximum error is only 0.75%, which is negligible compared to errors associated with spatial discretisation. As

% error		
Outlet length	$r = 0$	$r = 0.38d$
0	4.4×10^{-3}	0.75
3	6.7×10^{-3}	1.3×10^{-2}
6	6.3×10^{-3}	1.4×10^{-3}
9	2.0×10^{-3}	3.7×10^{-4}
24	0.0	0.0

TABLE 8.3: Percentage error of the axial velocity at the centreline and near-wall locations. The error decreases as the outlet length increases.

a result, the impact of the outlet length on the flow was small enough that an outlet length of only $3d$ was chosen for all simulations. This produced an error $< 0.05\%$.

8.3.3 h_z -type refinement

In § 8.3.1, a variety of meshing strategies were used to determine the most efficient strategy for this geometry using the numerical algorithm described in chapter 6. As part of this, a p -type investigation was conducted and a polynomial order of $p = 5$ was determined to provide sufficient accuracy for this investigation. The previous investigations identified the most efficient meshing strategy, the appropriate polynomial order and the inlet and outlet domain lengths to negate any boundary condition effects. In a further effort to reduce the computational cost, a further h_z -type analysis was conducted.

The aim of this h_z -type analysis was to determine the required resolution in the axial (or longitudinal) direction. Using fewer macro-elements reduces computation time, and consequently it is desirable to have a longer axial element length. In the h_z -type refinement study, axial element length was varied between $0.2d$ (giving approximately cube-shaped elements with a unit aspect ratio), $0.36d$, $0.4d$, $0.5d$ and $0.75d$.

Figure 8.7 shows the effect that changing the h_z -type refinement has on the L_2 -norm. The L_2 -norm is sampled at the time of peak flow through the aneurysm (i.e. 0.4 s), this corresponds to the time of peak energy in the system. As the axial element length is reduced, so too does the change in L_2 -norm. Such convergence is expected as the spatial resolution is increased. Table 8.4 shows the percentage difference in L_2 -norm

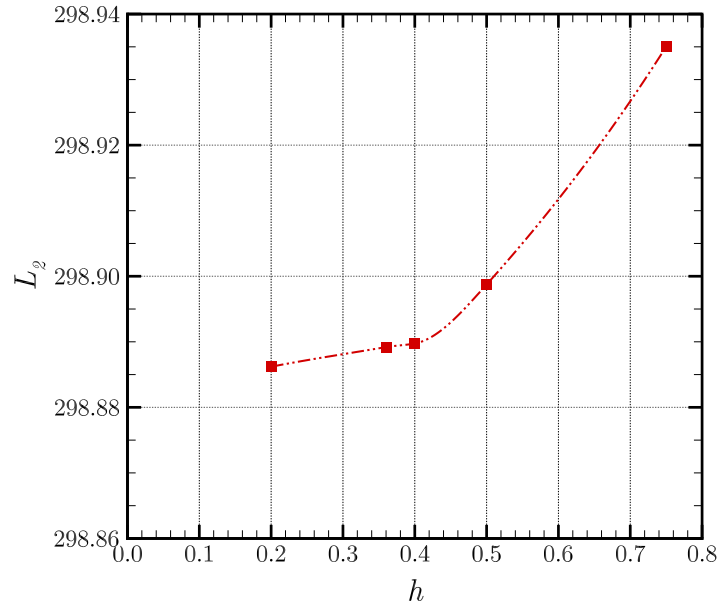


FIGURE 8.7: Results of the h -type refinement study. The L_2 -norm is measured at $t = 0.4$ s for each level of refinement. Note: only the axial length of the elements was changed.

as a function of element length. Error was calculated relative to an estimate of the mesh independent value. This value was calculated using a Richardson-type extrapolation.

As is clearly evident from table 8.4, for the straight pipe case, extra h_z -type refinement in the axial direction has little effect on the accuracy of the simulation. As this study is primarily interested in the effect a moving wall, the smaller cube-shaped elements are maintained in the region of interest (i.e. $h_z = 0.2$). This ensures that the highest level of accuracy is maintained in this region. Outside this region, in the inlet and outlet sections where the flow is less critical to this investigation, the element size in the axial direction is set to $h_z = 0.75$.

8.3.4 Solid domain p -type refinement

In this section, the spatial resolution of the solid domain is analysed. To simplify the meshing process, the solid mesh is created with macro-elements which completely coincide with the exterior fluid elements. In this way the h -type refinement for the solid is fixed. A p -type refinement study was conducted in which the polynomial order was increased from $p = 2$ to $p = 6$.

Each end of the elastic region was fixed in space. The pressure boundary condition

h_z	% error
$0.75d$	0.0255
$0.5d$	0.0133
$0.4d$	0.0103
0.36	0.0101
$0.2d$	0.0091

TABLE 8.4: Percentage error in the L_2 -norm with reference to a theoretical 100% accurate case defined using a Richardson extrapolation. The error decreases as the element length decreases.

described in equation 8.5 was applied to the perianeurysmal interface. As a forcing function, the outlet pressure boundary condition for the fluid was applied to the inner surface of the solid. In flow through an aneurysm unsteady flow structures locally alter the pressure at the fluid-structure interface. However, the change in mean pressure is many orders of magnitude greater than the local variations caused by the unsteady flow. As such, these boundary conditions closely match those encountered by the solid in the fluid-structure interaction. The neo-Hookean wall model was used with a mean Young's-modulus of 0.8 MPa (that of a healthy artery).

The maximum displacement in the lateral direction was monitored as the polynomial order was increased. The maximum lateral displacement occurred at $t = 0.5$ s and at a position exactly half way along the elastic region for all levels of resolution. Figure 8.8 shows the maximum lateral displacement, u_{max} , as a function of increasing polynomial order. The convergence behaviour described for the fluid domain throughout § 8.3.1 is clearly evident here. In fact, for the solid the solution converges to a mesh independent value at a much lower polynomial order, $p = 3$, than the fluid cases.

Table 8.5 shows the percentage error in the solution compared to the most refined case. Here, the most resolved case is assumed to contain no error. These results correlate well with the convergence behaviour shown in figure 8.8. Using a polynomial order of 3 or greater gives a mesh independent solution (error $< 0.02\%$). These results suggest that for a neo-Hookean solid continuum, less elements are required to spatially resolve the system than for similar fluid elements. As the equations governing each are so similar this is likely due to the state parameters, viscosity and Young's modulus.

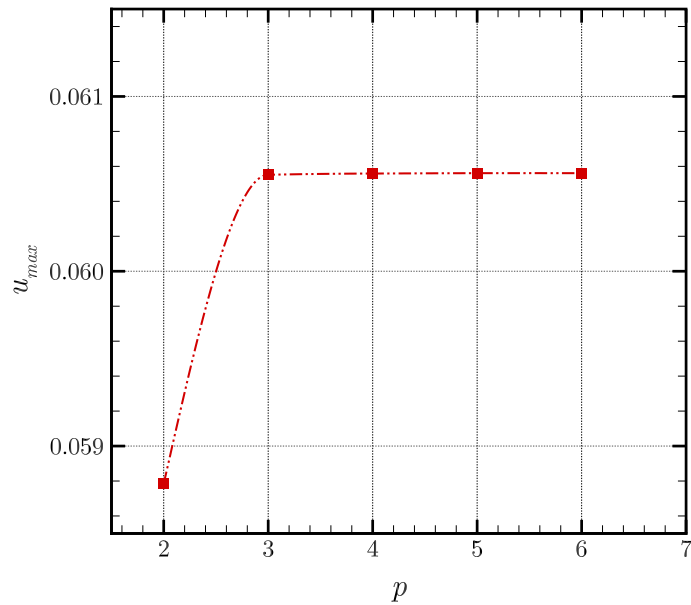


FIGURE 8.8: Results of the p -type refinement study for the solid domain. The maximum lateral displacement, u_{max} , is measured at $t = 0.5$ s for each level of refinement.

p	% error
2	2.9338
3	0.0138
4	0.0027
5	0.0002
6	0.0000

TABLE 8.5: Percentage error in maximum lateral displacement, u_{max} . The error decreases rapidly as the polynomial order is increased.

The Young's modulus in this case is several orders of magnitude larger than viscosity.

While using a polynomial order $p = 3$ provides a sufficiently resolved solution for this investigation, a polynomial order of $p = 5$ is chosen. Using a polynomial order that matches that of the fluid provides an efficient and accurate method for passing information between the fluid and solid meshes. Matching the polynomial order ensures both macro and quadrature nodes are coincident at the fluid-structure interface. As such, vector fields do not require interpolation between the two regions, a direct copy

of information can be passed. This is both highly efficient and more accurate than interpolation. The polynomial order of $p = 5$ is well resolved spatially and will produce a solution with only 0.002% error.

8.3.5 Fluid-solid coupling p -type refinement

In the preceding sections the spatial resolution of both the fluid and solid mesh components were analysed. It was concluded that a polynomial order of $p = 5$ and $p = 3$ for fluid and solid, respectively was required to attain a sufficiently mesh-independent solution. Before proceeding, the spatial resolution is tested once more for a fully coupled fluid-structure interaction solution. This determines whether the use of the arbitrary Lagrangian-Eulerian solver affects the spatial resolution of the mesh.

For this investigation, the full computational domain was solved with physiologically accurate fluid and solid boundary conditions (see chapter 7 and § 8.2). A healthy artery wall was simulated with stiffness of 0.8 MPa. A p -type grid resolution study was conducted in which the polynomial order was increased from $p = 3$ to $p = 6$.

As was anticipated given the results of the preceding sections, figure 8.9 shows the classic convergence behaviour. Figure 8.9(a) and 8.9(b), respectively, show the L_2 -norm and z -velocity component for the fluid region. After an initial variance, each plot begins to converge to a single value. A polynomial order of $p = 5$ initiates the converged section and exhibits a low percentage error. Table 8.6 records the error relative to the most resolved case for each metric. For each fluid measurement the error at $p = 5$ is less than 0.1%, which is well within the desired level of accuracy for the simulations. This correlates well with the p -type study conducted in § 8.3.1 in which the polynomial that delivered the desired level of accuracy for a fluid solve alone was $p = 5$.

Similarly, for the solid, figure 8.9(c) shows the variation in maximum radial displacement, u_{max} , as a function of polynomial order. Just as the fluid components correlated well with previous results, the solid solver too exhibits an analogous convergence behaviour. Again convergence is reached at a polynomial order of $p = 4$. Table 8.6 shows that the error associated with the solid region is less substantial than the fluid at $p = 4$ the error is merely 0.0027%.

This fluid-structure interaction spatial resolution study confirms the findings of § 8.3.1. For both fluids and solids the solution reaches a mesh independent state at a polynomial order of $p = 5$. This mesh and this level of resolution can now be used with

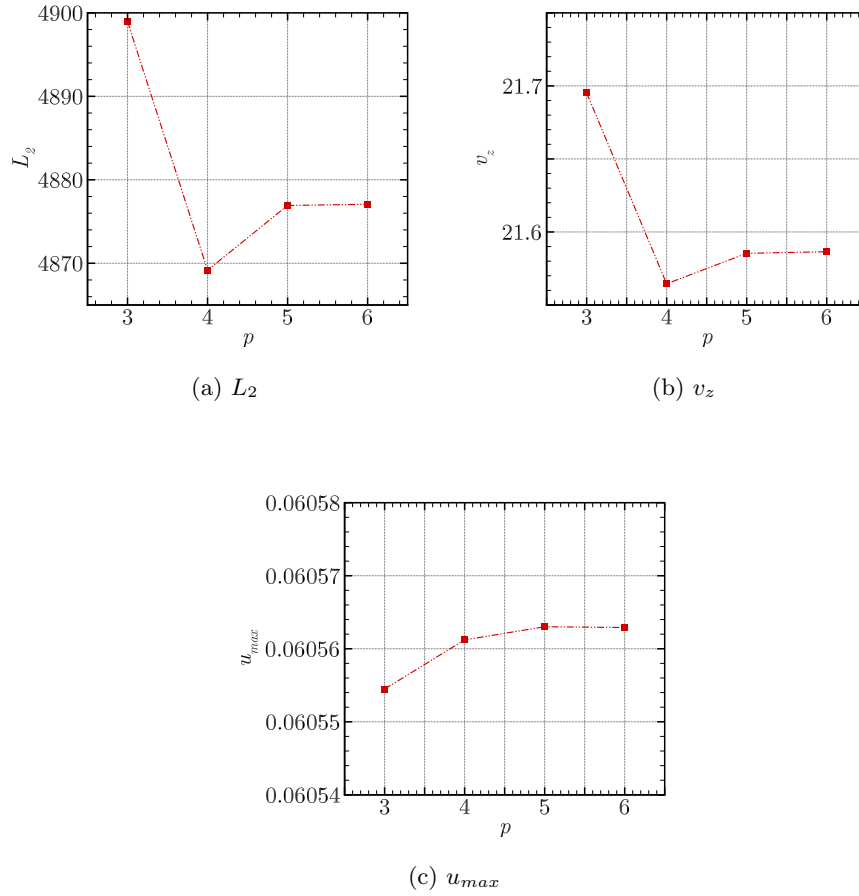


FIGURE 8.9: Results of the spatial resolution study using the fully coupled FSI algorithm. In each plot the polynomial order was used to change the spatial resolution of the mesh. (a) shows the L_2 -norm of the fluid domain, measured at $t = 0.4$ s at the time of peak velocity inlet. (b) shows the maximum fluid velocity along the centreline at $t = 0.4$ s. (c) shows the peak displacement of the wall at $t = 0.5$ s.

confidence in the proceeding aneurysm initiation study.

8.4 Temporal resolution

The continuum mechanics governing equations describe both spatial and temporal changes. In § 8.3 the appropriate spatial resolution of the computational mesh was determined to ensure a mesh independent solution was being produced. It is just as important to ensure that a sufficiently small time step is being used to capture the physics of the system. Depending on the flow properties different structures can develop over different time scales. If a large time step is used, there may not be sufficient

% error			
p	L_2	v_z	u_{max}
3	0.4487	0.5036	0.0139
4	0.1619	0.1016	0.0027
5	0.0028	0.0051	0.0001
6	0.0000	0.0000	0.0000

TABLE 8.6: Percentage error in fluid parameters L_2 -norm and axial velocity component v_z and as well as the solid domain parameter u_{max} relative to the most resolved case.

temporal resolution to simulate the formation of these structures thus introducing error into the simulation. The following investigation determines the appropriate time step required to resolve the flow in a distensible aneurysm and determine how many boundary condition cycles are necessary to capture the asymptotic fluid-structure response.

8.4.1 Time step

Firstly the temporal resolution is assessed and the appropriate time step is selected that captures the physics of the aneurysm problem. As an Eulerian reference frame is used for the fluid domain, large time steps may cause the solution to diverge as fluid moves fast enough to pass through an entire element within a time step. This alludes to a Courant stability condition. Courant stability conditions relate the stability to a quantity such as

$$\varsigma_f = \frac{1}{Re} \frac{\Delta x}{\Delta t} < 1, \quad (8.9)$$

for the fluid and

$$\varsigma_s = E \frac{\Delta x}{\Delta t^2} < 1, \quad (8.10)$$

for the solid, where ς is the Courant condition, E is the Young's modulus of the solid, Re is the Reynolds number, Δx is the characteristic element length and Δt is the time step. Given the restrictions on spatial resolution applied by the grid resolution study, this investigation seeks to determine the largest possible time step that allows an accurate and stable solution.

A number of time steps were tested ranging from 0.0001 s, to 0.05 s. As with the spatial resolution study, the L_2 -norm and v_z (component of the velocity in the z -

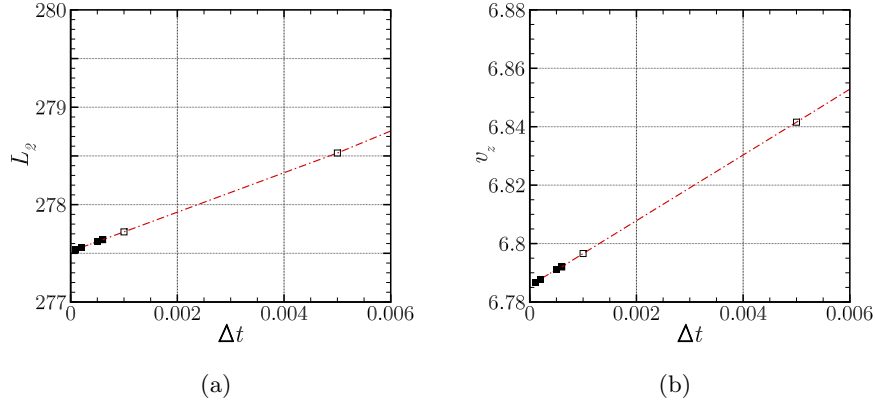


FIGURE 8.10: Results of the time step independence study are presented. Closed symbols (■) represent simulations that run in a stable fashion, open symbols (□) represent simulations that diverge later in the simulation. (a) shows the change in L_2 -norm and (b) shows the change in the velocity component in the z -direction at the centre of the aneurysm bulge. All measurements were conducted at $t = 0.05$ s.

direction) were used to assess the global and local error in the solution. The z -velocity component was measured at the centre of the aneurysm bulge. Measurements were taken at $t = 0.05$ s, and while some simulations ultimately diverged, all were capable of integrating to this point in time. Figure 8.10 shows the results of the time step independence study. As the time step is reduced the solution converges to a particular value. The closed symbols on each sub-plot represents simulations that are stable, while open symbols represent those that diverge.

Table 8.7 shows the percentage error for each time step. The error is measured relative to a theoretical fully resolved value at $\Delta t = 0$, calculated using a Richardson extrapolation. These results show that once a time step small enough to satisfy the stability criterion is used, the effect the time step has on the results is small. In order to reduce the computational cost of each simulation the largest stable time step $\Delta t = 0.0006$ s is chosen for all further investigations. At this time step the error is only 0.026% in L_2 -norm and 0.096% in v_z .

8.4.2 Time period

Finally, a small study was conducted to determine if the fluid-solid coupling caused any interactions to occur on a longer time scale than the boundary condition period. A

% error		
Δt	L_2	v_z
0.05	1.482	3.548
0.01	0.754	1.659
0.005	0.347	0.826
0.001	0.055	0.163
0.0006	0.026	0.096
0.0005	0.019	0.082
0.0002	0.002	0.034
0.0001	0.009	0.018

TABLE 8.7: Percentage error in the L_2 -norm and z velocity component v_z relative to a theoretical resolved value (calculated using a Richardson type extrapolation). Time steps below the double horizontal line are stable, those above diverge.

fully coupled fluid-structure interaction simulation was conducted for a healthy aorta. The boundary conditions and geometry described in § 8.2 were used with a stiffness of 0.8 Mpa for the artery wall and a time-averaged Reynolds number of 410 for the fluid.

Figure 8.11 shows the results of the time period analysis. Two parameters were monitored throughout the time period, the L_2 -norm (in sub-plots 8.11(a) and 8.11(b)) and v_z the z -component of velocity (in sub-plots 8.11(c) and 8.11(d)). These plots indicate that the first time period produces very different results to subsequent cycles. This is caused by transient conditions in the pipe created by the initial imposition of a Poiseuille velocity profile throughout. It takes nearly the entire first period to flush this initial condition from the computational domain. Subsequent cycles exhibit very small deviation from the asymptotic solution state.

Figures 8.11(b) and 8.11(d) plot the percentage error in each parameter compared to the asymptotic periodic solution. The periodic solution was calculated by averaging the last three time periods of the time saturated simulation. Data is plotted with respect to a scaled time

$$t^* = t - (n - 1)T, \quad (8.11)$$

where t is the physical time, T is the boundary condition period (in this case $T = 1$ s) and n indicates the n^{th} period. Plotting relative to the scaled time t^* allows each time

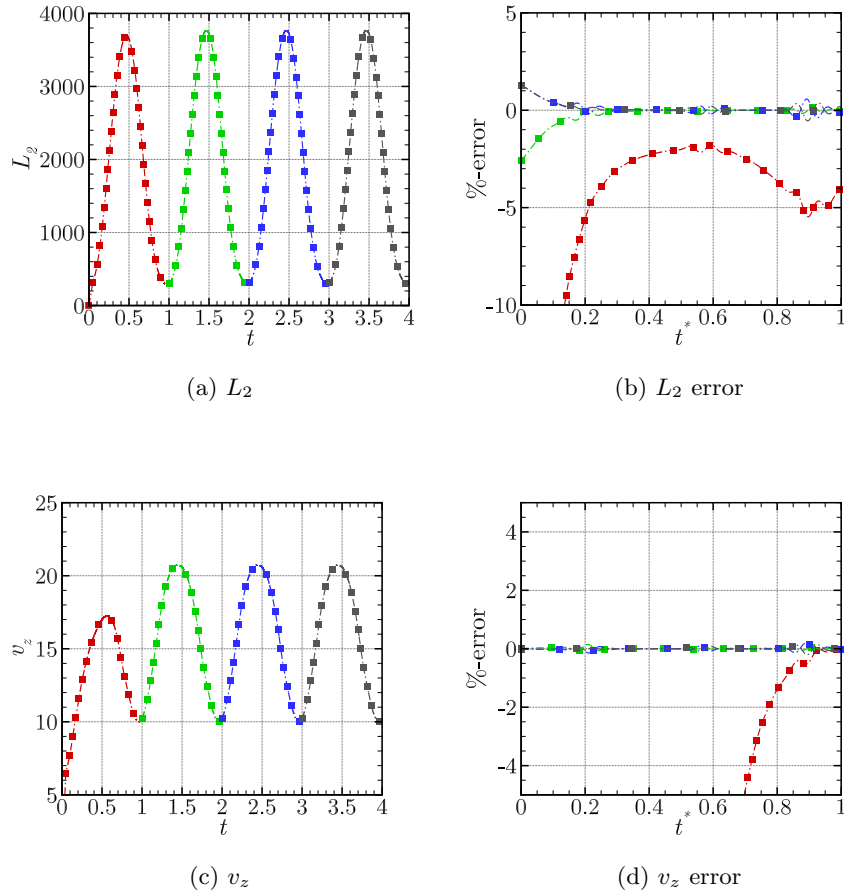


FIGURE 8.11: Results of the time period study. In each sub-plot red, green, blue and grey lines and symbols represent the first, second, third and fourth boundary condition time periods respectively. (a) shows the time evolution of the L_2 -norm, a global measure of energy in the solution. (b) shows the percentage error in L_2 -norm relative to the time saturated value. (c) shows the time history of v_z velocity component at a point along the centre line of the pipe. (d) shows the percentage error in v_z relative to the time saturated value. In each case the error in the latter periods is minimal.

period to be compared with ease. The first time period exhibits errors in excess of 20%, while subsequent cycles are subject to less than 1% error.

From this study two conclusions can be drawn. Firstly, there are no long-timescale phenomena observed in the FSI in a straight pipe. Measurement of the L_2 -norm and v_z showed no discernible variation as more time periods were simulated. Secondly, the initial conditions in the pipe are inaccurate and take a full cycle to be flushed from the computational domain. This was observed in the large error in the L_2 -norm and v_z for the first period when compared to the time-averaged data (see figure 8.11).

As a result of this investigation, simulations will be evolved for 4 inlet waveform cycles to eliminate transient startup errors from the reported results. This is sufficiently long to remove the errors associated with the initial conditions and to capture all interactions in the system.

8.5 Results

Having determined the spatial and temporal accuracy of the mesh, the effect of local variations in wall stiffness is investigated. First § 8.5.1 describes the flow through a pipe with rigid-walls. Section 8.5.2 discusses the effect of a moving wall boundary condition compared to a rigid-wall. Section 8.5.3 describes how a local variation in the wall stiffness can effect the flow dynamics in the aneurysm both globally and locally. In order to assess the impact on the potential initiation of an aneurysm the wall shear stress is studied in the context of varying stiffness.

8.5.1 Flow in a rigid pipe

Before discussing the flow characteristics in an abdominal aorta in the context of aneurysm initiation, the flow in a healthy artery with a rigid-wall is characterised. This case will form the reference case for the aneurysm initiation study; it epitomises the majority of the work currently conducted in this field (Salsac *et al.* 2006; Lasheras 2007) and serves as a point of comparison for quantifying the affect a dynamic wall has on the haemodynamics. The aorta was idealized using the dimensions and boundary conditions described in chapter 7. Briefly, this corresponds to an aorta of diameter 20 mm, with a time varying velocity inlet and pressure outlet boundary conditions, similar to those experienced in a subject at rest. The input flow conditions correspond to a peak Reynolds number of $Re_{peak} = 750$, a time-averaged Reynolds number of $Re_{mean} = 410$ and a Womersley number of 9.7.

The velocity profile of the flow in a straight pipe is determined by the relative strength of transient inertial effects to the viscous forces (see the discussion in § 1.6.1). The Womersley number is a non-dimensionalised parameter which describes the balance of these forces. At high Womersley numbers such as those involved in arterial flow, the velocity profile forms a top-hat profile, in which the flow is characterised by transient changes in the flow occurring in the near-wall region first with bulk movement of the flow slow to follow.

The input waveform of the flow rate, is replotted in figure 8.12(a). The time evolution of the velocity field was measured in the centre of the refined region in the axial plane. Figure 8.12(b) shows, at a few instants of time, the profiles of the axial velocity component v_z . During the systolic acceleration phase, $t^* = 0.0 - 0.5$, the peak velocity increases. The flow develops the characteristic top-hat profile (or flattened Poiseuille profile) of the Womersley solution. When the Womersley number is small ($\alpha \sim 1$), viscous forces dominate and the velocity profiles are parabolic in shape. However, for a Womersley number of $\alpha = 9.7$, which is the case in the abdominal aorta, the unsteady inertial forces dominate, and the flow approaches a top-hat profile with thin boundary layers. At peak systole, the thickness of the boundary layer scales as

$$\delta_t \propto \frac{d}{\alpha}, \quad (8.12)$$

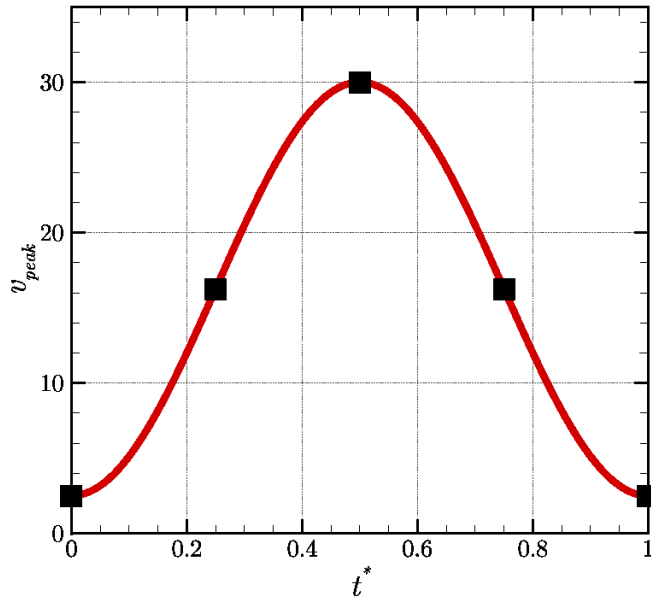
where δ_t is the transient boundary layer thickness (Fung 1997).

The effect of the dominant inertial forces is highlighted in comparing the profile at $t^* = 0.25$ and $t^* = 0.75$. At these two times the flow rate through the pipe is identical, however a distinct difference in the velocity profile is evident. During the acceleration phase ($t^* = 0.25$) the centreline velocity is lower and the velocity in the boundary layer is greater compared to the velocity profile in the decelerating phase ($t^* = 0.75$). This demonstrates that the change in flow in the boundary layer leads the change in the flow of the overall profile.

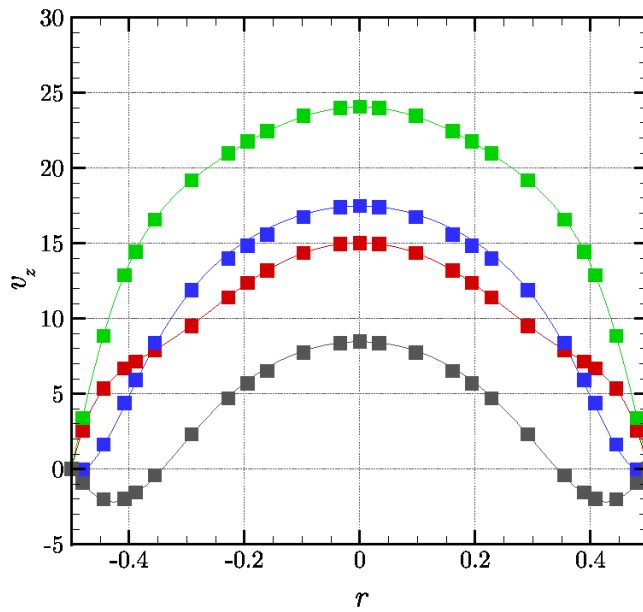
After the peak systole, the flow decelerates first along the walls. Despite the bulk fluid motion remaining in the forward direction, the flow along the wall reverses (see $t^* = 1.0$). For the time varying velocity profile used in this study, the bulk flow never reverses as the area-averaged flow rate is always positive. Having completed the deceleration phase the flow sets forward again with the increase in forward momentum first being observed in the boundary layer. Interestingly, despite the development of an inflectional velocity profile during diastole, the flow remains entirely laminar throughout the entire cardiac cycle. Salsac *et al.* (2006) state that a transition to turbulence does not occur at these high values of Womersley number because the characteristic time for the growth of the instability is much longer than the period of the pulsatility.

8.5.1.1 Analytical solution

As a first approximation, the healthy abdominal aorta can be modelled as an infinitely long straight pipe. The flow of a viscous fluid in an infinite tube under a periodic



(a)



(b)

FIGURE 8.12: (a) peak flow velocity (v_z) waveform at the inlet. (b) velocity profiles measured across the healthy abdominal aorta with a rigid-wall at various times throughout a single cardiac cycle. Velocity profiles were taken at the non-dimensionalised times indicated in (a); red, green, blue and grey represent the velocity profiles at the non-dimensionalised times $t^* = 0.25, 0.5, 0.75,$ and 1.0 , respectively. Comparison is made between the simulated data (single points) and the velocity profiles calculated with the Womersley solution (solid lines).

pressure gradient was first mathematically described by Womersley (1955). Helps & McDonald (1954) and Womersley (1955) calculated analytical solutions for the arterial pulsating flow. They started by expressing the time-varying pressure gradient as a Fourier series of sinusoidal modes. The axial velocity component $v_z(r, t)$ can be related to the time varying pressure gradient by

$$v_z(r^*, t^*) = \frac{ReG_0^*}{4} (1 - r^{*2}) + \frac{Re}{i} \sum_{n=1}^{\infty} \frac{G_n^*}{\alpha_n^2} \left(1 - \frac{J_0(r^* i^{3/2} \alpha_n)}{J_0(i^{3/2} \alpha_n)} \right) e^{int^*}, \quad (8.13)$$

where the length r has been non-dimensionalised by the radius $\frac{d}{2}$ giving the non-dimensionalised radius r^* and the time is normalised by the pulsation frequency ω to t^* . $i = \sqrt{-1}$ is the imaginary number, J_0 is the Bessel function of the first kind of order 0, G_n^* are the Fourier coefficients of the pressure gradient which have been normalised by the radius r and time t , and

$$\alpha_n = \frac{d}{2} \sqrt{\frac{n\omega}{\nu}}, \quad (8.14)$$

is the dimensionless Womersley number associated with the n^{th} harmonic of the Fourier series expansion of the time varying pressure gradient.

An analogous expression can be derived relating the velocity profile to an area-averaged inlet velocity by taking the surface integral of equation 8.13 and dividing by the area,

$$\bar{v}(t) = \frac{\int_0^{2\pi} \int_0^R v_z(r) r dr d\theta}{\pi R^2}. \quad (8.15)$$

Given an area average flow is to be imposed of the form

$$\bar{v} = A_n \cos(\omega_n t) + B_n \sin(\omega_n t) \quad (8.16)$$

where A_n and B_n are the Fourier coefficients of the n^{th} mode. The velocity profile is described by

$$v_z(r, t) = (c_r J_r^0(r) - c_i J_i^0(r)) \cos(\omega t) - (c_i J_r^0(r) + c_r J_i^0(r)) \sin(\omega t), \quad (8.17)$$

where

$$\begin{aligned}
c_r &= \frac{A_n J_r - B_n J_i}{J_r^2 + J_i^2} \\
c_i &= \frac{-A_n J_i - B_n J_r}{J_r^2 + J_i^2} \\
J_r &= \text{Real} \left\{ 1 + \frac{2i^{1/2} J_1 \left(i^{3/2} \alpha \right)}{\alpha J_0 \left(i^{3/2} \alpha \right)} \right\} \\
J_i &= \text{Imag} \left\{ 1 + \frac{2i^{1/2} J_1 \left(i^{3/2} \alpha \right)}{\alpha J_0 \left(i^{3/2} \alpha \right)} \right\} \\
J_r^0 &= \text{Real} \left\{ 1 - \frac{J_1 \left(i^{3/2} \alpha \frac{r}{R} \right)}{J_0 \left(i^{3/2} \alpha \right)} \right\} \\
J_i^0 &= \text{Imag} \left\{ 1 - \frac{J_1 \left(i^{3/2} \alpha \frac{r}{R} \right)}{J_0 \left(i^{3/2} \alpha \right)} \right\}
\end{aligned} \tag{8.18}$$

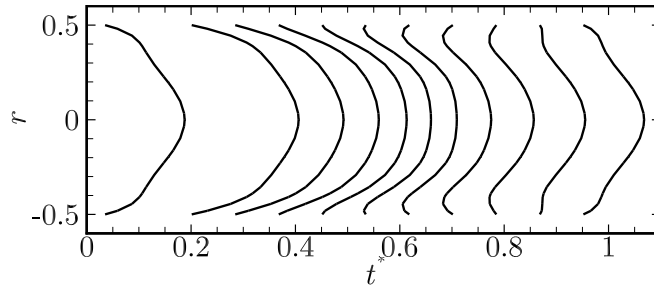
and J_ν is the complex Bessel function of the first kind of order ν . This solution was developed by Professor Spencer Sherwin and provided via private correspondence.

Figure 8.12(b) compares the simulated velocity profile in the rigid pipe to those calculated using the Womersley solution. Excellent agreement is observed with the simulated velocity profile (data points in figure 8.12(b)) falling within 0.4% of the Womersley solution (lines in figure 8.12(b)). The Womersley solution predicts an inflectional flow profile which remains laminar as a result of the unsteadiness of the flow preventing the instability from developing. This supports the lack of turbulence observed in the rigid artery model. The small difference in the theoretical and simulated velocity profiles are within the spatial uncertainty of the mesh.

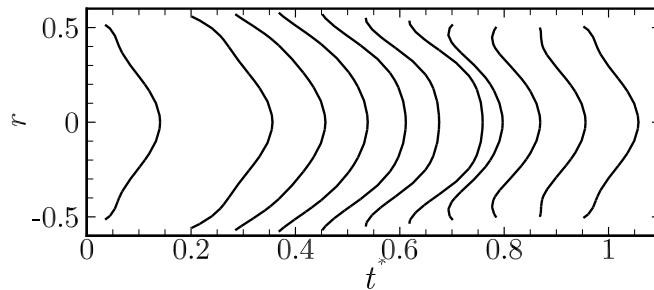
8.5.2 Flow in a healthy artery

Of principal interest to this investigation is how the motion of the wall affects the flow in a straight pipe. As such, figure 8.13 compares the axial velocity profile in a rigid pipe to the flow in a healthy artery with uniformly flexible walls. Figure 8.13(a) shows the time evolution of the axial velocity component (v_z) for a rigid pipe in the y - z plane. The flow reversal predicted by the Womersley profile is observed in the non-dimensionalised time period $t^* = 0.55 - 0.85$. As discussed in § 8.5.1 this is indicative of a Womersley profile in which the transient inertial forces first affect the near-wall region prior to being evident in the bulk flow; i.e. the greatest change is found in the boundary layer.

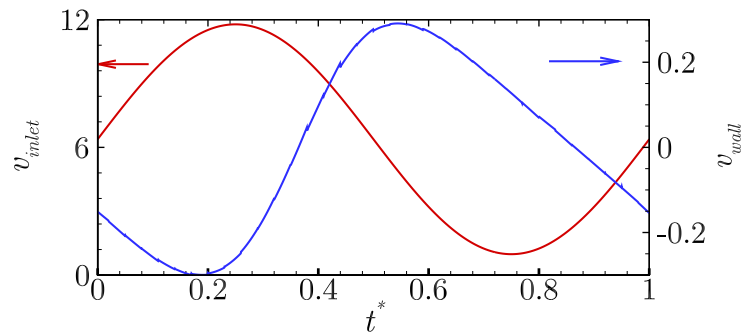
Figure 8.13(b) shows an identical plot for the case where the walls are elastic with a



(a)



(b)



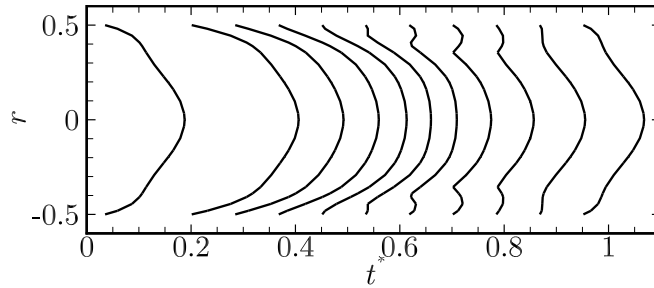
(c)

FIGURE 8.13: Visualisation of the time evolution of axial velocity field v_z in a straight pipe in the y - z plane. (a) shows the rigid-walled case, and (b) shows the case of a elastic-walled pipe with uniform stiffness $E = 0.8$ MPa. (c) shows both the velocity inlet condition and the wall velocity as a function of non-dimensionalised time. Note: for the case of the wall velocity, an expanding wall corresponds to a negative velocity.

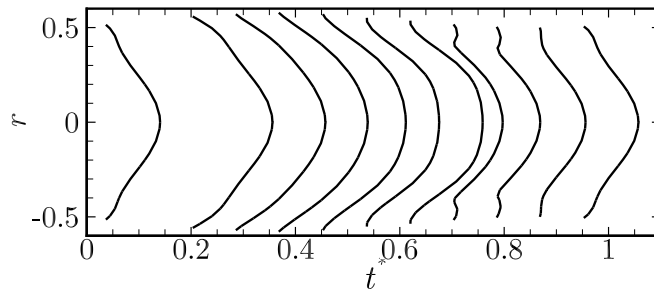
stiffness of 0.8 MPa (that of a healthy artery). In comparison to the rigid-wall case, the period of reversed flow is reduced by the elastic-wall from 0.3 s to 0.2 s. Furthermore, the onset of the reversed flow is delayed from $t^* = 0.55$ s to $t^* = 0.75$ s. The added inertia of the wall modifies the effective Womersley number of the vessel. This occurs in two forms; firstly the diameter of the vessel increases, and secondly the motion of the wall introduces extra transient inertia into the elastic region. In determining the new velocity profile with the distended and moving wall, the modified Womersley number must be considered. An analytical solution is described later in § 8.5.5.1. In this section, the change in effective Womersley number is related to a change in the transient boundary layer thickness which in turn changes the velocity profile.

The motion of the wall has a dramatic effect on the flow. The additional inertia acts in the wall-normal direction, perpendicular to the bulk motion of the fluid. Figure 8.13(c) shows the velocity inlet boundary condition and velocity of the wall, respectively. The motion of the artery wall is driven by the time-varying pressure boundary condition which is 0.1 s out of phase with the inlet velocity. The pressure-velocity phase lag may contribute to the delayed onset of the flow reversal in the elastic-walled case. When the bulk fluid motion driven by the inlet velocity boundary condition is starting to reverse, the phase lag causes the wall to continue to constrict. The changing vessel volume contributes momentum to the flow in the downstream direction in order to conserve mass (for an analytical argument of this point the reader is directed to the Reynolds transport theorem analysis conducted in § 8.5.5.1). The extra velocity introduced by this process reduces the onset and duration of the reversed flow.

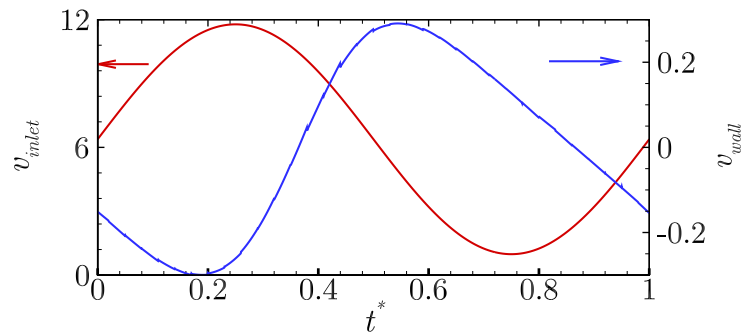
Also evident in figure 8.13(b) is a reduction in the magnitude of v_z at the peak systolic time $t^* = 0.2$ s compared to the rigid case in figure 8.13(a). This may be anticipated as the increased vessel diameter drives a reduction in the velocity magnitude in order to conserve mass. However, the area-averaged flow rate (figure 8.15) for each case shows a reduced peak flow rate suggesting this is not the sole contributing factor. Another hypothesis is that the velocity of the wall introduces components of velocity in the non-axial direction. In order to validate this hypothesis the velocity magnitude was plotted for the rigid pipe in figure 8.14(a) and for the elastic-walled case in figure 8.14(b). The relative difference in the velocity magnitudes (in figure 8.14) is less than the difference between velocity profiles (in figure 8.13), this indicates that a small amount of velocity in the radial direction is introduced by the velocity of the wall.



(a)



(b)



(c)

FIGURE 8.14: Visualisation of the time evolution of velocity magnitude in a straight pipe in the y - z plane. (a) shows the rigid-walled case, and (b) shows the case of a elastic-walled pipe with uniform stiffness $E = 0.8$ MPa. (c) shows both the velocity inlet condition and the wall velocity as a function of non-dimensionalised time. Note: for the case of the wall velocity, an expanding wall corresponds to a negative velocity.

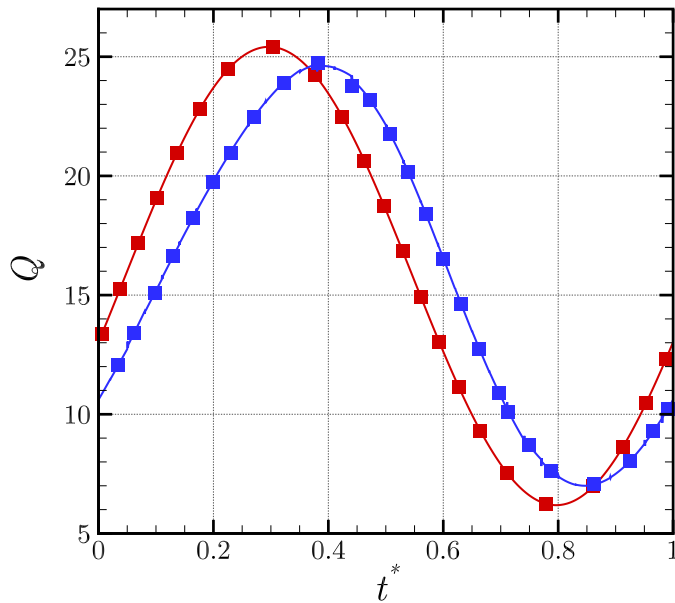


FIGURE 8.15: Flow rate through outlet boundary in a rigid pipe (red) and elastic artery (blue).

It is clear that the motion of the wall causes a reduction in both the peak axial velocity component and the peak velocity magnitude. Figure 8.15 shows the time evolution of the flow rate through the outlet of both the rigid and elastic pipe cases. A reduction in the peak flow rate (at peak systole) is observed in the elastic case, this is matched by an increase in the peak diastole flow rate. The result of this is to maintain the mean flow rate across the entire cardiac cycle regardless of the elasticity of the walls. Note: the phase difference between the flow rates for the rigid case and elastic case matches the phase difference between the pressure and velocity boundary conditions.

8.5.3 Flow dynamics with localised stiffness variations

To assess the impact of heterogeneous stiffness properties, the stiffness of a thin band of material was altered (see figure 8.1(a)). Figure 8.16 shows the variation in the axial component of velocity v_z throughout the cardiac cycle. The black lines represent the case of flow in a rigid pipe, while coloured lines and symbols show the case of flow through an elastic artery. The most prominent feature of figure 8.16 is the difference in peak velocity in the rigid pipe cases compared to the elastic pipe cases. During the

systolic acceleration phase the rigid-wall cases have a higher peak velocity than the elastic cases. This trend is reversed during the diastolic deceleration phase in which the peak velocity of the elastic cases is greater than the rigid pipe case. As discussed in § 8.5.2 this is due to flow being directed in the wall-normal direction as the wall moves. During the systolic phase this motion is acting to subtract flow from the axial direction and during the diastolic phase it is acting to add flow. Figure 8.16(f) shows the velocity profile at a time when the wall motion is zero. At this snapshot in time there is negligible difference between the velocity profile predicted with a rigid or elastic wall.

Figure 8.16 also shows how the locally varied wall stiffness affects the axial velocity component of the flow. As the section of wall is stiffened, the peak velocity trends towards the rigid-wall case (this is shown in more detail in figure 8.18). This trend is expected since as the stiffness of the entire artery wall is increased to infinity the rigid-wall solution is approached. For the elastic-walled cases simulated here, the wall predominantly has the stiffness of a healthy artery with a localised band of material with altered stiffness. As such, changes in stiffness have a less significant effect (i.e. the material maintains a stiffness of 0.8 MPa along much of its length, with only a small stiffness fluctuation in the small banded region). Figure 8.17 shows the relationship between the peak axial velocity at $t^* = 0.37$ as a function of wall stiffness. A nearly linear relationship between the peak velocity and the inverse stiffness is observed at this snapshot of the cardiac cycle (similar linear trends of varying gradient are observed at different times). The relationship is not perfectly linear due to the neo-Hookean material model used for the wall. If a Hookean model were used a linear relationship governs the wall displacement (or strain) in response to the force applied (stress),

$$\varepsilon = \frac{\sigma}{E}. \quad (8.19)$$

If it is assumed that the wall motion is linearly proportional to any change in the flow dynamics; a linear relationship between the peak axial velocity and the inverse stiffness can be expected. Figure 8.17 indicates that as the thin band of material is stiffened the impact it has on the flow is diminished. In fact any change in stiffness beyond 6.0 MPa ($7.5 \times E_{healthy}$) will change the flow by less than 0.08% based on a Richardson extrapolation of the results. Conversely, reductions in stiffness will have a profound impact on the peak flow rate.

Variation in the stiffness has both a global and local effect on the wall motion.

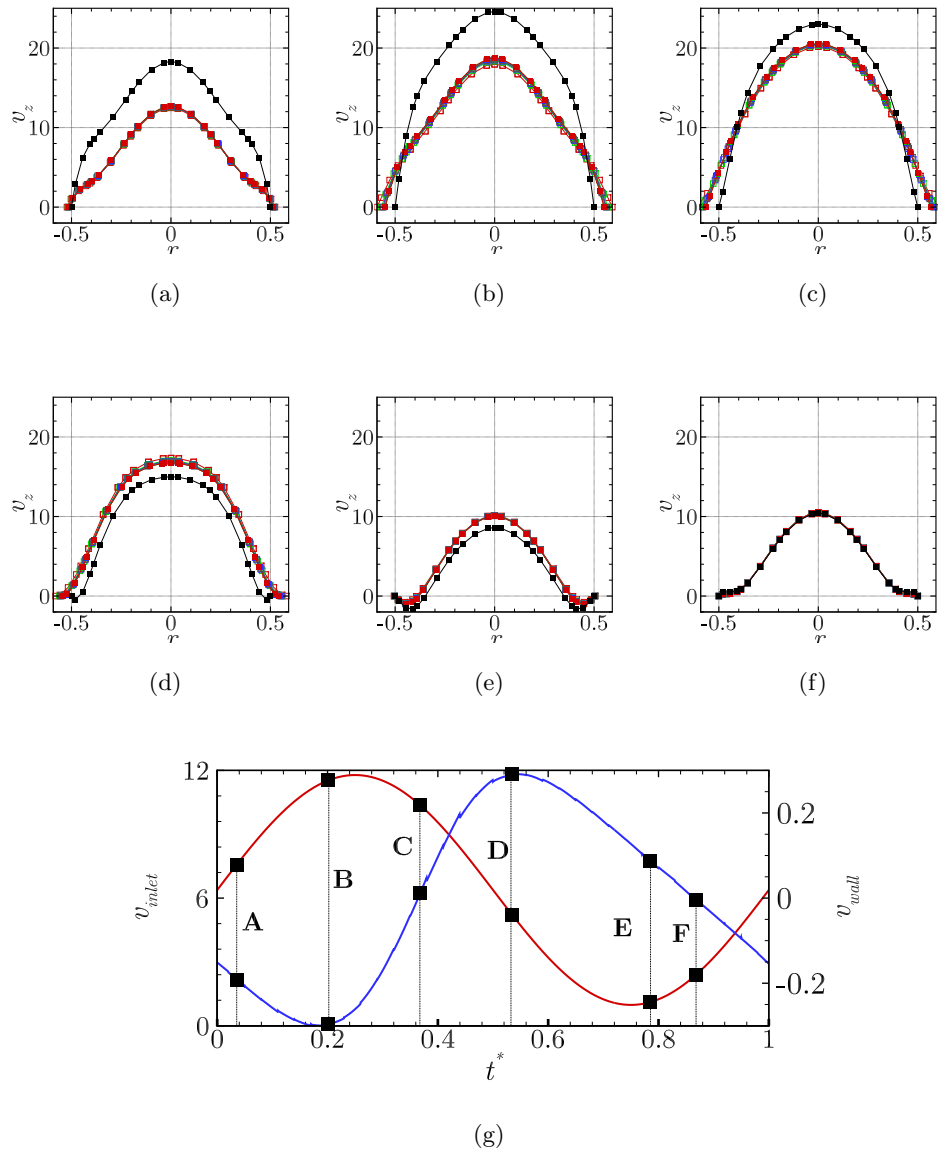


FIGURE 8.16: Plots of axial velocity in the y - z plane in the centre of the stiffened band ($z = 12$), velocity is normalised using the period of oscillation and diameter of the vessel. Subplots (a)-(f) show the axial velocity component for various wall stiffnesses at times A-F shown in (g). In each plot filled black squares (■), filled red squares (■), filled green squares (■), filled blue squares (■), open grey squares (□), open blue squares (□), open green squares (□), and open red squares (□) represent the cases of a fully **rigid pipe**, the region with **6 MPa**, **4 MPa**, **2 MPa**, 0.8 MPa (healthy-uniform), **0.6 MPa**, **0.4 MPa**, and **0.2 MPa**, respectively. (g) shows the velocity inlet (red) and wall velocity (blue) a negative wall velocity indicates the volume is expanding.

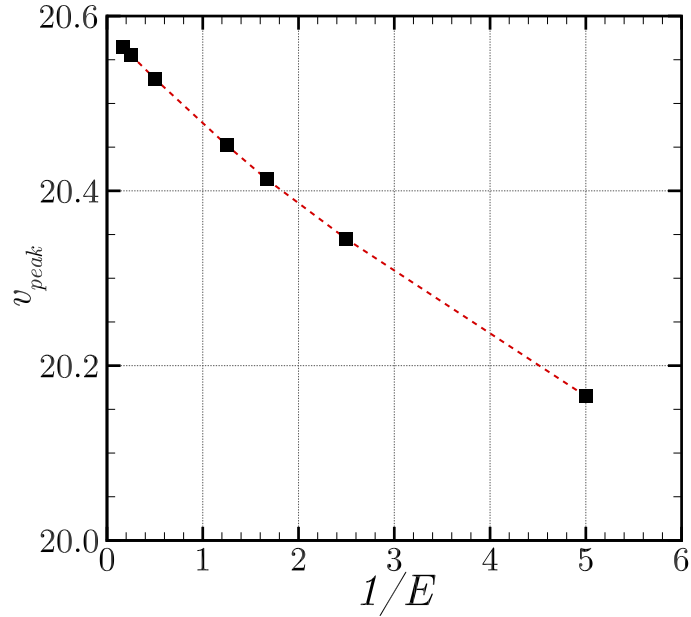


FIGURE 8.17: The peak axial velocity at non-dimensionalised time $t^* = 0.37$ plotted as a function of $\frac{1}{E}$.

Globally, if the stiffness is reduced it acts to increase the total dilation of the wall as the less stiff region can stretch more. Conversely, an increase in stiffness will cause a global reduction in the resulting dilation. Locally, there is a slight variation in the expansion shape. Figure 8.19 shows the local change in wall profile as a result of varying the stiffness. A stiffer band causes a localised constriction of the artery akin to a mini stenotic geometry while the less stiff geometry causes a localised dilation of the geometry above that of the normal wall motion. Figure 8.19 also shows the change in global dilation as a result of the varying stiffness. Note that an increase in the wall displacement corresponds to a greater wall-normal velocity: detail of this are shown in figure 8.20. In terms of the size of the impact that a change in local stiffness has on the flow, the results shown in figures 8.17 and 8.18 indicate that an increase in stiffness above 0.8 MPa has a less significant effect than a local weakening of the wall of the same order of magnitude. This is a result of the inverse relationship between stiffness and wall motion (for a given stress, see equation 8.19). Increases in stiffness form the asymptotic region of this relation, while decreases in stiffness move away from the asymptote where relative changes in wall motion resulting from changes in stiffness

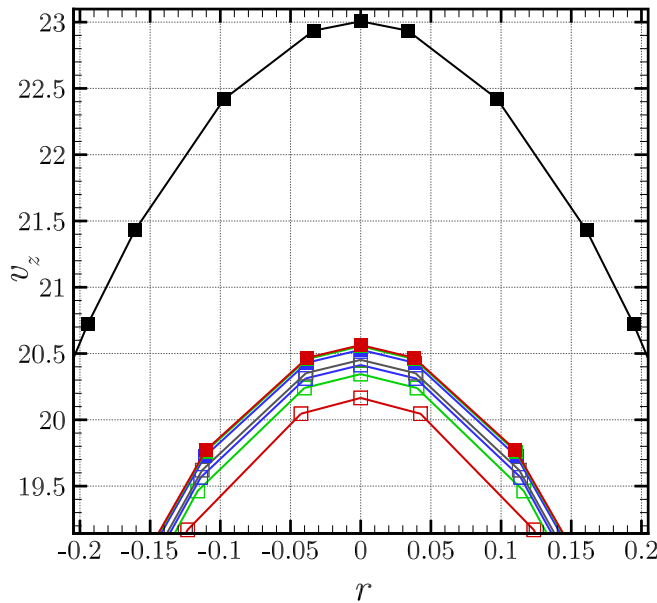


FIGURE 8.18: Axial velocity in the y - z plane in the centre of the stiffened band ($z = 12$) at $t^* = 0.3868$, velocity is normalised using the period of oscillation and diameter of the vessel. Filled black squares (■), filled red squares (■), filled green squares (■), filled blue squares (■), open grey squares (□), open blue squares (□), open green squares (□) and open red squares (□) represent the cases of a fully **rigid pipe**, the region with **6 MPa**, **4 MPa**, **2 MPa**, **0.8 MPa** (healthy-uniform), **0.6 MPa**, **0.4 MPa** and **0.2 MPa**, respectively with the rest of the wall being an elastic 0.8 MPa.

are greater.

The results presented in figure 8.16 describe the effects of wall dilation on the bulk flow. However, local variations in the flow resulting from the local variation in wall motion are not well represented. This is because the local change in wall profile arising from the local change in stiffness is small relative to the length of the artery. The small length scale of the localised variation in stiffness leads to a minimal change in the bulk flow. The change in surface profile has a greater effect in the boundary layer. Figure 8.20 shows the variation in the wall-normal component of velocity, v_y , at the centre of the localised stiffness region throughout the cardiac cycle.

Figure 8.20 shows the elastic case, which varies significantly in comparison to the inelastic case. This is particularly evident at the wall boundary where for an inelastic-wall the no-slip boundary condition forces the velocity to be zero while the elastic boundary is free to move. The motion of the elastic-wall causes a non-zero velocity

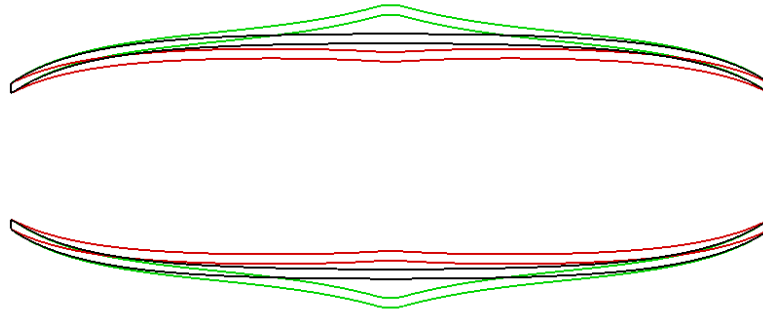


FIGURE 8.19: Wall displacement, exaggerated by a factor of 5 for visualisation. Black lines show the case of a uniform healthy artery stiffness of 0.8 MPa, red lines represent the case of 0.8 MPa with a 6.0 MPa central band, and green lines represent the case of 0.8 MPa with a 0.2 MPa central band.

in the boundary layer. The effect of the local change in wall stiffness is evident when looking at the wall-normal velocity component in the stiffened region. As the local stiffness increases, the magnitude of the peak wall-normal velocity also increases. As with the axial velocity component (v_z), as the wall is stiffened it approaches the rigid-wall solution: this is true of all but time $t^* = 0.8684$ in figure 8.20(f). At this time the trend reverses due to the phase lag between the wall motion and the inflow velocity. The phase lag is also responsible for the difference in the v_y velocity profile between the elastic cases and the rigid case at time $t^* = 0.5348$ in figure 8.20(c). Note that this occurs at both times when the magnitude of the wall-normal velocity is a minimum.

To emphasize the local nature of the effect on the flow, figure 8.21 shows the wall-normal velocity v_y at a location 1 diameter downstream of the altered stiffness region. When comparing figure 8.21 to figure 8.20 it is immediately apparent from the partial collapse in the data that the difference between the less stiff (0.2 MPa) and stiffened (6 MPa) elastic cases is much less significant downstream. The variation of the velocity with stiffness alteration is on a scale closer to that observed for the axial wall component in figure 8.16, which demonstrated the global effect of a local alteration in wall stiffness.

To finalise this discussion on the effect that local stiffness has on local flow dynamics, figure 8.22 shows the vorticity in the vicinity of the region of varying stiffness. The small variation in wall profile in this region changes the vorticity distribution along the wall. For the case when the material is stiffened, figure 8.22(e) shows that the local

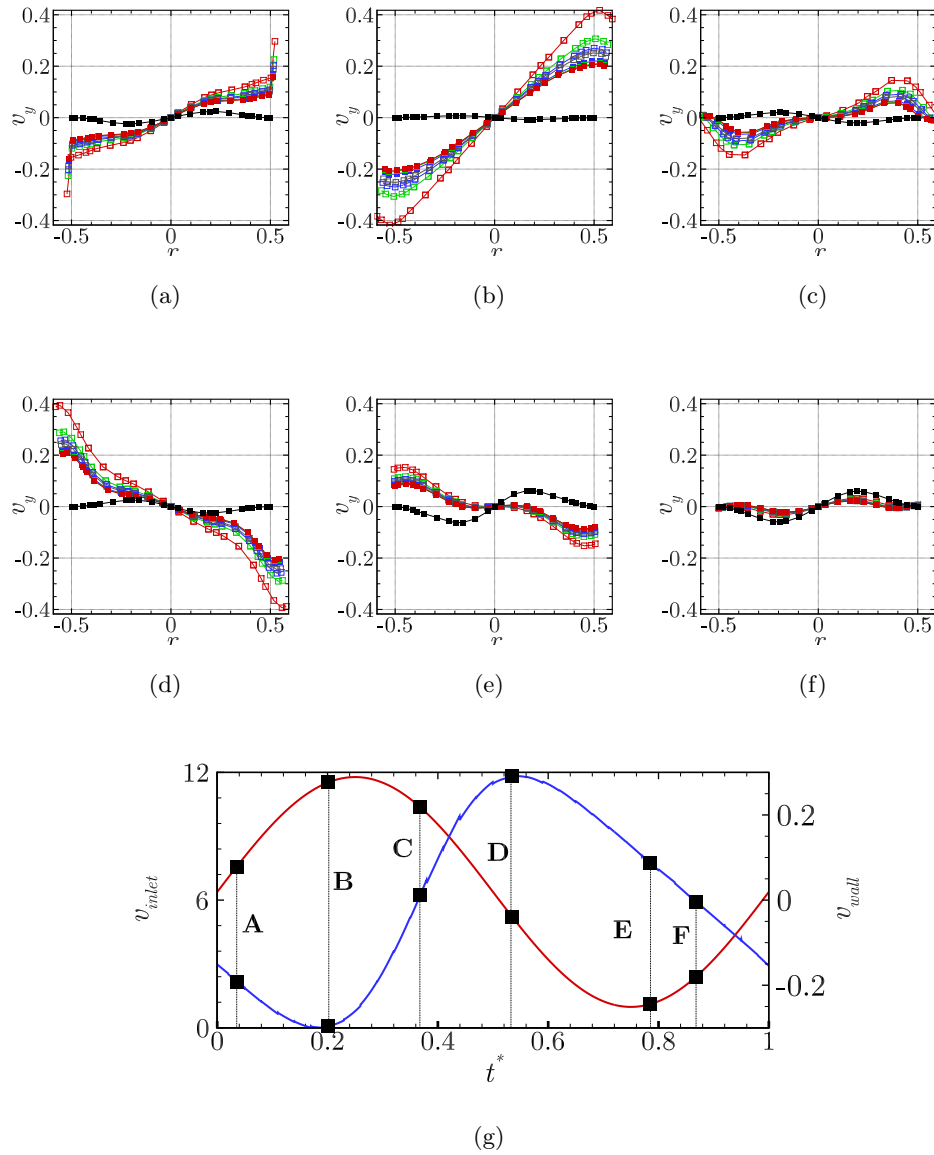


FIGURE 8.20: Plots of the wall-normal velocity in the y - z plane in the centre of the stiffened band ($z = 12$), velocity is normalised using the period of oscillation and diameter of the vessel. Sub-plots (a)-(f) show the wall-normal velocity component for various wall stiffnesses at times A-F shown in (g). In each plot filled black squares (■), filled red squares (■), filled green squares (■), filled blue squares (■), open grey squares (□), open blue squares (□), open green squares (□), and open red squares (□) represent the cases of a fully **rigid pipe**, the region with **6 MPa**, **4 MPa**, **2 MPa**, **0.8 MPa** (healthy-uniform), **0.6 MPa**, **0.4 MPa**, and **0.2 MPa**, respectively. (g) shows the velocity inlet (red) and wall velocity (blue) a negative wall velocity indicates the volume is expanding.

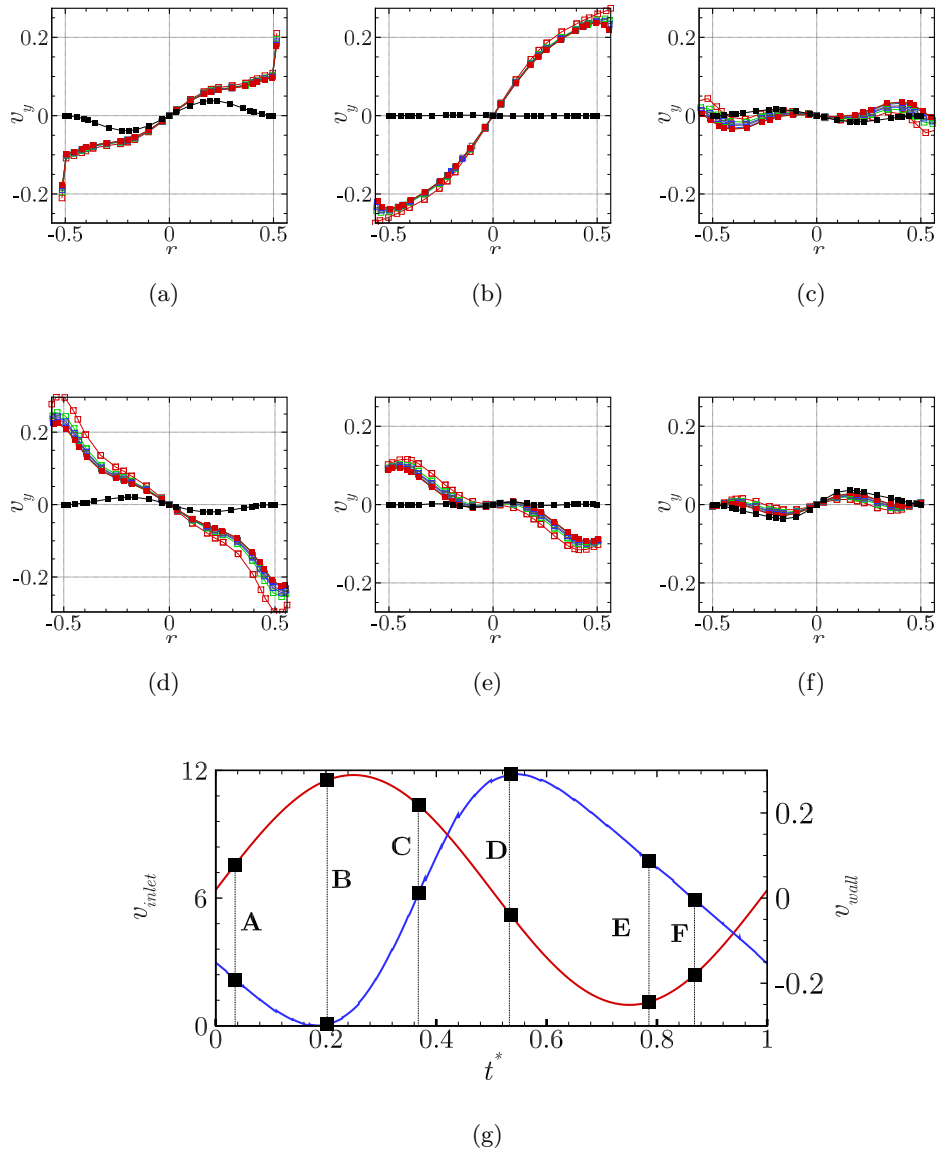


FIGURE 8.21: Plots of the wall-normal velocity in the y - z plane in the downstream of the stiffened band ($z = 13$), velocity is normalised using the period of oscillation and diameter of the vessel. Sub-plots (a)-(f) show the wall-normal velocity component for various wall stiffnesses at times A-F shown in (g). In each plot filled black squares (■), filled red squares (■), filled green squares (■), filled blue squares (■), open grey squares (□), open blue squares (□), open green squares (□), and open red squares (□) represent the cases of a fully **rigid pipe**, the region with **6 MPa**, **4 MPa**, **2 MPa**, **0.8 MPa** (healthy-uniform), **0.6 MPa**, **0.4 MPa**, and **0.2 MPa**, respectively. (g) shows the velocity inlet (red) and wall velocity (blue) a negative wall velocity indicates the volume is expanding.

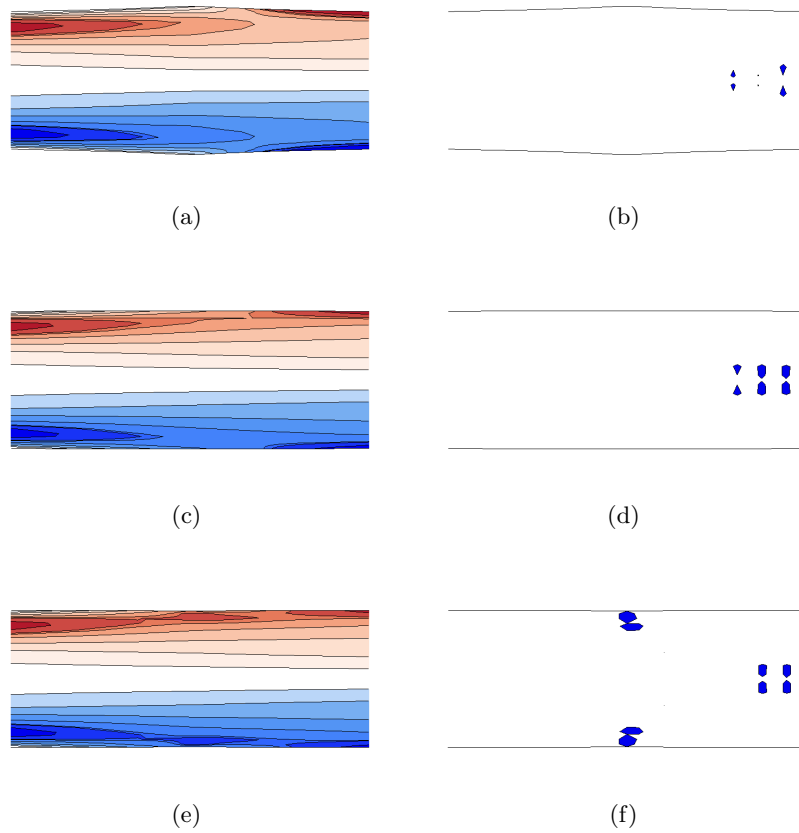


FIGURE 8.22: Left: contours of vorticity in the y - z plane in the region of varying stiffness. Vorticity contours are constant and vary from -75 to 75 (depicted by blue and red respectively). Right: the λ_2 field with contour levels of -0.0001 shown. Small negative values of λ_2 identify vortical regions of the flow. (a) and (b) shows the case of a 0.2 MPa region; (c) and (d) the uniform stiffness 0.8 MPa (healthy wall); and (e) and (f) is the stiffened case of 6 MPa.

restriction of the artery wall causes a region of greater vorticity to form close to the wall, figure 8.22(f) confirms that this is in fact a vortex core forming as a result of the restriction (a negative λ_2 implies that a vortex core is present). For the case of a less stiff wall the extra wall motion reduces the vorticity magnitude upstream of the disturbance and increases it downstream.

These results demonstrate that models which use a rigid-wall fail to capture the full flow dynamics in an aorta. The peak axial velocity predicted with a rigid-pipe model exceed the healthy elastic-wall case by over 32% . Furthermore, large variations in velocities close to the wall were observed. Section 8.5.5 will discuss the impact this has on the wall shear stresses which are integral to the healthy function of the endothelial

cells in the arterial wall. In the proceeding sections the rigid-wall model will be used as a comparison only to demonstrate the inadequacy of such models in describing the haemodynamic environment in the large arteries. Comparisons to the uniformly stiff healthy elastic-wall case will provide the basis upon which the heterogeneous wall results are discussed.

8.5.4 Wall shear stress in a perfectly rigid aorta

The evolution of the wall shear stress was calculated over time using equation 1.4. For the case of flow in a rigid-walled aorta where the flow is laminar and axisymmetric the wall shear stress may be approximated by equation 1.1. Using this approximation, and substituting the description of the Womersley velocity profile in equation 8.13, the analytical expression for the wall shear stress may be written as

$$\tau_{WSS}(t^*) = -\frac{\partial v^*}{\partial r^*} \Big|_{r^*=1} = \frac{ReG_0^*}{2} + \sum_{n=1}^{\infty} \frac{ReG_n^*}{2} \frac{2}{i^{3/2}\alpha_n} \frac{J_1(i^{3/2}\alpha_n)}{J_0(i^{3/2}\alpha_n)} e^{int}, \quad (8.20)$$

where

$$G_0^* = \frac{8}{\pi Re} Q_0^*, \quad (8.21)$$

and

$$G_n^* = \frac{2i\alpha_n}{Re \left(1 - \frac{2}{i^{3/2}\alpha_n} \frac{J_1(i^{3/2}\alpha_n)}{J_0(i^{3/2}\alpha_n)} \right)} Q_n^*, \quad (8.22)$$

where Q_n^* are the Fourier coefficients of the input flow rate, and quantities denoted by a (*) indicate that it has been non-dimensionalised by the input flow rate and viscosity (Salsac *et al.* 2006).

This analytical expression for the wall shear stress in a rigid-walled artery is compared to the wall shear stress calculated in the rigid-walled simulation using equation 1.4 in figure 8.23. The correlation between the analytical expression and the calculated wall shear stress is excellent for this simple laminar flow case. The wall shear stress ranges from -1.38 Pa to 3.56 Pa, the extrema occurring respectively at the peak diastole and peak systole. The simulated WSS measurements were within 2% of the analytical solution at all times. This shows an excellent correlation despite the assumptions made in the analytical solution. These include assumptions of a perfectly laminar and axisymmetric flow and a uniform wall geometry (i.e. it assumes the geometry is a flat plate). Other investigations have recorded wall shear stresses in rigid-walled pipes, Salsac *et al.* (2006) found the wall shear stress varied in the range of -3 Pa to 4.9 Pa.

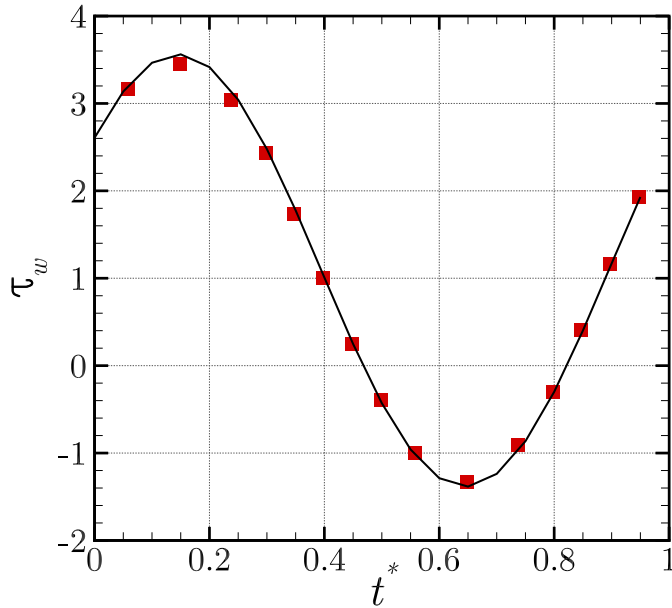


FIGURE 8.23: Variation of wall shear stress as a function of time inside a rigid-walled artery. The black line represents the analytical solution while the red squares, ■, show the results of the simulation.

In vivo measurements have also been conducted which would account for a moving wall, Oyre *et al.* (1997) reported a wall shear stress range of -1.3 Pa to 4.9 Pa, Cheng *et al.* (2002) found the peak wall shear stress in a resting patient to be only 2 Pa. The wall shear stress range found in this investigation is well within the range described within the literature, the difference in the wall shear stress between Salsac *et al.* (2006) and this study is likely due to the difference in inlet velocity profile. This study has a minimum inlet velocity of 2.5 cm/s compared to -8.8 cm/s (Salsac *et al.* 2006), which would allow for a greater near-wall velocity gradient in the reverse flow direction and therefore a greater negative wall shear stress. Furthermore, Salsac *et al.* (2006) uses a physiologically realistic heart beat waveform which includes sharper velocity gradients compared to the sinusoidal profile considered in this investigation.

Regardless of these small differences, the variation in the calculated wall shear stress correlates well with the analytical solution and is within the previously reported range of wall shear stress values. As this is a rigid-walled simulation and analytical model, the wall tangent shear stress model is sufficient to accurately predict the shear stress. The wall shear stress is the parameter that is physiologically relevant at the level of

the endothelial response. Figure 8.23 showed that the WSS fluctuates in a healthy abdominal aorta. Any departure from the healthy pattern of WSS strongly affects the morphology, metabolism and gene expression of the endothelial cells (Salsac *et al.* 2006; Lasheras 2007).

8.5.5 Wall shear stress in an elastic aorta

With an elastic wall, the flow dynamics inside an artery vary dramatically compared to rigid-walled models (examples of these variations were discussed in § 8.5.2). This section describes the repercussions of the changed flow dynamics in terms of the wall shear stress. Section 8.5.5.1 analytically describes how a change in the wall geometry will cause a change in the wall shear stress distributions. Section 8.5.5.2 goes on to compare the wall shear stress distributions in an elastic artery to that of a rigid pipe.

8.5.5.1 Analytical approach

The purpose of this section is to propose an analytical model of the flow through a bulging pipe to aid explanations of the root of changes in wall shear stress as a result of a changing geometry. Much of the discussion included later in this thesis relates changes in wall shear stress to three factors.

1. **The change in geometry causes a spatial acceleration or deceleration.**
In order to conserve mass if the local radius of the pipe changes, the velocity of the fluid through the pipe must change to ensure a constant fluid flux.
2. **The temporal dependence of the wall geometry, i.e. the velocity of the wall causes a change in the pipe volume** The changing volume of the pipe changes the downstream flow rate at a point in order to conserve mass flow rate.
3. **An increase in mass flow rate is associated with a thinner boundary layer** A thinner boundary layer corresponds to large velocity gradients, strain rates and consequently, wall shear stresses.

The ultimate goal is to describe what happens to the wall shear stress in the changing arterial environment. Primarily this may be linked to the boundary layer thickness. As such, the boundary layer is defined by referring to the momentum equation of the Navier–Stokes equations,

$$\frac{\partial \mathbf{v}}{\partial t} + (\mathbf{v} \cdot \nabla) \mathbf{v} = -\nabla P + \nu \nabla^2 \mathbf{v}. \quad (8.23)$$

The momentum equation of the Navier–Stokes equations represent a balance of the four forces, term by term these are:

$$\begin{array}{cccccc}
 \text{Transient} & + & \text{Convective} & = & \text{Net pres-} & + & \text{Net viscous} \\
 \text{inertia per} & & \text{inertia per} & & \text{sure force} & & \text{forces on} \\
 \text{unit volume} & & \text{unit volume} & & \text{on the sur-} & & \text{the surface} \\
 & & & & \text{face of the} & & \text{of the in-} \\
 & & & & \text{infinitesi-} & & \text{finitesimal} \\
 & & & & \text{mal control} & & \text{control} \\
 & & & & \text{volume} & & \text{volume}
 \end{array}$$

To determine the relative importance of these terms under differing flow conditions the Navier–Stokes equations are re-cast into a non-dimensionalised form using a characteristic velocity V , frequency ω , and length L . In the particular context of flow through an artery $V = v_{mean}$ (the mean flow speed), ω is the heart rate and $L = d$ (the diameter of the artery). Using these characteristic quantities the non-dimensionalised variables are

$$v^* = \frac{v}{v_{mean}}, \quad t^* = \omega t, \quad P^* = \frac{p}{\rho v_{mean}^2}, \quad \nabla^* = \frac{1}{D}. \quad (8.24)$$

Substituting these quantities into equation 8.23 yields the non-dimensionalised Navier–Stokes equations

$$\begin{aligned}
 \frac{\alpha^2}{Re} \frac{\partial \mathbf{v}^*}{\partial t^*} + (\mathbf{v}^* \cdot \nabla^*) \mathbf{v}^* &= -\nabla^* P^* + \frac{1}{Re} \nabla^{*2} \mathbf{v}^*, \\
 \nabla^* \cdot \mathbf{v}^* &= 0,
 \end{aligned} \quad (8.25)$$

where,

$$Re = \frac{v_{mean} d}{\nu}, \quad (8.26)$$

and

$$\alpha = d \sqrt{\frac{\omega}{\nu}}. \quad (8.27)$$

These form the complete set of field equations for an incompressible fluid, it is clear that the Reynolds number and the Womersley number are the only two physical parameters. This implies that two flows in geometrically similar vessels but with different sizes will exhibit identical flow dynamics if both the Reynolds number, Re , and Womersley number, α , are the same. Thus the Reynolds and Womersley numbers may be said to govern the balance of forces in a flow (Fung 1997).

The Reynolds number expresses the ratio of the convective inertial forces to the shear force. A large Reynolds number indicates a predominant convective inertial effect; a small Reynolds number indicates a predominant shear effect. Similarly, the Womersley

number expresses the ratio of the transient inertial forces to the shear force. If the Womersley number is large, the oscillatory inertial forces dominate.

The concept of a boundary layer was presented by Prandtl (1904). It can be understood by comparing the significance of various terms in the Navier–Stokes equations. If an ideal inviscid fluid is considered (i.e. $\nu = 0$) the last term in equation 8.23 vanishes. At a boundary, an ideal fluid may not penetrate the wall but its tangential velocity is unrestricted. For a viscous fluid the non-slip condition must apply regardless of the magnitude of the viscosity of the fluid. Prandtl (1904) postulates that if the viscosity is small, the influence of the no-slip condition and final term in equation 8.23 is limited to a small layer adjacent to the solid wall. Conversely, in this scenario, far from the wall the influence of the last term in equation 8.23 is insignificant and can be neglected. In this case the boundary layer thickness δ can be deduced by comparing proper terms in equation 8.23. The boundary layer is therefore defined as the region in which the viscous forces are dominant in the Navier–Stokes equations.

First consider an oscillating velocity field of frequency, ω , and velocity amplitude, V . The first term of equation 8.23 shows that the transient inertial force is of order $\rho\omega V$. The last term in equation 8.23 shows that the order of magnitude of the viscous forces is $\frac{\mu V}{\delta_t^2}$, where δ_t is the transient boundary layer thickness (a length scale used to non-dimensionalise the viscous term in the Navier–Stokes equations as a result of the definition of a boundary layer). In the transient boundary layer these terms are of similar orders of magnitude and balance each other to determine the flow. Hence

$$\rho\omega V \simeq \frac{\mu V}{\delta_t^2} \quad (8.28)$$

or

$$\delta_t \simeq \sqrt{\frac{\nu}{\omega}}. \quad (8.29)$$

In a tube flow let the characteristic length be the radius R , then the ratio of R to δ_t is the Womersley number

$$\frac{R}{\delta_t} \simeq \alpha. \quad (8.30)$$

Hence, if the Womersley number is large, the transient boundary layer is thin compared to the tube radius. This supports the discussion of Womersley profiles in § 8.5.1 in which it was shown that at high Womersley numbers the flow becomes plug like with changes in flow first occurring (as a result of the oscillatory nature of the flow) close to the

walls. When the Womersley number is low the flow approaches a Poiseuille flow profile in which the boundary layer thickness is equal to the entire tube radius.

Also of significance are the convective inertial forces: these are particularly important in the aneurysm context in which the changing shape will cause a convective acceleration. In a convective boundary layer of thickness δ_c the magnitude of the convective inertial forces $\frac{\rho V^2}{L}$ compete with the viscous forces $\frac{\mu V^2}{\delta_c^2}$. Thus the convective boundary layer may be described as

$$\delta_c \simeq \sqrt{\frac{\mu L}{\rho U}}. \quad (8.31)$$

In a tube flow let the characteristic length be the radius R , then the ratio of R to δ_c is the square root of the Reynolds number

$$\frac{R}{\delta_c} \simeq \sqrt{Re}. \quad (8.32)$$

Therefore, if the Reynolds number is large, the convective boundary layer is very thin. In a pipe flow at a distance from the wall much larger than δ_t and δ_c the flow may be considered ideal and the effect of viscous forces neglected.

Having defined some relationships between the non-dimensionalised physical parameters and relationships between the physical parameters and the boundary layer thickness, changes in local Reynolds and Womersley numbers can be used to describe changes in boundary layer thickness and consequently wall shear stresses.

In an artery model with an elastic wall, both the radius and the flow velocity can change. To determine the boundary layer thickness at a particular location the Reynolds transport theorem may be employed. Consider the bulging pipe shown in figure 8.24 with an arbitrary control volume shown. For an arbitrary moving and deformable control volume the Reynolds transport theorem is

$$\frac{dm}{dt} = \frac{d}{dt} \left(\int_{CV} \rho dV \right) + \int_{CS} \rho V_r \underline{\mathbf{n}} dA_{out} - \int_{CS} \rho V_r \underline{\mathbf{n}} dA_{in}, \quad (8.33)$$

where

$$V_r = V - V_{CS} \quad (8.34)$$

is the relative velocity between the fluid (V) and the control surface (V_{CS}), m is the mass and A_{out} and A_{in} are the areas of the control surface through which fluid flows.

If the fluid is incompressible the mass flux

$$\frac{dm}{dt} = 0, \quad (8.35)$$

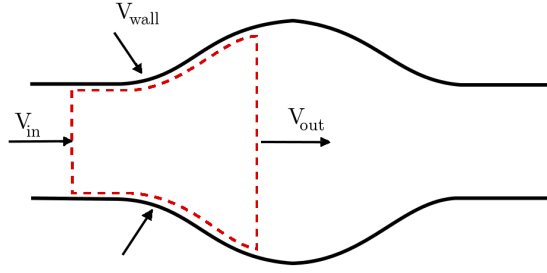


FIGURE 8.24: An example of the control volume used to determine the flow rate at any position along the pipe. The control volume deforms with the walls and has velocity flowing through its inlet on the left and out the outlet on the right.

giving the relationship

$$0 = \frac{d}{dt} \left(\int_{CV} \rho d\mathcal{V} \right) + \int_{CS} \rho V_r \underline{\mathbf{n}} dA_{out} - \int_{CS} \rho V_r \underline{\mathbf{n}} dA_{in} \quad (8.36)$$

For the control volume shown in figure 8.24 there is an input upstream of the elastic region, inflow as a result of the wall motion, and an output at the region at which the boundary layer thickness is of interest. i.e.

$$0 = \frac{d}{dt} \left(\int_{CV} \rho d\mathcal{V} \right) + \int_{CS} \rho V_r \cdot \underline{\mathbf{n}} dA_{out} - \left(\int_{CS} \rho V_{r,inlet} \cdot \underline{\mathbf{n}} dA_{in} + \int_{CS} \rho V_{r,wall} \cdot \underline{\mathbf{n}} dA_{in} \right). \quad (8.37)$$

If the control volume is fixed to the wall, the relative velocity between the control surface and the wall/fluid flow is zero, similarly if the control volume is fixed in space relative to the longitudinal axis, the relative velocity is simply the velocity of the fluid. As such, the final Reynolds transport equation is:

$$0 = \frac{d}{dt} \left(\int_{CV} \rho d\mathcal{V} \right) + \int_{CS} \rho V_{out} \cdot \underline{\mathbf{n}} dA_{out} - \int_{CS} \rho V_{in} \cdot \underline{\mathbf{n}} dA_{in}, \quad (8.38)$$

where the first term accounts for the change in volume of the artery and the motion of the wall, the second term describes the mass flow rate at the outlet of the control volume (location of interest) and the final term represents the mass flow rate at the inlet to the control volume. In this analysis, the location of the control volume inlet is fixed at the inlet to the elastic region. At this location the area of the control surface is constant as the elastic walls cannot move. Therefore at a particular instant in time, the final term is constant and known from the velocity inlet boundary conditions. Hence,

the Reynolds transport theorem can be re-written as

$$\int_{CS} \rho V_{out} \cdot \mathbf{n} dA_{out} = \rho Q(t) - \frac{d}{dt} \left(\int_{CV} \rho dV \right), \quad (8.39)$$

where $Q(t)$ is the volumetric flow rate at the inlet.

Equation 8.39 shows that if the volume of the aneurysm is increasing with time, the flow rate at the outlet is reduced. Conversely a decreasing control volume will cause an increase in the flow rate at the control volume outlet. Furthermore, if the radius at the outlet is greater than the radius at the inlet, the velocity at the outlet will be less than the velocity at the inlet.

Consider the relationship shown in equation 8.32. If the local velocity increases, the boundary layer becomes thinner and consequently the wall shear stress increases. By considering equation 8.32 in conjunction with equation 8.39, it can be seen that an increasing volume or an increasing radius of the pipe causes a reduction in the local fluid velocity, an increase in boundary layer thickness, and consequently a decrease in the local wall shear stress. Conversely, a decreasing volume or radius causes an increase in the local fluid velocity, a thinning of the boundary layer, and consequently an increase in the local wall shear stress.

This analysis can be taken further to derive an analytical expression for the flow through an incipient aneurysm with moving walls.

Salsac *et al.* (2006) present an analytical solution to flow through an incipient aneurysm with rigid walls. An analytical solution for the wall shear stress in a slowly expanding pipe is derived via an extension of the analytical solution for a straight pipe in § 8.5.1.1. In formulating this expression it is assumed that changes in the axial velocity occur very slowly along the longitudinal axis, i.e. the expansion is at a very small rate. In the case of a slowly expanding pipe the radial velocity, v_r , can no longer be neglected. Salsac *et al.* (2006) defines a characteristic length, \mathcal{L} along which the local radius varies, i.e.

$$\mathcal{L} = r_0 \frac{dr}{dz}, \quad (8.40)$$

where r_0 is the original pipe radius, z is the axial direction and r is the radius of the pipe at location z . The definition in equation 8.40 is rearranged to form a new small parameter

$$\varepsilon = \frac{\mathcal{L}}{r_0}, \quad (8.41)$$

which is used to define a new set of parameters,

$$Z^* = \varepsilon z^*, \quad P^* = \varepsilon p^*, \quad v_r^* = \varepsilon V_r^*, \quad (8.42)$$

where Z^* is the new non-dimensionalised axial position, P^* is the non-dimensionalised pressure and V_r^* is the new radial velocity. To extend the Salsac *et al.* (2006) approach to the case of an elastic bulging pipe the small parameter of equation 8.41 is defined not simply as a linear approximation of the radial position of the wall, but instead as the instantaneous gradient of the radius in the axial direction,

$$\varepsilon = \frac{\mathcal{L}}{r_0} = \frac{dr}{dz}. \quad (8.43)$$

If the change in radius is small this allows consideration of the case of a continually changing radius rather than a simple expanding pipe case. This definition permits the slightly bulging pipe case of this investigation to be considered (see figure 8.19).

A first-order approximation of the momentum equations decouples the flow into axial and radial velocity components, i.e. the axial velocity component reduces to a similar form as that of the straight pipe equations in § 8.5.1.1. The dimensionless longitudinal velocity $v_z^*(Z^*, r^*, t^*)$ is given by

$$v_z^*(Z^*, r^*, t^*) = \frac{ReG_0^*(Z^*)}{4} (R^{*2} - r^{*2}) + \frac{Re}{i} \sum_{n=1}^{\infty} \frac{G_n^*(Z^*)}{\alpha_n^2} \left(1 - \frac{J_0(i^{3/2}\alpha_n \frac{r^*}{R^*})}{J_0(i^{3/2}\alpha_n)} \right) e^{int^*}, \quad (8.44)$$

where $R^*(Z^*) = \frac{r(Z^*)}{r_0}$ is the local dimensionless radius, $\alpha_n(Z^*) = r(Z^*) \sqrt{\frac{n\omega}{\nu}}$ is the local Womersley number corresponding to the n^{th} harmonic of the input arterial flow rate and $G_n^*(Z^*)$ is the n^{th} Fourier coefficient of the pressure gradient $\frac{\partial P^*}{\partial Z^*}$.

As in § 8.5.1.1 it is preferential to recast equation 8.44 in terms of the flow rate Q_n^* rather than the pressure gradient. The pressure coefficients $G_n^*(Z^*)$ are then calculated using,

$$G_0^*(Z^*) = \frac{8}{\pi Re R^{*4}} Q_0^*; \quad G_n^*(Z^*) = \frac{i\alpha_n^2}{\pi Re R^{*4} [1 - F(\alpha_n)]}; \quad (8.45)$$

where

$$F(\alpha_n) = \frac{2}{i^{3/2}\alpha_n} \frac{J_1(i^{3/2}\alpha_n)}{J_0(i^{3/2}\alpha_n)}, \quad (8.46)$$

and J_1 is the Bessel function of the first kind with order one.

In addition, the radial velocity takes the form (Salsac *et al.* 2006):

$$V_r^* = \frac{2Q_0}{\pi R^{*2}} \frac{dR^*}{dY^*} \frac{r^*}{R^*} \left(1 - \frac{r^{*2}}{R^{*2}} \right) + \sum_{n=1}^{\infty} \frac{Q_n}{4\pi R^{*2}} \frac{dR^*}{dY^*} \frac{i\alpha_n^2 F(\alpha_n)^2}{(1-f(\alpha_n))^2} \left(\frac{r^*}{R^*} - \frac{J_1\left(i^{3/2}\alpha_n \frac{r^*}{R^*}\right)}{J_0\left(i^{3/2}\alpha_n\right)} \right) e^{int}. \quad (8.47)$$

In equations 8.44 and 8.47 the velocity is now dependent on the local wall gradient through the inclusion of the small parameter defined in equation 8.43. To account for the motion of the wall the Fourier components of the flow rate must include a component from the inlet boundary condition as well as the changing volume of the vessel,

$$Q_n^* = Q_{n,inlet}^* + Q_{n,wall}^*. \quad (8.48)$$

This is a direct result of the Reynolds transport theorem analysis in equation 8.39.

The wall shear stress can be approximated by taking the gradient of the axial velocity component at the wall location,

$$\tau_{WSS}(t^*) = - \left. \frac{\partial v^*}{\partial r^*} \right|_{r^*=R^*} = \frac{ReG_0^*(Z^*)}{2} + \sum_{n=1}^{\infty} \frac{ReG_n^*(Z^*)}{2} \frac{2}{i^{3/2}\alpha_n} \frac{J_1\left(i^{3/2}\alpha_n\right)}{J_0\left(i^{3/2}\alpha_n\right)} e^{int} \quad (8.49)$$

where G_0^* and G_n^* are as described in equation 8.45.

Each of the Fourier coefficients in equation 8.45 are dependent on the parameter $R^*(Z^*) = \frac{r(Z^*)}{r_0}$. Consider the differential control volume shown in figure 8.25. This shows that for a particular control volume, r_0 is the radius of the control volume on the inlet side and r^* is the radius of the control volume at the outlet side. If the differential control volume is located in the diverging section of the aneurysm, $R^* > 1$, conversely if the differential control volume is located in the converging section of the aneurysm, $R^* < 1$. Because the wall shear stress involves a fourth-order relationship with R^* , small changes in this ratio have a greater effect than other terms which are of order $\mathcal{O}(1)$. Thus if the wall is diverging and $R^* > 1$, the coefficients G_0^* and G_n^* are reduced and so too is the wall shear stress. Similarly if the wall is converging and $R^* < 1$, the coefficients G_0^* and G_n^* are increased and the wall shear stress also increases. This matches the findings of § 8.5.5.2 in which the diverging wall at the distal neck is associated with a reduction in the wall shear stress and the converging wall near the distal neck is associated with an increase in wall shear stress.

Similarly, analysis of the Fourier coefficients in equation 8.45 in association with the Reynolds transport relationship in equation 8.39 supports these findings. At times

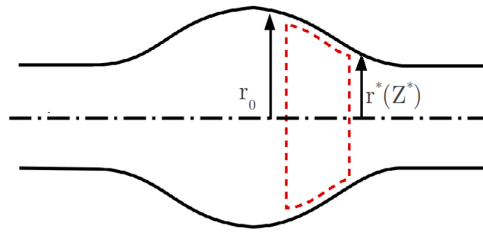


FIGURE 8.25: An example of a differential control volume. Depending on the axial location of the control volume, the ratio $R^*(Z^*) = \frac{r(Z^*)}{r_0}$ may be greater than or less than unity.

when the wall is collapsing and the volume is decreasing the flow rate increases: this leads to an increase in both G_0^* and G_n^* and consequently an increase in the wall shear stress at these times.

8.5.5.2 Simulated wall shear stresses

In § 8.5.4 an analytical expression for the wall shear stress was compared with rigid-walled results. Here, the variation in the wall shear stress with an elastic-wall is considered. Figure 8.26 shows contours of the variation in wall shear stress in the elastic region of interest through time. Figure 8.26(a) shows the case of a rigid pipe, the wall shear stress pattern is dominated by continuous horizontal bands. This shows that at a particular time the wall shear stress is spatially invariant along the length of the artery. This correlates well with the velocity distribution in a rigid smooth-walled artery in which the velocity profile is expected to be laminar throughout the cardiac cycle. The structure of figure 8.23 can be seen when looking at a vertical transect of figure 8.26(a), the wall shear stress reaches a maximum at peak systole before decreasing to a minimum at peak diastole. As the inlet velocity has a non-zero mean the intensity of contours around the peak systole is greater than the peak diastole.

Figure 8.26(b) shows the case when the wall has a uniform elasticity of $E = 0.8$ MPa. The elasticity of the wall allows it to balloon outward and form the shape shown in figure 8.19. Each contour plot shows the extents of the elastic region only, not the rigid sections up- or down-stream. The variation in shape drastically affects the banded contour profile of the wall shear stress. The peak wall shear stress occurs during systole as expected. However, rather than the peak shear stress occurring continuously across

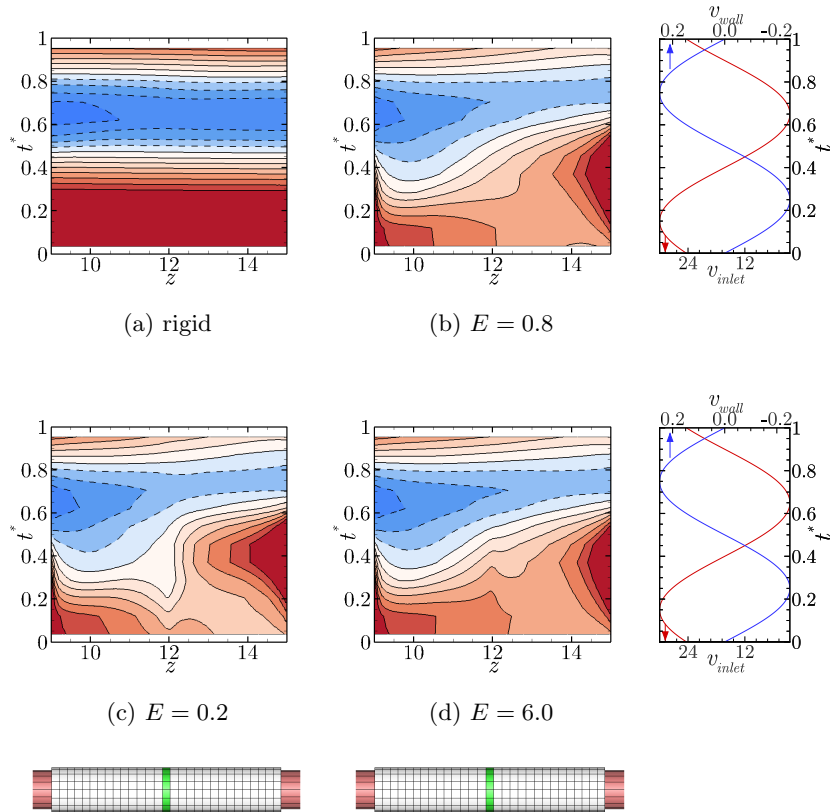


FIGURE 8.26: The variation of wall shear stress (WSS) in a straight pipe as a function of both time and space. Contours show WSS with high low levels represented by red and blue, respectively. Negative values are represented by dashed contour lines. The contour levels are equispaced and vary from -3 Pa to 3 Pa . Sub-plot (a) represents the WSS distribution in a straight pipe with rigid-walls. Sub-plots (b)-(d) represent the WSS in a straight pipe with a localised variation in wall stiffness of 0.8 MPa (healthy), 0.2 MPa and 6.0 MPa , respectively. The figures on the right show the velocity inlet (red) and wall-normal velocity (blue). A negative wall-normal velocity indicates that the wall is expanding.

the section of artery, it occurs predominantly at the distal neck formed by the change in shape. Similarly the minimum wall shear stress occurs at the peak diastole localised around the proximal neck. A close comparison of the time at which the maximum and minimum wall shear stress occurs in the rigid and elastic cases reveals that the peak wall shear stresses occur later in the time cycle for the elastic-walled cases (see figure 8.27). In fact the peak wall shear stresses occur at times of peak wall velocity $t^* = 0.4$ in rigid-walled cases. Equations 8.39 and 8.32 describe how the presence of the wall velocity causes the boundary layer to change size. As the boundary layer changes in size so too does the local strain rate. This in turn changes the wall shear stress which

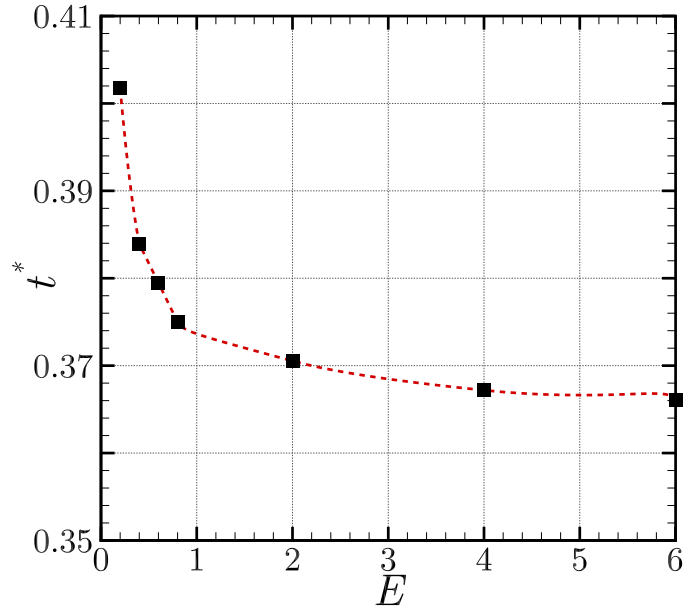


FIGURE 8.27: The time at which peak wall shear stress occurs at the distal neck as a function of wall stiffness. Results are for an elastic region with stiffness of 0.8 MPa with a stiffened region with a stiffness of E MPa

is strain rate dependent (equation 1.4). In the near-wall region the wall motion has a greater effect on the flow than the bulk motion of the fluid. This is why a delayed onset of peak wall shear stress is observed.

Figures 8.26(c) and 8.26(d) also show cases of an elastic-wall. However, they feature a localised change in stiffness (thickness $0.2D$) centred around $z = 12$. As discussed in § 8.5.3 this altered stiffness band causes both global and local effects. Globally the change in stiffness affects the amount the wall will displace; a lower stiffness (figure 8.26(c)) causes a greater dilation of the artery wall. Conversely a higher stiffness (figure 8.26(d)) causes a smaller dilation. The effect of the global change can be observed in comparing each of the plots in figure 8.26. As the stiffness is increased the peak wall shear stress occurs earlier in the time cycle (see figure 8.27). When comparing the elastic cases only, the peak wall shear stress is more localised around the distal neck as the stiffness increases. Also evident is that as the stiffness is increased the peak wall shear stress occurs earlier, i.e. closer to the peak systolic flow of the rigid-walled case. With a reduced stiffness and increased dilation of the wall, the change in volume of the artery is increased.

Equation 8.39 shows that the flow rate at the distal neck increases as a result of two processes. Firstly, as the local geometry is akin to a converging nozzle at any instant in time, the flow rate must increase at the outlet in order to conserve mass. This effect is enhanced by large wall motions as the wall gradient is larger for these cases. In addition to this effect an increase in the flow rate at the distal neck may also occur as a result of the motion of the wall itself for the case when the wall is contracting, the negative rate of change in volume causes an increase in the flow rate through the distal neck. An increase in the wall-normal velocity (which is a maximum after the peak systolic velocity) simultaneously increases the flow rate through the distal neck and therefore the peak velocity. The result of this increase in the flow velocity is an increase in the local Reynolds number at the distal neck and as described by equation 8.32 the convective boundary layer is thinner. A thinner boundary layer corresponds to an increase in velocity gradients near the wall and as a result, an increase in the wall shear stress. With a stiffer wall the wall displacement is reduced and consequently so too is the effect on the wall shear stress. Figure 8.27 shows that as the wall stiffness is decreased (and consequently the motion of the wall increases) the onset of peak wall shear stress is delayed. This indicates that the wall motion has a greater effect on the flow conditions as the wall stiffness is reduced. When the wall is rigid the peak in wall shear stress correlates directly with the peak in inflow rate.

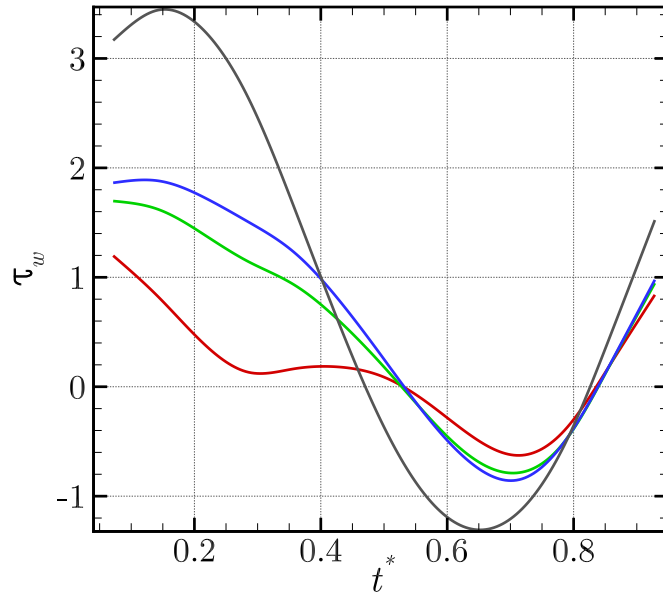
Also evident in figures 8.26(c) to 8.26(d) is that a variation in the wall shear stress contours around the $z = 12$ position where the wall stiffness is locally changed. As discussed in § 8.5.3 and pictured in figure 8.19 the local change in stiffness causes a local variation in the wall geometry. This local change in wall shape and velocity causes a local change in the fluid flow at that location. Figure 8.26(c) shows that with a less stiff section the wall shear stress in this local region is lower for a longer period than for the stiffer case in figure 8.26(d).

Figure 8.28(a) shows the variation in wall shear stress at the centre of the altered stiffness region. This supports the finding in figure 8.26(c) whereby the local wall shear stress is lower for more of the cardiac cycle. Upstream near the proximal neck, (figure 8.28(b)) changes in stiffness have little affect on the wall shear stress distribution. Downstream at the distal neck (figure 8.28(a)) large variations in the peak wall shear stress are observed. The control volume analysis in § 8.5.5.1 provides an explanation for this phenomenon. Figure 8.19 shows that the change in wall displacement as a result of

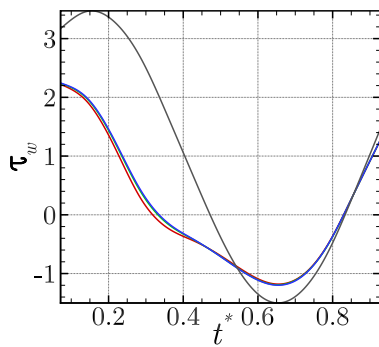
the change in stiffness is largely localised to the region of altered stiffness. Therefore, far upstream of the change in stiffness, the wall motion is nearly independent of the stiffness at the central location. As such the change in volume of the wall upstream of this point is almost the same regardless of the wall stiffness. This leads to the same flow rate through a control volume with an outlet at this location. At the position of altered stiffness, the wall motion is very different depending on the stiffness, leading to a change in the flow dynamics at this location. Equation 8.49 describes how the local wall gradient and change in radius at this location can affect the wall shear stress. A less stiff wall leads to a local increase in radius at this location, equation 8.49 shows this leads to a decrease in the wall shear stress. Conversely, a stiffer wall leads to a local decrease in radius and consequently an increase in wall shear stress. As with the upstream case, downstream at the distal neck the local wall displacement varies negligibly with the stiffness of the upstream region (see figure 8.19). Despite this, a large difference in the local wall shear stress is observed. Unlike the upstream case, downstream of the altered elastic band the flow is affected by the increase or decrease in volume upstream. Equation 8.39 shows that including this region in the control volume will affect the local velocity downstream and as a result of equation 8.32 the wall shear stress is further altered.

Further supporting this finding is figure 8.29 which shows the time-averaged wall shear stress in the elastic artery. The rigid-walled case shows an almost uniform time-averaged wall shear along the artery length. This is expected given the banded nature of the wall shear stress distribution shown in figure 8.26(a). The cases which include an elastic-wall show a large variation in the time-averaged wall shear stress through the elastic region ($z = 9 - 15$). The elastic cases are dominated by a sharp decline in the wall shear stress at the proximal neck before the wall shear stress begins to increase beyond the initial wall shear stress value. The wall shear stress gradient continue to increase until the distal neck is reached. The peak time-averaged wall shear stress is observed at the distal neck.

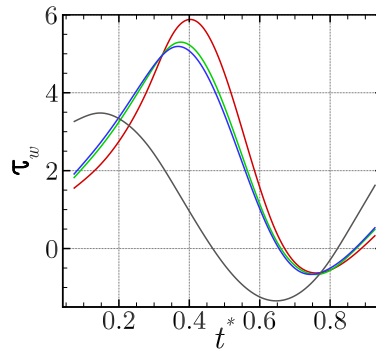
Also evident in figure 8.29 is the local variation in wall shear stress at the location of the local change in wall stiffness. For the case of a uniform stiffness ($E = 0.8$ MPa) the wall shear stress gradient is smooth, in contrast to the stiffened and less stiff cases. A less stiff artery causes a greater local wall motion and this causes a local increase in the boundary layer thickness and consequently a reduction in the local wall shear



(a) $z = 12$



(b) $z = 10$



(c) $z = 15$

FIGURE 8.28: The wall shear stress plotted as a function of time at (a) the centre of the altered stiffness region $z = 12$, (b) near the proximal neck $z = 10$ and (c) the distal neck $z = 15$. The black line represents the rigid-walled reference case, red, green and blue lines represent the cases with a local variation in wall stiffness of $E = 0.2$ MPa, 0.8 MPa (healthy), and 6.0 MPa respectively.

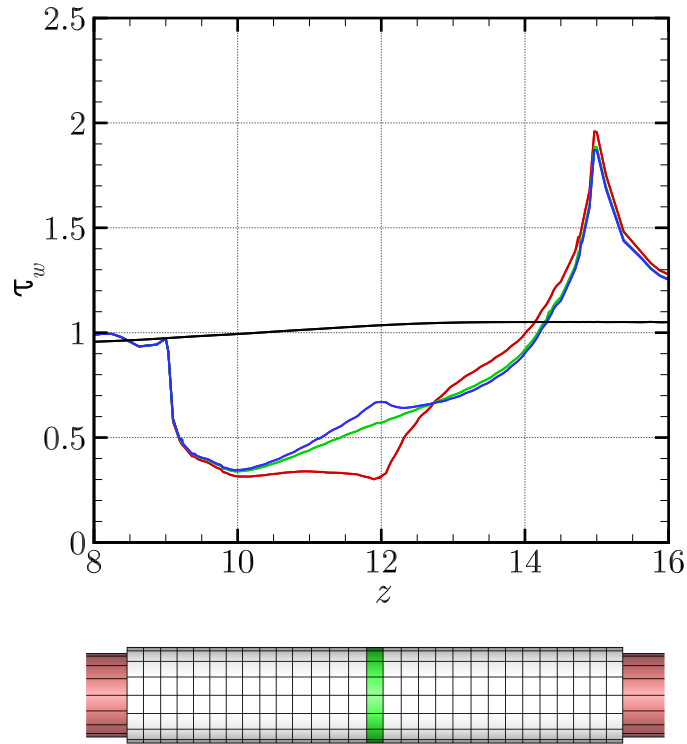


FIGURE 8.29: Comparison of the time-averaged wall shear stresses with varying local wall stiffness. The black line represents the rigid-walled reference case, red, green and blue lines represent the cases with a local variation in wall stiffness of $E = 0.2$ MPa, 0.8 MPa (healthy), and 6.0 MPa respectively. Note: for the elastic-walled cases a stiffness of $E = 0.8$ MPa is applied outside the region of local stiffness variation.

stress. Conversely, a stiffer artery causes a reduction in the local wall motion and velocity. A stenotic geometry forms which causes a local acceleration of the fluid and a corresponding thinning of the boundary layer, the thinner layer is synonymous with an increase in the wall shear stress (equation 8.32).

The minima of wall shear stress occurring immediately behind the proximal neck is a result of the local expansion of the artery wall. This causes an increase in the boundary layer thickness as the increasing radius causes a decrease in local flow velocity (equation 8.39). The wall shear stress begins to increase again at the point where the wall displacement gradient has reached a maximum and the spatial deceleration of the fluid catches up to re-establish contact between the bulk fluid flow and the wall motion. To determine the axial position of the minimum or maxima in wall shear stress

analytically, one must solve

$$0 = \frac{d\tau_{WSS}}{dZ^*}, \quad (8.50)$$

where τ_{WSS} may be given by equation 8.49. This shows that the minima of wall shear stress will occur at a location where

$$\frac{dR^*}{dZ^*} = \frac{d^2r(Z^*)^*}{dZ^{*2}}, \quad (8.51)$$

is also minimised, i.e. where the wall displacement gradient has reached a maximum.

The peak wall shear stress observed at the distal neck in figure 8.29 is much higher in the elastic-artery case than in the rigid-walled case. This increase in the wall shear stress is due to two factors. Firstly, the wall profile at the distal neck forms a converging nozzle shape causing a spatial acceleration (seen through the convective acceleration term in the Navier-Stokes equations) as the fluid speeds up to conserve the mass flux through the pipe. Equation 8.32 describes how the increase in local velocity is associated with a thinning of the boundary layer and as a result a local increase in the strain-rate and consequently the wall shear stress. The artery wall motion also acts to enhance this effect, the motion of the wall after peak systole forces extra fluid through the distal neck as the volume of the artery decreases (see equation 8.39). This causes the flow rate through the distal neck to be greater than that which would occur in a rigid-walled artery alone. This allows the peak wall shear stress to far exceed the wall shear stress predicted using a rigid-walled aneurysm model. The time-averaged wall shear stress at the distal neck is 85% higher in the elastic case. Furthermore, figures 8.28(c) and figure 8.29 show that the peak wall shear stress at the distal neck is greatest in the 0.2 MPa case in which the total wall motion is greatest.

Further to the discussion of wall shear stress, figure 8.30 shows the time-averaged wall shear stress magnitude. The oscillatory nature of the flow means that a time-averaged wall shear stress result can obscure the total shear felt at the wall as negative values of shear artificially reduce the intensity of the time-averaged wall shear stress. In terms of healthy endothelial cell function, wall shear stress magnitude may be more important to consider as shear stress direction is not important. Figure 8.30 shows that the wall shear magnitude in the elastic-wall case is close to 50% lower than the rigid-wall case across the majority of the aorta. The wall shear stress at the distal neck still exceeds the wall shear stress magnitude for the elastic cases.

Experiments, in which the temporal distribution of shear stresses applied to the en-

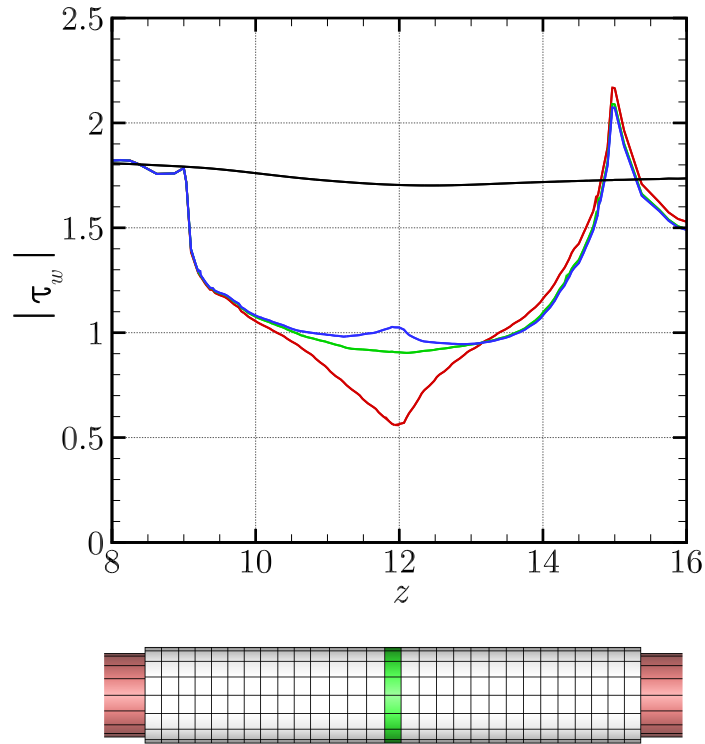


FIGURE 8.30: Comparison of the time-averaged wall shear stress magnitude with varying local wall stiffness. The black line represents the rigid-walled reference case, red, green and blue lines represent the cases with a local variation in wall stiffness of $E = 0.2$ MPa, 0.8 MPa (healthy), and 6.0 MPa respectively. Note: for the elastic-walled cases a stiffness of $E = 0.8$ MPa is applied outside the region of local stiffness variation.

endothelial cells could be carefully controlled, have shown that the endothelial behaviour depends not only on the magnitude of the shear stresses, but also on their spatial and temporal variations. The Oscillating Shear Index (OSI) quantifies the pulsatility and primary direction of the flow. It ranges from 0 (forward flow throughout the cardiac cycle) to 1 (fully reversed flow). An OSI index of 0.5 corresponds to a purely oscillating flow with a WSS mean of 0. Figure 8.31 shows the oscillating shear index distribution along the healthy aorta. Salsac *et al.* (2006) found the OSI of a rigid-walled healthy aorta to be 0.4, while others have calculated the OSI in a healthy artery to be 0.32 (Oyre *et al.* 1997). Figure 8.31 shows the oscillating shear index distribution along a rigid-walled artery to be 0.22. An $OSI = 0.22$ implies the flow is mostly forward which is to be expected given the inlet velocity profile for these simulations. The difference

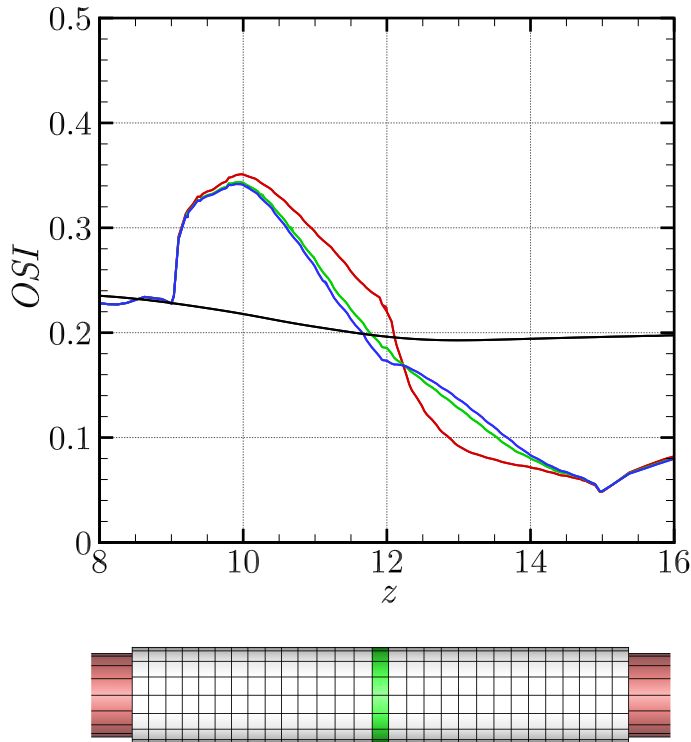


FIGURE 8.31: Comparison of the oscillating shear index (OSI) along the pipe with varying local wall stiffness. The black line represents the rigid-walled reference case, red, green and blue lines represent the cases with a local variation in wall stiffness of $E = 0.2$ MPa, 0.8 MPa (healthy), and 6.0 MPa respectively. Note: for the elastic-walled cases a stiffness of $E = 0.8$ MPa is applied outside the region of local stiffness variation.

in velocity profile is the likely cause of the discrepancy between the OSI values quoted in the literature and those determined here. The inclusion of an elastic-wall drastically changes the distribution of OSI. At the proximal neck the OSI reaches 0.38 and at the distal neck it dips as low as 0.04. This implies that the proximal neck is more prone to reverse flow and the distal neck is dominated by forward flow. Such local variation of the OSI away from the healthy range (0.32-0.42) at the proximal and distal necks may lead to endothelial cell damage in these locations. The locations of high wall shear stress gradients correspond strongly with the extreme values of OSI.

8.5.6 Effects of stiffened band thickness

The results presented in § 8.5.5 focus on the effect of varying the local stiffness of a band of material at the centre of the elastic region of the aorta. The results were discussed

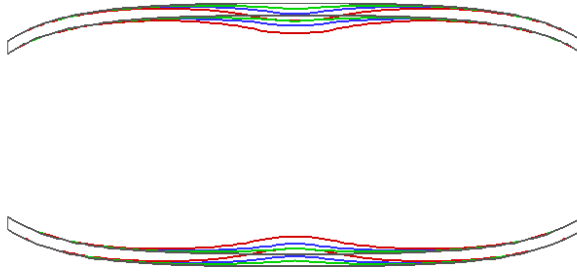


FIGURE 8.32: Wall displacement, exaggerated by a factor of 5 for visualisation. Grey lines show the case of a uniform healthy artery stiffness of 0.8 MPa; green, blue, and red lines represent the case of a 6.0 MPa stiffened region with thicknesses of $0.2d$, $0.4d$ and $0.8d$, respectively.

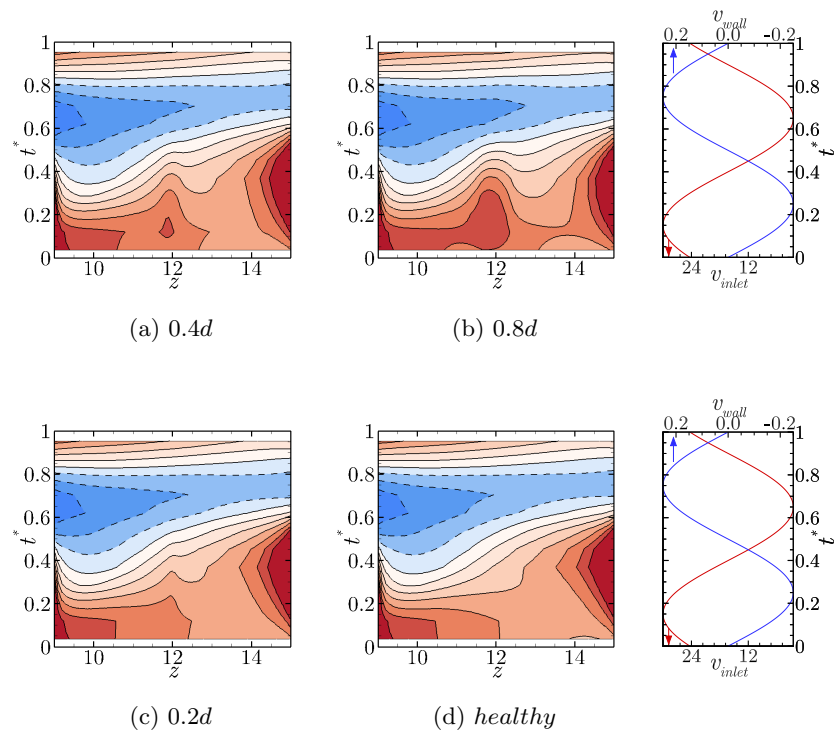


FIGURE 8.33: The variation of wall shear stress (WSS) in a straight pipe as a function of both time and space. Contours show WSS with high low levels represented by red and blue, respectively. Negative values are represented by dashed contour lines. The contour levels are equispaced and vary from -3 Pa to 3 Pa. Sub-plots (a)-(c) represented the WSS in a straight pipe with a locally stiffened zone (6.0 MPa) of thickness $0.4d$, $0.8d$ and $0.2d$ respectively. Sub-plot (d) shows the uniform healthy stiffness case. The figures on the right show the velocity inlet (red) and wall velocity (blue) as a function of time. A negative wall-normal velocity indicates that the wall is expanding.

in relation to the magnitude of the wall displacement and velocity in both a global and local context. This section focuses on the affect that varying the thickness of the stiffened region has on the wall shear stress distribution in the aorta.

Three scenarios were tested, those relating to a stiffened band of width $0.2d$ (presented in § 8.5.5), $0.4d$ and $0.8d$. Each scenario consisted of a constant stiffness of 0.8 MPa outside of the local stiff zone and 6.0 MPa in the stiffened zone. Comparison is made to an elastic artery case. Figure 8.32 shows the displacement of each of the scenarios relative to an artery with uniform stiffness. As the thickness of the stiffened region is increased the outward displacement at the centre of the stiffened region is decreased forming a more stenotic geometry (Note: the stenotic shape forms as a result of the smaller expansion of the stiff band relative to the surrounding material. At subsequent times such as peak diastole the artery forms a straight pipe shape). Associated with this reduced wall motion in the vicinity of the stiffened band is a global reduction in the total wall motion. This is expected as a greater proportion of the wall is less susceptible to changes in pressure. The increase in the stiffened band thickness is analogous to a localised increase in the wall stiffness in that both create an exaggeration of the wall motion effect.

Figure 8.33 shows contours of the variation in wall shear stress in the elastic region of interest through time. In figure 8.33(d) the case of an artery with a uniform stiffness is presented. As discussed in § 8.5.5 a region of high shear stress is present around the proximal neck at peak systole and a low wall shear stress region forms around the distal neck around peak diastole. For an elastic-walled artery, the wall shear stress distribution through time is driven more by the wall velocity (in phase with the pressure wave) than the inlet velocity waveform. This is a result of the spatial variation of the wall shear stress being directly related to a change in the wall geometry. Changes in the wall geometry occur as a result of the changing pressure conditions felt by the artery wall.

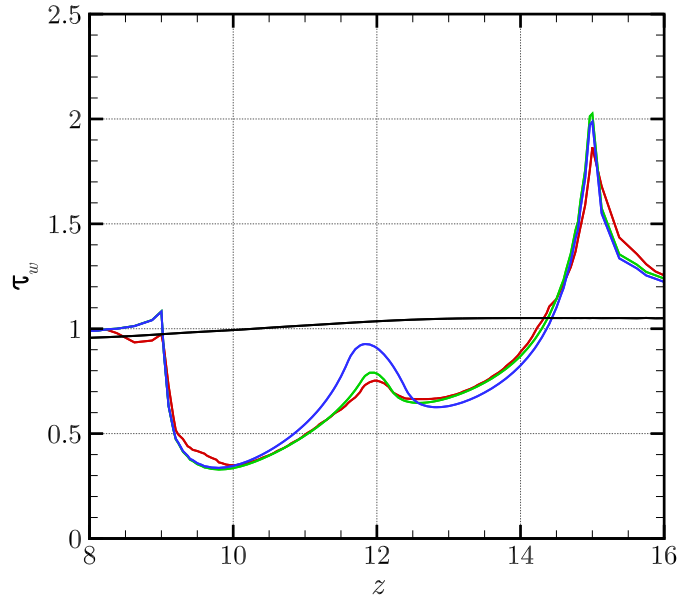
Figure 8.33(c) shows the case of a wall with a stiffened band of size $0.2d$ centred around $z = 12$. Along the line of constant position at this stiffened location, is a localised increase in wall shear stress. Figures 8.33(a) and 8.33(b) show the case of a stiffened band of thickness of $0.4d$ and $0.8d$ respectively. The presence of the increased stiffness region size is reflected in a more pronounced wall shear stress increase along the $z = 12$ position as the thickness of the stiffened region increases.

In conjunction with the localised increase in wall shear stress, as the size of the stiffened region increases, the width of the region of increased wall shear stress also increases. This is a result of the wider stiffened region causing a wider section through which the fluid velocity is high with a thinner boundary layer. Furthermore, the increased thickness of the stiffened region reduces the overall motion of the wall, both the high and low wall shear stress regions extend further along the artery wall from the proximal and distal necks. This is approaching the banded contour profile seen in figure 8.26(a) for a rigid-walled case. As the thickness of the stiffened region increases, the global displacement of the artery wall decreases; the geometry of the wall is closer to that of the rigid-wall case.

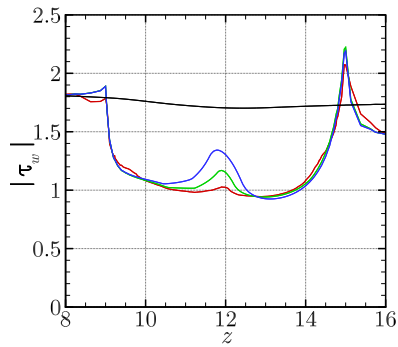
Further supporting this finding is figure 8.34, which shows the time-averaged wall shear stress in the elastic artery. As the thickness is increased the wall shear stress at the thickened location increases both in peak value and in the width of the increased region. In this way, the larger stiffened zone has a greater local effect on the wall shear stress distribution in the artery. Furthermore, the increase in wall shear stress localised around the variation in stiffness is greater for the thickest stiffened region, this correlates well with the case of a greater wall displacement gradient. The greater wall displacement gradient leading to the centre of the stiffened region corresponds to an $R^* < 1$. Equation 8.49 shows that this corresponds to a thinning of the boundary layer and an increase in the wall shear stress. After the stiffened region the wall shear stress decreases again as the flow exits the stenotic geometry and $R^* > 1$. Interestingly, the case in which the thickest region is the widest corresponds to a lower wall shear stress in the downstream region. This occurs despite the reduced global wall motion which would suggest a greater wall shear stress in this region as the flow is more attached to the walls and the wall velocity is affecting the boundary layer less. This indicates that the wall displacement gradient has a greater impact on the wall shear stress than the change in flow rate associated with a greater wall motion. Equation 8.49 supports this finding as it shows that

$$\tau_{WSS} \propto \frac{1}{R^{*4}} \propto Q^*.$$

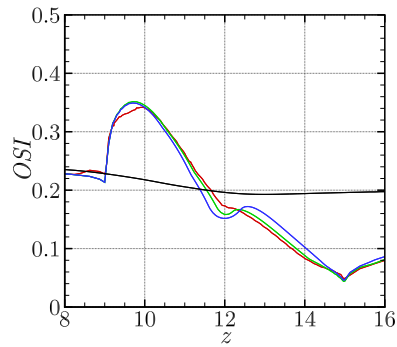
The fourth-order dependence on the radius implies that small changes in the radius of the vessel will lead to greater changes in the wall shear stress than small changes in flow rate. Similar trends are also observed in the wall shear stress magnitude (figure 8.34(b)) and the oscillating shear index (figure 8.34(c)) in which the thicker wall



(a)



(b)



(c)

FIGURE 8.34: Comparison of time-averaged wall shear stress, (a), time-averaged wall shear stress magnitude, (b), and oscillating shear index, (c), with varying wall stiffened region thickness. The black line represents the rigid-walled reference case; red, green, and blue lines represent the cases with a local variation in wall stiffened region thickness of $0.2d$, $0.4d$ and $0.8d$ respectively. Note: for the elastic-walled cases a stiffness of $E = 0.8$ MPa is applied outside of the stiffened region which has a stiffness of $E = 6.0$ MPa.

stiffness exaggerate the trends observed when increasing the stiffness.

Increasing the thickness of the local variation in wall stiffness has been shown to increase the local effect of the variation in wall stiffness. This trend was established for all stiffened region sizes studied. These results may not hold true as the size of the stiffened region exceeds 50% of the total elastic zone. In this case, the wall geometry may differ substantially from those formed in this study. Investigations into larger stiffened regions is beyond the scope of this work which is limited to analysing the effect of a localised lesion or calcification on aneurysm formation.

8.5.7 Flow in an expanded pipe with a rigid-wall

Much of the discussion in sections 8.5.5 and 8.5.6 has revolved around a local change in shape as a result of the wall motion causing a change in the wall shear stress distribution. This, in combination with the additional wall-normal velocity, is responsible for the variation in wall shear stress in an elastic-walled pipe. In this investigation flow through an expanded pipe is simulated in order to isolate the effect that the geometry change has on the flow dynamics. In order to perform this simulation the geometry formed by the uniform stiffness elastic-walled case at peak systole was captured and the identical velocity inlet and pressure outlet conditions applied with the wall position fixed.

Figure 8.35 shows contours of the variation in wall shear stress in the elastic region of interest through time. It is striking how similar the wall shear stress distribution in the expanded rigid-wall case looks in comparison to the uniform elastic-walled case. Both exhibit the high wall shear stress region at the proximal neck at peak systole and a low negative wall shear stress region at the peak diastole. Again, equation 8.49 supports this finding as the fourth-order dependence on the radius implies small changes in the radius of the vessel will lead to greater changes in the wall shear stress. The subtle differences appear in the timing of the extrema in wall shear stress. For the rigid-walled expanded case the peak values coincide with the peaks in inlet velocity waveform, just as in the rigid-walled case. In contrast to this the wall shear stress distribution of the elastic-walled cases follows the phase of the pressure waveforms. This indicates that while the spatial distribution of wall shear stress is largely driven by the geometry of the wall, the temporal distribution is dependent on the velocity of the wall itself.

Figure 8.36 compares the time-averaged wall shear stress, wall shear stress magnitude and oscillating shear index in elastic arteries to an expanded rigid artery. The

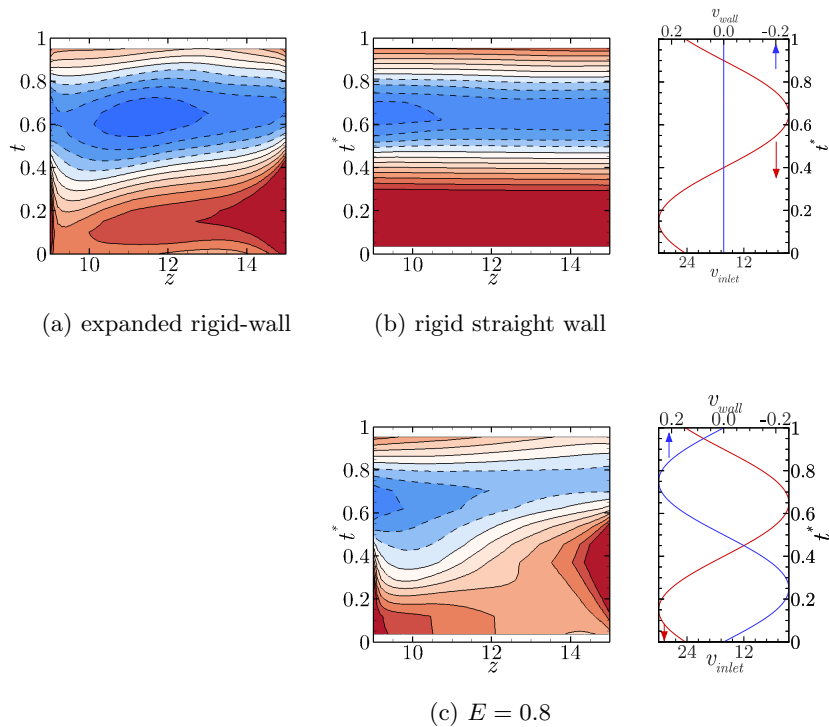
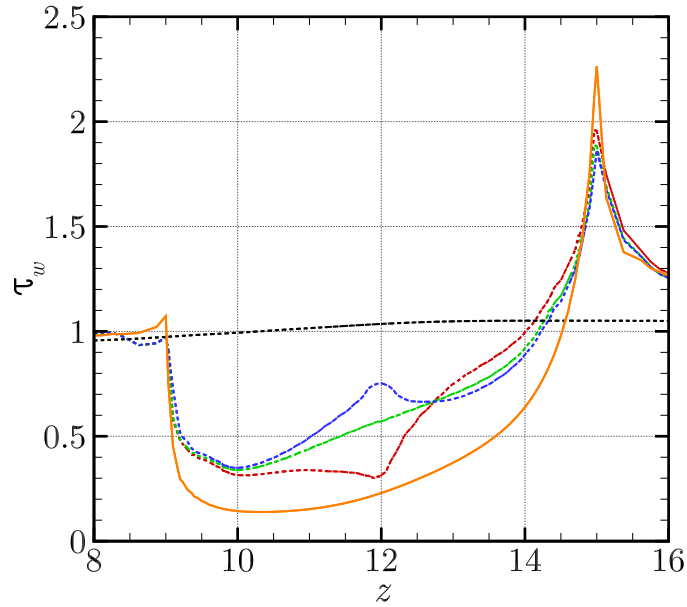
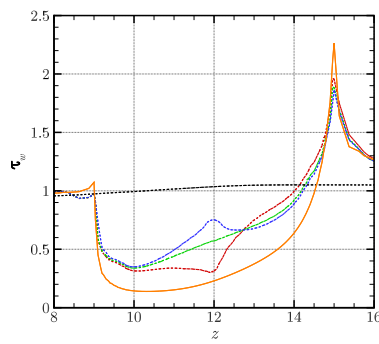


FIGURE 8.35: The variation of wall shear stress in an expanded rigid pipe as a function of time and space. Contours show WSS with high low levels represented by red and blue, respectively. Negative values are represented by dashed contour lines. The contour levels vary from -3 Pa to 3 Pa . Sub-plot (a) represents the expanded rigid pipe case, (b) represents the straight rigid pipe case and (c) represents the healthy elastic-walled case. The figures on the right show the velocity inlet (red) and wall velocity (blue) as a function of time. A negative wall-normal velocity indicates the wall is expanding.

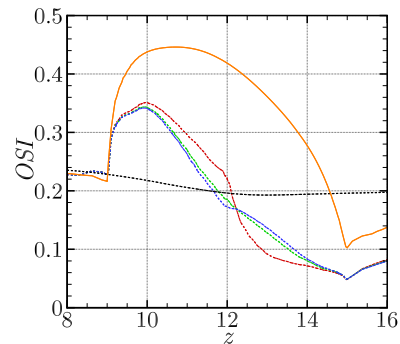
profile of the time-averaged wall shear stress distribution for the expanded rigid pipe case is very similar to the distribution in the elastic arteries. With a rigid-wall and the expanded geometry, the reduction in wall shear stress is more pronounced along the length of the expanded region and the peak wall shear stress at the proximal neck is greater. This occurs because the rigid-walled expanded case maintains the most extreme wall geometry for the entire time cycle. As such, it is subject to the most adverse wall gradients throughout the entire time period, and as a result the wall shear stress pattern is more extreme (i.e. for the entire time period the spatial acceleration and deceleration at the distal and proximal necks, respectively, is at their largest for the entire time cycle). In the elastic-walled case these spatial gradients occur at this order of magnitude only transiently. This is evidence that it is the change in geometry which



(a)



(b)



(c)

FIGURE 8.36: Comparison of (a) time-averaged wall shear stress, (b) time-averaged wall shear stress magnitude, and (c) oscillating shear index, with varying wall shape. The black line represents the rigid-walled reference case; red, green, and blue lines represent cases with an elastic-wall with local wall stiffness of $E = 0.2$ MPa, 0.8 MPa (healthy) and 6.0 MPa respectively. The orange line represents the case of a rigid-walled expanded artery. Note: for the elastic-walled cases a stiffness of $E = 0.8$ MPa is applied outside of the region of stiffness variation.

is the leading factor in defining the wall shear stress distribution throughout the artery.

The wall shear stress magnitude in figure 8.36(b) exhibits a substantially different trend for the rigid-walled expanded case. After the initial decrease in time-averaged wall shear stress magnitude at the distal neck, it retraces 50% of the reduction in wall shear stress before reaching the centre of the expanded region at $z = 12$. Around this central point there is a brief plateau in the wall shear stress magnitude before the substantial increase in wall shear stress magnitude at the distal neck. The increase and decrease in the wall shear stress at the distal and proximal necks, respectively, matches the results for an elastic-walled artery well as well as the analytical expressions described in § 8.5.5.1. This indicates that in these regions where the change in wall geometry is greatest, the spatial acceleration is the dominant cause of the change in wall shear stress. As mentioned in the discussion of the rigid-wall expanded artery wall shear stress results the greater time-averaged wall shear stress change in these locations can be attributed to the expanded geometry remaining constant throughout the time period rather than only forming transiently. In the central region after the flow has reattached to the wall, the shape does not change significantly. In this relatively uniform diameter section the flow is able to adopt a close approximation of the Womersley profile. As such it exhibits periods of reverse flow in the boundary layer (see figure 8.12); such periods of reverse flow are suppressed in the moving-wall cases (see figure 8.13). This leads to a greater wall shear stress magnitude in the expanded rigid-walled case throughout the centre of the expanded region. The suppression of the reverse flow in the moving-walled case is most prominent in the centre of the arterial bulge, suggesting it is directly related to the velocity of the wall which is greatest in the central region.

The results of the oscillating shear index presented in figure 8.36(c) support this analysis of the wall shear stress magnitude, as it shows that the shear index is much closer to 0.5 (completely oscillating flow about a mean of zero) near the centre of the deformed region. Note the peak in OSI is highest near where the minima in wall shear stress occurs. This location corresponds to the location where the wall displacement gradient reaches its maximum.

8.6 Closure

It is well documented that the structural function of the intimal endothelial layer is sensitive to local haemodynamic parameters. Experiments, in which the temporal dis-

tribution of shear stresses applied to the endothelial cells could be carefully controlled, have shown that the endothelial behaviour depends not only on the magnitude of the shear stresses, but also on their spatial and temporal variations (Salsac *et al.* 2006). Many have postulated that the endothelial response mechanisms play a key role in vasoregulation and lesion mitigation in regions of adversely spatially varying wall shear stresses (Nichols & O'Rourke 1990; Fung 1997; Lasheras 2007; Humphrey & Taylor 2008; Sforza *et al.* 2009). As such, the characterisation of the changes in wall shear stress resulting from wall stiffness variations around lesions and sites of disease is essential to understand the initiation process of abdominal aortic aneurysms.

This investigation has made simple comparative measurements of the spatial and temporal distribution of the flow through an elastic artery. Furthermore, it has measured the wall shear stress distribution in the elastic artery and compared the results against rigid-walled models and cases in which a localised variation in wall stiffness is present. This study has shown that the flow inside an elastic artery is characterised by the transient formation of regions of higher and lower wall shear stresses than are found in a rigid-walled artery model. In fact the presence of an elastic wall creates a spatial variation in the wall shear stress which is not present in rigid-walled approximations. On this basis it is reasonable to conclude that rigid-walled models of the healthy aorta are insufficient to accurately describe the wall shear stress environment in the aorta.

The presence of an elastic wall was found to delay the onset and reduce the strength of flow reversal in the boundary layer during the diastolic phase in comparison to rigid-walled models. This result was reflected in the measurements of wall shear stress which exhibited shorter periods of negative wall shear stress in comparison to the rigid-walled models. The motion of the boundary wall dominates the flow dynamics and temporal wall shear stress distribution in elastic cases. This was evident in both the discussion of flow dynamics and the wall shear stress distribution in which a phase shift of 0.1 was detected for the peak values of wall shear stress and axial flow magnitude for the elastic cases. This phase shift matches the phase lag between the velocity inlet and pressure outlet boundary conditions.

In addition to the change in axial velocity, the wall motion was shown to have a profound impact on the wall-normal velocity and boundary layer thickness. The spatial variation of the wall shear stress was shown to develop as a result of the change in wall profile as the elastic wall moved. The expansion of the artery wall caused a diverging

nozzle geometry to form at the proximal neck and a converging nozzle to form at the distal neck. The result of this geometry change was a dramatic decrease in the wall shear stress at the proximal neck before an increase in wall shear stress at the distal neck beyond what is encountered in a rigid-walled model. The diverging-converging nozzle shape causes a spatial acceleration of the fluid in order to conserve mass flow rate. This is associated with a change in local velocity and consequently a change in the local Reynolds number and boundary layer thickness. A change in the boundary layer thickness causes an increase in strain-rate in the case of boundary-layer thinning and a decrease in strain-rate in the case of boundary-layer thickening. The change in boundary layer thickness can therefore be directly attributed to the changes in wall shear stress. The transient nature of the wall further compounds these effects as the changing luminal volume causes an increase or decrease in the flow rate at the distal neck.

It was found that local variations in the wall stiffness slightly affected the wall shear stress distribution in the artery. On a global scale, a local increase in the wall stiffness decreased the peak dilation of the wall, conversely a decrease in stiffness increased the peak dilation. Global changes in the wall dilation affect the peak wall shear stress at the distal neck as a smaller volume change occurs leading to lower peak flow rate through the distal neck and consequently lower levels of wall shear stress. Local effects were also associated with the local change in wall stiffness. A departure from the uniform ballooning shape was clearly evident; stiffer sections caused a localised stenotic geometry while weaker walls formed an exaggerated ballooning at the stiffness variation location. Such changes in geometry led to similar wall shear stress changes as the locally changed wall gradient caused flow to detach from the wall when the wall was diverging and a thinning of the boundary layer when the wall gradient was converging.

This investigation aimed to address aim 2c and determine how a heterogeneous wall stiffness affects the haemodynamics in the context of aneurysm initiation. The original hypotheses outlined in § 1.8.3 are supported by the findings of this investigation. It was shown that local variations in the wall stiffness caused local variations in the wall shear stress distribution in the artery. A stiffer artery was shown to create a geometry similar to a stenosis which caused a local variation in the wall shear stress distribution. Similarly, the reduction in wall stiffness led to the extra ballooning of the artery in the local region which was shown to reduce the local wall shear stress at that location. In

terms of the final hypothesis relating to the width of the stiffened region, the results showed that an increase in the width of the local stiffened region led to an exaggeration of the haemodynamic changes. This is contrary to the initial hypothesis in which it was believed a less adverse flow condition would result from the increased thickness. The reason for this is that the increased width acts to exaggerate the geometry formed by the artery wall under pressure rather than reducing the wall gradients as was hypothesised.

In terms of the initiation of aneurysms, these results show that the wall shear stress distribution in an artery is very complex. Previous studies that have focused on rigid-walled models are likely to have underestimated the maximum and minimum wall shear stress in a healthy artery. Large variation in the wall shear stresses are present around the proximal and distal neck of the artery where tethering causes large variation in wall shapes. Localised lesion or stiffening in the centre of an artery can alter the wall shear stress distribution both local to the lesion and throughout the artery. The variation in wall shear stress does not exceed the healthy range described in Salsac *et al.* (2006), however, the results do show that the local variation is substantial in comparison to the local wall shear stress for a healthy elastic artery. The time-averaged wall shear stress was 31% higher for the stiffest case tested and 47% lower for the least stiff case tested. Such variation in wall shear stress may be sufficient to change the local endothelial function of the wall and lead to aneurysm initiation.

Chapter 9

Investigation 2: Haemodynamics and wall shear stress in an established aneurysm

9.1 Introduction

The investigation presented in chapter 8 studied the effect of localised wall stiffness on the haemodynamics in an aorta. It demonstrated the possible link between the local variation in wall stiffness and aneurysm initiation. In this chapter, the haemodynamics of an established aneurysm is considered.

After the formation of an aneurysm the haemodynamics within the bulbous structure are significantly different to those found in a healthy artery. The new complex haemodynamic environment drives the continued growth of the aneurysm through the disruption of the shear sensitive mechanotransduction process. Haemodynamic studies have not been able to show a sufficient peak pressure to cause rupture on a mechanical basis (Steiger *et al.* 1988). Instead aneurysm growth may be understood by a passive fatigue-based yielding to blood pressure and the associated reactive healing of the wall (Sforza *et al.* 2009).

The disruption of the normal mechanotransduction process due to changed haemodynamic stimuli may occur through both high and low wall shear stresses. High wall shear stresses cause endothelial injury (Kondo *et al.* 1997), which initiates wall remodelling and possible degradation. Furthermore, high wall shear stress can cause the over-production of nitric oxide (NO) upon which the endothelium is dependent. This has a variety of effects including altering gene expression and altering the arterial tone and stiffness (Sforza *et al.* 2009). Low wall shear stresses are associated with localised blood stagnation. Stagnation causes a dysfunction in the production of nitric oxide that

leads to a buildup of red blood cells and leukocytes. The aggregation of blood cells can suffocate the arterial wall, starving it of important nutrients leading to cell death and allowing white blood cells and fibrin into the arterial wall which locally degrades the stiffness (Sforza *et al.* 2009). Changes in wall stiffness at regions of high and low wall shear stress will subsequently alter the haemodynamics throughout the aneurysm which may in turn cause a change in the wall remodelling process and wall stiffness in these regions.

Presented in this chapter are the results of an investigation into the haemodynamics in established aneurysms. This study analyses the effect of a non-uniform wall stiffness on the haemodynamics in an aneurysm and subsequently the impact this has on the health of the artery.

This study aims to address aim 2a and 2b from § 1.8: that is, to investigate the effect of a heterogeneous wall stiffness on the haemodynamics in an aneurysm. To this end, blood flow through a typical medium sized fusiform aneurysm is considered.

A wall comprised of three layers with different mechanical properties was simulated. A hyperelastic neo-Hookean constitutive model is used to simulate the wall motion. The effect of wall elasticity on the blood flow through the aneurysm was assessed. To determine which non-uniform distribution of wall stiffness led to the most significant changes in haemodynamics, the stiffness of the wall was varied locally in the distal neck, proximal neck and central bulge region of the aneurysm.

The detailed set of hypotheses relating to this investigation can be found in § 1.8.2.

9.2 Geometry

Figure 9.1 shows the computational domain used for this investigation. It represents blood flow through a medium-sized abdominal aortic aneurysm. A mathematical description of the fusiform bulge shape is provided in § 7.2.2. The aspect ratio is $L/d = 3$, the dilation ratio is $D/d = 2$, and an aortic diameter of $d = 20$ mm was justified in § 7.2.2. Just as with the aneurysm initiation study of chapter 8, the length of the elastic-wall region shown in figure 9.1 is 120 mm (or $6d$). Figure 9.1 shows the macro element mesh used in the meshing of the aneurysm. Gauss–Legendre–Lobatto quadrature points are used to interpolate within each of the macro elements shown. By using these quadrature points a highly accurate fine mesh is formed (see § 9.3 for details of the accuracy).

The elastic region only occupies the central region of the computational domain; with the fluid domain computed both upstream ($9d$) and downstream ($9d$) of this region (see figure 9.1). While this region does not represent anatomical vascular structure, it is included to ensure that the inlet and outlet boundary conditions do not affect the flow in the region of interest. Further details of the choice of inlet and outlet length can be found in § 9.3.2.

Downstream of the elastic region is a flared section leading to the outlet. This section has an inflow velocity boundary condition imposed through the wall. The flare has a length of $3d$ and expands from the pipe diameter d to $1.5d$ at the exit. The reader is referred to section 8.2 for an explanation of the numerical necessity of the flared region.

Hexahedral mesh elements are used to discretise the three-dimensional flow domain. To maximise accuracy in the elastic region where the moving arterial wall introduces multi-dimensional flow dynamics, the mesh is much denser. In this region the mesh elements are approximately $0.2d \times 0.2d \times 0.2d$ (i.e. aspect ratio of unity). Outside of the elastic region, less resolution is required to describe the flow (see § 9.3.3), as such the mesh is coarser.

Figure 9.1(c) shows the solid domain mesh used. This mesh consists of three macro element layers. Each layer corresponds to a single layer in the arterial wall. Details of the layer thicknesses can be found in § 7.4.1. The accuracy of the solid domain mesh is discussed in § 9.3.4.

The established aneurysm investigation involves a local change in wall stiffness. The results presented in § 9.5.4.1, 9.5.4.2 and 9.5.4.3 include a stiffer band of material in the proximal, central, and distal regions respectively. In each case, a third of the aneurysm bulge is stiffened i.e. the stiffened region is $1d$ wide. All three layers of the wall are stiffened by the same amount.

9.2.1 Fluid and solid properties and boundary conditions

The fluid and solid properties and boundary conditions used in this investigation are identical to those used in the aneurysm initiation study of chapter 8. A summary is provided in table 9.1. For further details on the boundary conditions and the justification of the choice of material properties the reader is referred to § 8.2 and chapter 7.

Summary

Fluid property

Dynamic viscosity μ	$3.85 \times 10^{-3} \text{ Pa} \cdot \text{s}$
Density ρ	1060 kg/m^3
Inlet velocity mean \mathbf{v}_{mean}	16.25 cm/s
Inlet velocity peak \mathbf{v}_{peak}	30 cm/s
Outlet pressure systolic \mathbf{P}_{sys}	120 mmHg
Outlet pressure diastolic \mathbf{P}_{dia}	70 mmHg
Phase lag (velocity-pressure)	0.1 s
Heart rate (period) T	1 s
Time-averaged Reynolds number Re_{mean}	410
Peak Reynolds number Re_{peak}	750
Womersley number α	9.67

Fluid boundary condition

Inlet	Pouisseule profile (Finol <i>et al.</i> 2003b)
Outlet	Time varying pressure (Mills <i>et al.</i> 1970)
Walls	no-slip
FSI interface	$\mathbf{v}_f = \mathbf{v}_s$
Flared inlet	$v_t = 4 - 2 \cos(2\pi t)$

Solid property

Stiffness (healthy) E_{mean}	0.800 MPa
Aneurysm stiffness range	$0.200\text{-}6.000 \text{ MPa}$
Density ρ_s	1160 kg/m^3

Solid boundary condition

Inlet and outlet	Fixed, i.e. $\mathbf{u} = (0, 0, 0)$
Perianeurysmal environment	$P_{ext} = P_{dia} - 0.2 \frac{P_{peak} - P_{dia}}{2} \cos\left(\frac{2\pi}{T}t\right)$
FSI interface	$\sigma_s \cdot \mathbf{n} = P_f$.

TABLE 9.1: Summary of the properties and boundary conditions used in the aneurysm investigation.

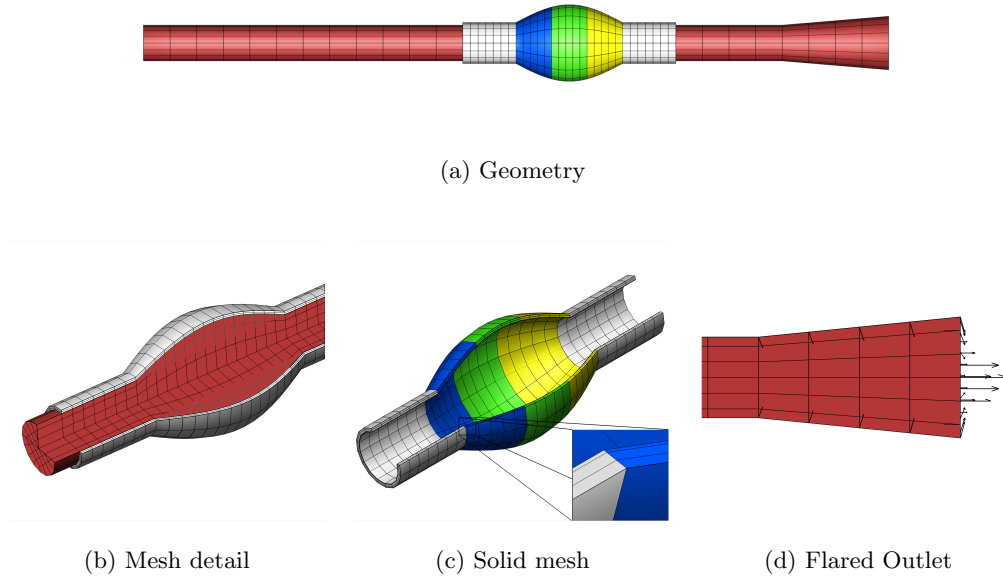


FIGURE 9.1: Mesh detail used in aneurysm investigation, blood flows from left to right. (a) shows macro elements in the entire computational domain. Red regions represent blood flow, the blue region is the proximal region to be stiffened, green is the lumen region and yellow is the distal region. (b) shows a detailed cross-section of the mesh, clearly visible is the cube-shaped elements in the fluid region and the thinner layer of solid elements. (c) shows a detailed cross-section of the solid mesh with its three macro element layers. The outlet flare with vectors representing the inlet boundary conditions and outflow at the end is shown in (d).

9.3 Solution validation

Rigorous validation of the numerical techniques, domain size, and mesh independence were conducted as part of this research. The numerical techniques developed in this thesis are validated in chapter 6. This section mimics the mesh optimisation and independence studies presented in § 8.3 for the aneurysm geometry shown in figure 9.1. Subsection 9.3.1 describes the mesh optimisation analysis that determined the most efficient meshing strategy. Any boundary condition effects were negated in the domain analysis (see § 9.3.2), ensuring a physiologically accurate solution was simulated. Sections 9.3.3 and 9.3.4 establish the level of spatial accuracy of the mesh. Finally, the accuracy of the temporal discretisation will be examined in § 9.4. As indicated in 8, an error threshold of $< 1\%$ for global error measures and $< 2\%$ for local error measures was used to direct the choice of spatial and temporal resolution; and domain size.

9.3.1 Mesh optimisation and p -type refinement

As discussed in § 8.3.1, the spectral- hp element method allows both h -type and p -type refinement of a computational mesh. To determine the most time efficient mesh for a prescribed level of accuracy, a mesh optimisation analysis was performed.

The four meshes created for the mesh optimisation study were based on the same meshing strategies used in § 8.3.1. Each mesh shown in figure 9.2 employed a different level of h -type refinement. Mesh 1 in figure 9.2(a) uses the strategy of very few macro elements. Such a mesh requires a higher polynomial order, p , to attain spatial convergence. Conversely, Mesh 4 employs a large number of macro elements; this allows a smaller polynomial order to be used to attain spatial convergence. Meshes 2 (figure 9.2(b)) and 3 (figure 9.2(c)) employ intermediate levels h -type refinement.

The optimisation study involved completing a p -type grid independence study for each mesh. This follows the methodology outlined in § 8.3.1. Global and local flow measurements were taken to assess the spatial resolution of each mesh at each level of p -type refinement. The L_2 -norm is used to measure the overall difference between the solutions from different meshes and resolutions. Local variations in the solutions are observed by monitoring v_z , the z -component of velocity, and the strain-rate-magnitude at a point within the global domain. The time taken for the simulation to run was also recorded to give an indication of the computational cost associated with each meshing strategy. In the results presented in figure 9.3, these parameters are sampled along the centreline at the midpoint of the aneurysm bulge, $(x, y, z) = (0, 0, 12D)$.

The results presented in figure 9.3 show the p -type grid independence studies conducted for each mesh. As expected, as the polynomial order is increased for each mesh the solution converges to a consistent value. Meshes 1 and 3 exhibit some numerical wiggle in the strain-rate-magnitude data. The sparse nature of these two meshes meant they were run at higher polynomial orders compared with Mesh 4. Mesh 4 exhibits stable convergence behaviour in both global and local error cases. Table 9.2 provides a numerical estimate of the error associated with each mesh. The error is calculated relative to the most resolved case for each mesh. The assumption is made that each mesh has reached a mesh independent state at the highest resolution case. The data presented in table 9.2 supports the results shown in figure 9.3. As the polynomial order is increased the error in each case decreases. In all cases the error is small (error < 2%) for the more resolved cases. The smallest error is observed in the global L_2 -norm error

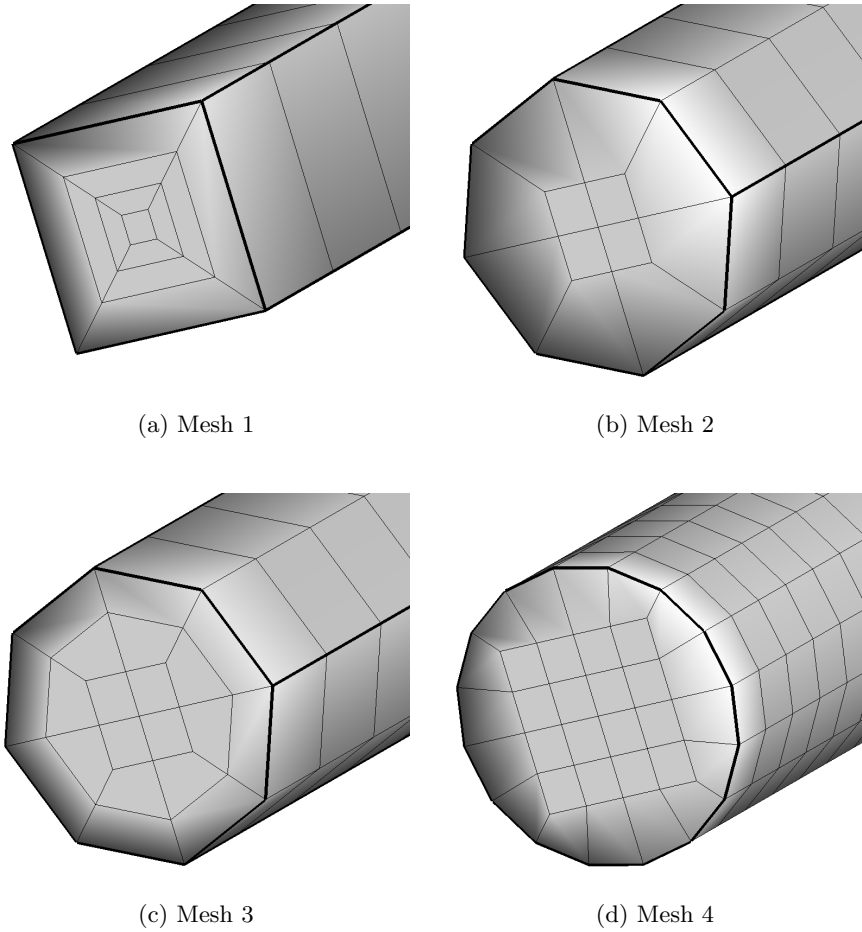
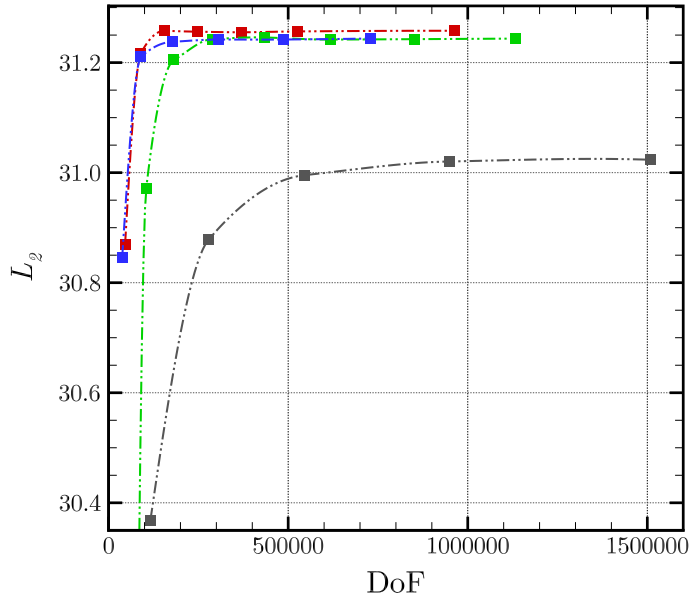


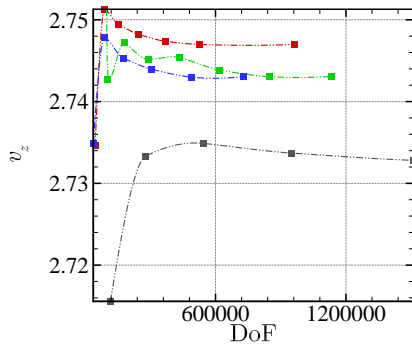
FIGURE 9.2: Macro element meshes used in mesh optimisation investigation. Meshes 1-4 show an increasing level of h -type refinement. The meshes were created by linking successive 2D planes of elements. To ensure accuracy at the boundary element, depth (plane spacing) was set to match the width of the element closest to the boundary. Note: a curvilinear mapping of the element faces onto the circular pipe is used - the flat faces depicted on the pipe walls here is a product of the plotting package used, which accentuates the poor representation of the geometry at the limit of small p -type resolution.

estimate, with error converging to less than $10^{-3}\%$. The greatest error was observed in the strain-rate-magnitude as is expected with the use of C^0 -continuous elements.

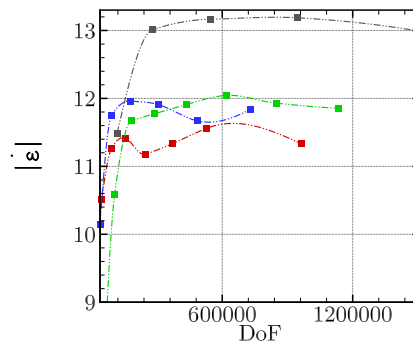
A dominant feature of figures 9.3(a) and 9.3(b) is Mesh 4 converging to a different value than the other meshes. The maximum difference between Meshes 1-3 and Mesh 4 was 0.75% in L_2 -norm, 0.51% in v_z and up to 12.7% in strain-rate-magnitude. The larger difference in strain-rate-magnitude data is a result of the higher number of C^0 -continuous elements in Mesh 4, producing a smoother first-order vector field. In the mesh optimisation study for the aneurysm initiation study such a difference was not



(a)



(b)



(c)

FIGURE 9.3: Results of the p -type grid independence study for each mesh 1-4 shown in figure 9.2. In each sub-plot red, green, blue and gray lines and symbols represent meshes 1, 2, 3 and 4 respectively. For all sub-plots and meshes as the number of degrees of freedom (polynomial order) is increased the mesh solution converges to a stable value. (a) shows the L_2 -norm, a global measure of energy in the solution. (b) shows the v_z velocity component at a point along the centre line of the pipe and (c) shows the magnitude of strain rate at a point on the pipe centreline. All values were taken at time of peak energy.

% error						
p	Mesh 1			Mesh 2		
	L_2	v_z	$ \dot{\epsilon} $	L_2	v_z	$ \dot{\epsilon} $
5	1.23	0.45	7.23	14.11	21.21	40.94
6	0.12	0.156	0.66	0.86	0.01	10.76
7	6.5×10^{-6}	12.94	0.69	0.12	0.14	1.52
8	5.3×10^{-3}	12.68	1.35	2.3×10^{-3}	0.07	0.67
9	8.6×10^{-3}	3.02	6.6×10^{-3}	6.6×10^{-3}	0.08	0.44
10	3.6×10^{-3}	2.19	1.98	5.7×10^{-3}	0.02	1.59
12	0.0	0.0	0.0	0.0	0.0	0.0

p	Mesh 3			Mesh 4		
	L_2	v_z	$ \dot{\epsilon} $	L_2	v_z	$ \dot{\epsilon} $
4	1.27	0.29	14.3	2.11	0.63	11.54
5	0.11	0.17	0.77	0.46	0.01	0.17
6	0.02	0.08	1.02	0.08	0.07	1.38
7	5.8×10^{-3}	0.58	0.24	9.8×10^{-3}	0.03	1.53
8	5.7×10^{-3}	1.45	0.28	0.0	0.0	0.0
9	0.0	0.0	0.0	-	-	-

TABLE 9.2: Percentage error in each mesh when compared to the most resolved case. Error is shown for global measures (L_2 -norm) and local measures (v_z and $|\dot{\epsilon}|$).

featured. The bulge in the aneurysm geometry causes a more complicated flow pattern that is not completely dominated by flow in the axial direction; as such resolution in the x - y plane is paramount. While the percentage difference between the meshes is small (for L_2 -norm and v_z) justification for the difference is required.

The numerical solver used in this investigation is capable of solving flow through non cube-shaped elements through the use of a curvature routine that applies a smooth curve passing through the macro element nodes on a specified curved boundary. The routine then places the Gauss–Legendre–Lobatto quadrature nodes at appropriate locations on the curved boundaries so as to preserve the third-order accuracy. The algorithm used to predict the curvature fits a circle to subsequent sets of three macro element nodes. It fits this circular curvature to each set of neighbouring nodes on the curved boundary in all three directions. The routine then applies a blending operation to provide a smooth curve across the entire boundary.

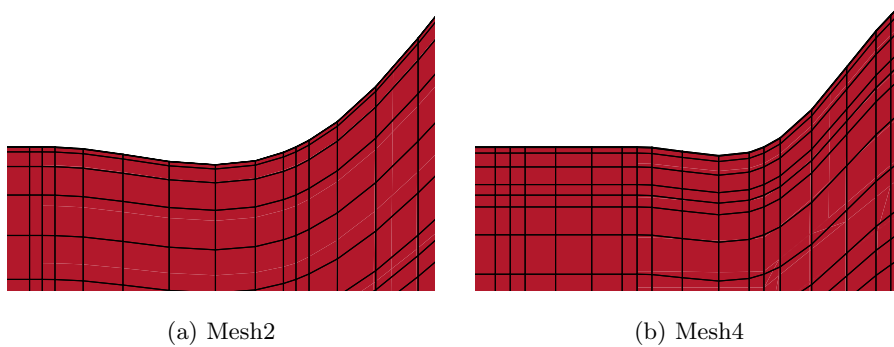


FIGURE 9.4: Curvature at the proximal neck generated using the two different meshing strategies.

The spacing of the macro nodes is paramount to the accuracy of the curvature routine. If macro nodes are spaced differently between meshes the curve approximated will also differ. This numerical artefact is prevalent in this mesh optimisation study. Figure 9.4 shows a slice through the proximal neck region for Mesh 2 and Mesh 4. These images demonstrate that the curvature of the neck region is different in each case. It is clear from this figure that a smaller region is affected in Mesh 4 as a result of the smaller macro element mesh size in the axial direction.

The different geometry will affect the way the characteristic aneurysm vortex is shed, and hence the flow structures in general (Sheard *et al.* 2007). This is one reason for the difference observed between meshes. This concept is supported by Mesh 2 and 4 which have identical axial element sizes and therefore curvatures. These two meshes produce very similar grid independent results. A further confounding factor is the dependence of the L_2 -norm on domain size. Figure 9.5 shows the volume of each mesh at each polynomial order. The variation in mesh volume with each mesh is clear. Mesh 4 has a 0.11% smaller volume than that of the analytical volume, and Mesh 1 has a 0.91% smaller volume than the analytical volume. This correlates well with figure 9.4. This figure shows that Mesh 4 reproduces the analytically prescribed curve with much greater accuracy and as a result it is the best candidate for the aneurysm study.

Despite the superiority in Mesh 4 in relation to reproducing the analytical geometry, an attempt is made to reconcile the solution produced by each mesh. To account for

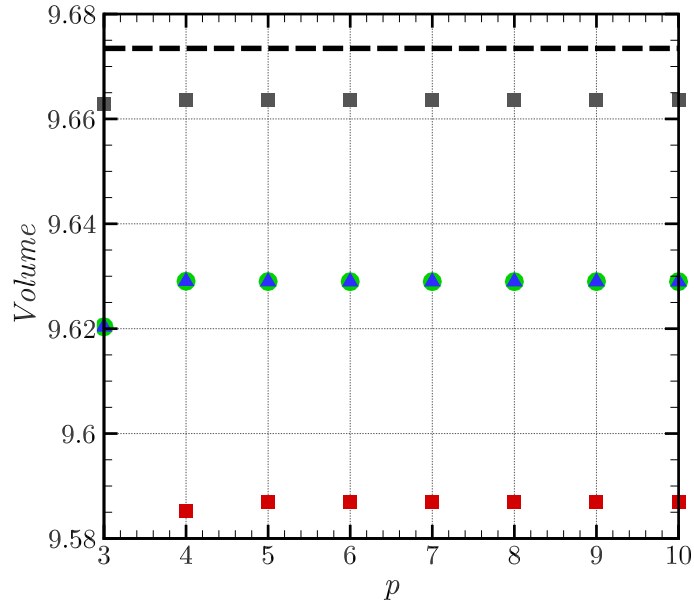
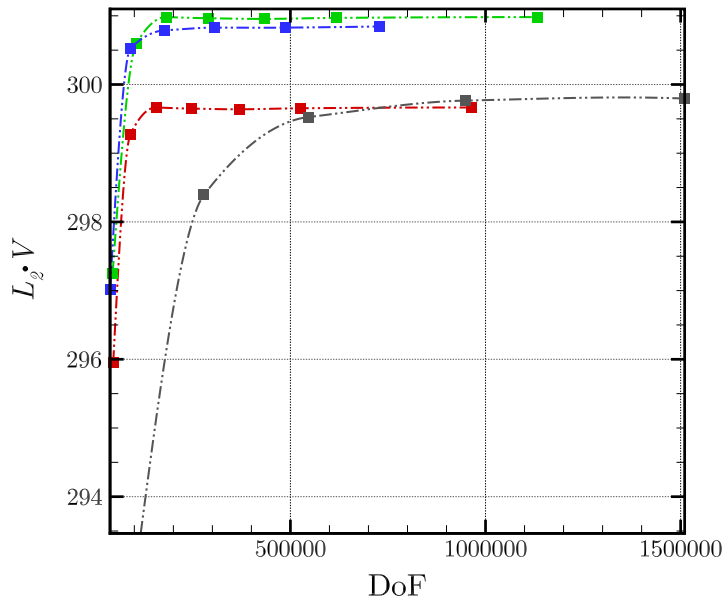


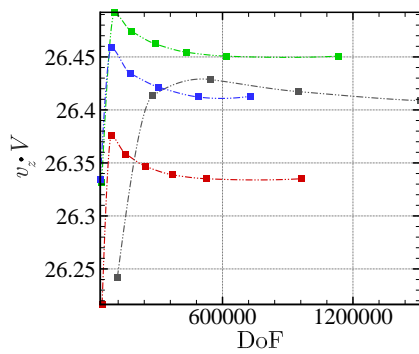
FIGURE 9.5: Volume of each mesh plotted as a function of increasing polynomial order. red, green, blue and grey symbols represent meshes 1, 2, 3 and 4 respectively. The volume that should be achieved using the analytical expression for the curve is 9.67 (shown using the dashed black line). The volume of meshes 1 and 2 is near identical which is to be expected as they have the same spacing between element planes i.e. axial element length. The smaller macro elements in Mesh 4 allow for a more accurate curvature and hence larger volume.

the difference in volume between the meshes the data from figure 9.3 is re-scaled by the volume of each mesh (figure 9.6). The maximum difference in each case is now only 0.35% in L_2 -norm, 0.27% in v_z and up to 8.7% in strain-rate-magnitude down from 0.75%, 0.51% and 12.7% respectively. As expected the greatest improvement came in the volume dependent L_2 -norm. The remaining difference in these results is a product of the different geometry at the proximal and distal necks affecting the flow characteristics.

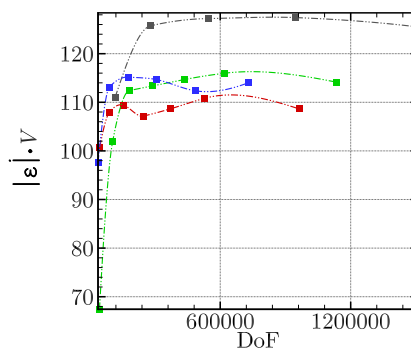
The most appropriate mesh for the aneurysm study provides a grid independent solution at the lowest computational cost. Figure 9.6 and table 9.2 showed each meshing strategy is capable of producing a spatially resolved mesh. Figure 9.7 shows the physical time taken to complete 100 time steps (t_{100}) in the solver for each mesh at each level of resolution. This clearly shows that Mesh 4 which is based on more macro elements and a relatively low polynomial order is more efficient than the other meshes.



(a)



(b)



(c)

FIGURE 9.6: Results of the p -type grid independence study for each mesh 1-4 shown in figure 9.2 with volume adjustment. In each sub-plot red, green, blue and gray lines and symbols represent meshes 1, 2, 3 and 4 respectively. For all sub-plots and meshes as the number of degrees of freedom (polynomial order) is increased the mesh solution converges to a stable value. (a) shows the L_2 -norm a global measure of energy in the solution. (b) shows the v_z velocity component at a point along the centre line of the pipe and (c) shows the magnitude of strain rate at a point on the pipe centreline. All values were taken at time of peak energy.

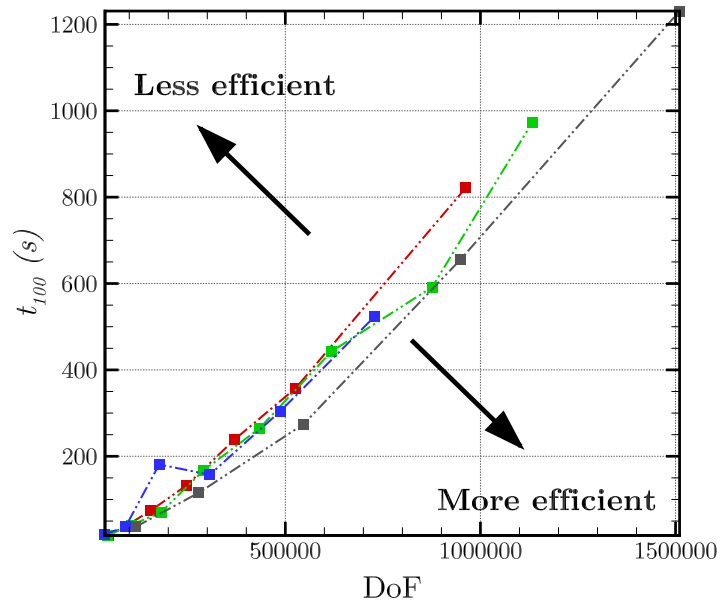


FIGURE 9.7: Simulation time required to complete 100 time steps, t_{100} , is plotted with respect to the number of degrees of freedom for each simulation. As in figure 9.3, red, green, blue and grey lines and symbols represent meshes 1, 2, 3 and 4 respectively. A more efficient simulation has a shorter run time at higher resolution. Mesh 4 is the most efficient mesh.

Figure 9.6 and table 9.2 present a clear case that using all of the meshes a grid independent solution can be achieved. Mesh 4 with the use of relatively low polynomial orders provides the most stable, accurate and efficient solution. Furthermore, figures 9.4 and 9.5 demonstrate that of all the meshes, Mesh 4 is least affected by the curvature routine. As such, this mesh is used throughout the aneurysm study. In order to minimise the computational cost of this study a polynomial order of $p = 5$ ($DoF = 622080$) is chosen. This level of resolution ensures the mesh is within its mesh independent convergence region, provides less than 0.5% error across both global and local error measurements and limits the computational cost of each simulation.

9.3.2 Domain size

Following the grid-independence methodology outlined in chapter 8, a domain size analysis is conducted for the aneurysm geometry case. To ensure that the blood flow through the region of interest is physiologically accurate it is imperative that the proximity of the boundary conditions do not affect the results. As in §8.3.2, five inlet and

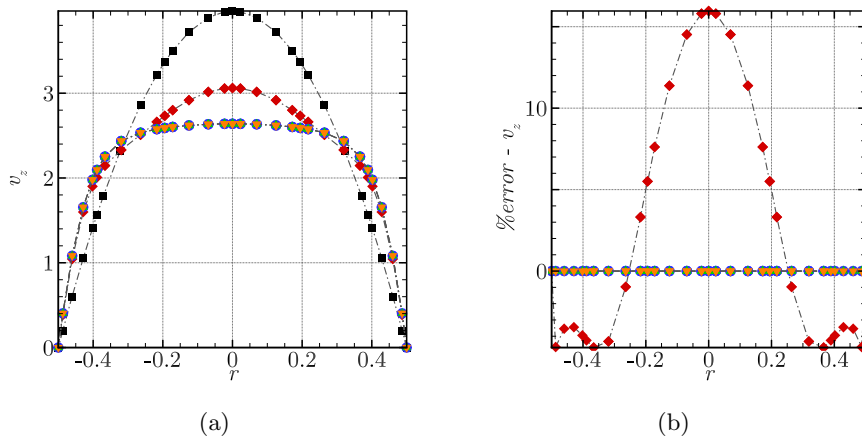


FIGURE 9.8: Velocity profile at the start of aneurysm bulge, velocity is normalised using the period of oscillation and diameter of the vessel. Black squares \blacksquare , red diamonds \blacklozenge , blue circles \bullet , green triangles \blacktriangle , and orange inverted triangles \blacktriangledown represent the profile for an inlet length $0d$, $3d$, $6d$, $9d$ and $24d$ upstream respectively. (a) shows the velocity profile across the pipe diameter and (b) shows the percentage error of each velocity profile relative to the longest inlet case in (a). As the inlet length is increased, the difference in velocity profiles becomes negligible.

outlet lengths were simulated in each case, $0d$, $3d$, $6d$, $9d$ and $24d$.

9.3.2.1 Upstream

Simulations were conducted using a constant outlet length and varying the upstream length. The flow was monitored at a series of points throughout the aneurysm bulge. Figure 9.8(a) shows the velocity profile at the entrance to the aneurysm at $t = 0.5$ s for each of the inlet length cases. For the case of $0D$ upstream the velocity distribution is that of the perfect Poiseuille profile that is described at the inlet. As the inlet length is increased the flow has time to adopt the Womersley profile which is the natural state for oscillating flow. Figure 9.8(b) demonstrates that increasing the inlet length beyond $6d$ yields a negligible change in the velocity profile.

To illustrate precisely the effect of changing the inlet length, figure 9.8(b) plots the error-norm of the axial velocity across the diameter of the pipe at the entrance to the aneurysm. As the inlet length is increased, the change in velocity diminishes dramatically. This correlates well with the velocity profile plots of figure 9.8. The percentage change of flow as a result of varying the inlet length is listed in table 9.3. The inlet length has a greater effect on the peak velocity than in the near-wall region. These

% error		
Inlet length	$r = 0$	$r = 0.35d$
0	50.37	14.67
3	15.96	4.25
6	1.3×10^{-4}	1.5×10^{-4}
9	9.9×10^{-5}	1.2×10^{-4}
24	0.0	0.0

TABLE 9.3: Percentage error of the axial velocity at the centreline and near-wall locations. The error decreases as the inlet length increases.

results show that with an inlet length of $9d$ or greater, the effect of the inlet boundary condition is less than 0.01%. This is sufficiently accurate for this investigation, an inlet length of $9d$ is used hereafter.

9.3.2.2 Downstream

Having established an inlet length of $9d$, a series of simulations were conducted to determine the appropriate outlet length. The inlet length was fixed at $9d$, while the outlet length (including flared region) was varied between $0d$ and $24d$. The flow was monitored at identical locations to the upstream domain study. Figure 9.9(a) shows the velocity profile at the aneurysm bulge outlet at $t = 0.5$ s for each of the outlet length cases. The presence of the aneurysm bulge dramatically changes the flow when compared with the inlet flow and indeed the flow through a straight pipe discussed in chapter 8. Figure 9.9(b) demonstrates that increasing the outlet length beyond $6d$ yields a negligible change in the velocity profile.

Once more, to illustrate the effect of changing the outlet length, figure 9.9(b) shows the error-norm of the axial velocity across the diameter of the pipe at the exit of the elastic region. As the inlet length is increased, the change in velocity diminishes. Table 9.4 shows the percentage error for each outlet length. The impact of the outlet length on the flow is small enough that an outlet length of only $3d$ was chosen for all simulations.

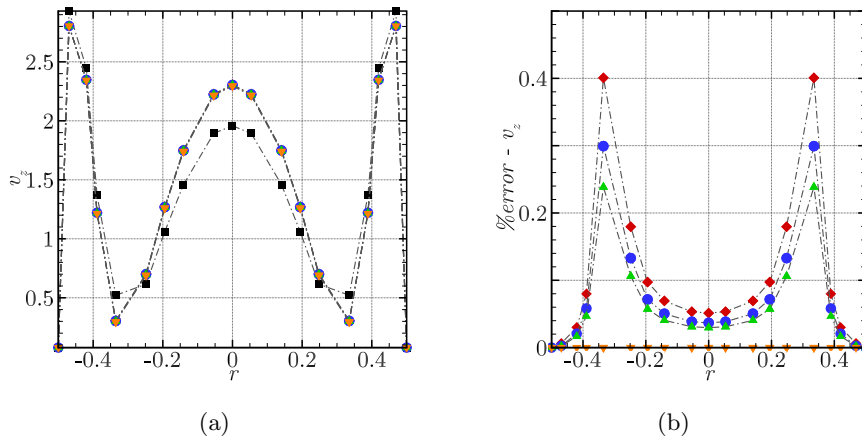


FIGURE 9.9: Velocity profile at end of aneurysm bulge, velocity is normalised using the period of oscillation and diameter of the vessel. Black squares \blacksquare , red diamonds \blacklozenge , blue circles \bullet , green triangles \blacktriangle , and orange inverted triangles \blacktriangledown represent the profile for an outlet length $0d$, $3d$, $6d$, $9d$ and $24d$ downstream respectively. (a) shows the velocity profile across the pipe diameter and (b) shows the percentage error of each velocity profile relative to the longest inlet case in (a). As the outlet length is increased, the difference in velocity profiles becomes negligible.

% error		
Outlet length	$r = 0$	$r = 0.35d$
0	1.46	7.67
3	5.1×10^{-2}	0.40
6	3.6×10^{-2}	0.29
9	2.9×10^{-2}	0.23
24	0.0	0.0

TABLE 9.4: Percentage error of the axial velocity at the centreline and near-wall locations. The error decreases as the outlet length increases.

h_z	% error
$1.0d$	0.482
$0.5d$	0.217
$0.33d$	0.137
$0.25d$	0.109
$0.2d$	0.101
$0.167d$	0.103

TABLE 9.5: Percentage error in the L_2 -norm with reference to a theoretical 100% accurate case defined using a Richardson extrapolation. The error decreases as the element length decreases.

9.3.3 h_z -type refinement

Having completed the p -type grid resolution study, a further h_z -type analysis was conducted in an effort to reduce the computational cost (see similar study conducted in § 8.3.3). Efficiency gains may be made by reducing the resolution of the mesh in regions where the flow is relatively constant.

This h_z -type analysis endeavoured to determine the minimum required resolution in the axial direction (h_z). Using fewer macro elements reduces computation time; consequently it is desirable to have a longer axial element length. In the h_z -type refinement study axial element length was varied between $0.167d$, $0.2d$ (giving approximately cube-shaped elements with a unit aspect ratio), $0.25d$, $0.33d$, $0.5d$ and $1.0d$.

Figure 9.10 shows the effect that changing h_z -type refinement has on the L_2 -norm. The L_2 -norm is sampled at the time of peak flow through the aneurysm (i.e. 0.4 s), this corresponds to the time of peak energy in the system. As the axial element length is reduced, the solution exhibits stable convergence properties. Such convergence is to be expected as the spatial resolution is increased. Table 9.5 shows the percentage error of each element length. Error was calculated relative to an estimate of the mesh independent value. This value was calculated using a Richardson-type extrapolation.

Table 9.5 shows extra h -type refinement in the axial direction has a significant effect on the solution. The effect was beyond the changes observed for the straight pipe case shown in table 8.4. This investigation focuses on the flow through the aneurysm bulge with a moving wall. In order to attain highly accurate results the h_z refinement in

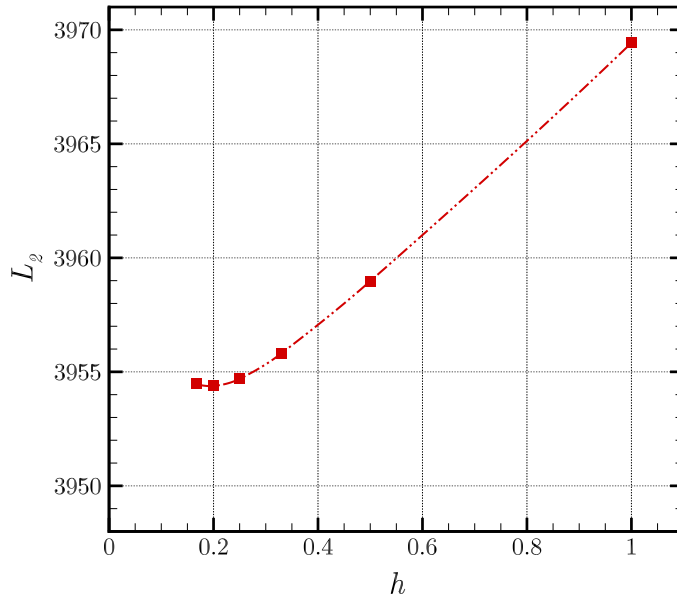


FIGURE 9.10: Results of the h -type refinement study. The L_2 -norm is measured at $t = 0.4$ s for each level of refinement. Note: only the axial length of the elements was changed.

this region is kept at $0.2d$. This forms an aspect ratio of unity for the wall elements that provides the most numerically stable elemental matrices (poor aspect ratios can lead to poorly conditioned matrices). This ensures that the highest level of accuracy is maintained in this region. Outside this region, in the inlet and outlet sections where the flow is less critical, the element size in the axial direction is set to $h_z = 0.75$. The results presented in § 8.3.3 suggest that in straight pipe sections the refinement in the z -direction is less critical than in the aneurysm geometry by an order of magnitude.

9.3.4 Solid domain p -type refinement

In this section, the spatial resolution of the solid domain is analysed. To simplify the meshing process, the solid mesh is created with macro elements which completely coincide with the exterior fluid elements. In this way the h -type refinement for the solid is fixed. A p -type refinement study was conducted in which the polynomial order was increased from $p = 2$ to $p = 6$.

Each end of the elastic region was fixed in space. The pressure boundary condition described in equation 7.10 was applied to the perianeurysmal interface. As a forcing function, the outlet pressure boundary condition for the fluid was applied to the inner

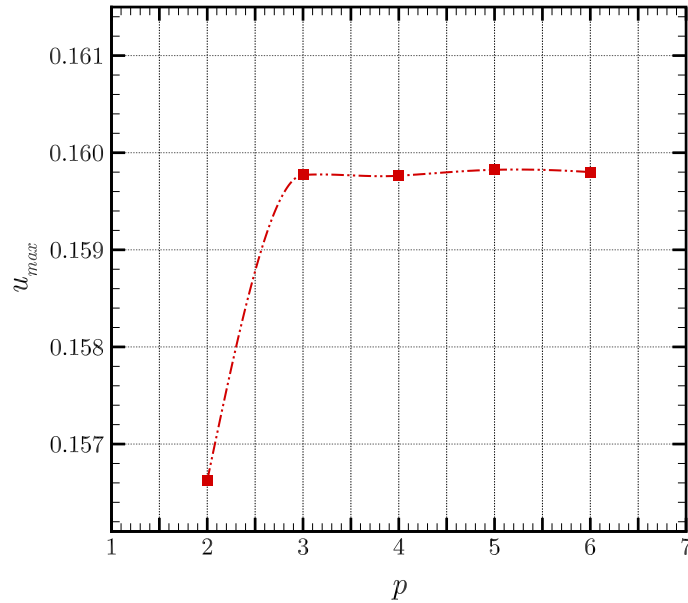


FIGURE 9.11: Results of the p -type mesh refinement study for the solid domain. The maximum lateral displacement, u_{max} , is measured at $t = 0.5$ s for each level of refinement.

surface of the solid. The neo-Hookean wall model was used with a mean Young's modulus of 0.8 MPa (that of a healthy artery).

The maximum displacement in the lateral direction was monitored as the polynomial order was increased. The maximum lateral displacement occurred at $t = 0.5$ s and at a position exactly half way along the elastic region for all levels of resolution. Figure 9.11 shows the maximum lateral displacement, u_{max} , as a function of increasing polynomial order. The solid solution converges to a mesh independent value at a much lower polynomial order, $p = 3$, than in the fluid cases.

Table 9.6 shows the percentage error in the solution compared to the most refined case. Here, the most resolved case is assumed to contain no error. These results correlate well with the convergence behaviour shown in figure 9.11. Using a polynomial order of 3 or greater gives a mesh independent solution (error $< 0.02\%$). These results suggest that for a neo-Hookean solid continuum fewer elements are required to spatially resolve the system than for similar fluid elements.

While using a polynomial order $p = 3$ provides a sufficiently resolved solution for this investigation, a polynomial order of $p = 5$ is chosen. Using a polynomial order that

p	% error
2	1.986
3	0.018
4	0.023
5	0.014
6	0.000

TABLE 9.6: Percentage error in the maximum lateral displacement u_{max} . The error decreases rapidly as the polynomial order is increased.

matches that of the fluid domain provides an efficient and accurate method for passing information between the fluid and solid meshes. Matching the polynomial order ensures both macro and quadrature nodes are coincident at the fluid-structure interface. As such vector fields do not require interpolation between the two regions, a direct copy of information can be made. This is both highly efficient and more accurate than interpolating. The polynomial order of $p = 5$ is well resolved spatially and will produce a solution with only 0.014% error.

9.3.5 Fluid-solid coupling p -type refinement

In the preceding sections the spatial resolution of both the fluid and solid mesh components were analysed. It was concluded that a polynomial order of $p = 5$ and $p = 3$ for fluid and solid, respectively was required to sufficiently resolve the solution. Before proceeding, the spatial resolution is tested once more for a fully coupled fluid-structure interaction. This determines whether the use of the arbitrary Lagrangian–Eulerian solver affects the spatial resolution of the mesh.

For this investigation, the full computational domain was solved with physiologically accurate fluid and solid boundary conditions (see chapter 7 and § 9.2). A healthy artery wall was simulated with a stiffness of 0.8 MPa. A p -type grid resolution study was conducted in which the polynomial order was increased from $p = 3$ to $p = 6$.

As was anticipated given the results of the preceding sections, figure 9.12 shows a mesh independent solution is achieved. Figure 9.12(a) and 9.12(b), respectively, show the L_2 -norm and z -velocity component for the fluid region. After an initial variance, each plot begins to converge to a single value. A polynomial order of $p = 5$ initiates

% error			
p	L_2	v_z	u_{max}
3	1.7915	6.1535	0.0185
4	0.0664	2.1695	0.0701
5	0.0359	0.4323	0.0149
6	0.0000	0.0000	0.0000

TABLE 9.7: Percentage error in fluid parameters L_2 -norm and z -velocity component v_z as well as the solid domain parameter u_{max} relative to the most resolved case.

the converged section and exhibits a low percentage error. Table 9.7 records the error relative to the most resolved case for each metric. For each fluid measurement the error at $p = 5$ is less than 0.5%, which is well within the desired level of accuracy for the simulations. This correlates well with the p -type study conducted in § 9.3.1 in which the polynomial that delivered the desired level of accuracy for a fluid solve alone was $p = 5$.

Similarly, for the solid, figure 9.12(c) shows the variation in maximum radial displacement, u_{max} , as a function of polynomial order. Just as the fluid components correlated well with previous results, the solid solver too exhibits analogous convergence behaviour. Table 9.7 shows that the error associated with the solid region is less substantial than the fluid region. Using a polynomial order of $p = 4$ the error for the solid domain is merely 0.07%.

This fluid-structure interaction spatial resolution study confirms the findings of § 9.3.1. For both fluids and solids the solution reaches a mesh independent state at a polynomial order of $p = 5$. This mesh and this level of resolution can now be used with confidence in the proceeding aneurysm study.

9.4 Temporal resolution

In following the mesh validation of chapter 8, a temporal resolution study was conducted. The following investigation determines the appropriate time step required to resolve the flow in a distensible aneurysm and determine how many boundary condition cycles are necessary to capture the natural fluid-structure interaction.

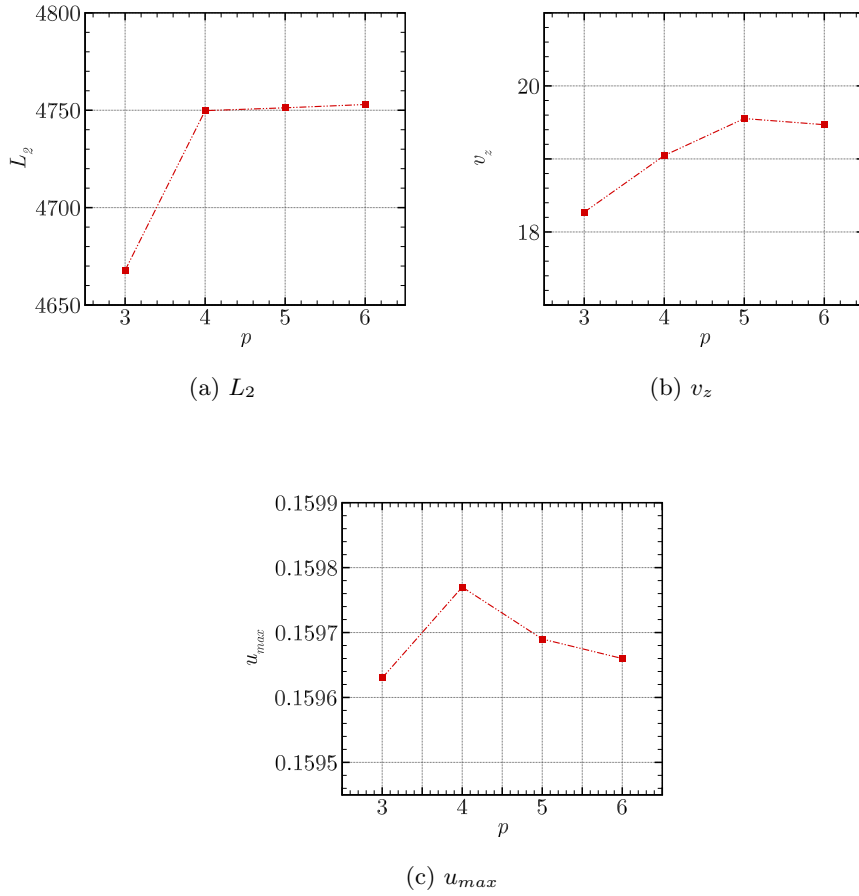


FIGURE 9.12: Results of the spatial resolution study using the fully coupled FSI algorithm. In each plot the polynomial order was used to change the spatial resolution of the mesh. (a) shows the L_2 -norm of the fluid domain, measured at $t = 1.4$ s at the time of peak velocity inlet. (b) shows the maximum fluid velocity along the centreline at $t = 1.4$ s. (c) shows the peak displacement of the wall at $t = 1.5$ s.

9.4.1 Time step

Firstly the temporal resolution is assessed and the appropriate time step is selected that captures the physics of the aneurysm problem. As an Eulerian reference frame is used for the fluid domain, large time steps may cause the solution to diverge as fluid moves fast enough to pass through an entire element within a time step.

A number of time steps were tested ranging from 0.0001 s, to 0.05 s. As with the spatial resolution study, the L_2 -norm and v_z (component of the velocity in the z -direction) were used to assess the global and local error in the solution. The z -component of velocity was measured at the centre of the aneurysm bulge. Measurements

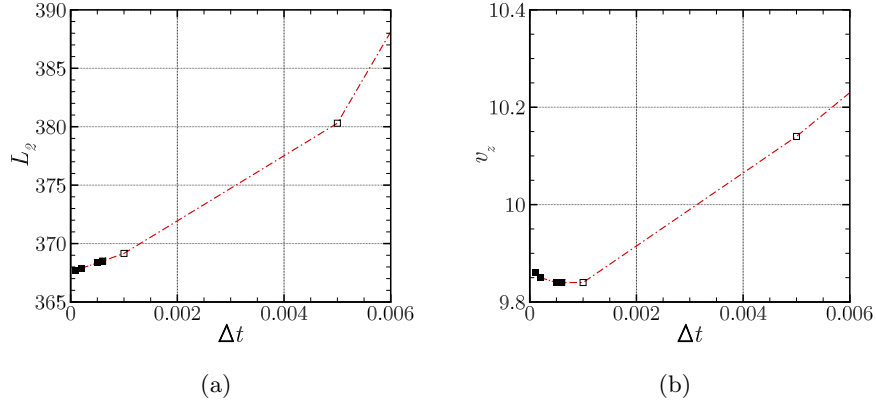


FIGURE 9.13: Results of the time step independence study are presented. Closed symbols (■) represent simulations that run in a stable fashion, open symbols (□) represent simulations that diverge later in the simulation. (a) shows the change in L_2 -norm and (b) shows the change in the velocity component in the z -direction at the centre of the aneurysm bulge. All measurements were made at $t = 0.05$ s.

were taken at $t = 0.05$ s, and while some simulations ultimately diverged, all were capable of running to this point in time. Figure 9.13 shows the results of the time step independence study. As the time step is reduced the solution converges to a single value. The closed symbols on each sub-plot represents simulations that were stable, while open circles represent those that ultimately diverged.

Table 9.8 shows the percentage error for each time step. The error is measured relative to a theoretical fully resolved case at $\Delta t = 0$, calculated using a Richardson extrapolation. These results show that once a time step small enough to satisfy the stability criterion is used the effect the time step has on the results is small. In order to reduce the computational cost of each simulation the largest stable time step $\Delta t = 0.0006$ s is chosen for all further aneurysm investigations. At this time step the error is only 0.241% in L_2 -norm and 0.17% in v_z .

9.4.2 Time period

As in chapter 8, a final validation case was conducted to determine if the fluid-solid coupling caused any interactions to occur over a longer time scale than the boundary condition period. This is more likely in an aneurysm bulge given the complex flow structures that can form compared to the flow through a straight pipe. A fully coupled

% error		
Δt	L_2	v_z
0.05	20.486	16.482
0.01	14.182	7.817
0.005	3.451	3.235
0.001	0.420	0.181
0.0006	0.241	0.173
0.0005	0.197	0.160
0.0002	0.075	0.283
0.0001	0.031	0.384

TABLE 9.8: Percentage error in the L_2 -norm and z -velocity component v_z relative to a theoretical resolved value (calculated using a Richardson extrapolation). Time steps below the double horizontal line are stable, those above diverge.

fluid-structure interaction simulation was conducted using the boundary conditions and geometry described in § 9.2.

Figure 9.14 shows the results of the time period analysis. Two parameters were monitored throughout the time period, the L_2 -norm (in sub-plots 9.14(a) and 9.14(b)) and v_z the z -component of velocity (in sub-plots 9.14(c) and 9.14(d)). As was observed for straight pipes in § 8.4.2, these plots indicate that the first time period produces very different results to subsequent cycles. This is caused by transient conditions in the aneurysm created by the initial imposition of a Poiseuille velocity profile throughout. Subsequent cycles exhibit very small deviation from the asymptotic solution state.

Figure 9.14(b) and 9.14(d) plot the percentage error in each parameter compared to the asymptotic periodic solution. The periodic solution was calculated by averaging the last three time periods of the time saturated simulation. Data is plotted with respect to a scaled time

$$t^* = t - (n - 1)T, \quad (9.1)$$

where t is the physical time, T is the boundary condition period (in this case $T = 1$ s) and n indicates the n^{th} period. Plotting relative to the scaled time t^* allows each time period to be compared with ease. The first time period exhibits errors in excess of 20%, while subsequent cycles are subject to less than 1.1% error.

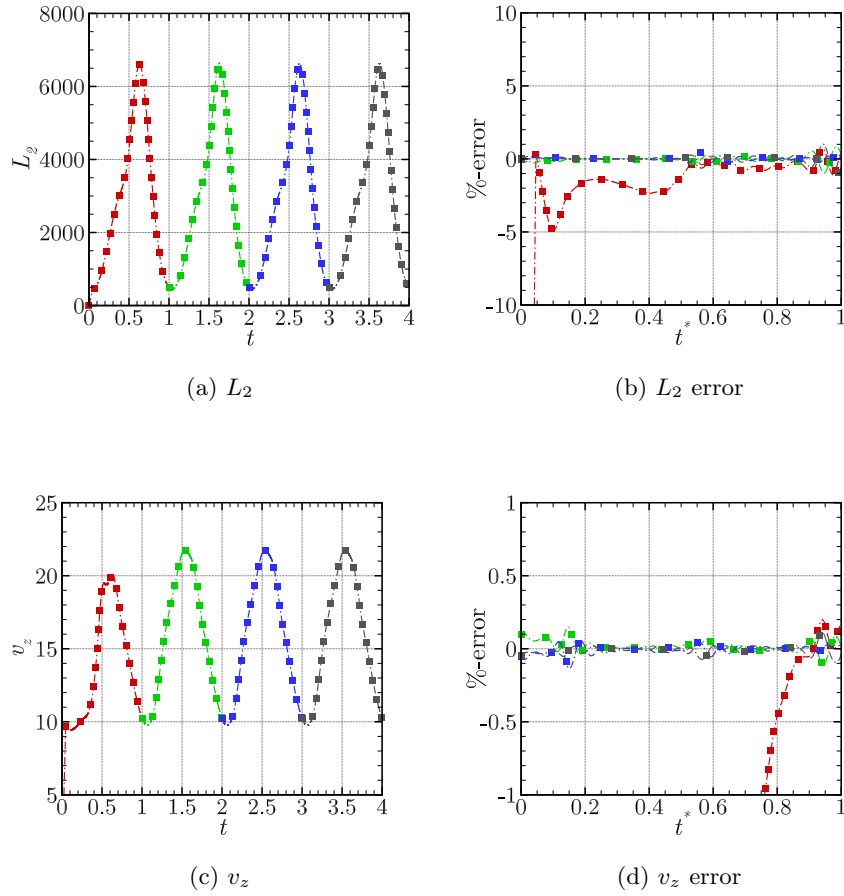


FIGURE 9.14: Results of the time period study. In each sub-plot red, green, blue and grey lines and symbols represent the first, second, third and fourth boundary condition time periods respectively. (a) shows the time evolution of the L_2 -norm, a global measure of energy in the solution. (b) shows the percentage error in L_2 -norm relative to the time saturated value. (c) shows the time history of v_z velocity component at a point along the centre line of the pipe. (d) shows the percentage error in v_z relative to the time saturated value. In each case the error in the latter periods is minimal.

These results are very similar to those presented in § 8.4.2 for straight pipes. As such similar conclusions can be drawn. Firstly, there are no long-timescale phenomena observed in the FSI in an aneurysm. Measurement of the L_2 -norm and v_z showed no discernible variation as more time periods were simulated. Secondly, the initial conditions in the pipe are inaccurate and take at least a full cycle to be flushed from the computational domain. This was observed in the large error in the L_2 -norm and v_z for the first period when compared to the asymptotic data (see figure 9.14).

As a result of this investigation simulations will be evolved for 4 inlet waveform

cycles to eliminate transient startup errors from the reported results.

9.5 Results

Having determined the spatial and temporal accuracy of the mesh, the effect of local variations in wall stiffness is investigated. First, § 9.5.1 describes the flow through an abdominal aortic aneurysm with rigid-walls. Section 9.5.2 discusses the effect of the fluid-structure interaction on the aneurysm haemodynamic environment. Section 9.5.4 describes how a local variation in the wall stiffness can affect the flow dynamics and the consequential change in the wall shear stress distribution as a result of this. Finally, § 9.5.6 discusses how the perianeurysmal environment affects the flow in an aneurysm.

9.5.1 Flow in a rigid-walled aneurysm

Before analysing the effect of an elastic arterial wall on the flow topology in aneurysms, the spatial and temporal evolution of the flow is characterised in a typical rigid-walled abdominal aortic aneurysm model. Figure 9.15 depicts the flow through an aneurysm throughout the cardiac cycle. Similarly, figure 9.16 uses negative λ_2 field iso-contours to give a three-dimensional representation of where vortex rings are present. Time progresses with the sequential numbering of the frames as shown on the velocity waveform in figure 9.15(m) and 9.16(m). Analysis of these flow fields reveals the important features of haemodynamics in fusiform aneurysms. The flow is dominated by the formation of separated flow regions in the aneurysm bulge. The internal shear layer is composed of an array of coherent vortex rings that traverse the length of the aneurysm. These findings support the observations made by Salsac *et al.* (2006) and Finol *et al.* (2003b).

During the acceleration portion of the systole, the flow remains laminar and is predominantly attached to the bulging walls (figures 9.15(a) and 9.15(b)). The exception is a very small recirculation region at the proximal neck (the result of the dramatic change in wall geometry) and a weak vortex close to the distal neck which is an artefact from the previous cardiac cycle. Salsac *et al.* (2006) explains that the flow remains attached in the divergent section of the pipe as a result of the positive pressure gradient generated at the beginning of systole: temporal acceleration of the flow at this point is greater than the convective deceleration.

Figure 9.15(b) shows that, during the acceleration portion of the cardiac cycle, the

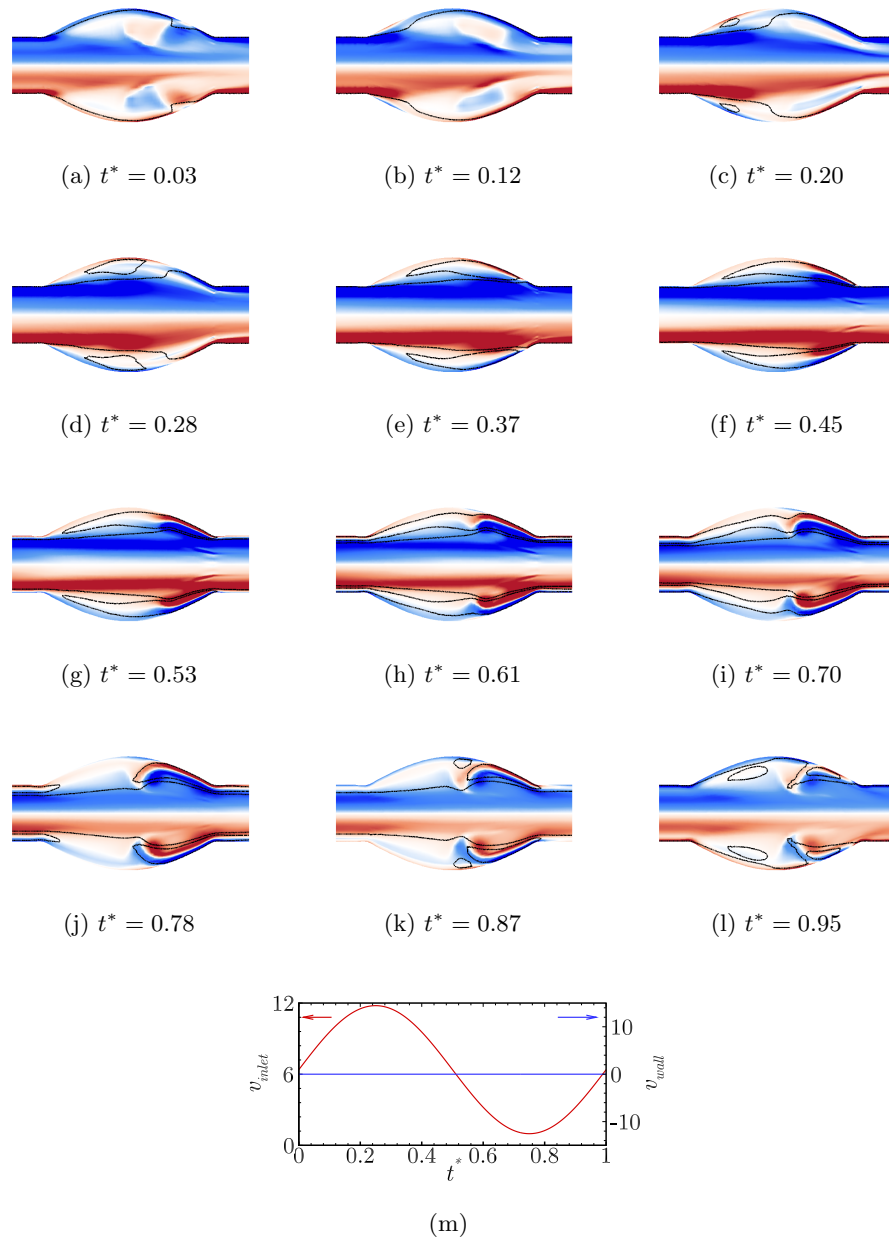
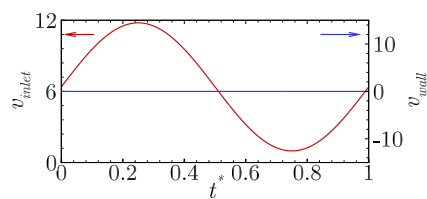
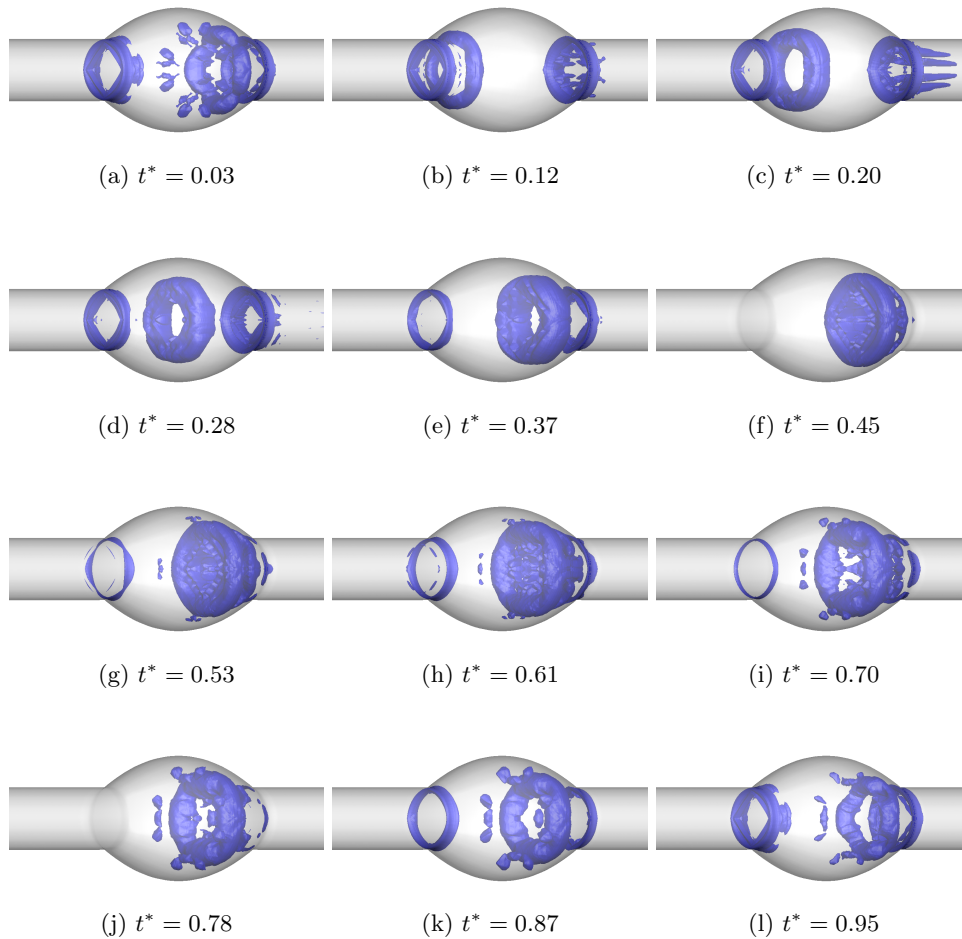


FIGURE 9.15: Flow through an aneurysm with a rigid-wall model. Contours show vorticity in the y - z plane and range between -50 and 50. Positive vorticity (anticlockwise whorl) is represented by red contours and negative vorticity (clockwise whorl) is represented by blue contours. Line contours show the regions of flow with axial velocity component of +1 and -1 (dashed lines are negative).



(m)

FIGURE 9.16: Flow through an aneurysm with a rigid-wall model throughout the cardiac cycle. An iso-surface of an arbitrary small negative value of the λ_2 field is plotted to reveal vortex structures in the flow.

high vorticity (and as a result strain-rate) is confined to a very thin boundary layer. Salsac *et al.* (2006) found that the flow remains attached to the entire wall during the entire acceleration of the cardiac cycle. In contrast to this, figure 9.15 shows small areas of recirculation at the proximal and distal necks. These effects are small and are likely the result of the different inlet flow conditions. The flow profile used by Salsac *et al.* (2006) has a greater systolic acceleration which promotes a positive pressure gradient and reduces the recirculation region at the proximal neck. Furthermore, the Salsac *et al.* (2006) profile reaches peak diastole much earlier in the cycle and allows a flushing time which limits the residual recirculation from the previous cardiac cycle at the distal neck.

After peak systole is reached, the flow begins a deceleration phase (figures 9.15(c) to 9.15(i)). During this time, while the bulk of the flow (near the centreline) is still moving forward the flow reverses close to the wall inside the aneurysms bulge. This velocity profile encourages the flow to detach from the proximal neck as the temporal acceleration no longer dominates the convective acceleration. The result is a recirculating flow region in the proximal half of the aneurysm, which slowly moves down the length of the aneurysm. The iso-surface plots of the λ_2 field in figures 9.16(c) to 9.16(i) confirm that this is a large-scale vortex ring that is ejected from the proximal neck. As a result of the presence of the large-scale intense vortex ring, the shear layer adjacent to the vortex ring exhibits a region of vorticity opposite in sign to that of the local vortex. Salsac *et al.* (2006) postulate that this is a result of the Kelvin–Helmholtz instability causing small-scale vortices to form. Further downstream the converging nozzle shape of the wall causes a positive pressure gradient near the wall keeping the flow attached with vorticity limited to a thin boundary layer.

Post ejection, the proximal vortex ring travels through the aneurysm and slowly grows in both ring and vortex diameter (see figures 9.16(c) to 9.16(i)). At time $t^* = 0.45$ (figures 9.15(j) and 9.16(j)) the vortex ring starts to impinge on the distal neck of the abdominal aortic aneurysm. This corresponds to a sharp increase in the wall shear stress at this location (see § 9.5.3). The shear layer trailing the vortex ring extends the full length of the aneurysm bulge and is localised around the central region within the diameter of the healthy pipe. At the point of impact, the boundary layer is characterized by vorticity and shear stresses of the opposite sign. Furthermore, the large velocities near the wall associated with the whorl of the vortex causes a very thin boundary layer

to form. Elsewhere the flow is largely detached from the walls and the corresponding vorticity in the shear layer is weak.

The close proximity of the vortex ring to the wall after $t^* = 0.45$ in figures 9.16(k) and 9.16(l) causes the shear layer to be drawn into a secondary vortex ring behind the large vortex ring with opposite sign. This secondary vortex ring interacts with the primary vortex ring inducing a mutual strain which forces the pair of vortex rings to drift back into the aneurysm bulge. This process is helped by the reducing flow rate at this time which causes a negative mean flow velocity in the near-wall region. A result of this is that the vortex ring is drawn upstream back into the aneurysm bulge despite the bulk flow remaining in the forward direction. The reduction in flow velocity also corresponds to a reduction in the intensity (observed by a reduction in vorticity of 34%) of the primary vortex and subsequently the induced secondary vortex ring.

Salsac *et al.* (2006) identified a loss in two-fold symmetry in the instantaneous velocity field behind the primary vortex core after the primary vortex impacted with the distal neck. This symmetry breaking was not observed in this investigation. Salsac *et al.* (2006) found that the vortex ring was tilted slightly, though this could well have been an artefact of the experimental set up used in their investigation. After the initial impact of the primary vortex ring on the distal neck the secondary vortex does break axisymmetry as it is destroyed by the much stronger primary vortex ring; this is observed in figures 9.16(k) to 9.16(l).

Toward the end of the cardiac cycle the flow disturbances weaken owing to vortex entanglement (energy cascade) and viscous dissipation. At the onset of the next cardiac cycle the weakened pair of vortex rings remain close to the distal neck before they are flushed from the aneurysm altogether with the onset of the systolic acceleration phase.

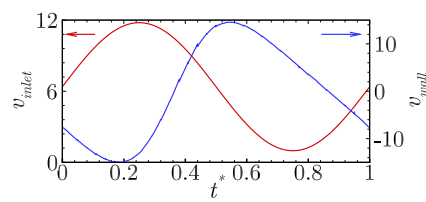
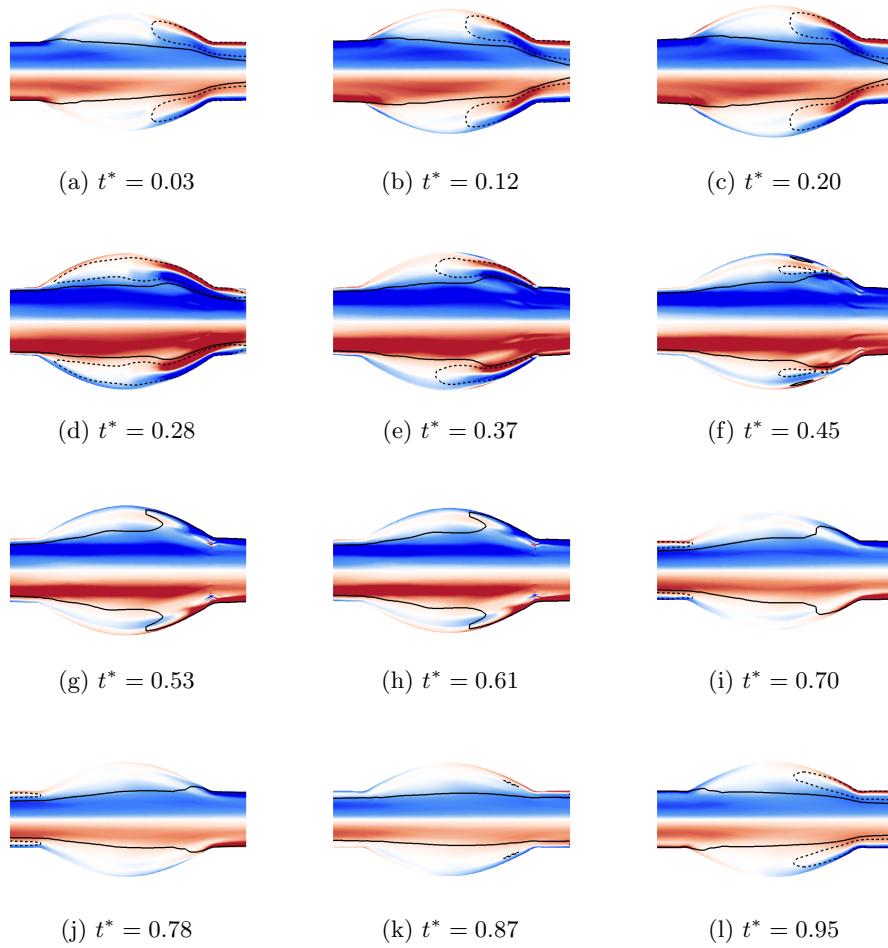
9.5.2 Flow conditions with a healthy arterial wall stiffness

In section 9.5.1 the flow in a rigid-walled abdominal aortic aneurysm model was considered. As suggested by Lasheras (2007) and Humphrey & Taylor (2008) the flow in an aneurysm may be adversely affected by the motion of the wall. The results presented in figures 9.17 and 9.18 show the temporal evolution of the flow in a typical abdominal aortic aneurysm with a uniformly elastic wall. Time progresses with the sequential numbering of the frames as shown on the velocity waveform in figure 9.17(m) and 9.18(m). Analysis of these flow fields reveals the striking difference between rigid-

walled models and elastic-walled models for simulating flow through an aneurysm. In the elastic-walled case, the flow is dominated by the formation of separated flow regions in the aneurysm bulge. The formation of vortex rings occurs at both the proximal neck and the distal neck, which proceed to interact in a complex manner as the cardiac cycle progresses.

Throughout the cardiac cycle the flow field varies dramatically from that seen in a rigid-walled aortic aneurysm. Initially, in figure 9.17(a) the flow is similar to the rigid-walled simulations. It consists of a very thin shear layer, a small recirculation region forming locally at the proximal neck and the remnants of a vortex ring structure at the distal neck (figure 9.18(a)). Unlike the rigid-walled case, the shear layer in the elastic-walled case does not extend over the full length of the aneurysm bulge. At this time, the flow far from the central axis in the aneurysm bulge is reasonably stagnant, and as a result, the initial movement of the wall provides sufficient velocity to alter the local shear layer at the centre of the aneurysm bulge.

During the systolic acceleration phase, a very different evolution in flow occurs. As the sequence over figures 9.17(a) to 9.17(c) and 9.18(a) to 9.18(c) show, two vortex rings form and begin to increase in strength (described herein as the local peak of the absolute value of vorticity in a recirculation region). Firstly, a vortex ring forms at the proximal neck just as in the rigid-walled case. This is a result of the large change in geometry causing a spatial acceleration. At the distal neck, a dual vortex structure is present. This double distal vortex structure consists of a wall shear layer vortex and an inner strong distal-vortex structure. The evolution of these vortices is schematically depicted in figure 9.19. The wall shear layer vortex (vortex C' in figure 9.19) is formed as a result of the reverse flow in the boundary layer caused by the expanding motion of the wall (see dashed contour lines in figure 9.17 depicting negative axial velocity). During this time the pressure acting on the wall causes it to accelerate outwards, in turn increasing the volume of the aneurysm. Reynolds transport theorem (equation 8.39) shows, in order to conserve mass, the flow rate through the outlet must reduce. As this is a high Womersley number flow, the change in transient inertia occurs first in the boundary layer causing a large flow reversal in the near-wall region. This local reverse flow undergoes a spatial deceleration similar to that which occurs at the proximal neck as the flow moves over the distal neck into the aneurysm bulge. This causes the flow to curl toward the wall causing a region of positive vorticity at the distal neck. The



(m)

FIGURE 9.17: Flow through an aneurysm with elastic-walls throughout the cardiac cycle. The wall has a uniform stiffness of $E = 0.8$ MPa. Contours show vorticity in the y - z plane and range between -50 and 50. Positive vorticity (anticlockwise whorl) is represented by red contours and negative vorticity (clockwise whorl) is represented by blue contours. Line contours show the regions of flow with axial velocity component of +1 and -1 (dashed lines are negative).

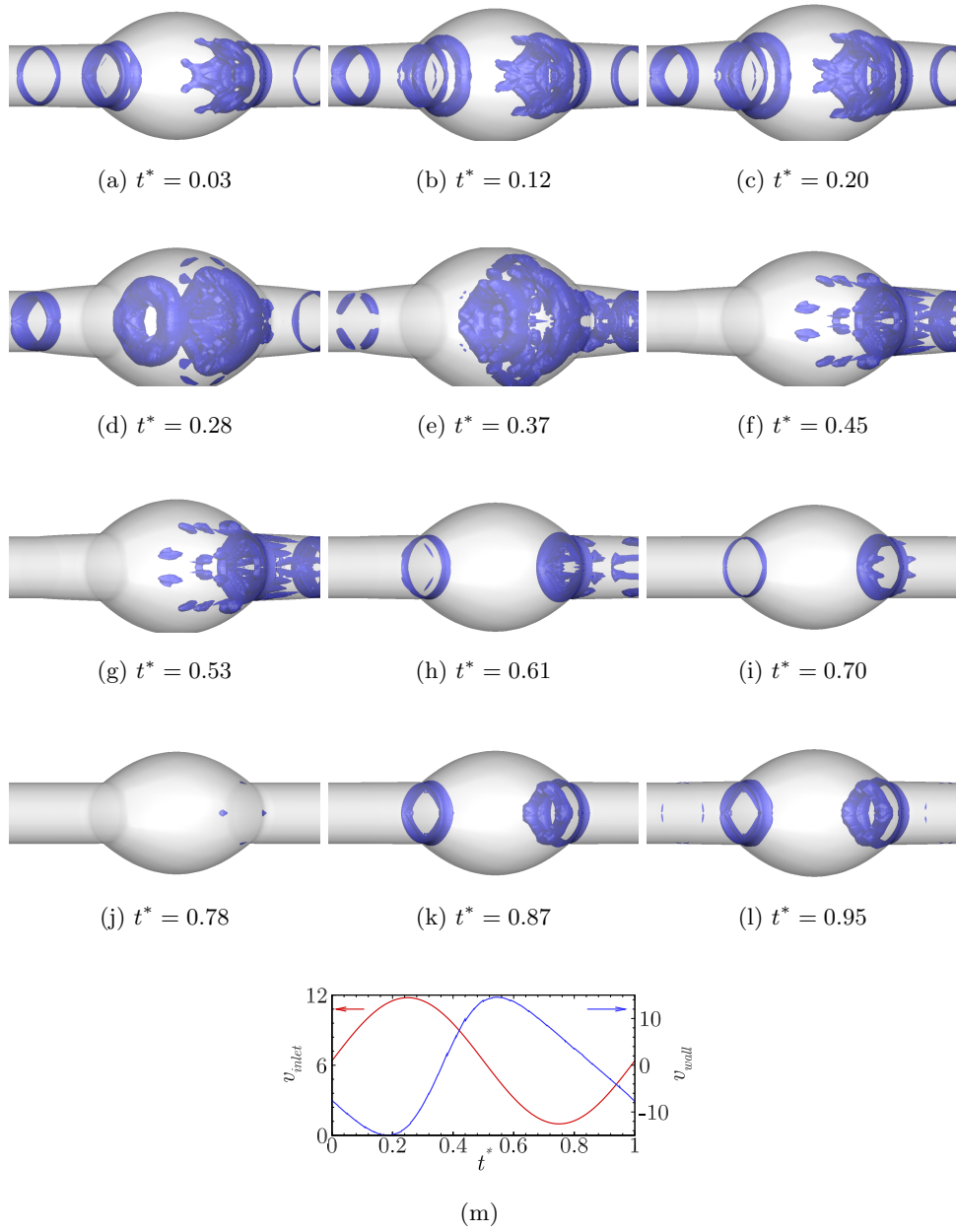


FIGURE 9.18: Flow through an aneurysm with elastic-walls throughout the cardiac cycle. The wall has a uniform stiffness of $E = 0.8$ MPa. An iso-surface of an arbitrary small negative value of the λ_2 field is plotted to reveal vortex structures in the flow.

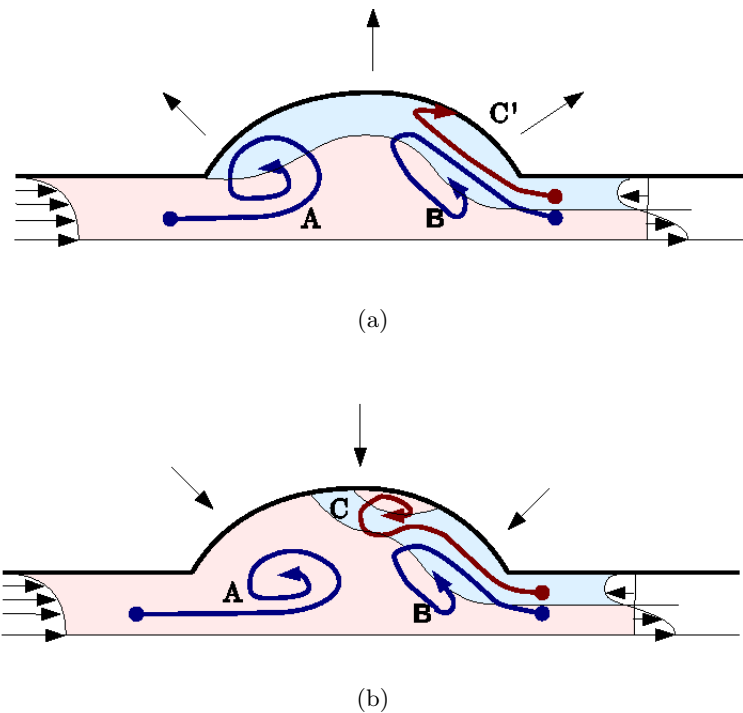


FIGURE 9.19: Schematic representation of the formation of the proximal vortex A and the inner distal vortex B. In sub-plot (b) the shear layer C' is drawn up into the secondary vortex ring vortex C.

inner strong distal vortex (vortex B in figure 9.19) forms around the shear layer which forms between the positive-velocity (downstream) flow coming from the inlet and the negative velocity (upstream) in the distal neck shear layer (a result of the wall motion). The long interface of forward and reverse flow causes the elongation of this vortex core.

After peak systole is reached, the inlet flow begins a deceleration phase and similarly the outward velocity of the wall begins to decelerate (see figures 9.17(c) to 9.17(f)). During this time the wall velocity is still in the outward normal direction, causing the aneurysm bulge to continue to expand. However, the inlet velocity begins to decrease. Figures 9.17(c) to 9.17(f) and figures 9.18(c) to 9.18(f) show that the recirculation region which formed during the systolic acceleration phase at the proximal neck (vortex A in figure 9.19) detaches from the proximal neck forming a vortex ring which begins to travel down the length of the aneurysm. The wall motion continues to draw fluid from the distal neck during this phase: in fact the effect it has on the flow is increased as the inlet velocity decreases. This causes the inner distal vortex B to extend farther into

the domain as a large portion of the aneurysm bulge is subject to reverse flow in the boundary layer. Similarly the wall shear layer vortex C' increases in strength (by 37%) and extends further upstream into the aneurysm bulge, in fact the shear layer extends the full length of the aneurysm bulge.

At time $t^* = 0.37$, shown in figure 9.17(e), the aneurysm has reached its full expansion and begins to collapse back toward its original position. At this point in the cardiac cycle, the flow rate from the boundary is insignificant when compared to the inlet velocity flow rate ($< 10\%$), and as such the inflow jet dominates the flow. This is observed in figure 9.17(e) by the reattachment of forward flow through the distal neck, with the recirculation region of negative flow being isolated in the extrema of the aneurysm bulge. This isolation causes the vortex core to reduce in length and increase in strength of 16% as circulation is conserved. As the systolic deceleration continues, figures 9.17(e) and 9.18(e) show the shear layer being drawn up into a secondary vortex ring of opposite sign to the primary distal neck vortex. This process is aided as the wall begins to collapse inwards adding extra curl to inner shear layer. The velocity of the wall is greatest at the centre of the aneurysm bulge and decreases slowly across the length of the bulge. This causes a velocity gradient which encourages the shear layer roll up observed in these figures. Through the mutually induced strain exerted by the vortex ring pair and the reversed flow in the outer regions of the aneurysm, the distal vortex ring pair (vortex B and C) moves back into the aneurysm bulge in the direction of the proximal neck vortex ring (vortex A).

Due to the location of the shear layer around which the inner strong distal vortex B forms, it is forced to follow close to the aneurysm wall. The proximal vortex (vortex A) having formed close to the central axis is subject to smaller wall forces acting to expand its radius. As such, when the proximal and distal vortices meet, the proximal vortex (vortex A) has a smaller radius than the strong inner distal vortex B. Under an inviscid flow assumption a three-vortex-ring system may undergo a leap frogging phenomenon, in which the inner vortex ring is drawn through the outer distal vortex ring. However, as this is a low Reynolds number flow, the viscous forces are non-negligible. As the proximal and distal neck vortex pairs collide they undergo a vortex merging process which causes a very large recirculation region to form extending throughout the aneurysm bulge.

After the coalescence of the proximal and distal vortex pair, the inlet velocity con-

tinues to decelerate while the wall, having reached its maximum expansion, continues to accelerate back towards the unstressed state. Figures 9.17(f) to 9.17(i) depict this period. Despite the decelerating inlet velocity, the diminishing volume contributes forward momentum to the flow (see equation 8.39). Figure 9.20 shows the contributions from the velocity inlet and from the wall motion to the total flow rate. During this time ($t^* = 0.5$ to 0.70) the flow rate produced as a result of the wall motion is much greater than the flow rate through the velocity inlet, indicating the flow conditions will be driven primarily by the motion of the wall. The increasing flow rate produced by the collapse of the wall in figures 9.17(f) to 9.17(i) causes a flushing of the flow structures developed in the previous phase. As the flow returns to the forward direction throughout the aneurysm geometry the shear layer changes direction and increases in intensity.

Also of interest is the shear layer near the proximal neck. During systolic acceleration, the expanded wall geometry causes a region of negative vorticity to occur. The expanding vessel contributes flow with velocity gradients in the same direction as the recirculation region formed by the change in geometry. As the wall begins to collapse, the contribution to the velocity gradients changes direction and causes a separation of the recirculation region from the wall and a shear layer with opposing velocity gradients to form.

The final stages of the cardiac cycle coincide with an increasing velocity at the inlet and a decreasing wall velocity. At time $t^* = 0.78$ in figure 9.17(j), the flushing initiated in the previous phase is enhanced as the temporal acceleration at the velocity inlet contributes to the flushing of the flow structures from the aneurysm bulge. As the inlet flow rate increases and the wall velocity decreases the shear layer near the proximal neck returns to its original sign as the flow becomes laminar in the forward direction along the wall. Finally, figures 9.17(k) and 9.17(l) show the onset of the wall expansion and the reverse flow in the boundary layer at the distal neck, this initiates the roll up of the shear layer into a pair of vortex rings which remain at the start of the next cardiac cycle.

Figures 9.17 and 9.18 highlight the significant difference in the flow dynamics when considering an elastic-walled aneurysm model compared to a rigid-walled model. Unlike their rigid-walled counterparts, realistic elastic-walled models are subject to complicated multi-vortex-ring interactions with much more dynamic boundary layer flows.

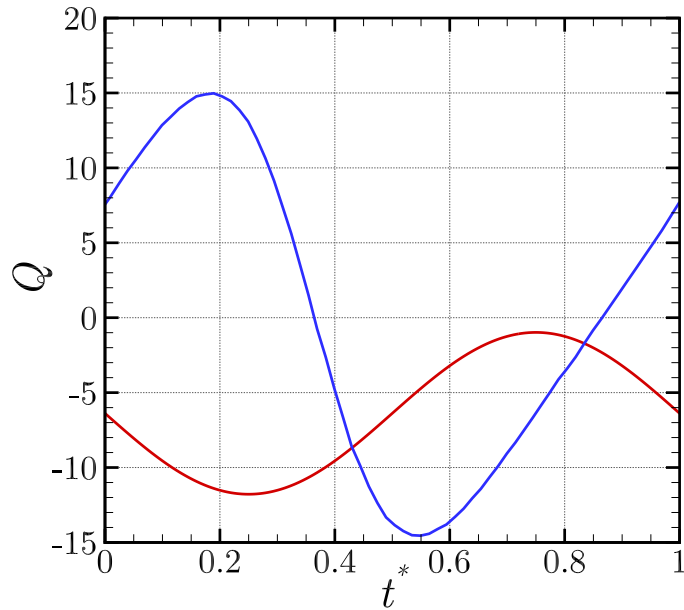


FIGURE 9.20: Flow rate through the inlet (red curve) and as a result of the wall motion (blue curve) across a single cardiac cycle. A positive flow rate, Q , indicates flow is exiting the domain, a negative flow rate indicates flow is entering the domain.

In § 9.5.3 the ramifications of the complex haemodynamics is considered in terms of its effect on the wall shear stress.

9.5.3 The effect of wall elasticity on wall shear stress in an aneurysm

The results presented in § 9.5.1 and 9.5.2 describe in detail the flow in an aneurysm using a rigid and elastic-wall model. The large displacement of the wall in the elastic-wall model drastically affects the effective flow rate in the aneurysm bulge and as a result causes dramatic changes to the flow dynamics. In this section the effect that the altered flow conditions have on the wall shear stress is realised both in space and time.

Figure 9.21 shows the wall shear stress distribution in the elastic region throughout the cardiac cycle. Figure 9.21(a) depicts the wall shear stress distribution in a rigid-walled aneurysm model. Upstream and downstream of the aneurysm bulge, the banded wall shear stress distribution described in chapter 8 is evident. In these sections the pipe diameter is constant and a Womersley velocity profile forms. As shown in § 8.5.4, the Womersley profile formed is predominantly forward flowing with a short period of flow reversal in the transient boundary layer. This is reflected in the wall shear stress

distribution in the regions outside of the aneurysm bulge by the spatially invariant wall shear stress distribution. The shear stress distribution is predominantly positive as a function of time with only a short period of negative wall shear stress (with a corresponding smaller wall shear stress magnitude).

Inside the aneurysm bulge, the wall shear stress distribution is substantially different. Initially, the systolic acceleration causes the flow to remain fairly laminar and attached along the entire length of the bulge. As time progresses, the recirculation region seen forming in figure 9.15(b) begins to move down the length of the aneurysm. The recirculation region causes the local velocity near the boundary wall to reverse. The result of this is a negative velocity gradient and a corresponding negative wall shear stress. The motion of the proximal vortex core along the length of the aneurysm bulge may be tracked by the peak in negative wall shear stress indicated by the white dashed line on figure 9.21(a).

Once the proximal neck vortex reaches the distal neck, the size and strength of the negative wall shear stress region increases. This is a result of two factors. Firstly at this time; the inlet flow rate is at its smallest which corresponds to a period of reversed flow in the transient boundary layer. The reverse flow in the transient boundary layer causes a negative strain-rate and consequently a negative wall shear stress. The close proximity of the vortex to the wall causes a local increase in the velocity and corresponding local Reynolds number. Secondly, this flow reversal on the transient boundary layer also contributes to the swirl of the vortex increasing its strength and pushing it further into the aneurysm bulge. These two factors increase the strength of the negative wall shear stress region and enlarge its size.

After $t^* = 0.5$ a region of positive wall shear stress develops at $z = 12.5$. This is upstream of the large negative wall shear stress region developed by the proximal vortex ring. Comparison of these results with figure 9.15(h) indicates that this region of positive wall shear stress is associated with the local change in shear layer which occurs as the secondary vortex ring C detaches from the wall. The primary vortex ring draws the shear layer into a secondary vortex ring of opposite rotation. The proximity of this vortex ring to the wall induces a local strain-rate at the wall in the opposite direction. As the vortex core moves closer to the axis and begins to move out of the aneurysm under the action of the increasing inlet flow rate, the region of positive wall shear stress increases.

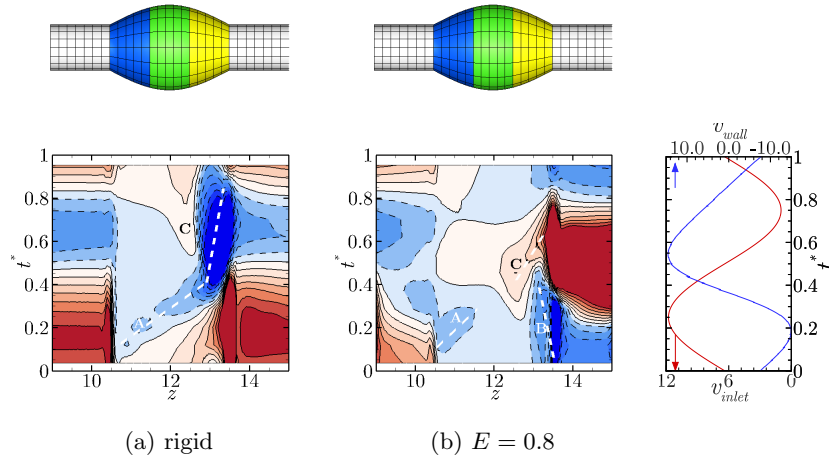


FIGURE 9.21: The variation of wall shear stress (WSS) in an aneurysm as a function of time and space. Contours show WSS with high WSS represented by red and low WSS represented by blue, negative values are depicted using dashed contour lines. The contour levels are equispaced and vary from -3.35 Pa to 3.35 Pa. Sub-plots (a) and (b) represent the WSS in an aneurysm with rigid-walls and elastic-walls respectively. The figures on the right show the velocity inlet (red) and wall velocity (blue).

Finally, figure 9.21(a) depicts a significant decrease in wall shear stress at the proximal neck and increase at the distal neck. From the analysis conducted in § 8.5.5.1, it is understood that this occurs as a result of the aneurysm geometry. At the proximal neck, the diameter is locally increasing which through the spatial deceleration causes a local reduction in the flow rate. Equation 8.32 shows that a decrease in the local flow rate decreases the local Reynolds number and consequently increases the boundary layer thickness. A larger boundary layer thickness results in lower wall shear stresses. Similarly at the distal neck, the diameter is decreasing, by a similar argument this leads to an increase in the local flow rate and consequently a thinner boundary layer with high wall shear stresses.

Figure 9.21(b) shows, in stark contrast to figure 9.21(a), the impact that the altered flow dynamics discussed in § 9.5.2 has on the wall shear stress distribution in an elastic-walled aneurysm. The most significant change is the phase shift in wall shear stress, which is evidently driven by the wall motion rather than the inlet velocity. Other changes include the non-uniform shear stress distribution in the “straight” sections of the aneurysm bulge, the length and time scale of the effect of the proximal vortex (vortex A in figure 9.19), and the complex shear environment at the distal neck.

Firstly, consider the regions of “straight” elastic-wall from $z = 9 - 10.5$ and $z = 13.5 - 15$. As in the aneurysm initiation cases discussed in chapter 8 these sections undergo a slight distension to form a diverging nozzle shape at the proximal neck and a converging nozzle at the distal neck. This causes a spatial acceleration or deceleration of the flow and affects the local Reynolds number which in turn affects the boundary layer thickness (equation 8.32). This causes the wall shear stress to decrease spatially in the proximal neck region and increase spatially in the distal neck region. This finding is supported by the time-averaged wall shear stress results presented in figure 9.22, which shows that in these regions, the wall shear stress is constant for the rigid pipe cases.

Inside the aneurysm bulge the differences in the wall shear stress distribution is a result of the complex vortex structures. Initially, the wall motion causes reverse flow along the length of the aneurysm wall. This creates a negative strain rate and a negative wall shear stress distribution. The proximal neck vortex is shed at an identical time to the rigid-wall case; at the point when the inlet velocity starts its deceleration phase. The proximal vortex position may be tracked by following the region of elevated negative wall shear stress highlighted in figure 9.21(b) by the dashed white line. The rotation of this shed vortex ring causes a local increase in the negative velocity at the wall which causes a thinning of the boundary layer (as described in equation 8.32). At the same time as the proximal vortex is developing and being shed at the proximal neck, the inner strong distal-vortex ring (vortex B) and wall shear layer vortex (vortex C') are formed at the distal neck. The spatial deceleration of the reverse flow at the distal neck in combination with the increase in local reverse flow causes a highly negative shear-rate to form near the distal neck. This is coupled with the close proximity of the strong inner distal-vortex to the wall locally thinning the boundary layer and resulting in an increased wall shear stress.

As the wall starts to collapse back toward its initial state at time $t^* = 0.35$, a local increase in the wall shear stress distribution occurs at around $z = 12.5$. This coincides with the rollup of the wall shear layer C' into the vortex ring C. This forms a vortex-ring pair with the strong inner distal vortex B. The motion of the wall and strength of the inner distal vortex ring pulls the shear layer into a vortex ring which detaches from the wall. The local shear layer adjacent to the wall shear layer vortex (vortex C) has a local forward velocity and consequently positive wall shear stress. As the reverse flow in the aneurysm diminishes (with collapsing wall), the flow becomes

laminar along the length of the aneurysm bulge in the forward direction. Unlike the rigid-walled case, figure 9.21(b) does not show the proximal vortex core traversing the full length of the aneurysm before it collides with the distal neck. Instead, it travels only half way through the aneurysm before it interacts with the distal vortex pair and is enveloped. As the relative size of the proximal vortex pair causes it to leapfrog through the middle of the distal vortex pair, the wall shear stress dynamics at the distal neck are dominated throughout time by the distal vortex pair.

As in the rigid pipe case, the distal neck is dominated by the extrema in wall shear stresses. As the distal neck is downstream of the elastic region, it is subject to changes in flow rate resulting from both the inlet velocity and the wall motion (see equation 8.39). This amplifies any changes in the wall shear stress at this location. The large amount of reverse flow in the boundary layer causes the negative wall shear stress region at the distal neck during the peak systolic acceleration ($t^* = 0.0 - 0.25$). In contrast, the rigid-walled case is dominated by forward flow during this time and is subject to positive wall shear stresses. The opposite reversal occurs later in the cycle. The collapsing wall and the presence of the vortex rings combine to induce a positive wall shear stress at the wall. At this time, the flow in the boundary layer is positive and undergoing a spatial acceleration due to the wall geometry. As this is a high-Womersley-number flow, changes in flow rate occur initially in the inertial boundary layer. As such, the wall shear stress changes very quickly in response to the wall motion which provides a much greater flow rate range (see figure 9.20).

The time-averaged wall shear stress distributions shown in figure 9.22 complement the findings presented in figure 9.21. In the region outside the aneurysm bulge, the wall shear stress is constant for the rigid pipe case. In the elastic case the wall shear stress dramatically decreases at the proximal end ($z = 9 - 10.5$) and increases at the distal neck ($z = 13.5 - 15$). As previously discussed, this is a result of the changing wall diameter leading to a spatial acceleration which alters the local velocity and consequently boundary layer thickness. The boundary layer thickness is linked to the wall shear stress via a change in strain rate. In both the rigid-walled model and the elastic-walled model the time-averaged wall shear stress is reasonably consistent in the upstream half of the aneurysm bulge (from $z = 10.5 - 12.5$). As the input velocity profile is never negative, and the expansion of the aneurysm is quite rapid, the flow detaches along this upstream section and is subject to low wall shear stresses ($\tau_{WSS} \simeq 0$). At $z = 13$ a

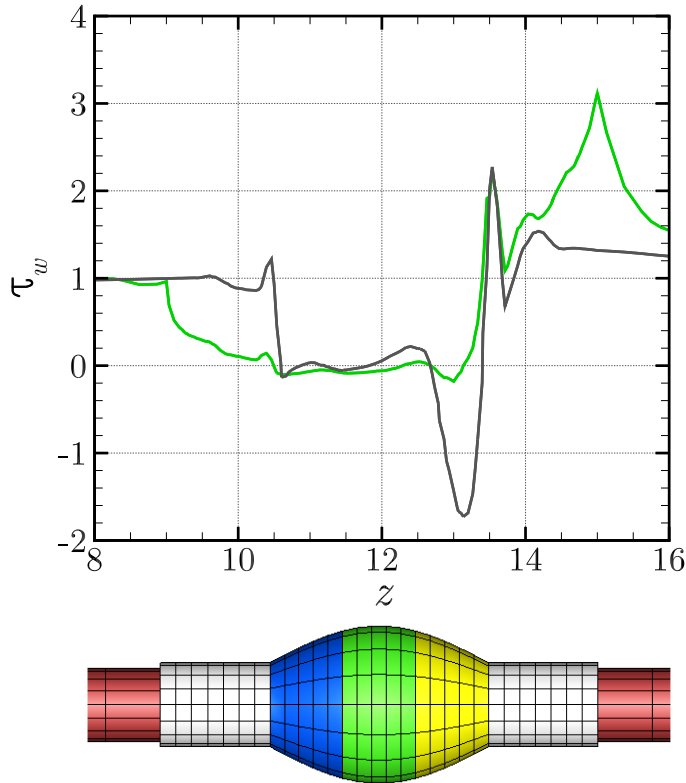


FIGURE 9.22: Comparison of the time-averaged wall shear stresses with rigid and elastic-walls. The grey line represents the rigid-walled reference case, while the green lines represent the elastic-walled case with a wall stiffness of $E = 0.8$ MPa (healthy).

very low wall shear stress is observed in the rigid-walled case which is not present in the elastic-walled case. This negative wall shear stress in the rigid-walled case corresponds to where the proximal vortex reaches the distal neck. As a result of the reversed flow at this time in the rigid-wall cycle, the proximal vortex stays for a significant time at this location and interacts with the shear layer causing the large decrease in time-averaged wall shear stress. The elastic-walled case does not exhibit this minimum in wall shear stress at $z = 13$. In elastic-walled cases the local shear layer is predominantly driven by the wall motion. With a substantial section of elastic-wall upstream, the flow rate at the distal neck is driven primarily by the motion of the wall. The result of this is the formation of the distal vortex pair (vortices B and C in figure 9.19) which form as a result of the reverse flow in the boundary layer and the forward flow through the centre of the bulge. These vortices interact with the proximal vortex before it reaches

the distal neck preventing it from having an impact on the boundary layer or the wall shear stress. There is a small reduction in the wall shear stress at $z = 13$ as a result of the thinning of the boundary layer as the vortex is flushed from the aneurysm. The regions of high and low wall shear stresses seen above the distal neck in figure 9.22 are predominantly driven by the motion of the wall. As such, these average through time to zero.

Finally, both the rigid-wall case and the elastic-wall case exhibit a spike in time averaged wall shear stress at the distal neck. The large change in geometry causes an increase in the local flow rate before the neck that thins the boundary layer (equation 8.32) and increases the wall shear stress. This occurs temporarily as the flow re-adjusts to the new pipe diameter. As was found in the incipient aneurysm case, the elastic-wall model causes a much higher wall shear stress downstream at the end of the elastic region due to the larger flow rates achieved in the elastic-walled case (see equation 8.39).

Figure 9.23 shows the time-averaged wall shear stress magnitude in both the elastic and rigid-walled aneurysm models. This plot shows many of the features observed in figure 9.22. It highlights the effect of the wall motion on the peak wall shear stress downstream of the elastic region. The peak wall shear stress at both the major changes in geometry (the distal neck $z = 13.5$ and the end of the elastic region $z = 15$) experience elevated wall shear stress magnitudes. At the end of the distal region the elastic-wall region has a time averaged wall shear stress 69% higher than the wall shear stress in the rigid-walled aneurysm.

The Oscillating Shear Index (OSI) quantifies the pulsatility and primary direction of the flow. It ranges from 0 (forward flow throughout the cardiac cycle) to 1 (fully reversed flow). An OSI of 0.5 corresponds to a pure oscillating flow with a WSS_{mean} of 0. Figure 8.31 shows the oscillating shear index distribution along the length of the aneurysm. The average OSI across the entire elastic region is 0.4 for the rigid-walled case and is slightly elevated to 0.437 for the elastic-walled case. Primarily this is seen in the extended section with increased oscillating shear index between $z = 9$ and $z = 12$. This includes a section which experiences flow which is predominantly negative ($OSI > 0.5$). Salsac *et al.* (2006) found the OSI of a rigid-walled healthy aorta to be 0.4, while others have calculated the OSI in a healthy artery to be 0.32 (Oyre *et al.* 1997). These results show elevated levels of oscillating shear index above the healthy norm,

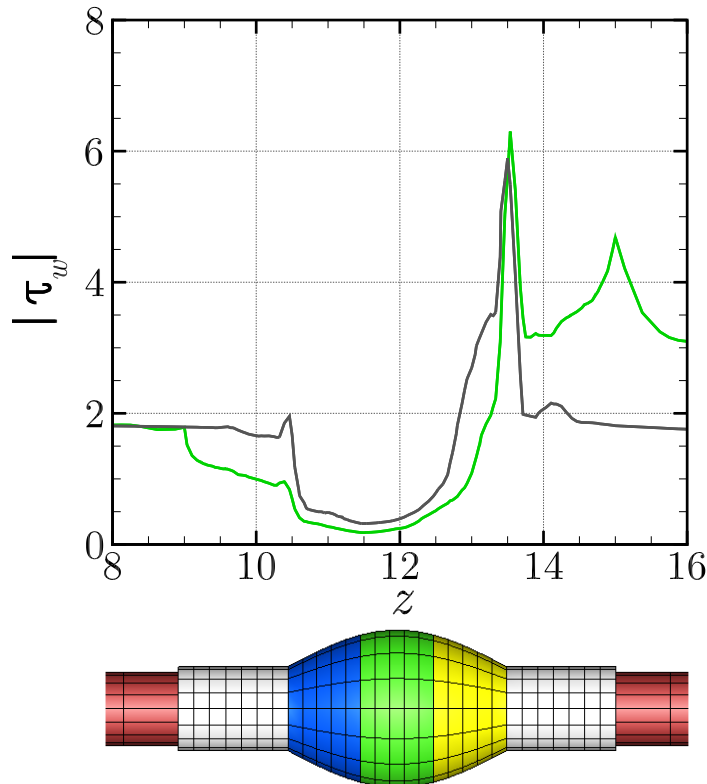


FIGURE 9.23: Comparison of the time-averaged wall shear stress magnitude with rigid and elastic-walls. The grey line represents the rigid-walled reference case, while the green lines represent the elastic-walled case with a wall stiffness of $E = 0.8$ MPa (healthy).

this is most significant when compared to the healthy elastic artery results discussed in chapter 8 which found the healthy $OSI = 0.22$. This indicates that the near-wall flow dynamics experience substantially different flow conditions to a healthy artery. Such differences in the OSI may affect endothelial function and exacerbate the growth of the aneurysm.

The results presented in this section show that the wall shear stress distribution in an elastic-walled aneurysm is very different to the distribution produced from the rigid-wall model. The differences in wall shear stress are caused by the large impact that the wall motion has on the flow near the wall in an aneurysm. The wall motion causes complex vortex interactions that affect the flow in the centre of the aneurysm and drives changes in flow direction in the wall shear layer. In terms of time-averaged measurements the wall shear stress at the distal neck has a much greater magnitude in the elastic-

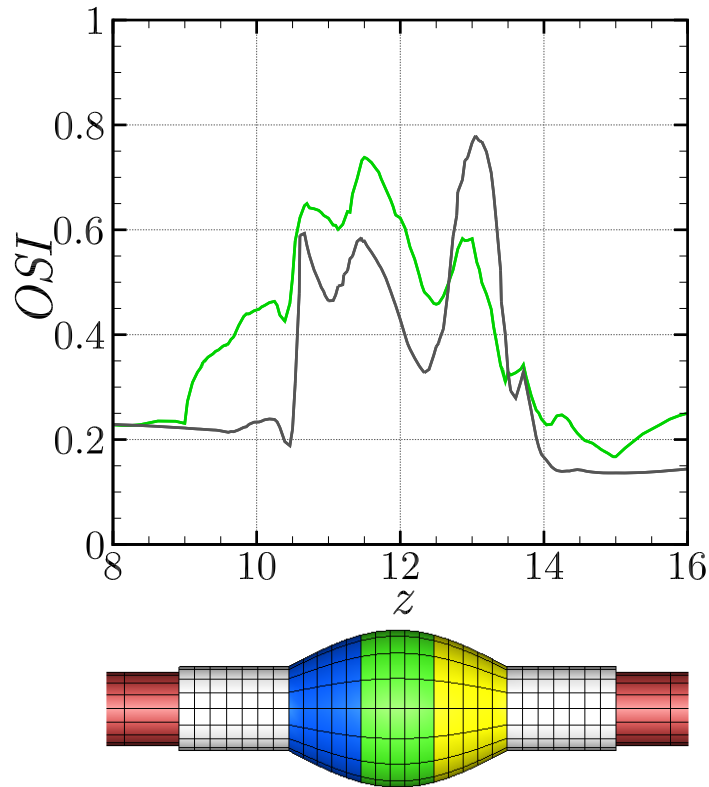


FIGURE 9.24: Comparison of the time-averaged oscillating shear index with rigid and elastic-walls. The grey line represents the rigid-walled reference case, while the green lines represent the elastic-walled case with a wall stiffness of $E = 0.8$ MPa (healthy).

walled case. Despite this, the elastic-walled case is subject to smaller wall shear stress gradients just upstream of the distal neck as the proximal vortex does not interact directly with the shear layer. This occurs as the effect of the proximal neck vortex is suppressed by the distal neck vortices. In any case, the dramatic differences in wall shear stress observed between the elastic-walled case and the rigid-walled case suggest that rigid-walled models are insufficient in describing the haemodynamic environment in an aneurysm.

9.5.4 The effect of heterogeneous wall properties

In section 9.5.3 the different haemodynamics in elastic and rigid-walled aneurysm models was identified. The impacts of these results were discussed in the context of the wall shear stress to assess the efficacy of using a rigid-wall model to assess the risk of rupture in an aneurysm. In the following sections, the wall stiffness at various locations

along the aneurysm bulge is altered to determine if a non-uniform stiffness distribution may cause an adverse haemodynamic environment. The wall stiffness was changed in the proximal, central and distal thirds of the aneurysm. The stiffness was varied from 0.6 MPa to 6.0 MPa with a healthy 0.8 MPa stiffness applied elsewhere in the elastic region.

9.5.4.1 Proximal region

Figures 9.25 and 9.26 show the temporal evolution of the flow for the cases when the proximal neck was weakened to 0.6 MPa and stiffened to 6.0 MPa, respectively. In comparison to the healthy case shown in figure 9.17, the weakened case shown in figure 9.25 features many of the same flow structures. Both involve the shedding of a vortex ring from the proximal neck and the development of a vortex ring pair at the distal neck. As time progresses, the proximal vortex ring travels through the aneurysm bulge to interact with the distal vortex pair and eventually gets flushed downstream. Subtle differences are evident: The flow features associated with the wall motion, namely the distal vortex ring pair, are of a greater strength (the vorticity is 39% greater for the inner distal vortex ring) in the reduced-stiffness proximal case and extend further upstream toward the proximal neck than in the simply healthy case. This is likely caused by the additional wall motion at the proximal neck causing an increase in the reverse flow in the boundary layer. A greater strain rate in the boundary layer leads to stronger shear layers and vortices forming. Furthermore, the location of additional wall motion (and increased wall velocity) also contributes to the distribution of the vortices. The strength of the reverse flow extends further upstream to the proximal neck as the peak wall motion is shifted toward the proximal neck (see figure 9.29). This results in the distal vortex ring pair forming and moving further upstream than in the healthy case.

The flow evolution depicted in figure 9.26 for the stiffened proximal wall case presents a very different flow field to that of the weakened and healthy cases. The wall motion is substantially less in the proximal region and this causes a reduction in the reverse flow in the boundary layer downstream at the distal neck. This suppresses the formation of a strong distal-vortex pair. Greater similarity is found between the evolution of the proximal vortex in the rigid-walled model in figure 9.15. The proximal vortex ring traverses the length of the aneurysm bulge and contributes to the reverse

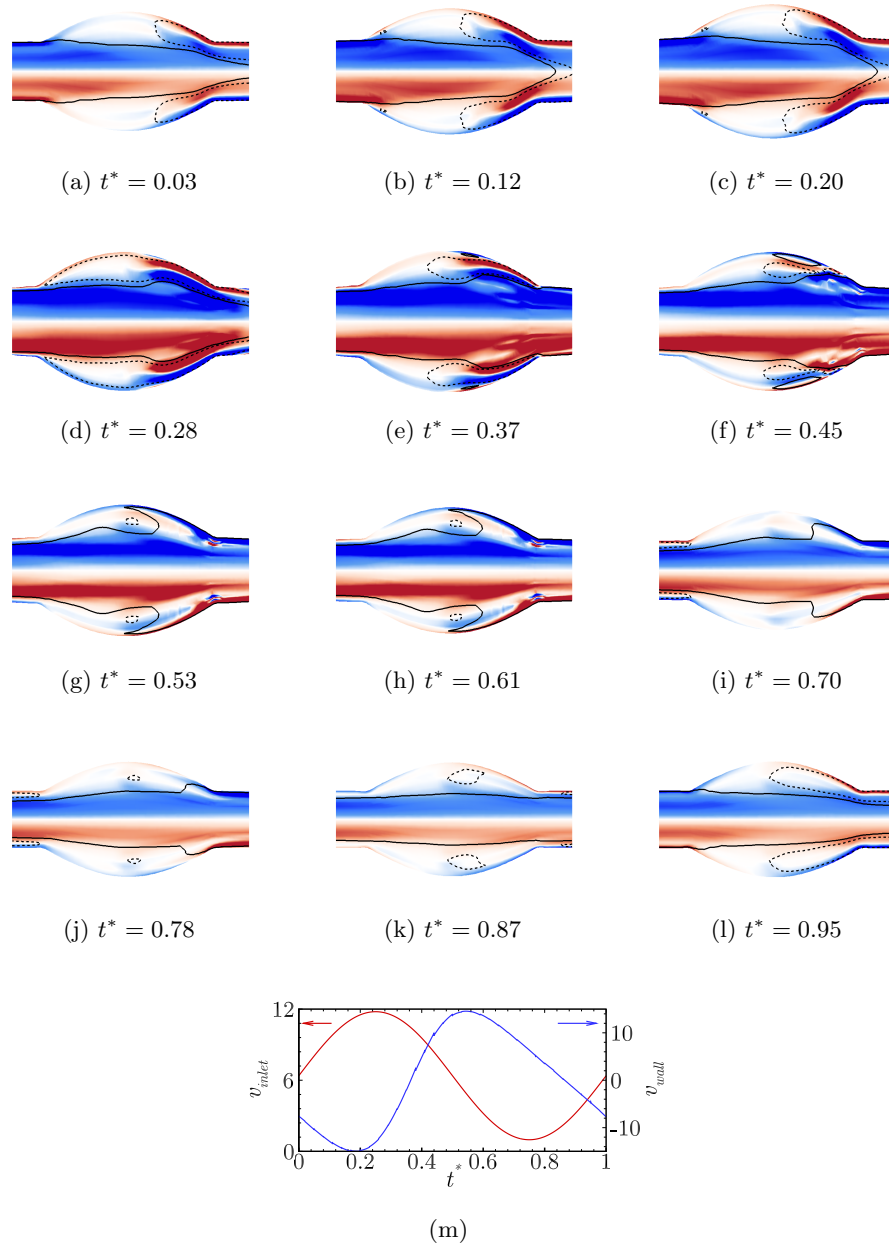
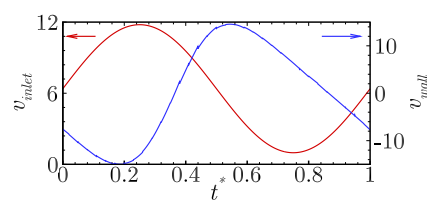
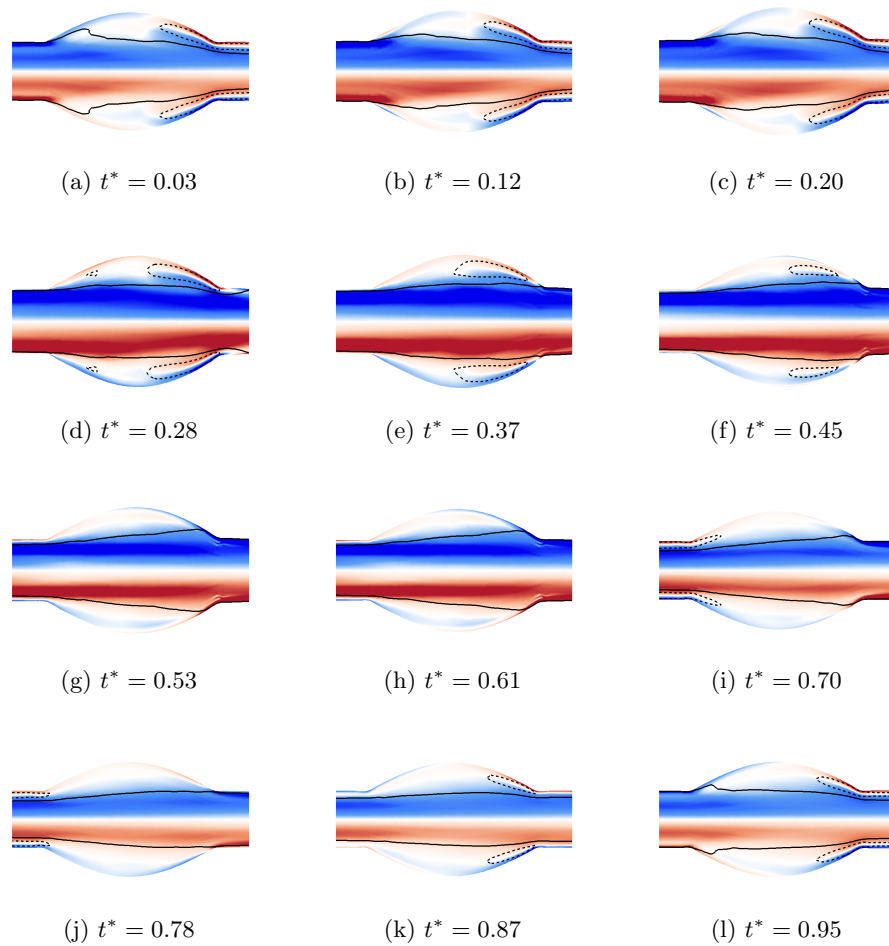


FIGURE 9.25: Flow through an elastic aneurysm throughout the cardiac cycle. The wall in the proximal third of the aneurysm bulge is weakened from $E = 0.8$ MPa to $E = 0.6$ MPa. Contours show vorticity in the y - z plane and range between -50 and 50. Positive vorticity (anticlockwise whorl) is represented by red contours and negative vorticity (clockwise whorl) is represented by blue contours. Line contours show the regions of flow with an axial velocity component of +1 and -1 (dashed lines are negative).

flow at the distal neck. However, as some wall motion is present, the shear layer at the distal neck is still subject to flow reversal. This causes a weak recirculation region to form which prevents the proximal vortex from impacting directly on the wall at the distal neck.

The effect of the change in wall stiffness is easily seen in terms of the wall shear stress in figure 9.27. For the case of the less stiff proximal region (figure 9.27(c)) the extra flow at the upstream proximal end of the aneurysm manifests itself in multiple ways. Firstly the proximal vortex is shed with greater vortex strength and is drawn closer to the wall due to the additional wall normal velocity. This creates a region of lower negative wall shear stress as the proximal vortex is shed at $t^* = 0.2$ and $z = 10.8$. The trajectory of this vortex A is indicated in figure 9.27. The additional reverse flow at the proximal neck also causes the fluid to be reversed further along the aneurysm bulge. This was shown in figure 9.25(e) and is reflected in the wall shear stress distribution in figure 9.27(c) by the extended period of lower wall shear stress which extends from the distal neck to meet the shear layer created by the proximal vortex. The increased reverse flow closer to the proximal neck also increases the strength and axial position of the strong inner vortex core (vortex B in figure 9.19) which forms in the shear layer between the reverse flow in the boundary layer and the forward flow through the centre of the aneurysm. The position of this vortex draws the shear layer into the secondary vortex ring (vortex C in figure 9.19) closer to the proximal neck than in the uniform elastic case. The strength of vortex C is also increased as a direct consequence of the strength of the inner-distal vortex B, this is reflected in the wall shear stress by an increase in the peak wall shear stress at $t^* = 0.5$ at $z = 12.5$. The effect of the secondary vortex is seen in the wall shear stress as it is flushed from the aneurysm bulge. The white lines on figure 9.27(c) indicate its trajectory. This is matched by the flushing observed in figure 9.25(g) to 9.25(i). Finally, the distal neck experiences a larger range of wall shear stresses compared to the healthy case as the greater flow rate generated by the wall motion causes steeper velocity gradients near the wall through a thinning of the boundary layer (equation 8.32). In conclusion, the increase in wall motion at the proximal neck causes a greater amount of reverse flow over a larger section of the aneurysm bulge which leads to more extreme values of wall shear stress both spatially and temporally.

The wall shear stress distribution in the stiffened proximal region is shown in fig-



(m)

FIGURE 9.26: Flow through an elastic aneurysm throughout the cardiac cycle. The wall in the proximal third of the aneurysm bulge is stiffened from $E = 0.8$ MPa to $E = 6.0$ MPa. Contours show vorticity in the y - z plane and range between -50 and 50 . Positive vorticity (anticlockwise whorl) is represented by red contours and negative vorticity (clockwise whorl) is represented by blue contours. Line contours show the regions of flow with an axial velocity component of $+1$ and -1 (dashed lines are negative).

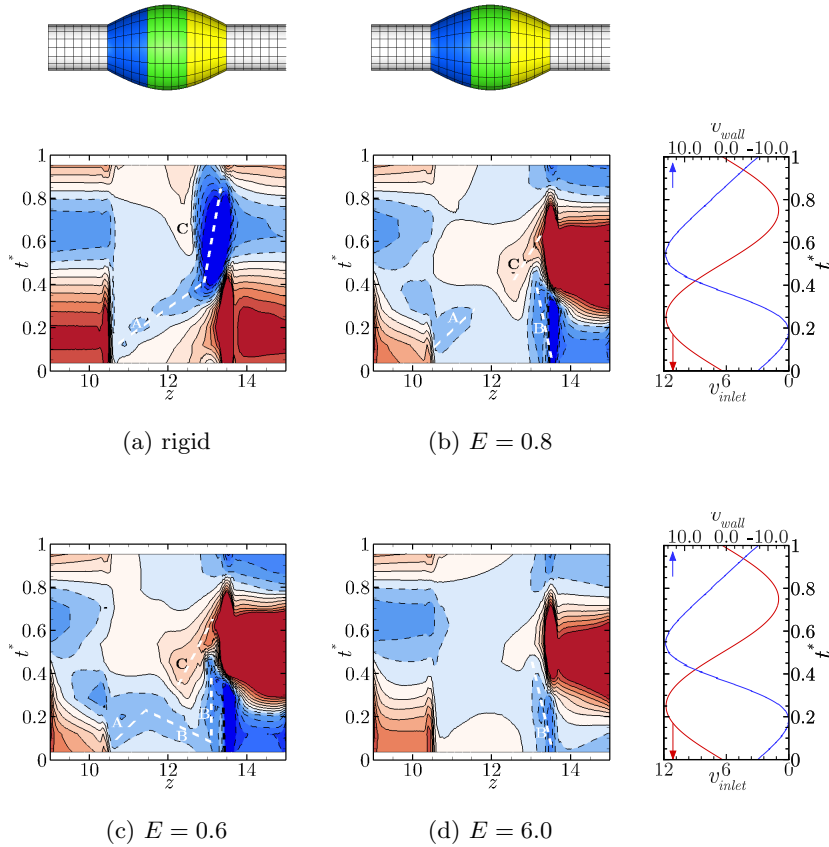


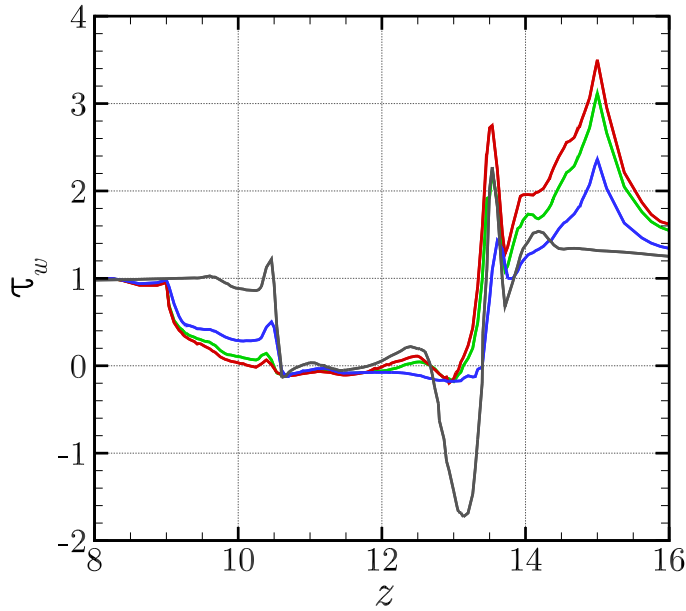
FIGURE 9.27: The variation of wall shear stress (WSS) in an aneurysm as a function of time and space. Contours show WSS with high low levels represented by red and blue, respectively. Negative values are represented by dashed contour lines. The contour levels are equispaced and vary from -3.35 Pa to 3.35 Pa. Sub-plots (a)-(d) represent the WSS in an aneurysm with rigid-walls, uniformly elastic-walls of stiffness $E = 0.8$ MPa, a local weakening of the proximal wall to $E = 0.6$ MPa and a local stiffening of the proximal wall to $E = 6.0$ MPa respectively. The figures on the right show the velocity inlet (red) and wall velocity (blue).

ure 9.27(d). In this case an overall reduction in the wall shear stress magnitude is seen. Figure 9.28(b) confirms that this is the case. The reduced wall motion reduces the maximum and minimum volume rate of change of the aneurysm. At lower flow rates the local Reynolds number is reduced causing a thicker boundary layer to form (see equation 8.32). A thicker boundary layer will cause a reduction in the wall shear stress magnitude. Furthermore, the strength of all vortices produced is diminished, consequently reducing the strength of any shear layer interactions that occur. The distal vortices are weaker due to the smaller flow rate contribution from the wall. The weakness of the vortices is reflected in the velocity gradients in the boundary layer, which leads to a reduction in the local wall shear stress magnitude. The strength of the

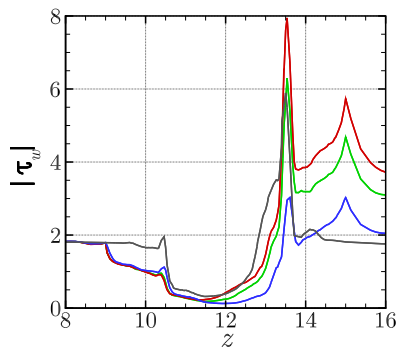
proximal vortex is also reduced as the stiffer wall causes a smaller wall displacement at the proximal neck. The smaller wall displacement limits the spatial acceleration experienced by the fluid as it rolls off the proximal neck. The limited vortex strength and reduced flow reversal in the boundary layer towards the proximal neck causes the detachment of the vortex C to be delayed and occur closer to the distal neck, this is reflected in the wall shear stress by a reduction in the size of the positive wall shear stress area at $t^* = 0.5$ and $z = 12.5$. In conclusion, the decrease in wall motion at the proximal neck causes a decrease in the amount of reverse flow over a larger section of the aneurysm which leads to a smaller range of wall shear stress both spatially and temporally.

The time-averaged results presented in figure 9.28 support the findings described herein. An increase in wall motion at the upstream proximal end leads to an increase in the wall shear stress magnitude both in terms of peak values (as the velocities are greater and therefore boundary layer is thinner) and in terms of regions with elevated wall shear stress. Conversely a stiffer proximal neck corresponds to a reduction in the wall shear stress magnitude throughout the aneurysm bulge both in terms of peak values and spatial distribution. The stiffened wall case does exhibit a larger time-averaged wall shear stress at the proximal neck due to the smaller displacement at this location. This allows the flow to remain attached to the wall: equation 8.49 indicates that if the gradient of the wall is less (i.e. the convective acceleration is less) the resultant wall shear stress will be greater.

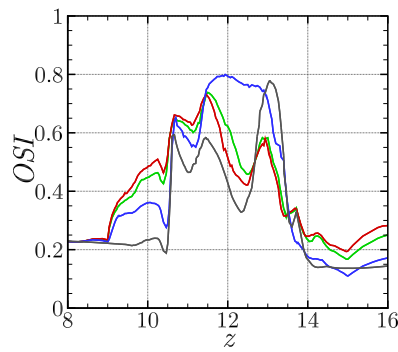
Figure 9.28(c) shows that as expected with the increase in wall motion and flow reversal, the oscillating shear index increases. Of particular interest is the increase in the oscillating shear index for the stiffened wall case around $z = 11.5 - 13$. This indicates an increase in the time spent with reverse flow in the distal portion of the aneurysm bulge. Physically this may be described by considering the wall motion shown in figure 9.29(b). The reduced wall motion at the proximal neck causes a decrease in the total flow rate caused by the change in geometry. This has already been shown to cause a reduction in the relative strength of the proximal and distal vortex structure. From $t^* = 0.35 - 0.85$ when the wall is collapsing back towards the unstressed state, the flow rate generated as a result of the collapsing wall volume in the distal section is greater than that produced upstream. The local wall geometry of the distal neck being that of a converging nozzle causes the mean wall velocity to be directed upstream. As the flow



(a)



(b)



(c)

FIGURE 9.28: Comparison of the axial distributions of the (a) time-averaged wall shear stress, (b) the time-averaged wall shear stress magnitude, and (c) the oscillating shear index, with varying stiffness in the proximal region. The grey line represents the rigid-walled reference case, red, green and blue lines represent the cases with a local variation in proximal wall stiffness of $E = 0.6$ MPa, $E = 0.8$ MPa (uniformly healthy) and $E = 6.0$ MPa respectively. Note for the elastic-walled cases a stiffness of $E = 0.8$ MPa is applied outside beyond the altered stiffness region.

produced at the wall upstream is smaller than that produced at the distal neck the net flow is preferentially in the reverse flow direction. This causes the increase in OSI seen in figure 9.28(c). The same logic may be applied to the less stiff proximal region case. In this scenario the upstream flow is greater than the downstream flow causing a mean wall flow direction in the positive direction. This is observed by the reduction in OSI (below 0.5 indicating predominantly forward flow) for the less stiff case. Contributing to the forward flow in the boundary layer in the less stiff and uniformly elastic cases is the roll up of the shear layer into the secondary distal vortex ring C. When this vortex ring detaches from the wall it causes the local boundary layer flow to be in the forward direction. This roll up is present in the rigid-walled, uniformly elastic and weakened proximal wall case but not present in the stiffened elastic-wall case. As the wall motion is reduced at the proximal section the strength of the inner distal vortex B and proximal vortex A is reduced to the point that it does not cause the roll up of the shear layer into vortex C until the flushing of the vortices occurs. As a result, this does not contribute forward flow in the boundary layer which in turn results in a high OSI.

In this section the effect of a variable stiffness in the proximal third of a typical fusiform abdominal aortic aneurysm has been considered. It was shown that changes in the stiffness in the proximal region can have a dramatic effect on the flow through an aneurysm as the changes in flow propagate downstream. A decrease in wall stiffness, which causes an increase in wall motion, increases the strength of the vortex structures generated in the aneurysm. Consequently, the wall shear stress magnitude is increased in downstream sections as it is predominantly related to the boundary layer flow rate and the strength of vortices in the near-wall region. An increase in wall stiffness resulted in the weakening of vortex structures. This was primarily noted in the absence of the secondary vortex ring C in the middle part of the aneurysm. Instead, the shear layer remains attached until much of the flushing process has occurred and the shear layer is shed from the aneurysm. The resultant wall shear stresses were of lesser magnitude and the oscillating shear index was increased locally as a result of the vortex C suppression. In terms of the healthy function of the endothelial cells the stiffened wall had a significantly different OSI profile which may cause endothelial injury. However, the greater wall shear stress magnitudes throughout the aneurysm bulge which formed in the weakened proximal wall case suggest this is the less desirable scenario.

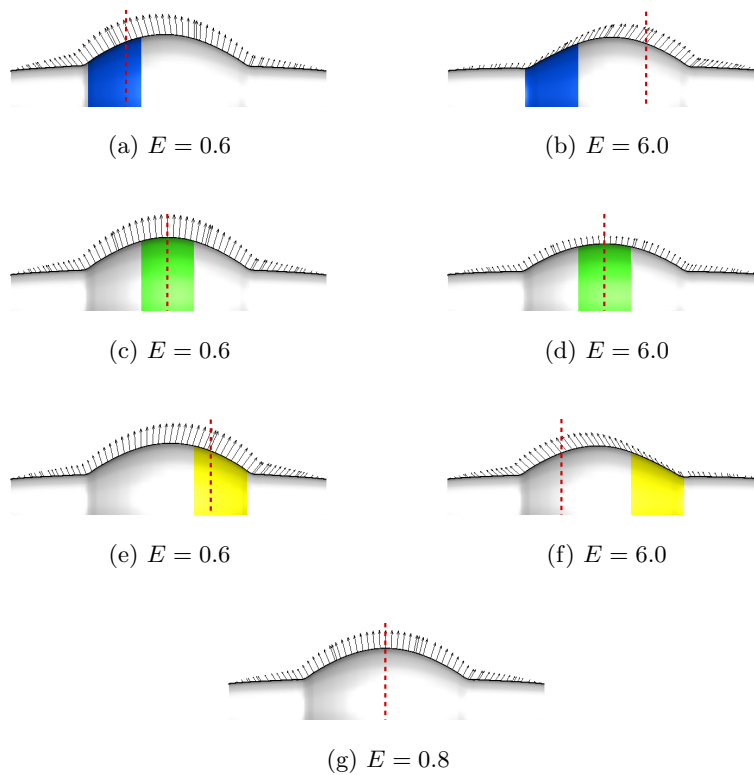


FIGURE 9.29: The velocity of the wall under various stiffness conditions taken at an arbitrary point during the systolic expansion. The red dashed line in each case indicates the location of maximum net wall velocity. Figures (a) and (b) show the cases of altered stiffness in the proximal section; (c) and (d) show the cases of altered stiffness in the central section; and (d) and (e) show the cases of altered stiffness in the distal section. plot (f) is the case when a uniform stiffness is prescribed throughout the aneurysm.

9.5.4.2 Central region

Figures 9.30 and 9.31 show the temporal evolution of the flow field for the cases when the central bulge region was weakened to 0.6 MPa and stiffened to 6.0 MPa, respectively. In figure 9.30 many of the flow features depicted in the healthy case (figure 9.17) and the less stiff proximal case (figure 9.25) are evident. Just as in the Proximal less stiff case: The flow features associated with the wall motion, namely the distal vortex ring pair are of a greater strength in the reduced central stiffness case and extend further upstream toward the proximal neck than in the simply healthy case. The greater freedom of the wall at this central location allows the wall displacement both globally and locally to be increased. Reynolds transport theorem (equation 8.39) suggests that in order to conserve mass, the reverse flow in the boundary layer increases as the pressure in the

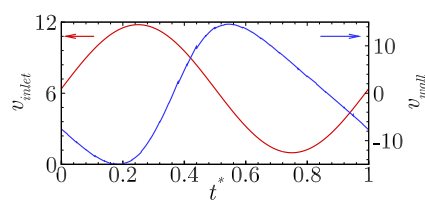
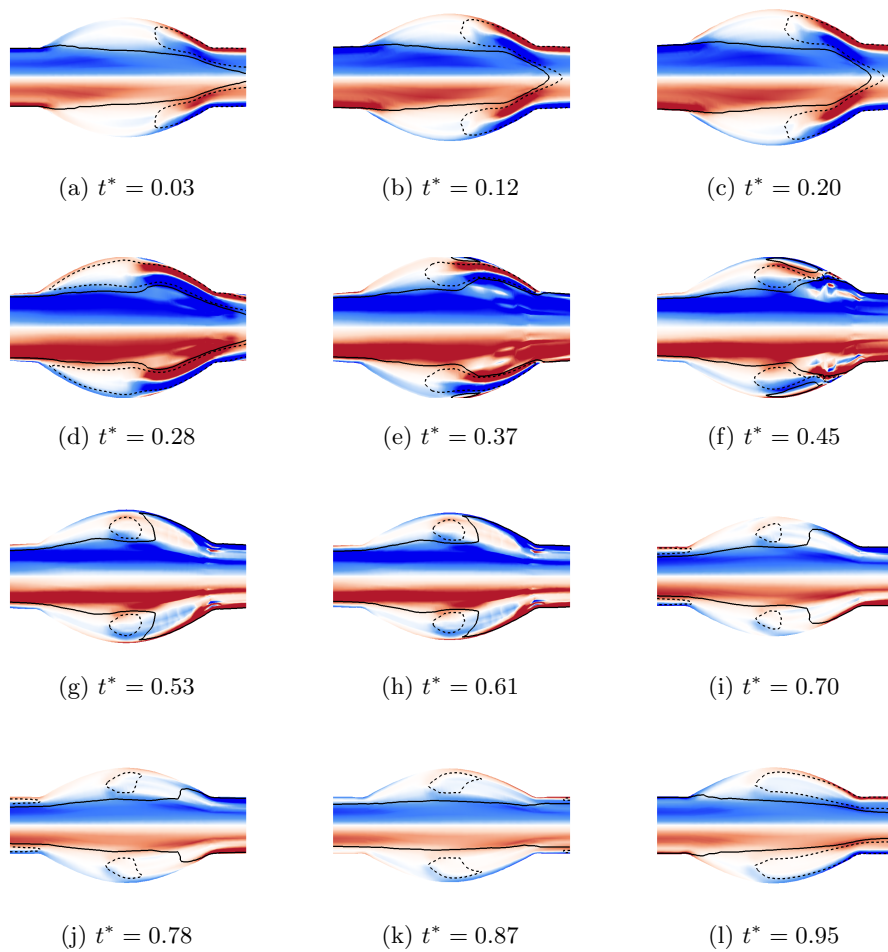
aneurysm bulge increases. This leads to a larger strain-rate in the shear layers between both the wall and flow (vortex C' in figure 9.19) and the reverse flow in the boundary layer and forward flow through the lumen (vortex B in figure 9.19). This leads to the stronger vorticity fields in each of the shear layers as well as the formation of strong vortex rings.

Furthermore, the location of additional wall motion (and increased wall velocity) contributes to the distribution of the vortices. Figure 9.29 shows the wall velocity distribution in each of the heterogeneous wall stiffness cases. In the case of a less stiff central region the region of maximum wall motion is at the centre of the aneurysm bulge. This is in contrast to the less stiff proximal case, the flow reversal is less strong at the proximal neck in the weakened central region case. This is reflected in the location of the vortex structures developed in the aneurysm bulge. The distal vortex pair extends further toward the proximal neck in the proximal weakened case than in the central weakened case. Similarly, in the central weakened case the vortices move further into the domain than the simple uniformly stiff case.

The flow evolution depicted in figure 9.31 for the stiffened central wall case presents a very different flow field to that of the weakened and healthy cases. As with the stiffened proximal case, the wall motion is substantially less and this causes a reduction in the reverse flow in the boundary layer downstream at the distal neck. This prevents the formation of a strong distal-vortex pair.

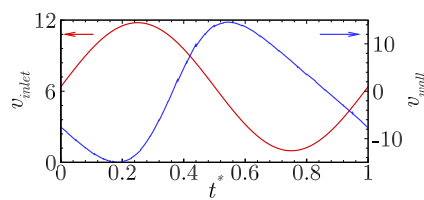
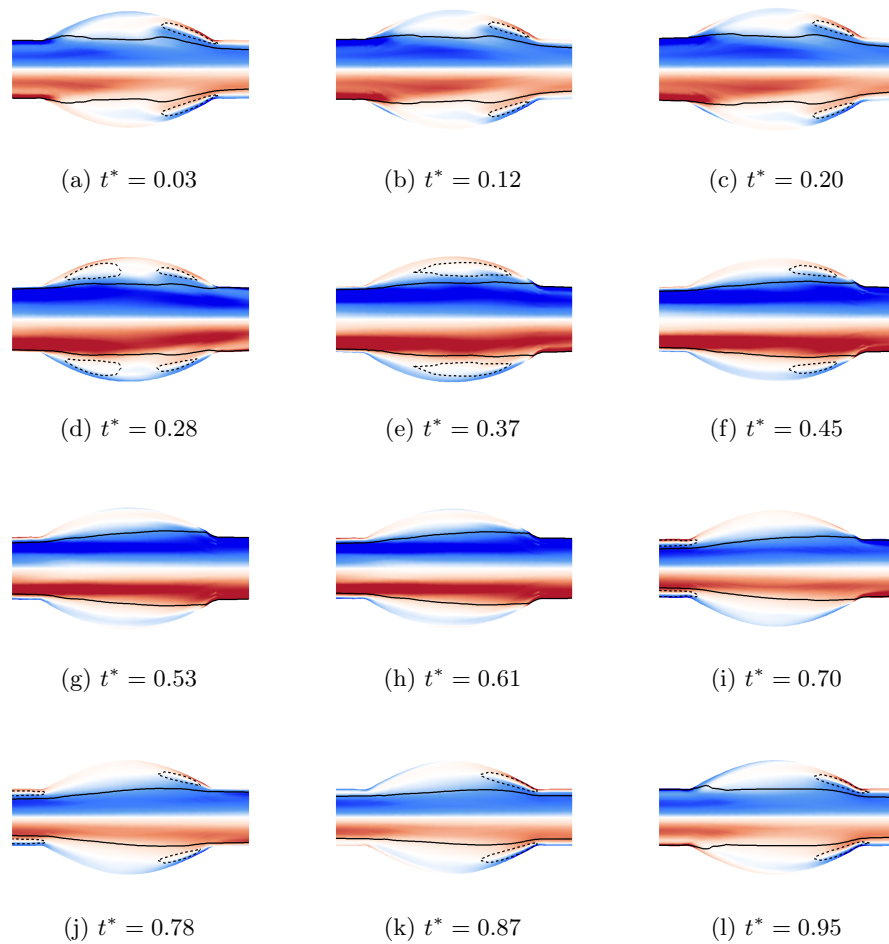
Consistent with the results from the weakened proximal case, the weakened central region exhibits a stronger proximal vortex being shed and drawn closer to the wall due to the additional wall normal velocity (figure 9.32(c)). A lower negative wall shear stress is observed as the proximal vortex is shed at $t^* = 0.2$ and $z = 10.8$. The additional reverse flow in the central region causes the fluid to be reversed in the boundary layer for a greater length of the aneurysm bulge compared to the uniformly elastic case which is reflected in the wall shear stress distribution (figure 9.32(c)). The position of the strong distal vortex draws the shear layer into the secondary vortex ring (Vortex C in figure 9.19) closer to the proximal neck than in the uniform elastic case but less than the proximal case.

Interestingly, the strength of vortex C is greater in the central stiffened case as a result of the greater wall normal velocity at the central location at which the vortex forms, causing a greater curling velocity gradient. The strength of vortex C is also



(m)

FIGURE 9.30: Flow through an elastic aneurysm throughout the cardiac cycle. The wall in the central third of the aneurysm bulge is weakened from $E = 0.8$ MPa to $E = 0.6$ MPa. Contours show vorticity in the y - z plane and range between -50 and 50. Positive vorticity (anticlockwise whorl) is represented by red contours and negative vorticity (clockwise whorl) is represented by blue contours. Line contours show the regions of flow with an axial velocity component of +1 and -1 (dashed lines are negative).



(m)

FIGURE 9.31: Flow through an elastic aneurysm throughout the cardiac cycle. The wall in the central third of the aneurysm bulge is stiffened from $E = 0.8$ MPa to $E = 6.0$ MPa. Contours show vorticity in the y - z plane and range between -50 and 50 . Positive vorticity (anticlockwise whorl) is represented by red contours and negative vorticity (clockwise whorl) is represented by blue contours. Line contours show the regions of flow with an axial velocity component of $+1$ and -1 (dashed lines are negative).

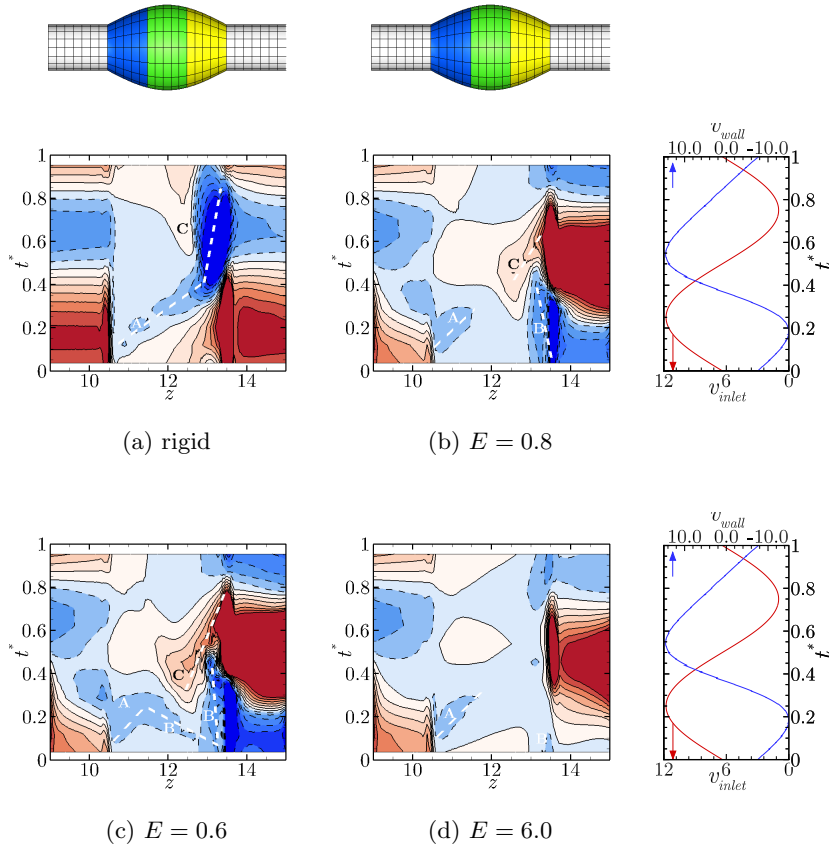


FIGURE 9.32: The variation of wall shear stress (WSS) in an aneurysm as a function of both time and space. Contours show WSS with high low levels represented by red and blue, respectively. Negative values are represented by dashed contour lines. The contour levels are equispaced and vary from -3.35 Pa to 3.35 Pa. Sub-plots (a)-(d) represent the WSS in an aneurysm with rigid-walls, uniformly elastic-walls of stiffness $E = 0.8$ MPa, a local weakening of the central wall to $E = 0.6$ MPa and a local stiffening of the central wall to $E = 6.0$ MPa respectively. The figures on the right show the velocity inlet (red) and wall velocity (blue).

increased as a direct consequence of the strength of the inner-distal vortex B. The white lines on figure 9.32(c) indicate the trajectories of vortices A, B and C. This is matched by the flushing observed in figure 9.31(g) to 9.31(i). Finally, as with the proximal neck case the distal neck experiences a larger range of wall shear stresses compared to the healthy case.

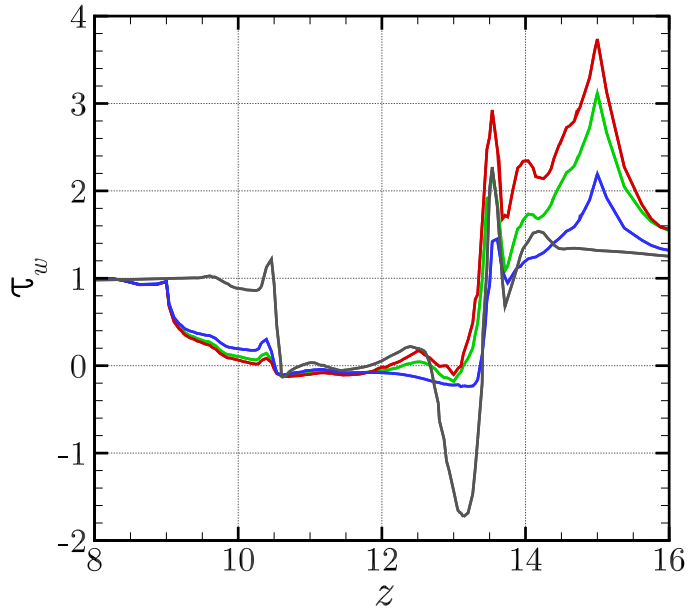
The stiffened case (figure 9.32(d)) shows an overall reduction in the wall shear stress magnitude. Figure 9.33(b) confirms this is the case. As was observed for the stiffer proximal case in § 9.5.4.1, the strength of all vortices produced is diminished, reducing the strength of any shear layer interactions that occur. The distal vortices are weaker (by 68% than the healthy case and 23% than the proximally stiffened case) due to the

smaller flow rate contribution from the wall. Similarly vortex C is suppressed due to the limited vortex strength and reduced flow reversal in the boundary layer. A region of slightly positive wall shear stress is observed at the centre of the aneurysm bulge at $t^* = 0.55$. This is caused by the motion of the aneurysm wall at this time causing forward flow in the boundary layer over the flattened central region. The formation of secondary vortex structures is suppressed further than the stiffened proximal case due to the more uniform wall profile throughout the domain (see figure 9.34).

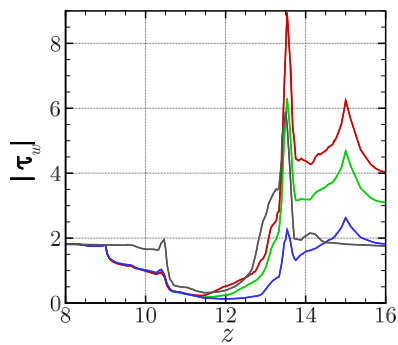
The time-averaged results presented in figure 9.33 support the findings described herein. The increase and decrease of wall stiffness has an identical impact on the peak wall shear stress and wall shear stress distribution as for the proximal stiffened case.

Figure 9.33(c) shows that as expected with the increase in wall motion and flow reversal, the oscillating shear index increases. As with the proximal wall case there is an elevation in the oscillating shear index for the stiffened wall case around $z = 11.5 - 13$. Physically this may be described by considering the wall motion shown in figure 9.29(d). The reduced wall motion in the central location causes a decrease in the total flow rate caused by the change in geometry. From $t^* = 0.35 - 0.85$ when the wall is collapsing back towards its initial state, the flow rate generated as a result of the collapsing wall volume in the distal section is greater than that produced immediately upstream in the central stiffened zone. The local wall geometry being that of a converging nozzle causes the mean wall velocity to be directed upstream at the wall. As the flow produced immediately upstream at the stiffened central location is smaller than that produced at the distal neck, the net flow is preferentially in the reverse flow direction. This causes the increase in OSI seen in figure 9.28(c). The reverse flow in the stiffened central region case is greater than the reverse flow in the stiffened proximal case. This may be the result of the wall geometry formed, depicted in figure 9.34. The wall geometry in the proximal stiffened case shows a much more gradual wall gradient from the proximal neck. This may allow the fluid to remain attached to the wall allowing a less steep velocity gradient and consequently reduced reverse flow.

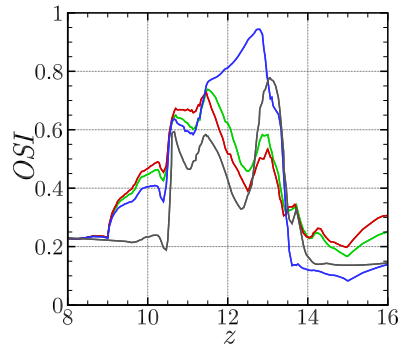
In this section the effect of a variable stiffness in the central third of a typical fusiform abdominal aortic aneurysm has been considered. It was shown that changes in the stiffness in the central region can have a similar effect both globally and locally, to the proximal case. While the OSI was significantly different in the stiffened central region case compared to the uniformly stiff case, the increased wall shear stress and



(a)



(b)



(c)

FIGURE 9.33: Comparison of the axial distributions of the (a) time-averaged wall shear stress, (b) the time-averaged wall shear stress magnitude, and (c) the oscillating shear index, with varying stiffness in the central region. The grey line represents the rigid-walled reference case, red, green and blue lines represent the cases with a local variation in central wall stiffness of $E = 0.6$ MPa, $E = 0.8$ MPa (uniformly healthy) and $E = 6.0$ MPa respectively. Note for the elastic-walled cases a stiffness of $E = 0.8$ MPa is applied beyond the stiffened region.

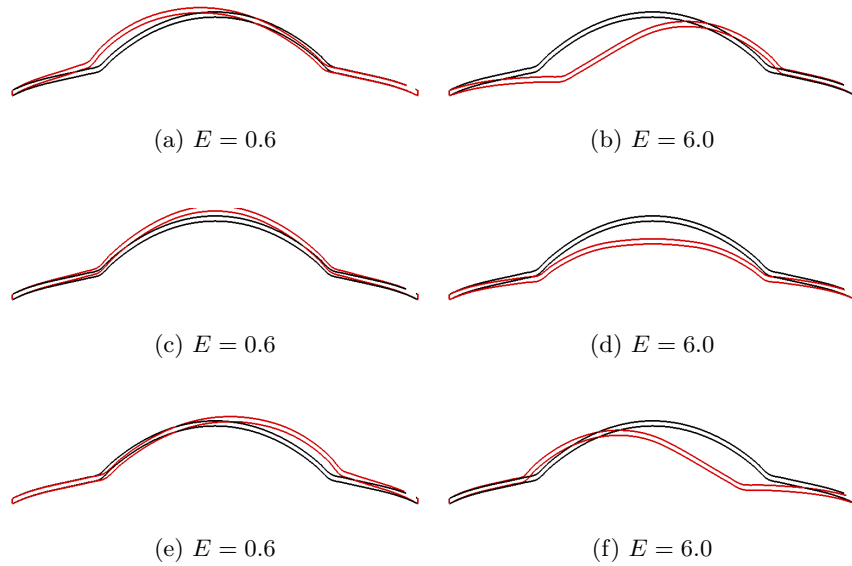


FIGURE 9.34: The displacement of the wall formed at peak distension under various stiffness conditions. The displacement is amplified by a factor of 4 for visualization purposes. Red lines represent the case with an altered stiffness, black lines represent the case of uniform stiffness ($E = 0.8$) MPa. Figures (a) and (b) show the cases of altered stiffness in the proximal section; (c) and (d) show the cases of altered stiffness in the central section; and (d) and (e) show the cases of altered stiffness in the distal section.

wall shear stress gradients in the less stiff central region case indicates that this is the less desirable haemodynamic scenario for the healthy function of endothelial cells and aneurysm rupture prognosis.

9.5.4.3 Distal region

Having considered the effect of an altered stiffness region in both the proximal and central thirds of an aneurysm, the effect of wall stiffness in the distal third is finally considered. Figures 9.35 and 9.36 show the temporal evolution of the flow field for the cases when the distal region was weakened to 0.6 MPa and stiffened to 6.0 MPa, respectively. The less stiff distal neck case shares many features with the less stiff proximal and central region cases and indeed with the uniform stiffness case of figure 9.17. The primary differences are observed in figure 9.35(f) in which some complex interactions are observed during the breakup and flushing of the distal vortex pair. The complex interaction is likely caused by the large wall normal velocity in the distal region at this time. Figure 9.29(e) shows how the greater wall motion at the distal neck causes a shift of the peak wall velocity into the distal neck region. The additional wall normal

velocity forces the wall shear layer away from the wall. Once separated, this vortex interacts with the strong distal vortex pair at the distal neck. Furthermore the steep wall gradients in this location mean the flow is subject to strong spatial accelerations at the distal neck which strains the flow further. Similar vortex distribution phenomena are observed elsewhere in the aneurysm bulge with strong vortices forming as a result of the increased wall motion.

The location of additional wall motion (and increased wall velocity) also contributes to the distribution of the vortices. Figure 9.29 shows the wall velocity distribution in each of the heterogeneous wall stiffness cases. As the maximum wall motion (and wall velocity) occurs at the distal neck, the distal neck vortex pair is pulled further from the centreline of the aneurysm and restricted to the distal region of the bulge.

The flow evolution depicted in figure 9.36 for the stiffened distal wall section presents a very different flow field to that of the weakened and healthy cases. Like the previous stiffened cases, the wall motion is substantially reduced, causing a reduction in the reverse flow in the boundary layer at the distal neck. This prevents the formation of a strong distal-vortex pair. In the stiffened distal neck case the lack of sufficient wall motion upstream of the weakened distal vortex precludes the shear layer from rolling up into a secondary vortex ring. Instead, the shear layer is simply detached by the motion of the wall as it begins to move back towards its initial state in figure 9.36(f).

The change in flow dynamics induced by the change in wall stiffness affects the wall shear stress. For the weaker distal neck case (figure 9.37(c)) the extra flow at the distal neck affects the wall shear stress in multiple ways consistent with the weakened proximal and central region cases. The presence of the proximal vortex creates a lower negative wall shear stress as it is shed at $t^* = 0.2$ and $z = 10.8$. The presence of vortex B and C (in figure 9.19 is reflected in the wall shear stress distribution by the positive wall shear stress which forms at $t^* = 0.5$ and $z = 12.5$. As the maximum wall velocity occurs at the distal neck, the strong forward shear layer associated with the secondary vortex ring does not extend as far into the aneurysm bulge and remains localised around the distal neck. The distal neck experiences a larger range of wall shear stresses compared to the healthy case. The greater flow rate generated by the wall motion causes steeper velocity gradients near the wall which results in a thinner boundary layer (equation 8.32). Despite this, the peak wall shear stress magnitude is less than in the weakened proximal and central region cases as the wall gradient (shown

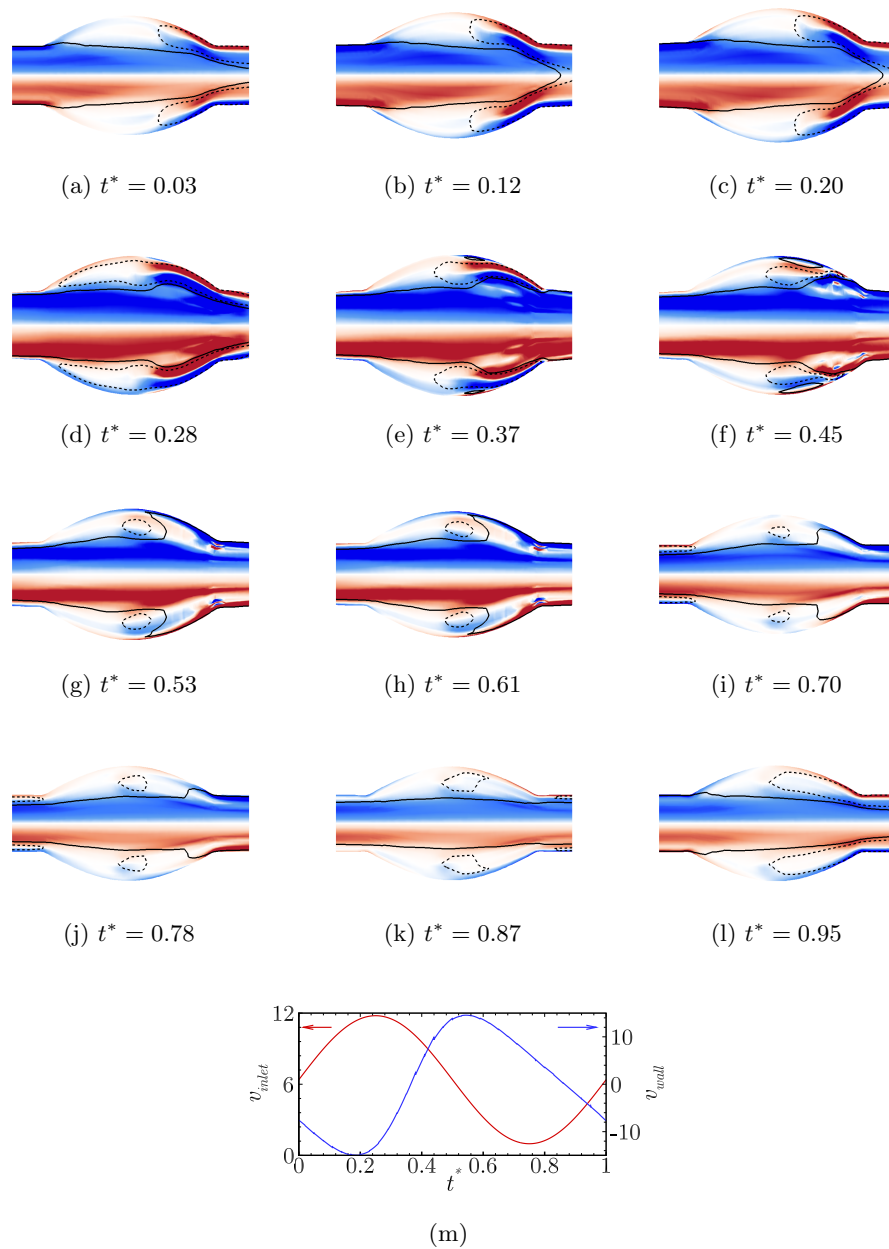
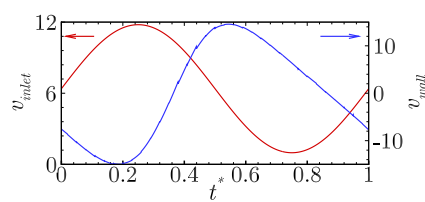
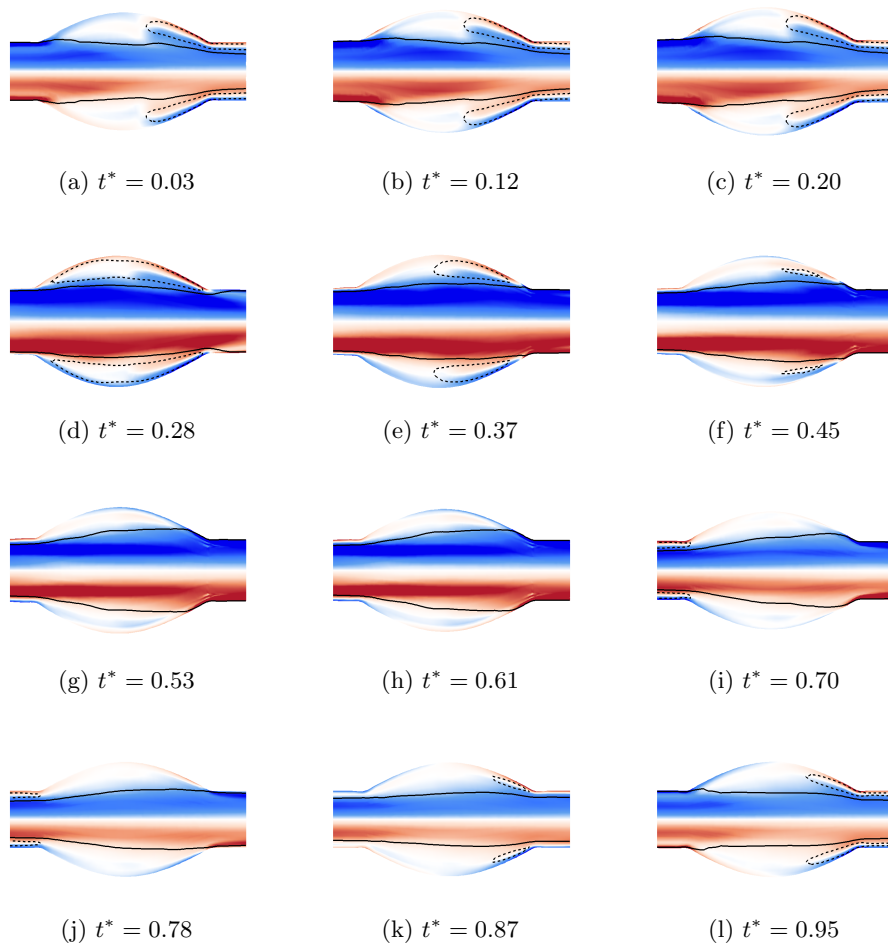


FIGURE 9.35: Flow through an elastic aneurysm throughout the cardiac cycle. The wall in the distal third of the aneurysm bulge is weakened from $E = 0.8$ MPa to $E = 0.6$ MPa. Contours show vorticity in the y - z plane and range between -50 and 50. Positive vorticity (anticlockwise whorl) is represented by red contours and negative vorticity (clockwise whorl) is represented by blue contours. Line contours show the regions of flow with an axial velocity component of +1 and -1 (dashed lines are negative).



(m)

FIGURE 9.36: Flow through an elastic aneurysm throughout the cardiac cycle. The wall in the distal third of the aneurysm bulge is stiffened from $E = 0.8$ MPa to $E = 6.0$ MPa. Contours show vorticity in the y - z plane and range between -50 and 50. Positive vorticity (anticlockwise whorl) is represented by red contours and negative vorticity (clockwise whorl) is represented by blue contours. Line contours show the regions of flow with an axial velocity component of +1 and -1 (dashed lines are negative).

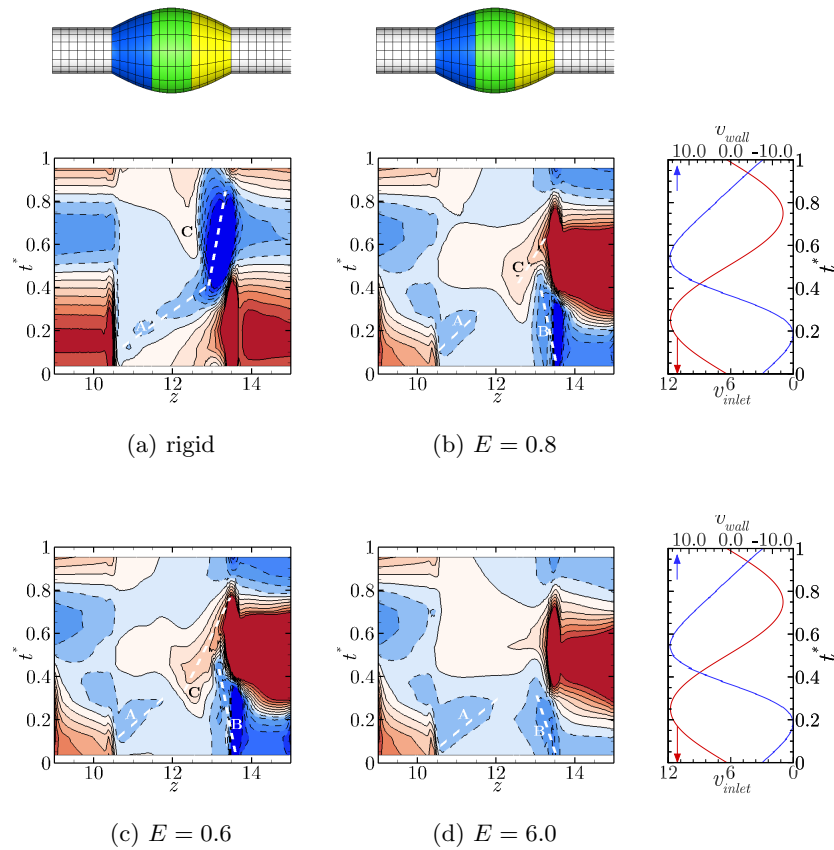


FIGURE 9.37: The variation of wall shear stress (WSS) in an aneurysm as a function of both time and space. Contours show WSS with high WSS represented by red and low WSS represented by blue, negative values are represented by dashed contour lines. The contour levels are equispaced and vary from -3.35 Pa to 3.35 Pa. Sub-plots (a)-(d) represent the WSS in an aneurysm with rigid-walls, uniformly elastic-walls of stiffness $E = 0.8$ MPa, a local weakening of the distal wall to $E = 0.6$ MPa and a local stiffening of the distal wall to $E = 6.0$ MPa respectively. The figures on the right show the velocity inlet (red) and wall velocity (blue).

in figure 9.34) is less for the weakened distal case. Smaller wall gradients cause less severe spatial accelerations and consequently less thinning of the boundary layer.

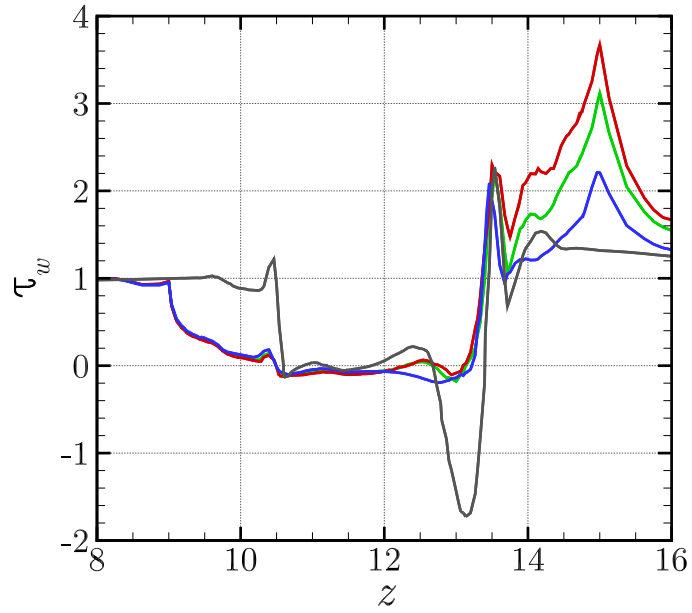
The stiffened case (figure 9.37(d)) shows an overall reduction in the wall shear stress magnitude. Figure 9.38(b) confirms this is the case. This is in line with the findings for the proximal and central region stiffened cases and is a result of the reduced wall motion see equations 8.32 and 8.39. Locally, the strength of the shear layer at the distal neck is greater than both the proximal and central region cases as a result of the local increase in wall velocity. As was found in the previous stiffened cases, the limited vortex strength and reduced flow reversal in the boundary layer completely suppresses

the formation of vortex C. Despite the suppression of vortex C, a region of positive wall shear stress is observed at the centre of the aneurysm bulge at $t^* = 0.55$. For this case the stiffened distal region causes a greater flow rate contribution from the proximal third of the aneurysm (see figure 9.29). This causes a net forward flow in the boundary layer over the flattened central region which corresponds to the positive shear layer (and shear stress) in this region at this time. In conclusion, the decrease in wall motion at the distal neck of the aneurysm decreases the amount of flow in the aneurysm and reduces the wall shear stress in the aneurysm. The formation of secondary vortex structures is suppressed as a result of the reduced distal vortex strength.

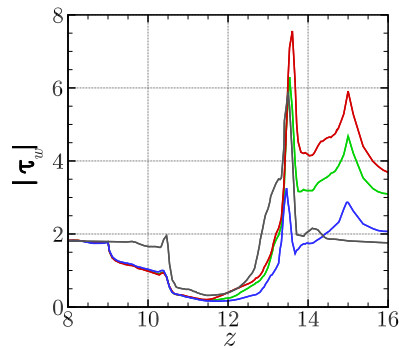
The time-averaged results presented in figure 9.38 support these findings. An increase in wall motion in the distal region leads to an increase in the wall shear stress magnitude and distribution. The stiffened wall case does exhibit a larger time-averaged wall shear stress at the proximal neck due to the smaller displacement at this location. This allows the flow to remain attached to the wall, equation 8.49 indicates that if the gradient of the wall is less (i.e. the convective acceleration is less) the resultant wall shear stress will be greater.

Figure 9.38(c) confirms that as the wall motion and flow reversal is increased, the oscillating shear index increases. The region of increased reverse flow, $z = 11.5 - 13$, found in the stiff proximal region and stiff central region cases is also evident in the distal neck case, albeit of lesser significance. Because it is the distal wall region which has the greatest motion and velocity (see figure 9.29), the flow upstream is not subject to the local changes in flow conditions caused by the change in stiffness (some effects are felt from the altered wall geometry e.g. see figure 9.34). As such, the wall from $z = 11.5 - 13$ is not subject to large changes in flow rate which occur due to the wall motion as this region sits predominantly upstream of where the increased flow rate is occurring. The OSI does increase in the region $z = 12.5 - 13$ in which the wall stiffness has been altered and the wall motion is greater.

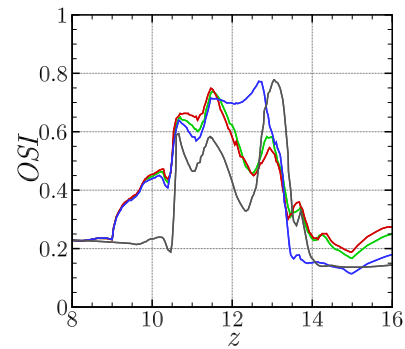
In this section the effect of a variable stiffness in the distal third of a medium sized fusiform abdominal aortic aneurysm has been considered. It was shown that changes in the stiffness in the distal region can affect the wall shear stress distribution. Changes in the wall shear stress distribution as a result of the heterogeneous wall stiffness in the distal region were less substantial than for changes in stiffness in other locations. The increased wall shear stress and wall shear stress gradients in the less-stiff distal region



(a)



(b)



(c)

FIGURE 9.38: Comparison of the axial distributions of the (a) time-averaged wall shear stress, (b) the time-averaged wall shear stress magnitude, and (c) the oscillating shear index, with varying stiffness in the distal region. The grey line represents the rigid-walled reference case, red, green and blue lines represent the cases with a local variation in distal wall stiffness of $E = 0.6$ MPa, $E = 0.8$ MPa (uniformly healthy) and $E = 6.0$ MPa respectively. Note for the elastic-walled cases a stiffness of $E = 0.8$ MPa is applied beyond the stiffened region.

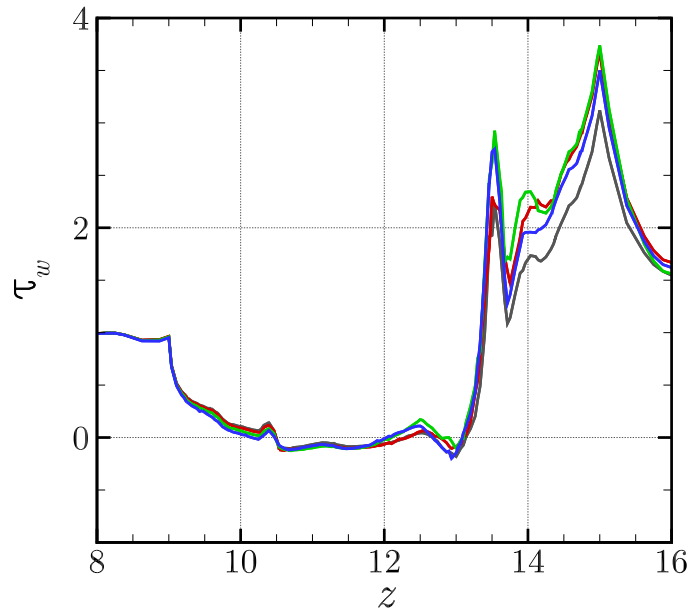
indicates that this is the less desirable haemodynamic scenario for the healthy function of endothelial cells and aneurysm rupture prognosis.

9.5.5 Comparison of heterogeneous wall stiffness scenarios

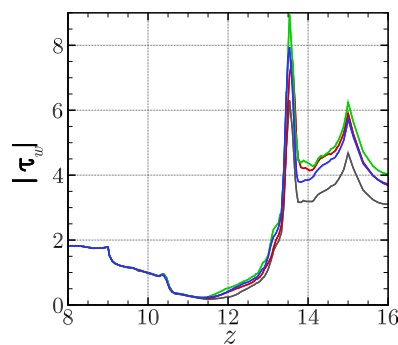
In this section the wall shear stress distribution in each of the wall stiffness cases is compared to assess which wall stiffness scenario represents the least favourable haemodynamic environment for healthy endothelial cell function. Figures 9.39 and 9.40 compare the time-averaged wall shear stress and oscillating shear stress distributions when the wall stiffness is made less-stiff and more-stiff respectively. In each case (stiffened or weakened) variations in the wall shear stress distribution pattern is minimal, this is a result of the comparable flow dynamics in each of the stiffened or weakened cases. Despite the similarity in the wall shear stress distribution, the magnitude of wall shear stress experienced with differing wall stiffness distributions does vary in a significant manner.

For the weakened wall cases shown in figure 9.39, a weakening of the central region of the aneurysm causes the greatest increase in the wall shear stress magnitude. All cases exhibit a greater wall shear stress magnitude than the uniformly elastic case. As discussed in the previous sections, this is a result of the extra flow induced by the additional wall motion. At the distal neck of the aneurysm, the wall shear stress is 21.4% higher in the central weakened case than in the distal weakened case. Negligible differences are seen in the wall shear stress magnitude at the distal neck for central and proximally stiffened cases. Variations in the OSI distribution for the weakened wall cases are negligible.

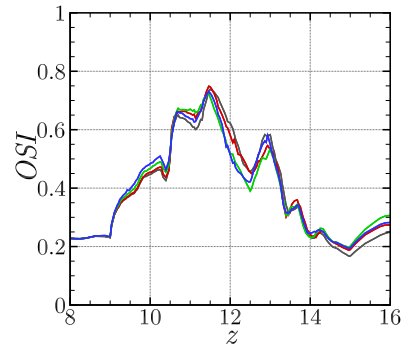
For the stiffened wall cases shown in figure 9.40, a stiffening of the central region of the aneurysm also causes the change in the wall shear stress magnitude. However, in the case of stiffening, the wall shear stress is reduced. Following high wall shear stress theory (Lasheras 2007), the least favourable haemodynamic scenario at the distal neck ($z = 13.5$) corresponds to the stiffened distal neck case. At the distal neck of the aneurysm the wall shear stress is 30.1% higher in the stiffened distal case than in the stiffened central case. In terms of the OSI, significant differences are observed in the OSI distribution as the location of the stiffened region is varied. The least favourable of these is the centrally stiffened case. The OSI distribution is heavily dependent on the wall gradient formed and wall velocity distribution in the aneurysm.



(a)

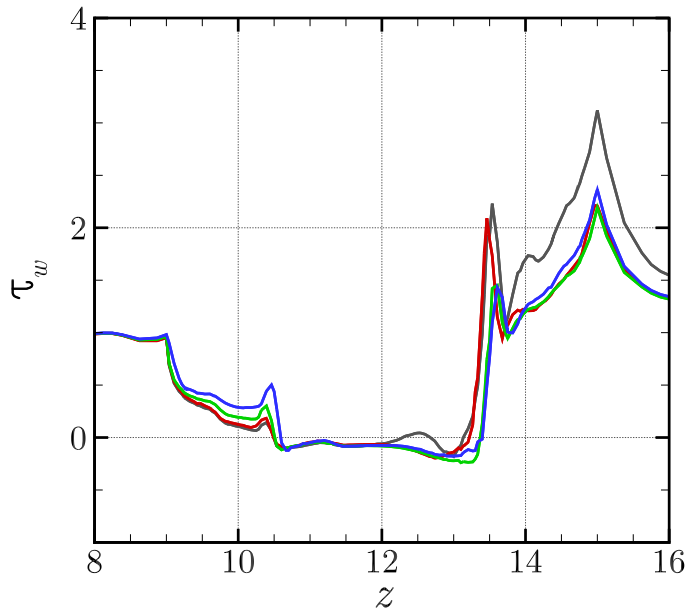


(b)

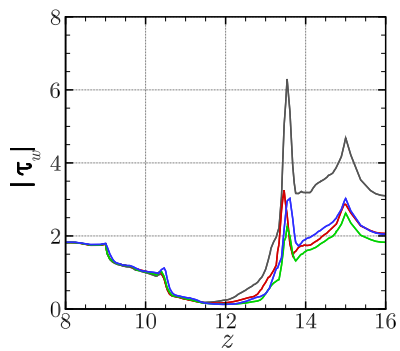


(c)

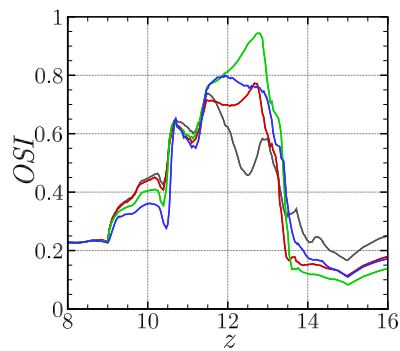
FIGURE 9.39: Comparison of the time-averaged wall shear stress (a), the time-averaged wall shear stress magnitude (b), and the oscillating shear index (c). The grey line represents the uniformly stiff reference case, red, green and blue lines represent the cases with a local variation in wall stiffness of $E = 0.6$ MPa in the distal, central and proximal regions respectively. Note: a stiffness of $E = 0.8$ MPa is applied beyond the stiffened region.



(a)



(b)



(c)

FIGURE 9.40: Comparison of the time-averaged wall shear stress (a), the time-averaged wall shear stress magnitude (b), and the oscillating shear index (c). The grey line represents the uniformly stiff reference case, red, green and blue lines represent the cases with a local variation in wall stiffness of $E = 6.0$ MPa in the distal, central and proximal regions respectively. Note: a stiffness of $E = 0.8$ MPa is applied beyond the stiffened region.

From these results it is evident that a weakening of the aneurysm wall presents a greater risk to rupture than a stiffening of the wall. In their review, Lasheras (2007) describes the possibility of both high and low wall shear stress distributions causing an undesirable haemodynamic environment which may propagate the growth of an aneurysm. In both the weakened and stiffened cases, the wall shear stress in the proximal section of the bulge is dominated by a very low wall shear stress region. Salsac *et al.* (2006) reported values of wall shear stress in a rigid-wall aneurysm ranging from -0.09 – 0.35 Pa in this region, for which these results correlate well. Salsac *et al.* (2006) also detailed the healthy flow in an aneurysm corresponds to a time-averaged wall shear stress mean of 0.27 Pa, a time-averaged wall shear stress magnitude of 1.5 Pa and an OSI of 0.4 . The results presented in this thesis show a large deviation from the healthy time-averaged values expected in the aorta. The regions of high wall shear stress at the distal neck are of significant concern as they exceed the healthy artery values predicted in section 8.5.5 by over 430%.

Interestingly, the wall stiffness surveys conducted by Claridge (2010) among others, indicates that aneurysms are predominantly found with stiffer walls. These results suggest that as an aneurysm forms, the undesirable haemodynamics environment is partially mitigated, or the propagation of the aneurysm is hindered by the stiffening of the wall. This may be caused by the active mechanotransduction process responding to reduce the adverse haemodynamic conditions.

In conclusion, a weakened aneurysm wall at the central location presents the least desirable wall shear stress distribution in the aneurysm. It is characterised by an increase in the wall shear stress at the distal neck above all other heterogeneous wall stiffness arrangements tested.

9.5.6 Effects of the perianeurysmal environment

The flow dynamics described in § 9.5.2 detail the complex flow evolution in an elastic-walled aneurysm with large wall motion. The elasticity of the wall dominates the flow mechanics in the near-wall region as its motion alters the flow rate throughout the aneurysm (see equation 8.39). The total wall movement and consequently the degree to which the wall motion affects the flow will also be dependent on the perianeurysmal environment, which depending on the force feedback response will limit the wall motion to differing degrees.

Stefanadis *et al.* (1995) measured the dilation of a healthy artery wall in two patients throughout the cardiac cycle. They reported a change in vessel diameter of $\Delta D = 1.2 - 2.5$ mm (i.e. a 10% change in diameter). The results presented in chapter 8 found that using an external pressure which matched the diastolic pressure at diastole and varied by 20% of the change in luminal pressure throughout the cycle, the healthy artery response was a dilation of $\Delta d = 1.54$ mm. This is well within the range of values quoted in Stefanadis *et al.* (1995). In the aneurysm simulations with a healthy wall stiffness, the dilation of the artery wall was $\Delta D = 6.4$ mm, and given that the diameter of the aneurysm bulge is $D = 40$ mm, this represents a 16% increase in diameter. The large dilation is a consequence of the undeformed shape of the aneurysm. It allows a larger wall motion in response to an equivalent stress as the wall aneurysm shape can flatten without addition of extra internal stress to the aneurysm wall.

It is expected that as the aneurysm bulge increases in size, the resistance of the perianeurysmal environment to movement should also increase. This is a result of the compression and effective stiffening of the perianeurysmal environment upon the formation of an aneurysm in conjunction with the proximity of internal organs and vertebral structures. As such, the results presented in § 9.5.2 may under-estimate the perianeurysmal response causing a wall motion greater than is physiologically reasonable to occur. This is not to say that these results are not valid. The results clearly indicate that in an elastic artery the flow dynamics are complicated by the motion of the wall; flow dynamics that are not observed when using a rigid-walled model.

To determine the effect of the perianeurysmal environment (and the effect of an overall reduction in wall motion), a study was undertaken in which the force exerted by the perianeurysmal environment was varied for a healthy aneurysm ($E = 0.8$ MPa). The external pressure boundary condition was varied according to

$$P_{ext} = P_{dia} - f \frac{P_{peak} - P_{dia}}{2} \cos\left(\frac{2\pi}{T}t\right), \quad (9.2)$$

where P_{ext} is the pressure applied to the external surface of the artery wall, P_{dia} is the diastolic pressure in the lumen, P_{peak} is the peak systolic pressure in the lumen, T is the period of the heart beat and f is a multiplicative factor which increases the perianeurysmal response. The factor, f , was varied from 0.2-0.9, a factor of $f = 0.2$ was used in all previous aneurysm studies reported in this thesis and was used to give a physiologically accurate wall distortion for the healthy arterial case. A factor $f = 1.0$ corresponds to the case of a perfectly rigid outer wall.

Figure 9.41 shows snapshots of the flow at a series of times throughout the cardiac cycle using various values of the perianeurysmal pressure factor, f . As the perianeurysmal pressure factor is increased and the subsequent wall motion is decreased, the flow exhibits a weaker distal vortex (vortex B in figure 9.19) this is best observed at time $t^* = 0.28$ in figure 9.41. Initially as the wall motion is decreased, the reduced reverse flow in the boundary layer and consequentially the reduced strength of vortex B results in the suppression of vortex C. The reduced strength of vortex B means it does not draw the shear layer C' into the secondary distal vortex ring. As the perianeurysmal pressure factor is increased further, the effect of the wall motion is further reduced. This causes the weakening of the distal vortex to the point where the proximal vortex A begins to dominate the flow field in the distal region at times $t^* > 0.6$. As this occurs, the strength of the shear layer at $t^* = 0.7$ increases again (see $f = 0.8$) until the proximal vortex A draws the shear layer into the secondary vortex ring C. This shows a clear progression from the uniformly elastic case with a weak perianeurysmal pressure response to the rigid-walled case.

The change in flow dynamics with variation in the perianeurysmal pressure factor is reflected in a transition in the wall shear stress distribution. Figure 9.42 shows the spatial and temporal distribution of wall shear stress throughout the elastic region of the aneurysm. These results reflect the change in flow dynamics observed in figure 9.41 which involves a reduction in the strength of the distal vortex and corresponding shear layer C' , a suppression of the creation of vortex C, and finally the domination of the proximal vortex A (as the perianeurysmal pressure factor is increased). The precedence of the proximal vortex is denoted in figure 9.42 by the transition from a wall shear stress pattern that has peaks which match the phase of the wall motion to that which matches the phase of the inlet velocity conditions (as the perianeurysmal pressure factor is increased). The trajectories of the vortices A, B and C from figure 9.19 are tracked on figure 9.42 by the dashed white lines.

In conclusion the perianeurysmal environment plays a key role in determining the flow dynamics in the aneurysm. Large wall motions lead to the formation of secondary vortex rings at the distal neck which have been shown to interact with vortices shed from the proximal neck. At intermediate levels of wall motion the flow exhibits a weaker shear layer at the distal neck and the suppression of the secondary vortex ring. Similar vortex C suppression was observed in the heterogeneous wall stiffening cases

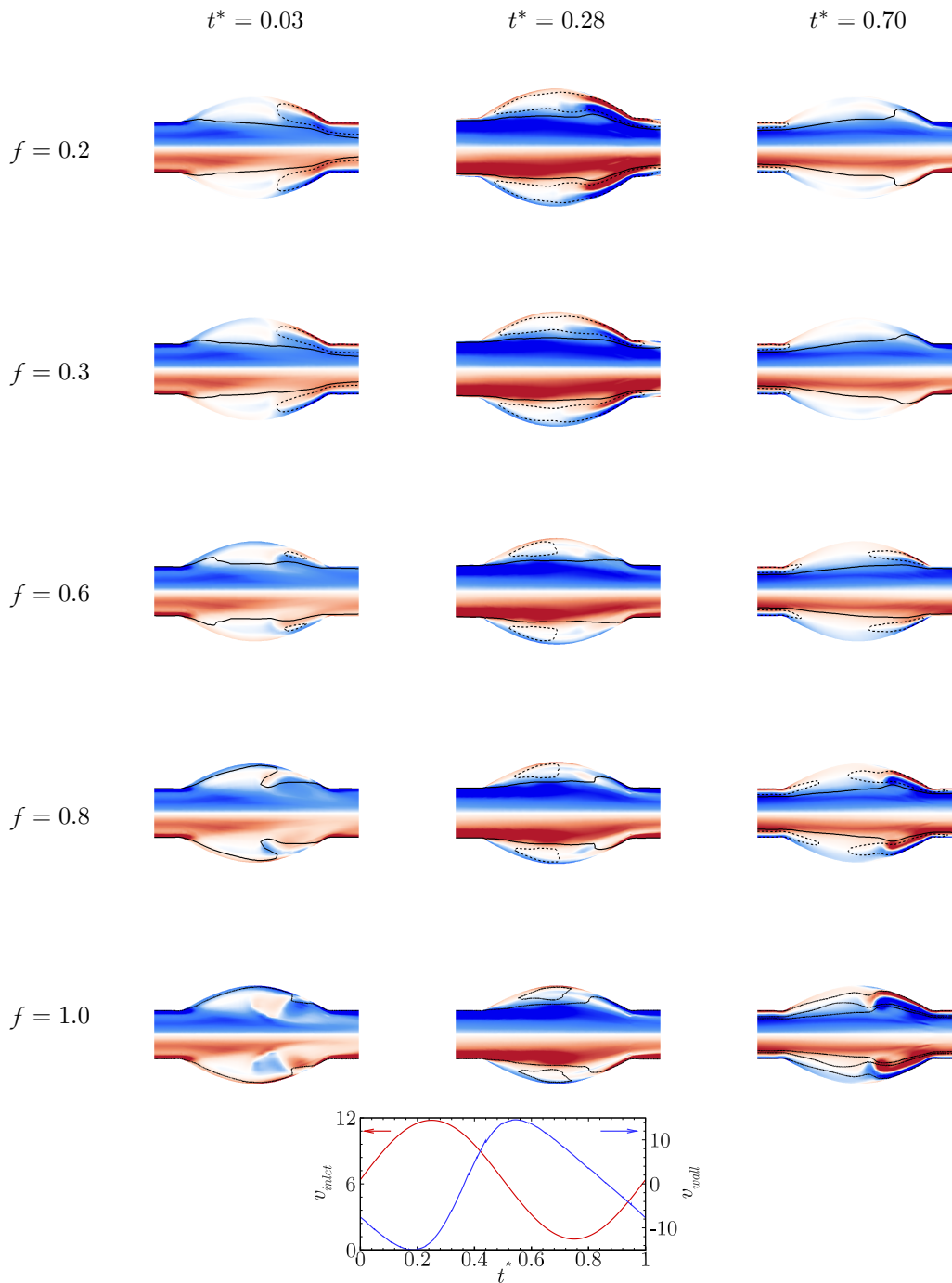


FIGURE 9.41: The effect of the perianeurysmal environment on the flow through an elastic aneurysm. The wall has a uniform stiffness of $E = 0.8$ MPa and the perianeurysmal pressure factor f is varied from the standard case of 0.2 to the completely rigid case of 1.0. Contours show vorticity in the y - z plane. Positive vorticity (anticlockwise whorl) is represented by red contours and negative vorticity (clockwise whorl) is represented by blue contours. Line contours show the regions of flow with an axial velocity component of +1 and -1 (dashed lines are negative).

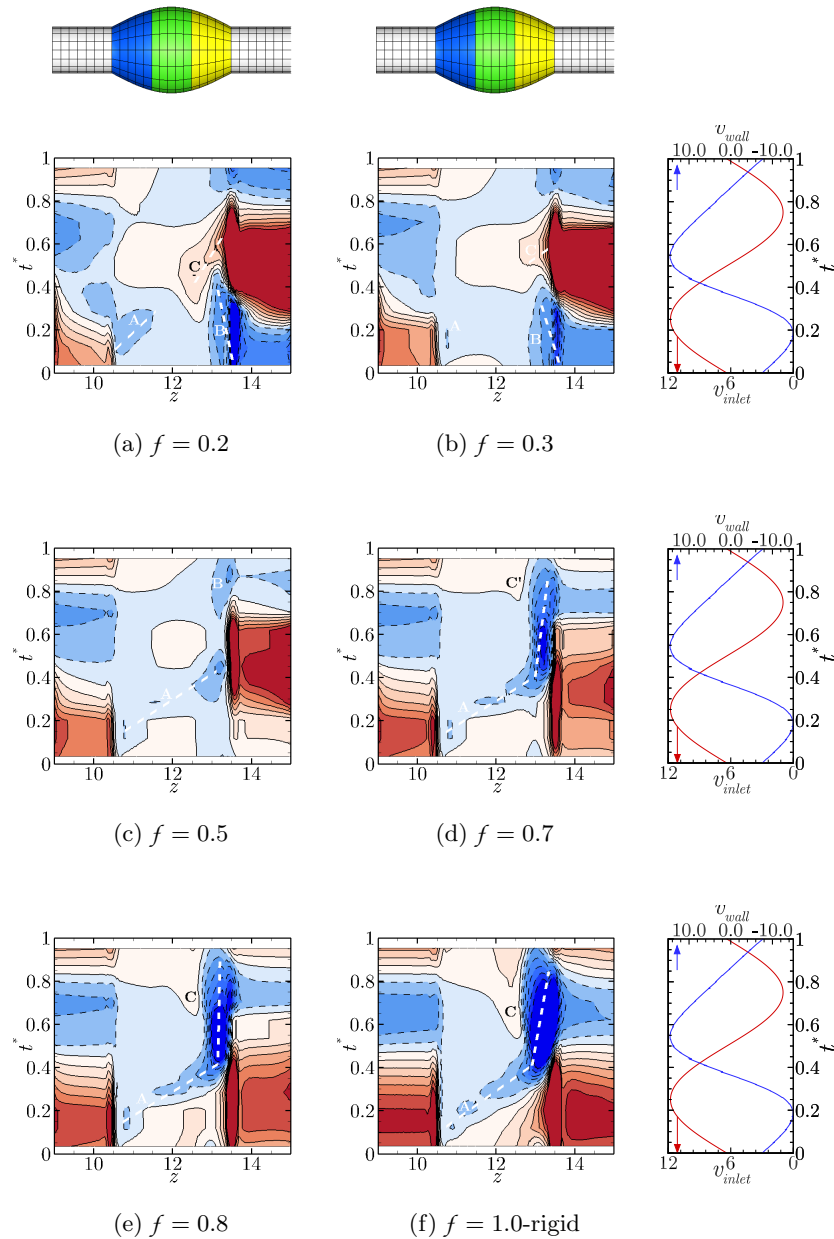


FIGURE 9.42: The variation of wall shear stress (WSS) in an aneurysm as a function of time and space. Contours show WSS with high WSS represented by red and low WSS represented by blue, negative values are represented by dashed contour lines. The contour levels are equispaced and vary from -3.35 Pa to 3.35 Pa. Sub-plots (a) - (f) represent the WSS in an aneurysm with uniformly elastic-walls of stiffness $E = 0.8$ MPa with a perianeurysmal pressure factor, $f = 0.2 - 1.0$. The figures on the right show the velocity inlet (red) and wall velocity (blue).

in which a stiffer wall section precluded the distal vortex from achieving sufficient strength to draw the shear layer C' into a secondary vortex ring. At high levels of the perianeurysmal response, the flow is akin to the flow in a rigid-walled aneurysm. Under these circumstances the proximal vortex ring dominates the flow in the aneurysm and its strength is sufficient to induce the shear layer roll up into vortex C .

9.6 Closure

It is well documented that the formation and growth of an aneurysm is linked to an irregular haemodynamic environment (Finol *et al.* 2003b; Salsac *et al.* 2006; Lasheras 2007; Humphrey & Taylor 2008; Sforza *et al.* 2009). Many studies analyse the effect of the irregular geometry on the flow dynamics. Specifically, wall shear stress and wall shear stress gradients are considered as the healthy function of the intimal endothelial layer is shear sensitive. The results presented in this chapter describe a complex vortex structure interaction which occurs as a result of additional vortices created in response to the motion of the elastic-wall. The results highlight the significant difference in the flow dynamics when considering an elastic-walled aneurysm model compared to a rigid-walled model. Unlike their rigid-walled counterparts, realistic elastic-walled models are subject to complicated multi-vortex ring interactions with much more dynamic boundary layer flows. Rigid-wall models fail to capture the distal vortex pair created in an aneurysm and can therefore not accurately assess the impact the flow has on the wall shear stress distribution in an aneurysm.

This investigation has made simple comparative measurements of the spatial and temporal distribution of the flow through an aortic aneurysm. Furthermore, it has measured the wall shear stress distribution in an elastic aneurysm and compared the results against rigid-walled models and cases in which a localised variation in wall stiffness is present. This study has shown the flow inside an elastic aneurysm is characterised by the transient formation of a proximal vortex ring and distal vortex ring pair; and the presence of altered boundary layer flow conditions as a result the wall motion. In fact, the presence of an elastic wall creates a spatial variation in the wall shear stress which is not present in rigid-walled approximations. On this basis it is reasonable to conclude that rigid-walled models of the aorta are insufficient to accurately describe the wall shear stress environment in an aneurysm.

The differences in wall shear stress are caused by the large impact that the wall

motion has on the flow near the wall in an aneurysm. The wall motion causes complex vortex interactions to affect the flow in the centre of the aneurysm and drives changes in flow direction in the wall shear layer. In terms of time-averaged measurements the wall shear stress at the distal neck has a much greater magnitude than in the rigid-walled case. Despite this, the elastic-walled case is subject to smaller wall shear stress gradients just upstream of the distal neck as the proximal vortex does not interact directly with the shear layer. This occurs as the proximal neck vortex interacts with the wider distal neck vortices. In any case, the dramatic differences in wall shear stress observed between the elastic-walled case and the rigid-walled case suggest that rigid-walled models are insufficient in describing the haemodynamic environment in an aneurysm.

The effect of local variations in wall stiffness was determined at a variety of locations throughout the aneurysm bulge. Weakening of the aneurysm wall led to large wall displacements and an increase in the wall shear stress magnitude at the distal neck. The increase in wall motion caused the induced flow rate to exceed the fluctuations in flow rate at the velocity inlet. This in turn caused the flow in the boundary layer to be dominated by the wall action in conjunction with the proximity of vortices. A greater wall motion invariably led to an increase in the strength of both the proximal and distal vortex rings. The increase in vortex strength was directly linked to an increase in the wall shear stress in the vicinity of the vortex structures. The weaker wall cases also led to the roll up of a secondary vortex ring in the distal third of the bulge. The formation of the secondary vortex ring was not observed in the stiffer wall cases. While all weakened walled cases exhibited similar changes in wall dynamics compared to the uniformly stiff case, a weakened region upstream of the distal neck provided the greatest change in wall shear stress distribution. Both the weakened proximal neck and central region studies revealed a similar wall response and wall shear stress distribution. The case of a weakened central region represents the least favourable haemodynamic conditions for healthy endothelial wall function.

In contrast to the heterogeneous weakened wall distributions, the stiffened wall cases exhibited a wall shear stress distribution which was protective (relatively) of endothelial response. A stiffening of the wall reduced the wall motion and consequently the strength of the distal vortices. The reduced strength of the inner distal vortex led to the suppression of the secondary distal vortex ring. A combination of the reduced vortex

strength and the reduced volume rate of change of the aneurysm led to a reduction in the shear stresses that endothelial cells would be subjected to. The least protective distribution was the stiffening at the distal neck. At the distal neck the wall shear stress is 30.1% higher in the distal stiffened case than in the central stiffened case or proximal stiffened case. In terms of the OSI, significant differences are observed in the OSI distribution as the location of the stiffened region is varied. The least favourable of these is the centrally stiffened case. The OSI distribution is heavily dependent on the wall gradient formed and wall velocity distribution in the aneurysm.

From these results it is evident that a weakening of the aneurysm wall presents a greater risk to rupture than a stiffening of the wall. In their review, Lasheras (2007) describes the possibility of both low and high wall shear stress distributions causing an undesirable haemodynamic environment which may propagate the growth of an aneurysm. In both the weakened and stiffened cases, the wall shear stress in the proximal section of the bulge was dominated by a very low wall shear stress region. Salsac *et al.* (2006) reported values of wall shear stress in a fixed-walled aneurysm model ranging from $-0.09 - 0.35$ Pa in this region, for which these results correlate quite well. Salsac *et al.* (2006) also detailed the healthy flow in an aneurysm corresponds to a time-averaged wall shear stress mean of 0.27 Pa, a time-averaged wall shear stress magnitude of 1.5 Pa and an OSI of 0.4. The results presented in this thesis show a large deviation from the healthy time-averaged values expected in an aneurysm. The regions of high wall shear stress at the distal neck are of significant concern as they exceed the healthy artery values by over 430%.

Finally, a study was conducted to determine the effect of the perianeurysmal environment on the haemodynamics in an aneurysm. It was shown that an increase in the perianeurysmal response leads to the reduction in wall motion. As the wall motion was decreased, the strength of the distal vortex was diminished and the roll up of the shear layer into the secondary vortex was suppressed. As the perianeurysmal response was increased further, the distal vortex became very weak and the proximal vortex began to dominate the flow dynamics. With a sufficiently stiff wall, the distal vortex no longer protected the distal neck from the impact of the proximal vortex ring. The strength of this vortex was sufficient to draw the shear layer into a secondary vortex ring. This study describes the transition of flow régimes from one dominated by the motion of the wall to one in which the wall geometry and inlet velocity profile are dominant. Very

different wall shear stress distributions occur in each case.

This investigation set out to address aims 2a and 2b by assessing the impact of varying wall mechanical properties on the haemodynamics in a fusiform abdominal aortic geometry. The original hypotheses outlined in § 1.8.3 have been supported in this investigation. Evidence was found to support the first hypothesis relating to the effect of the perianeurysmal environment. As the force feedback from the perianeurysmal environment was increased the wall motion reduced in magnitude across the domain. The interaction of proximal and distal vortex structures which is prevalent with large wall motion was suppressed and the flow dynamics approached that seen in a rigid-walled aneurysm model. The second question in § 1.8.3 asked what effect local wall stiffness will have on the haemodynamics in an aneurysm. It was postulated that a local increase in wall stiffness would introduce secondary regions of flow separations and potentially the development of a secondary vortex ring system as a result of the local variations in wall geometry. While this study did identify the formation of a secondary vortex ring pair at the distal neck; it was concluded that this was not the result of the local variation in wall stiffness. Rather, the large wall motion caused significant flow reversal in the boundary layer at the distal neck which formed a strong vortex system at this location. The location of the change in wall stiffness did affect the distribution of the vortices and affected how far into the domain the vortices travelled. Furthermore, in terms of wall shear stress it was shown that changes in wall motion upstream had a greater impact on the wall shear stress at the distal neck. The secondary distal vortex pair was most prevalent in cases when the wall was weakened and suppressed when the wall was stiffened. These flow dynamics were driven by the global change in wall motion which occurred as a result of the stiffening and weakening rather than any local effects.

Chapter 10

Conclusions

The prevalence of abdominal aortic aneurysms is increasing with an ageing population. Aneurysms present a major health risk; in the event of aneurysm rupture, patients exhibit a mortality rate of 70-95% (Lindholt *et al.* 2005). Treatment of aneurysms involves invasive surgery, which carries an inherent risk, therefore it is preferable to intervene only when an aneurysm is close to rupture. Currently, the aneurysm initiation, growth and rupture mechanisms are not fully understood and accurate predictions of aneurysm growth-rate and rupture time frame cannot be made. Research in this field has identified haemodynamic stimuli as the principal factor leading to aneurysm growth. As such, in-depth fluid-dynamic investigations can contribute greatly to developing appropriate models for patient prognosis and treatment. Previous investigations into aneurysm haemodynamics have largely been focused on blood flows with rigid-wall dynamics. To realistically model the flow, a moving boundary condition must be applied to account for the elasticity of the aneurysm wall.

This research aimed to address the current shortcomings in the literature by developing a complex fluid-structure solver and utilising it to determine the effects of an elastic-wall model on aneurysm haemodynamics. As such the outcomes presented in this thesis are twofold. Firstly, a computational tool was developed capable of accurately modelling the non-linear solid mechanics and coupled fluid-structure interactions. The algorithms used in this computational tool were described at length and verified against a series of benchmark test cases. Subsequently, the new solver was utilised to simulate blood flow through idealised artery and aneurysm models. The results presented in this thesis improve on the current standard of artery wall modelling by incorporating the effects of heterogeneous wall mechanical properties in a multi-layered wall.

10.1 FSI algorithm

In order to accurately model the fluid-structure interactions in an aneurysm a computational tool was developed. Previous studies into aneurysm FSI have failed to:

1. fully couple the wall response to the motion of the fluid,
2. accurately model the location of the artery wall, or,
3. account for the complex nature of the wall in terms of mechanical properties, inertial effects, and non-linear constitutive models.

To overcome these shortfalls a novel approach to numerically modeling non-linear solid mechanics was developed in conjunction with an adaptation of the ALE coupling scheme. A monolithic ALE solver was suggested with a modified iterative over unequal time step coupling routine. The unequal time stepping algorithm ensures information is updated in the fluid solver at each fluid time step using an extrapolation/interpolation method on intermediate time steps and a full iterative feedback method during time steps when both the fluid and the solid are being updated. To preserve the relative spacing of mesh nodes in the fluid region as the domain size changes, a Hookean solid model is used to regulate the mesh movement.

The arbitrary Lagrangian–Eulerian time stepping scheme developed in this thesis allows the coupling of the fluid and solid mechanics solvers. This enables the solver to handle the complex fluid-structure interactions found in arterial flows. This work is integral to aim 1 defined in chapter 1. While the mathematical background of the ALE technique is well defined, this algorithm represents a novel contribution to the field with its new information transfer scheme.

In order to model the non-linear wall response, an algorithm which solved a neo-Hookean constitutive model was developed. Spectral elements were used for the spatial discretisation while a backward differencing time stepping scheme was proposed for the temporal evolution. A two-step operator splitting scheme was proposed in order to implicitly solve for the displacement at the next time step. As such this algorithm is capable of modelling both the inertial and non-linear response of the wall, which is important in biological applications.

The combination of a two-step operator splitting scheme, the inclusion of the inertial term and the use of a spectral element spatial discretisation makes this a new technique

for solving the governing equations for an incompressible neo-Hookean solid. When simulating the response of the arterial wall in an aneurysm, a hyperelastic material model such as the neo-Hookean model is essential. This algorithm in conjunction with the new fluid-structure interaction coupling scheme described in § 3.5.1 represents a new and highly accurate tool for investigating FSI in aneurysms. A series of verification simulations were presented to test the accuracy and stability of the algorithm. In each case high levels of accuracy were achieved.

10.2 Aneurysm initiation

It is well documented that the healthy function of an arterial wall is reliant on a balance of haemodynamic parameters to which intimal endothelial cells are sensitive. As such, the characterisation of the changes in wall shear stress resulting from wall stiffness variations around lesions and sites of disease is essential to understand the initiation process of abdominal aortic aneurysms.

This investigation has made simple comparative measurements of the spatial and temporal distribution of the flow through an elastic artery. Furthermore, it has measured the wall shear stress distribution in the elastic artery and compared the results against rigid-walled models and cases in which a localised variation in wall stiffness is present. This study has shown that the flow inside an elastic artery is characterised by the transient formation of regions with higher and lower wall shear stresses which are not predicted using a rigid-walled artery model. In fact the presence of an elastic wall creates a spatial variation in the wall shear stress which is not detected in rigid-walled approximations. On this basis it is reasonable to conclude that rigid-walled models of the healthy aorta are insufficient to accurately describe the wall shear stress environment in the aorta.

The presence of an elastic wall was found to delay the onset and reduce the strength of flow reversal in the boundary layer during the diastolic phase in comparison to rigid-walled models. In addition, the wall motion was shown to have a profound impact on the wall normal velocity and boundary layer thickness. The spatial variation of the wall shear stress was shown to develop as a result of the change in wall profile as the elastic wall moved. The result of this geometry change was a dramatic decrease in the wall shear stress at the proximal neck before an increase in wall shear stress at the distal neck beyond what is encountered in a rigid-walled model. The shape adopted during

systole causes a spatial acceleration of the fluid, which is associated with a change in local velocity and consequently a change in the local Reynolds number, boundary layer thickness and wall shear stress. The transient nature of the wall motion further compounds these effects as the changing luminal volume causes an increase or decrease in the flow rate at the distal neck.

Local variations in the wall stiffness caused only slight variations in the wall shear stress distribution in the artery. On a global scale, a local increase in the wall stiffness decreased the peak dilation of the wall which altered the peak wall shear stress in regions downstream (predominantly the distal neck). Local variations in wall stiffness were also associated with the local change in wall shear stress. The locally altered wall gradient caused flow to detach from the boundary when the wall was diverging and a thinning of the boundary layer when the wall gradient was converging.

This investigation aimed to address aim 2c and determine how a heterogeneous wall stiffness affects the haemodynamics in the context of aneurysm initiation. The original hypotheses outlined in § 1.8.3 have been supported in this investigation. In terms of the initiation of aneurysms these results show that the wall shear stress distribution in an artery is very complex. Previous studies that have used a rigid wall assumption are likely to have underestimated the maximum and minimum wall shear stress in a healthy artery. Large variation in the wall shear stresses are present around the proximal and distal neck of the artery where tethering causes large variation in wall shapes. Localised lesion or stiffening in the centre of an artery can alter the wall shear stress distribution both local to the lesion and throughout the artery. The variation in wall shear stress does not exceed the healthy range described in Salsac *et al.* (2006), however the results do show that the local variation is substantial in comparison to the local wall shear stress for a healthy elastic artery. The time averaged wall shear stress was 31% higher for the stiffest case tested and 47% lower for the least stiff case tested. Whether lower or higher wall shear stresses present a greater risk of endothelial injury is beyond the scope of this work. However, such variation of wall shear stress in either direction may be sufficient to change the local endothelial function of the wall and lead to aneurysm initiation.

10.3 Haemodynamics in established aneurysms

It is well documented that the formation and growth of an aneurysm is linked to an irregular haemodynamic environment (Finol *et al.* 2003b; Salsac *et al.* 2006; Lasheras 2007; Humphrey & Taylor 2008; Sforza *et al.* 2009). Many studies have analysed the effect of the irregular geometry on the flow dynamics. This study described the complex vortex structure interaction which occurs as a result of additional vortices created at the distal neck in response to the motion of the elastic wall. The results highlight the significant difference in the flow dynamics when considering an elastic-walled aneurysm model compared to a rigid-walled model.

This investigation has made simple comparative measurements of the spatial and temporal distribution of the flow and wall shear stress distribution through an aortic aneurysm. The differences in wall shear stress are caused by the large impact that the wall motion has on the flow near the wall. In addition to the vortex ring shed from the proximal neck, the wall motion causes significant flow reversal in the boundary layer which causes the formation of a distal vortex. The proximity of these vortices to the aneurysm wall affects the shear layer at the wall and consequently the wall shear stress. A secondary distal vortex ring was found to develop in cases when the wall motion was high. At intermediate levels of wall motion the secondary distal vortex ring was suppressed. The wall was protected from the presence of the strong proximal vortex ring by its interaction with the primary distal vortex ring.

The effect of local variations in wall stiffness was determined at a variety of locations throughout the aneurysm bulge. Weakening of the aneurysm wall led to large wall motions, an increase in vortex strength and a corresponding increase in the wall shear stress magnitude at the distal neck. Conversely stiffening of the wall led to a reduction in the wall shear stresses and vortex strengths. The weaker wall cases also led to the roll up of a secondary vortex ring at the distal neck, as the wall began to collapse back to its initial position. The formation of the secondary vortex ring was not observed in the stiffer-wall cases.

While all weakened-wall cases exhibited similar changes in wall dynamics compared to the uniformly stiff case, a weakened region upstream of the distal neck provided the greatest change in wall shear stress distribution. The case of a weakened central region represents the least favourable haemodynamic conditions for healthy endothelial wall function. In terms of the stiffened cases, the least protective distribution was the

stiffening at the distal neck. In terms of the OSI, significant differences were observed in the OSI distribution as the location of the stiffened region is varied. The least favourable of these is the centrally stiffened case. The OSI distribution is heavily dependent on the wall gradient and wall velocity distribution in the aneurysm. A weakening of the aneurysm wall presents a greater risk to rupture than a stiffening of the wall.

In their review, Lasheras (2007) describes the possibility of both high and low wall shear stress distributions causing an undesirable haemodynamic environment which may propagate the growth of an aneurysm. In both the weakened and stiffened cases, the wall shear stress in the proximal section of the bulge is dominated by a very low wall shear stress region. Salsac *et al.* (2006) reported values of wall shear stress in a fixed wall aneurysm ranging from -0.09 to 0.35 Pa in this region, for which these results correlate well. Salsac *et al.* (2006) also detailed the healthy flow in an aneurysm corresponds to a time averaged wall shear stress mean of 0.27 Pa, time averaged wall shear stress magnitude of 1.5 Pa and an OSI of 0.4 . The results presented in this thesis show a large deviation from the healthy time averaged values expected in an aneurysm. The regions of high wall shear stress at the distal neck are of significant concern as they exceed the healthy artery values by over 430% .

Finally, a study was conducted to determine the effect of the perianeurysmal environment on the haemodynamics in an aneurysm. It was shown that an increase in the perianeurysmal response led to a reduction in wall motion. As the wall motion was decreased the strength of the distal vortex was diminished and the roll up of the shear layer into the secondary vortex was suppressed. As the perianeurysmal response was increased further, the distal vortex became very weak and the proximal vortex began to dominate the flow dynamics. With a sufficiently stiff wall, the distal vortex no longer protected the distal neck from the impact of the proximal vortex ring. The strength of this vortex was sufficient to draw the shear layer into a secondary vortex ring. This study describes the transition of flow régimes from that being dominated by the motion of the wall to one in which the wall geometry and inlet velocity profile are dominant. Very different wall shear stress distributions occur in each case.

This investigation aimed to address aims 2a and 2b in assessing the impact of varying wall mechanical properties on the haemodynamics in a fusiform abdominal aortic geometry.

10.4 Directions for future work

The fluid-structure interactions in abdominal aortic aneurysms have been investigated in detail in this study. Even so, some further advancements in the model remain. Future work should focus on a number of key areas: the effect of the perianeurysmal environment, geometry considerations, physiological boundary conditions pressure pulse wave velocities, and long-term modelling of the aneurysm life cycle.

The perianeurysmal environment was shown to have a profound affect on the wall motion and consequently the haemodynamic structures that formed in the aneurysm bulge. Greater understanding of the perianeurysmal force response is required. Further investigations could be conducted into a non axisymmetric perianeurysmal response which would simulate the presence of vertebral structures and organs. Such asymmetry should dramatically affect the flow evolution.

In order to isolate the effect of the wall motion on the flow structures in an aneurysm an idealised fusiform model was used. Many investigations have been conducted on patient-specific models citing the complexity of the aneurysm shape as having a profound impact on the flow structures that form (e.g. Leung *et al.* 2006). Having identified the role of the fluid structure interaction in aneurysms, more complex geometries should be considered. Of particular interest would be models which include upstream and downstream branches which have been reported to influence wall motion and correlate with the location of aneurysms (see Lasheras 2007).

Furthermore, to increase the physiological relevance of the simulations impedance boundary conditions such as Windkessel models should be applied. Such boundary conditions would allow investigations into the effect of velocity-pressure phase lag on the flow in the aneurysms. This could highlight ways of altering the stiffness of the wall to improve the haemodynamic environment in the aneurysm.

Once the appropriate physiological conditions have been implemented, an interesting study might be to analyse the effect of the wall stiffness on the pulse wave velocity. Quantification of a range of frequencies and speeds which cause constructive interference of the waves as they reflect off bifurcations could be a useful tool in determining healthy haemodynamic conditions. Correlations of this range with various stiffnesses could highlight different distributions which would act to exacerbate the negative effects of this interaction.

Low flow has been suggested as a possible factor in the growth of aneurysms. An

interesting study might be to assess how flushing-time and low wall shear stresses are affected by varying wall stiffnesses. Analysis of the correlation between low wall shear stresses and flushing time in this context could provide some insight into low flow theories for aneurysm growth.

Finally, in terms of the computational model, fluid structure growth models represent the most complete analysis tool in assessing the life cycle of an aneurysm. These models incorporate not only the temporal evolution of the geometry, the non-linear wall properties, and the haemodynamics, but also the cell mechanobiology in response to the haemodynamic stimuli. Humphrey & Taylor (2008) believe it is important to go beyond the coupling of fluid and structural mechanics in FSI models to incorporate long-term growth and remodelling processes of the evolving arterial wall. The work conducted in this thesis forms an important role in feeding into fluid-structure growth models by providing an accurate tool for assessing the fluid-structure interaction. What remains is an accurate model for determining the biological impact (in terms of wall stiffness and thickness) of haemodynamic stimuli.

Reference list

- AMES, W. 1965 *Non-linear Partial Differential Equations in Engineering*. Academic, New York.
- ANLIKER, M., HISTAND, M. & OGDEN, E. 1968 Dispersion and attenuation of small artificial pressure waves in the canine aorta. *Circulation Research* **23** (4), 539–551.
- ANLIKER, M., WELLS, M. & OGDEN, E. 1969 The transmission characteristics of large and small pressure waves in the abdominal vena cava. *IEEE Transactions on Biomedical Engineering* **16** (4), 262–273.
- ARZANI, A., DYVERFELDT, P., EBBERS, T. & SHADDEN, S. C. 2012 In vivo validation of numerical prediction for turbulence intensity in an aortic coarctation. *Annals of biomedical engineering* **40** (4), 860–870.
- ÅSTRAND, H., RYDÉN-AHLGREN, Å., SANDGREN, T. & LÄNNE, T. 2005 Age-related increase in wall stress of the human abdominal aorta: An in vivo study. *Journal of vascular surgery* **42** (5), 926–931.
- ATABEK, H. 1968 Wave propagation through a viscous fluid contained in a tethered, initially stressed, orthotropic elastic tube. *Biophysical Journal* **8** (5), 626–649.
- ATABEK, H. 1980 Blood flow and pulse propagation in arteries. In *Basic Hemodynamics and its Role in Disease Processes* (ed. D. Patel & R. Vaishnav), pp. 255–361. Baltimore University Park Press.
- ATANACKOVIC, T. & GURAN, A. 2000 *Theory of elasticity for scientists and engineers*. Birkhauser.
- ATTINGER, E. O. 1964 Pulsatile blood flow. In *Proceedings of the First International Symposium on Pulsatile Blood Flow*. New York, United States of America.
- BAEK, S., GLEASON, R., RAJAGOPAL, K. & HUMPHREY, J. 2007 Theory of small on large: Potential utility in computations of fluid-solid interactions in arteries. *Computer Methods in Applied Mechanics and Engineering* **196** (31-32), 3070–3078.
- BAEK, S., RAJAGOPAL, K. & HUMPHREY, J. 2006 A theoretical model of enlarging intracranial fusiform aneurysms. *Journal of Biomechanical Engineering* **128** (1), 142.

- BATHE, K. & LEDEZMA, G. 2007 Benchmark problems for incompressible fluid flows with structural interactions. *Computers & Structures* **85** (11), 628–644.
- BATHE, K. & ZHANG, H. 2009 A mesh adaptivity procedure for CFD and fluid–structure interactions. *Computers & Structures* **87** (11), 604–617.
- BAZILEVS, Y., CALO, V., ZHANG, Y. & HUGHES, T. 2006 Isogeometric fluid–structure interaction analysis with applications to arterial blood flow. *Computational Mechanics* **38** (4), 310–322.
- BELYTSCHKO, T., KARABIN, M. & LIN, J. 1986 Fluid–structure interaction in water–hammer response of flexible piping. *Journal of Pressure Vessel Technology* **108** (3), 249.
- BELYTSCHKO, T. & KENNEDY, J. 1978 Computer models for sub-assembly simulation. *Nuclear Engineering and Design* **49** (1-2), 17–38.
- BELYTSCHKO, T., KENNEDY, J. & SCHOEBERLE, D. 1980 Quasi-Eulerian finite element formulation for fluid–structure interaction. *Journal of Pressure Vessel Technology* **102** (1), 62.
- BEN DRISS, A., BENESSIANO, J., POITEVIN, P., LEVY, B. I. & MICHEL, J. B. 1997 Arterial expansive remodelling induced by high flow rates. *American Journal of Physiology - Heart and Circulation Physiology* **272** (2), H851–H858.
- BENSON, D. 1989 An efficient, accurate, simple ALE method for nonlinear finite element programs. *Computer Methods in Applied Mechanics and Engineering* **72** (3), 305–350.
- BINNIE, A. M. & FOWLER, J. S. 1947 A study by a double refraction method of the development of turbulence in a long cylindrical tube. *Proceedings of the Royal Society London* **192**, 32–44.
- BLACKBURN, H. & SHERWIN, S. 2004 Formulation of a Galerkin spectral element–Fourier method for three-dimensional incompressible flows in cylindrical geometries. *Journal of Computational Physics* **197** (2), 759–778.
- BLACKBURN, H., SHERWIN, S. & BARKLEY, D. 2008 Convective instability and transient growth in steady and pulsatile stenotic flows. *Journal of Fluid Mechanics* **607** (1), 267–277.
- BLACKMAN, B. R., GARCIA-CARDENA, G. & GIMBRONE, M. A. 2002 A new in vitro model to evaluate differential responses of endothelial cells to simulated arterial shear stress waveforms. *Journal of Biomechanical Engineering* **124**, 397–407.

- BLOM, F. 1998 A monolithical fluid–structure interaction algorithm applied to the piston problem. *Computer Methods in Applied Mechanics and Engineering* **167** (3), 369–391.
- BODARD, N. & DEVILLE, M. O. 2006 Fluid structure interaction by the spectral element method. *Journal of Scientific Computing* **27**, 123–135.
- BOWER, A. 2009 *Applied mechanics of solids*. CRC.
- BRUNO, G., TODOR, D. R., LEWIS, I. & CHYATTE, D. 1998 Vascular extracellular matrix remodelling in cerebral aneurysms. *Journal of Neurosurgery* **89** (3), 431–440.
- BUCHANAN, J. R., KLEINSTREUER, C., TRUSKEY, G. A. & LEI, M. 1998 Relation between non-uniform haemodynamics and sites of altered permeability and lesion growth at the rabbit aorto-celiac junction. *Atherosclerosis* **143** (1), 27–40.
- BUTLER, C., RYAN, K. & SHEARD, G. 2012 Haemodynamic forces on in vitro thrombi: A numerical analysis. *Medical & Biological Engineering & Computing* **50** (5), 493–502.
- CABRERA-FISCHER, E., ARMENTANO, R., PESSANA, F., GRAF, S., ROMERO, L., CHRISTEN, A., SIMON, A. & LEVENSON, J. 2002 Endothelium-dependent arterial wall tone elasticity modulated by blood viscosity. *American Journal of Physiology-Heart and Circulatory Physiology* **282** (2), H389–H394.
- ČANIĆ, S., TAMBAČ, J., GUIDOBONI, G., MIKELIĆ, A., HARTLEY, C. & ROSENSTRAUCH, D. 2006 Modeling viscoelastic behaviour of arterial walls and their interaction with pulsatile blood flow. *SIAM Journal on Applied Mathematics* **67** (1), 164–193.
- CARMO, M., COLOMBO, L., BRUNO, A., CORSI, F., RONCORONI, L., CUTTIN, M., RADICE, F., MUSSINI, E. & SETTEMBRINI, P. 2002 Alteration of elastin, collagen and their cross-links in abdominal aortic aneurysms. *European Journal of Vascular and Endovascular Surgery* **23** (6), 543–549.
- CEBRAL, J. R., YIM, P., LOHNER, R., SATO, O. & CHOYKE, P. 2002 Blood flow modeling in carotid arteries with computational fluid dynamics and MRI imaging. *Academic Radiology* **9** (11), 1286–1299.
- CHAYTTE, D. & LEWIS, I. 1997 Gelatinase activity and the occurrence of cerebral aneurysms. *Stroke* **28** (4), 799–804.
- CHENG, C., PARKER, D. & TAYLOR, C. 2002 Quantification of wall shear stress in large blood vessels using Lagrangian interpolation functions with cine phase-contrast magnetic resonance imaging. *Annals of Biomedical Engineering* **30** (8), 1020–1032.

- CHESKIDOV, A., CONSTANTIN, P., FRIEDLANDER, S. & SHVYDKOY, R. 2008 Energy conservation and Onsager's conjecture for the Euler equations. *Nonlinearity* **21** (6), 1233.
- CHIEN, S., LI, S. & SHYY, J. Y. J. 1998 Effects of mechanical forces on signal transduction and gene expression in endothelial cells. *Hypertension* **31** (1), 162.
- CHIU, J., CHEN, L., CHEN, C., LEE, P. & LEE, C. 2004 A model for studying the effect of shear stress on interactions between vascular endothelial cells and smooth muscle cells. *Journal of Biomechanics* **37** (4), 531–539.
- CHIU, J., CHEN, L., LEE, P., LEE, C., LO, L., USAMI, S. & CHIEN, S. 2003 Shear stress inhibits adhesion molecule expression in vascular endothelial cells induced by coculture with smooth muscle cells. *Blood* **101** (7), 2667–2674.
- CLARIDGE, M. 2010 Clinical assessment of arterial stiffness. PhD thesis, University of Birmingham.
- COUADE, M., PERNOT, M., PRADA, C., MESSAS, E., EMMERICH, J., BRUNEVAL, P., CRITON, A., FINK, M. & TANTER, M. 2010 Quantitative assessment of arterial wall biomechanical properties using shear wave imaging. *Ultrasound in Medicine & Biology* **36** (10), 1662–1676.
- COURANT, R. & HILBERT, D. 1989 *Methods of Mathematical Physics..* Wiley.
- COX, R. 1969 Comparison of linearized wave propagation models for arterial blood flow analysis. *Journal of Biomechanics* **2** (3), 251–265.
- DARDIK, A., CHEN, L., FRATTINI, J., ASADA, H. & AZIZ, F. 2005 Differential effects of orbital and laminar shear stress on endothelial cells. *Journal of Vascular Surgery* **41** (5), 869–880.
- DAVIES, P., DEWEY JR, C., BUSSOLARI, S., GORDON, E. & GIMBRONE JR, M. 1984 Influence of hemodynamic forces on vascular endothelial function. *in vitro* studies of shear stress and pinocytosis in bovine aortic cells. *Journal of Clinical Investigation* **73** (4), 1121.
- DAVIES, P., MUNDEL, T. & BARBEE, K. 1995 A mechanism for heterogeneous endothelial responses to flow *in vivo* and *in vitro*. *Journal of Biomechanics* **28** (12), 1553–1560.
- DE HART, J., BAAIJENS, F., PETERS, G. & SCHREURS, P. 2003a A computational fluid–structure interaction analysis of a fiber-reinforced stentless aortic valve. *Journal of Biomechanics* **36** (5), 699–712.

- DE HART, J., PETERS, G., SCHREURS, P. & BAAIJENS, F. 2003b A three-dimensional computational analysis of fluid–structure interaction in the aortic valve. *Journal of Biomechanics* **36** (1), 103–112.
- DEMPERE-MARCO, L., OUBEL, E., CASTRO, M., PUTMAN, C., FRANGI, A. & CEBRAL, J. 2006 CFD analysis incorporating the influence of wall motion: Application to intracranial aneurysms. In *Medical Image Computing and Computer-Assisted Intervention–MICCAI 2006*, pp. 438–445. Springer.
- DETRANO, R., WONG, N., DOHERTY, T., SHAVELLE, R., TANG, W., GINZTON, L., BUDOFF, M. & NARAHARA, K. 1999 Coronary calcium does not accurately predict near-term future coronary events in high-risk adults. *Circulation* **99** (20), 2633–2638.
- DI MARTINO, E., BOHRA, A., VANDE GEEST, J., GUPTA, N., MAKAROUN, M. & VORP, D. 2006 Biomechanical properties of ruptured versus electively repaired abdominal aortic aneurysm wall tissue. *Journal of Vascular Surgery* **43** (3), 570–576.
- DI MARTINO, E., GUADAGNI, G., FUMERO, A., BALLERINI, G., SPIRITO, R., BIGLIOLI, P. & REDAELLI, A. 2001 Fluid–structure interaction within realistic three-dimensional models of the aneurysmatic aorta as a guidance to assess the risk of rupture of the aneurysm. *Medical Engineering & Physics* **23** (9), 647–655.
- DI MARTINO, E., MANTERO, S., INZOLI, F., MELISSANO, G., ASTORE, D., CHIESA, R. & FUMERO, R. 1998 Biomechanics of abdominal aortic aneurysm in the presence of endoluminal thrombus: Experimental characterization and structural static computational analysis. *European Journal of Vascular and Endovascular Surgery* **15** (4), 290–299.
- DOBRIN, P. 1989 Pathophysiology and pathogenesis of aortic aneurysms. current concepts. *The Surgical Clinics of North America* **69** (4), 687.
- DOKOS, S., LEGRICE, I., SMAILL, B., KAR, J. & YOUNG, A. 2000 A triaxial-measurement shear-test device for soft biological tissues. *Journal of Biomechanical Engineering* **122** (5), 471–478.
- DONEA, J., FASOLI-STELLA, P. & GIULIANI, S. 1977 Lagrangian and Eulerian finite element techniques for transient fluid–structure interaction problems. In *Transactions of the 4th International Conference on Structural Mechanics in Reactor Technology*.
- DONEA, J., HUERTA, A., PONTHOT, J. & RODRÍGUEZ-FERRAN, A. 2004 Arbitrary Lagrangian–Eulerian methods. *Encyclopedia of Computational Mechanics* .
- DORBIN, P. B. 1978 Mechanical properties of arteries. *Physiological Review* **58** (2), 397–441.

- DRIESSEN, N., WILSON, W., BOUTEN, C. & BAAIJENS, F. 2004 A computational model for collagen fibre remodelling in the arterial wall. *Journal of Theoretical Biology* **226** (1), 53–64.
- EGELHOFF, C., BUDWIG, R., ELGER, D., KHRAISHI, T. & JOHANSEN, K. 1999 Model studies of the flow in abdominal aortic aneurysms during resting and exercise conditions. *Journal of Biomechanics* **32** (12), 1319–1329.
- EL-KHATIB, F. & DAMIANO, E. 2003 Linear and non-linear analyses of pulsatile blood flow in a cylindrical tube. *Biorheology* **40** (5), 503–522.
- EULER, L. 1844 Principia pro motu sanguinis per arterias determinando. *Opera posthuma mathematica et physica anno* pp. 814–823.
- FIGUEROA, A. C., BAEK, S., TAYLOR, C. & HUMPHREY, J. 2009 A computational framework for fluid-solid-growth modeling in cardiovascular simulations. *Computer Methods in Applied Mechanics and Engineering* **198** (45-46), 3583–3602.
- FIGUEROA, C., VIGNON-CLEMENTEL, I., JANSEN, K., HUGHES, T. & TAYLOR, C. 2006 A coupled momentum method for modeling blood flow in three-dimensional deformable arteries. *Computer Methods in Applied Mechanics and Engineering* **195** (41-43), 5685–5706.
- FILLINGER, M., MARRA, S., RAGHAVAN, M. & KENNEDY, F. 2003 Prediction of rupture risk in abdominal aortic aneurysm during observation: Wall stress versus diameter. *Journal of Vascular Surgery* **37** (4), 724–732.
- FINLAYSON, B. 1972 *The method of weighted residuals and variational principles: With application in fluid mechanics, heat and mass transfer*. Academic Press.
- FINOL, E. & AMON, C. 2002 Flow-induced wall shear stress in abdominal aortic aneurysms: Part i-steady flow hemodynamics. *Computer Methods in Biomechanics & Biomedical Engineering* **5** (4), 309–318.
- FINOL, E., DI MARTINO, E., VORP, D. & AMON, C. 2003a Fluid–structure interaction and structural analyses of an aneurysm model. In *Proceedings of the 2003 Summer Bioengineering Conference; 25–29 June 2003; Key Biscane, Florida*, pp. 75–76.
- FINOL, E., KEYHANI, K. & AMON, C. 2003b The effect of asymmetry in abdominal aortic aneurysms under physiologically realistic pulsatile flow conditions. *Journal of Biomechanical Engineering* **125** (2), 207.
- FORMAGGIA, L., GERBEAU, J., NOBILE, F. & QUARTERONI, A. 2001 On the coupling of 3D and 1D Navier–Stokes equations for flow problems in compliant vessels. *Computer Methods in Applied Mechanics and Engineering* **191** (6-7), 561–582.

- FÖRSTER, C., WALL, W. & RAMM, E. 2007 Artificial added mass instabilities in sequential staggered coupling of non-linear structures and incompressible viscous flows. *Computer Methods in Applied Mechanics and Engineering* **196** (7), 1278–1293.
- FOUTRAKIS, G., YONAS, H. & SCLABASSI, R. 1999 Saccular aneurysm formation in curved and bifurcating arteries. *American Journal of Neuroradiology* **20** (7), 1309–1317.
- FRANCK, R. & LAZARUS, R. 1964 Mixed Eulerian–Lagrangian method. *Methods in Computational Physics* **3**, 47–67.
- FRIEDMAN, M., HUTCHINS, G., BRENT BARGERON, C., DETERS, O. & MARK, F. 1981 Correlation between intimal thickness and fluid shear in human arteries. *Atherosclerosis* **39** (3), 425–436.
- FRY, D. 1968 Acute vascular endothelial changes associated with increased blood velocity gradients. *Circulation Research* **22** (2), 165–197.
- FUNG, Y. 1993 *Biomechanics: Mechanical Properties of Living Tissues*. New York: Springer-Verlag.
- FUNG, Y. 1997 *Biomechanics: Circulation*. New York: Springer-Verlag.
- FUNG, Y., FRONEK, K. & PATITUCCI, P. 1979 Pseudoelasticity of arteries and the choice of its mathematical expression. *American Journal of Physiology-Heart and Circulatory Physiology* **237** (5), H620–H631.
- GAO, F., WATANABE, M. & MATSUZAWA, T. 2006 Stress analysis in a layered aortic arch model under pulsatile blood flow. *Biomedical Engineering Online* **5** (1), 25.
- GERBEAU, J., VIDRASCU, M. & FREY, P. 2005 Fluid–structure interaction in blood flows on geometries based on medical imaging. *Computers & Structures* **83** (2), 155–165.
- GIANNOPAPA, C. 2006 Fluid structure interaction in flexible vessels. PhD thesis, Technische Universiteit Eindhoven.
- GLOWINSKI, R. 2008 *Numerical methods for non-linear variational problems*. Springer Verlag.
- GLOWINSKI, R. & TALLEC, P. L. 1989 *Augmented Lagrangian and operator splitting methods in non-linear mechanics*. SIAM, 9.
- GOTTLIEB, D. & ORSZAG, S. 1981 *Numerical analysis of spectral methods: Theory and applications*. Society for Industrial and Applied Mathematics.

- GROTBERG, J. & JENSEN, O. 2004 Biofluid mechanics in flexible tubes. *Annual Review of Fluid Mechanics* **36** (1), 121.
- GUNZBURGER, M., NICOLAIDES, R. & PRESS, C. U. 1993 *Incompressible computational fluid dynamics: Trends and advances*. Cambridge University Press.
- HAGENBACH, E. 1860 Über die bestimmung der zähigkeit einer flüssigkeit durch den ausfluss aus röhren. *Annalen der Physik* **185** (3), 385–426.
- HALE, J., MCDONALD, D. & WOMERSLEY, J. 1955 Velocity profiles of oscillating arterial flow, with some calculations of viscous drag and the Reynolds number. *The Journal of Physiology* **128** (3), 629.
- HARTER, L., GROSS, B., CALLEN, P. & BARTH, R. 1982 Ultrasonic evaluation of abdominal aortic thrombus. *Journal of Ultrasound in Medicine* **1** (8), 315–318.
- HELPS, E. & MCDONALD, D. 1954 Observations on laminar flow in veins. *The Journal of Physiology* **124** (3), 631.
- HILBERT, D. 1986 An efficient Navier–Stokes solver and its application to fluid in elastic tubes. *Colloquia Mathematica Societatis Janos Bolya* **50** (1), 439–447.
- HIRT, C., AMSDEN, A. & COOK, J. 1974 An arbitrary Lagrangian–Eulerian computing method for all flow speeds. *Journal of Computational Physics* **14** (3), 227–253.
- HOFFMANN, B. 2008 Ultrasound guide for emergency physicians.
- HOLZAPFEL, G. & WEIZSÄCKER, H. 1998 Biomechanical behavior of the arterial wall and its numerical characterization. *Computers in Biology and Medicine* **28** (4), 377–392.
- HUGHES, T., LIU, W. & ZIMMERMANN, T. 1981 Lagrangian–Eulerian finite element formulation for incompressible viscous flows. *Computer Methods in Applied Mechanics and Engineering* **29** (3), 329–349.
- HUMPHREY, J. D. & TAYLOR, C. A. 2008 Intracranial and abdominal aortic aneurysms: Similarities, differences, and need for a new class of computational models. *Annual Review of Biomedical Engineering*. **10** (1), 221–246.
- INZOLI, F., BOSCHETTI, F., ZAPPA, M., LONGO, T. & FUMERO, R. 1993 Biomechanical factors in abdominal aortic aneurysm rupture. *European Journal of Vascular Surgery* **7** (6), 667–674.
- ISSA, R. 1986 Solution of the implicitly discretised fluid flow equations by operator-splitting. *Journal of Computational Physics* **62** (1), 40–65.

- JIANG, J., JOHNSON, K., WIEBEN, O., MYKLEBUST, O., MARDAL, K. & STROTHER, C. 2009 Computational fluid dynamics (CFD)-based flow analysis in aneurysms: A comparison study with 4D phase-contrast MR in an in vivo canine aneurysm. In *Proceedings 17th Scientific Meeting, International Society for Magnetic Resonance in Medicine*.
- JOG, C. & PAL, R. 2011 A monolithic strategy for fluid–structure interaction problems. *International Journal for Numerical Methods in Engineering* **85** (4), 429–460.
- KARNIADAKIS, G., ISRAELI, M. & ORSZAG, S. 1991 High-order splitting methods for the incompressible Navier–Stokes equations. *Journal of Computational Physics* **97** (2), 414–443.
- KARNIADAKIS, G. E. & SHERWIN, S. J. 1999 *Spectral/hp Element Methods for CFD*. Oxford University Press.
- KASSIOTIS, C., IBRAHIMBEGOVIC, A., NIEKAMP, R. & MATTHIES, H. 2011 Nonlinear fluid–structure interaction problem. Part i: Implicit partitioned algorithm, non-linear stability proof and validation examples. *Computational Mechanics* **47** (3), 305–323.
- KONDO, S., HASHIMOTO, N., KIKUCHI, H., HAZAMA, F., NAGATA, I., KATAOKA, H. & MACDONALD, R. 1997 Cerebral aneurysms arising at nonbranching sites: An experimental study. *Stroke* **28** (2), 398–404.
- KORN, G. & KORN, T. 2000 *Mathematical Handbook for Scientists and Engineers: Definitions, Theorems, and Formulas for Reference and Review*. Dover Publications.
- KOTERAS, J., GULLERUD, A., CRANE, N. & HALES, J. 2006 Presto users guide version 2.6. *SAND2006-6093, Sandia National Laboratories, Albuquerque, NM* .
- KRINDEL, P. & SILBERBERG, A. 1979 Flow through gel-walled tubes. *Journal of Colloid and Interface Science* **71** (1), 39–50.
- KU, D., GIDDENS, D., ZARINS, C. & GLAGOV, S. 1985 Pulsatile flow and atherosclerosis in the human carotid bifurcation. positive correlation between plaque location and low oscillating shear stress. *Arteriosclerosis, Thrombosis, and Vascular Biology* **5** (3), 293–302.
- KUMARAN, V. 1995a Stability of the flow of a fluid through a flexible tube at high Reynolds number. *Journal of Fluid Mechanics* **302** (1), 117–139.
- KUMARAN, V. 1995b Stability of the viscous flow of a fluid through a flexible tube. *Journal of Fluid Mechanics* **294** (1), 259–281.
- KÜTTLER, U. & WALL, W. 2008 Fixed-point fluid–structure interaction solvers with dynamic relaxation. *Computational Mechanics* **43** (1), 61–72.

- LALLY, C., REID, A. & PRENDERGAST, P. 2004 Elastic behavior of porcine coronary artery tissue under uniaxial and equibiaxial tension. *Annals of Biomedical Engineering* **32** (10), 1355–1364.
- LAMB, H. 1898 On the velocity of sound in a tube, as affected by the elasticity of the walls. *Manchester Memoirs* **42** (9).
- LASHERAS, J. C. 2007 The biomechanics of arterial aneurysms. *Annual Review of Fluid Mechanics* **39** (1), 293–319.
- LAURENT, S., GIRERD, X., MOURAD, J., LACOLLEY, P., BECK, L., BOUTOUYRIE, P., MIGNOT, J. & SAFAR, M. 1994 Elastic modulus of the radial artery wall material is not increased in patients with essential hypertension. *Arteriosclerosis, Thrombosis, and Vascular Biology* **14** (7), 1223–1231.
- LE TALLEC, P. & MARTIN, C. 1996 A non-linear elasticity model for structured mesh adaptation. In *Proceedings of the Third ECCOMAS Computational Fluid Dynamics Conference, Paris, France*, pp. 174–180.
- LE TALLEC, P. & MOURO, J. 2001 Fluid–structure interaction with large structural displacements. *Computer Methods in Applied Mechanics and Engineering* **190** (24), 3039–3067.
- LEE, K. & XU, X. 2002 Modelling of flow and wall behaviour in a mildly stenosed tube. *Medical Engineering & Physics* **24** (9), 575–586.
- LEITE, R. 1959 An experimental investigation of the stability of Poiseuille flow. *Journal of Fluid Mechanics* **5** (81), 35.
- LEONTINI, J., STEWART, B., THOMPSON, M. & HOURIGAN, K. 2006 Wake state and energy transitions of an oscillating cylinder at low Reynolds number. *Physics of Fluids* **18** (6), 067101.
- LERICHE, E. & LABROSSE, G. 2001 High-order direct Stokes solvers with or without temporal splitting: Numerical investigations of their comparative properties. *SIAM Journal on Scientific Computing* **22** (4), 1386–1410.
- LEUNG, J., WRIGHT, A., CHESHIRE, N., CRANE, J., THOM, S., HUGHES, A. & XU, Y. 2006 Fluid–structure interaction of patient specific abdominal aortic aneurysms: A comparison with solid stress models. *BioMedical Engineering OnLine* **5** (1), 33.
- LI, Z. & KLEINSTREUER, C. 2005 Fluid–structure interaction effects on sac-blood pressure and wall stress in a stented aneurysm. *Journal of Biomechanical Engineering* **127** (4), 662.

- LI, Z., U-KING-IM, J., TANG, T., SOH, E., SEE, T. & GILLARD, J. 2008 Impact of calcification and intraluminal thrombus on the computed wall stresses of abdominal aortic aneurysm. *Journal of Vascular Surgery* **47** (5), 928–935.
- LINDGREN, E. R. 1958 The transition process and other phenomena in viscous flow. *Arkiv fur Physik* **12**, 1–169.
- LINDHOLT, J., JUUL, S., FASTING, H. & HENNEBERG, E. 2005 Screening for abdominal aortic aneurysms: Single centre randomised controlled trial. *bmj* **330** (7494), 750.
- LINDSAY, J. & HURST, J. 1979 *The aorta*. Saunders.
- LOPEZ-CANDALES, A., HOLMES, D., LIAO, S., SCOTT, M., WICKLINE, S. & THOMPSON, R. 1997 Decreased vascular smooth muscle cell density in medial degeneration of human abdominal aortic aneurysms. *The American Journal of Pathology* **150** (3), 993.
- LORKOWSKI, S. & CULLEN, P. 2001 *Atherosclerosis: Pathogenesis, Clinical Features and Treatment*. John Wiley & Sons, Ltd.
- LUCHINI, P., LUPO, M. & POZZI, A. 1991 Unsteady Stokes flow in a distensible pipe. *ZAMM-Journal of Applied Mathematics and Mechanics/Zeitschrift für Angewandte Mathematik und Mechanik* **71** (10), 367–378.
- MALVERN, L. 1969 *Introduction to the Mechanics of a Continuous Medium*.
- MARDAL, K., JIANG, J., VALSEN-SENDSTAD, K. & STROTHER, C. 2010 Comparison of flow based on CFD and MRI in canine aneurysm models .
- MESA MÚNERA, E. 2011 Characterization of brain tissue phantom using an indentation device and inverse finite element parameter estimation algorithm. PhD thesis, Universidad Nacional de Colombia, Sede Medellín.
- MILLS, C., GABE, I., GAULT, J., MASON, D., ROSS JR, J., BRAUNWALD, E. & SHILLINGFORD, J. 1970 Pressure-flow relationships and vascular impedance in man. *Cardiovascular Research* **4** (4), 405–417.
- MILNOR, W. 1989 *Properties of the vascular wall*, pp. 58–101.
- MOK, D. & WALL, W. 2001 Partitioned analysis schemes for the transient interaction of incompressible flows and non-linear flexible structures. In *Trends in Computational Structural Mechanics, Barcelona*.
- MOORE JR, J., MAIER, S., KU, D. & BOESIGER, P. 1994 Haemodynamics in the abdominal aorta: a comparison of in vitro and in vivo measurements. *Journal of Applied Physiology* **76** (4), 1520–1527.

- MORRISON, A. 1999 Robbins pathologic basis of disease. *JAMA: The Journal of the American Medical Association* **282** (18), 1776–1777.
- MOSORA, F., HARMANT, A., BERNARD, C., FOSSION, A., POCHE, T., JUCHMES, J. & CESCOTTO, S. 1993 Modelling the arterial wall by finite elements. *Archives of Physiology and Biochemistry* **101** (3), 185–191.
- MOWER, W., QUIÑONES, W. & GAMBHIR, S. 1997 Effect of intraluminal thrombus on abdominal aortic aneurysm wall stress. *Journal of Vascular Surgery* **26** (4), 602–608.
- MÜLLER, W. & FERBER, F. 2008 *Technische Mechanik für Ingenieure*. Hanser Verlag.
- NAGEL, T., RESNICK, N., DEWEY, C. & GIMBRONE, M. 1999 Vascular endothelial cells respond to spatial gradients in fluid shear stress by enhanced activation of transcription factors. *Arteriosclerosis, Thrombosis, and Vascular Biology* **19** (8), 1825–1834.
- NESBITT, W., WESTEIN, E., TOVAR-LOPEZ, F., TOLOUEI, E., MITCHELL, A., FU, J., CARBERRY, J., FOURAS, A. & JACKSON, S. 2009 A shear gradient-dependent platelet aggregation mechanism drives thrombus formation. *Nature medicine* **15** (6), 665–673.
- NEWMAN, A., ARNOLD, A., BURKE, G., O’LEARY, D. & MANOLIO, T. 2001 Cardiovascular disease and mortality in older adults with small abdominal aortic aneurysms detected by ultrasonography: The cardiovascular health study. *Annals of Internal Medicine* **134** (3), 182.
- NICHOLS, W. W. & O’ROURKE, M. F. 1990 *McDonald’s blood flow in arteries: Theoretic, experimental and clinical principles*. Edward Arnold.
- NOH, W. 1963 Cel: A time-dependent, two-space-dimensional, coupled Eulerian–Lagrange code. *Tech. Rep.*. Lawrence Radiation Lab., Univ. of California, Livermore.
- OLAFSSON, E., HAUSER, W. & GUDMUNDSSON, G. 1997 A population-based study of prognosis of ruptured cerebral aneurysm mortality and recurrence of subarachnoid hemorrhage. *Neurology* **48** (5), 1191–1195.
- OLSEN, J. & SHAPIRO, A. 1967 Large-amplitude unsteady flow in liquid-filled elastic tubes. *Journal of Fluid Mechanics* **29** (3), 513–538.
- ONDA, H., KASUYA, H., YONEYAMA, T., TAKAKURA, K., HORI, T., TAKEDA, J., NAKAJIMA, T. & INOUE, I. 2001 Genomewide-linkage and haplotype-association studies map intracranial aneurysm to chromosome 7q11. *The American Journal of Human Genetics* **69** (4), 804–819.

- OSCUII, H., SHADPOUR, M. & GHALICHI, F. 2007 Flow characteristics in elastic arteries using a fluid–structure interaction model. *American Journal of Applied Sciences* **4** (8), 516–524.
- OUBEL, E., CRAENE, M. D., PUTMAN, C. M., CEBRAL, J. R. & FRANGI, A. F. 2007 Analysis of intracranial aneurysm wall motion and its effects on haemodynamic patterns. In *Proc. SPIE*, , vol. 6511, pp. 65112A–1–65112A–8.
- OYRE, S., PEDERSEN, E., RINGGAARD, S., BOESIGER, P. & PAASKE, W. 1997 In vivo wall shear stress measured by magnetic resonance velocity mapping in the normal human abdominal aorta. *European Journal of Vascular and Endovascular Surgery* **13** (3), 263–271.
- PAPAHARILAOU, Y., EKATERINARIS, J., MANOUSAKI, E. & KATSAMOURIS, A. 2007 A decoupled fluid structure approach for estimating wall stress in abdominal aortic aneurysms. *Journal of Biomechanics* **40** (2), 367–377.
- PATERA, A. 1984 A spectral element method for fluid dynamics: Laminar flow in a channel expansion. *Journal of Computational Physics* **54** (3), 468–488.
- PERKTOLD, K. & RAPPITSCH, G. 1995 Computer simulation of local blood flow and vessel mechanics in a compliant carotid artery bifurcation model. *Journal of Biomechanics* **28** (7), 845–856.
- PETERSSON, N. 2001 Stability of pressure boundary conditions for Stokes and Navier–Stokes equations. *Journal of Computational Physics* **172** (1), 40–70.
- PFENNINGER, W. 1961 *Transition in the inlet length of tubes at high Reynolds numbers*, pp. 970–980. Pergamon.
- PIERSON, K., HALES, J., ALVIN, K. & MITCHELL, J. 2004 ADAGIO/ANDANTE users guide version 2.0. *Memo, Sandia National Laboratories, Albuquerque, NM* .
- PIETRABISSA, R. & INZOLI, F. 1994 Computational analysis of the fluid dynamics of a pulsatile flow in an elastic tube. *Journal of Biomechanics* **27** (6), 861–861.
- POISEUILLE, J. L. M. 1847 Sur ie mouvement des liquides de nature differente dans les tubes de tres petits diametres. *Annales de Chimie et de Physique* **3** (21), 76–110.
- PONTRELLI, G. 2001 Non-linear problems in arterial flows. *Nonlinear Analysis-Theory Methods and Applications* **47** (7), 4905–4916.
- POTKIN, B., BARTORELLI, A., GESSERT, J., NEVILLE, R., ALMAGOR, Y., ROBERTS, W. & LEON, M. 1990 Coronary artery imaging with intravascular high-frequency ultrasound. *Circulation* **81** (5), 1575–1585.

- POZRIKIDIS, C. 2011 *Introduction to theoretical and computational fluid dynamics*, 2nd edn. Oxford University Press, Inc.
- PRANDTL, L. 1904 Über flüssigkeitsbewegung bei sehr kleiner reibung. In *Proceedings of 3rd International Mathematics Congress, Heidelberg*.
- PRESS, W. 2007 *Numerical recipes: The art of scientific computing*. Cambridge University Press.
- QIU, Y. & TARBELL, J. 2000a Interaction between wall shear stress and circumferential strain affects endothelial cell biochemical production. *Journal of Vascular Research* **37** (3), 147–157.
- QIU, Y. & TARBELL, J. 2000b Numerical simulation of pulsatile flow in a compliant curved tube model of a coronary artery. *Journal of Biomechanical Engineering* **122** (1), 77.
- QUARTAPELLE, L. 1993 *Numerical solution of the incompressible Navier–Stokes equations*, 3rd edn. Birkhauser Basel.
- RAGHAVAN, M., KRATZBERG, J., CASTRO DE TOLOSA, E., HANAOKA, M., WALKER, P. & DA SILVA, E. 2006 Regional distribution of wall thickness and failure properties of human abdominal aortic aneurysm. *Journal of Biomechanics* **39** (16), 3010–3016.
- RAGHAVAN, M. & VORP, D. 2000 Toward a biomechanical tool to evaluate rupture potential of abdominal aortic aneurysm: Identification of a finite strain constitutive model and evaluation of its applicability. *Journal of Biomechanics* **33** (4), 475–482.
- REINALD, N., FOURNIER, B., NAVEAU, A., COUTY, L., LEMITRE, M., SEGUIER, S., COULOMB, B., GOGLY, B., LAFONT, A. & DURAND, E. 2010 Fusiform aneurysm model in rabbit carotid artery. *Journal of vascular research* **47** (1), 61–68.
- RESTREPO, C., STRONG, J., GUZMÁN, M. & TEJADA, C. 1979 Geographic comparisons of diffuse intimal thickening of the aorta. *Atherosclerosis* **32** (2), 177–193.
- REUDERINK, P. 1991 Analysis of the flow in a 3D distensible model of the carotid artery bifurcation. PhD thesis, Eindhoven Technical University.
- REUDERINK, P., VAN DE VOSSE, F., VAN STEENHOVEN, A., VAN DONGEN, M. & JANSSEN, J. 1993 Incompressible low-speed-ratio flow in non-uniform distensible tubes. *International journal for numerical methods in fluids* **16** (7), 597–612.
- REYNOLDS, O. 1883 An experimental investigation of the circumstances which determine whether the motion of water shall be direct or sinuous, and of the law of resistance in parallel channels. *Proceedings of the Royal Society of London* **35** (224–226), 84–99.

- RISSLAND, P., ALEMU, Y., EINAV, S., RICOTTA, J. & BLUESTEIN, D. 2009 Abdominal aortic aneurysm risk of rupture: Patient-specific FSI simulations using anisotropic model. *Journal of Biomechanical Engineering* **131** (3), 031001.
- ROCKWELL, R. 1969 *Nonlinear analysis of pressure-and shock waves in blood vessels*.
- RODKIEWICZ, C., SINHA, P. & KENNEDY, J. 1990 On the application of a constitutive equation for whole human blood. *Journal of Biomechanical Engineering* **112** (2), 198.
- RUECKERT, D., SONODA, L., HAYES, C., HILL, D., LEACH, M. & HAWKES, D. 1999 Nonrigid registration using free-form deformations: Application to breast MR images. *IEEE Transactions on Medical Imaging* **18** (8), 712–721.
- SALSAC, A., SPARKS, S., CHOMAZ, J. & LASHERAS, J. 2006 Evolution of the wall shear stresses during the progressive enlargement of symmetric abdominal aortic aneurysms. *Journal of Fluid Mechanics* **560** (1), 19–51.
- SALSAC, A. V. 2005 Changes in the hemodynamic stresses occurring during the enlargement of abdominal aortic aneurysms. PhD thesis, University of California, San Diego.
- SATTA, J., LÄÄRÄ, E. & JUVONEN, T. 1996 Intraluminal thrombus predicts rupture of an abdominal aortic aneurysm. *Journal of Vascular Surgery* **23** (4), 737–739.
- SCHENK, O. & GÄRTNER, K. 2004 Solving unsymmetric sparse systems of linear equations with PARDISO. *Future Generation Computer Systems* **20** (3), 475–487.
- SCHERZINGER, W. & HAMMERAND, D. 2007 Testing of constitutive models in LAME. *SAND07-5872, Sandia National Laboratories, Albuquerque, NM* .
- SCHMERMUND, A., DENKTAS, A., RUMBERGER, J., CHRISTIAN, T., SHEEDY, P., BAILEY, K. & SCHWARTZ, R. 1999 Independent and incremental value of coronary artery calcium for predicting the extent of angiographic coronary artery disease: comparison with cardiac risk factors and radionuclide perfusion imaging. *Journal of the American College of Cardiology* **34** (3), 777–786.
- SCHULZE-BAUER, C., MÖRTH, C. & HOLZAPFEL, G. 2003 Passive biaxial mechanical response of aged human iliac arteries. *Journal of Biomechanical Engineering* **125** (3), 395.
- SCOTTI, C. M., SHOKOLNIK, A. D., MULUK, S. C. & FINOL, E. A. 2005 Fluid–structure interaction in abdominal aortic aneurysms: Effects of asymmetry and wall thickness. *BioMedical Engineering OnLine* **4** (1), 64.
- SFORZA, D. M., PUTMAN, C. M. & CEBRAL, J. R. 2009 Haemodynamics of cerebral aneurysms. *Annual Review of Fluid Mechanics* **41** (1), 91–107.

- SHEARD, G. 2009 Flow dynamics and wall shear-stress variation in a fusiform aneurysm. *Journal of Engineering Mathematics* **64** (4), 379–390.
- SHEARD, G. & RYAN, K. 2007 Pressure-driven flow past spheres moving in a circular tube. *Journal of Fluid Mechanics* **592** (1), 233–262.
- SHEARD, G. J., EVANS, R. G., DENTON, K. M. & HOURIGAN, K. 2007 Undesireable haemodynamics in aneurysms. In *Proceedings of the IUTAM Symposium on Unsteady Separated Flows and Their Control Unpublished*. Hotel Corfu Chandris, Corfu, Greece.
- SHOJIMA, M., OSHIMA, M., TAKAGI, K., TORII, R., HAYAKAWA, M., KATADA, K., MORITA, A. & KIRINO, T. 2004 Magnitude and role of wall shear stress on cerebral aneurysm computational fluid dynamic study of 20 middle cerebral artery aneurysms. *Stroke* **35** (11), 2500–2505.
- SOMMERFELD, A. 1908 Ein beitrag zur hydrodynamisehen erkliirung der turbulenten flfissigkeitsbewegun. In *4th International Congress on Mathematics*. Rome.
- SONESSON, B., SANDGREN, T. & LÄNNE, T. 1999 Abdominal aortic aneurysm wall mechanics and their relation to risk of rupture. *European Journal of Vascular and Endovascular Surgery* **18** (6), 487–493.
- STEFANADIS, C., STRATOS, C., VLACHOPOULOS, C., MARAKAS, S., BOUDOULAS, H., KALLIKAZAROS, I., TSIAMIS, E., TOUTOUZAS, K., SIOROS, L. & TOUTOUZAS, P. 1995 Pressure-diameter relation of the human aorta: A new method of determination by the application of a special ultrasonic dimension catheter. *Circulation* **92** (8), 2210–2219.
- STEBBENS, W. 1963 Histopathology of cerebral aneurysms. *Archives of Neurology* **8** (3), 272.
- STEBBENS, W. E. 1989 Histopathology of cerebral aneurysms. *Journal of Neurosurgery* **70**, 823–831.
- STEIGER, H., LIEPSCH, D., POLL, A. & REULEN, H. 1988 Hemodynamic stress in terminal saccular aneurysms: A laser-doppler study. *Heart and Vessels* **4** (3), 162–169.
- STEINMAN, D. & ETHIER, C. 1994 The effect of wall distensibility on flow in a two-dimensional end-to-side anastomosis. *Journal of Biomechanical Engineering* **116** (3), 294–301.
- STETTLER, J., NIEDERER, P. & ANLIKER, M. 1981 Theoretical analysis of arterial hemodynamics including the influence of bifurcations. *Annals of Biomedical Engineering* **9** (2), 145–164.

- STOKES, G. 1967 Classical works in fluid mechanics and hydraulics. *La Houille Blanche* (7), 765–772.
- STREETER, V., KEITZER, W. & BOHR, D. 1964 *Energy dissipation in pulsatile flow through distensible tapered vessels*.
- SYNGE, J., SCHILD, A. & SCHILD, A. 1978 *Tensor calculus*, 5th edn. Dover Publications.
- THOMPSON, R., LIAO, S. & CURCI, J. 1997 Vascular smooth muscle cell apoptosis in abdominal aortic aneurysms. *Coronary Artery Disease* **8** (10), 623.
- THUBRIKAR, J., LABROSSE, M., ROBICSEK, F., AL-SOUDI, J. & B. FOWLER, M. 2001 Mechanical properties of abdominal aortic aneurysm wall. *Journal of Medical Engineering & Technology* **25** (4), 133–142.
- TOLOUEI, E., BUTLER, C., FOURAS, A., RYAN, K., SHEARD, G. & CARBERRY, J. 2011 Effect of haemodynamic forces on platelet aggregation geometry. *Annals of Biomedical Engineering* **39** (5), 1403–1413.
- TORII, R., OSHIMA, M., KOBAYASHI, T., TAKAGI, K. & TEZDUYAR, T. 2008 Fluid–structure interaction modeling of a patient-specific cerebral aneurysm: Influence of structural modeling. *Computational Mechanics* **43** (1), 151–159.
- TRAUB, O. & BERK, B. 1998 Laminar shear stress mechanisms by which endothelial cells transduce an atheroprotective force. *Arteriosclerosis, Thrombosis, and Vascular Biology* **18** (5), 677–685.
- TRULIO, J. 1966 Theory and structure of the afton codes. *Tech. Rep.*. DTIC Document.
- VAN BRUMMELEN, E., HULSHOFF, S. & DE BORST, R. 2003 Energy conservation under incompatibility for fluid–structure interaction problems. *Computer Methods in Applied Mechanics and Engineering* **192** (25), 2727–2748.
- VAN LOON, R., ANDERSON, P., VAN DE VOSSE, F. & SHERWIN, S. 2007 Comparison of various fluid–structure interaction methods for deformable bodies. *Computers & Structures* **85** (11), 833–843.
- VIGNON-CLEMENTEL, I., FIGUEROA, A. C., JANSEN, K. & TAYLOR, C. 2006 Out-flow boundary conditions for three-dimensional finite element modeling of blood flow and pressure in arteries. *Computer Methods in Applied Mechanics and Engineering* **195** (29–32), 3776–3796.
- VORP, D., LEE, P., WANG, D., MAKAROUN, M., NEMOTO, E., OGAWA, S. & WEBSTER, M. 2001 Association of intraluminal thrombus in abdominal aortic aneurysm with local hypoxia and wall weakening. *Journal of Vascular Surgery* **34** (2), 291–299.

- VORP, D., RAGHAVAN, M., MULUK, S., MAKAROUN, M., STEED, D., SHAPIRO, R. & WEBSTER, M. 1996 Wall strength and stiffness of aneurysmal and non-aneurysmal abdominal aorta. *Annals of the New York Academy of Sciences* **800** (1), 274–276.
- VORP, D., RAGHAVAN, M. & WEBSTER, M. 1998 Mechanical wall stress in abdominal aortic aneurysm: Influence of diameter and asymmetry. *Journal of Vascular Surgery* **27** (4), 632–639.
- WALL, W. 1999 Fluid-struktur-interaktion mit stabilisierten finiten elementen. PhD thesis.
- WANHAINEN, A. 2008 How to define an abdominal aortic aneurysm-influence on epidemiology and clinical practice. *Scandinavian Journal of Surgery* **97** (2), 105.
- WILMAN, A., RIEDERER, S., HUSTON III, J., WALD, J. & DEBBINS, J. 1998 Arterial phase carotid and vertebral artery imaging in 3D contrast-enhanced MR angiography by combining fluoroscopic triggering with an elliptical centric acquisition order. *Magnetic resonance in medicine* **40** (1), 24–35.
- WINSLOW, A. 1963 “equipotential” zoning of two-dimensional meshes. *Tech. Rep.*. California Univ., Livermore (USA). Lawrence Livermore Lab.
- WITZING, K. 1914 Über erzwungene wellenbewegungen zaher, inkompressibilen flüssigkeiten in elastischen röhren. PhD thesis, Inaugural thesis.
- WOLTERS, B., RUTTEN, M., SCHURINK, G., KOSE, U., DE HART, J. & VAN DE VOSSE, F. 2005 A patient-specific computational model of fluid–structure interaction in abdominal aortic aneurysms. *Medical Engineering & Physics* **27** (10), 871–883.
- WOMERSLEY, J. 1955 Method for the calculation of velocity, rate of flow and viscous drag in arteries when the pressure gradient is known. *The Journal of Physiology* **127** (3), 553.
- WOMERSLEY, J. 1957a *An elastic tube theory of pulse transmission and oscillatory flow in mammalian arteries*, 5th edn. Wright Air Development Center.
- WOMERSLEY, J. 1957b Oscillatory flow in arteries: The constrained elastic tube as a model of arterial flow and pulse transmission. *Physics in Medicine and Biology* **2** (2), 178.
- WOOTTON, D. & KU, D. 1999 Fluid mechanics of vascular systems, diseases, and thrombosis. *Annual Review of Biomedical Engineering* **1** (1), 299–329.
- WYGNANSKI, I., SOKOLOV, M. & FRIEDMAN, D. 1975 On transition in a pipe. Part 2. The equilibrium puff. *J. Fluid Mech* **69** (2), 283–304.

- XIE, J., ZHOU, J. & FUNG, Y. 1995 Bending of blood vessel wall: stress-strain laws of the intima-media and adventitial layers. *Journal of biomechanical engineering* **117** (1), 136.
- YANENKO, N. 1971 *The Method of Fractional Steps*. Gordon and Breach, London.
- YOUNG, T. 1808 Hydraulic investigations, subservient to an intended Croonian lecture on the motion of the blood. *Philosophical Transactions of the Royal Society of London* **98** (1), 164–186.
- ZAGZOULE, M., KHALID-NACIRI, J. & MAUSS, J. 1991 Unsteady wall shear stress in a distensible tube. *Journal of Biomechanics* **24** (6), 435–439.

Appendices

Appendix A

Wall shear stress

Of particular significance to the healthy function of the artery wall is wall shear stress. The endothelial cells in the intimal layer respond to the fluid shear stress at the wall by secreting chemicals vital to the mechanotransduction process (Lasheras 2007). Furthermore, an amenable wall shear stress environment is vital to platelet adhesion and the leukocyte extravasation processes in which blood cells first roll along the wall before stopping and transmigrating through the endothelial wall layer (Sforza *et al.* 2009). The significance of the wall shear stress makes it the primary flow quantity considered in the haemodynamics literature.

Physically, the wall shear stress is simply the shear force per unit area felt at the wall location. As described in chapter 3, a shear stress is a stress which causes a shear strain. A shear strain acts in the plane along a face of a differential element. While normal strains are measured by a dilation or change in length, shear strain may be conceptualised as the change in angle between two line elements. In fluids, shear stresses cause a spatial variation in the velocity field. A fundamental example of this is in a boundary layer near a wall (figure A.1). The no-slip boundary condition at the wall dictates that the speed of the fluid at the boundary (relative to the boundary) is zero, but at some height from the wall the flow speed reaches the free stream velocity. The region between these two points is aptly named the boundary layer. Figure A.1 shows for a simple 2D case the boundary layer consists of a spatially varying velocity. For Newtonian fluids (which this discussion is limited to), the two-dimensional shear stress parallel to a flat plate, such as is depicted in figure A.1 is given by

$$\tau(x_2) = -\mu \frac{\partial v_1}{\partial x_2}. \quad (\text{A.1})$$

where τ is the shear stress, μ is the dynamic viscosity, v_1 is the x_1 -component of the

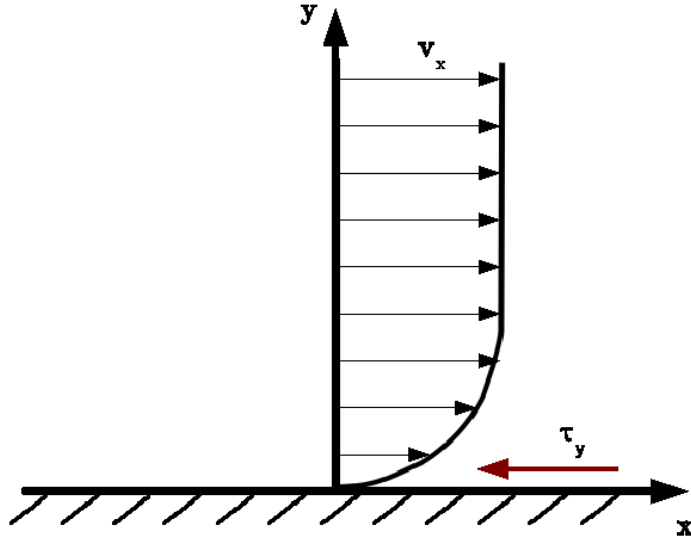


FIGURE A.1: A shear stress τ_y causes the velocity to change in the wall-normal direction, y , to enforce the non-slip boundary condition at the wall.

velocity vector \mathbf{v} and x_2 is the component of the position vector normal to the wall. However for the case of flow in an aneurysm, the wall is no longer a flat plate and the flow is three-dimensional rather than two-dimensional. For such cases a broader definition of the shear stress is required. In three dimensions the shear stress is a tensor defined as (Pozrikidis 2011)

$$\begin{aligned}
 \boldsymbol{\tau} &= \mu \boldsymbol{\gamma}_T, \\
 &= \mu (\nabla \mathbf{v} + \nabla \mathbf{v}^T), \\
 &= \mu \begin{bmatrix} \tau_{11} & \tau_{12} & \tau_{13} \\ \tau_{21} & \tau_{22} & \tau_{23} \\ \tau_{31} & \tau_{32} & \tau_{33} \end{bmatrix}, \tag{A.2}
 \end{aligned}$$

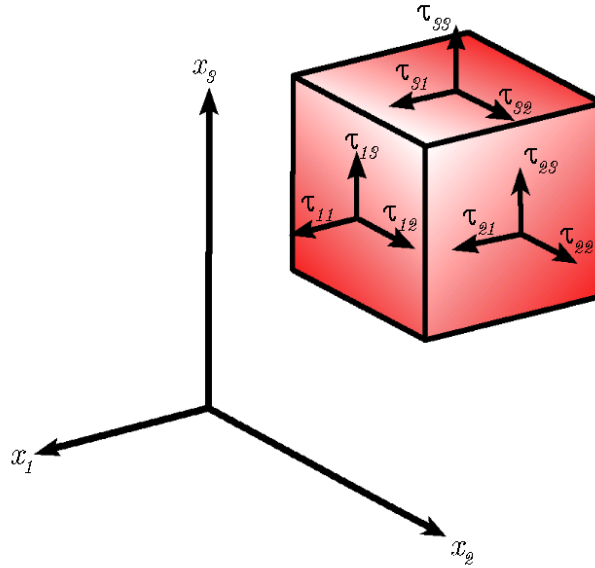


FIGURE A.2: Components of the shear stress tensor in three dimensions. The total force on any particular surface corresponds to the columns in the shear stress tensor.

where

$$\begin{aligned}
 \tau_{11} &= \left(\frac{dv_1}{dx_1} + \frac{dv_2}{dx_2} + \frac{dv_3}{dx_3} \right) + \frac{dv_1}{dx_1}, \\
 \tau_{22} &= \left(\frac{dv_1}{dx_1} + \frac{dv_2}{dx_2} + \frac{dv_3}{dx_3} \right) + \frac{dv_2}{dx_2}, \\
 \tau_{33} &= \left(\frac{dv_1}{dx_1} + \frac{dv_2}{dx_2} + \frac{dv_3}{dx_3} \right) + \frac{dv_3}{dx_3}, \\
 \tau_{12} = \tau_{21} &= \left(\frac{dv_1}{dx_2} + \frac{dv_2}{dx_1} \right), \\
 \tau_{13} = \tau_{31} &= \left(\frac{dv_1}{dx_3} + \frac{dv_3}{dx_1} \right), \\
 \tau_{23} = \tau_{32} &= \left(\frac{dv_2}{dx_3} + \frac{dv_3}{dx_2} \right).
 \end{aligned} \tag{A.3}$$

Figure A.2 shows a means by which the shear stress tensor of equation A.2 may be interpreted. It shows a 3D differential element and the corresponding stresses acting on its faces. This shows that rows of the shear stress tensor describe the contribution from each face to the shear stress in a particular principal direction. The columns of the shear stress tensor describe the shear stress on a particular face of the differential element. It is important to note that the shear stress components τ_{11} , τ_{22} and τ_{33} are not hydrostatic normal stresses. The shear rate tensor is the deviatoric component of

the the total fluid stress tensor

$$\sigma_{ij} = -P\mathbf{I}\delta_{ij} + \tau_{ij}, \quad (\text{A.4})$$

where δ is the Kronecker-delta function and P is the hydrostatic pressure. The hydrostatic pressure term $P\mathbf{I}\delta_{ij}$ is sometimes described as the volumetric stress tensor or mean normal stress tensor (Pozrikidis 2011). For an incompressible Newtonian fluid, in order to conserve continuity, the pressure

$$P = \frac{1}{3}\text{tr}(\boldsymbol{\tau}), \quad (\text{A.5})$$

which is the mean normal stress. This term is responsible for the change in volume of the stressed body. The shear stress tensor $\boldsymbol{\tau}$ is the deviatoric component of the stress that acts to change the spatial relationships within a differential element. While the shear stress components τ_{11} , τ_{22} , and τ_{33} may act in the face-normal direction of the differential element, they may still contribute to the deviatoric (or spatial) change and hence the shear stress.

The wall shear stress is simply defined as the shear stress felt at the wall, i.e. the components of the shear stress tensor effective on a differential element with a face that coincides with the boundary. Firstly it is recognised that a simple definition of the wall shear stress could be given by

$$\boldsymbol{\tau}_{WSS} = \boldsymbol{\tau} \cdot \underline{\mathbf{n}}, \quad (\text{A.6})$$

where $\underline{\mathbf{n}}$ is the unit normal vector to the plane of interest. Note: these being tensor quantities the order of operations is important. If the local coordinates of the differential element and the global (wall coordinates) align then the wall shear stress on the face with normal $\underline{\mathbf{n}} = (\underline{n}_1, \underline{n}_2, \underline{n}_3) = (1, 0, 0)$ becomes

$$\boldsymbol{\tau}_{WSS}^{(1,0,0)} = \begin{bmatrix} \tau_{11} \\ \tau_{21} \\ \tau_{31} \end{bmatrix}, \quad (\text{A.7})$$

which is the stress components on the wall depicted in figure A.2. Mathematically it is clear that the wall shear stress at any point is a vector having components in each of the principal coordinate directions.

It becomes quickly apparent that for the case of flow through an aneurysm the description of the wall shear stress given in equation A.1 is inadequate. The aneurysm-focused literature presents a variety of definitions for the wall shear stress based on

differing assumptions. The first is equation A.1. This model assumes that at the infinitesimal limit the curvature of the wall is insignificant, as such flow may be approximated as the local variation in flow in a radial direction.

Some papers use the definition for the wall shear stress derived from the Hagen–Poiseuille equation

$$\tau = \frac{8\mu \cdot v_z}{d}, \quad (\text{A.8})$$

where d is the diameter of the vessel and v_z is the axial velocity component. While this definition incorporates the curvature of the wall into its derivation it assumes that the vessel is of constant diameter, i.e. a straight pipe and that the velocity profile is parabolic and symmetric i.e. the Hagen–Poiseuille solution. For the case of blood flow through aneurysms this is insufficient to describe the wall shear stress as the dilation of the vessel causes d to vary, and the pulsatile flow will invoke a Womersley profile, not a Hagen–Poiseuille profile.

To accurately describe the wall shear stress in an aneurysm, a generic method is required, for describing the shear stress on a wall with arbitrary wall profile and flow characteristics. Salsac *et al.* (2006) defines the wall shear stress as

$$\boldsymbol{\tau}_{WSS} = 2\mu (\boldsymbol{\tau} \cdot \underline{\mathbf{n}}) \cdot \underline{\mathbf{t}}, \quad (\text{A.9})$$

with $\underline{\mathbf{n}}$ representing the unit normal vector to the plane in which the shear stress is acting, $\underline{\mathbf{t}}$ being a tangent vector in the direction of maximum shear in the shearing plane, and $\boldsymbol{\tau}$ the deviatoric stress tensor described in equation A.2. Equation A.9 is a generalization of equation A.6 which is capable of determining the shear stress components on any plane.

In terms of endothelial health, the maximum wall shear stress is more significant than the wall shear stress in a single direction $\underline{\mathbf{t}}$. As such, in defining the wall shear stress it makes sense to define the shear stress as a vector acting in the wall-normal plane and determine its magnitude. Note: this is not typical of wall shear stress analysis which often takes only the component of the dominant direction of shear (e.g. Finol *et al.* 2003b; Salsac *et al.* 2006).

Rather than specifying the direction of shear, the shear stress in a particular plane with unit normal vector $\underline{\mathbf{n}}$ can be determined by projecting the deviatoric component of the stress tensor onto the plane with unit normal vector $\underline{\mathbf{n}}$,

$$\boldsymbol{\tau}^{(\underline{\mathbf{n}})} = 2\mu \underline{\mathbf{n}} \cdot \boldsymbol{\tau} \cdot (\mathbf{I} - \underline{\mathbf{n}} \otimes \underline{\mathbf{n}}), \quad (\text{A.10})$$

where $(\mathbf{I} - \underline{\mathbf{n}} \otimes \underline{\mathbf{n}})$ is the projection matrix, $\tau^{(\underline{\mathbf{n}})}$ is the shear stress in the plane with normal vector $\underline{\mathbf{n}}$. When the plane is located at the wall and the normal vector $\underline{\mathbf{n}}$ of the plane is identical to that of the wall

$$\boldsymbol{\tau}^{(\underline{\mathbf{n}})} = \boldsymbol{\tau}_{WSS}. \quad (\text{A.11})$$

For a Newtonian fluid flowing in Cartesian two-dimensional coordinates, above an infinite flat plate, such as the case in figure A.1, the normal vector is

$$\underline{\mathbf{n}} = \begin{bmatrix} \underline{n}_1 \\ \underline{n}_2 \end{bmatrix} = \begin{bmatrix} 0 \\ 1 \end{bmatrix}, \quad (\text{A.12})$$

the deviatoric stress tensor is

$$\begin{aligned} \boldsymbol{\tau} &= 2\mu \begin{bmatrix} \tau_{11} & \tau_{12} \\ \tau_{21} & \tau_{22} \end{bmatrix} = 2\mu \begin{bmatrix} \frac{\partial v_1}{\partial x_1} & \frac{1}{2} \left(\frac{\partial v_1}{\partial x_2} + \frac{\partial v_2}{\partial x_1} \right) \\ \frac{1}{2} \left(\frac{\partial v_1}{\partial x_2} + \frac{\partial v_2}{\partial x_1} \right) & \frac{\partial v_2}{\partial x_2} \end{bmatrix} \\ &= 2\mu \begin{bmatrix} 0 & \frac{1}{2} \frac{\partial v_1}{\partial x_2} \\ \frac{1}{2} \frac{\partial v_1}{\partial x_2} & 0 \end{bmatrix}, \end{aligned} \quad (\text{A.13})$$

and the wall shear stress vector becomes

$$\boldsymbol{\tau}_{WSS} = 2\mu \begin{bmatrix} \underline{n}_2 [\tau_{12} (\underline{n}_1^2 - \underline{n}_2^2) + (\tau_{22} - \tau_{11}) \underline{n}_1 \underline{n}_2] \\ -\underline{n}_1 [\tau_{12} (\underline{n}_1^2 - \underline{n}_2^2) + (\tau_{22} - \tau_{11}) \underline{n}_1 \underline{n}_2] \end{bmatrix}, \quad (\text{A.14})$$

To determine the principal wall shear stress in the wall plane, the magnitude of $\boldsymbol{\tau}_{WSS}$ is taken and the property of the unit normal vector ($\underline{n}_1^2 + \underline{n}_2^2 = 1$) is employed

$$\begin{aligned} |\boldsymbol{\tau}_{WSS}| &= 2\mu \sqrt{(\underline{n}_1^2 + \underline{n}_2^2) [\tau_{12} (\underline{n}_1^2 - \underline{n}_2^2) + (\tau_{22} - \tau_{11}) \underline{n}_1 \underline{n}_2]^2} \\ &= 2\mu [\tau_{12} (\underline{n}_1^2 - \underline{n}_2^2) + (\tau_{22} - \tau_{11}) \underline{n}_1 \underline{n}_2] \end{aligned} \quad (\text{A.15})$$

Substituting the stress tensor and normal vectors from equations A.12 and A.13 recovers equation A.1.

Salsac *et al.* (2006) use the relationship for the wall shear stress presented in equation A.15. Unlike equation A.8, equation A.15 is sufficiently general to consider both a generic boundary layer velocity profile, and at the infinitesimal limit the normal vectors account for the wall structure. Despite these improvements equation A.15 is not without its pitfalls. Firstly it assumes the flow is two-dimensional. For laminar flows in rigid pipes this is a reasonable assumption to make as the flow is well bounded, leading to negligible fluid motion in the wall-normal direction. For the case of an aneurysm, however, vortex formation and impingements at the proximal and distal necks will cause

a small velocity gradient in the wall-normal direction. Large aneurysm flows typically have non-axisymmetric flow patterns which require a full three-dimensional analysis of the flow to accurately determine the wall shear stress. Furthermore, if the assumption of a rigid-wall is relaxed, as is the case for both this investigation and *in vivo* flows, the velocity of the fluid at the wall may have a significant component in the wall-normal direction. Under these conditions it is essential that the definition for the wall shear stress include the contribution from all three velocity components. Performing the same projection onto a plane normal to the vessel wall, the wall shear stress in three dimensions may be written

$$\boldsymbol{\tau}_{WSS} = 2\mu \begin{bmatrix} (\tau_{11} - \tau_{22})\underline{n}_{122} + (\tau_{11} - \tau_{33})\underline{n}_{133} + \\ \tau_{12}(\underline{n}_2 - 2\underline{n}_{211}) + \tau_{13}(\underline{n}_3 - 2\underline{n}_{311}) - 2\tau_{23}\underline{n}_{123} \\ (\tau_{22} - \tau_{11})\underline{n}_{211} + (\tau_{22} - \tau_{33})\underline{n}_{233} + \\ \tau_{12}(\underline{n}_1 - 2\underline{n}_{122}) + \tau_{23}(\underline{n}_3 - 2\underline{n}_{322}) - 2\tau_{13}\underline{n}_{123} \\ (\tau_{33} - \tau_{11})\underline{n}_{311} + (\tau_{33} - \tau_{22})\underline{n}_{322} + \\ \tau_{13}(\underline{n}_1 - 2\underline{n}_{133}) + \tau_{23}(\underline{n}_2 - 2\underline{n}_{233}) - 2\tau_{12}\underline{n}_{123} \end{bmatrix}, \quad (\text{A.16})$$

where

$$\underline{n}_{ijk} = \underline{n}_i \underline{n}_j \underline{n}_k. \quad (\text{A.17})$$

Investigations that do not include these extra terms when calculating the wall shear stress may well underestimate the wall shear stress in the wall plane. Many investigations into elastic-walled aneurysms have reported a reduction in the peak wall shear stress achieved (Perktold & Rappitsch 1995; Dempere-Marco *et al.* 2006; Oubel *et al.* 2007). None of these papers indicate how they define the wall shear stress; failure to use the full three-dimensional form of the wall shear stress may partially explain the reduced wall shear stress observed in their investigations (the resulting motion of the arterial wall is expected to slightly reduce the local axial velocity component and therefore simplistic wall shear stress calculations fail to capture the full shearing forces on the flow).

The definitions in equations A.15 and A.16 provide the wall shear stress in a particular plane with unit normal vector \underline{n} . For the simple flow case shown in figure A.1 the plane in which the shear stress is a maximum is the wall plane. With a moving wall, the

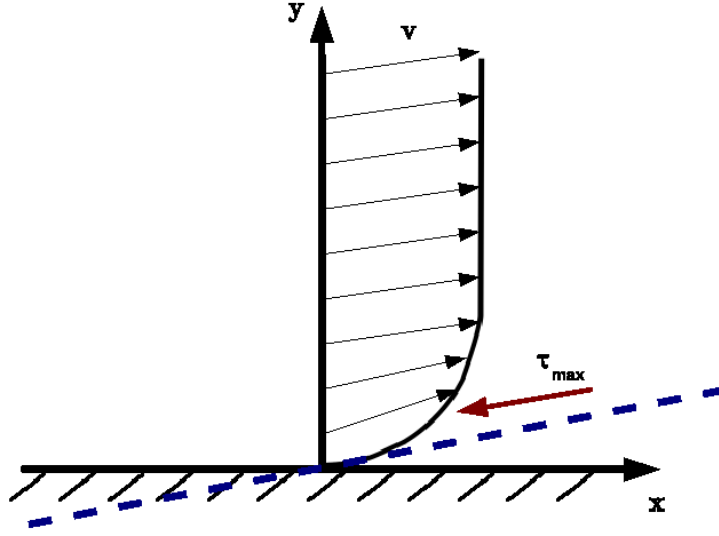


FIGURE A.3: A non-zero wall-normal component of velocity causes the maximum shear stress τ_{max} to occur in the blue-dashed plane rather than the plane of the wall.

wall-normal velocity component makes it possible to have a shear stress greater than the shear in the wall-normal plane (e.g. figure A.3). To determine the shear stress at the wall location in the plane which provides maximum shearing involves solving the eigenvalue problem,

$$|\boldsymbol{\tau} - \lambda \mathbf{I}| = \begin{bmatrix} \tau_{11} - \lambda & \tau_{12} & \tau_{13} \\ \tau_{21} & \tau_{22} - \lambda & \tau_{23} \\ \tau_{31} & \tau_{32} & \tau_{33} - \lambda \end{bmatrix} = 0, \quad (\text{A.18})$$

where λ is the eigenvalue which maximises the stress tensor. In two dimensions the eigenvalues are given by

$$\lambda = \frac{\tau_{11} + \tau_{22}}{2} \pm \sqrt{\left[\frac{1}{2}(\tau_{11} - \tau_{22})\right]^2 + \tau_{12}^2} \quad (\text{A.19})$$

Each eigenvalue λ corresponds to the principal normal stress in a particular direction. The direction in which each of the principal normal stresses act is described by the corresponding eigenvector. Each eigenvector describes the unit normal vector to the plane in which the normal stress is maximised. In this plane, the shear stress is equal to zero. The plane in which the shear stress is maximised is 45 degrees out of phase with the maximum normal stress plane; the value of the maximum shear stress is

$$\tau_{max} = \frac{1}{2} |\lambda_1 - \lambda_2|, \quad (\text{A.20})$$

where $\lambda_1 > \lambda_2$. For an in-depth discussion and derivation of the properties of these eigenvalues and equation A.20 the reader is referred to texts such as Atanackovic & Guran (2000) and Pozrikidis (2011).

Again due to the motion of the wall, the full three-dimensional stress tensor must be used to determine the maximum shear stress. In this case finding the characteristic equation for the stress matrix is a third-order polynomial

$$|\tau_{ij} - \lambda\delta_{ij}| = -\lambda^3 + I_1\lambda^2 - I_2\lambda + I_3 = 0 \quad (\text{A.21})$$

where I_1 , I_2 and I_3 are the invariants of the deviatoric stress which may be written

$$\begin{aligned} I_1 &= \tau_{11} + \tau_{22} + \tau_{33} \\ &= \tau_{kk}, \\ I_2 &= \begin{vmatrix} \tau_{22} & \tau_{23} \\ \tau_{32} & \tau_{33} \end{vmatrix} + \begin{vmatrix} \tau_{11} & \tau_{13} \\ \tau_{31} & \tau_{33} \end{vmatrix} + \begin{vmatrix} \tau_{11} & \tau_{12} \\ \tau_{21} & \tau_{22} \end{vmatrix} \\ &= \tau_{11}\tau_{22} + \tau_{22}\tau_{33} + \tau_{11}\tau_{33} - \tau_{12}^2 - \tau_{23}^2 - \tau_{31}^2 \\ &= \frac{1}{2}(\tau_{ii}\tau_{jj} - \tau_{ij}\tau_{ji}), \\ I_3 &= \det(\tau_{ij}) \\ &= \tau_{11}\tau_{22}\tau_{33} + 2\tau_{12}\tau_{23}\tau_{31} - \tau_{12}^2\tau_{33} - \tau_{23}^2\tau_{11} - \tau_{31}^2\tau_{22}. \end{aligned} \quad (\text{A.22})$$

The eigenvalues λ are determined using the standard cubic equation (Korn & Korn 2000), and once determined they can be used to determine the maximum shear stress using

$$\tau_{max} = \frac{1}{2}|\lambda_1 - \lambda_3| \quad (\text{A.23})$$

where $\lambda_1 > \lambda_2 > \lambda_3$.

For simple flows such as those depicted in figure A.1, equations A.15 and A.20 are analogous. This is because the nature of the flow makes the wall shear stress in the wall-normal plane naturally correspond to the plane of maximum shear stress. However, with a non-zero wall-normal velocity this is no longer the case; if the maximum shear stress (regardless of the shearing direction) is physiologically important then the wall shear stress should be calculated using the eigenvalue approach described herein. If it is only shear tangent to the wall which is physiologically relevant then the stress projection technique should be employed. Physiological studies of endothelial cell response do not indicate which definition of shear stress is most important to the endothelial cell response. As such, the physiological merit of each shear stress definition cannot be

determined and the resolution of this question is beyond the scope of this work. This thesis merely provides the techniques required in either case.

In this thesis the wall tangent shearing approach (equation A.16) is employed rather than the maximum shearing in any plane (equation A.20). This approach assumes that shear forces at a tangent to the wall surface are the only ones pertinent to the healthy function of the artery wall.